

Camille L. Bertrand
Editor

Electrostatics Theory and Applications

Physics Research and Technology

NOVA

ELECTROSTATICS: THEORY AND APPLICATIONS

No part of this digital document may be reproduced, stored in a retrieval system or transmitted in any form or by any means. The publisher has taken reasonable care in the preparation of this digital document, but makes no expressed or implied warranty of any kind and assumes no responsibility for any errors or omissions. No liability is assumed for incidental or consequential damages in connection with or arising out of information contained herein. This digital document is sold with the clear understanding that the publisher is not engaged in rendering legal, medical or any other professional services.

PHYSICS RESEARCH AND TECHNOLOGY

Additional books in this series can be found on Nova's website
under the Series tab.

Additional E-books in this series can be found on Nova's website
under the E-book tab.

PHYSICS RESEARCH AND TECHNOLOGY

ELECTROSTATICS: THEORY AND APPLICATIONS

**CAMILLE L. BERTRAND
EDITOR**



Nova Science Publishers, Inc.
New York

Copyright © 2011 by Nova Science Publishers, Inc.

All rights reserved. No part of this book may be reproduced, stored in a retrieval system or transmitted in any form or by any means: electronic, electrostatic, magnetic, tape, mechanical photocopying, recording or otherwise without the written permission of the Publisher.

For permission to use material from this book please contact us:

Telephone 631-231-7269; Fax 631-231-8175

Web Site: <http://www.novapublishers.com>

NOTICE TO THE READER

The Publisher has taken reasonable care in the preparation of this book, but makes no expressed or implied warranty of any kind and assumes no responsibility for any errors or omissions. No liability is assumed for incidental or consequential damages in connection with or arising out of information contained in this book. The Publisher shall not be liable for any special, consequential, or exemplary damages resulting, in whole or in part, from the readers' use of, or reliance upon, this material. Any parts of this book based on government reports are so indicated and copyright is claimed for those parts to the extent applicable to compilations of such works.

Independent verification should be sought for any data, advice or recommendations contained in this book. In addition, no responsibility is assumed by the publisher for any injury and/or damage to persons or property arising from any methods, products, instructions, ideas or otherwise contained in this publication.

This publication is designed to provide accurate and authoritative information with regard to the subject matter covered herein. It is sold with the clear understanding that the Publisher is not engaged in rendering legal or any other professional services. If legal or any other expert assistance is required, the services of a competent person should be sought. **FROM A DECLARATION OF PARTICIPANTS JOINTLY ADOPTED BY A COMMITTEE OF THE AMERICAN BAR ASSOCIATION AND A COMMITTEE OF PUBLISHERS.**

Additional color graphics may be available in the e-book version of this book.

LIBRARY OF CONGRESS CATALOGING-IN-PUBLICATION DATA

Electrostatics : theory and applications / [edited by] Camille L. Bertrand.

p. cm.

Includes index.

ISBN 978-1-61728-044-3 (eBook)

1. Electrostatics. I. Bertrand, Camille, L.

QC571.E445 2009

537'.2--dc22

2010012165

Published by Nova Science Publishers, Inc. / New York

CONTENTS

Preface	vii
Chapter 1 Asymmetric Electrostatic Forces and a New Electrostatic Generator <i>Katsuo Sakai</i>	1
Chapter 2 Corona Treatment of Polymer Films <i>T.A. Yovcheva</i>	53
Chapter 3 Numerical Simulation for Electrostatic Field, Flow Field and Particle Behavior in a Wire-Plate Electrostatic Precipitator <i>Hong Lei</i>	83
Chapter 4 ESD Protection Designs With Low-Capacitance Consideration for Radio-Frequency Integrated Circuits <i>Ming-Dou Ker, Chun-Yu Lin and Yuan-Wen Hsiao</i>	125
Chapter 5 Food Industry Electrostatic Powder Coating <i>Nutsuda Sumonsiri and Sheryl A. Barringer</i>	159
Chapter 6 Electrostatic Capacitance Extraction of Arbitrary-shaped Conducting Bodies Using Method of Moments with Rectangular Subdomain Modeling <i>Saswati Ghosh</i>	171
Chapter 7 Electrostatics of Planar System of Conducting Strips <i>Yuriy Tasinkevych</i>	189
Chapter 8 Review of Electroporation <i>Sadhana Talele</i>	223
Chapter 9 Measurements on the Principal Electric Parameters of the Atmosphere <i>Florian Mandija</i>	259

Chapter 10	A Route to Molecular Electrostatics through Atomic Charges Generated by Means of Fast and Robust Empirical Schemes <i>Dmitry A. Shulga, Alexandr A. Oliferenko, Sergey A. Pisarev, Vladimir A. Palyulin and Nikolay S. Zefirov</i>	309
Index		325

PREFACE

Electrostatics is the branch of science that deals with the phenomena arising from stationary or slow-moving electric charges. Electrostatic phenomena arise from the forces that electric charges exert on each other and include many examples, from the apparently spontaneous explosion of grain silos, to the damage of electronic components during manufacturing, to the operation of photocopiers. Among other topics, this book reviews research on asymmetric electrostatic forces and new electrostatic generators; the food industry's electrostatic powder coating, electrostatic capacitance extraction of arbitrary-shaped conducting bodies and the electrostatics of planar systems of conducting strips.

It is well known that there are three kinds of electrostatic force: gradient force, image force, and Coulomb force. A gradient force acts on a non-charged body that is placed in a convergent electric field. An image force acts on a charged body placed near a conductive plate. A Coulomb force acts on a charged body placed in an electric field. As for the shape of these bodies, only symmetric forms have been treated in the past. The representative example for all three force types is a sphere. Forty years ago, only the potential of a spherical body could be calculated. In contrast, today, we can calculate the potential of any shape by computer simulation.

In Chapter 1, a simulation of the electrostatic force that acts on asymmetrically shaped conductors is carried out. As a result, three interesting phenomena were found.

Firstly, it is assumed that the gradient force arises only in a convergence electric field, but the simulation herein demonstrated that the same force acts on an asymmetric conductor in a parallel electric field. I call this force the Asymmetric Force (AF).

Secondly, it is thought that, when any face of a charged conductor is pointed toward a conductive plate, the image force remains the same. However, the simulation showed that the image force exerted on an asymmetric conductor changes when different faces are pointed toward a conductive plate. I call this force the Asymmetric Image Force (AIF).

Thirdly, it is commonly believed that, if the direction of an electric field is reversed, the absolute value of the Coulomb force remains the same. However, the simulation demonstrated that the absolute value of the Coulomb force on an asymmetric conductor changes when the direction of the electric field is reversed. I call this force the Asymmetric Coulomb force (ACF).

In this work, a simulation and an experiment of the AF, a simulation of the AIF, and a simulation and an experiment of the ACF are presented.

New static electricity applications that use these three asymmetric forces are expected to develop. In particular, an electrostatic generator utilizing the ACF is promising. Thus, I present a concrete design and a prospective performance of this electrostatic generator. It is expected that the earth environmental problem and the energy crisis can be simultaneously solved with this new electrostatic generator.

Finally, I will introduce an unusual phenomenon in which the direction of the ACF does not change, even if the electric field surrounding the asymmetric charged conductor is reversed. This unusual phenomenon is made possible by appropriately designing the shape of the conductor; thus, it resembles the phenomenon in which a yacht can advance diagonally in a head wind.

Chapter 2 is a brief review of the investigations devoted to polymer film changes initiated by corona treatment and their possible applications. Polymer films, among which are polypropylene, polyethylene terephthalate and polytetrafluoroethylene, are most widely used as materials for the production of stable charged films. One of the simplest and most widespread methods for charging the polymers involves the use of corona discharge in air at room temperature. The corona discharge creates high energy oxygen-containing charged particles, which are accelerated by the electric field of the corona and then interact with the surface of the polymer films.

Firstly, changes in electret surfaces initiated by corona treatment, which are analyzed by XPS and an optical method, are discussed. The XPS investigations show that oxygen content in negative corona charged samples is several times higher than the ones of positive corona charged samples. The optical method of disappearing diffraction pattern is proposed to determine the surface modifications of the charged polymer films. The strongest surface modification is observed at the center of the samples and they are greatly affected by the applied corona voltage and the corona device configuration. The electric charges are mainly deposited onto the surface and do not penetrate into the sample bulk when corona charged films are formed under not very strong charging conditions (air ambient, room temperature and humidity, 5kV corona voltage).

Secondly, the influence of different treatments (low pressure and low-energy laser irradiation) on charged polymer film stability and its possible applications are discussed. The sharp surface potential decay in charged films stored under pressure lower than atmospheric down to 0.1mbar is observed. It is possible to calculate pressure at which sharp decay occurs if the initial surface potential is known. Preliminarily placing the charged films under pressure less than 1mbar can be used as a method for stabilizing the surface charge. The different surface potential decay and the relevant steady state surface potential values for charged films being under different irradiation conditions (continuous He-Ne, pulsed CuBr and quasi-continuous CO₂ lasers) are revealed. These results can find applications in optical storage and processing of information as a direct registration of information on electret films using low energy lasers.

Thirdly, the influence of corona treatment on holographic recording in photopolymer films is discussed. An additional induced polarizability, which is due to an electric charging, influences the exposure characteristics and diffraction efficiency of the holographic recordings in amorphous side-chain azobenzene polymers. The additional electric corona charging seems to be a promising method for increasing both the diffraction efficiency and the sensitivity of the azo-polymer recording media.

The behavior of charged particles in turbulent gas flow in electrostatic precipitators (ESPs) is crucial information needed to design and optimize electrostatic precipitators, so a three-dimensional numerical simulation was performed to predict electrostatic fields, electro-hydrodynamic (EHD) turbulent flow and particle charging and tracing in a wire-plate ESP. For electrostatic field, the traditional finite difference method (FDM) has been widely applied to calculate two-dimensional electrical field in the wire-plate ESP on the base of the symmetry assumption. In Chapter 3 we analyze the reason why the traditional FDM method by Leutert and McDonald only converges in the first quadrant of single discharge electrode, and we give the numerical method suitable to obtain a convergence solution in the other quadrants. Based on an analogy between the electric equation and the fluid dynamics equation, we propose the upwind (or downwind) scheme to calculate the electrostatic field in the case of positive (or negative) corona. For EHD flow, the classic $k-\varepsilon$ model is applied to describe the EHD turbulent flow in a wire-plate ESP, and a non-dimensional EHD number is introduced to analyze the interactions between the cross-flow and the electric wind. The electric wind has the arrays of large-scale, spanwise counter-rotating vortical structures, and three different types of singularities are located at equally spaced intervals. On average, each wire generates four equal circulatory cells, two upstream and two downstream for the wire. The cross-flow weakens the intensity of EHD flow. With the increase of the inlet velocity, the cross-flow causes the two circulatory cells near the corona wire to merge into one circulatory cell. For particles, a Monte-Carlo simulation is applied to describe *in situ* particle charging and tracing. In the current model we consider the effect of the fluid turbulence on the particle movement; give the particle charging history; and clarify the magnitude of the electric field force, the drag force, the gravitational force, the buoyancy force, the virtual mass force, the Basset history force, the Saffman lift force and the pressure gradient force on particle motion.

As discussed in Chapter 4, radio-frequency (RF) circuits have been widely designed and fabricated in CMOS processes due to the advantages of high integration and low cost for mass production. Electrostatic discharge (ESD), which has become one of the most important reliability issues in IC products, must be taken into consideration during the design phase of all ICs, including the RF front-end circuits. Without ESD protection circuits at all I/O pads, the RF performance of a wireless transceiver can be easily damaged by ESD stresses, because RF front-end circuits are always fabricated in advanced CMOS processes. Usually the I/O pads are connected to the gate terminal of MOS transistor or silicided drain/source terminal, which leads to a very low ESD robustness if no ESD protection design is applied to the I/O pad. Once the RF front-end circuit is damaged by ESD, it can not be recovered and the RF functionality is lost. Therefore, on-chip ESD protection circuits must be provided for all I/O pads in RF ICs.

Chapter 5 discusses powder coating, which is an important process in the food industry, especially for snack foods. Powder coating creates variety in food, producing different flavors and appearance. Electrostatic coating has been adopted in order to provide better efficiency and lower the dust produced during coating. Electrostatic coating is usually done with a corona system to charge the powder. There are two systems used to coat the food: a tumble drum coating system and a conveyor belt coating system. The tumble drum coating system is used to coat all sides of the food product. The conveyor belt coating system only coats one side of the product but most consumers do not notice this. The efficiency of electrostatic coating is affected by characteristics of the powder, including particle size, density, resistivity, and flowability. Surface characteristics of the food to be coated are also important.

These factors affect the transfer efficiency, adhesion, dust, evenness, and functionality of the powder on the targets. An understanding of these factors can be used to predict the coating performance in food production and help the processor choose the best system for coating food products.

Chapter 6 presents the evaluation of capacitance of arbitrary-shaped conducting bodies using Method of Moments. The conducting surfaces are modeled by planar rectangular subdomains in which the charge density is assumed to be constant over each subsection. The exact formulation for the matrix element is evaluated for rectangular subsection. The capacitances of different conducting structures, e.g. square, circular, triangular, wedge-shaped plate and also multiconducting bodies e.g. transmission lines with square, circular cross section are evaluated here. In the next part of the chapter, work is extended for the evaluation of static charge distribution and capacitance of conducting bodies from the measured electric field components due the same. The computed results show good agreement with other available results in literature.

The spatial distributions of electric field and charge are the most frequent subjects of classical electrostatic problems. In Chapter 7, the spatial spectrum of the charge distribution on planar systems of strips is studied. Due to the charge singularities at the strip edges and strong dependence of the spectrum on the distribution details over the entire system, the direct application of the Fourier transformation to the charge spatial distribution yields results with unsatisfactory accuracy. Here a method of direct evaluation of the charge spatial spectrum is proposed and discussed; the spatial distribution is obtained from it by the inverse Fourier transformation for certain auxiliary purposes and final verification of numerical results. The solution is constructed as a linear combination of the template functions, evaluated in spectral domain, satisfying the electric boundary conditions on the strips, and having known spatial spectrum. The same functions are applied in the solution of the complementary problem of strips in external electric field. The flexibility of the method is illustrated in two examples. Namely, the quasi-periodic system of strips with periodicity broken by inclusion of one narrower strip is considered first. Also, the problem of acoustic beam forming analysis is treated by the presented method.

Electroporation also called *Electroporabilization*, is the use of high magnitude electric field pulses to alter the permeability of a cell membrane. This change in permeability is achieved by using an electric field pulse to induce nanoscopic ‘pores’ in the cell membrane. These pores are commonly called ‘electropores,’ which is why the process is commonly referred to as *electroporation*. Many biotechnological applications and research require transport of macromolecules such as genes, antibodies, and chemical drugs, into a host cell. For any particular application, choosing a given transfer process is based on its efficacy, ease of use and side effects. A characteristic shared by most of the chemical and biological techniques is that they are usually cell-type dependent and have relatively poor efficiencies.

Therefore, methods which are both versatile and efficient are being searched for and investigated. Electroporation, first reported in 1982 (Neumann *et al.*, 1982), is one of the methods reported to be effective for such delivery. Since its inception, this method has been a valuable tool for *in vitro* delivery of small and large molecules into a large variety of cells. During this time, electroporation has been performed on living plants, animals, and humans (*in vivo* electroporation), with an increasing focus on therapeutic uses (Dev *et al.*, 2000; Smith and Nordstrom, 2000; Muramatsu *et al.*, 1998).

Chapter 8 covers important aspects of electroporation including induced transmembrane potential, formation of pores, relation between pore radii and pore energy, pore density and current through electropores. This knowledge is useful for simulating electroporation results which can be helpful for making informed decisions about electroporation system parameters.

In the latest research developments, a great interest in the scientific community is dedicated also on study of the atmospheric state in the lower part of the troposphere. This part of the atmosphere is our living environment, and so it is the source of our breathing air. The atmospheric studies are a multidisciplinary science. It concerns on the measurement of both, the physical and chemical atmospheric parameters. In Chapter 9, the author is concentrated on the continuous monitoring of the physical atmospheric parameters, especially electrical parameters of lower part of the troposphere. The principal electrical parameters of the atmosphere are atmospheric ion concentration, density current, atmospheric electric fields, aerosol concentration, etc.

Atmospheric ion and aerosol concentration are the principal electrical parameters monitored in my measurement campaigns. Atmospheric ions belong on the small air ion group. In the case of aerosol monitoring, there are done two types of measurements; aerosol number concentration, for the aerosol particles in the size interval (0.3-100 μm), and aerosol mass concentration, for three aerosol groups PM1, PM2.5 and PM10.

The electrical state of the atmosphere is strongly connected with the area category. So, all the monitoring process is carried out in four main areas; urban, rural, seashore and mountain.

Based on the measurement results, the author studied the daily and annual variation of the atmospheric ion and aerosol particle concentration.

During the measurements are recorded also the principal meteorological parameters. These parameters are air temperature, atmospheric pressure, relative humidity and wind speed. There are carried out the correlations among atmospheric and aerosol concentration and the above mentioned meteorological parameters.

Analyzing the variation of the concentrations, the author determined the recombination and the attachment coefficients, so giving a clear picture of the electrostatic interaction among atmospheric ions and aerosol particles in certain areas.

The concentrations of both atmospheric ions and aerosol particles are also altitude dependent, in the exponentially decay form. The measurements on the different altitudes enable to determine the scale height of their concentrations and the analytical functions.

It is important to mention that the author's research activities on the atmospheric electricity are developed mainly in the fair weather conditions of the atmosphere.

Chapter 1

ASYMMETRIC ELECTROSTATIC FORCES AND A NEW ELECTROSTATIC GENERATOR

Katsuo Sakai*

Electrostatic Generator Research Center.
Moegino 25-64, Aoba-ku, Yokohama Japan

Abstract

It is well known that there are three kinds of electrostatic force: gradient force, image force, and Coulomb force. A gradient force acts on a non-charged body that is placed in a convergent electric field. An image force acts on a charged body placed near a conductive plate. A Coulomb force acts on a charged body placed in an electric field. As for the shape of these bodies, only symmetric forms have been treated in the past. The representative example for all three force types is a sphere. Forty years ago, only the potential of a spherical body could be calculated. In contrast, today, we can calculate the potential of any shape by computer simulation.

In this work, a simulation of the electrostatic force that acts on asymmetrically shaped conductors is carried out. As a result, three interesting phenomena were found.

Firstly, it is assumed that the gradient force arises only in a convergence electric field, but the simulation herein demonstrated that the same force acts on an asymmetric conductor in a parallel electric field. I call this force the Asymmetric Force (AF).

Secondly, it is thought that, when any face of a charged conductor is pointed toward a conductive plate, the image force remains the same. However, the simulation showed that the image force exerted on an asymmetric conductor changes when different faces are pointed toward a conductive plate. I call this force the Asymmetric Image Force (AIF).

Thirdly, it is commonly believed that, if the direction of an electric field is reversed, the absolute value of the Coulomb force remains the same. However, the simulation demonstrated that the absolute value of the Coulomb force on an asymmetric conductor changes when the direction of the electric field is reversed. I call this force the Asymmetric Coulomb force (ACF).

In this work, a simulation and an experiment of the AF, a simulation of the AIF, and a simulation and an experiment of the ACF are presented.

New static electricity applications that use these three asymmetric forces are expected to develop. In particular, an electrostatic generator utilizing the ACF is promising. Thus, I

* E-mail address: gy7a-ski@asahi-net.or.jp

present a concrete design and a prospective performance of this electrostatic generator. It is expected that the earth environmental problem and the energy crisis can be simultaneously solved with this new electrostatic generator.

Finally, I will introduce an unusual phenomenon in which the direction of the ACF does not change, even if the electric field surrounding the asymmetric charged conductor is reversed. This unusual phenomenon is made possible by appropriately designing the shape of the conductor; thus, it resembles the phenomenon in which a yacht can advance diagonally in a head wind.

1. Asymmetric Force (AF)

1.1. Purpose

In a convergent electric field, all bodies are forced to move in the convergent direction by an electrostatic force. This is the gradient force. The other two electrostatic forces (the image force and the Coulomb force) act only on charged bodies, but the gradient force can also act on neutral objects. This is a very useful characteristic. However, a gradient field is not particularly useful. If a non-charged material could be forced to move in a parallel electric field by electrostatic force, this would be a very useful phenomenon.

Thus, the following hypothesis is proposed.

Hypothesis: When a convergent field is changed to a parallel field, if the shape of a non-charged conductor is changed precisely in proportion to the change of the field, the same electrostatic force will act on the altered non-charged conductor.

The above phenomena are proposed to be mathematically equivalent. As a note, in this paper, only the electrostatic force that acts on a conductive body was simulated for simplification.

Therefore, it is a main purpose of this chapter to prove this hypothesis. In addition, finding the optimal shape for this force and confirming this force experimentally are the second and third purposes of this chapter.

1.2. Simulation Methods and Results

If these two forces that act on the original conductor in a convergent field and the altered conductor in parallel field could be calculated analytically, this task would be easy. However, there is no formula that can be used to calculate these forces for all shapes. There exists only an approximate formula for small spheres in a convergent field [1]. This situation is shown schematically in Figure 1. The following is the approximate formula for a small conductive sphere.

$$F_g = 2\pi r^3 \varepsilon_0 \nabla E_0^2 \quad (1)$$

where r: Radius of the sphere.

E_0 : Intensity of the convergent field around the sphere

ε_0 : Vacuum permittivity

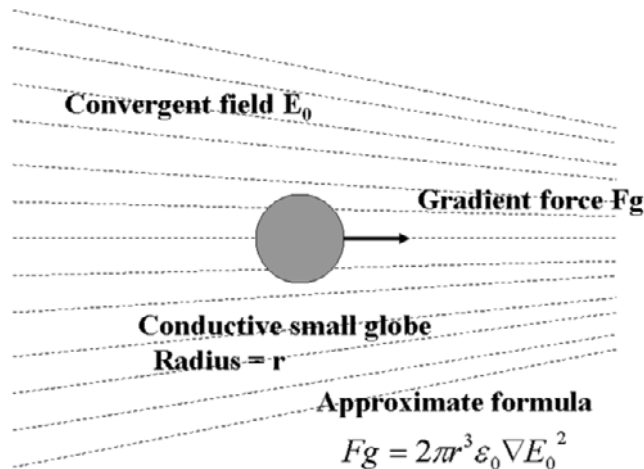


Figure 1. Schematic view of the gradient force and an approximate formula for a sphere.

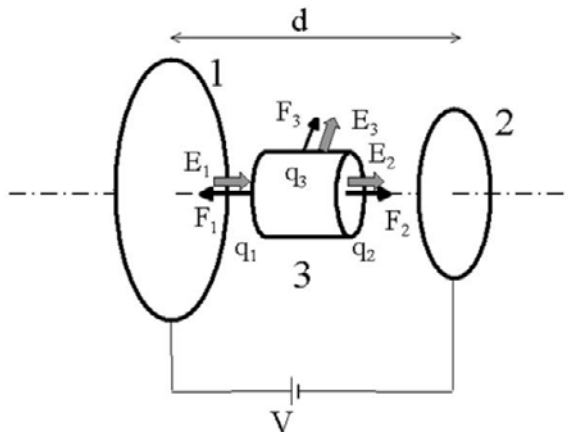


Figure 2. Schematic layout for simulating the electrostatic force acting on a cylinder in a convergent field.

Therefore, I used a simulation method to calculate these forces. It would be ideal to simulate these forces in three dimensions. However, the simulation program, which was written by the author, is only a bi-dimensional program, employing an axi-symmetric finite difference method. Fortunately, this simulation program can treat an axi-symmetric body. Hence, a cylinder-shaped conductor was selected in place of the conductive small sphere; this cylinder-shaped conductor is hereafter referred to as a cylinder.

Figure 2 shows a cylinder placed in the convergent field. This field is formed by two disc electrodes that have different diameters.

Figure 2 shows a schematic layout for the simulation. A large circle electrode (1), a small circle electrode (2), and a cylinder (3) were aligned along the z axis (the dotted line in Figure 2). The radii of the large electrode, the small electrode, and the cylinder were 250 μm , 100 μm , and 100 μm , respectively. The distance between the large and small electrodes was 600 μm , and the width of the cylinder was 300 μm . A positive voltage of 600 V was applied to the

large circle electrode in order to generate a convergent electric field between it and the grounded small circle electrode. The cylinder was electrically floated.

E_1 , E_2 , and E_3 are the electric field intensities on the left surface, the right surface, and the circumference surface of the cylinder, respectively, while q_1 , q_2 , and q_3 are the charge quantities of the left surface, the right surface, and the circumference surface of the cylinder, respectively. F_1 , F_2 , and F_3 are the electrostatic forces acting on the left surface, the right surface, and the circumference surface of the cylinder, respectively.

The total electrostatic force F_e that acts on the conductor was calculated using the following formula, (2)

$$F_e = F_1 + F_2 \quad (2)$$

F_3 , which acts on the circumference surface of the cylinder, was not included in formula (2) because it cancels out at an interval of 180 degrees and ultimately becomes zero.

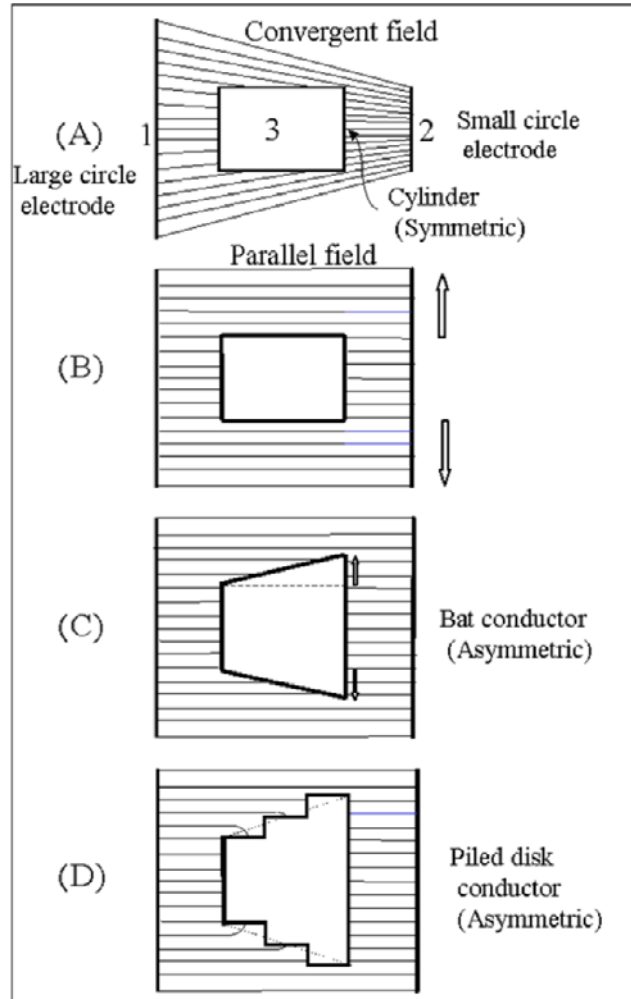


Figure 3. Schematic diagram of electric field patterns and conductor shapes. (A) A convergent field and a cylinder. (B) A parallel field and a cylinder. (C) A parallel field and a baseball-bat-shaped conductor. (D) A parallel field and a piled disk conductor.

The details of this simulation are explained in Appendix 1.

The gradient force that acts on a non-charged cylinder in a convergent field (see Figure 3(A)) was simulated using an axi-symmetric finite difference method.

Then, the electrostatic force that acts on a cylinder in a parallel field (see Figure 3 (B)) and the force that acts on a piled disk conductor in a parallel field (see Figure 3 (D)) were simulated.

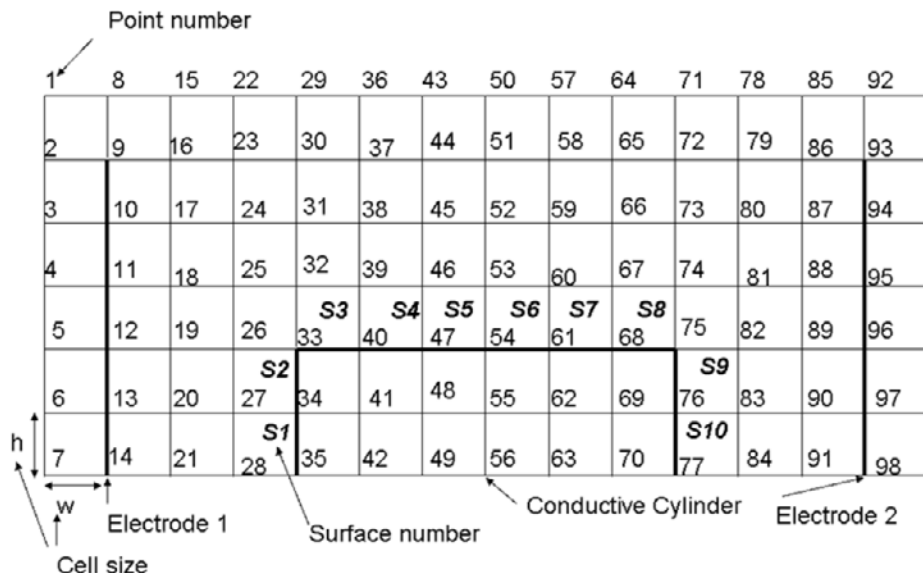


Figure 4. A design of cells (mesh) for simulating the electrostatic force that acts on a non-charged cylinder in a parallel electric field.

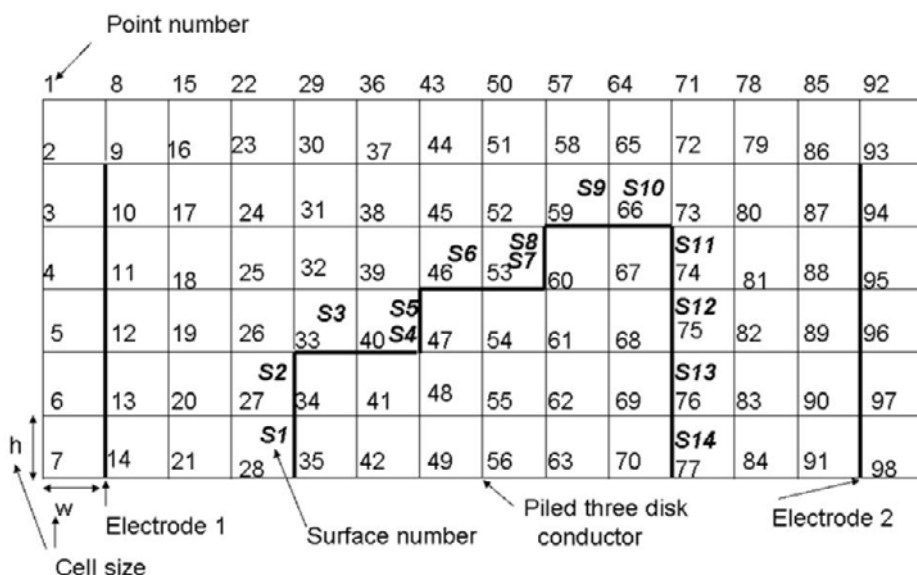


Figure 5. A design of cells (mesh) for simulating the electrostatic force that acts on a non-charged piled three-disk conductor in a parallel electric field.

To prove the hypothesis of this paper, first, the radius of the small circle electrode was increased from 100 μm to 250 μm (see Figure 3 (B)). As a result, the electric field between the electrodes changed from asymmetric (convergent) to symmetric (parallel). Next, the radius of the right surface of the cylinder was increased from 100 μm to 200 μm , and the shape of the conductor changed from a symmetric cylinder to an asymmetric bat (see Figure 3 (C)). In this step, the shape of the cylinder must be changed precisely in proportion to the change of the field. However, only 150 μm or 200 μm can be selected in this simulation program; therefore, 200 μm was selected as an approximate value.

As mentioned above, the simulation program, which was written by the author, cannot deal with this bat shape (three dimensions). Hence, the bat shape conductor was replaced with a piled three-disk conductor (see Figure 3 (D)). The radii of the three disks were 100 μm , 150 μm , and 200 μm , and the width of the disks was 100 μm .

Figure 4 shows the design of the cells (mesh) used for simulation (B), and Figure 5 shows the design of the cells (mesh) used for simulation (D). The design of the cells (mesh) used for simulation (A) and an explanation of the cells are given in Appendix 1 (See Figure 49).

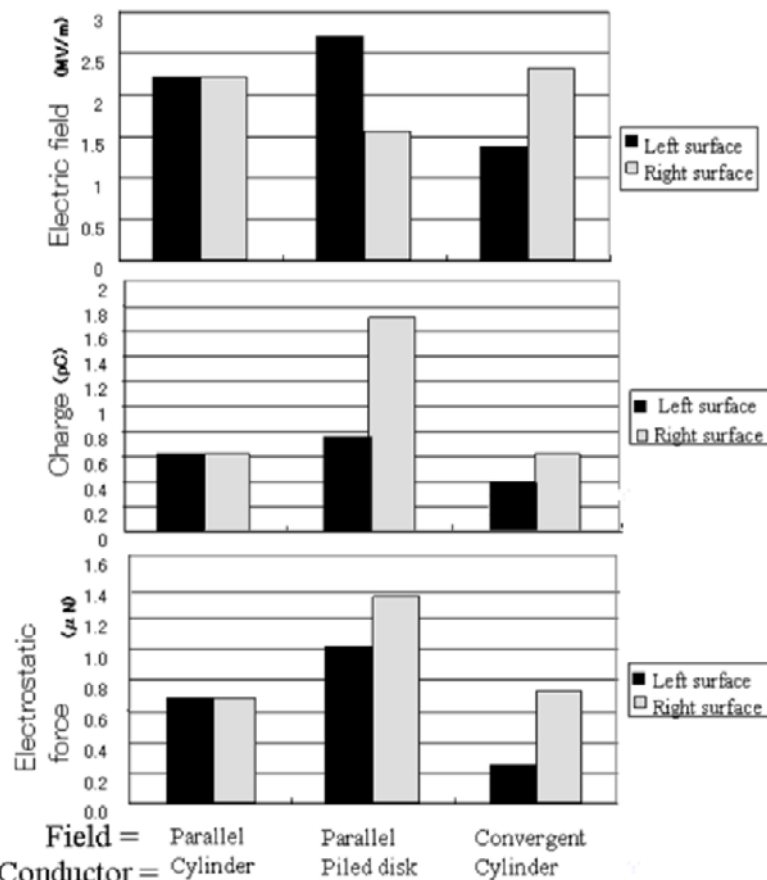


Figure 6. Field intensity, charge quantity, and electrostatic force as a function of field pattern and conductor shape. These variables were simulated for a cylinder or a piled disk conductor in a parallel field or a convergent field.

Figure 6 shows the simulation results: the field intensity, charge quantity, and electrostatic force of both side surfaces of the cylinder and the piled three-disk conductor under a convergent or parallel field (see Figure 3 (A), (B), and (D)).

For the cylinder placed in the parallel field (see Figure 3 (B)), the field intensity on both surfaces is the same, and consequently, the electrostatic force acting on both surfaces is also the same. For the cylinder placed in the convergent field (see Figure 3 (A)), the field intensity on the right surface is stronger than that on the left surface; as a result, the electrostatic force of the right surface is stronger than that of the left. For the piled disk conductor placed in the parallel field (see Figure 3 (D)), the field intensity on the right surface is weaker than that on the left; nevertheless, the electrostatic force of the right surface is stronger than that of the left because the surface area of the right surface is four times greater than that of the left.

The electrostatic force of the right surface is stronger than that of the left for the conditions in both Figure 3 (A) and (D), and the differences between the right and left electrostatic forces for both conditions are similar. I propose that this simulation result almost proves the above-mentioned hypothesis.

If the shape of the cylinder had been changed precisely in proportion to the change of the field in Figure 3 (C), and if the electrostatic force acting on this changed cylinder could be simulated, then it would completely agree with the simulated force for Figure 3 (A).

This force (see Figure 3 (A)) is called the gradient force, because the field has a gradient (convergence). Meanwhile, the other force (see Figure 3 (D)) acts on an asymmetric conductor, therefore I named this force the Asymmetric Force (AF).

When a non-charged, small conductive sphere is placed in a gradient (convergent) electric field, the gradient force acts on it. This gradient force can be calculated by formula (1). On the other hand, when a non-charged cylinder is placed in a parallel electric field, the AF acts on it. The formula and the simulation of the AF are completely different in appearance, but I suggest that the two are mathematically equivalent. I will prove this in Appendix 2.

1.3. Cause of the AF

In the previous chapter, the AF acting on a piled three-disk conductor in a parallel field (see Figure 3 (D)) was simulated. This three-disk conductor has three left surfaces (shown in Figure 3 (D)), where the total area of the three left surfaces is the same as that of the right surface. Nevertheless, the electrostatic force on the right surface is stronger than the total electrostatic force on the combined left surfaces. If a symmetric conductor that has the same area on the left and right surfaces is placed in a parallel field, the electrostatic forces that act on the two surfaces must be the same.

Figure 7 shows the simulation results of the field intensity, charge quantity, and electrostatic force of the first, second, and third left surfaces of the piled conductor.

It can clearly be seen in Figure 7 that the field intensity on the first left surface is much larger than that on the second and third left surfaces; hence, the electrostatic forces that act on the second and third left surfaces are negligible in comparison to that acting on the first left surface. This is because the direction of lines of electric force that runs straight from the left electrode toward the second and third left surface is strongly bent towards the conductor,

finally aiming perpendicularly to the circumference surfaces of the first and second disks, as shown in Figure 8.

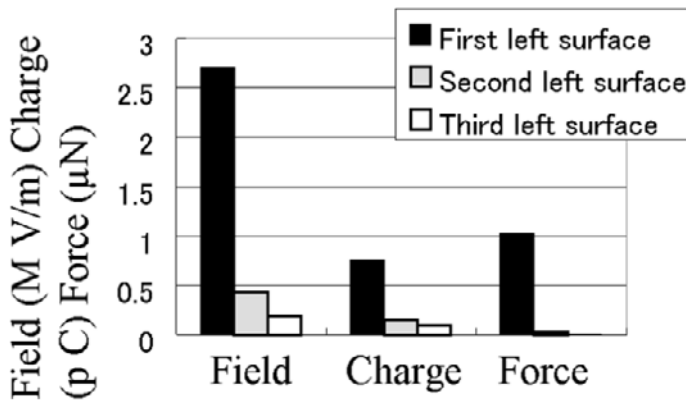


Figure 7. Field intensity, charge quantity, and electrostatic force as a function of the specific surface of the piled three-disk conductor. These are simulated for a piled conductor in a parallel field (see Figure 3 (D)).

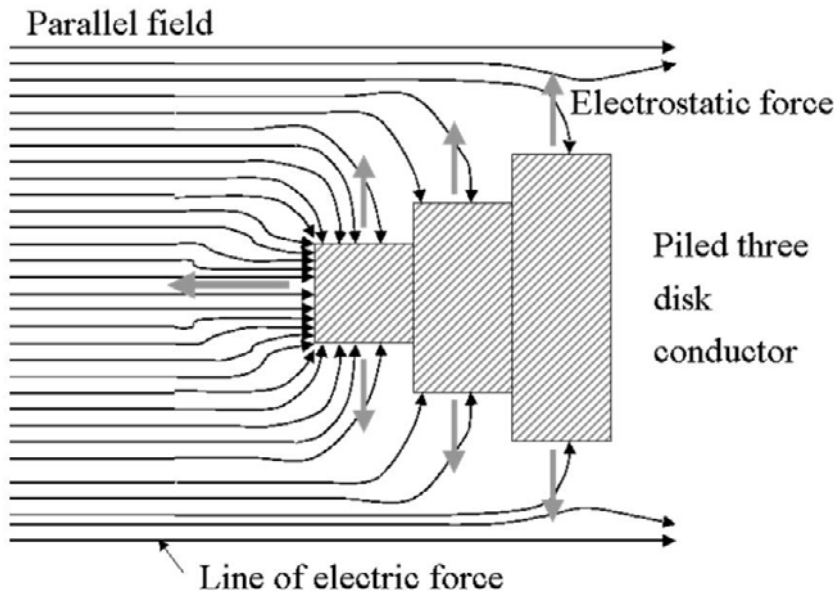


Figure 8. Schematic diagram of the electric force that is concentrated on the asymmetric piled disk conductor in a parallel field.

As a result, the electrostatic force acts on the circumference surfaces perpendicularly. These forces cancel each other at an interval of 180 degrees and ultimately become zero.

This means that the second left surface is electrically shielded by the circumference surface of the first left disk, and the third left surface is electrically shielded by the circumference surface of the second left disk.

On the contrary, the right surface is not shielded. Therefore, many lines of electric force point from the surface to the right electrode. The number of those lines of electric force is the

same as the number of lines of electric force that point toward the first left surface and the circumference surfaces of the three disks.

As a result, the electrostatic force acting toward the right becomes larger than the electrostatic force acting toward the left.

Therefore, when an asymmetric conductor consists of surfaces that are perpendicular to the electric field and surfaces that are parallel to the electric field, electrical shielding of a large part of one side (left or right) of the perpendicular surfaces by parallel surfaces causes the AF to arise.

1.4. Simulation of the Best Shape for the AF

It has been shown that the AF arises when the second and third left vertical surfaces are selectively electrically shielded by parallel surfaces. Accordingly, it would be expected that the AF becomes strongest when the area of the first left vertical surface is minimized with respect to the area of the right vertical surface. Therefore, a suitable shape for this requirement must be a bolt or a cup, as shown in Figure 9.

To investigate the effect of the ratio of the first left surface area to the right surface area on the AF and to determine the optimum shape of the conductor, numerical simulations were carried out for the following different surface area ratios for the bolt and cup conductors: 5, 10, 20, 30, 40, 50, 70, and 90%.

The simulation results are shown in Figure 10.

Figure 10 shows that the AF of the cup conductor is larger than the AF of the bolt conductor. In particular, when the ratio of the first left surface to the right surface is less than 15%, the AF becomes three times larger than that of the bolt. Therefore, the cup shape is better than the bolt shape; specifically, a thin-walled cup should generate the largest AF.

These results can be explained by the same theory that is given above. The second left surface of the cup (the inner bottom) is perfectly electrically shielded by the surrounding thin wall. In contrast, the second left surface of the bolt cannot be perfectly electrically shielded by the narrow center stick.

Further details of these simulations have been reported in reference [2].

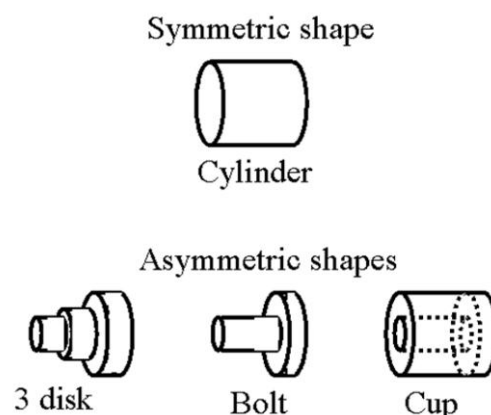


Figure 9. Shapes of conductors used to simulate the AF.

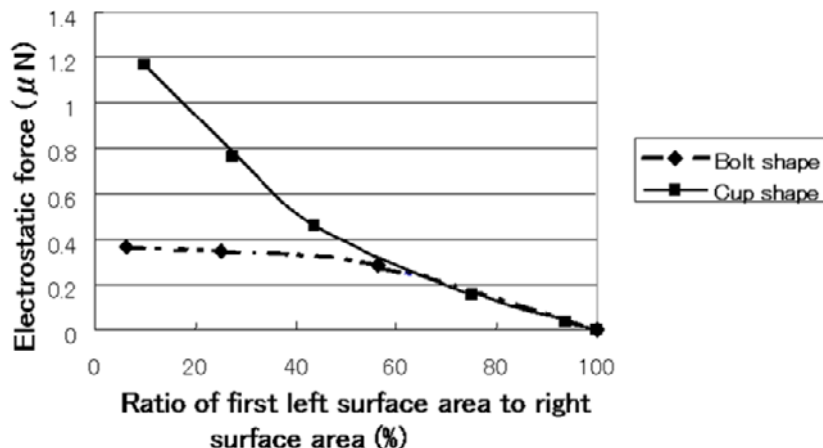


Figure 10. The AF as a function of the ratio of the first left surface area to the right surface area for asymmetric conductors in a parallel field.

1.5. A Simple Experiment Confirming the Existence of the AF

The simulation of the AF was done with the simple structure shown in Figure 2. However, it was difficult to execute a confirmation experiment using this structure. The dimensions of this structure are difficult to achieve experimentally, and the cup shape is very difficult to produce. Therefore, the distance between the electrodes was increased from 0.6 mm to 98 mm. Furthermore, the shape of the conductor was changed from a cup to a box. Figure 11 shows a schematic layout of the experimental setup that was used to confirm the AF.

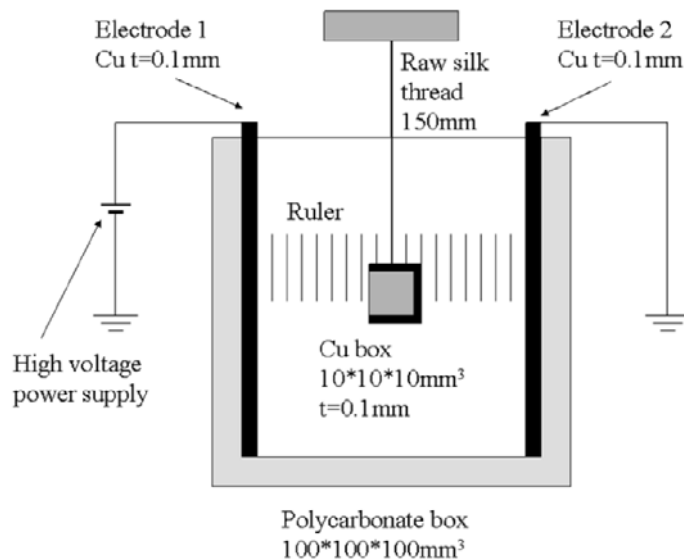


Figure 11. Schematic layout of the experimental setup used to confirm the AF.

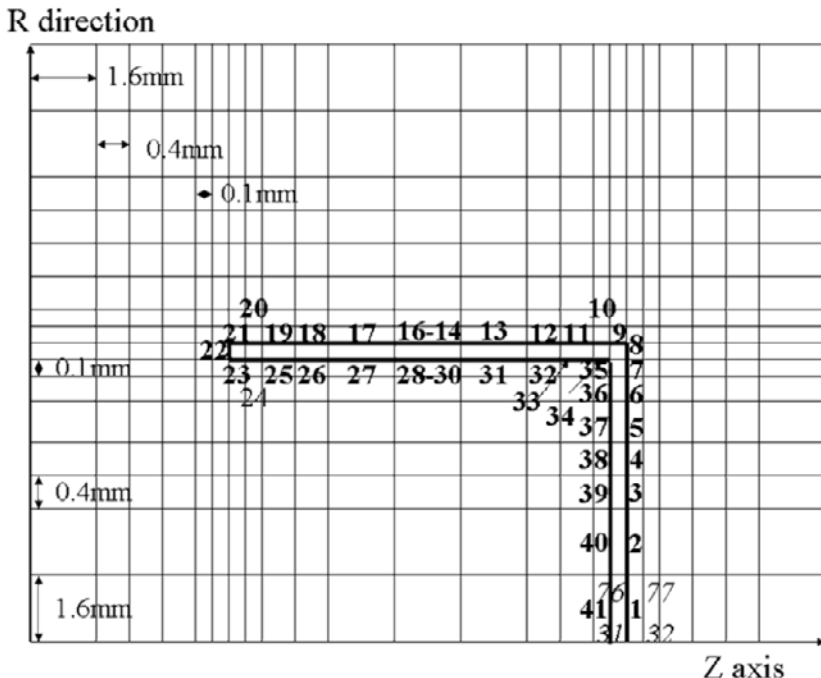


Figure 12. A design of cells (mesh) to simulate the electrostatic force that acts on a charged cup in a parallel electric field.

Before discussing the results of the experiment, I will present a simulation result of the electrostatic force that acts on a box conductor in this situation. This is done because the dimensions of the situation were largely changed. Figure 12 shows the main part of the cell structure used in this simulation. I used a cup in this simulation because my simulation program cannot treat a box, as previously mentioned.

Figure 12 is slightly more complicated in comparison to Figure 49. However, both figures are basically the same. Therefore, an explanation is omitted (an explanation of the cell design is shown in Appendix 1 along with Figure 49).

After running the simulation, the electrostatic force that was found to act on the cup was converted into the electrostatic force that would act on the box, according to the area ratio of the bottom face.

Figure 13 shows the converted electrostatic force as a function of the field intensity between the electrodes. It is apparent that the total electrostatic force increases with the square of the electric field intensity.

Now, I return to Figure 11 for an explanation of the experimental setup and procedure. Initially, a large, transparent, polycarbonate box was prepared. Thin copper plates with dimensions of $100 \times 100 \text{ mm}^2$ and thickness of 0.1 mm were attached to the left and right walls of a large box as left and right electrodes. The left electrode was connected to a high voltage power supply, and the right electrode was grounded.

A small left open box conductor ($10 \times 10 \times 10 \text{ mm}^3$) that was made from a thin copper plate with a thickness of 0.1 mm was floated by an insulating raw silk thread with a length of 150 mm connected to the center of both electrodes. A ruler was attached to the back wall of the

large box to measure the position of the box. A Matsusada Precision Model HAR-50PS was used as a high voltage power supply.

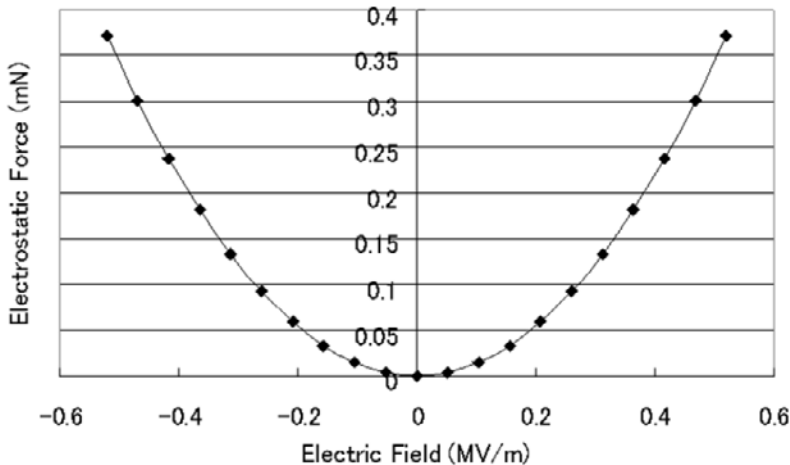


Figure 13. Simulation results of the total electrostatic force acting on a non-charged box in a parallel electric field as a function of the field intensity.

The experiment was performed as follows.

- ① The left and right electrodes were grounded, and the box was put into contact with one of the grounded electrodes for discharging.
- ② The box was centered between the grounded electrodes, and the position of the box was measured using the ruler.
- ③ A high voltage was applied to the left electrode; as a result, the box conductor was shifted by a short distance to the right. This altered position of the box was measured using the ruler. The difference between the position measured in step ② and the position measured in step ③ is the shifted distance of the box.
- ④ Steps ①→③ were repeated three times at different voltages (10 kV, 15 kV, 20 kV, 25 kV, 30 kV).
- ⑤ Finally, the high voltage power supply and the ground line were switched, and the same experiment was repeated.

Figure 14 shows the measured average shifted distance of the non-charged box as a function of the applied voltage.

In Figure 14, it is apparent that the measured shifted distance of the non-charged box increases almost with the square of the applied voltage. This is the same pattern that was observed for the simulation results shown in Figure 13.

The shifted distance D of the non-charged box floating in a strong electric field was measured as described above. This shifted distance D is related to the length L and the height Y of the thread as shown in Figure 15.

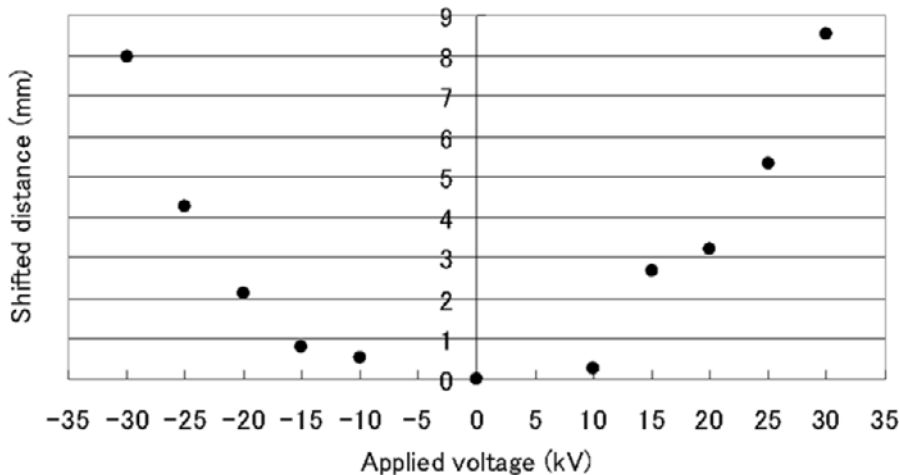


Figure 14. The measured average shifted distance of a non-charged box in a parallel field as a function of the applied voltage.

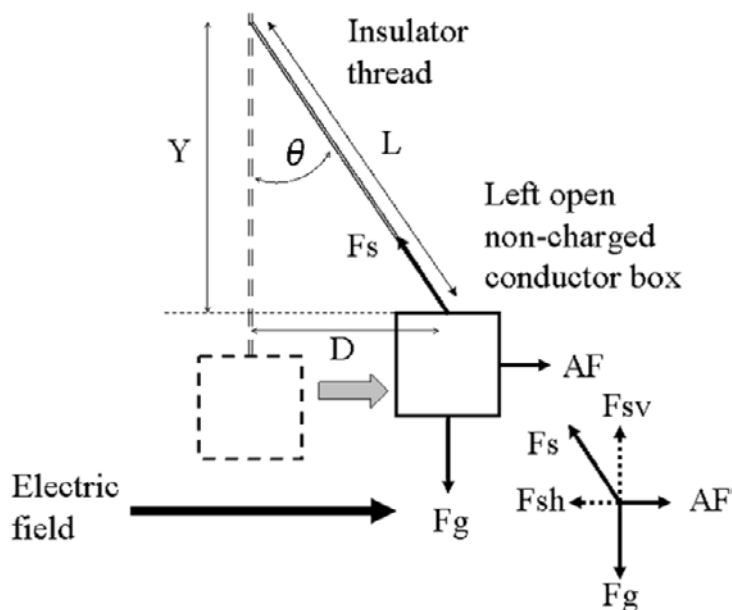


Figure 15. Schematic diagram of the electrostatic force (AF), the gravity force, and the tensile force that act on a non-charged box in a strong parallel field.

The ratio $L:D:Y$ is the same as the ratio of the tensile strength of the thread F_s :the electrostatic force AF :the gravity force F_g . The horizontal component of the tensile force F_{sh} is equal to the AF , and the vertical component of the tensile force F_{sv} is equal to the gravity force F_g . Therefore, the AF was calculated from the shifted distance D , the thread length L , and the gravity force F_g , using the following formula (3):

$$AF = Fg \times \tan \theta = Fg \times \frac{D}{Y} = Fg \times \frac{D}{\sqrt{L^2 - D^2}} \quad (3)$$

where $L=150$ mm, and $Fg=4.39$ mN, which was calculated from the area of the box, 5 cm^2 , the thickness of the Cu plate, 0.1 mm, and the specific gravity of Cu, 8.96.

Figure 16 shows the AF calculated from the measured shifted distance of the box with the simulated AF as a function of the electric field intensity.

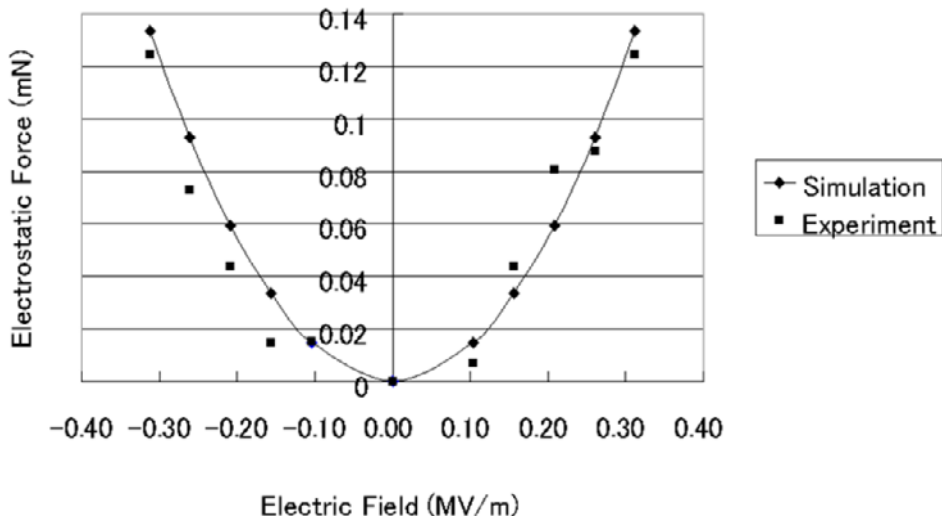


Figure 16. Simulated and experimentally measured AF acting on a non-charged box as a function of the electric field intensity.

As a result, the measured AF shows good agreement with the simulated AF. This result confirms the AF that acts on a non-charged asymmetric conductor in a parallel electric field actually exists.

Further details of this simulation and the experiment have been reported in reference [3].

1.6. Applications

Electrostatic transportation of non-charged asymmetric conductors can be realized by using the AF. Traditional electrostatic transportation methods usually require a charged transfer body and a change in potential at the transfer electrodes. In contrast, this new electrostatic transportation method requires neither of these. It needs only an electrostatic field in place of an alternating electric field. The electrostatic field can be easily generated by electrets in place of electrodes. As a result, the structure of this new electrostatic transportation machine becomes very simple.

Electrostatic acceleration of non-charged asymmetric conductors can be realized by using the AF as well. Traditional electrostatic accelerators usually require a charged target body and an increased potential of the accelerative electrodes that is generated by high voltage power supplies. In contrast, this new electrostatic accelerator does not require either of these; it

needs only a constant electrostatic field in place of an increasing electrostatic field. The constant electrostatic field can be easily generated by electrets. As a result, the structure of this new electrostatic accelerator machine becomes very simple.

A new type of electrostatic motor can also be realized by using the AF. The traditional electric motor consists of moving electrodes and fixed electrodes. The moving electrodes are given charges, and the fixed electrodes are applied to an alternating voltage. In contrast, this new electrostatic motor requires neither; the moving electrodes are not given charges, and the fixed electrodes are applied to a constant voltage. The constant voltage can be easily generated by electrets. As a result, the structure of the new electrostatic motor becomes very simple.

1.7. Conclusion

- 1) The following hypothesis has been almost proven by simulation.

Hypothesis: When a convergent field is changed to a parallel field, if the shape of the non-charged conductor is changed precisely in proportion to the change of the field, the same electrostatic force will act on the changed conductor.

Thus, this force is termed the AF

2) It is thought that the AF is caused by surfaces that are perpendicular to the electric field that are also electrically shielded along with surfaces that are parallel to the electric field.

3) The AF is the strongest when the conductor is cup-shaped.

4) The existence of the AF has been confirmed by a simple experiment.

5) Electrostatic transporters, electrostatic accelerators, and electrostatic motors can be greatly improved by using the AF.

2. The Asymmetric Image Force (AIF)

2.1. Purpose

When a charged body is placed near an electrode, an electrostatic force acts on this body. This force is known as the image force. If the body is a spherical conductor, the force is calculated by the following formula (4) [4].

$$f = \frac{q^2}{4\pi\epsilon_0(2r)^2} \quad (4)$$

where q: Quantity of charge on the sphere.

r: Distance between the sphere's center and the grounded electrode.

ϵ_0 : Vacuum permittivity

This force does not change even if the sphere is turned in either direction because the shape is symmetric. In contrast, if an asymmetric charged conductor is turned to the right or left, this force may change.

Therefore, confirming this expectation is the purpose of this chapter.

2.2. Simulation Result

Figure 17 shows the cell layout (mesh) of the simulation of the image force that acts on a charged cup.

In this step, the electrostatic force that acts on a charged cup near a grounded electrode was simulated. The height, radius, and thickness of the cup are 10 mm, 5 mm, and 1 mm, respectively.

The quantity of charge on this cup is +2.0 nC. The distance between the grounded electrode and the cup varied from 1.0 mm to 9.0 mm. In the first simulation, the mouth of the cup was pointed toward the grounded electrode. In the second simulation, the bottom of the cup was pointed toward the grounded electrode, as shown in Figure 17.

The conventional image force that acts on a spherical conductor near a grounded electrode was calculated according to formula (4). The radius of the sphere is 5 mm, and the quantity of charge on the sphere is +2.0 nC.

Figure 18 shows the simulated image forces and the calculated image force.

From Figure 18, it is apparent that when the bottom of the cup is pointed toward the grounded electrode, the simulated image force is large, and when the mouth of the cup is pointed toward the grounded electrode, the simulated image force is small.

I called this changeable image force the Asymmetric Image Force (AIF).

(Caution: when the distance is 1 mm, the calculated image force becomes smaller than the simulated force. This is not a real phenomenon. It is well known in toner development research that the real image force is about two times bigger than the image force calculated by formula (4) when a toner is placed on an electrode [5].)

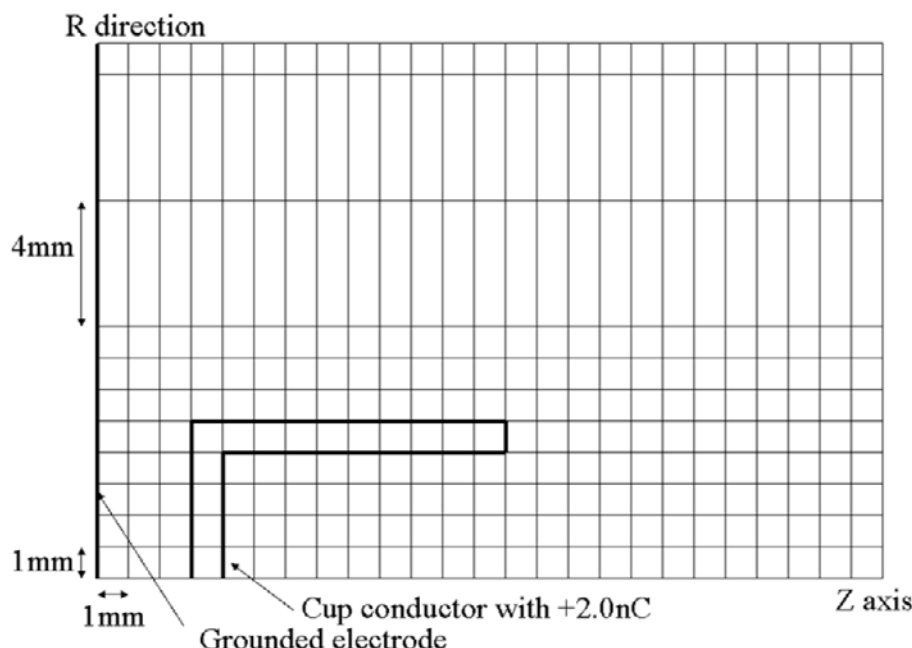


Figure 17. A design of cells (mesh) for simulating the image force that acts on a charged cup near a grounded electrode.

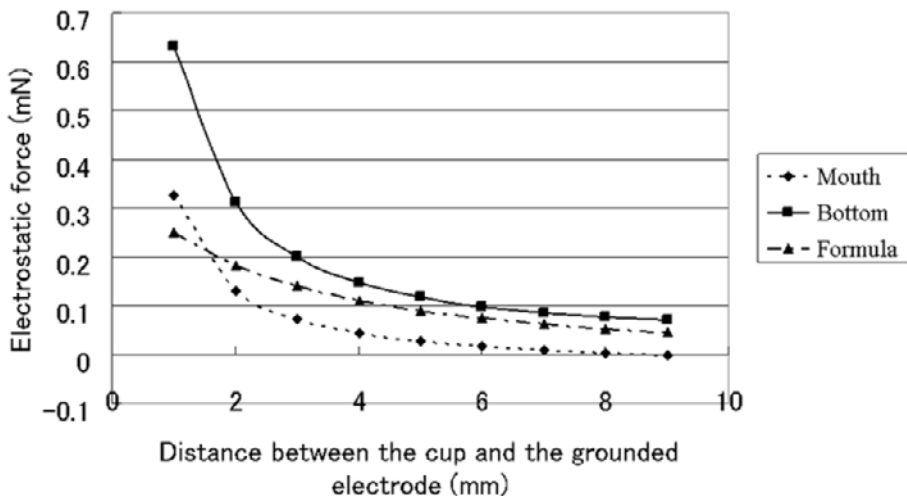


Figure 18. Simulation results for the image force acting on a charged cup and the calculated image force acting on a charged sphere near a grounded electrode.

2.3. Experimental Results

I attempted to confirm these simulation results using an experimental setup that is explained in the next chapter. However, the experiment failed because the force of gravity on the charged box in air did not balance the electric force near the electrode. The charged box always came into contact with the electrode when it was made to approach the electrode.

Thus, another instrument is needed to measure the AIF.

2.4. Cause of the AIF

It is proposed that this force is caused by the charge distribution rather than electric shielding, because there are charges on the cup, but there is not an electric field surrounding the cup.

Figure 19 shows the simulated charge distribution of the cup.

It is apparent in Figure 19 that about half of the charges gather on the first left surface (outer bottom) when the bottom is pointed toward the grounded electrode, but only 20% of the charges gather on the first left surface (edge of the mouth) when the mouth is pointed toward the grounded electrode, as shown in Figure 19.

This decrease in the number of charges gathering on the first left surface occurs because the area of the first left surface in the former situation is large, and the area of the first left surface in the latter situation is very small. As a result, a large electrostatic force acts on the bottom in the former situation, but a weak electrostatic force acts on the edge in the latter situation.

Many of the other charges are trapped on the circumference surface of the cup. The electrostatic force that acts on those charges is perpendicular to the circumference surface. These forces cancel each other at an interval of 180 degrees, thus becoming zero.

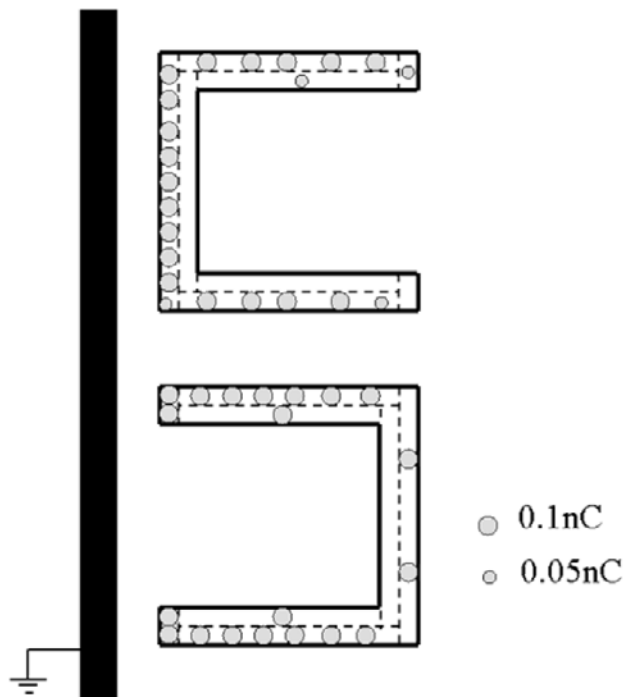


Figure 19. Charge distribution in a cup placed near a grounded electrode. The bottom of the upper cup is pointed toward the electrode, and the mouth of the lower cup is pointed toward the electrode. Both cups have a charge of +2.0 nC each.

Therefore, the cause of the AIF is the following.

The charged conductor has a small first left (or right) vertical surface, a large first right (or left) vertical surface, and a horizontal surface. When the large surface is pointed toward a grounded electrode, many charges can gather at the large surface. In contrast, when the small surface is pointed toward the grounded electrode, only a small amount of charge can gather at the small surface. The other charges are stopped at the horizontal surface, and the electrostatic force that acts on those charges does not contribute to the overall electrostatic force because it cancels out at an interval of 180 degrees.

2.5. Applications

At this point, I cannot present any electrostatic applications that would use the AIF.

2.6. Conclusion

The following expectation is confirmed by a simulation. If the direction of an asymmetric charged conductor near a grounded electrode is turned to the right or left, the magnitude of the image force on the conductor should change.

3. The Asymmetric Coulomb Force

3.1. Purpose

When a point charge is placed in an electric field, an electrostatic force acts on this charge. This force is known as the Coulomb force and can be calculated by the formula (5).

$$f = qE \quad (5)$$

where: q: Quantity of the charge

E: Intensity of the field

This formula is used not only for point charges, but also small charged conductive spheres. In this case, the absolute value of this force does not change when the direction of the electric field is reversed. However, it is expected that if the shape of the charge carrier is asymmetric, then the absolute value of the force will change when the direction of the electric field is reversed, in analogy with the AF and AIF.

I named this changeable Coulomb force the Asymmetric Coulomb Force (ACF). Therefore, confirming ACF by a simulation and an experiment is the first purpose of this chapter. The second purpose of this chapter is to clarify the cause of the ACF.

3.2. Simulation Results

ACF is similar to AF. The box (cup) conductor is neutral in the AF case. In contrast, the box (cup) conductor is charged in the ACF case. Therefore, the experimental setup for confirming the ACF is the same as that used for the AF (see Figure 11). Thus, the cell layout for the ACF simulation is also the same as the cell layout for the AF simulation. Hence, I can use the cell layout of the AF (see Figure 12) as the cell layout of the ACF. However, I changed the radius of the cup from 5.0 mm to 5.6 mm. As a result, the area of the bottom surface of the cup is the same as the area of the bottom surface of the box that was used in the following experiment. Figure 20 shows the new cell layout used to simulate the ACF.

Because the simulation method (the axi-symmetric finite difference method) of the ACF is the same as that of the AF, the explanation is shortened here. I explain the simulation procedure only with Figure 21.

In the corresponding experiment that will be explained later, the box is charged by electrostatic induction. Therefore, the quantity of the induction charge is simulated first. When electrode 1 is grounded, a voltage of 10 kV is applied to electrode 2, and the cup is brought into contact with the grounded electrode (see Figure 21), the induction charge on the cup is simulated as -1.026 nC.

Therefore, in this simulation, the cup conductor was initially charged to -1.026 nC, then electrode 1 was grounded and electrode 2 was set to a high voltage (from +10 kV to +30 kV). I defined this condition as a forward electric field for the negative charge (see Figure 21); in this case, the electrostatic force pulled the charged cup toward the right side.

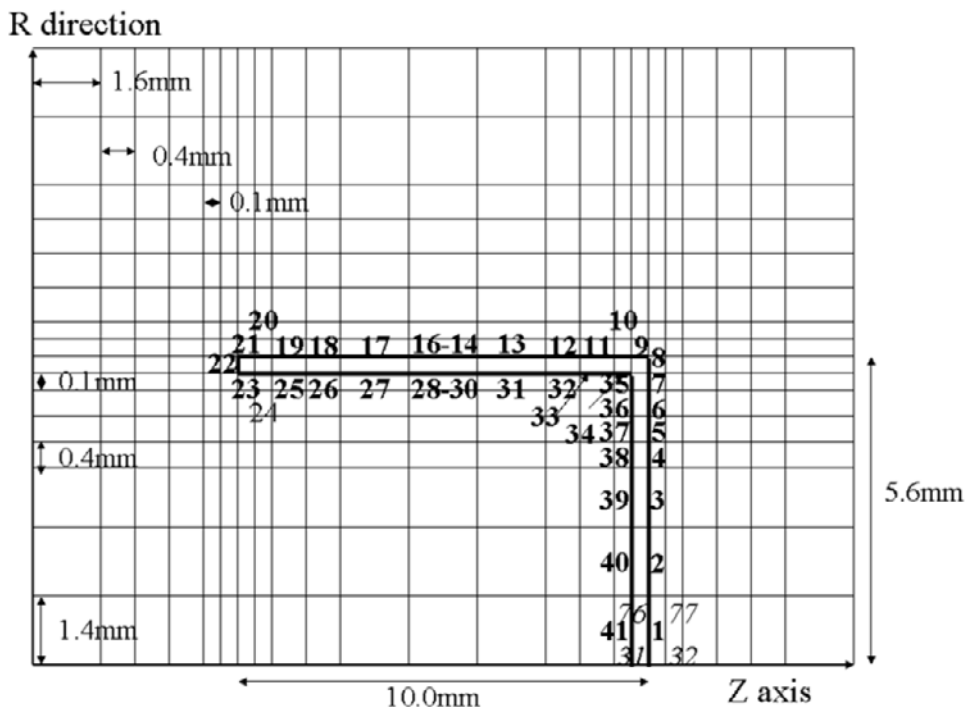


Figure 20. A design of cells (mesh) to simulate the electrostatic force that acts on a charged cup in a parallel electric field.

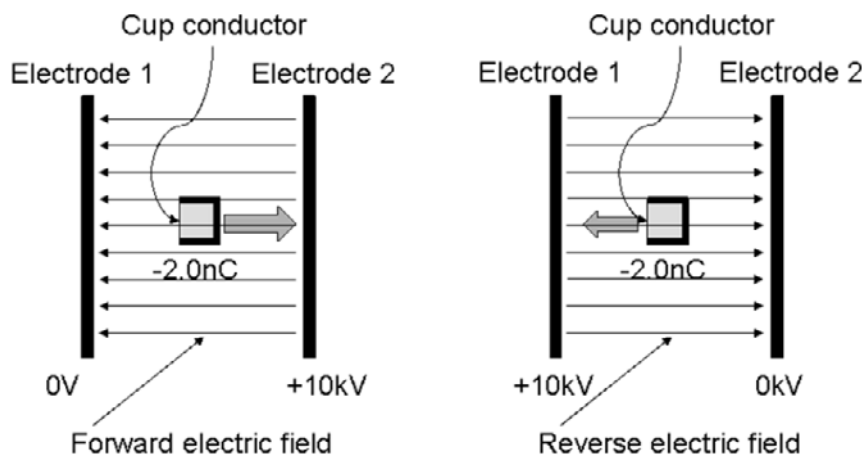


Figure 21. Explanation of the forward electric field and the reverse electric field.

Next, the cup was charged to -2.052 nC , and third, the cup was charged to -3.078 nC , and the electrostatic forces that act on the charged cup were simulated. Finally, electrode 1 was set at a high voltage and electrode 2 was grounded. I defined this condition as a reverse electric field for the negative charge (see Figure 21); in this case, the electrostatic force pulled the charged cup toward the left side.

Figure 22 shows the simulated electrostatic force in the forward electric field and the reverse electric field scenarios as a function of the field intensity between the electrodes.

In Figure 22, it is apparent that when the absolute value of the forward electric field intensity is equal to that of the reverse electric field, the electrostatic force that acts on the charged cup in the forward field is larger than the electrostatic force in the reverse field. It is also apparent that when the electric field becomes strong, the electrostatic force generally increases.

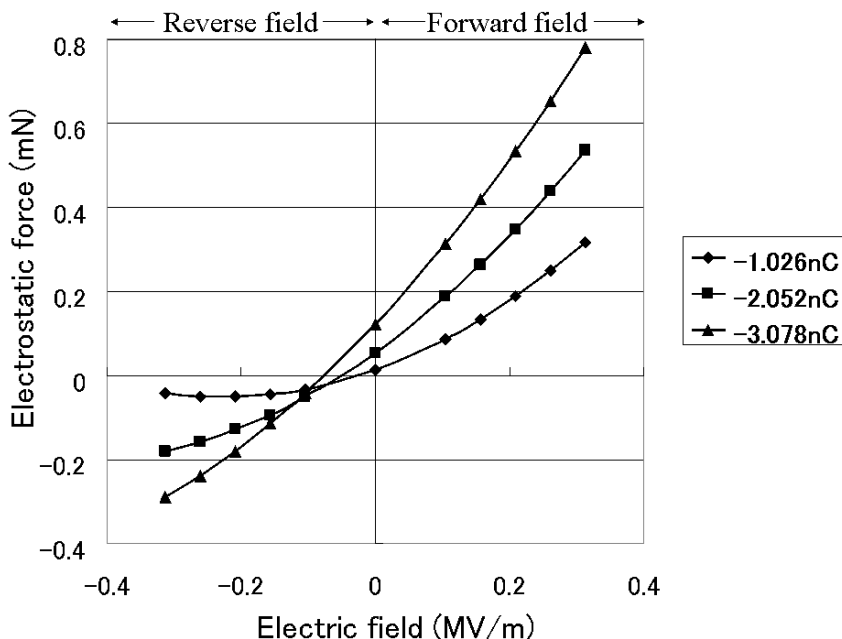


Figure 22. Simulation results for the electrostatic force acting on a negatively charged cup in a forward electric field and a reverse electric field.

(In the case that the quantity of the charge is small (-1.026 nC) and the reverse electric field is strong (-0.3 MV/m), the electrostatic force becomes small. This result can be explained by AF.

In the case in which the electric field is 0.0 MV/m, the electrostatic force does not become zero. This result can be explained by the AIF. If the distance between the cup and the right-side electrode is large enough, this unexpected result no longer occurs.)

3.3. Experiment Results

Because the experiment equipment for the ACF is the same as that of the AF (Figure 11), the explanation is shortened here. I explain the experiment procedure only with Figure 23.

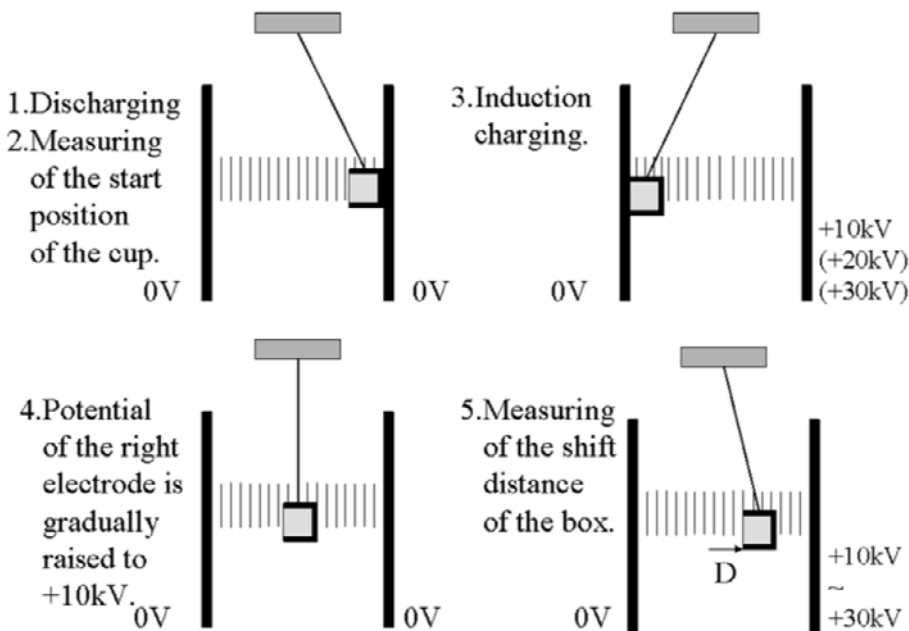


Figure 23. Schematic of the procedure of the experiment to confirm the ACF.

This experiment was performed using the following procedure:

- ① The left and right electrodes were grounded, and the box conductor was brought into contact with the grounded electrode for discharging.
- ② The non-charged box conductor was centered between the electrodes, and the position of this box was measured using the ruler.
- ③ The right electrode was charged to V1 (+10 kV), and the box conductor was brought into contact with the grounded left electrode for induction charging. It was then kept away from the electrode so that a negative charge was maintained on the box conductor.
- ④ The right electrode was grounded again, and it was gradually charged to the target high voltage V2 (+10 kV), creating a forward electric field for negative charges between the electrodes. As a result, the box conductor shifted toward the right side. This position of the box was measured using the ruler. The difference between the position measured in step ④ and the position measured in step ② was the shifted distance of the box.
- ⑤ ① → ④ This procedure was repeated with varying values of V1 (+20 kV, +30 kV) and V2 (+15 kV, +20 kV, +25 kV, +30 kV).
- ⑥ Finally, the left electrode was charged to a positive high voltage and the right electrode was grounded, creating a reverse electric field for negative charges between the electrodes, and the same experiment was performed again.

The following three photographs show the typical three positions of the left open box of the experiment.

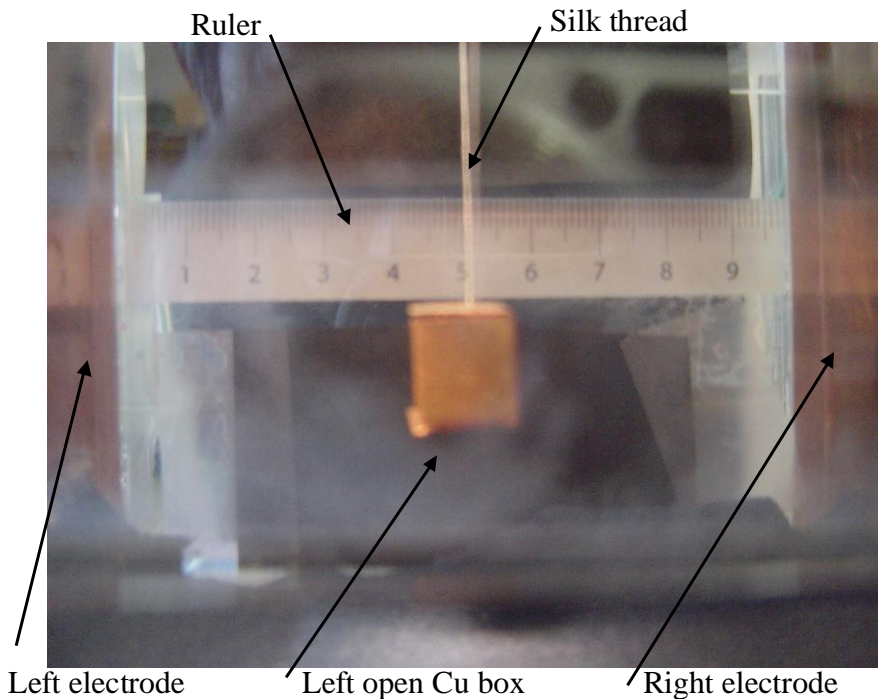


Photo 1. The original position of the left open box that has no charge in no electric field.

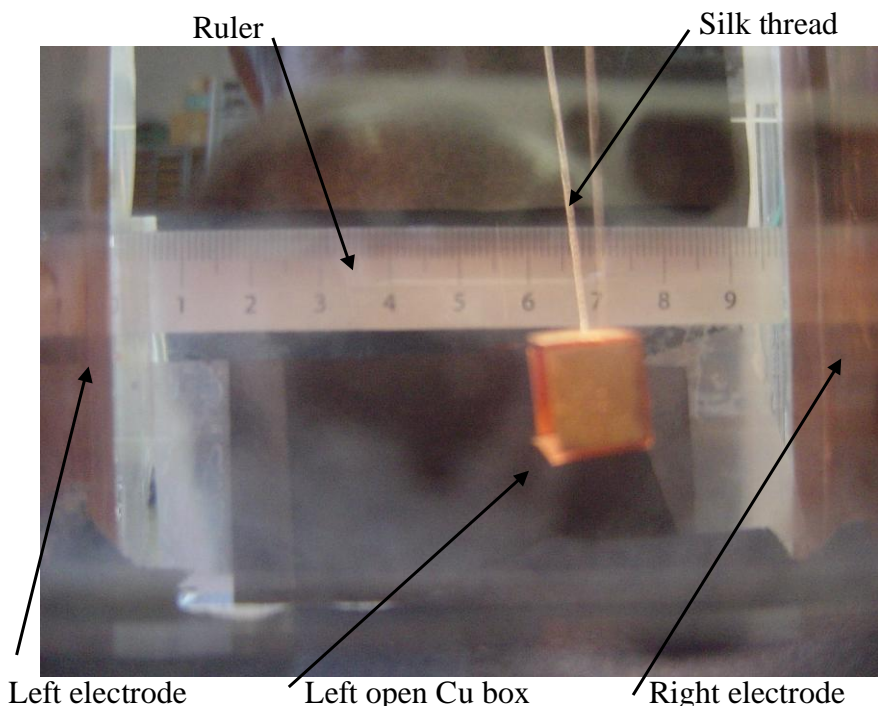


Photo 2. The shifted position of the left open box that has charge of -2.0nC in forward electric field of $+0.2\text{MV/m}$.

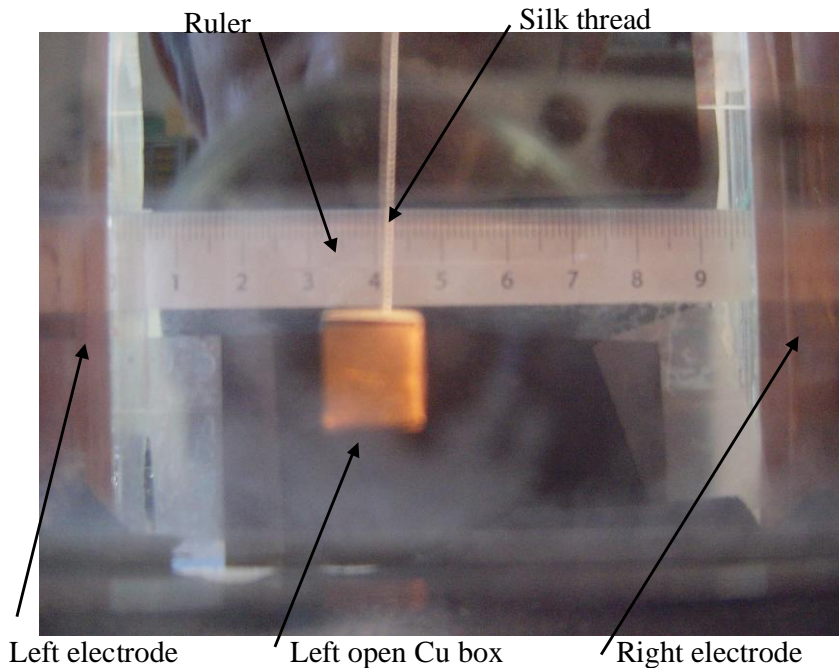


Photo 3. The shifted position of the left open box that has charge of -2.0nC in reverse electric field of -0.2MV/m .

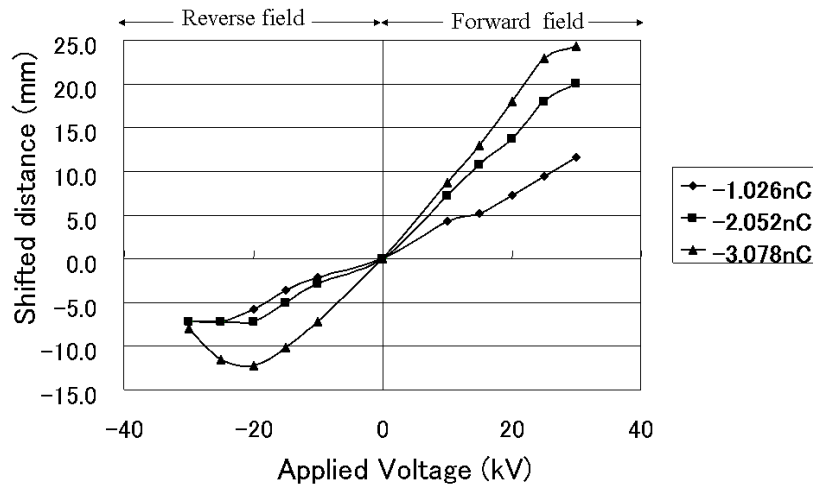


Figure 24. The measured shifted distance of the box in the forward electric field and the reverse electric field as function of the applied voltage.

Figure. 24 shows the measured shifted distance of the box as a function of the applied high voltage.

It is apparent from in Figure 24 that the measured shifted distance of the box in a forward electric field is large, but it is small in a reverse electric field. Furthermore, we can see that the pattern inof Figure 24 (experiment) is similar to that of Figure 22 (simulation).

However, to appropriately compare between Figure 22 (simulation) and Figure 24 (experiment), the shifted distance of the box must be changed converted to the electrostatic force.

3.4. A Comparison of the Experimental and Simulation Results

The shifted distance D of the charged box conductor floating in a strong electric field was measured as described above. This shifted distance D is related to the length L and the height Y of the thread, as shown in Figure 25.

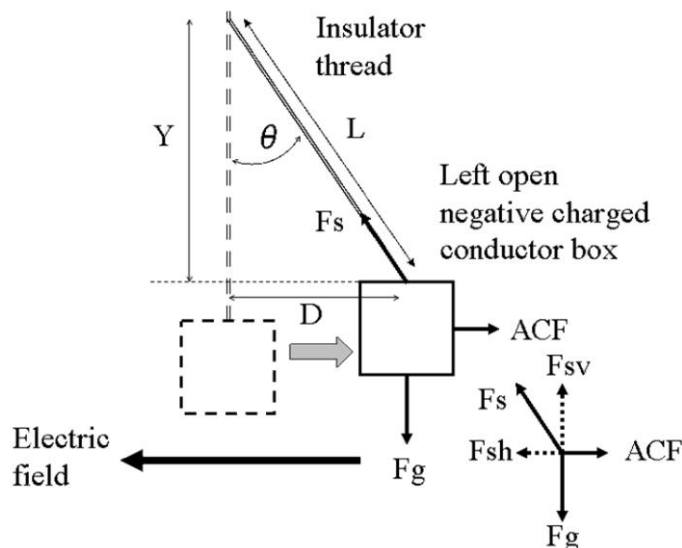


Figure 25. Schematic diagram of the electrostatic force (ACF), the gravity force, and the tensile force acting on a charged box in a strong electric field.

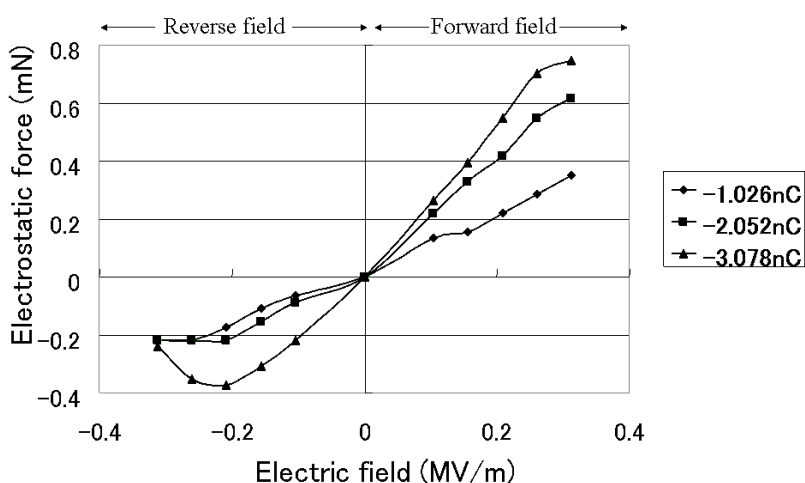


Figure 26. Experimentally measured ACF acting on a charged box as a function of the electric field intensity.

In Chapters 1-5, I explained how to calculate the electrostatic force that acts on the box from the shifted distance. Therefore, the explanation is omitted here.

The experimentally measured ACF acting on the charged box in a strong electric field is shown in Figure 26.

The overall pattern of the experimental result is very similar to that of the simulation (see Figure 22). However, it is difficult to compare the results of the experiment and the results of the simulation when the three simulation results and the three experiment results are shown simultaneously on one graph. Thus, Figure 27 shows the results obtained for a charge of -2.052 nC. The other results can be confirmed in reference [6].

It is apparent in Figure 27 that the experimental result shows good agreement with the simulation result as a general rule and that ACF due to the forward electric field is larger (by a factor of 2 or more) than ACF due to the reverse electric field. Therefore, the ACF has almost been confirmed via simulation and experimentation.

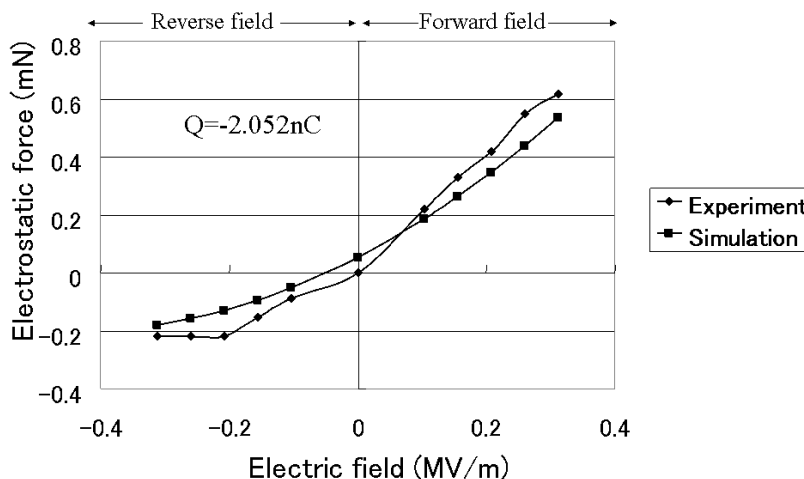


Figure 27. Experimentally measured and simulated ACF acting on a charged box as a function of the electric field intensity. The charge quantity is -2.052 nC.

3.5. Cause of the ACF

As mentioned above, the existence of the ACF has been confirmed experimentally. Therefore, I next focus on the cause of the ACF.

For this purpose, a cup-shaped conductor was divided into two parts, as shown in Figure 28. The first part is a pipe, and the other is a disk. The electrostatic forces that act on these three conductors were simulated using the same simulation method described previously. In this simulation, the same charge of -2.06 nC was placed on the three conductors. The cell layouts of the pipe and the disc were omitted, because they can be easily determined from Figure 20.

Figure 29 shows the simulated electrostatic forces of the three conductors in the forward electric field and the reverse electric field as a function of the field intensity between the electrodes. The Coulomb force calculated by formula (5) is also shown in Figure 29. For this calculation, the charge q was fixed at -2.06 nC.

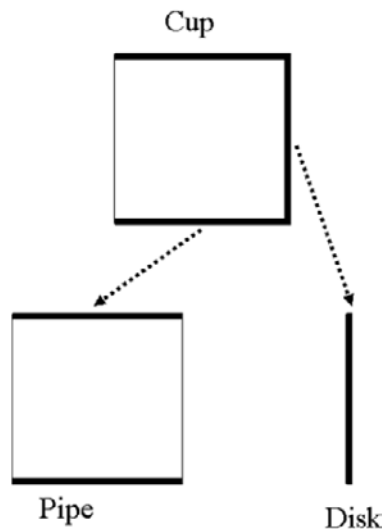


Figure 28. Original cup conductor and the cup divided into two parts (pipe and disk).

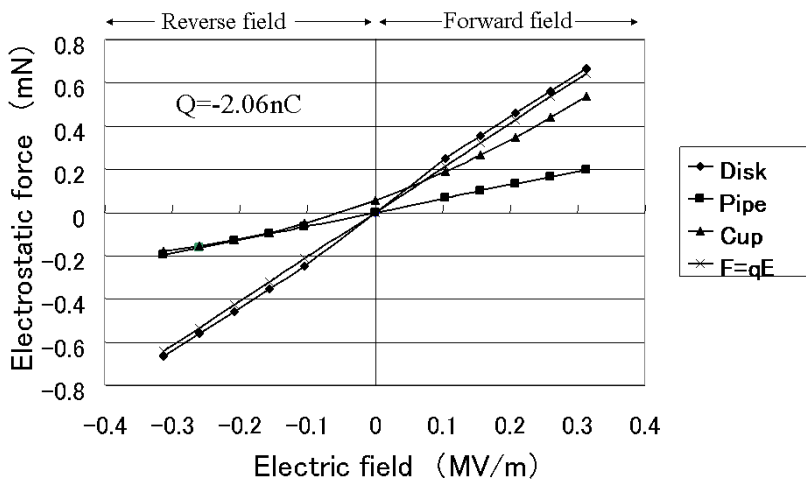


Figure 29. The simulated electrostatic forces that act on the three differently shaped conductors and the calculated Coulomb force.

In Figure 29, the triangle data points show the electrostatic force that acts on the cup, the square data points show the electrostatic force that acts on the pipe, and the diamond data points show the electrostatic force that acts on the disk. The X data points show the result calculated from formula (5).

The following results are apparent from Figure 29.

- (1) The simulation results of the disk and the cylinder are point symmetric. Both shapes are symmetric. The calculation result of the Coulomb force is point symmetric as well. This means that the absolute value of the electrostatic force in the forward field is equal to that in the reverse field.

- (2) The simulated electrostatic force of the disk shows good agreement with the calculated Coulomb force. It is not presently clear whether this consensus occurred by chance.
- (3) The electrostatic force of the disk is about three times stronger than the electrostatic force of the pipe.
- (4) The simulation result of the cup is not point symmetric. In the forward field, the electrostatic force of the cup is similar to the electrostatic force of the disk. In the reverse field, the electrostatic force of the cup is equal to the electrostatic force of the pipe.

As a result, the electrostatic force of the cup in the forward field is about three times stronger than the electrostatic force of the cup in the reverse field.

These results suggest that the charge distribution of the cup is similar to the charge distribution of the disk in the forward field, and the charge distribution of the cup is similar to the charge distribution of the pipe in the reverse field.

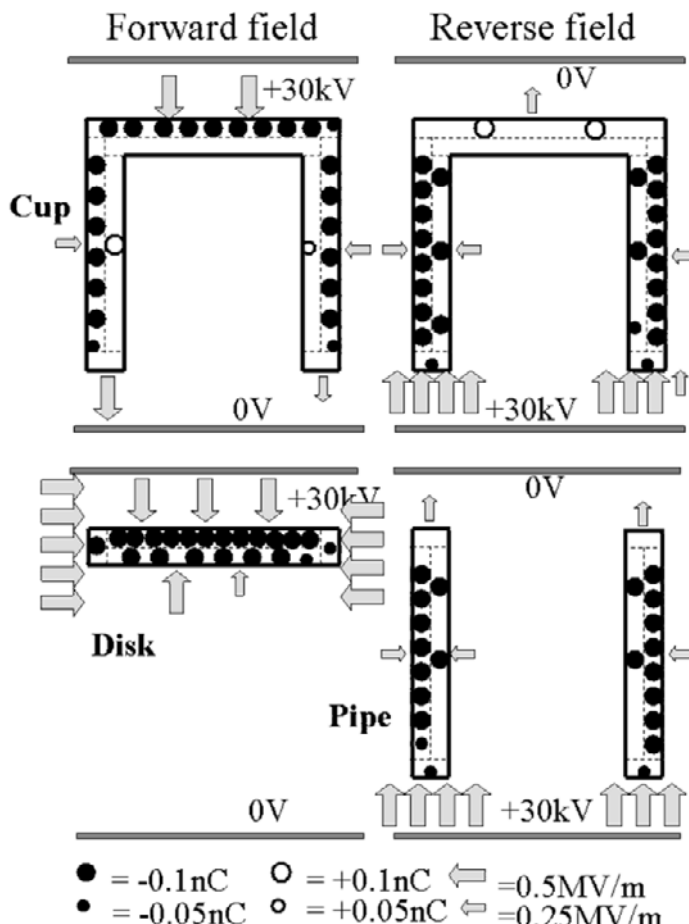


Figure 30. Charge distribution for the three different conductors in the forward and reverse fields.

Therefore, I simulated the charge distribution of the three conductors in both electric fields. Figure 30 schematically shows the simulation results.

In Figure 30, the black circles represent electrons, and the blank circles represent holes. The large circles and small circles represent 0.1 and 0.05 nC, respectively. The arrow marks represent the direction and intensity of the electric field. The large and small arrows represent 0.5 MV/m and 0.25 MV/m, respectively.

(Caution: In Figure 30, the circles and arrows are divided on the left and right with different numbers for convenience. For example, the left edge of the pipe has four arrows, and the right edge of the pipe has three arrows in the reverse electric field. However, this does not mean that the intensity of the electric field on the left edge is 2.0 MV/m and the intensity of the right edge is 1.5 MV/m. The correct meaning is that the intensity of the edge is 3.5 MV/m.)

(Caution: There are a few holes in Figure 30. They were generated by electrostatic induction.)

It is apparent in Figure 30 that the charge distribution of the cup is the same as the charge distribution of the pipe in the reverse field. However, the charge distribution of the cup is not the same as the charge distribution of the disk in the forward field. Therefore, this phenomenon cannot be explained solely by the charge distribution.

It is apparent in Figure 30 that the outer bottom of the cup has a large amount of charge in the forward field. On the other hand, the edge of the mouth of the cup does not have a large charge. As a result, a strong forward electrostatic force acts on the cup in the forward field.

Of course, the outer circumference surface is charged as well, but the electrostatic force that acts on those charges is perpendicular to the circumference surface and cancels out at an interval of 180 degrees.

In contrast, when the cup is placed in the reverse electric field, all of the electrons leave the outer bottom of the cup, but none of the electrons stop at the inner bottom of the cup because this place is electrically shielded by the surrounding cup wall. If this region was not shielded, many electrons would stop here and a strong electrostatic force in the reverse direction would be generated.

Because none of the electrons stop at the inner bottom, all of the electrons move toward the mouth of the cup. A few electrons migrate to the edge, but many electrons stop at the circumference surface of the cup.

This occurs because the area of the edge is too small for many electrons to gather. Electrons repulse each other with electrostatic force; thus, only a few electrons can remain in the small area.

As mentioned above, the electrons on the circumference surface make no contribution to the effective electrostatic force. Finally, only the electrostatic force that acts on the edge remains. However, this force is weak. Of course, the intensity of the electric field on the edge is strong, but the quantity of electrons on the edge is small. Therefore, a weak reverse electrostatic force acts on the cup in the reverse field.

Therefore, the cause of the ACF is summarized in the following:

When a charged conductor consists of four parts, that is a small first left surface, a large second left surface, a large right surface, and a circumference surface, and the left and right surfaces are perpendicular to the electric field and the circumference surface is parallel to the electric field, in the reverse electric field, the large second left surface is electrically shielded by the circumference surface and only a few charges can gather at the non-shielded small first left surface. The other charges that remain on the circumference surface cannot generate an

effective electrostatic force. In contrast, in the forward electric field, the large right surface is not shielded, and many charges can gather at the right surface.

3.6. Conclusion

- (1) The existence of the ACF that acts on a charged asymmetric conductor in a parallel electric field has been confirmed by a simulation and an experiment.
- (2) The cause of the ACF has been clarified. Selective electric shielding and an unbalanced charge distribution are the main reasons behind this force.

4. A New Electrostatic Generator (an Application of the ACF)

4.1. Purpose

As mentioned in the abstract, a new electrostatic generator can be designed to use the ACF. Therefore, it is the first purpose of this chapter to clarify the difference between the traditional generator and the new generator. A determination of the expected performance of the new generator is the second purpose. The concrete design and manufacturing method of the new generator comprise the third purpose. A prediction of the performance of this new generator is the fourth purpose.

4.2. Basic Theory

The idea behind an electrostatic generator has been defined by lifting the charge to a high potential by mechanical force against the electric force that acts on this charge. It is impossible for the mechanical force to carry the charge directly. Therefore, the charge is placed on a suitable body. We call this body the charge carrier.

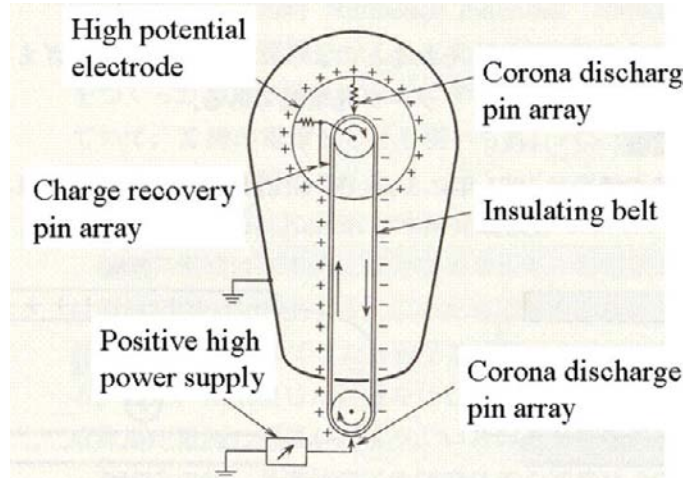


Figure 31. Schematic layout of the Van de Graaff electrostatic generator [7].

The most popular electrostatic generator is the Van de Graaff type electrostatic generator. This was invented by Dr. Van de Graaff in 1931 in the USA. Today, it is used with a large voltage power supply. It can produce ten million volts. In this machine, an insulating belt is used as a charge carrier. Figure 31 shows an example of this generator.

The insulating belt is moved in the direction of the arrow by a motor. The bottom corona discharge pin array places positive ions on the insulating belt. The positive ions on the insulating belt are carried to the high voltage electrode sphere by the mechanical force of a motor.

Corona discharge occurs between the negative charge on the recovery pin array and the positive ions on the insulating belt. As a result, the positive ions on the insulating belt are neutralized by the negative corona ions. Then, positive charges (holes) are added to the high voltage electrode sphere.

The principle of this electrostatic generator is shown schematically in Figure 32.

In Figure 32, the bold line represents the potential, and the arrows represent the forces. The small black circles represent the electrons, and the gray plates represent the charge carriers.

In the Van de Graaff electrostatic generator, the charge carrier is directly transported by a strong mechanical force, F_m , against the electrostatic force F_e .

In contrast, in the new electrostatic generator, the charge carrier is firstly moved in the forward electric field caused by electrets according to the electrostatic force F_{e1} . In this process, the charge carrier gains kinetic energy from the electric field. Then, the carrier is moved in the reverse electric field, expending the given energy against electrostatic force F_{e2} .

The shape of this charge carrier is asymmetric.

Therefore, the ACF acts on this charge carrier. Thus, the absolute value of F_{e1} is larger than that of F_{e2} . As a result, the charge carrier can arrive at a potential that is larger (-200 V) than the initial potential (0 V).

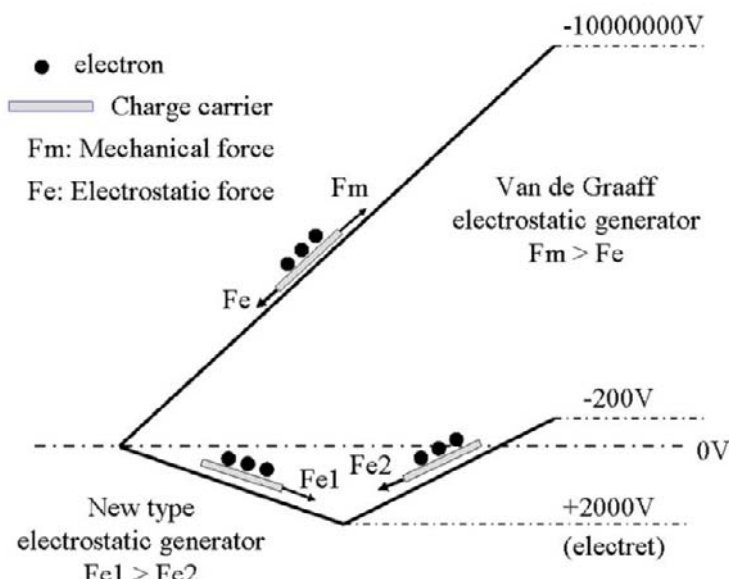


Figure 32. Schematic explanation of the principles behind the two electrostatic generators.

The new electrostatic generator cannot produce ten million volts, but it does not require mechanical force. If the lifetime of the electret was infinite, the new electrostatic generator could generate electric energy forever without adding energy.

As a result, this new electrostatic generator can solve the CO₂ problem and the energy crisis at the same time.

4.3. Simulation Results of the Energy Gained Using the New Electrostatic Generator

Now that the basic principle of the new electrostatic generator is clear, I show the smallest unit of the new generator concretely and simulate the energy gained by the smallest unit. Figure 33 shows the schematic layout of the new generator.

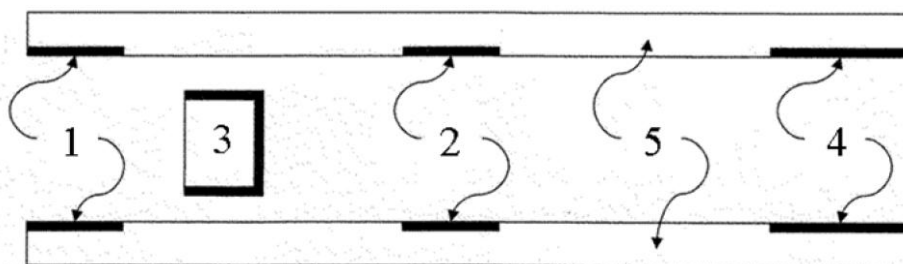


Figure 33. Schematic layout of one unit of the new electrostatic generator.

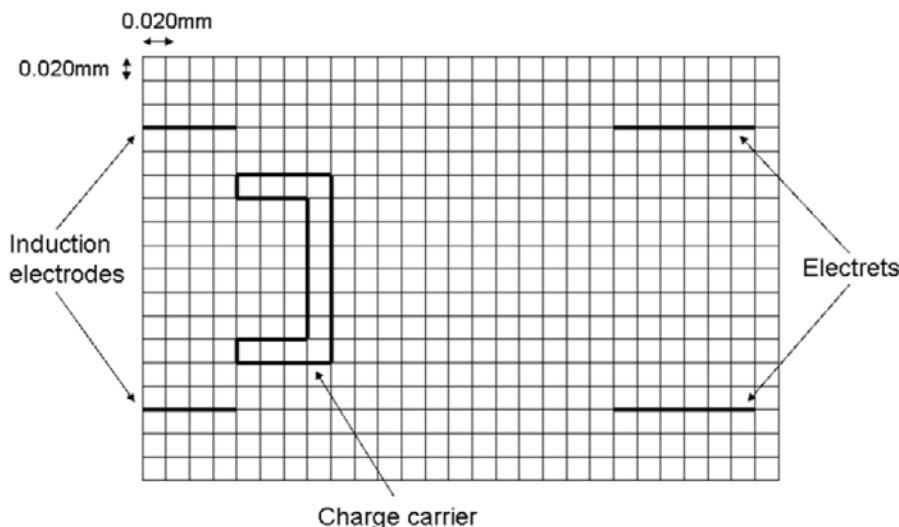


Figure 34. A design of cells (mesh) to simulate the electrostatic force that acts on a charge carrier in one unit of the new electrostatic generator.

This generator mainly consists of electrets 2, induction electrodes 1, and recovery electrodes 4. All of them are disposed on insulating base board 5. The distance between the boards is 0.240 mm. The width of the induction electrodes, the electrets, and the recovery

electrodes is 0.080 mm, 0.120 mm, and 0.160 mm respectively. The electrets, the induction electrodes, and the recovery electrodes have the same length of 38.000 mm. The distance between the electrets and the induction electrodes is 0.320 mm, and the distance between the electrets and the recovery electrodes is 0.320 mm as well.

The electrets have a semi-permanent positive charge density of $+0.1 \text{ mC/m}^2$. The induction electrodes are grounded. The recovery electrodes are kept at a voltage of -260 V. As a result, the electric potential of the electrets is approximately +2600 V. Therefore, the electrets and the induction electrodes produce a forward electric field for a negative charge between them.

The electrets and the recovery electrodes produce a reverse electric field for a negative charge between them.

The long open box 3 is used for a charge carrier that carries negative charge (electron) from the induction electrodes to the recovery electrodes through the electrets. The height of the long box is 0.160 mm, and the width of the long box is 0.08 mm. The thickness of the wall of the long box is 0.02 mm. The length of the long box is 38.000 mm.

Figure 34 shows the left half of the cell design (mesh) for the simulation of one unit of the new electrostatic generator. As mentioned previously, I used the axi-symmetric finite difference method to simulate the electrostatic force that acts on a cup. This time, I must simulate the electrostatic force that acts on a long box; therefore, I used the normal (XY) finite difference method. Both methods are basically equivalent; therefore, a detailed explanation is not given.

At first, the quantity of induction charge to the charge carrier from the induction electrode was simulated. Figure 34 shows the position of the charge carrier at which the induction charge was simulated. At this location, the potential of the charge carrier was fixed to zero volts. The total surface charge of the charge carrier was calculated according to formula (13) (see Appendix 1).

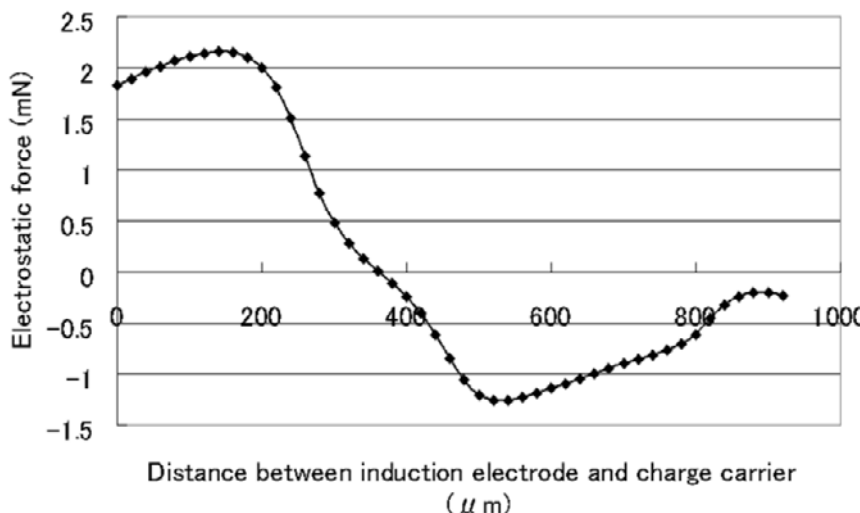


Figure 35. ACF vs. distance between the charge carrier and the induction electrode.

The resulting charge was 0.586 nC. Therefore, this charge carrier was given 0.586 nC in this simulation. The ACF that acts on this conductor was simulated using formula (2) at an

interval of 0.020 mm. The recovery electrodes were grounded in this simulation for simplicity. Figure 35 shows the results of the simulation.

The vertical axis shows the ACF, and the horizontal axis shows the distance between the induction electrode and the charge carrier (left side). The ACF in the forward field is positive; therefore, the charge carrier gains kinetic energy. This energy w was calculated by formula (6).

$$w = \sum F * s \text{ [J]} \quad (6)$$

where: $F=ACF \text{ [N]}$

$s=20*E-6 \text{ m}$

The resulting energy was 5.70E-7 J.

In contrast, the ACF becomes negative in the reverse electric field. Then, the charge carrier loses some of its kinetic energy. The energy loss is calculated as 4.17E-7 J. As a result, the charge carrier maintains some kinetic energy, 1.53E-7 J, when it arrives between the recovery electrodes. The carried charge quantity Q is -5.86E-10 C. This charge Q can be lifted to a higher potential by the extra energy w . This possible potential V is calculated by formula (7).

$$V = \frac{w}{Q} \text{ [V]} \quad (7)$$

The resulting potential is 261 V.

The carried charge cannot be recovered perfectly, because the recovery electrodes do not comprise a perfect Faraday gauge. The remaining charge on the charge carrier can be simulated by grounding the charge carrier between the recovery electrodes. The simulated remaining charge was -0.61E-10 C. As a result, the recovered charge was -5.25E-10 C, and the recovery rate was 90%.

In this one process, a charge of -5.25E-10 C was lifted to -261 V from 0 V.

The generated electric energy, We , can be calculated by formula (8).

$$We = Q * V \text{ [J]} \quad (8)$$

The resulting energy was 1.37E-7 J. This is a small amount of energy, but a large amount of energy can be obtained by gathering those small units. The concrete design of the new electrostatic generator that can generate a large amount of energy is explained in the following chapter.

4.4. Manufacturing Method of a New Electrostatic Generator

Figure 36 shows a very simple structure of the box-type electrode that is used as the charge carrier.

This simple electrode 3 can easily be made as follows.

- (1) A copper foil is placed on insulating base 6.
- (2) The unwanted part of the copper foil is removed by etching.

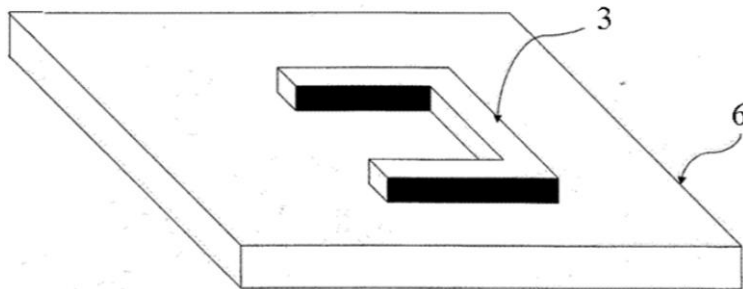


Figure 36. Simple structure of the box-type electrode that is used as the charge carrier.

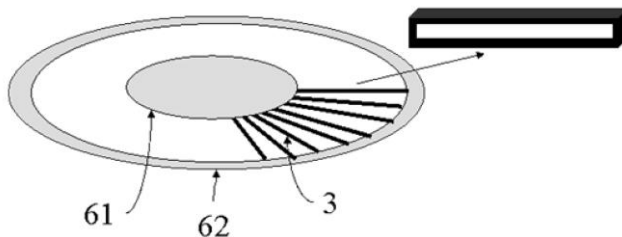


Figure 37. Ideal structure of the box-type electrodes to be used as charge carriers.

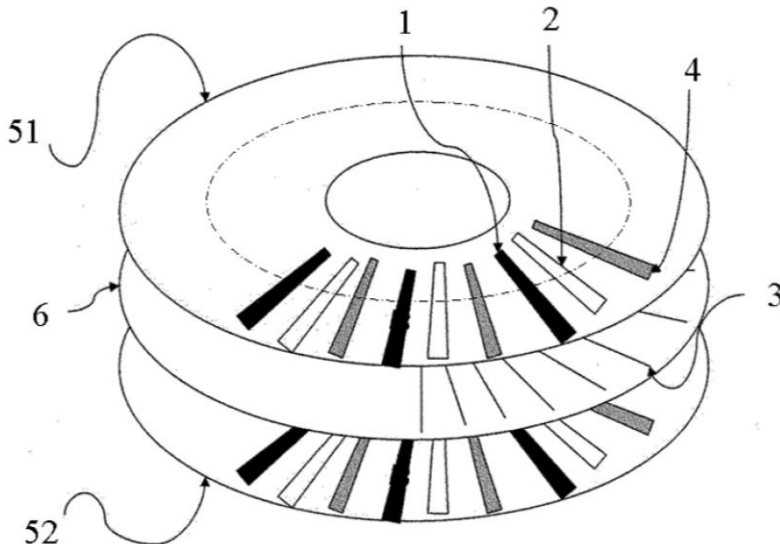


Figure 38. Schematic layout of the one set of three disks of the new electrostatic generator.

This is a very simple method, but the use of space is inefficient, because the thickness of the base is large and the thickness of the electrode is small.

Figure 37 shows an ideal structure of the electrode that is used as the charge carrier.

In this ideal charge carrier disc, many long box electrodes 3 are oriented radially to the circumference 62 from the core 61 of the insulating base disc. This charge carrier disc is sandwiched between two electrode discs. Figure 38 shows one set of three disks of the new electrostatic generator.

In Figure 38, mark 6 shows the charge carrier disc. Marks 51 and 52 show the upper electrode disc and the lower electrode disc, respectively. Mark 3 shows the charge carrier electrode. Marks 1, 2, and 4 show the induction electrode, the electrets, and the recovery electrode, respectively. These electrodes and electrets are made on one side of the electrode disc.

The lower electrode disc has the same structure as the upper electrode disc. However, the electrode surfaces of the two electrode discs face each other. These two electrode discs are fixed, and the charge carrier disc rotates at a high speed.

The three discs have the same radius of 60 mm. The three electrodes and the electret have the same length of 38 mm. They are oriented radially from 20 mm to 58 mm from the center of the disk. Figure 39 shows the concrete design of one unit of the new electrostatic generator. The measurements given in Figure 39 are the measurements of a part displayed by an alternating long and short dashed line in Figure 38, and the units are millimeters.

The marks (1, 2, 3, 4, 51, 52) used in Figure 39 correspond to those in Figure 38. The measurements of each part are the same as for the above-mentioned simulation. However, one pair of induction electrodes was added.

They are drawn at the right side in Figure 39. The distance between the recovery electrode and the added induction electrode is 0.20 mm. As a result, the width of one unit of the new electrostatic generator is 1.32 mm. In addition, two more charge carriers were added. As for the die center distance, 0.44 mm was selected to avoid interference.

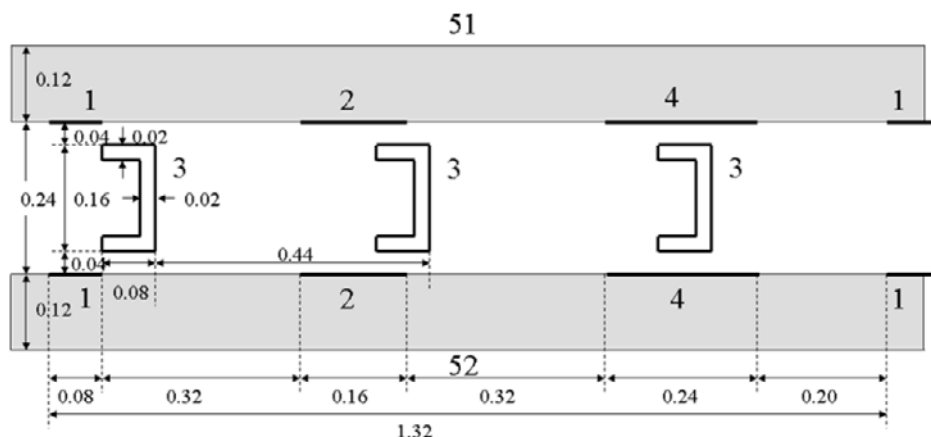


Figure 39. A detailed layout of one unit of the new electrostatic generator.

The induction electrodes and the recovery electrodes can be easily made by the above-mentioned etching method. The electrets can be made as follows.

- (1) The base plate (a polycarbonate disc) is warmed to 100-120 degrees.
- (2) The unwanted part of this disc is covered by a mask.
- (3) This covered disc is exposed to a corona discharge.
- (4) Then, this disc is rapidly cooled to the freezing point.

As a result, corona ions are trapped on the polycarbonate surface, which becomes an electret. Figure 40 shows the manufacturing method of the charge carrier disc. The charge

carrier disc can be made by an improved etching method. It is made through the following process.

- (1) A polycarbonate disk with a thickness of 0.12 mm is cut as shown in Figure 40 (1) to make the slits. The length and the width of the slits are 38 mm and 0.22 mm, respectively. The die center distance of slits is 0.44 mm. An enlarged image of the small area of the center of the slits, displayed by an alternating long and short dashed line in Figure 40 (1) right, is shown at Figure 40 (1) left.
- (2) The slits are filled with sacrifice resin. Mark 62 shows the filled slits, and mark 61 shows the polycarbonate base.
- (3) Copper foils ($t=0.02$ mm) are placed on both sides of the disc. Mark 30 shows the copper foils.
- (4) The unwanted part of the copper foil is removed by etching.
- (5) The polycarbonate base between the sacrifice resin is cut.
- (6) The walls of the right side of the sacrifice resin are plated with copper when a voltage is applied to both the top and bottom copper foils. However, the walls of the left side of the sacrifice resin are not plated, because the electric field is weak. Mark 31 shows the plated copper.
- (7) The sacrifice resin is dissolved in and is removed.

Now, we can manufacture the new electrostatic generator that is shown in Figure 38. In the next section, I will predict the performance of the new electrostatic generator.

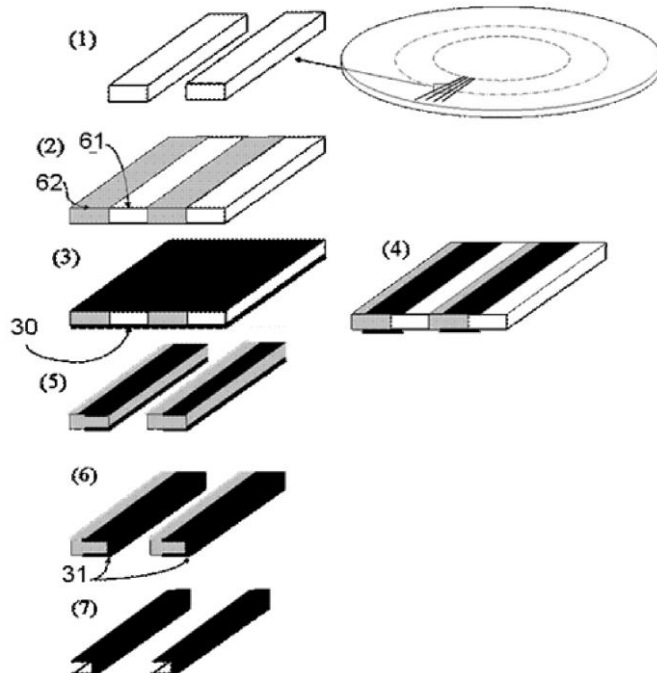


Figure 40. Manufacturing method of the charge carrier disc of the new electrostatic generator.

4.5. Predicted Performance of the New Electrostatic Generator

As mentioned before, the gained electric energy was simulated as 1.37E-7 J, when the charge carrier arrived at the recovery electrode. Therefore, the generated electric power P of one set of three discs can be calculated by formula (9).

$$P = n * m * 1.37E-7 \text{ W} \quad (9)$$

where n: Number of charge carriers that arrive at one recovery electrode in 1 sec.

m: Number of recovery electrodes on one electrode disc.

The value of n was calculated to be 9280 according to the pitch and velocity of the charge carrier. As mentioned above, the pitch is 0.44 mm, and the velocity is 4.083 m/sec when the rotational speed of the charge carrier disc is 1000 rpm.

The number m of the recovery electrodes on the electrode disk was calculated to be 185 according to the pitch of the unit and the circumference length of the charge carrier. As mentioned above, the pitch is 1.32 mm and the circumference length is 245.0 mm at the center of the recovery electrodes, which is displayed by an alternating long and short dashed line in Figure 38.

Here, n=9280 and m=185 are substituted into expression (9), and P is 0.236 W.

This is the electric power generated by one set of three discs of the new electrostatic generator shown in Figure 38. The thickness of one set is 0.480 mm, as mentioned before. However, the thickness can be reduced to 0.360 mm by using a double-electrode disc. The structure of this disk is drawn schematically in Figure 41.

The marks in Figure 41 correspond to those in Figure 39. The thickness of the electrode disc and the charge carrier disc combined is 0.360mm. Therefore, 2778 of these pairs of disks can be piled to 1 m. The diameter of the disc is 120 mm, so one side of length of the desk holder becomes 140mm.

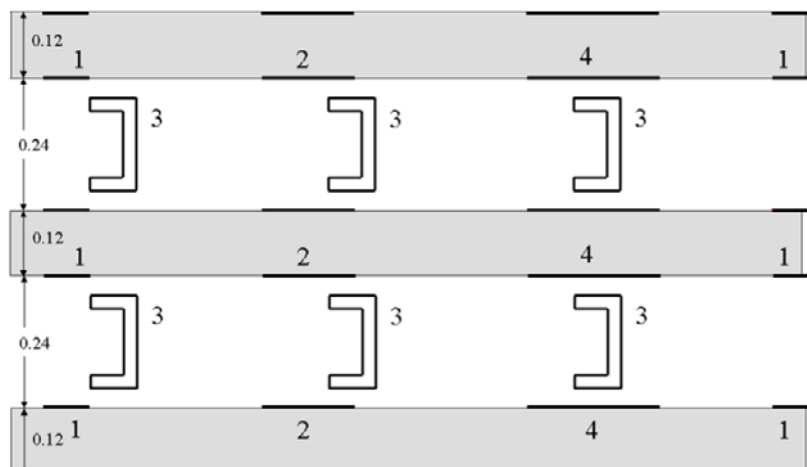


Figure 41. Schematic drawing of the piled discs of the new electrostatic generator.

Then, 49 disc holders can be placed in 1 m². As a result, 136,122 pair of discs will be packed into 1 m³. As mentioned above, one set can generate 0.236 W, therefore, the total electric power that a 1-m³ box of the new electrostatic generator can generate is 32.125 kW.

An ordinary home needs an electric power of 3 kW. Therefore, a 45.5-cm³ box of this new electrostatic generator can supply the needed electric power.

Nevertheless, an electric car will require much more power. The charge density of the electret used in the simulation is 0.1 mC/m². The maximum charge density of the electret that we can use today is 1.0 mC/m² [8]. As a result, the generated electric power is 3212.5 kW/m³ (explained in the following paragraph). This amount of electric power can easily run a car.

The electric field intensity is directly proportional to the charge density of the electrets. Additionally, the quantity of the induction charge of the charge carrier is directly proportional to the electric field intensity. Therefore, if the charge density increases by a factor of 10, the electric field intensity and the induction charge also increase by the same factor. As a result, the electrostatic force increases by a factor of 100. Finally, the generated electric power increases by a factor of 100 as well.

Electrets cannot produce a charge density greater than 1.0 mC/m². However, ferroelectric substances can usually produce charge densities of 10 mC/m². This material can generate an electric power of 321250 kW/m³. The maximum charge density of ferroelectric material that we can use today is 160 mC/m² [9]. As a result, the generated electric power is 82240000 kW/m³.

In the above-described calculation, it was assumed that the air resistance that arises with the high rotational speed of the charge carrier disc is zero. This assumption can be made valid by making the inside of the set a vacuum. A vacuum has three other advantages as well. One of them is that the corona discharge never occurs. The second is that the charge on the charge carrier will never leak into the air moisture. If either of these occurs, the electret charge will be quickly neutralized. The third advantage is that oxidation of the surface of the charge carrier never occurs. If this occurs, the electrostatic force does not act on the surface of the charge carrier perpendicularly. As a result, the ACF decreases.

In the above-mentioned calculation, it was assumed that the friction resistance that arises due to the high rotational velocity of the charge carrier disc is zero. This can be a valid assumption if the disc floats in the air by electrostatic force. The corresponding details are clarified in my Japanese laid open patent [10].

4.6. Conclusion

- (1) The differences in the principles of the traditional electrostatic generator and the new electrostatic generator employing the ACF have been clarified. The former needs a mechanical force to lift up a charge carrier, but the latter can lift up a charge carrier by using only an electrostatic force, without the need for a mechanical force.
- (2) The electric energy that will be generated by one cycle by a minimum unit of the new generator is expected to be 1.37E-7 J.
- (3) A concrete design and a manufacturing method of the new generator have been proposed. It can be made by conventional etching methods and corona discharge.
- (4) The performance of the new generator is predicted to be 32 kW/m³ when the charge density of the electrets is 0.1 mC/m².

4.7. Other Applications of the ACF

Application of the ACF includes not only an electrostatic generator, but also an electrostatic transporter, an electrostatic accelerator, and an electrostatic motor. These three applications can be realized by an apparatus that has a structure similar to that of the above-mentioned electrostatic generator.

5. A Miracle Charge Carrier that Can Move forward in a Reverse Field

5.1. Background

As mentioned above, the basic theory of the new electrostatic generator is explained with Figure 33. The charge carrier is forced to the back by the electrostatic force in the reverse field. In Figure 33, Fe2 represents this force. If the direction of this force is reversed and the charge carrier is forced to move forward in the reverse field, the new electrostatic generator can generate a greater electric power.

A negatively charged charge carrier usually experiences a backward electrostatic force in a reverse electric field. Therefore, if the carrier moves forward in a reverse field, it is a miracle. It is an unbelievable phenomenon.

However, we know that a yacht can move forward as a result of wind power in a head wind. This phenomenon can be explained by the shape and the direction of the sails of the yacht. Therefore, if we select a suitable shape for the charge carrier, this miracle may occur.

I have attempted to solve this phenomenon, and I found a solution by simulation. I cannot yet confirm this simulation result with a real experiment. The shape of the charge carrier is complex; therefore, I can not make it correctly with handmade methods.

Thus, I will present only the simulation result now.

5.2. Simulation Result

Figure 42 shows a conception diagram of the miracle charge carrier.

In Figure 42, mark 3 shows the charge carrier. Marks 4 and 2 show the upper electrode and the lower electrode, respectively. When a large positive voltage is applied to the upper electrode and the lower electrode is grounded, then a forward electric field for a negative charge is formed between the electrodes. When the upper electrode is grounded and a large positive voltage is applied to the lower electrode, then a reverse electric field for a negative charge is formed between the electrodes. Figure 42 shows this state.

The miracle charge carrier 3 consists of a main plane 31 and two side planes 32 and 33 and five shield members 34, as shown in Figure 42. The direction of the main plane is perpendicular to the electric field, which is drawn as dotted lines in Figure 42. The direction of the two side planes is diagonal to the electric field. The direction of the shield members is parallel to the electric field. The shield members are attached to the back of the main and side planes.

They can shield the back of these three planes from the electric field. As a result, the electrostatic forces that act on the back of these three planes cancel each other.

(Caution: In reality, the electric line of force bends at the circumference of the charge carrier. However, it is drawn as a straight line for simplification in Figure 42.)

Figure 43 shows the detailed measurements of this charge carrier. The electrostatic force that acts on this charge carrier was simulated with these measurements.

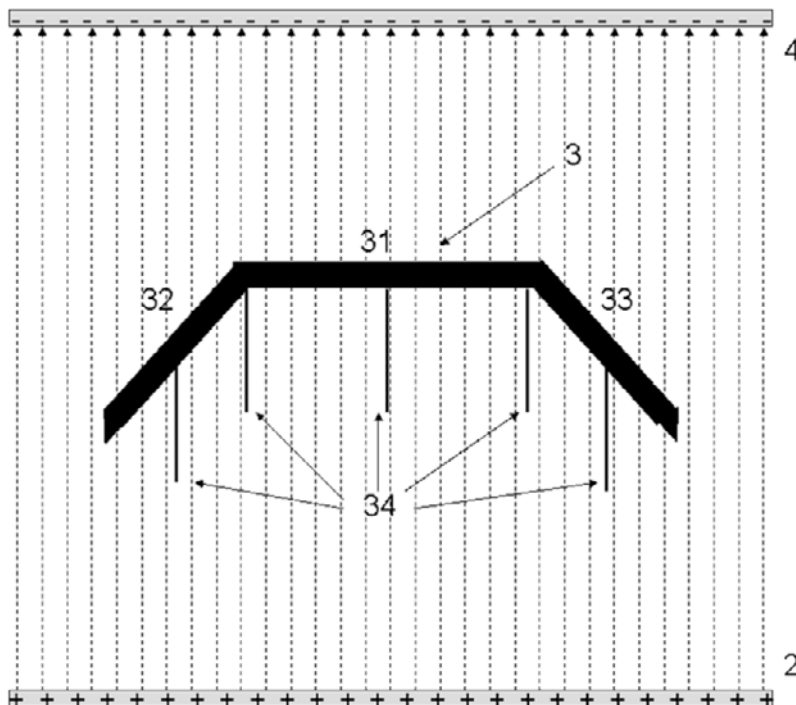


Figure 42. A conception diagram of the miracle charge carrier.

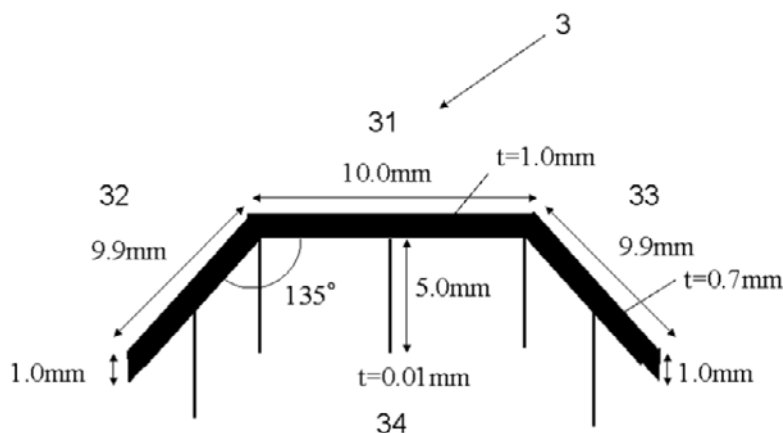


Figure 43. Detailed measurements of the miracle charge carrier.

This charge carrier has ten surfaces and three edges. Thus, thirteen electrostatic forces act on the ten surfaces and the three edges. This situation is drawn schematically in Figure 44.

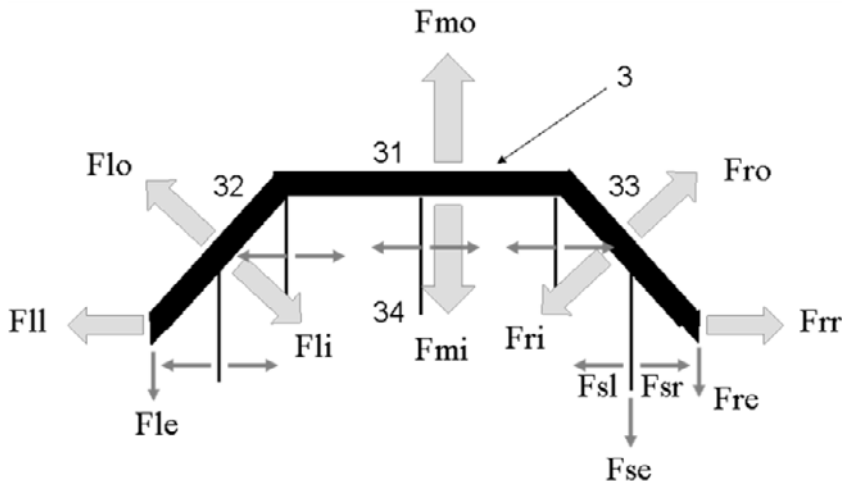


Figure 44. Schematic drawing of the thirteen forces that act on the ten surfaces and the three edges of the miracle charge carrier.

The thirteen electrostatic forces are the following forces.

- F_{mo} acts on the outside of the main plane.
- F_{mi} acts on the inside of the main plane.
- F_{lo} acts on the outside of the left side plane.
- F_{li} acts on the inside of the left side plane.
- F_{ro} acts on the outside of the right side plane.
- F_{ri} acts on the inside of the right side plane.
- F_{ll} acts on the left vertical surface of the left side plane.
- F_{rr} acts on the right vertical surface of the right side plane.
- F_{sl} acts on the left surfaces of the five shield members.
- F_{sr} acts on the right surfaces of the five shield members.
- F_{le} acts on the edge of the left side plane.
- F_{re} acts on the edge of the right side plane.
- F_{se} acts on the edges of the five shield members.

These thirteen electrostatic forces were simulated by the following simulation method.

The simulation was done with the XY bi-dimensional finite difference method. Figure 45 shows the cell layout (mesh) used for the simulation. In this simulation, the charge carrier was given a charge of -3.0 nC, and it was placed in an electric field of $\pm 2.08 \text{ MV/m}$.

In Figure 45, the measurements show the width and height of each cell, and the numbers shows the number of cells. The individual lines that outline the cells are eliminated for simplification.

Figure 46 shows the simulation result.

The following results are apparent in Figure 46.

- (1) The inside force of the main plane (F_{mi}) and those of the two side planes (F_{li} , F_{ri}) decrease largely with the shield members. The outside force of the main plane (F_{mo}) decreases by half with the shield members.
- (2) The outside forces of the two side planes (F_{lo} , F_{ro}) increase slightly with the shield members.
- (3) The left and right forces of the shield members (F_{sl} , F_{sr}) appear strongly with the shield members.
- (4) The edge forces of the three edges (F_{le} , F_{re} , F_{se}) are small.
- (5) The left force of the left side plane (F_{ll}) and the right force of the right side plane (F_{rr}) decrease slightly with the shield members.

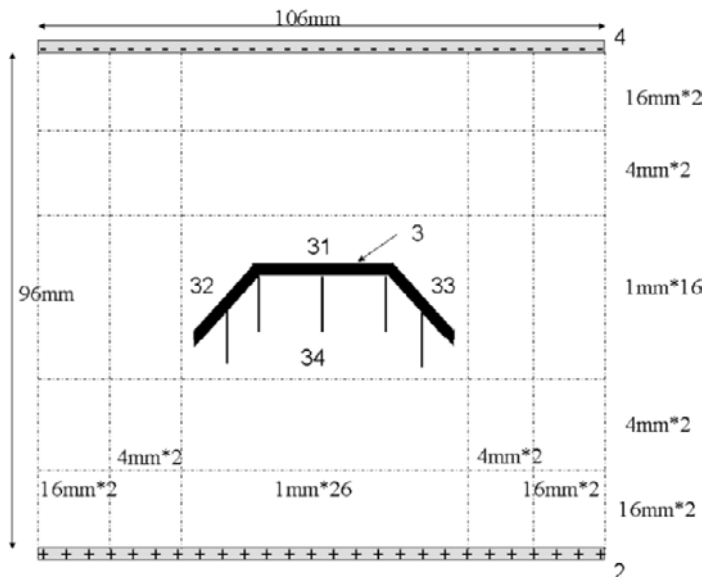


Figure 45. A design of cells (mesh) for simulating the electrostatic force that acts on a miracle charge carrier in a parallel electric field.

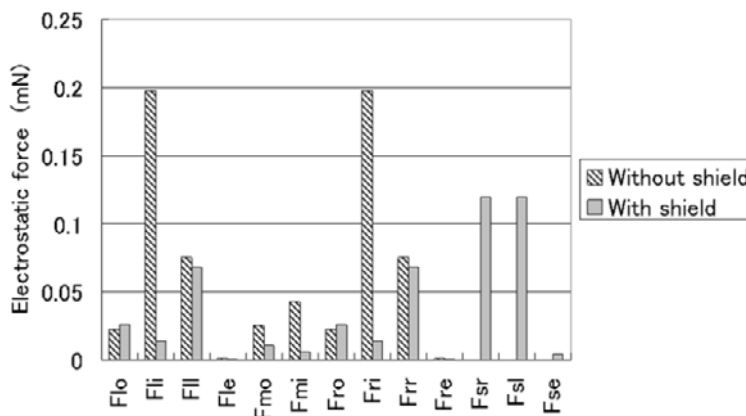


Figure 46. Simulation results of the thirteen electrostatic forces that act on the thirteen regions of the miracle charge carrier.

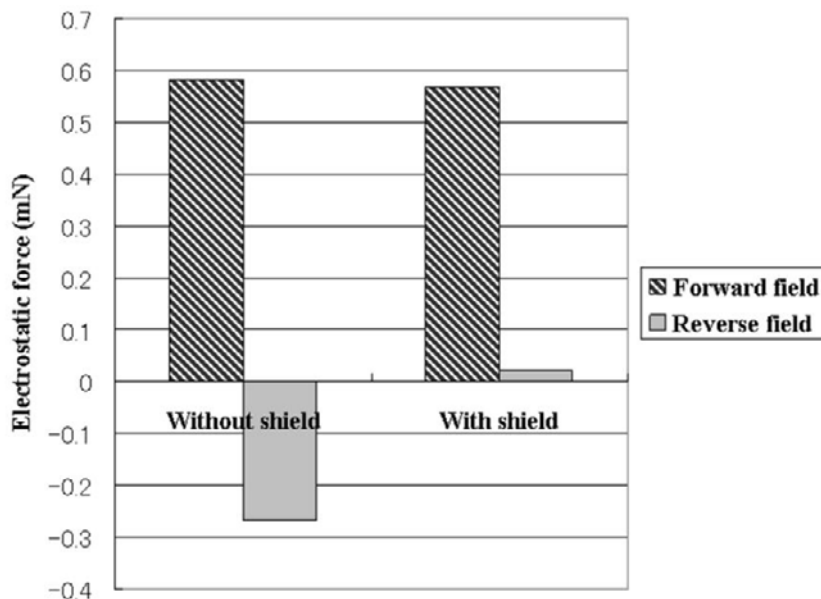


Figure 47. The electrostatic force that acts on the miracle charge carrier in a forward or reverse electric field with or without shield members.

The left and right forces of the shield members (F_{sl} , F_{sr}) cancel each other, because they act in opposite direction. The left force of the left side plane (F_{ll}) and the right force of the right side plane (F_{rr}) cancel each other for the same reason. The parallel component of the outside force of the left side plane (F_{lo}) and the parallel component of the outside force of the right side plane (F_{ro}) also cancel each other for the same reason. Finally, the parallel component of the inside force of the left side plane (F_{li}) and the parallel component of the inside force of the right side plane (F_{ri}) cancel each other for the same reason.

I then summed all of the outside forces of the main plane (F_{mo}) and the vertical component of the outside forces of the two side planes (F_{lo} , F_{ro}); this sum is the total upper force. Additionally, I summed up the inside force of the main plane (F_{mi}) and the vertical component of the inside forces of the two side planes (F_{li} , F_{ri}) and the three edge forces(F_{le} , F_{re} , F_{se}). This is the total lower force. Finally, I summed up the two total forces. This is the final force that acts on the miracle charge carrier. Figure 47 shows the four final forces that act on the miracle charge carrier in a forward or reverse electric field with or without shield members.

The following results are apparent in Figure 47.

- (1) The electrostatic force that acts on the miracle charge carrier in the forward electric field decreased slightly when five shield members were attached to the back side of the carrier.
- (2) In contrast, the force in the reverse electric field decreased significantly, and the direction was reversed.

This result means that a miracle charge carrier that has a negative charge can move forward to a negative potential in a reverse electric field.

5.3. Conclusion

It was found by a simulation that, if the back side is electrically shielded, a charged specially shaped conductor can progress from a low potential to a higher potential for the charge by an electrostatic force that is generated by a electric field.

Conclusion

- 1) The electrostatic force that acts on asymmetric conductors was simulated, and the following three asymmetric forces were found.
 - A. The asymmetric force (AF), which acts on a neutral asymmetric conductor in a parallel electric field. Mathematically, this force must be equivalent to the gradient force that acts on a neutral symmetric conductor in a convergent electric field.
 - B. The Asymmetric Image Force (AIF), which acts on a charged asymmetric conductor near an electrode. The magnitude of the force changes with the shape and direction of the conductor.
 - C. The Asymmetric Coulomb Force (ACF), which acts on a charged asymmetric conductor in a parallel electric field. When the direction of the field is reversed, the absolute value of the force changes, even if the absolute value of the field remains the same.
- 2) The existence of AF and ACF was confirmed experimentally.
- 3) The causes these three forces were made clear. The asymmetric conductors that experience these three forces have perpendicular planes and parallel planes, with respect to the electric field, and a large area of the perpendicular planes of one side are electrically shielded by the parallel planes. Only a small amount of charge can gather at the small area of the non-shielded perpendicular plane on one side, but many charges gather on the large parallel plane and do not contribute to the effective force.
- 4) A concrete design and a production method for a new electrostatic generator driven by ACF were devised, and the generator's performance was predicted. The performance can be used to simultaneously solve the environmental problem and the energy crisis.
- 5) A miracle charge carrier was devised. This specially shaped carrier can move from a low potential to a higher potential for the carried charge by the electrostatic force that is generated by an electric field.

Appendix 1. An Explanation of the Simulation Method (A Bi-Dimensional Axi-Symmetric Finite Difference Method)

Here, I will explain how to simulate the electrostatic force that acts on a non-charged cylinder that is floating in an electric field (see Figure 2). This simulation is performed by using a bi-dimensional axi-symmetric finite difference method.

First, the simulation target space between the two circle electrodes was divided into small parts, as schematically shown in Figure 48.

The space was divided into 5 parts in the R direction and 12 parts on the Z axis in this simulation, although, in Figure 48, it is only divided into 5 on the Z axis for clarity. I call this divided small space a part. As shown in Figure 48, the shape of the 12 parts on the Z axis is cylindrical and the shape of the other 48 parts is a pipe shape. The bold line circles show the edges of the conductor parts, and the normal line circles are the edges of the insulator (air) parts. The potential along these circles is the same everywhere. Each part has three (cylinder) or four (pipe) surfaces, that is, the left surface, the right surface, the outer circumference surface, and the inner circumference surface.

The surface charge density and the electric field intensity of each surface are determined by a simulation, and the electrostatic force acting on the surface is calculated by those two values.

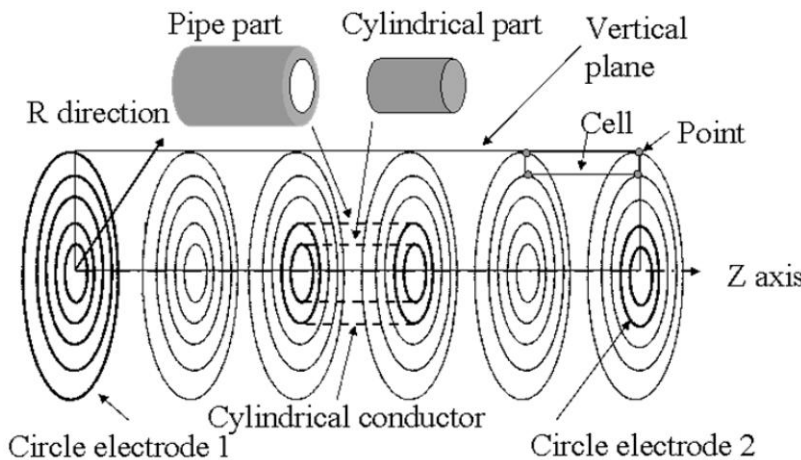


Figure 48. Schematic drawing of the space between the electrodes for the axi-symmetric finite difference method.

This is a very simple simulation. Therefore, we can describe the simulation air space in three dimensions. However, in the case of a complicated simulation, it may be difficult to describe it in three dimensions. Thus, we usually choose one plane that includes the Z axis of the target space. Because the space is axi-symmetric, we describe only one side of the Z axis. For example, only the upper part of the vertical plane was converted into a bi-dimensional picture, which is shown in Figure 49. In this conversion, a section of the parts (the pipe and the cylinder) was changed into a cell. Furthermore, the circumference line of the parts (the pipe and the cylinder) was changed to a point. Figure 49 shows the details of the converted vertical half plane.

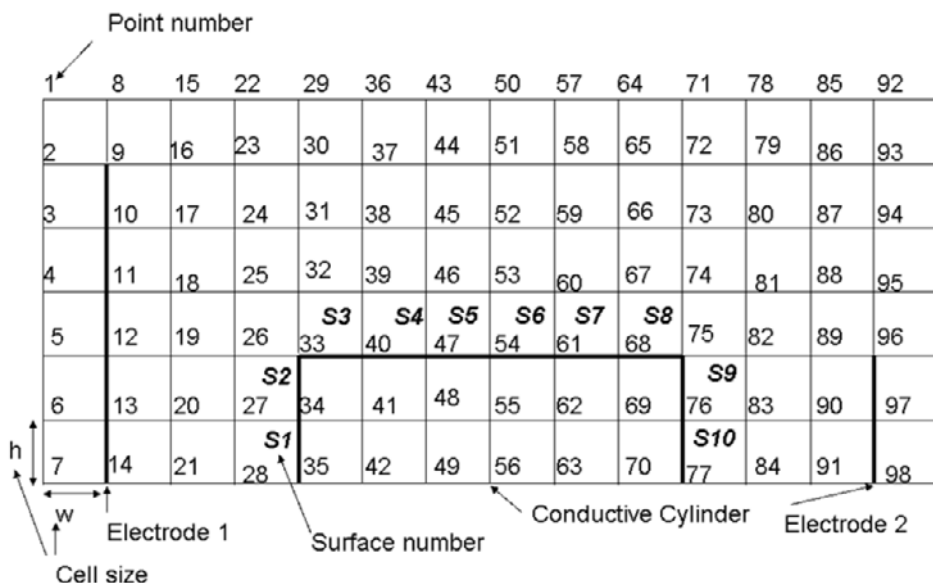


Figure 49. A design of cells (mesh) for simulating the electrostatic force that acts on a non-charged cylinder in a convergent electric field.

The mesh is usually cut over larger air space that include the simulation target, as shown in Figure 49. In the figure, a normal digit represents a lattice point number. The potential of each lattice point is calculated by the simulation. For example, the potential of lattice point 52 is calculated with the following formula from the electric potential of the four neighboring lattice points.

$$V_{52} = \frac{V_{51} + V_{53} + V_{45} + V_{59}}{4} \quad (10)$$

The same formula is used at all lattice points. For this coalition linear equation, the potential is solved using the Gaussian method of elimination from a lattice point that is already known. For example, a value of +600 V is given to lattice points 9, 10, 11, 12, 13, and 14 because electrode 1 includes lattice points 9, 10, 11, 12, 13, and 14. A value of 0 V is given to lattice points 96, 97, and 98 because electrode 2 includes these lattice points. Because the cylinder includes 21 lattice points from 33 to 77, the potential of these points are forced to be the same.

In Figure 49, the oblique digits S1 - S10 represent the ten surfaces of the cylinder. The electric field intensity, E_n , of the surface area of the cylinder is calculated using the potentials of the four corner points of the cell. For instance, the electric field intensity E_1 of surface 1 is calculated from the potential of the four points V27, V28, V34, and V35, and the width of cells, w , is determined by formula (11):

$$E_1 = \frac{(V_{27} + V_{28})/2 - (V_{34} + V_{35})/2}{w} \quad (11)$$

The surface charge density of each surface δ_n is calculated from the field intensity E_n of the surface and the vacuum permittivity ϵ_0 , using formula (12):

$$\delta_n = \epsilon_0 E_n, \quad (12)$$

The charge on each surface q_n is calculated from the surface charge density δ_n and area of the surface S_n , using formula (13):

$$q_n = \delta_n S_n, \quad (13)$$

The electrostatic force F_n acting on each surface is calculated using formula (14):

$$F_n = \frac{q_n E_n}{2} = \frac{\epsilon_0 S_n E_n^2}{2} \quad (14)$$

The above is a simple explanation of the simulation method. However, in practice, various problems can arise. The details of the simulation method are described in references [11], [12], [13].

Figure 49 shows the design of cells (mesh) used for this simulation. F_1 is the sum of the electrostatic forces that act on the left side surfaces S_1 and S_2 of this cylinder. F_2 is the sum of the electrostatic forces that act on the right side surfaces S_9 and S_{10} of this cylinder. Finally, F_3 is the sum of the electrostatic force that act on the circumference surfaces S_3 , S_4 , S_5 , S_6 , S_7 , and S_8 of this cylinder. The electrostatic force F_e that acts on the cylinder was calculated using formula (2):

$$F_e = F_1 + F_2 \quad (2)$$

The force F_3 that acts on the circumference surface of the cylinder was not included in formula (2) because it cancels out at an interval of 180 degrees and ultimately becomes zero.

Appendix 2. Relationship between the Approximate Formula for the Gradient Force and the Simulation Method of the Electrostatic Force Acting on a Non-Charged Cylinder in a Convergent Field

This axi-symmetric bi-dimensional finite difference method cannot deal with a sphere; therefore, a spherical conductor with radius r is replaced by a cylinder that envelops the spherical conductor. The radius of both side surfaces of the cylinder is r , and the width is $2r$ (see Figure 50).

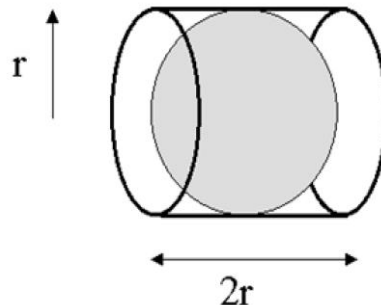


Figure 50. A spherical conductor (radius = r) and a cylinder (radius = r , width = $2r$).

The electrostatic force F_1 that acts on the left surface of the cylinder is calculated by formula (15):

$$F_1 = \frac{\epsilon_0 S_1 E_1^2}{2}, \quad (15)$$

where ϵ_0 is the vacuum permittivity, S_1 is the area of the left surface and E_1 is the field intensity on the left surface.

The electrostatic force F_2 that acts on the right surface is calculated with formula (16):

$$F_2 = \frac{\epsilon_0 S_2 E_2^2}{2}, \quad (16)$$

where ϵ_0 is the vacuum permittivity, S_2 is the area of the right surface and E_2 is the field intensity on the right surface. The magnitude of E_2 is larger than that of E_1 , because this field converges to the right.

The total electrostatic force F_e is calculated with formula (2):

$$F_e = F_1 + F_2. \quad (2)$$

The direction of F_1 is to the left (-) while that of F_2 is to the right (+), and formula (2) is transformed into formula (17),

$$F_e = -\frac{\epsilon_0 S_1 E_1^2}{2} + \frac{\epsilon_0 S_2 E_2^2}{2} \quad (17)$$

The areas of the left and right surfaces of the cylinder are the same and equal to πr^2 , so formula (17) becomes formula (18):

$$F_e = \frac{\epsilon_0 \pi r^2 (E_2^2 - E_1^2)}{2}. \quad (18)$$

The width of the cylinder w is multiplied by the denominator and the numerator in formula (18):

$$F_e = \frac{\epsilon_0 \pi r^2 w (E_2^2 - E_1^2)}{2w} . \quad (19)$$

The width of the cylinder w is equal to $2r$, and formula (19) becomes formula (20):

$$F_e = \frac{\epsilon_0 \pi r^3 (E_2^2 - E_1^2)}{w} \quad (20)$$

$(E_2^2 - E_1^2)/w$ represents the gradient of the field intensity squared at the right and left surfaces of the cylinder, so formula (20) becomes formula (21):

$$F_e = \epsilon_0 \pi r^3 \nabla E^2 \quad (21)$$

This formula is derived based on the assumption that the electric field intensity is not changed when the cylinder is placed in the electric field, but it actually becomes stronger because the electric field concentrates in the left and right surfaces of the cylinder. The concentration rate is not known, but, if it is $\sqrt{2}$, then formula (21) is transformed into formula (22):

$$F_e = 2\epsilon_0 \pi r^3 \nabla E^2 . \quad (22)$$

Formula (22) is the same as the gradient force approximate formula (1).

Therefore, the simulated electrostatic force acting on the cylinder in the convergent field must be the gradient force.

Nevertheless, the shape of the conductor is not a sphere, it is a cylinder. Therefore, I now attempt to simulate an electrostatic force acting on an analogous spherical conductor in a convergent field.

Figure 51 shows a spherical conductor (dotted line) and a piled six-disk conductor as an approximately spherical conductor.

The radius of the sphere is R , and the radius of the first left and first right disks of the piled conductor is $R/2$. The width of the piled conductor is $\sqrt{3} R$. E_{10} and E_{20} are the original electric field intensity, and E_1 and E_2 are the changed electric field intensity after the piled conductor is placed in the convergent field. The field concentration rate on the first left and first right surfaces of the piled conductor is assumed to be 3.0. It is actually about 2.7 in the simulation of the piled three-disk conductor that was described in Chapters 1-3, but considering the electrostatic force acting on the second and third surfaces of the piled conductor (see Figure 7), it is assumed to be 3.0 here.

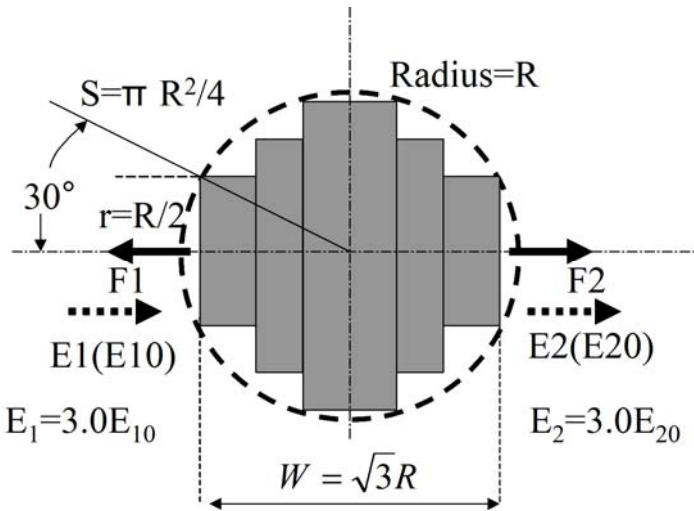


Figure 51. A spherical conductor (radius = R) and a piled six-disk conductor as an approximately spherical conductor (radius of the first left and right surfaces = R/2, width = $\sqrt{3}$ R).

Caution: As mentioned above, I assumed that the concentration rate of the electric field on the surface of the cylinder that is shown in Figure 50 is $\sqrt{2}$, but I use 3.0 here, because the radius of this cylinder is only half of that of the cylinder that is shown in Figure 50).

The electrostatic forces that act on the second left and right surfaces and on the third left and right surfaces are neglected (see Figure 7).

Therefore, the piled six-disk conductor can actually be replaced with a cylinder whose radius is R/2 and whose width is $\sqrt{3}$ R.

The electrostatic force F_e that acts on the cylinder is calculated with formula (20) with $r=R/2$, $w=\sqrt{3} R$, $E_1 = 3.0 \times E_{10}$, and $E_2 = 3.0 \times E_{20}$ are substituted into formula (20), which then becomes formula (23):

$$\begin{aligned}
 F_e &= \frac{\varepsilon_0 \pi (\frac{R}{2})^2 \sqrt{3} R ((3.0 \times E_{20})^2 - (3.0 \times E_{10})^2)}{2w} \\
 &= \frac{9\sqrt{3}\varepsilon_0\pi R^3 (E_{20}^2 - E_{10}^2)}{8w} \\
 &= \frac{1.95\varepsilon_0\pi R^3 (E_{20}^2 - E_{10}^2)}{w}.
 \end{aligned} \tag{23}$$

$(E_{20}^2 - E_{10}^2)/w$ represents the gradient of the field intensity squared at the left and right surfaces of the cylinder, and formula (23) is transformed into formula (24):

$$\begin{aligned}
 F_e &= 1.95\varepsilon_0\pi R^3 \nabla E^2 \\
 &\doteq 2\varepsilon_0\pi R^3 \nabla E^2
 \end{aligned} \tag{24}$$

Formula (24) is the same as the gradient force approximate formula (1). Of course, this is not an exact simulation of a spherical conductor. An exact simulation would require a three-dimensional simulation method. Therefore, an exact simulation of a spherical conductor is required in further work.

References

- [1] *Handbook of electrostatic (Japan)* (1998) p.1196.
- [2] K. Sakai, An overlooked electrostatic force that acts on a non-charged asymmetric conductor in a symmetric (parallel) electric field, *J. Electrostat.* **67** (2009) 67-72.
- [3] K. Sakai, An experimental result which confirm the fourth electrostatic force, *Proceedings of ESA Annual Meeting on Electrostatics 2008* (2008).
- [4] The fourth edition of physics and chemistry dictionary (Japanese), p.309.
- [5] L. B. Schein, Electrostatic Proximity force, Toner Adhesion, and a New Electrophotographic Development System, *Proc. ESA/IEJ/IEEE-IAS/SFE Joint Conference on Electrostatics 2006* 68-75.
- [6] K. Sakai, The electrostatic force that acts on the charged asymmetric conductor in normal and reverse electric fields, *Proceedings of 2009 Electrostatics Joint Conference* (2009).
- [7] *Handbook of electrostatic (Japan)* (1998) p.962.
- [8] T. Tsutsumino, Y. Suzuki, N. Kasagi, Y. Sakane, Seismic power generator using high-performance polymer electret, *Proc. Int. Conf. MEMS'06*, Jun. 2006, Istanbul, pp.98-101.
- [9] Kageyama, K., Kato, H. and Watanabe, S.: Fabrication and Evaluation of Electret Condenser Microphone using Poled Ferroelectric Ceramics, *Journal of Solid Mechanics and Materials Engineering*, *Journal of Solid Mechanics and Materials Engineering*, vol. 2, No. 7, pp 877-887 (2008).
- [10] K. Sakai, Japanese laid open patent 2010-098925.
- [11] Yasuyuki Matsubara, Improved Finite Difference Expression for Laplace's and Poisson's Equations on the Surface of Dielectrics, *J. Electrostatics Japan* **16** (1992) 440-442.
- [12] Yasuyuki Matsubara, A Guide to the Calculation of Electric Field Part III Application of the Finite Difference Method to Electric field in an Oil Tank, *J. Electrostatics Japan* **16** (1992) 530-538.
- [13] Yasuyuki Matsubara, A Method to Calculate the Potential of Ungrounded Conductors, *Proceedings of the Institute of Electrostatics Japan* (1994) 181-184.

Chapter 2

CORONA TREATMENT OF POLYMER FILMS

T.A. Yovcheva*

Department of Experimental Physics,
University of Plovdiv ‘P. Hilendarski’,
Tzar Assen Str. 24, 4000 Plovdiv, Bulgaria

Abstract

This chapter is a brief review of the investigations devoted to polymer film changes initiated by corona treatment and their possible applications. Polymer films, among which are polypropylene, polyethylene terephthalate and polytetrafluoroethylene, are most widely used as materials for the production of stable charged films. One of the simplest and most widespread methods for charging the polymers involves the use of corona discharge in air at room temperature. The corona discharge creates high energy oxygen-containing charged particles, which are accelerated by the electric field of the corona and then interact with the surface of the polymer films.

Firstly, changes in electret surfaces initiated by corona treatment, which are analyzed by XPS and an optical method, are discussed. The XPS investigations show that oxygen content in negative corona charged samples is several times higher than the ones of positive corona charged samples. The optical method of disappearing diffraction pattern is proposed to determine the surface modifications of the charged polymer films. The strongest surface modification is observed at the center of the samples and they are greatly affected by the applied corona voltage and the corona device configuration. The electric charges are mainly deposited onto the surface and do not penetrate into the sample bulk when corona charged films are formed under not very strong charging conditions (air ambient, room temperature and humidity, 5kV corona voltage).

Secondly, the influence of different treatments (low pressure and low-energy laser irradiation) on charged polymer film stability and its possible applications are discussed. The sharp surface potential decay in charged films stored under pressure lower than atmospheric down to 0.1mbar is observed. It is possible to calculate pressure at which sharp decay occurs if the initial surface potential is known. Preliminarily placing the charged films under pressure less than 1mbar can be used as a method for stabilizing the surface charge. The different surface potential decay and the relevant steady state surface potential values for charged films being under different irradiation conditions (continuous He-Ne, pulsed CuBr and quasi-

* E-mail address: temiov@uni-plovdiv.bg

continuous CO₂ lasers) are revealed. These results can find applications in optical storage and processing of information as a direct registration of information on electret films using low energy lasers.

Thirdly, the influence of corona treatment on holographic recording in photopolymer films is discussed. An additional induced polarizability, which is due to an electric charging, influences the exposure characteristics and diffraction efficiency of the holographic recordings in amorphous side-chain azobenzene polymers. The additional electric corona charging seems to be a promising method for increasing both the diffraction efficiency and the sensitivity of the azo-polymer recording media.

1. Introduction

Synthetic polymer films are widely used as materials for the production of stable charged films that are of scientific, commercial and technical interest. Corona treatment, one of the simplest and most widespread methods for polymer charging, causes surface sample changes which may be analyzed by different methods. The understanding of charged surface changes is required in different polymer film applications, such as microelectronic devices, modern optics and optoelectronics, adhesion and biomedical technology. On the other hand, for numerous applications it is very important to store electric charges for a long time under different conditions and that is why the influence of various factors, causing charge decay, must be taken into account. Therefore, the investigations of the surface sample changes and the charge stability of corona treated polymer films are motivated by both scientific and applied research interests.

2. Materials (PP, PET and PTFE)

In the last decades, synthetic polymer films have been widely used as materials for the production of stable charged films (electret state) that have found commercial and technical interest.

To store electret charges for a long time, the dielectric materials should have constant and stable properties over a large temperature and frequency range. Polymer films, among which are polyolefin polymers like polypropylene (PP) [1], polyethylene terephthalate (PET) and polytetrafluoroethylene (PTFE) [2], are the most widely used ones and have been found to be very suitable materials for this purpose.

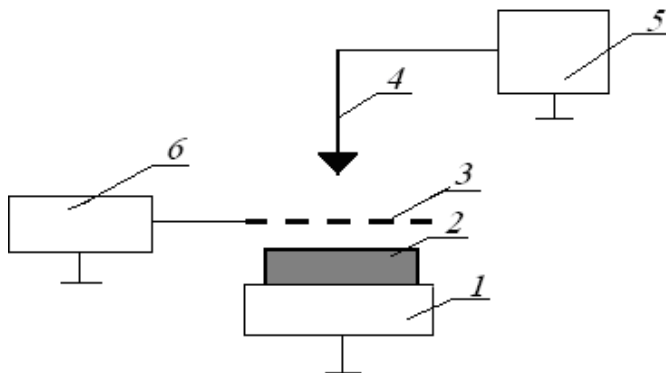
This is due to their high resistance, low cost, easy production, promising technological potentialities, low density, high mechanical and thermal stability, resistance to corrosion, low relative weight.

Nonmetalized samples of 20µm polypropylene (PP) and polytetrafluoroethylene (PTFE) films as well as nonmetalized samples of 40µm, 36% crystalline poly (ethylene terephthalate) (PET) film were studied. Initially the films were cleaned in an ultrasonic bath with alcohol for 4 minutes (2 minutes on each side), then washed in distilled water and dried on filter paper under room conditions.

3. Positive and Negative Corona Treatment

The corona treatment of the samples was carried out by one of the simplest and most widespread methods for charging the polymers [3], the method of the corona discharge using a point-to-plane three-electrode corona discharge system. The experimental set up of the system consisting of a corona electrode (needle), a grounded plate electrode and a grid placed between them is represented in Figure 1.

The distance between the grounded plate electrode and the grid was 10mm; the distance from the grid to the corona electrode was 7mm. The samples were placed on the grounded plate electrode and were charged for 1 minute under normal relative humidity of 45% and atmospheric pressure of 101.3kPa. The samples can be charged under different conditions (electrodes polarity and temperature from the range (20–100)°C. Positive or negative 5kV voltages were applied to the corona electrode. Voltages of the same polarity as that of the corona electrode were applied to the grid and their values could have been chosen from the range (350 – 1200)V. Introducing a grid between the corona electrode and sample limits the electret surface potential to that of the grid and produces a more uniform distribution of charge on the electret surface. The electret surface potential of the charged samples was measured by the vibrating electrode method with compensation [4] by which the estimated error was better than 5%.



1 - Grounded electrode; 2 - Sample; 3 – Grid; 4 - Corona electrode (needle); 5 - Power supply to the corona electrode; 6 - Power supply to the grid.

Figure 1. Experimental set up for charging the electret samples.

4. Investigation of Changes in Charged Surfaces Initiated by Corona Treatment

The corona treatment of polymer films initiates changes in the sample surfaces. The investigation of charged surface changes is necessary for different polymer film applications, such as microelectronic devices, modern optics and optoelectronics, adhesion and biomedical technology.

4.1. Analyzed by XPS

Analysis by X-ray Photoelectron Spectroscopy (XPS) provides one method for investigating changes in the physical and chemical properties of polymer surfaces after treatment in plasma [5] and corona discharge [6, 7]. The purpose of such treatments is to improve the adhesion properties of the materials, hence in treated samples, surface potential is not measured. On the other hand, in studying electret properties, only surface potential is measured, and the possible changes in surface properties are not studied. In [8], an attempt was made to use XPS analysis to find changes on the surfaces of polymer electrets. Reference [9] reports on the use of XPS to study mechanisms for charge stabilization in PTFE electrets produced in corona discharge.

In [10], XPS was used to clarify how different polarities of corona initiate various changes in the surfaces of 20 μm PP film electrets subject to corona discharge. The samples were charged in three-electrode corona discharge system (Figure 1) using positive and negative corona polarities at both temperatures – 20°C and 75°C. Studies with XPS were carried out in a VG ESCALAB Mk II ultra-vacuum chamber with electronic spectrometer under a base pressure of 1×10^{-8} Pa. Photoelectron spectra were obtained using an Al K α excitation source ($h\nu=1486.6\text{eV}$) at a total instrumental resolution of $\sim 1\text{eV}$. The spectra of C1s, O1s and N1s lines were recorded. All recorded lines were calibrated to the C1s line at 284.6eV. The surface composition of the mixed oxide layers was determined from the ratio of the corresponding peak intensities to the photo ionisation cross sections [11].

The parameters of all investigated samples groups are shown in Table 1. The initial surface potential values were measured using a vibrating electrode method with compensation. The effective surface charge density values were calculated from the following formula:

$$\sigma_{\text{eff}} = \varepsilon \cdot \varepsilon_0 \cdot V / d, \quad (1)$$

Here $d = 20\mu\text{m}$ is the sample thickness; $\varepsilon = 2.2$ is the relative permittivity of polypropylene; $\varepsilon_0 = 8.85 \times 10^{-12} \text{ F/m}$, and V is the electret surface potential.

Figures 2 and 3 respectively show the XPS spectra of C1s lines and O1s lines for the five groups listed in Table 1. The N1s lines are not shown because nitrogen was not detected in any of the samples.

Table 1. Charging parameters of the PP electret films produced in corona discharge

Group No.	Charging temperature $T, ^\circ\text{C}$	Corona voltage U_c, kV	Initial value of surface potential V_o, V	Effective surface charge density $\sigma_{\text{eff}}, \text{C/m}^2$
1	20	0	0	0
2	20	-5 kV	-740 V	7.2×10^{-4}
3	20	+5 kV	+650 V	6.3×10^{-4}
4	75	-5 kV	-730 V	7.1×10^{-4}
5	75	+5 kV	+670 V	6.5×10^{-4}

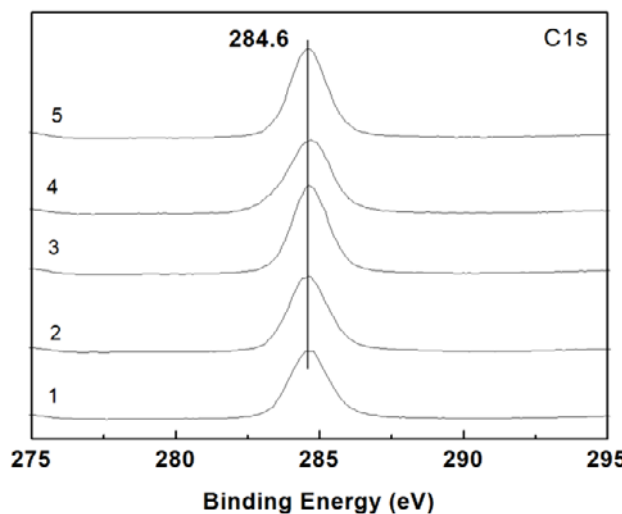


Figure 2. C1s XPS spectrum of a PP film: 1- untreated; 2 - 5 – treated by corona discharge at various voltages, see Table 1.

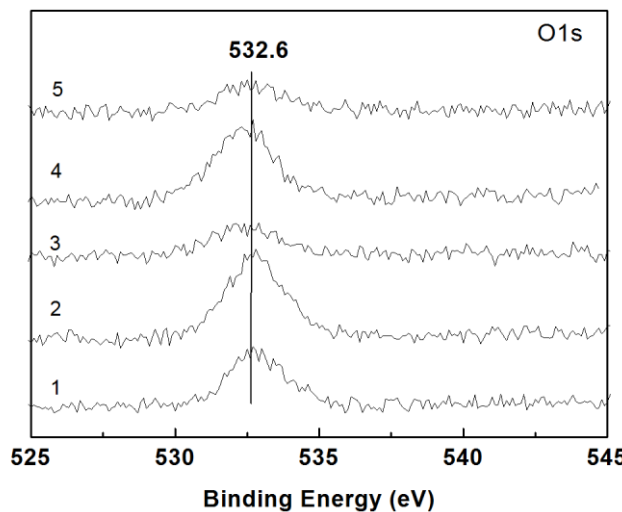


Figure 3. O1s XPS spectrum of a PP film: 1- untreated; 2 - 5 – treated by corona discharge at various voltages, see Table 1.

From the C1s and O1s peaks the atomic ratios (O/C) for all groups of samples were calculated. Some important $\frac{(O/C)_n}{(O/C)_p}$ relations of the various (O/C) atomic ratios were presented in Table 2, where the subscripts n and p respectively denote positive and negative corona polarity and the subscripts 20 and 75 represent the °C temperatures at which the electrets were charged.

Table 2. Some various (O/C) atomic ratios

$\frac{(O/C)_{20n}}{(O/C)_{20p}}$	$\frac{(O/C)_{75n}}{(O/C)_{75p}}$	$\frac{(O/C)_{20n}}{(O/C)_{75n}}$	$\frac{(O/C)_{20p}}{(O/C)_{75p}}$	$\frac{(O/C)_{20n}}{(O/C)_{ref}}$	$\frac{(O/C)_{20p}}{(O/C)_{ref}}$
2.40	2.42	1.24	1.25	1.29	0.54

The results show that oxygen content in negative corona charged samples is approximately 2.4 times higher than that of positive corona charged samples. This correlation is the same for samples charged at both 20°C and 75°C. Furthermore, the oxygen content in the negatively charged samples is 29% higher than that of the reference group; while for the positively charged samples it is 46% lower. The atomic ratios (O/C) for electrets charged at 20°C and 75°C are independent of corona polarity and have nearly the same value of about 1.245.

After samples were cleaned, rinsed in distilled water, and dried in air, it was normal to observe the presence of oxygen [atomic ratio (O/C) in the order of 0.028] in the reference group. When polymers are subjected to corona discharge in air, various ion groups initiated by the corona, deposit onto sample surfaces. The authors [12] ascertain that air corona is characterized by high concentrations of O, HO₂, H₂O₂ and O₃ groups. According to [13], if positive corona occurs in air, the prevailing ions are of the type (H₂O)_nH⁺, (H₂O)_nNO⁺ and (H₂O)_n(NO₂)⁺. If negative corona occurs in air, the most important ions are the CO₃⁻ and (H₂O)_nCO₃⁻ ions.

In negative corona, the electric field stimulates deposition of oxygen ions or oxygen-containing groups, initiated by the corona discharge in air, onto polymer surface and causes a 29% increase in the atomic ratio (O/C) in comparison with the reference group. According to [7], those functional groups deposited on the surface are polar, and hence they have a dipole moment. They can orient in the electret field and cause the observed peaks in the TSCD curves representing the temperature dependence of the surface potential for PTFE electrets [14] and PET electrets [15].

In a positive corona, the corona electric field stimulates desorption of the oxygen atoms deposited on the surfaces of untreated samples. This factor can explain the observed 46% drop in the atomic ratio (O/C) compared to the reference group.

When the charging temperature at which corona electrets are formed rises, the thermal desorption rate increases and, consequently, adsorbed oxygen is decreased. Furthermore, at the higher charging temperature, the oxygen content is expected to be just as low irrespective of its quantity at the lower charging temperature. Hence, regardless of corona polarity, the atomic ratios O/C for electrets charged at 75°C and 20°C would be approximately the same.

In XPS analysis pressure is in the order of 10⁻⁸Pa, and one can expect surface potential decay of the samples as it was shown in [16, 17]. When the pressure was lower than 10⁻²Pa for the positively charged samples the relative surface potential was 0.3 and for the negatively charged samples was 0.2. According to [18, 19], relaxation of the electret state for PP films is a surface process at insufficiently high temperatures. Hence, the decay of surface potential with pressure can be determined by the state of charges contained in surface traps. That assumption is confirmed by the good agreement between the two ratios. Specifically, the ratio

of the change in oxygen content for negatively and positively charged samples is $29\% / 46\% = 0.63$, while the ratio of surface potential values for negatively and positively charged samples in lower pressures is $0.2 / 0.3 = 0.66$.

In [12, 13] it was shown that corona discharge created charged particles that containing oxygen. It is shown in [18, 20] that if one uses these charging parameters (Table 1) the observed processes are on the surface and not in the bulk. Consequently, we could assume the presence of oxygen adsorption processes on the sample surfaces as well as oxygen desorption during the charging the samples. These processes are most probably stimulated in different ways by the positive and negative coronas, and that is the reason for the experimentally observed difference in oxygen content.

4.2. Analyzed by an Optical Method

In order to control the result of different treatment of polymer films, including corona treatment, several optical methods are used for precise refractive index (RI) measurements. A thorough review of the most applied experimental techniques is given by Meeten [21]. Generally, the methods which determined the refractive index near the surface of the polymer sample could be refractometric (critical angle), reflectometric and ellipsometric methods. Despite the fact that electret behaviour of PP films is quite intensively investigated making use of different methods [3], there are only several references [22, 23, 24] that studies the relation of the electret properties of PP films to their optical properties, and in particular to refractive index and its distribution on the charged surface. The refractive index and absorption studies have only been carried out with uncharged PP films in connection to exploring their structure and film thickness [25-27].

The refractive index measurement of polymer films with thickness less than $50\mu\text{m}$ is not very easy problem to solve. It is well known that Herschell's interference fringes make it difficult to exactly determine the critical angle in Abbe and Pulfrich refractometers [28], when sample thickness is very small. Recently, a new optical method using two wavelengths laser refractometer has been proposed for RI measurements of very small samples or microliter droplets – the method of the disappearing diffraction pattern (MDDP) [29].

In [22, 23], MDDP method was used to clarify how the corona treatment of $20\mu\text{m}$ polypropylene films changes the refractive index and its distribution on the sample surface. The refractive index was measured by a two-wavelength laser refractometer at two wavelengths of 532nm and 632.8nm. The principle scheme of the refractometric system is illustrated in Figure 4.

A sample (5) was put between the glass prism (3) and the reflecting grating (6). To ensure a good optical contact at both sides of the sample a thin layer of contact liquid having an appropriate refractive index was coated – benzyl alcohol – $n_r(632.8\text{nm}) = 1.5374$, $n_g(532\text{nm}) = 1.5449$. It is necessary matching liquid's RI to be higher than measured sample's RI.

The angle of the incident laser beam (1) from the lasers (L1) or (L2) on the prism's side wall was denoted as α . That angle α changed whenever the rotary stage (2), where the prism with the sample and the reflecting grating were firmly fixed, rotated. At a certain incidence angle α , the laser beam refracted consecutively by the prism (3), the liquid layer (4'), the

sample (5), the liquid layer (4") and reached the reflection grating (6). A diffraction pattern was observed on screen (7) (beam path (a) as shown in Figure 4).

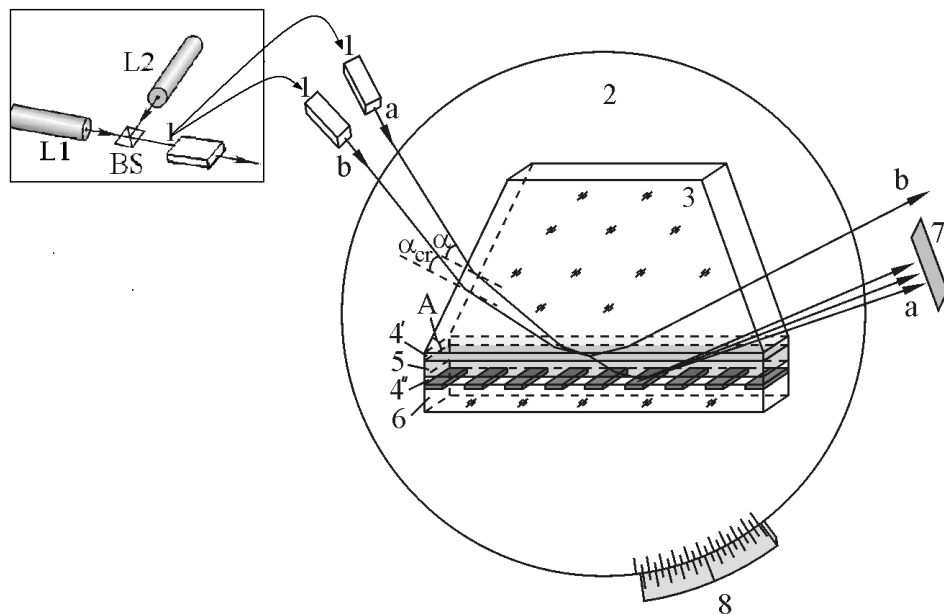


Figure 4. Experimental set-up: (BS) - beam splitter; (L1) - 532nm laser; (L2) - 632.8nm laser; (1)-incident laser beam; (2) - rotary stage with 1 arcmin resolution; (3) - glass prism with RI =N; (4'), (4")-liquid layer, (5) - sample; (6) reflection metal grating; (7) - screen; (8) - vernier.

If the angle α was reduced to a certain critical value α_{cr} a total internal reflection (TIR) occurred at the liquid (4') – sample (5) interface. Hence, the laser beam did not reach the reflection grating and a diffraction pattern was not observed on the screen (beam path (b) as shown in Figure 4). The position of the rotary stage, at which the diffraction pattern disappeared from the screen, was fixed. Then the graduated circle with a vernier (8) was used to measure the critical angle α_{cr} . Knowing α_{cr} the sample RI could be calculated by the following relation:

$$n = N \sin \left[A \pm \arcsin \frac{\sin \alpha_{\text{cr}}}{N} \right] \quad (2)$$

where A and N are respectively the prism refractive angle and a refractive index. In this experiment $A = 65^\circ$, N (532nm) = 1.7480, N (632.8nm) = 1.7347. The sign (+) and (-) correspond to clockwise and counter-clockwise determination of α_{cr} , respectively. The experimental uncertainty was $\Delta n_s = \pm 5 \times 10^{-4}$, mainly depending on the used rotary stage with 1 arcmin resolution.

For investigation of corona changes initiated in refractive index 20 μm polypropylene films were charged in a three-electrode corona discharge system (Figure 1). The samples were divided into 10 groups according to their charging conditions (corona polarity, grid voltage). A group of reference samples – samples that were not corona charged – was measured too.

Six samples from each of the groups were studied. Initial surface potential V_0 and critical angle α_{cr} were measured for each one of the samples, and α_{cr} values were used to calculate RI by the formula (2). Table 3 represents the experimental data.

Table 3. The experimental data for the RI and the initial surface potential

$IU_g I$ V	Group	V_0 (V)	n_g /532nm/	n_r /632.8nm/
0	Ref.	0	1.5078	1.5056
350	1.1	-259	1.5157	1.5120
500	1.2	-371	1.5159	1.5123
650	1.3	-488	1.5152	1.5117
800	1.4	-593	1.5152	1.5117
1000	1.5	-737	1.5157	1.5120
350	2.1	+270	1.5159	1.5126
500	2.2	+340	1.5152	1.5121
650	2.3	+476	1.5159	1.5126
800	2.4	+542	1.5149	1.5118
1000	2.5	+733	1.5155	1.5123

The results obtained showed that the RI values for the uncharged samples were lower than those for the electret samples. The electret samples RI did not depend on corona polarity and surface potential values. The average RI values of the electrets sample were 1.5154 for $\lambda = 532$ nm and 1.5122 for $\lambda = 632.8$ nm.

An additional experiment was carried out in order to determine the contact liquid influence on electret sample charge. It was observed that if electret samples were coated by benzyl alcohol, surface potential rapidly decreased after 1 minute to a very low value (10V – 15V) that did not depend on initial surface potential.

Material refractive index is connected to material polarizability and in its turn it depends on the availability of free and bound charges. When samples are corona charged at various grid voltages different quantities of electrical charges are injected into the samples, so that the values of the measured initial surface potential V_0 are different (Table 3). Therefore, different RI values for the different electret groups should be expected. Experimental results, however, showed that for all measured electret samples RI were the same.

In order to clarify this contradiction the following assumptions were made:

- A. In the case of PP corona electrets almost the whole amount of the electric charge is deposited on sample surfaces, and only a small part of the charge is injected into a certain depth of the bulk. Such charge distribution was reported for negatively charged 50 μ m PP corona electrets using the LIPP and TSC methods [19].
- B. When samples are coated by benzyl alcohol for 1 minute, their surface charge is removed. Furthermore, the charge that is injected into the volume does not change as benzyl alcohol cannot penetrate into the samples. The fast surface potential discharge is caused by the great difference in volume resistivity values for PP films ($\sim 10^{17}$ Ohm.m) and benzyl alcohol ($\sim 10^7$ Ohm.m). That assumption agrees well with [19]

where it was found that negatively charged 50 μm PP films got their surface charge removed for just 1 second when dipped in ethanol.

If surface potential is measured by the vibrating electrode method, one registers both surface charge and volume charge. But, the measured surface potential for electrets that have previously been coated by benzyl alcohol is only due to the injected charge trapped in electret bulk. In order to give an account of the influence of those volume charges in the measurements of refractive index by the MDDP method a laser irradiation penetration depth into the sample was calculated.

The “penetration depth” d_p is defined as a distance in the second medium (with lower RI), where the amplitude of the evanescent wave, created by the total internal reflection diminishes 1/e times (~ 0.368) and strongly depends on the wave’s polarization. In fact, the penetration depth near critical angle α_{cr} is connected with the longitudinal Goos-Hanchen shift – D [30]. For s-polarized wave with wavelength λ_0 and incidence angle α , it could be written:

$$d_p = \frac{\lambda_0}{2\pi N \sqrt{\sin^2 \alpha - \sin^2 \alpha_{cr}}} \quad (3)$$

where N is the prism refractive index.

The value of d_p was calculated to be 0.98 μm for $\lambda_0 = 0.633 \mu\text{m}$ and 0.82 μm for $\lambda_0 = 0.532 \mu\text{m}$ [22]. It was found out in [19] that volume injected charge was at 7 μm from the negatively charged surface of a 50 μm PP corona electret. Therefore, the laser irradiation penetration depth was smaller than the depth of the volume injected charges and when RI was measured the influence of the volume injected charge was not taken into account. Electret surface charge did not influence RI measurements too, as it was removed by benzyl alcohol coating. Nevertheless, RI for the electret samples was higher than RI for the reference uncharged samples and did not depend on surface potential value and polarity. Most probably that was due to structural changes of electret surfaces that occurred at the time of corona charging. Those could be broken or newly formed bonds, generated specific surface defects, additionally captured oxygen containing groups etc. [7, 13].

A modified optical two dimensional (2D) - laser micro-refractometer set-up was proposed for the investigation of refractive index (RI) distribution on the surface of 20 μm thick polypropylene film electrets, and by this distribution one can judge about the surface modification. The RI was measured at 35 points (7 x 5) – at five horizontal rows with 4mm distance between them, at seven different points at a 5mm distance for each row.

The electret samples were divided into 4 groups according to their charging conditions (corona device configurations and corona voltage supply U_c):

Group 1 - The point-grid three-electrode system (Figure 1); $U_c = 5\text{kV}$.

Group 2 - The point-grid three-electrode system (Figure 1); $U_c = 10\text{kV}$.

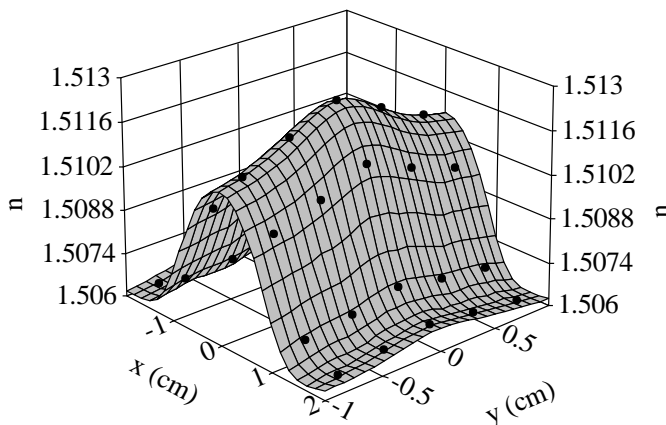
Group 3 - The point-to-plane two-electrode system (Figure 1 without the grid); $U_c = 5\text{kV}$.

Group 4 - The point-to-plane two-electrode system (Figure 1 without the grid); $U_c = 10\text{kV}$.

The experimental results were represented in Table 4. Figures 5 - 6 represent the experimental data as 3D plots for Group 1 and 3. The surface refractive index distribution for Group 2 is the same as the one for Group 1, however, the values of Group 2 are higher than the ones of Group 1. The surface refractive index distribution for Group 4 is the same as the one for Group 3, however, the values of Group 4 are higher than the ones of Group 3.

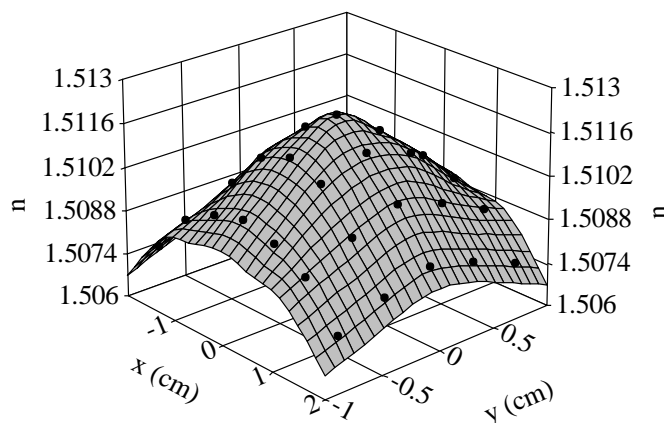
Table 4. Extreme refractive index values

n	Group				
	1	2	3	4	Ref.
n_{\max}	1.5124	1.5149	1.5121	1.5141	1.5056
n_{\min}	1.5064	1.5080	1.5075	1.5095	1.5056



Average initial surface potential: $V_0=910V$.

Figure 5. The surface refractive index distribution for Group 1.



Average initial surface potential: $V_0=1.4kV$.

Figure 6. The surface refractive index distribution for Group 3.

The surface refractive index distribution for the uncharged $20\mu m$, PP film was uniform; while for all the samples treated by the corona discharge method was not uniform. Electret

surface charge did not influence RI measurements too, as it was removed by benzyl alcohol coating used as matching liquid.

This was an indication that during corona charging some structural changes of surface occurred and depended on charging conditions.

For all the studied PP film electrets the RI values were highest in the sample center, just under the tip of the corona needle, and lowest – in the points that were outermost with reference to the center (Table 4). Consequently, the strongest surface modification was observed at the center of the electret samples. On one hand, that could be due to the fact that initially (within the first several seconds) corona was ignited straight under the corona electrode and charge injection took place in the center of the charged zone, where the initial potential was higher [31]. Besides, ionic wind was caused by the migration of ions in the corona discharge field [32]. The pressure of the ionic wind and the axial velocity of charged particles were high at the center of the samples [33].

The surface refractive index distribution for the polymer film electrets was greatly affected by the applied corona voltage as well as by the corona device configuration.

The results of the surface refractive index distribution for the electrets, obtained by the different corona device configuration at the same applied corona voltage, showed that the maximum values for RI did not differ from each other within the limits of the error.

The RI was high when high voltage was applied and the surface refractive index distribution was sharp at the centre, irrespective of the corona device configurations. The differences between the maximum and minimum RI values were greater for samples charged in a point-grid three-electrode set-up, where the grid played a restrictive role. After a sample was charged to the grid potential value, the charges did not reach the sample. When we used a point-to-plane set-up there was not a restricting element and during the whole corona charging process the charges reached the sample and caused some structural changes. This was probably the reason for the measured higher minimum RI values for samples charged in a point-to-plane set-up.

The surface RI investigations by the MDDP method were not influenced by the electret surface charge, because it was removed by benzyl alcohol coating during the measurements. Therefore, the corona treatment changes of the refractive index and its distribution on the sample surface were most probably due to structural changes of electret surfaces that occurred at the time of corona charging. Hence, the MDDP method used to measure RI in transparent polymer films can be used to determine their former history, i.e. to find out if surface modifications have occurred at a submicrometer depth, caused by ageing or various influences – charging in electric field, heating, mechanical deformation, irradiation by various beams, etc.

5. Influence of Different Treatment on Charged Films Stability

The influence of different factors on charge decay has been studied in order to obtain stable electrets for numerous applications. The various factors that influence electret charge decay, including humidity [18, 20], pressure [16, 17, 20], corona polarity [14, 34], gaseous media [35-37], and laser irradiation [38, 39] have been studied. However, the influence of low pressure and laser irradiation on charge decay of electrets has been insufficiently investigated.

5.1. Storage at Pressure Lower Than Atmospheric

Despite the studying of the influence of many factors on the electret behaviour, only a few publications are devoted to the influence of low pressure on charge decay of electrets [16, 17, 20, 40, 41]. Two models are proposed for explaining the pressure effect. The first one assumes that charge decay is a result of sparking breakdown in air [20, 41]. In the second one it is assumed that charge decay is due to desorption of ions from electret surface [16, 17, 40].

Recently, the pressure influence on PP, PTFE and PET films charged in positive and negative coronas were studied in [42, 43]. All the 30mm diameter samples were put onto the same diameter metal pads. Charging of the samples was performed under room conditions in a three-electrode corona discharge system (Figure 1). After charging, the initial surface potential V_0 was measured. Then the samples, together with their metal pads, were placed into a vacuum chamber, consisting of isolated bases and a jar bell, under a low pressure for 1hour. The pressures p created in the chamber were 0.1mbar, 1mbar, 10mbar, 20mbar, 66mbar, 132mbar or 1000mbar. After the samples and their metal pads were removed from the vacuum chamber surface potential V was measured again and normalized surface potential V/V_0 was calculated. The dependence of surface potential on electret storage pressure was investigated for five groups of samples: two of PP samples (respectively charged in a positive or in a negative corona), two of PTFE samples (charged in a positive or in a negative corona) and one of PET samples (charged in a negative corona). Each sample group was subdivided into five sets of samples and each set was charged to one of the following initial surface potentials V_0 : 350V, 500V, 650V, 800V and 950V respectively.

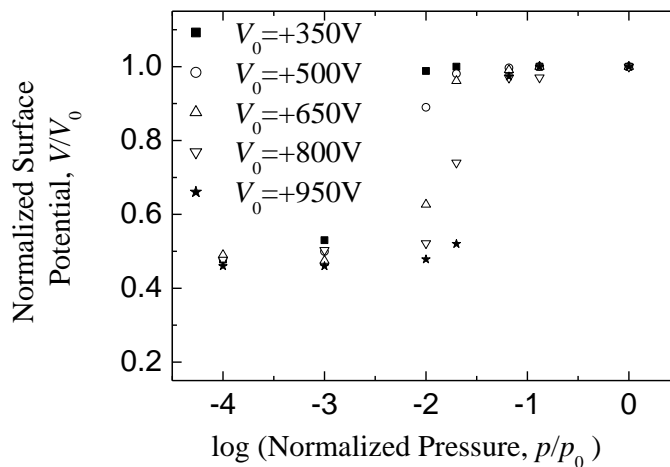


Figure 7. Dependence of the surface potential on pressure for PTFE films positively charged to different initial surface potential V_0 .

The dependences of normalized surface potential V/V_0 on normalized pressure p/p_0 for all samples are drawn and have similar behaviour. The dependences of the surface potential on pressure for PTFE films positively charged to different initial surface potential V_0 are presented in Figure 7. V_0 denotes the initial value of surface potential measured just after charging the electrets, and p_0 is the atmospheric pressure. Each point in the figure is a mean

value from six samples. The calculated standard deviation was better than 10% from the mean value with confidence level 90%.

The experimental results obtained show the following features:

- Three parts are observed in each curve. At higher pressures the surface potential is constant and equals initial surface potential. For each curve a relatively narrow region of pressures exists where a sharp decay of surface potential occurs. At lower pressures the surface potential is also constant but has different values for the different cases.
- The higher the initial surface potential, the higher the pressure at which the sharp decay occurs. Hence, the potential sharply decay region is shifted to the lower pressures when the initial surface potential value decreases. This feature holds for all samples.
- The final values of surface potential at low pressures for the samples charged in a positive corona are higher than those for the samples charged in a negative corona for both PP and PTFE samples.
- The final values of surface potential at low pressures are higher for the PTFE electrets than those for the PP electrets irrespective of the corona polarity.
- The final values of surface potential at low pressures for negatively charged samples are the highest for the PET electrets.

The results obtained show that two factors influence electrets' surface potential decay – the pressure p at which electrets were kept and the initial surface potential V_0 . Besides, the higher initial surface potential, the higher the pressure at which sharp decay occurs. Therefore, the ratio p/V_0 is the main factor determining surface potential sharp decay region. Thus for each group of experiments only one generalized curve can be drawn to represent the dependence of normalized surface potential on the ratio p/V_0 . Such generalized curves for all groups of experiments with the coefficient of determination $R^2 = 0.98$ are drawn and have similar behavior.

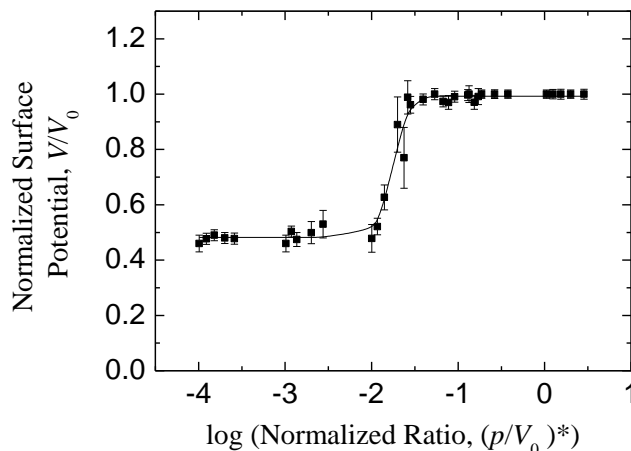


Figure 8. Generalized curve for positively charged PTFE films drawn by fitting the data of figure 7 to equation (4).

In Figure 8 the dependence of normalized surface potential V/V_0 on normalized ratio $(p/V_0)^* = (p/V_0)/(p_0/V_0^*)$, where p_0 is atmospheric pressure and $V_0^* = 1000\text{ V}$, for positively charged PTFE films are represented. The error bars mark the confidence intervals for the mean values with confidence level 90%. One can see that the error bars are shortest in the first section where the ratio p/V_0 has higher values and largest in the sharp decay region.

The experimental results are well described by the following equation:

$$\frac{V}{V_0} = a + \frac{b}{2} \left(1 + \operatorname{erf} \left(\frac{x-c}{\sqrt{2d}} \right) \right) \quad (4),$$

where V/V_0 is normalized surface potential, $x = \log(p/V_0)^*$ and a, b, c and d are parameters. Equation (4) is analogous to the equation in [44] that described linear desorption accompanied by surface diffusion. Equation (4) can be analysed if the $\operatorname{erf} \left(\frac{x-c}{\sqrt{2d}} \right)$ values for various cases are used [45].

If $x \gg c + \sqrt{2d}$, $\frac{V}{V_0} = a + b$; if $x \ll c - \sqrt{2d}$, $\frac{V}{V_0} = a$. Therefore, the parameter a has the meaning of a minimum value of the normalized surface potential; b is the difference between the maximum and minimum values of the normalized surface potential.

If $x = c$, $\operatorname{erf} \left(\frac{x-c}{\sqrt{2d}} \right) = 0$ and $\frac{V}{V_0} = a + \frac{b}{2}$, i.e. c is the midpoint of the range within which sharp surface potential decay occurs.

Using the values of the parameters the minimum value of the normalized surface potential - $(V/V_0)_{\min}$ and the values of the ratio (p/V_0) for the midpoint of surface potential sharp decay range - $(p/V_0)_{\text{mp}}$ were calculated and presented in Table 5. These values for PET, PP and PTFE are of the same order and differ for different sample materials. Thus, the midpoint ratio $(p/V_0)_{\text{mp}}$ of sharp decay range enables one to calculate pressure at which sharp decay will occur if the initial surface potential is known for different materials.

Table 5. Some important values

Sample	Corona polarity	$(V/V_0)_{\min}$	$(p/V_0)_{\text{mp}}$ [mbar/V]
PP	Positive	0.30 ± 0.02	0.019
	Negative	0.20 ± 0.01	0.024
PTFE	Positive	0.49 ± 0.02	0.020
	Negative	0.26 ± 0.01	0.022
PET	Negative	0.39 ± 0.02	0.019

The surface potential decay as a function of pressure could be due to spark breakdown of the air. During the spark breakdown process an electrical charge of opposite sign to the electret surface charge will be deposited on the electret surface. This process continues until the external field of electret is reduced to below the minimum sparking potential. In this case the surface potential decay should not be dependent on the sign of the surface charge (positive or negative), and the material of which electrets have been made. However, the results obtained show that the charge decay is different for different signs of the surface charge and for the different materials (PP, PTFE and PET). Hence, it seems that the surface potential decay is not caused by a spark breakdown process.

The samples were corona charged and the injected charges are trapped into charge traps of various depths in the thin surface layer [19, 46]. When placing such kinds of electrets under conditions of low pressure, liberation of trapped surface charges, stimulated by the electret own electric field, is quite likely to occur. When the surface charge is uniformly distributed over the surface of a round sample, the potential of the outer circumference of the sample will be less than that at the central part. Consequently, the electric field will have a component on the electret surface, pointing outwards. This field component will cause a charge drift along the sample surface. This fact has been previously substantiated and it has been shown that the creation of a certain mechanical relief on the electret surface [47] or production of electrets with island surface charge distribution [48] impedes the decay of the charge and increases the stability of the electrets. Hence, the surface potential decay seems to be due to liberation of trapped surface charges and a charge drift along the electret surface.

In further experiments the electret surface potential on the time of storage under room conditions for negatively charged PET films were studied for a month for two sets of samples [43]. For the first set the electrets were stored under room conditions after their production and for the second one they were preliminary placed under a pressure of 0.1mbar for 30 minutes. The dependences of normalized surface potential on the time of storage under room conditions are represented in Figure 9. The error bars mark the confidence intervals for the mean values with 90% confidence level.

Curve 1 corresponds to the electrets which were stored under room conditions after producing. Curve 2 corresponds to the samples which were placed after producing for 30 minutes under a low pressure of 0.1mbar. The surface potential measured just after removal of the electrets from the vacuum chamber is assumed to be the initial value. It can be seen that the electrets, which preliminary have been placed under low pressure, are more stable.

As it could be seen from Figure 9, the surface potential for the electrets preliminary kept at 0.1 mbar holds the same value for a month under room conditions. At the same time the surface potential decreases with time for samples which were not preliminary kept at low pressure. According to [46] phenolic – OH, carbonyl and carboxyl acid (COOH) have been identified as the functional groups incorporated onto the surface and low-molecular-weight oxidized materials have been also observed in the form of a globular morphology on the surface of the PET film electrets.

Hence, charge traps of different depths were available on the electret surface. When the electrets were kept under low pressure liberation of charges from shallow traps occurred and no charge detrapping was observed during subsequent keeping under room conditions. The TSC spectra showed a low temperature peak that was believed to be due to a charge released from the shallow traps [43]. The calculation of activation energies by the initial rise method confirmed the assumption that under low pressure charge detrapping from shallow traps

occurred and the mean activation energy was increased. Therefore, placing the electrets initially under low pressure for one hour can be used as a method for stabilizing the electret charges.

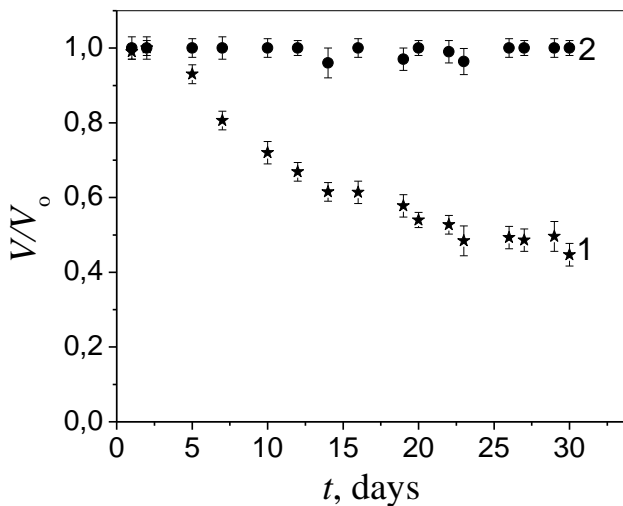


Figure 9. Time dependence of surface potential for negatively charged PET films.

In conclusion, it can be announced that knowing the dependence of the surface potential on pressure for polymer film of a definite material gives the possibility to determine the pressure at which sharp decay will occur if the initial surface potential is known. Furthermore, preliminary placing the electrets under pressure less than 1 mbar can be used as a method for stabilizing the electret charge.

5.2. Irradiation by a Low Energy Laser

Despite that a number of studies are devoted to the effect of various irradiations on polyolefin polymers so far little research has been reported on the influence of visible and infrared laser radiation on polymers [39, 49]. The study of the interaction of low energy laser radiation with polymer electret films is motivated not only by scientific but also by applied research interests. Theoretically, compared to traditional computers, the optical computer has a number of advantages in the processing, storage and distribution of information data.

A system for information storage and retrieval on dielectric materials using the selective formation of electret locations by modulated laser beams has been considered [50]. A reading system establishes the presence or absence of an electric field created by the stored charge on the electret locations in the dielectric tape. In [51], electrets with a suitable charge density and long lifetime for the fabrication of electret floppy disks for digital storage of information have been studied. It has been shown in [38] that CO₂ laser radiation allows direct laser writing of mid-infrared microstructures on polyethylene. The bonding of non-polar polymer films (PE, PP) to various polymer substrates is a problem, and needs costly preliminary treatment. In [39], an alternative tunable CO₂ laser processing of the polypropylene substrate is suggested, which improves its adhesive properties.

In [52-54], it has been investigated the influence of low energy laser radiation on 20 μm PP electret films. Three lasers have been used for the irradiation: a continuous wave He-Ne laser (632.8nm wavelength; 20mW output power), a pulsed copper vapor (Cu-Br) laser (510.5nm and 578nm wavelengths; 300mW average output power) and a quasi-continuous wave CO₂ laser (10.6 μm wavelength; 4W average output power) were used in the experiments.

Circularly shaped samples were cut out from the PP film and placed in a special holder, ensuring the same surface during charging, irradiation and measurement, which coincided with the laser beam cross-section, having a circular shape 8mm in diameter.

Samples of polypropylene were initially charged in a point-to-plane corona discharge system (Figure 1) using positive and negative corona polarities and $\pm 1\text{kV}$ grid voltage at 20°C temperature. Then they were irradiated by low energy laser for different time intervals. The surface potential was measured before (V_0) and after (V_{irr}) irradiation and the relative surface potential V_{irr}/V_0 was calculated, and each result was averaged over five measurements. Finally, V_{irr}/V_0 was plotted versus the cumulative energy E . The experimental dependencies of the electret surface potential versus irradiation energy of the CO₂ and the CuBr vapor laser are shown in Figure 10. Mark bars show the 90% confidential level for the average values of the relative surface potential.

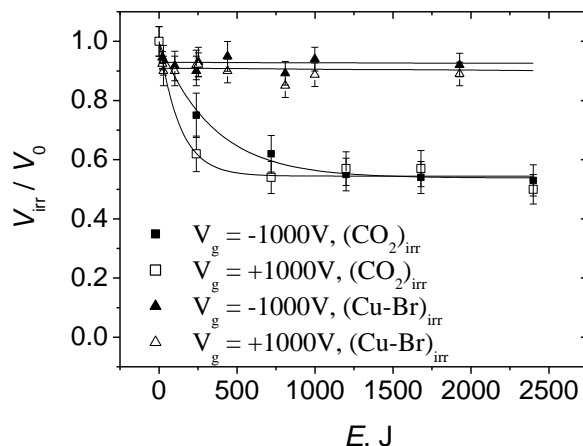


Figure 10. Dependence of the V_{irr}/V_0 on the radiation energy, CL = 90%.

The dependencies of the relative surface potential V_{irr}/V_0 of PP coronoelectrets, irradiated by He-Ne and Cu-Br lasers, show a similar behaviour. The V_{irr}/V_0 values drop slightly and remain constant within the investigated ranges independently of the corona polarity. The relative surface potential slightly drops to 0.95 at very low energy levels (~10J) and practically remains unchanged for energy values up to 122J in the case of He-Ne laser irradiation.

A weak drop of V_{irr}/V_0 values to 0.9 is observed at low energy level (~150J) which remains constant for irradiation energies up to 2000J in the case of Cu-Br laser irradiation.

The steady state level of the V_{irr}/V_0 values in the case of the Cu-Br laser is slightly lower than that of the He-Ne laser which implies that higher energy photons of the green copper

laser cause a larger drop in the relative surface potential than lower energy photons of the red He-Ne laser.

It follows that on irradiation with low energy He-Ne and Cu-Br laser light the relative potential of coronoelectrets is determined by the photon energy. This opens new perspectives in the search and development of new materials and technologies for laser registration of digital information

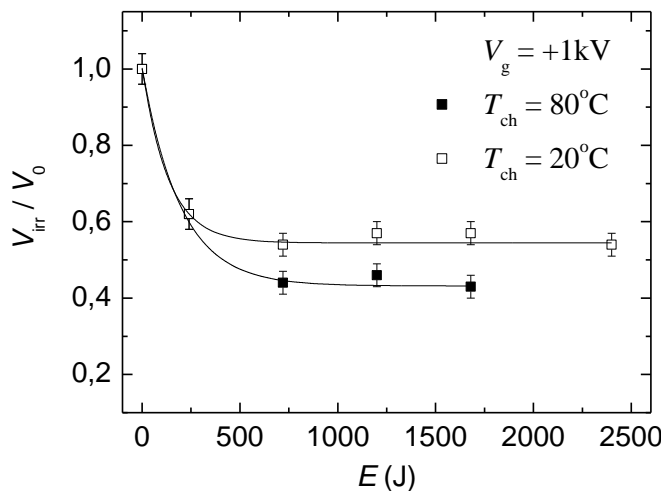


Figure 11. Dependence of the relative surface potential of positive PP electret samples on the energy of CO₂ laser radiation.

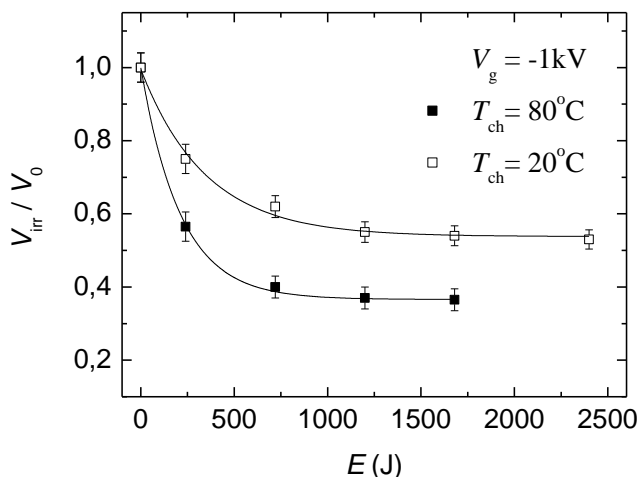


Figure 12. Dependence of the relative surface potential of negative PP electret samples on the energy of CO₂ laser radiation.

The behaviour is different when PP corona electrets are irradiated with CO₂ laser (energy levels up to 2400J) (Figure 10). It has been found that in this case the surface potential V_{irr}/V_0 drops exponentially with the irradiation energy E . For more detail investigation of this behaviour the samples charged at two different temperatures (T_{ch}): 20°C and 80°C are

studied. Figure 11 and Figure 12 show the experimental dependences. The error bars show the 90% confidence intervals for the average values of the relative potential.

The experimental results show that the relative surface potential V_{irr}/V_0 drops with the cumulative irradiation energy, following an exponential curve independently of the polarity and temperature of the charging. The samples reach a steady state level of the relative surface potential $(V_{\text{irr}}/V_0)_{\text{st}}$ at different cumulative energies E_{st} dependently of the corona polarity and the charging temperature (Table 6).

Table 6. Steady state values

Charging conditions			Steady state level	
No	V_g , (kV)	T_{ch} , (°C)	E_{st} , (J)	$(V_{\text{irr}}/V_0)_{\text{st}}$
1	+1	20	750	0.54
2	-1	20	1000	0.54
3	+1	80	750	0.43
4	-1	80	1000	0.37

The results obtained show that electrets charged in a negative corona have reached the steady state level $(V_{\text{irr}}/V_0)_{\text{st}}$ at greater cumulative energies of about 1000J. Lower values for $(V_{\text{irr}}/V_0)_{\text{st}}$ have been found for the samples charged at a higher temperature (80°C), compared to those for the electrets charged at 20°C, independently of the corona polarity.

It could be assumed that the observed behaviour is explained by the consecutive occurrence of two processes: adsorption of oxygen containing ions or ion groups during the corona discharge, and laser thermo-desorption during CO₂ laser irradiation, which depends on the cumulative energy of the laser radiation.

The corona discharge creates high energy charged oxygen-containing particles like ions and ion groups [13]. These particles are accelerated by the electric field of the corona and interact with the surface of the PP. Depending on the type of interaction; it was observed physical or chemical adsorption of charged particles, which determines the surface potential of the resulting electret.

Upon laser irradiation of the PP electret samples, the opposite process - desorption - can occur on the surface, as a result of energy interactions. Since this is stimulated by the laser radiation, it is called laser desorption [55]. It has been shown [39] that when PP films are irradiated with a CO₂ laser, resonance absorption of coherent light takes place and a strong thermal effect is observed, rather than an optical one. In this case, it could be talked about laser thermodesorption of the charged particles from the electret surface, which causes the reduction in its surface potential. This assumption is confirmed by the experimentally obtained dependencies of the relative surface potential on the irradiation energy (Figure 11 and Figure 12).

For PP coronoelectrets irradiated by CO₂ laser, the experimental results fitted very well to an exponential dependence of the type:

$$y = y_{\infty} + (1 - y_{\infty}) \exp\left(-\frac{E}{E_{\infty}}\right) \quad (5)$$

where $y = V_{\text{irr}}/V_0$ is the relative surface potential, $y_\infty = (V_{\text{irr}}/V_0)_{\text{st}}$ is the steady state level which is reached for $E \gg E_\infty$ and E_∞ is a constant characterizing the process.

Equation (5) is analogous to an equation characterizing the kinetics of adsorption-desorption processes [55].

In our case, these processes are not parallel but in series. Firstly, during the corona discharge, an adsorption takes place, as a result of which the accumulated surface charge determines V_0 at $E = 0$. Subsequently, laser thermo-desorption, depending on the irradiation energy, takes place upon CO₂ laser irradiation, and its development is described by the second term in equation (5). Above a certain value of the energy ($E \gg E_\infty$), the quantity of desorbed particles remains the same. At that point, the steady state level of the relative potential y_∞ can be determined.

XPS studies have been carried out for irradiated and non-irradiated samples to proof the thermo-desorption process during CO₂ laser irradiation. For all irradiated samples, it was observed a decrease of the O/C atomic ratio, which shows a decrease of the quantity of oxygen. As all charged groups of particles creating the electric charge are oxygen-containing [13], this implies a reduction of the relative surface potential V_{irr}/V_0 , as observed experimentally.

The lower steady state values found for the samples charged at a higher temperature (80°C), compared to those for the electrets charged at 20°C may be due to the more intensive thermo-desorption process during CO₂ laser irradiation, which is made easier by the modification of the surface upon charging at a higher temperature.

The different steady state levels for PP electrets obtained under different conditions after being irradiated with a CO₂ laser can find applications in optical storage and the processing of information on PP films, as for example the direct registration of information on PP electret films using a low energy CO₂ laser.

On the other hand, the relative surface potential for PP electrets irradiated with a laser He-Ne or a Cu Br laser does not change significantly. Hence those lasers can be used to read the information stored by the electrostatic field.

Low-energy semiconductor lasers which are characterized by small dimensions and low power consumption are the most economically advantageous to read stored information. It could be supposed that their effect on the surface potential of coronoelectrets will be similar to that of the above used lasers.

6. The Corona Treatment Influence on Holographic Recording

The influence of corona treatment on holographic recording in different media is discussed. An additional induced polarizability, which is due to an electric charging, influences the exposure characteristics, surface relief increasing and diffraction efficiency of the holographic recordings.

Glassy chalcogenide semiconductors have been widely used as holographic media for many years. Writing of holographic interference gratings on thin-film metal-semiconductor structures was carried out simultaneously with their charging in the corona field 10⁴ – 10⁶ V/cm. [56]. Initiation of a corona at the stage of interference grating recording is shown to improve the exposure contrast of metal-glassy chalcogenide semiconductor thin-film

structures, as well as the holographic sensitivity, diffraction efficiency, dynamic range, and contrast are also improved several times. In work [57] the formation of holographic gratings in an organic molecular glass for the simple case of an intensity grating in the s-polarization of the recording beams is investigated. An additional electrical corona field perpendicular to the sample leads to a magnification of the relief pattern and the relief gratings turned out to be stable in the long term, which is an important requirement in optoelectronic devices.

Azo-polymers are also very attractive holographic recording media and have been investigated in details twenty years ago [58, 59]. Up till now, the continuous interest in this area is based on the unique possibility to obtain significant change of the holographic characteristics by relatively easy change of polymer structure. It should be mentioned, that the photoinduced structural changes are manifested not only in the volume, but also on the surface, where fine surface relief has been observed [60, 61]. On the other side, it is well known that the polymer's surface relief of the thermoplastic holographic recording medium [62] is obtained by corona discharge treatment. In [63] it is shown that to obtain the maximum diffraction efficiency and the minimum noise level for a grating recorded in a photothermoplastic media, it is necessary to increase the potential of the corona-forming electrode with decreasing thickness of the thermoplastic layer. The main disadvantages of these materials are low spatial resolution (about 1000mm^{-1}), low sensitivity and relatively complicated production technology. It will be interesting to verify if additional induced polarizability due to electric charging will influence the exposure characteristics and diffraction efficiency of the holographic recordings in amorphous side-chain azobenzene polymers. The work [64] is devoted to the experimental verification of that idea.

Two types of azodyepolymers with chromophores in the side polymer chain were synthesized and investigated [64]:

- Type 1: Homopolymer from 4-acriloil-4'- cianoazobenzil - monomer (1).
- Type 2: Co-polymer with composition monomer 1 and methylmethacrylate (MMA) - in proportion 1:1.

The synthesis proceeded in three stages:

1. Azodye 4-(4-Hydroxylazo) benzonitrile (A) was synthesized by diazotation of 4-aminobenzenonitrile and coupling with phenol using standard technology.
2. Esterification between the dye (A) and acryloyl chloride led to the azodye monomer (1).
3. Monomers were polymerized by a free type radical polymerization in a dioxane solution using $\alpha\alpha'$ -azobisisobutironitrile as an initiator.

The polymerization of monomer (1) led to obtaining a homopolymer 1 (type 1) and copolymerization between MMA (Merck) and monomer (1) in proportion 1:1 led to polymer type 2.

Films with good optical quality and $7\mu\text{m}$ thickness have been obtained by solution of 1, 2 dichloretane casting onto clear glass substrates. The thickness of the films was measured by "Mitutoyo" Dinamic micrometer with uncertainty of $\pm 1\mu\text{m}$. The chemical structures of samples are shown in the Figure 13.

The samples from each of the two azo-polymer types were divided into 2 groups – uncharged and corona charged. Firstly, for same samples the corona treated were done in a point-to-plane three -electrode corona discharge system (Figure 1) with 1kV grid voltage at a temperature of 25°C for 3 minute. Then, for all the samples the holographic gratings have been recorded by the experimental setup shown in Figure 14.

The Ar²⁺ laser was used as a light source. The laser beam was filtered and expanded, with 20mW/cm² total intensity at wavelength $\lambda = 488\text{nm}$, and then it had been used for exposure. The initial laser beam was split into two secondary beams with a 1:1 intensity ratio. The value of the intersection angle of the Ar²⁺ laser was $2\Theta = 63.3^\circ$.

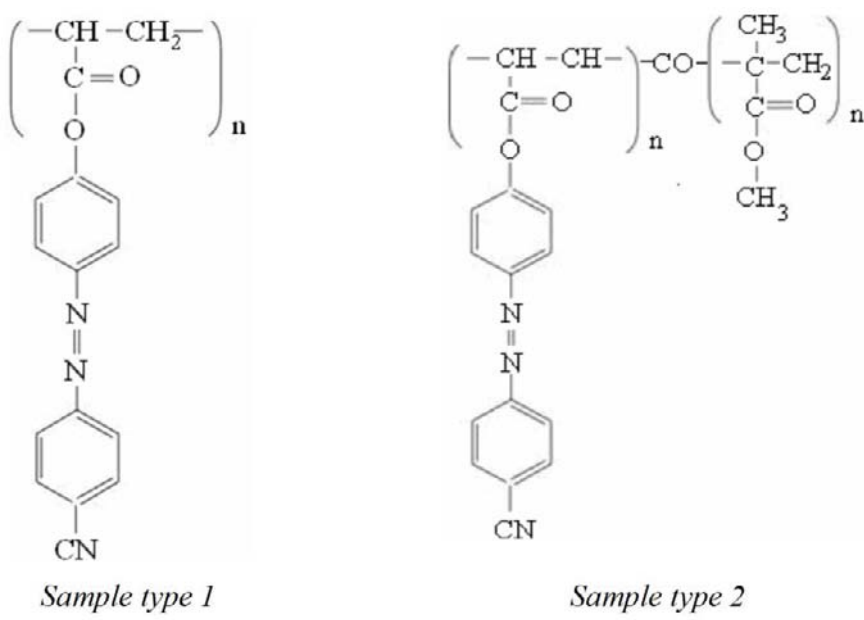


Figure 13. Chemical structure of the polymers.

The experimental grating recording with the Ar²⁺ laser was provided in Bragg regime with the Klein parameter $Q = \frac{2\pi\lambda d}{n_f\Lambda^2} = 66$, depending on the grating step ($\Lambda = 0.465\mu\text{m}$), the

thickness of the recording film ($d = 7\mu\text{m}$) and the film's refractive index ($n_f = 1.5$). The diffracted efficiency was monitored in real time with low-power He-Ne laser (1mW, 632.8nm), positioned at the Bragg's angle. Both, monitoring and recording beams were s-polarized. The spatial frequency of recorded gratings was 2150mm^{-1} . Special care had been taken of the sample's position in order to provide the successive grating recording on the same place of the sample before or after electric charging procedure.

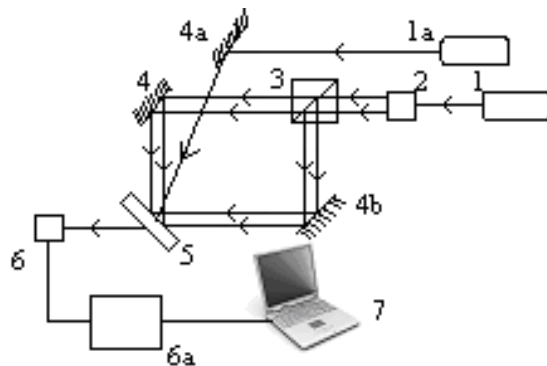


Figure 14. Holographic set-up: 1 – Ar^{2+} laser; 1a – He-Ne laser; 2 – expander - collimator; 3 – beam splitter; 4, 4a, 4b – mirrors; 5 – sample; 6 – sensor; 6a – “Ealing” power meter; 7 – PC.

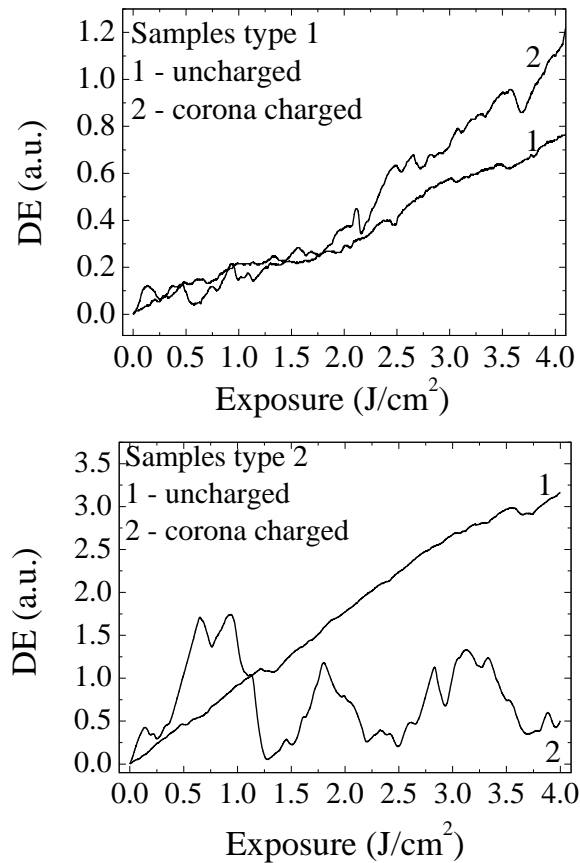


Figure 15. Exposure dependence on charged and uncharged samples.

The DE was calculated by PC (Figure 14) and it was in the form of the ratio $DE = I_d / I_o$, where I_d is the diffracted beam intensity of the monitoring (He-Ne) laser and I_o is the incident beam intensity of the monitoring (He-Ne) laser. The exposure dependences on the DE for charged and uncharged two types of samples are shown in the Figure 15.

The results obtained show different influences of the electric charge treatment on the DE of holographic recording in photopolymers. As it has been mentioned above, an additional corona-induced electrical field during the holographic recording leads to a magnification of the DE due to an increase of the relief pattern.

However, the spatial frequencies are relatively low - 233mm^{-1} and 500mm^{-1} . But, in this case of high spatial frequency (Bragg grating), it is reasonable to suppose that the additional refractive index modulation due to electric corona charge also occurs. The initial polarizability α of the corona discharge samples increases. With respect to local field effects, from the Lorentz-Lorenz equation, it has been the additional refractive index modulation Δn^e , according to the following relation:

$$\Delta n^e = \frac{(n^2 - 1)(n^2 + 2)}{6n} \cdot \frac{\Delta \alpha}{\alpha} \quad (6)$$

The total refractive index modulation is:

$$\Delta n = \Delta n_o + \Delta n^e \quad (7)$$

where Δn_o is an uncharged refractive index modulation.

According to the Kogelnik diffraction theory [65], the low value DE is proportional to $(\Delta n)^2$.

$$DE \propto \left(\frac{\pi d \Delta n}{\lambda \cos \Theta} \right)^2 = 2.8 \times 10^3 \cdot \Delta n^2 \quad (8)$$

where d is a constant film's thickness.

In this case: $d = 7\mu\text{m}$, $\lambda = 0.488\mu\text{m}$, $\Theta = 31.65^\circ$.

So, if $\Delta n^e < \Delta n_o$, it is logical to expect the increase of the DE:

$$DE \propto (\Delta n_o + \Delta n^e)^2 \approx (\Delta n_o)^2 \left(1 + 2 \frac{\Delta n^e}{\Delta n_o} \right) \quad (9)$$

The difference in sample polarizability is the reason of their DE behaviour. Unsaturated DE observed in the type 1 samples, is caused probably by its lower polarizability. In the type 2 samples, on the other hand, the over-modulation has caused \sin^2 -type DE behaviour. In this case α is bigger, one needs lower exposure (less than 1J/cm^2) in order to achieve maximum refractive index modulation. Obviously, the additional electric charge was caused by the noisy character of the DE in the process of re-orientation of the azo-molecules perpendicular to the light electric field.

The additional electric corona charge seems to be a promising method for increasing the DE (like for the type 1 samples), or sensitivity (like for the type 2 samples) of the azo-polymer recording media. The similar results have been observed at the investigation of electric charge influence of the diffraction efficiency of holograms, recorded in thin chalcogenide films [56, 57].

Conclusion

This chapter briefly reviews polymer film changes initiated by corona treatment and their possible applications. The corona treatment of polymer films initiates changes in the sample surfaces. The controllable and desirable changes of electret surface are necessary to different polymer film applications. The presence of oxygen adsorption processes on the sample surfaces as well as oxygen desorption during the samples charging stimulated in different ways by the positive and negative coronas was shown by X-ray Photoelectron Spectroscopy Analysis. Structural changes of sample surfaces that occurred during the corona charging were the most probable reasons that caused the corona treatment changes of the refractive index and its distribution on the sample surface measure by the method of the disappearing diffraction pattern. Hence, this method can be used to determine the transparent polymer films former history, i.e. to find out if surface modifications have occurred at a submicrometer depth, caused by ageing or various influences – charging in electric field, heating, mechanical deformation, irradiation by various beams, etc.

The influence of different factors—storage at pressure lower than atmospheric and irradiation by a low energy laser—on charge decay has been studied in order to obtain stable electrets for numerous applications. It was found that knowing the dependence of the surface potential on pressure for polymer film of a definite material gives the possibility to determine the pressure at which sharp decay will occur if the initial surface potential is known. Furthermore, preliminary placing the electrets under pressure less than 1 mbar can be used as a method for stabilizing the electret charge.

The study of the interaction of low energy laser radiation with polymer electret films is motivated by applied research interests for development of an information storage system and a reading system used in the optical computer. The different steady state levels for PP electrets obtained under different conditions after being irradiated with a CO₂ laser can find applications in optical storage and the processing of information on PP films, as for example the direct registration of information on PP electret films using a low energy CO₂ laser. On the other hand the relative surface potential for PP electrets irradiated with a He-Ne laser or a Cu-Br laser does not change significantly. Hence, those lasers can be used to read the information stored by the electrostatic field.

The influence of corona treatment on holographic recording in photopolymer films is discussed. It was shown that an additional induced polarizability, which is due to an electric charging, increases the sensitivity and the diffraction efficiency of the holographic recordings in amorphous side-chain azobenzene polymers.

References

- [1] Korakianiti, A.; Papaefthimiou, V.; Dalfou, T.; Kennou, S.; Gregoriou, V. *Macromol. Symp.* 2004, 205, 71-84.
- [2] Kestelman V. N.; Pinchuk L. S.; Goldade V. *Electrets in Engineering: Fundamentals and Applications*; Kluwer Academic Publishers: Norwell (USA), 2000; pp 22-24.
- [3] Sesler, G. M. in Electrets; Sesler, G. M.; Ed.; Springer-Verlag: Berlin-Heidelberg-New York, 1980; pp. 43-45.
- [4] Reedyk, C.; Perlman, M. M. *J. Electrochem. Soc.* 1968, 115, 49-51.

- [5] Morra, M.; Occhiello, E.; Garbassi, F. *Surf. Interface Analysis* 1990, 16, 412-417.
- [6] Suzer, S.; Argun, A.; Vatansever, O.; Aral, O. *J. Appl. Polym. Sci.* 1999, 74, 1846-1850.
- [7] O'Hare, L-A.; Leadley, S.; Parbhoo, B. *Surf. Interface Analysis* 2002, 33, 335-342.
- [8] Karmazova, P. G.; Marinova ,T. S; Krastev, V. I.; Mekishev, G. A. *Bulg. Chemical Commun.* 1995, 28, 94-104.
- [9] Chen, Q. *J. Electrostatics* 2003, 59, 3-13.
- [10] Yovcheva, T.; Avramova, I.; Mekishev, G.; Marinova, T. S. *J. of Electrostatics* 2007, 65, Issues 10-11, 667-671.
- [11] Scofield, J. H. *J. Electron Spectroscopy Rel. Phenom.* 1976, 8, 129-137.
- [12] Strobel, M.; Jones, V.; Lyons, C. S.; Ulsh, M.; Kushner, M.J.; Dorai, R.; Branch, M. C. *Plasmas and Polymers* 2003, 8, 61-95.
- [13] Giacometti, J.A.; Oliveira, Jr. O. N. *IEEE Trans. Electr. Insulation* 1992, 27, 924-943.
- [14] Karmazova, P. G.; Mekishev, G. A. *Sci. Work PU* 1984, 22, 17-21.
- [15] Turnhout, J. van Thermally stimulated discharge of polymer electrets; Elsevier Sci. Publ. Comp.: Amsterdam/Oxford/New York, 1975; pp. 222-225.
- [16] Mekishev, G. A.; Iovcheva, T. A.; Guentcheva, E.; Nedev, S. J. Mater. Sci.: *Mater. Electron* 2003, 14, 779-780.
- [17] Mekishev, G. A.; Yovcheva, T. A.; Gentcheva, E. A.; Nedev, S. R. *J. Electrostat* 2005, 63, 1009-1015.
- [18] Yovcheva, T. A.; Mekishev, G. A.; Marinov, A. T. *J. Phys.: Condens. Mat* 2004, 16, 455-464.
- [19] Ono, R.; Nakazawa, M.; Oda, T. *IEEE Transactions on Industry Applications* 2004, 40, 1482-1487.
- [20] Wild, J. W.; Stranathan, J. D. *J. Chem. Phys.* 1957, 27, 1055-1059.
- [21] Meeten, G. H. in Optical properties of polymers; Meeten, G. H.; Ed.: Elsevier *Appl. Sci.*: London and N. Y., 1986; pp. 17-40.
- [22] Yovcheva, T.; Sainov, S.; Mekishev, G. *J. of Optoelectronics and Advanced Materials* 2007, 9(7), 2087-2090.
- [23] Yovcheva, T.; Sainov, S.; Mekishev, G. *J. of Optoelectronics and Advanced Materials* 2008, 10(2), 373-376.
- [24] Yovcheva, T.; Babeva, Tz.; Nikolova, K.; Mekishev, G. *J. Opt. A: Pure Appl. Opt.* 2008, 10 (5), 055008 (4pp)
- [25] Stephan, M.; Große, S.; Stintz ,M.; Blankschein, U. *J. Appl. Pol. Sci.* 2007, 103, 258-262.
- [26] Seisa, E. A. *Int. Pol. Proc.* 2006, 21, 183-188.
- [27] Coelho, J.; Abreu, M.; Rodrigues, F. *J. Polymer testing* 2004, 23, 307-312.
- [28] Ioffe, B. Refractometric Methods in Chemistry; Chemistry Publ. Comp.: St. Peterburg (RU), 1960; pp. 131-173 (in Russian).
- [29] Sainov, S. *Rev. Sci. Instrum.* 1991, 62, 3106-3107.
- [30] Goos, F.; Hanchen, H. *Ann. Phys.* 1947, 1, 333-346.
- [31] Molinie, P. *J. Electrostatics* 1999, 45, 265-273.
- [32] Kawamoto, H.; Umez, S. *J. Phys. D: Appl. Phys.* 2005, 38, 887-894.
- [33] Zhao, L.; Adamiak, K. *J. Electrostatics* 2005, 63, 337-350.
- [34] Zhang, B.; Zhou, Y.; Wang, N.; Liang, X.; Guan, Z.; Takada, T. *J. Electrostatics* 2005, 63, 657-663.

- [35] Steinhauser, H.; Ellinghorst, G. *E Angew. Makromol. Chem.* 1984, 120, 177-191.
- [36] Karmazova, P. G.; Mekishev, G. A. *Bulg. J. Phys.* 1990, 17, 454-458.
- [37] Marat-Mendes, J. N.; Raposo, M.; Ribeiro, P.A. in Equilibrium structure and properties of surfaces and interfaces; Gonis, A., Stocks, G. M.; Eds.; Plenum press: New York and London, 1992; pp.353-359.
- [38] Ornelas-Rodriguez, M.; Calixto, S. *Opt. Eng.* 2001, 40, 921-925.
- [39] Bormashenko, E.; Pogreb, R.; Sheshnev, A.; Sutovski, S.; Shulzinger, A.; Nachum, L.; Kerbel, R. *Appl. Surf. Sci.* 2003, 220, 125-135.
- [40] Draughn, R. A.; Catlin, A. *J. Electrochem. Soc.* 1968, 115, 391-394.
- [41] Palaia, F. L.; Catlin, A. *J. Chem. Phys.* 1970, 52, 3651-3654.
- [42] Mekishev, G. A.; Yovcheva, T. A.; Viraneva, A. *J. of Non-Crystalline Solids* 2007, 353, 4453-4456.
- [43] Viraneva, A.; Yovcheva, T.; Gencheva, E.; Mekishev, G. *J. of Opt. and Adv. Mat.* 2008, 10(2), 302-305.
- [44] Keltzev, N. V. Bases of Adsorption Technique; Chemistry Publ. Comp.: Moscow (RU), 1984; pp. 183-187 (in Russian).
- [45] Gautschi, W, In Handbook of Mathematical Functions; Abramowitz, M.; Stegun, I. A.; Eds.; National bureau of standards, Applied mathematics, series 55; US Government Printing Office: Washington (USA), 1964; pp. 295-297.
- [46] O'Hare, L.-A; Smith, J. A.; Leadley, S. R.; Parbhoo, B.; Goodwin, J. A.; Watts, J. F. *Surface and Interface Analysis* 2002, 33, 617-625.
- [47] Mekishev, G. A.; Prikhodchenko, V. A.; Tairov, V. N.; Karmazova, P. G. *Bulg. J. Phys.* 1986, 13, 58-64.
- [48] Karmazova, P.; Mekishev, G. *Europhys. Lett.* 1992, 19, 481-484.
- [49] Mageramov, A. *High Energy Chem.* 2005, 39, 142-147.
- [50] Amanullah, K. *IEEE Trans. Cons. Electr.* 1994, 40, 42-46.
- [51] Amjadi, H.; Franz, C. *J. Electr.* 2001, 50, 265-277.
- [52] Yovcheva, T.; Eftimov, T.; Mekishev, G. Proc. 4-th Intern. Symp. Laser Techn. and Lasers, LTL Plovdiv, Bulgaria, 2005, 265-269.
- [53] Yovcheva, T. A.; Eftimov, T. A; Viraneva, A.,P.; Mekishev, G., Yanev, V. C.; Avramova, I. A. AIP Conference Proceedings 899, Sixth International Conference of the Balkan Physical Union 2007, 673.
- [54] Yovcheva, T.; Eftimov, T.; Yanev, V.; Viraneva, A.; Mekishev, G.; Avramova, I. *J. of Opt. and Adv. Mat.* 2007, 9, 471-474.
- [55] Lazneva E. Laser desorption; LGU Publ. Comp.: Leningrad (RU), 1990; pp.5-28 (in Russian). 201
- [56] Nastas, A. M.; Andriesh, A. M.; Bivol, V. V.; Prisakar, A. M.; Tridukh, G. M *Technical Physics*, 2009, 54(2), 305-308.
- [57] Reinke, N.; Draude, A.; Fuhrmann, T.; Franke, H.; Lessard, R. *Appl. Phys. B* 2004, 78 (2), 205-209.
- [58] Couture, J. A.; Lessard, R. A. *Appl. Opt.* 1988, 27, 3368-3374.
- [59] Natansohn, A.; Rochon, R.; Gosseline, J.; Xie, S. *Macromolecules* 1992, 25, 2268 - 2273.
- [60] Rochon, R.; Batalia, E.; Natansohn, A. *Appl. Phys. Letters* 1995, 66, 136-138.
- [61] Kim, D.; Tripathy, S.; Li, L.; Kumar, J. *Appl. Phys. Letters* 1995, 66, 1166-1168.
- [62] Urbach, J. G.; Meier, R. W. *Appl. Opt.* 1966, 5, 666-667.

- [63] Panasyuk, L. M.; Nastas, A. M. *Optics and Spectroscopy* 2003, 94(6), 959–961.
- [64] Yovcheva, T.; Beev, K.; Petrova, Tz.; Dragostinova, V.; Mekishev, G.; Sainov, S. *JOAM - Symposya* 2009, 1(3), 608-611.
- [65] Kogelnik, H. *Bell Syst. Techn. Journal* 1969, 48, 2909-2947.

Chapter 3

NUMERICAL SIMULATION FOR ELECTROSTATIC FIELD, FLOW FIELD AND PARTICLE BEHAVIOR IN A WIRE-PLATE ELECTROSTATIC PRECIPITATOR

Hong Lei

Key Laboratory of Electromagnetic Processing of Materials,
Ministry of Education, Northeastern University,
Shenyang, 110004, China

Abstract

The behavior of charged particles in turbulent gas flow in electrostatic precipitators (ESPs) is crucial information needed to design and optimize electrostatic precipitators, so a three-dimensional numerical simulation was performed to predict electrostatic fields, electro-hydrodynamic (EHD) turbulent flow and particle charging and tracing in a wire-plate ESP. For electrostatic field, the traditional finite difference method (FDM) has been widely applied to calculate two-dimensional electrical field in the wire-plate ESP on the base of the symmetry assumption. We analyze the reason why the traditional FDM method by Leutert and McDonald only converges in the first quadrant of single discharge electrode, and we give the numerical method suitable to obtain a convergence solution in the other quadrants. Based on an analogy between the electric equation and the fluid dynamics equation, we propose the upwind (or downwind) scheme to calculate the electrostatic field in the case of positive (or negative) corona. For EHD flow, the classic $k-\varepsilon$ model is applied to describe the EHD turbulent flow in a wire-plate ESP, and a non-dimensional EHD number is introduced to analyze the interactions between the cross-flow and the electric wind. The electric wind has the arrays of large-scale, spanwise counter-rotating vortical structures, and three different types of singularities are located at equally spaced intervals. On average, each wire generates four equal circulatory cells, two upstream and two downstream for the wire. The cross-flow weakens the intensity of EHD flow. With the increase of the inlet velocity, the cross-flow causes the two circulatory cells near the corona wire to merge into one circulatory cell. For particles, a Monte-Carlo simulation is applied to describe *in situ* particle charging and tracing. In the current model we consider the effect of the fluid turbulence on the particle movement; give the particle charging history; and clarify the magnitude of the electric field force, the drag force, the gravitational force, the buoyancy force, the virtual mass force, the Basset history force, the Saffman lift force and the pressure gradient force on particle motion.

1. Introduction

Exposure to airborne microorganisms may cause various respiratory and other health disorders. A significant number of illnesses and infections due to such exposures have been reported in a variety of residential and occupational environments. Thus, environmental protection has become a crucial problem of public concern, and governments are requested to set more stringent limits for the emissions of solid particle and other gaseous pollutants from industrial plants. The electrostatic precipitator(ESP), which is an air pollution control device to remove particles from a flowing gas by electric field force, has reached fairly good collection efficiencies. In industrial applications, the most commonly used ESP is the wire-plate type ESP shown in Figure 1. Equally spaced corona wires usually of negative polarity are located at the center of the grounded plates (or collecting electrodes), and are kept at a voltage high enough to discharge the ionic species. The space-charges (electrons or ions) generated by the corona are driven toward the grounded plates by the action of an electrostatic field. They collide with the fluid molecules and transfer momentum to them. In this way, the electric field force acting on the air is produced and leads to a secondary air flow, which is known as electric wind, ionic wind or corona wind in the ESP. The particles acquire electric charges of the same polarity as that of the discharge electrode. And the charged particles move toward the grounded plates under the influence of the electrostatic field and are removed by a rapping mechanism.

In general, in order to model the particle transport in industrial ESP, three major issues should be addressed.

- (1) Electric field: The electric-field distribution in the ESP is of prime importance for increasing the performance and optimizing the operating conditions of industrial ESP. The electric conditions inside the ESP are determined by the electric field and the corona-generated space-charge, and can be described by the steady-state Maxwell equations and a constitutive law relating current and voltage. In this case, the governing equations may be solved by a finite difference scheme, a finite element method or a control-volume method. The key problem in these numerical methods is the relation and the difference between the backward (or forward) difference scheme and the upwind (or downwind) scheme.
- (2) Flow field: There is strong coupling of the fluid flow with the electric field since the ions will transfer momentum gained in the electric field into the fluid flow. In the past, a number of attempts have been made to numerically calculate the EHD (electrohydrodynamic) flow in the ESP. These computational fluid dynamics (CFD) calculations are performed by using a laminar flow assumption, a $k - \varepsilon$ turbulence model, or a direct numerical simulation.
- (3) Particle behavior: Particle behaviors in the ESP, which involve in particle charging kinetics and turbulent particle transport, are modeled by Eulerian approach (i.e. modeling the particle phase as a second continuum phase and solving a differential equation for particle concentration) and Lagrangian approach (i.e. calculating individual particle trajectory). In the Eulerian approach, the most frequently used assumption for the local particle velocity is the sum of fluid velocity and particle terminal velocity. Furthermore, the Eulerian approach has a fatal deficiency because

the charge acquired on a particle in a non-uniform electric field is determined by the precharge assumption. In the Lagrangian approach, the particle motion in the turbulent flow can be described by Monte-Carlo method. But it is difficult to track a large number of particles at the same time due to CPU speed limitations.

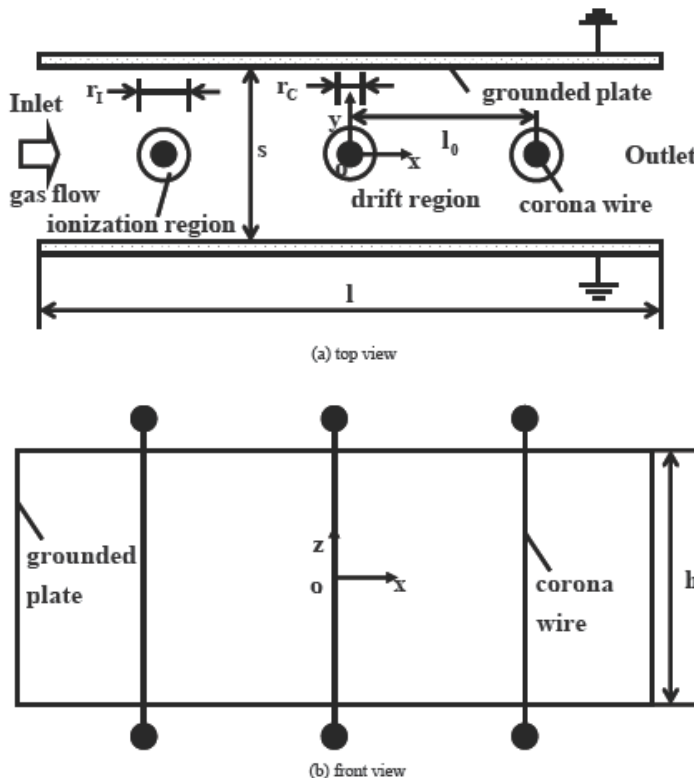


Figure 1. Schematic of wire-plate electrostatic precipitator.

The complete model is structured into several modules, each one dealing with a particular process, solving a self-consistent set of differential equations, and exchanging the necessary information with the other modules. In this paper, the model is organized into the following three sections. Firstly, the electrostatic field is solved under the assumption that it is not affected by the flow field and particle motion. The electric field and the space-charge are calculated by the control-volume method described in section 2. The aim of this section is to give detailed information on the application of upwind (or downwind) scheme for calculating electrical conditions in the ESP. Secondly, the Coulomb force is calculated from the numerical results of the electric field and the space-charge density, and then the turbulent EHD (electrohydrodynamic) flow field is obtained by solving the governing equations described in section 3. The aim of EHD section is to investigate the nature of the electric wind and the interactions between the cross-flow and the electric wind. At last, particle section involves in particle charging and tracing. Particle charging module considers the charges transfer from the ions to the dust particles and their progressive charging. Particle tracing module is used to compute the particle motion. It takes into consideration all the forces applied to the particles. The aim of this section is to investigate the effects of the turbulence

on the particle tracing and charging, and to clarify the magnitude of the Basset history force, the Saffman lift force, the virtual mass force and the pressure gradient force on particle motion.

2. Electric Field

The particle collection in electrostatic precipitator is largely dominated by the distribution of the electric field, which influences almost all the physical processes that occur in the ESP. The traditional finite difference method[1,2] has been widely used to calculate electrical conditions in the wire-plate ESP, but all these authors used two-dimensional and symmetric domain[1-14]. How to choose the calculational domains in traditional difference method is dependent on the backward (or forward) difference scheme for calculating the gradient of the space-charge density. In order to solve such a problem, the upwind (or downwind) scheme is introduced into the control-volume method.

2.1. Assumptions

- (1) The system is in a steady-state operating condition, and the electric conditions are modeled under clean-air condition.
- (2) Since the electrical migration velocity of ions under the Coulomb force is about 100 times larger than the convective velocity of ions on the conventional operation condition of the ESP [7,11], the electrostatic field doesn't depend on the flow field, but only depends on the configuration of the electrodes and the applied electric potential.
- (3) The discharge current remains constant and there are unipolar ion charges in the calculational domain.

2.2. Governing Equations

In the absence of magnetic effect, the steady-state Maxwell equations can be expressed as

$$\nabla \cdot (\epsilon_0 \vec{E}) = \rho \quad (1)$$

$$\nabla \cdot \vec{j} = \rho \quad (2)$$

$$\vec{j} = \rho \beta \vec{E} \quad (3)$$

where ϵ_0 is the free-space permittivity, E is the electric field strength, ρ is the space-charge density, j is the current density, and β is the ion mobility.

Equation (1) is the point form of Gauss's law, equation (2) presents the continuity of steady currents, and equation (3) is the point form of Ohm's law.

Since the electric field is irrotational (conservative) in the region of interest, it is derivable from the gradient of an electric potential V .

$$\vec{E} = -\nabla V \quad (4)$$

Substituting equation (4) into equation (1), the Poisson equation for the electric potential can be expressed as

$$\epsilon_0 \nabla^2 V = -\rho \quad (5)$$

The continuity equation (2) can be transformed into an equation involving V and ρ by using equations (1), (3) and (4). Upon making the appropriate substitutions and using vector algebra, the special form of the current continuity equation can be expressed as follows:

$$\epsilon_0 \nabla V \cdot \nabla \rho = \rho^2 \quad (6)$$

Equations (5) and (6) compose a coupled pair of the partial differential equations (PDEs), one of which is nonlinear. With appropriate boundary conditions and solution method, the scalar functions V and ρ can be numerically computed.

2.3. Numerical Method

2.3.1. Traditional Finite-Difference Technique

Accurate knowledge of the electric field and space-charge density distributions inside ESPs is vital to the modeling and analysis of device performance. The traditional finite difference method (FDM), proposed by Leuter[1] and McDonald[2], has been widely used to solve the partial differential equations (PDEs), namely, Poisson's equation(5) and current continuity equation (6). The solution domain in the wire-duct precipitator geometry is two dimensional, as shown in Figure 2. Due to the symmetry of multiwire precipitator, the domain consists solely of the rectangle ABCD. It is assumed that the solution will hold for all similar rectangles within the electrostatic precipitator. And the continuity equation is solved by using a backward difference method to yield the space-charge density distribution.

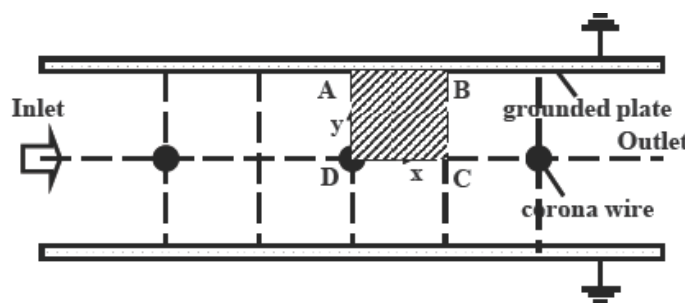


Figure 2. Numerical solution domain in the traditional finite-difference technique.

In the traditional FDM, the central difference scheme is applied to obtain the electric potential,

$$E_x = -\frac{\partial V}{\partial x} = \frac{V_E - V_W}{(\delta x)_e + (\delta x)_w} \quad (7)$$

and the backward difference scheme is applied to calculate the gradient of the space-charge density,

$$\left. \frac{\partial \rho}{\partial x} \right|_- = \frac{\rho_p - \rho_w}{(\delta x)_w} \quad (8)$$

where δx are mesh sizes in x axis, as shown in Figure 3. Here, E denotes the east side, W is the west side. For the single corona wire, the computational domain in the traditional finite-difference technique is the zone I shown in Figure 4.

Now we explain the physical meaning of the backward difference scheme. If the backward difference scheme is used to calculate the gradient of the space-charge density, the space-charge density at grid point P, as shown in Figure 3, is dependent on the information at the neighbor W, not at the other neighbor E. Therefore, the grid point in the upstream side should provide the full information for the grid point in the downstream in this scheme. Here, the upstream side and the downstream side are based on the direction of the coordinate system. In general, the backward difference scheme requires the positive charge or the negative charge to move in the positive direction of the coordinate system.

Certainly, if the forward difference scheme is used to calculate the gradient of the space-charge density, the space-charge density at grid point P is determined by the information at the neighbor E, not at the other neighbor W. Thus, the grid point in the downstream side should provide the full information for the grid point in the upstream in this scheme. In general, the forward difference scheme requires the positive charge or the negative charge to move in the negative direction of the coordinate system.

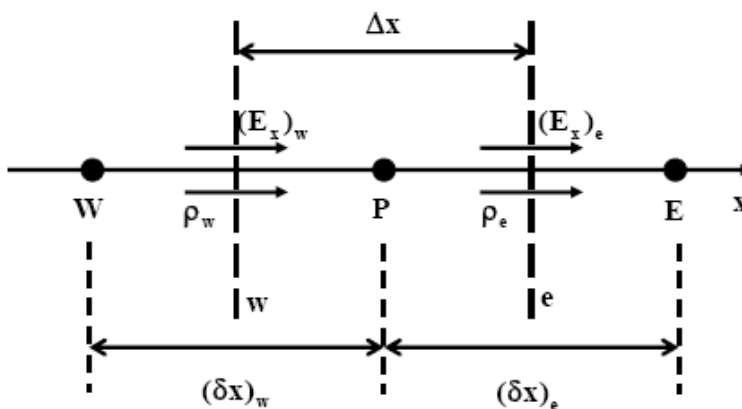


Figure 3. Control-volume for the one dimensional geometry.

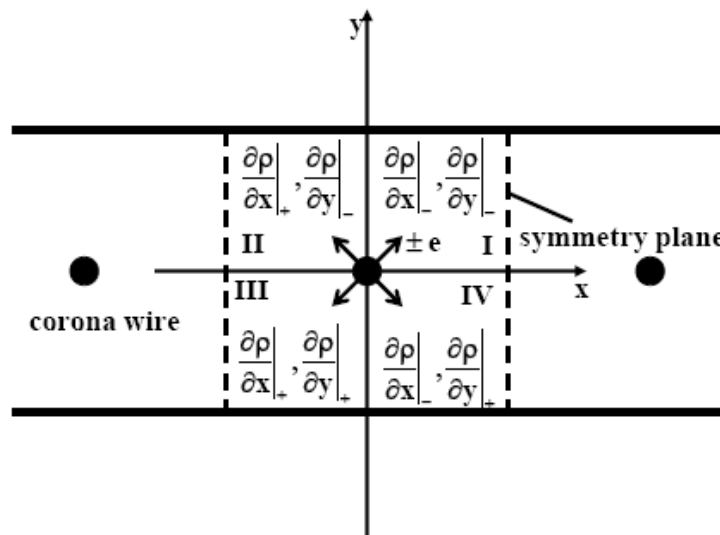


Figure 4. convergence domain for traditional finite difference method.

For the positive corona, the direction of the electric field strength follows the positive direction of the coordinate system in domain I, so the backward difference scheme complies with the physical rule that the positive charges move in the direction of the electric field strength.

Thus, the converged numerical solution can be obtained by the traditional FDM in domain I. But in zone III, the direction of the electric field strength follows the negative direction of the coordinate system, and the space-charge move in the negative direction of the coordinate system. Thus it conflicts with the backward difference scheme. Such a conflict also occurs in zones II and IV.

If we want to obtain the converged solution in zone I, II, III or IV, the corresponding difference scheme to calculate the gradient of the space-charge density should be defined as follows:

- (1) Zone I: backward difference scheme to calculate $\frac{\partial \rho}{\partial x}$, and backward difference scheme to calculate $\frac{\partial \rho}{\partial y}$.
- (2) Zone II: forward difference scheme to calculate $\frac{\partial \rho}{\partial x}$, and backward difference scheme to calculate $\frac{\partial \rho}{\partial y}$.
- (3) Zone III: forward difference scheme to calculate $\frac{\partial \rho}{\partial x}$, and forward difference scheme to calculate $\frac{\partial \rho}{\partial y}$.

(4) Zone IV: backward difference scheme to calculate $\frac{\partial \rho}{\partial x}$, and forward difference

scheme to calculate $\frac{\partial \rho}{\partial y}$.

For the negative corona, the direction of the electric field is opposite to that of the positive corona in zone I, and the negative charges move in the opposite direction of the electric field strength. Consequently, the direction of the charge motion, which is independent of the polarity of the charge, is the same in the same domain shown in Figure 4.

Backward difference scheme require the space-charges (positive or negative) to move in the positive direction of the coordinate system, and forward difference scheme require the space-charges (positive or negative) to move in the opposite direction of the coordinate system. Only if the difference scheme can satisfy the physical process, a converged solution can be obtained by FDM(finite difference method). Therefore, the backward difference scheme can be successfully applied to domain I, and the forward difference scheme can also be successfully applied to domain III. Difference schemes for the gradient of the space-charge density that ensure relative convergent calculations in all the domains are shown in Figure 4.

In conclusion, the traditional FDM can not follow the directions of the electric field strength in all zones. Consequently, such a defect limited its applications.

2.3.2. Control-Volume Method

Control-volume method is one of the popular numerical methods to solve the partial differential equations. It was initially proposed and developed in computational fluid dynamics(CFD), but it can be extensively applied to other research fields so long as the related differential equation has the same mathematic form[15-17]. Now, we make an analogy between the fluid flow problem and the electric-field problem in order to apply control-volume method to the present problem.

The steady and incompressible flow governed by the Navier-Stokes equations can be expressed as

$$(\rho^f \vec{u}^f \cdot \nabla) \vec{u}^f = -\nabla p + \nabla \cdot (\mu_1 \nabla \vec{u}^f) + \rho^f \vec{g} \quad (9)$$

where ρ^f is the fluid density, \vec{u}^f is the fluid velocity, p is the pressure, μ_1 is the fluid viscosity, and \vec{g} is the gravitational acceleration.

The Navier-Stokes equations and the governing equations for ESP can be expressed as the general differential equation

$$(\rho_0 \vec{U} \cdot \nabla) \varphi = \nabla \cdot (\Gamma \nabla \varphi) + S \quad (10)$$

where Γ is the diffusion coefficient and S is the source term. The terms and coefficients in this expression depend on the dependent variable φ . The three mathematical terms in the general differential equation (10) are the convection term, the diffusion term and the source

term. Table 1 gives the similarities and the differences between the governing PDEs for ESP and Navier-Stokes equations.

Table 1. Analogy among the governing equations for electrostatic field and steady fluid flow field

General equations	ρ_0	\vec{U}	Γ	ϕ	S
Navier-Stokes equations	ρ^f	\vec{u}^f	μ_1	\vec{u}^f	$-\nabla p + \rho^f \vec{g}$
Poisson equation for V	0	0	ϵ	V	ρ
charge conservation equation	β	\vec{E}	0	ρ	0
current continuity equation	1	\vec{j}	1	0	0

(a) Poisson's equation for electric potential

If we evaluate the derivative ∇V from the piecewise-linear profile, and use the standard method to treat with the diffusion term and the source term in the Poisson's equation for electric potential, the integrated equation over the control-volume shown in Figure 3 can be expressed as

$$\begin{aligned} & \frac{V_E - V_P}{\Delta x \cdot (\delta x)_e} - \frac{V_P - V_W}{\Delta x \cdot (\delta x)_w} + \frac{V_N - V_P}{\Delta y \cdot (\delta y)_n} - \frac{V_P - V_S}{\Delta y \cdot (\delta y)_s} \\ & + \frac{V_T - V_P}{\Delta z \cdot (\delta z)_t} - \frac{V_P - V_B}{\Delta z \cdot (\delta z)_b} = -\rho_p / \epsilon_0 \end{aligned} \quad (11)$$

where ρ_p is the average space-charge density in the control-volume P. Here, N, S, T and B denote north, south, top and bottom, respectively. It is useful to cast the discretization equation (11) into the following form:

$$a_p V_p = a_E V_E + a_w V_w + a_n V_N + a_s V_s + a_t V_T + a_b V_B + b \quad (12)$$

With

$$a_E = \frac{1}{\Delta x \cdot (\delta x)_e} \quad (13a)$$

$$a_w = \frac{1}{\Delta x \cdot (\delta x)_w} \quad (13b)$$

$$a_n = \frac{1}{\Delta y \cdot (\delta y)_n} \quad (13c)$$

$$a_s = \frac{1}{\Delta y \cdot (\delta y)_s} \quad (13d)$$

$$a_t = \frac{1}{\Delta z \cdot (\delta z)_t} \quad (13e)$$

$$a_b = \frac{1}{\Delta z \cdot (\delta z)_b} \quad (13f)$$

$$a_p = a_e + a_w + a_n + a_s + a_t + a_b \quad (13g)$$

$$b = \rho_p / \epsilon_0 \quad (13h)$$

(b) charge conservation equation

The current continuity equation does not have a diffusion term, but has a convection term and a source term. Thus, integrated equation over the control-volume shown in Figure 3 is expressed as

$$(E_x)_e A_e \rho_e - (E_x)_w A_w \rho_w + (E_y)_n A_n \rho_n \\ - (E_y)_s A_s \rho_s + (E_z)_t A_t \rho_t - (E_z)_b A_b \rho_b = -\rho_p^2 \Delta v / \epsilon_0 \quad (14)$$

where ρ_i ($i=e, w, n, s, t, b$) is the value of ρ at the control-volume face i . A_i is the area of the control-volume face i . $\Delta v = \Delta x \Delta y \Delta z$ represents the volume of the control-volume P .

Usually, the upwind scheme is applied to treat with the convection term in CFD. But in the electrostatic precipitator, there are positive corona and negative corona. For the positive corona, the direction of the electric field strength and the direction of the positive ion motion are the same. But for the negative corona, the negative ion motion is on the opposite direction of the electric field strength. In other words, the positive charges move from the upstream to the downstream, and the negative charges move from the downstream to the upstream. Here, the upstream side and the downstream side are based on the direction of the electric field.

For the positive charge, the upwind scheme can be applied to describe such a process: the space-charge density at each point is affected by the upstream conditions. In other words, the space-charge density at the interface is equal to that of the grid point on the upstream side.

$$\rho_e = \begin{cases} \rho_p & \text{if } (E_x)_e > 0 \\ \rho_E & \text{if } (E_x)_e < 0 \end{cases} \quad (15)$$

Thus, equation (14) can be rewritten as follows

$$a_p \rho_p = a_e \rho_E + a_w \rho_w + a_n \rho_N + a_s \rho_S + a_t \rho_T + a_b \rho_B + b \quad (16)$$

with

$$a_E = \max[-(E_x)_e A_e, 0] \quad (17a)$$

$$a_W = \max[(E_x)_w A_w, 0] \quad (17b)$$

$$a_N = \max[-(E_y)_n A_n, 0] \quad (17c)$$

$$a_S = \max[(E_y)_s A_s, 0] \quad (17d)$$

$$a_T = \max[-(E_z)_t A_t, 0] \quad (17e)$$

$$a_B = \max[(E_z)_b A_b, 0] \quad (17f)$$

$$\begin{aligned} a_P = & a_E + a_W + a_N + a_S + a_T + a_B \\ & + [(E_x)_e A_e - (E_x)_w A_w + (E_y)_n A_n - (E_y)_s A_s + (E_z)_t A_t - (E_z)_b A_b] \end{aligned} \quad (17g)$$

$$b = -\rho_p^2 \Delta v / \epsilon_0 \quad (17h)$$

For the negative charge, the downwind scheme can be applied to describe such a process: the space-charge density at each point is affected by the downstream conditions. In other words, the space-charge density at the interface is equal to that of the grid point on the downstream side.

$$\rho_e = \begin{cases} \rho_E & \text{if } (E_x)_e > 0 \\ \rho_P & \text{if } (E_x)_e < 0 \end{cases} \quad (18)$$

Thus, equation (14) can be rewritten as follows

$$a_P \rho_P = a_E \rho_E + a_W \rho_W + a_N \rho_N + a_S \rho_S + a_T \rho_T + a_B \rho_B + b \quad (19)$$

with

$$a_E = \max[(E_x)_e A_e, 0] \quad (20a)$$

$$a_W = \max[-(E_x)_w A_w, 0] \quad (20b)$$

$$a_N = \max[(E_y)_n A_n, 0] \quad (20c)$$

$$a_S = \max[-(E_y)_s A_s, 0] \quad (20d)$$

$$a_T = \max[(E_z)_t A_t, 0] \quad (20e)$$

$$a_B = \max[-(E_z)_b A_b, 0] \quad (20f)$$

$$\begin{aligned} a_P = & a_E + a_W + a_N + a_S + a_T + a_B \\ & - [(E_x)_e A_e - (E_x)_w A_w + (E_y)_n A_n - (E_y)_s A_s + (E_z)_t A_t - (E_z)_b A_b] \end{aligned} \quad (20g)$$

$$b = \rho_p^2 \Delta v / \epsilon_0 \quad (20h)$$

S. V. Patankar[18] pointed out that the algorithm, which satisfies the following three rules, will converge.

- (1) When a face is common to two adjacent control-volumes, the flux across it must be represented by the same expression in the discretization equations for the two adjacent control-volumes.
- (2) The coefficient a_p at the grid point P and the neighbor coefficients a_{nb} ($nb = E, W, N, S, T, B$) must always be positive.
- (3) The coefficient at the grid point P must be always equal to or greater than the sum of the neighbor coefficients (E, W, N, S, T, B).

Reference [15] shows that the control-volume method with the upwind (or downwind) scheme can satisfy the above three basic rules and is an unconditionally convergent numerical method.

2.4. Boundary Conditions

The boundary conditions used in this calculation are summarized in Table 2. The space-charge density near the wire, ρ_w , can be given by Peek's semi-empirical formula [19]

$$\rho_w = \frac{l_0 j_p}{\pi \beta r f [30\delta + 0.9(\delta/r_c)^{1/2}]} \times 10^{-5} \quad (21a)$$

$$\text{With } \delta = \frac{T_0}{T} \cdot \frac{P}{P_0} \quad (21b)$$

where l_0 is the wire-wire spacing, j_p is the average current density at the grounded plate, r_c is the corona wire radius, T_0 is 293K, P_0 is 1.01×10^5 Pa, P and T are the operating pressure and temperature [2,3]. And f is a factor to account for wire roughness. For perfectly smooth clean wire, the roughness factor f is equal to unity. For dirty scratched wires in the laboratory, f usually is between 0.5 to 0.7 [2].

Table 2. Boundary conditions for electric conditions

	Grounded plate	Corona wire	Side face, top, bottom
Electric potential	$V = 0$	$V = V_0$	$\partial V / \partial n = 0$
Space-charge density	$\partial \rho / \partial n = 0$	$\rho = \rho_w$	$\partial \rho / \partial n = 0$

The inter-electrode space may be divided into two regions: the ionization region close to the corona wire where the ionization occurs, and the drift region comprising the space between the ionization region and the grounded plate, as shown in Figure 1. Another boundary condition for the corona wire is to shift the inner boundary conditions at ionization radius r_I rather than at the wire radius r_C [6,16].

$$r_I = r_C + 0.03\sqrt{r_C} \quad (22)$$

The ionization radius r_I established by the corona discharge is typically the same order of magnitude as the wire radius r_C . This radius separates the unipolar space-charge region from the complicated bipolar ion process contained in the ionization regions. The space-charge density at the ionization radius r_I is also given by Peek's formula[6], and the electric potential at the ionization radius r_I is computed using the coaxial cylinder potential expression near the wire [6,16], where the internal radius is r_C and the external radius is $s/2$.

$$V_{r_I} = \frac{\ln \frac{s}{2r_I}}{\ln \frac{s}{2r_C}} V_0 \quad (23)$$

Here, s is the duct width, as shown in Figure 1. And V_0 is the voltage applied at the corona wire.

2.5. Numerical Experiments

Specially, the experiment of Kallio [20,21] will be used to perform the detailed numerical study for electric field, flow field and particle behavior. Specifications of the modeled ESP are listed in Table 3. The calculational domain was discretized by using a nonuniform grid with a densely packed grid near the corona wire to represent the strong gradient of the electric field. The governing equations were solved on the staggered grid. On this condition, the electric potential and the space-charge density were evaluated at the grid nodes while the electric field components were defined at the interface between gird nodes. The discretized

equations for the electric potential and the space-charge density were solved by using the tri-diagonal matrix algorithm coupled with the Gauss-Siedel routine.

The steps in the numerical procedure are outlined as follows:

- (1) Solve equation (5) with an initial guess of free space-charge density.
- (2) Calculate the space-charge density at the corona wire by using Peek's empirical formula[21a].
- (3) Calculate the space-charge density at every point in the grid by using equation (6).
- (4) Calculate the electric potential at every point in the grid by using equation (5).
- (5) Repeated steps (3) and (4) alternatively until convergence.

The convergence criteria were

$$\begin{cases} \max \left| \frac{V^{K+1} - V^K}{V^{K+1}} \right| < 10^{-6} \\ \max \left| \frac{\rho^{K+1} - \rho^K}{\rho^{K+1}} \right| < 10^{-6} \end{cases} \quad (24)$$

where K was the iteration number.

There are a wide range of published experimental values ($1.1 \times 10^{-4} - 2.2 \times 10^{-4} \text{ m}^2/\text{V}\cdot\text{s}$) for the electric mobility of gas ions created in a corona discharge [2] and it was assumed to be $1.8 \times 10^{-4} \text{ m}^2/\text{V}\cdot\text{s}$ for negative coronas in the present study.

The experimental data of Penney and Matick [22] were employed to validate the numerical result. The electric potential distribution in a direct current corona field was measured by a stationary-probe method. The voltage in the shielded fine-wire probe was applied to the shield in order to overcome the excess potential of the probe due to ionic charge transfer.

Figure 5 shows that the predicted results agree well with the experimental data of Penny and Matick. In the present work, first-order upwind (downwind) scheme is introduced to calculate the electrical condition.

Certainly, if two-order upwind (downwind) scheme or QUICK (Quadratic Upwind Interpolation of Convective Kinematics) scheme are introduced, the predicted results should be closer to the experimental data.

Table 3. Main dimensions of electrostatic precipitator

Dimension	Value
Length l	0.8128 m
Height h	0.6096 m
Width s	0.2032 m
Wire-wire spacing l_0	0.2032 m
Wire radius r_C	0.1016

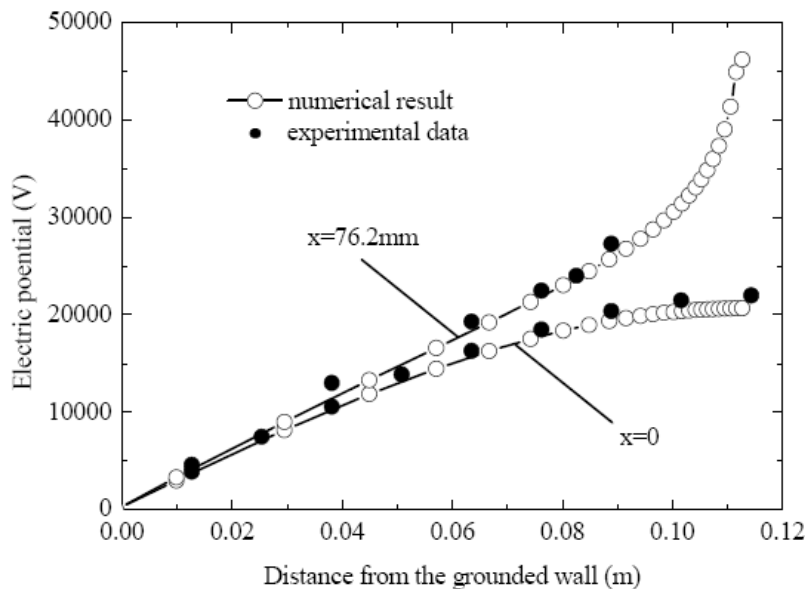


Figure 5. Comparisons of predicted electric potential with Penney's experimental data.

There was no information about the top and bottom plates in Kallio's paper [20,21], so the top and bottom plates were assumed to be insulated as shown in Table 2.

In this way, the electrical condition in the wire-plate electrostatic precipitator becomes two-dimensional. Here, we give the three-dimensional distribution for the space-charge density and the electric potential in the ESP, as shown in Figures 6 and 7.

They show that the horizontal distributions of the space-charge density and the electric potential have an annular shape, with the corona wires at the center of annulus.

Figure 6a shows that the space-charge density is the highest near the corona wire and the lowest near the inlet and outlet, and the influences of the inlet and outlet were not great. Therefore, the periodic boundary condition can be applied as an approximation.

From Figures 6b and 7b, all the isometric lines for the electric potential and the space-charge density are parallel to the corona wire because the top and bottom plates are treated as the insulated plate.

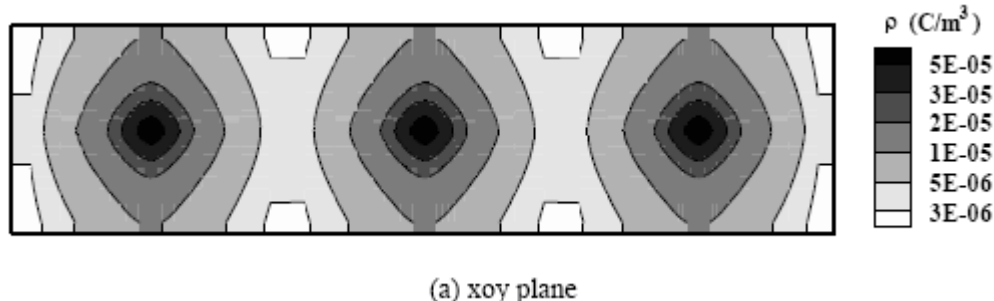


Figure 6. Continued on next page.

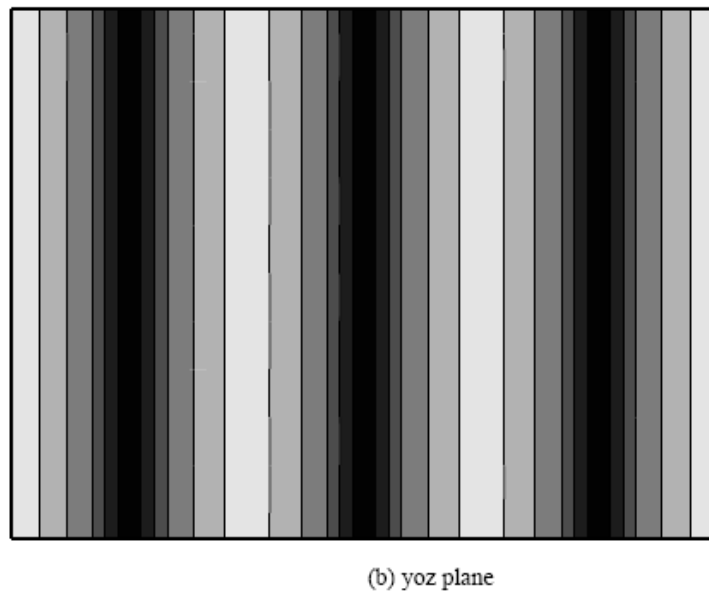
(b) yoz plane

Figure 6. Predicted space-charge density in the wire-plate electrostatic precipitator.

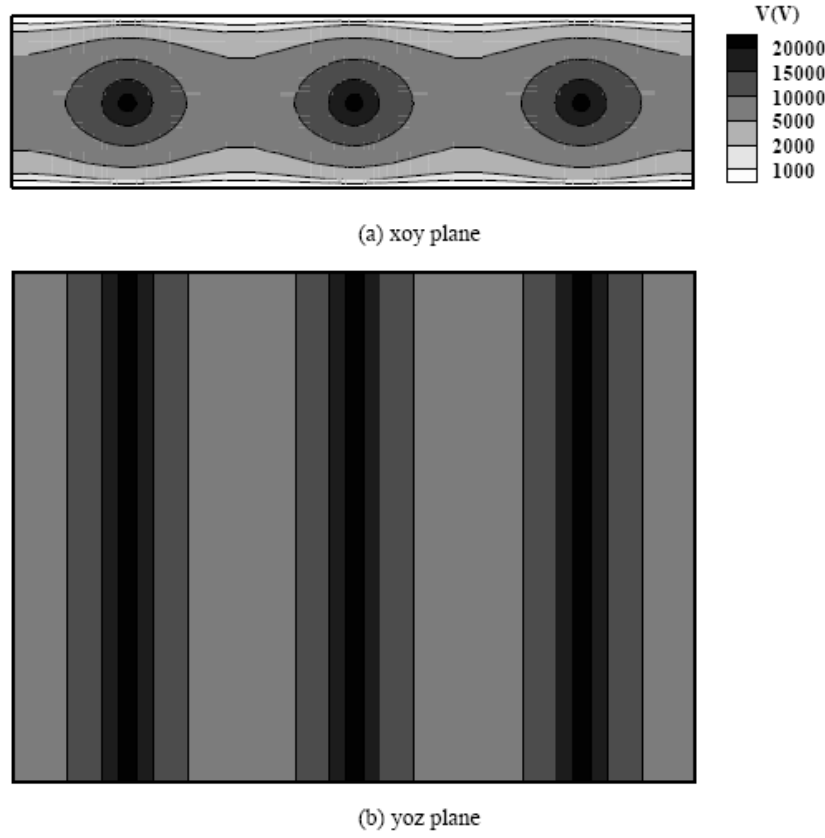


Figure 7. Predicted electric potential in the wire-plate electrostatic precipitator.

3. EHD Turbulent Flow Field

The existence of momentum coupling between the electrostatic field and fluid dynamic field gives rise to a feature known as the electric wind. This secondary gas flow results from corona-generated ions that collide at high velocity with neutral gas molecules residing in the space between the corona wire and grounded plate. The momentum imparted to the gas by the ion flux produces a highly directional gas flow toward the grounded plate in the absence of flow through the precipitator. Continuity demands that gas return to the corona region, thereby promoting a recirculating flow. The interaction of the electric wind with a superimposed inlet velocity was first theoretically investigated by Yamamoto [7] and Lai [8], who used a two dimensional streamline-vorticity numerical model. Soldati [12,13] performed direct numerical simulations(DNS) of the turbulent flow field in ESPs. Direct numerical solution of the time-dependent Navier-Stokes equations is not yet economically feasible despite recent advances in computer technology and numerical techniques. Consequently, the most cost-effective way to solve practical turbulent flow problems is the use of statistically averaged equations governing the mean flow variables [5,9,11,20,23-30]. These time-averaged equations contain correlations between fluctuating quantities which must be closed by some turbulence models before the equations can be solved. Thus, the classic $k - \epsilon$ model [31] is applied in the present study.

3.1. Assumptions

- (1) The fluid is not compressible because the mean flow velocity is lower than the sound velocity in the fluid.
- (2) The air flow in the ESP is a steady turbulent flow.
- (3) The process is isothermal because the viscous and electric losses are negligible with respect to the initial gas enthalpy.
- (4) The effects of the corona wires and particle motion on the fluid flow can be ignored because the diameter of the corona wire is very small and the particle concentration is very low.

3.2. Mathematic Model and Boundary Condition

Regarding the gas as a continuum phase, its behavior can be described by means of mass and momentum conservation equations laws. For a steady-state incompressible turbulent flow, the equations of continuity and momentum can be written as follows:

$$\frac{\partial(\rho^f \bar{u}_i^f)}{\partial x_i} = 0 \quad (i=1,2,3) \quad (25)$$

$$\frac{\partial(\rho^f \bar{u}_j^f \bar{u}_i^f)}{\partial x_j} = -\frac{\partial p}{\partial x_i} + \frac{\partial}{\partial x_j} \left[\mu_{eff} \left(\frac{\partial \bar{u}_i^f}{\partial x_j} + \frac{\partial \bar{u}_j^f}{\partial x_i} \right) \right] + \rho^f g_i + f_i \quad (i,j=1,2,3) \quad (26)$$

where x is the Cartesian coordinate, \bar{u}^f is the fluid mean velocity, p is the mean pressure, f is the Lorentz force, and μ_{eff} is the effective viscosity.

Since no mass sources exist, continuity equation (25) represents a balance between the incoming and outgoing mass fluxes within a fluid volume. The term on the left-hand side and the second term on the right-hand side of momentum equation (26) represent momentum transport by convection and diffusion, the first term on the right-hand side of equation (26) is the pressure gradient term, the third term on the right-hand side of equation (26) is the gravity term, and the last term on the right-hand side of equation (26) represents the momentum imparted to the gas by the Lorentz force, which can be written as

$$f_i = E_i \rho + j_i \times B_i \quad (i=1,2,3) \quad (27)$$

where j is the current density due to free charge motion and B is the local magnetic flux density field. In the electrostatic precipitator, the magnetic field force contribution is negligible owing to the low current densities available. There, Coulomb force becomes an electric body force on the gaseous medium.

$$f_i = E_i \rho \quad (i=1,2,3) \quad (28)$$

The effective dynamic viscosity is the sum of the molecular viscosity μ_l and the turbulent viscosity μ_t .

$$\mu_{\text{eff}} = \mu_l + \mu_t \quad (29)$$

The turbulent viscosity closure condition employed in the Launder and Spalding's $k - \varepsilon$ model is the Prandtl-Kolmogorov equation.

$$\mu_t = \rho^f C_\mu k^2 / \varepsilon \quad (30)$$

where k is the turbulent kinetic energy and ε is the turbulent dissipation rate, C_μ is an empirical constant.

The classic $k - \varepsilon$ model is used to model the turbulence, which requires solving the following two additional transport equations to determine turbulent kinetic energy k and dissipation rate of turbulent kinetic energy ε .

$$\frac{\partial(\rho^f \bar{u}_j^f k)}{\partial x_j} = \frac{\partial}{\partial x_j} \left[\left(\mu_l + \frac{\mu_t}{\sigma_k} \right) \frac{\partial k}{\partial x_j} \right] + G_k - \rho^f \varepsilon \quad (j=1,2,3) \quad (31)$$

$$\frac{\partial(\rho^f \bar{u}_j^f \varepsilon)}{\partial x_j} = \frac{\partial}{\partial x_j} \left[\left(\mu_t + \frac{\mu_t}{\sigma_\varepsilon} \right) \frac{\partial \varepsilon}{\partial x_j} \right] + C_1 G_k \frac{\varepsilon}{k} - \rho^f C_2 \frac{\varepsilon^2}{k} \quad (j=1,2,3) \quad (32)$$

where G_k represents the generation of turbulent kinetic energy due to the mean velocity gradients. It is defined as

$$G_k = \mu_t \frac{\partial \bar{u}_i^f}{\partial x_j} \left[\frac{\partial \bar{u}_i^f}{\partial x_j} + \frac{\partial \bar{u}_j^f}{\partial x_i} \right] \quad (i,j=1,2,3) \quad (33)$$

The values of various turbulence constants appearing in the above equations are as follows:

$$\sigma_k = 1.0, \sigma_\varepsilon = 1.3, C_1 = 1.44, C_2 = 1.92, C_\mu = 0.09$$

3.3. Boundary Conditions

Because of ESP's symmetry, half of the ESP was considered. Table 4 shows that four types of boundaries enclose the domain: the inlet, the outlet, the solid wall and the symmetry plane along the domain. The boundary conditions of k and ε at the inlet in Table 4 are the ones typically employed in predictions when no experimental boundary condition is available. Here, it should be noted that d is the characteristic length of ESP, and u_t^f and u_n^f are the fluid tangential velocity and the fluid normal velocity. The idea of the wall-function approach is employed to define the tangential velocity, turbulent kinetic energy, and dissipation rate of turbulent kinetic energy at the grid nodes near the wall.

Table 4. Boundary conditions for fluid flow

	inlet	outlet	Solid wall	Symmetry plane
velocity	$u^f = u_0$	$\frac{\partial u^f}{\partial n} = 0$	Wall-function	$u_n^f = 0, \frac{\partial u_t^f}{\partial n} = 0$
Turbulent kinetic energy	$k = 0.01u_0^2$	$\frac{\partial k}{\partial n} = 0$	Wall-function	$\frac{\partial k}{\partial n} = 0$
Turbulent dissipation rate	$\varepsilon = \frac{k_0^{1.5}}{d/2}$	$\frac{\partial \varepsilon}{\partial n} = 0$	Wall-function	$\frac{\partial \varepsilon}{\partial n} = 0$

3.4. Numerical Method

The calculational domain was discretized by using a nonuniform grid with a densely packed grid near the corona wire and near the wall. The control-volume method [18] was

chosen to solve these differential equations. These equations were solved by Semi-Implicit Method for Pressure-Linked Equations (SIMPLE) algorithm on a staggered grid where the pressure, turbulent kinetic energy, dissipation rate of turbulent kinetic energy, space-charge density and electric field components were evaluated at the grid nodes while the velocity components were defined at the interfaces between the grid nodes. The discretized equations were solved by using the tri-diagonal matrix algorithm coupled with the Gauss-Siedel routine. The convergence criteria were that the ratio of the difference of input and output fluxes to input flux was less than 0.1%, and the residual error of the mass source term was less than 10^{-8} .

3.5. Numerical Experiments

Figure 8 shows the distribution of Coulomb force in the ESP. Because the space-charge density and the electric field intensity decrease rapidly away from the corona wire, the Coulomb force increases rapidly with the decrease of the distance from the wire. And the magnitude of the Coulomb force at the wire surface is nearly 100 times greater than its magnitude at the collection plate opposite the corona wire, and is almost 1000 times greater than the value at the place between adjacent corona wires.

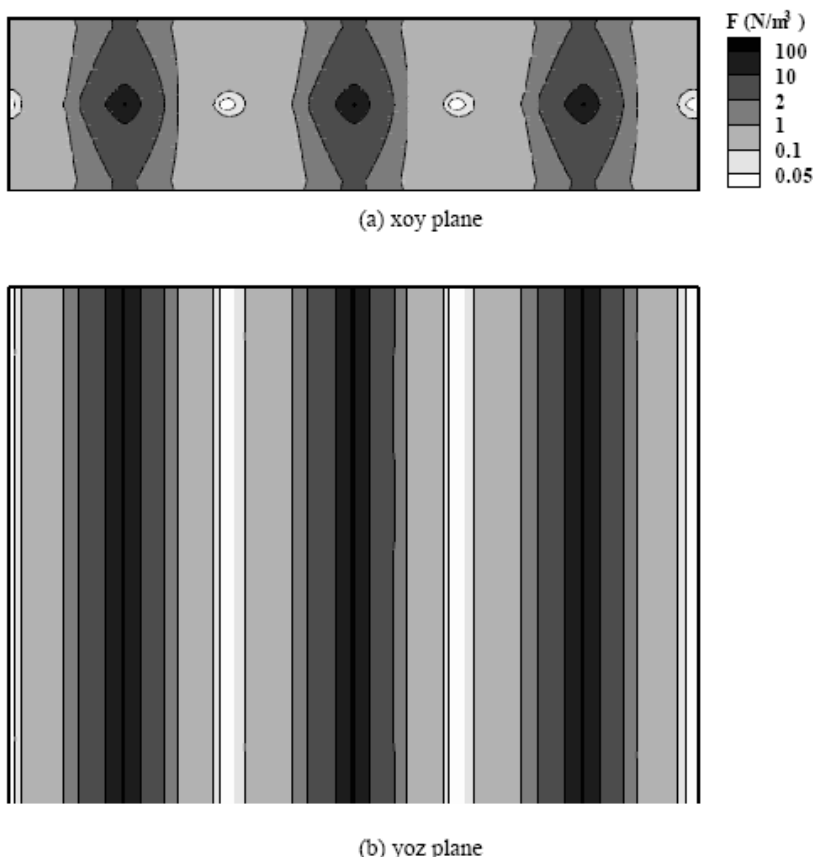


Figure 8. Predicted Coulomb force in the wire-plate electrostatic precipitator.

In order to get the electrohydrodynamic conditions similar to those used in practice, a non-dimensional parameter EHD number, N_{EHD} , which is the ratio between the electrostatic body force and the inertial force acting on the fluid [8], is introduced to investigate the magnitude of the interactions between the cross-flow and the electric wind.

$$N_{EHD} = \frac{i}{l_0 \rho^f \beta U^2} \quad (34)$$

where i/l_0 is the discharge current per unit length of corona wire, and U is the mean flow velocity. In the case of $N_{EHD} = \infty$, the cross-flow does not affect EHD flows. In the case of $N_{EHD} = 0$, it is a simple rectangular duct flow, unaffected by the Coulomb force.

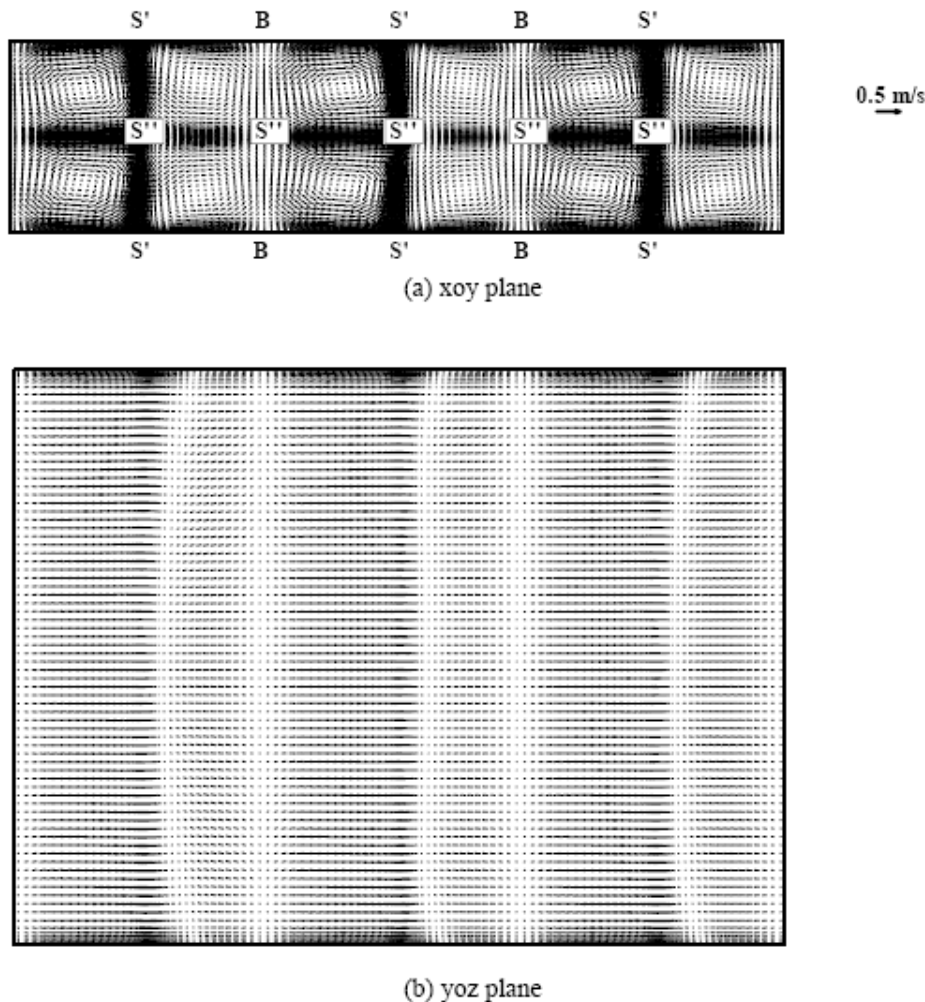


Figure 9. Predicted EHD turbulent flow field without inlet velocity in the wire-plate electrostatic precipitator.

$N_{EHD} = \infty$ means Coulomb force is the dominant force affecting the fluid flow in the ESP. The standard recirculating structure of electric wind is illustrated by Figure 9. At first, the air flows away from the corona wire until it impinges against the grounded plates, then separates and forms arrays of large-scale, spanwise counter-rotating vortical structures. It consists of two series of circulatory cells located symmetrically about the median plane $y=0$ and periodically in the x direction. In average, each wire generates four equal circulatory cells, two upstream and two downstream for the wire. And three different types of singularities are located at equally spaced intervals. Near the grounded plate, there are the separation points (S' point) generated by the impingement of the jets on the grounded plate, and the bonding points (B point) generated by the return flow toward the center of the channel. Another type is the saddle points (S'') in the center-line of the channel, which are located at the corona wires and at the place between adjacent corona wires.

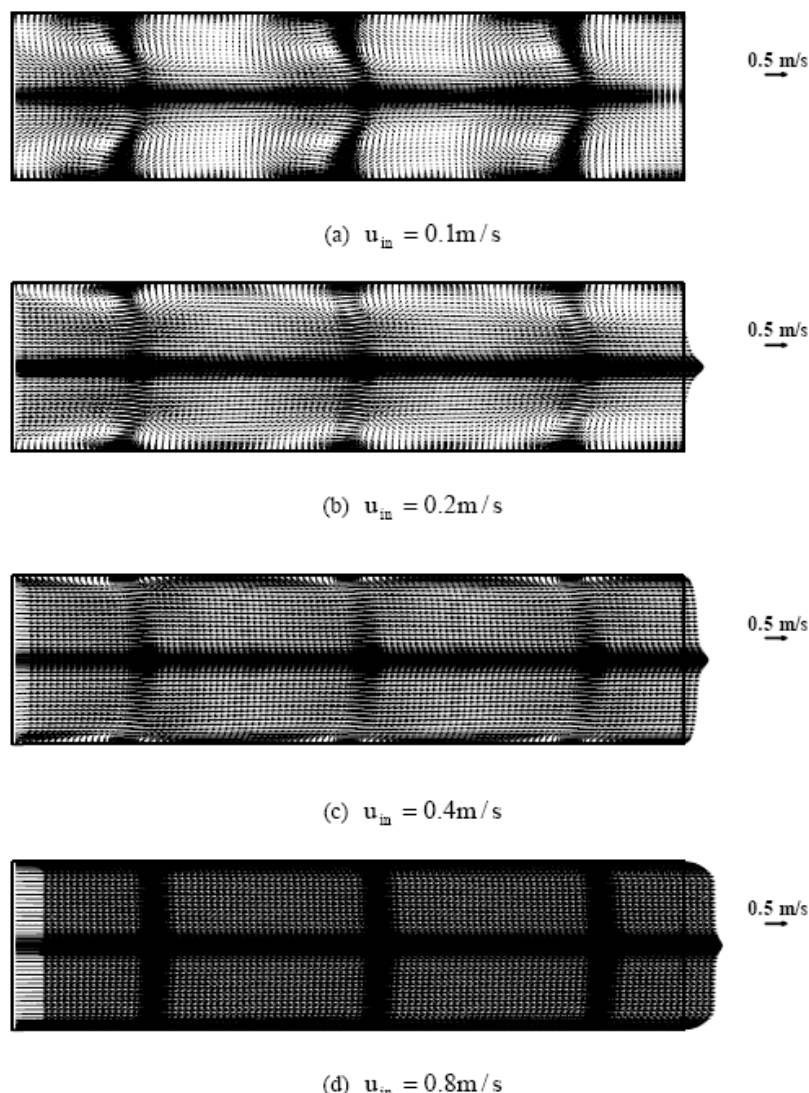


Figure 10. EHD turbulent flow field with different inlet velocities.

Figure 10 shows the cross-flow weakens the intensity of EHD flow, especially in the central region of the channel. As the precipitator inlet velocity is increased, the cross-flow causes the two circulatory cells near the corona wire to merge into one, leaving a total of six circulatory cells.

At $u_{in} = 0.1\text{m/s}$ and $N_{EHD} = 116.0$, arrays of large-scale vertical structures disappear and only one circulatory cell remains near every separation point (S' point) shown in Figure 10a, so the streamline near the grounded plate bends towards the discharge wire. The flow visualization also displayed this phenomenon [7,32]. Further suppression of the circulatory patterns is observed at $u_{in} = 0.2\text{m/s}$ and $N_{EHD} = 29.0$. In the case of $u_{in} = 0.4\text{m/s}$ and $N_{EHD} = 7.3$, the circulatory cells near the grounded plate become smaller. No significant perturbation of the flow field was predicted at $u_{in} = 0.8\text{m/s}$ and $N_{EHD} = 1.8$. The strong cross-flow weaken the large-scale circulatory cells and sweep off the great velocity gradient.

4. Particle Charging and Tracing

Eulerian approach and Lagrangian approach are popular to describe particle behavior in ESP. In the Eulerian approach, the governing equation for particle transport is written as follows:

$$\frac{\partial(U_i^p)C^p}{\partial x_i} = \frac{\partial}{\partial x_i} \left[D_t \frac{\partial C^p}{\partial x_i} \right] \quad (i=1,2,3) \quad (35)$$

Here, U^p is the local particle velocity, C^p is particle number concentration per unit volume, D_t is the turbulent eddy diffusivity coefficient. And the diffusion-like approach is justified only when the particle inertia is negligibly small. There is another problem of imposing boundary conditions on the grounded plate. Though a zero concentration or a zero concentration-gradients is the most popular boundary condition [11,26], the validity of such a boundary condition is questionable in many circumstances, e.g. when the particles of high momentum penetrate the boundary layer through a strong turbulence. To overcome the shortcoming of the current Eulerian method, a Lagrangian particle tracking method is applied to simulate the particle motion in the turbulence. Because a set of differential equations should be solved for one particle [9,12,14,23,25,27-30], it is difficult to trace many particles at the same time due to limited computational resources.

4.1. Assumptions

- (1) A particle in the air is simplified as a spherical particle, and the density and shape of the particle remain unchanged during its motion.
- (2) The particle doesn't rotate during its motion.
- (3) If the particle is trapped by the grounded plates, it should not come back to the system any more.

-
- (4) Collision and coagulation among particles are not considered.
 - (5) Particle motion does not affect the flow field because small particles are loaded in low concentration.

4.2. Particle Charging Kinetics

Particles in a corona field are charged simultaneously by both field and diffusion charging. The field charging occurs in the presence of a strong electric field and is dependent on particle properties. The rapid motion of ions in an electric field results in frequent collisions between the ions and the particles. When an uncharged particle is placed in an electric field, it distorts the electric field. The extent of the distortion of the field near the particle surface is dependent on the relative dielectric constant of the particle and the charges on the particle. After a sufficiently long charging time, a particle essentially attains the saturation charge, which produces an electric field on particle surface equal and opposite to the external field [33].

$$q_s = \frac{3\epsilon_r}{\epsilon_r + 2} \pi \epsilon_0 d_p^2 E_0 \quad (36)$$

where ϵ_r is the relative dielectric constant, d_p is the particle diameter, and E_0 is the external field.

The diffusion charging is the dominant charging process for very small particles or very weak electric fields. It takes into account the possible impact of ions on the particle surface due to their stochastic thermal velocity. This mechanism does not require an external electrical field. As the charge accumulates, it produces a field that tends to repel additional ions, reducing the charging rate. The ions, being in equilibrium with the gas molecules, have a Boltzmann distribution of velocities. As the charge on the particle increases, fewer and fewer ions have sufficient velocity to overcome the repulsive force, and the charging rate slowly approaches zero. In theory, the charging rate never reaches zero because the Boltzmann distribution of velocities has no upper limit [33].

The complete particle non-dimensional charging rate is the sum of the field charging rate and the diffusion charging rate. Recently, Lawless [34] gave a linear differential equation which has to be solved with respect to time based on the local fields experienced by the particle. Such a model accounts for the field charging and the additional diffusive charging current of ions transported by the electric field near the surface.

To calculate the charging rate of a particle at different locations, the above non-dimensional charging equations should be rewritten as

$$\frac{dq}{dt} = \frac{d\omega}{d\tau_q} \cdot \frac{2\pi d_p k_0 T \rho \beta}{q_e} \quad (37a)$$

with

$$\frac{d\omega}{d\tau_q} = \begin{cases} f(w) \frac{\omega - 3w}{\exp(\omega - 3w) - 1} & \text{if } \omega > 3w \\ \frac{3w}{4} \left(1 - \frac{\omega}{3w}\right)^2 + f(w) & \text{if } -3w \leq \omega \leq 3w \\ -\omega + f(w) \frac{-\omega - 3w}{\exp(-\omega - 3w) - 1} & \text{if } \omega < -3w \end{cases} \quad (37b)$$

Here, ω , w and τ_q are the non-dimensional particle charge, the non-dimensional electric field and the non-dimensional particle charging time, respectively. Their expressions are as follows:

$$\omega = \frac{qq_e}{2\pi\epsilon_0 d_p k_0 T} \quad (38)$$

$$w = \frac{Ed_p}{2k_0 T / q_e} \quad (39)$$

$$\tau_q = \frac{\rho\beta t}{\epsilon_0} \quad (40)$$

where q_e is the electronic unit charge, q is the charge on the particle, k_0 is Boltzmann constant, and t is the time.

The function $f(w)$ is the area fraction of the particle surface covered by the diffusive current. It can be determined by

$$f(w) = \begin{cases} \frac{1}{(w + 0.475)^{0.575}} & \text{if } w \geq 0.525 \\ 1 & \text{if } w < 0.525 \end{cases} \quad (41)$$

4.3. Particle Movement

4.3.1. Particle Trajectory Model

All the time-average data of the fluid field, including the velocity, the turbulent kinetic energy and the dissipation rate of turbulent kinetic energy can be known a priori. The effect of the fluid turbulence on the particle movement was considered, but the effect of particle movement on the fluid turbulence could be ignored if the particle concentration is very low. Lagrangian approach is based on tracking of individual particles from inlet to outlet of the ESP channel. And the particles' trajectories were evaluated by using the unsteady-state particle momentum balance equations.

$$\frac{1}{6} \pi d_p^3 \rho^p \frac{du_i^p}{dt} = F_i^D + F_i^g + F_i^b + F_i^E + F_i^V + F_i^B + F_i^p + F_i^S \quad (i=1,2,3) \quad (42)$$

where ρ^p is the particle density, and u_i^p is the velocity of the particle.

Here, the drag force F_i^D represents the drag force due to the relative velocity of the particle and the fluid, and is given by

$$F_i^D = \frac{1}{2} \cdot \frac{1}{4} \pi d_p^2 \cdot \rho^f C_D |u_i^f - u_i^p| (u_i^f - u_i^p) \quad (43)$$

with

$$C_D = \begin{cases} \frac{24}{C_c Re_p} & \text{if } Re_p \leq 0.1 \\ \frac{24}{Re_p} (1 + 0.15 Re_p^{0.687}) & \text{if } 0.1 < Re_p < 800 \\ 0.44 & \text{if } Re_p \geq 800 \end{cases} \quad (44)$$

where the particle Reynolds number Re_p and the Cunningham slip correction factor C_c can be expressed as [33]

$$Re_p = \rho^f |u_i^p - u_i^f| d_p / \mu_l \quad (45)$$

$$C_c = 1 + \frac{1000}{Pd_p} [15.06 + 7.00 \exp(-59Pd_p)] \quad (46)$$

Here, P is the absolute pressure.

The gravitational force F_i^g causes the particle to descend in the fluid and is given by

$$F_i^g = \frac{1}{6} \pi d_p^3 \rho^p g_i \quad (47)$$

Similarly, the buoyancy force F_i^b causes the particle to rise in the fluid and is given by

$$F_i^b = -\frac{1}{6} \pi d_p^3 \rho^f g_i \quad (48)$$

The electric field force \vec{F}_E acting on the charged particle is given by

$$\mathbf{F}_i^E = \mathbf{E}_i \mathbf{q} \quad (49)$$

The virtual mass force \mathbf{F}_i^V accounts for the relative acceleration of the particle and the fluid and is given by

$$\mathbf{F}_i^V = \frac{1}{12} \pi d_p^3 \rho_f \left(\frac{du_i^f}{dt} - \frac{du_i^p}{dt} \right) \quad (50)$$

The Basset history force \mathbf{F}_i^B due to the transient formation of a boundary layer near the particle surface is given by

$$\mathbf{F}_i^B = \frac{3}{2} d_p^2 \sqrt{\pi \rho_f \mu_l} \int_0^t \frac{\frac{du_i^f}{d\tau} - \frac{du_i^p}{d\tau}}{\sqrt{t-\tau}} d\tau \quad (51)$$

The pressure gradient force \mathbf{F}_i^P due to the acceleration of the fluid flow field is given by

$$\mathbf{F}_i^P = \frac{1}{6} \pi d_p^3 \rho_f \frac{du_i^f}{dt} \quad (52)$$

The Saffman lift force \mathbf{F}_i^S acting on the particle moving through the stream with a velocity gradient [35] is given by

$$\mathbf{F}_i^S = 1.61 d_p^2 (\mu_l \rho_f)^{1/2} |\nabla \times \mathbf{u}_i^f|^{-1/2} [(\mathbf{u}_i^f - \mathbf{u}_i^p) \times (\nabla \times \mathbf{u}_i^f)] \quad (53)$$

The equation (42) of motion for the particle, which was solved by stepwise integration over discrete time steps, yields the velocity of the particle at each point along the trajectory. The particle trajectories were predicted by

$$\frac{dx_i}{dt} = u_i^p \quad (54)$$

4.3.2. Particle Random Walk Model

The Eulerian approach can not properly handle the *in-situ* particle charging or the particle motion near the grounded plate. For Lagrangian method, how to specify the ever-changing flow field is one important problem related to particle motion in turbulent flow. The simplest way is the introduction of the eddy life-time model[36], which use a Gaussian probability distribution for fluctuating velocity $u_i'^f$ with a mean value of zero and the root mean square

fluctuating velocity $\overline{u_i'^f}$ as standard deviation. The instantaneous fluid velocity is then given by

$$u_i^f = \bar{u}_i^f + u_i'^f = \bar{u}_i^f + \xi \sqrt{2k/3} \quad (55)$$

In this model, the particle interacts with the fluid phase in the turbulent eddies over the eddy life-time τ_e . When the eddy life-time is reached, a new value of the fluid instantaneous velocity is obtained by applying a new value of random number ξ , whose value is distributed between -1 and 1. Each eddy is characterized by a Gaussian distributed random velocity fluctuation $u_i'^f$, which keeps constant over the characteristic life-time of the eddies. The expression of the life-time scale of the eddy τ_e is expressed as follows

$$\tau_e = 0.3 \frac{k}{\varepsilon} \quad (56)$$

The eddy life-time model assumes that flow field is frozen during each interval. But in fact, the velocities at adjacent points or the velocities at a point at subsequent instants are not perfectly random but are inter-related, so sometimes the assumption of frozen flow field may lead to some errors. However, these deficiencies can be improved if correlation functions between adjacent points or between subsequent intervals are taken into account.

In the present work, an improved Lagrangian simulation method proposed by Lu [37,38] is adopted, because the crossing trajectory and continuity effects are clearly observed and the particle diffusion coefficients obtained for the condition of high particle drift velocity is close to the theoretical values.

At the instant t , a particle and a fluid particle start out from the same position \vec{r}_s . After one time step of computation, Δt , they arrive at \vec{r}_p and \vec{r}_f , respectively. And the distance between \vec{r}_p and \vec{r}_f is Δs , as shown in Figure 11.

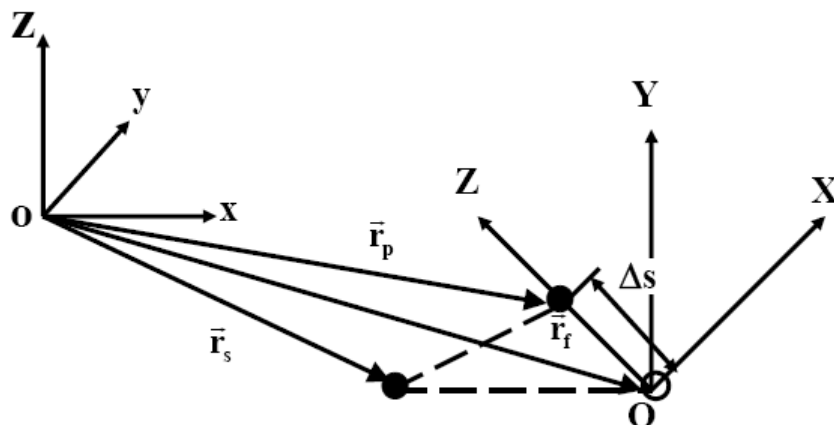


Figure 11. Coordinate system for particle tracing simulation.

Here, o-xyz is the absolute coordinate system, and O-XYZ is the relative coordinate system based on Δs . The fluctuating velocity of the fluid at position \vec{r}_s and \vec{r}_p are assumed to have the following relations.

$$\bar{W}_i(\vec{r}_p) = f(\Delta t)g_i(\Delta s)\bar{W}_i(\vec{r}_s) + \psi_i \quad (i=1,2,3) \quad (57)$$

where the normalized fluctuating component is defined on the coordinate system of O-XYZ as

$$\bar{W}_i = \frac{\bar{u}'^f_i}{\sqrt{\bar{u}'^f_j \bar{u}'^f_j}} \quad (i,j=1,2,3) \quad (58)$$

Here, the subscripts 1, 2 and 3 denote the directions of X, Y and Z axis shown in Figure 11, and the overbars indicate the ensemble average values. The random variables ψ_i is assumed to be Gaussian distribution with mean value and a variance $(\sigma_\psi)_i$ which are obtained by

$$\overline{\psi_i} = 0 \quad (59a)$$

$$(\sigma_\psi)_i = \sqrt{1 - f^2(\Delta t)g_i^2(\Delta s)} \quad (i=1,2,3) \quad (59b)$$

For the implementation of this model, it is essential to determine an appropriate expression for the correlation functions $f(\Delta t)$ and $g_i(\Delta s)$.

$$f(\Delta t) = \exp\left(\frac{-\Delta t}{\tau_f}\right) \quad (60)$$

$$g_i(\Delta s) = \exp\left(\frac{-\Delta s}{2\Lambda_i}\right) \cos\left(\frac{\Delta s}{2\Lambda_i}\right) \quad (i=1,2,3) \quad (61)$$

The Lagrangian integral timescales τ_f and the Eulerian length-scale Λ_i are deduced from statistical turbulence quantities, i.e. the turbulent kinetic energy k and the dissipation rate of turbulent kinetic energy ε in the case of $k - \varepsilon$ turbulence model.

$$\tau_f = 0.235 \frac{\bar{u}'^f_j \bar{u}'^f_j}{\varepsilon} \quad (j=1,2,3) \quad (62)$$

$$\Lambda_1 = 2.5\tau_f \sqrt{\bar{u}'^f_j \bar{u}'^f_j} \quad (j=1,2,3) \quad (63a)$$

$$\Lambda_2 = \Lambda_3 = 0.5\Lambda_1 \quad (63b)$$

Here, Λ_1 is the longitudinal length-scale, and Λ_2 and Λ_3 are transverse length-scales. For isotropic turbulence, the mean square velocity fluctuation $\overline{u_j'^f u_j'^f}$ are related to the turbulent kinetic energy k by $\overline{u_j'^f u_j'^f} = \frac{2}{3}k$ ($j=1,2,3$).

4.4. Boundary Conditions

There are two types of boundary conditions for particle tracing.

- (1) At the inlet, the particle's velocity is equal to the fluid velocity at the injection point and the particles are charge-free.
- (2) The calculation stops until the particle is removed by the grounded plate or escaped from the outlet.

4.5. Numerical Method

The solution for the fluid flow equations provides the hydrodynamic conditions for the calculation of the motion of the particle. The particle motion is coupled with the particle charging process: the variation of the particle's charge changes the particle's path, which in turn affects the particle's charging rate because the electro-corona field is not uniform. The calculation procedure is described as follows:

1. Particle's starting position and initial velocity are given at $t=0$. The initial fluctuating velocity components $u_i'^f$ at the particle position are obtained from Gaussian variables satisfying probability distribution function with variances $\overline{u_i'^f u_i'^f}$ ($i=1,2,3$). The instantaneous fluid velocity can be known by adding the known mean velocity and the fluctuating velocity.
2. After one time step, according to the fluid instantaneous velocity, the particle charging rate and the new position can be solved from equations (37), (42) and (54) simultaneously, so the fluid position \vec{r}_f , the particle's position \vec{r}_p and the particle's charge q can be obtained.
3. A relative coordinate system O-XYZ is established to obtain the fluid fluctuating velocity at \vec{r}_p from equation (57).
4. The numerical solution is repeated from step 2 to step 3 until the particle is trapped by the grounded plate or escapes through the ESP.

A fourth-order adaptive-step-size Gill method was adopted to solve these equations simultaneously, and the convergence criteria were

$$\left\{ \begin{array}{l} \max \left| \frac{u_i^{P,K+1} - u_i^{P,K}}{u_i^{P,K+1}} \right| < 10^{-5} \\ \left| \frac{q_r^{K+1} - q_r^K}{q_r^{K+1}} \right| < 10^{-5} \end{array} \right. \quad (64)$$

where $q_r = q/q_e$ is the amount of the charge on the particle, and K was the iteration number.

4.6. Numerical Experiments

Figure 12 shows the predicted trajectories of different sized particles. In contrast with the x and y directions, the particle movement in the z direction is not obvious. The $1\mu\text{m}$ particle entering the channel gradually moves toward the first wire, and then is pushed back toward the grounded plate.

After passing the second corona wire or the third corona wire, it is pushed toward the grounded plate again. Such a staggered shape of the particle paths comes from the increments in particle charge near the wires shown in Figure 13 and the strong electric field near the wires.

Figure 13 shows the particle size is one of the key factors to affect particle charging process. The bigger the particle, the more the particle's charge. For example, the charge on the $1\mu\text{m}$ particle is one order higher than that on the $0.1\mu\text{m}$ particle, and the charge on the $10\mu\text{m}$ particle is also one order higher than that on the $1\mu\text{m}$ particle. For the particle smaller than $1\mu\text{m}$, its charge always increases along with its whole trajectory, and one jump happens when it passes the corona wire. For the particle larger than $10\mu\text{m}$, the increase of particle's charge is not obvious after it passes the first corona wire, and there are the difference of the charge among the particles with the same size because of their different trajectories in the ESP.

Figure 14 shows some interesting phenomena. (1) The electric field and drag forces are the key forces acting on particles in the ESP. The drag force always maintains a balance with the electric field force except that the particle moves between the corona wires. And the electric field force and the drag force are usually one order greater than the other forces. (2) The variation frequencies of the Basset history force, the virtual mass force and the pressure gradient force are very high. (3) At the initial stage of the particle's movement, the electric field force increases rapidly with the increase of the particle's charge, and the gravitational force and the electric field force are at the same order. (4) Sometimes, the Basset history force is two orders higher than the gravitational force for the $0.1\mu\text{m}$ particle, and is in the same order of the gravitational force for the $1\mu\text{m}$ particle.

Thus, the Basset history force plays an important role for the motion of the particle less than $1\mu\text{m}$. (5) Two groups of forces follow the same variation rule along with the particle's trajectory although they are not in the same order.

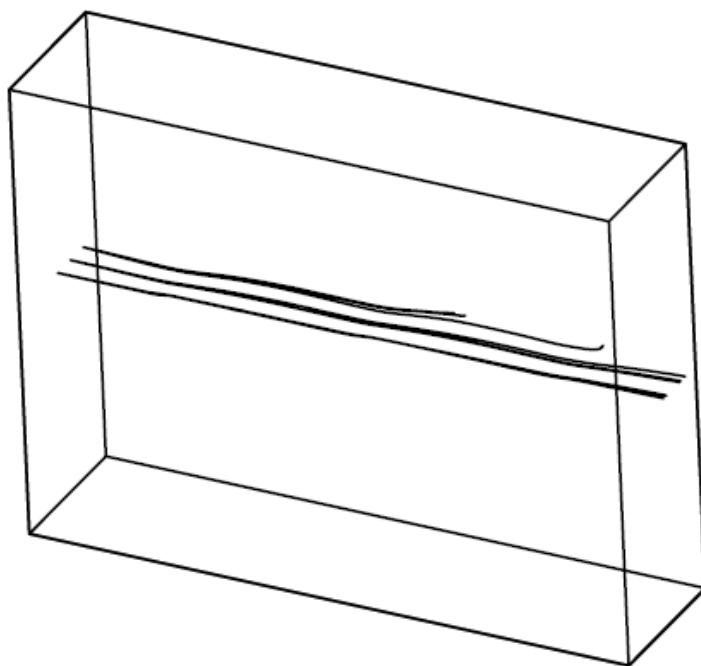
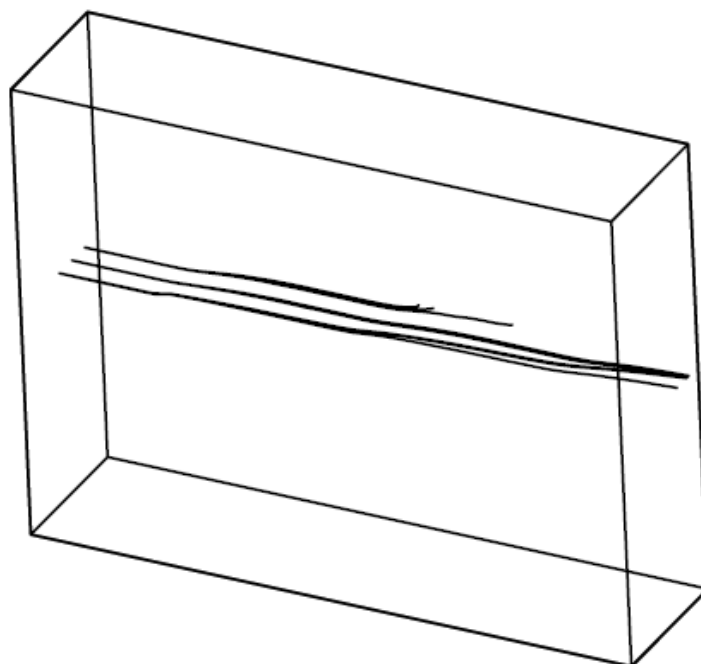
(a) $0.1\mu\text{m}$ (b) $1\mu\text{m}$

Figure 12. Continued on next page.

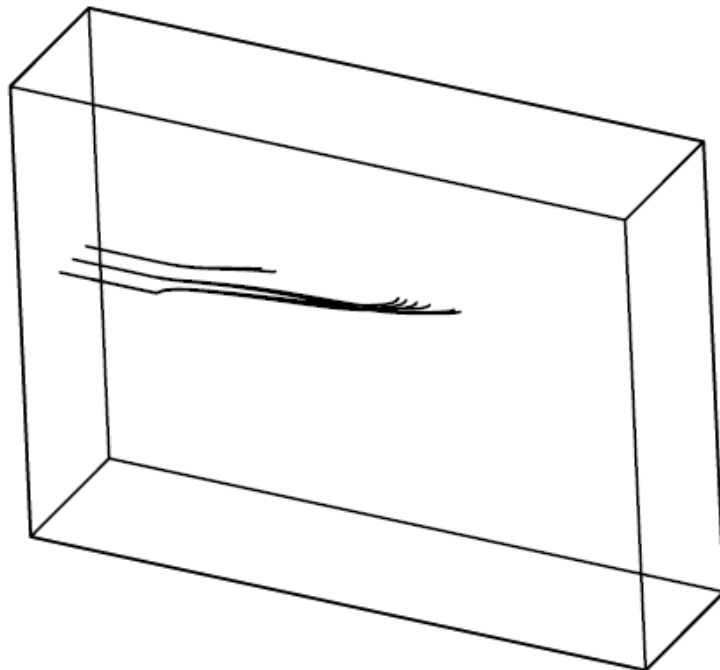
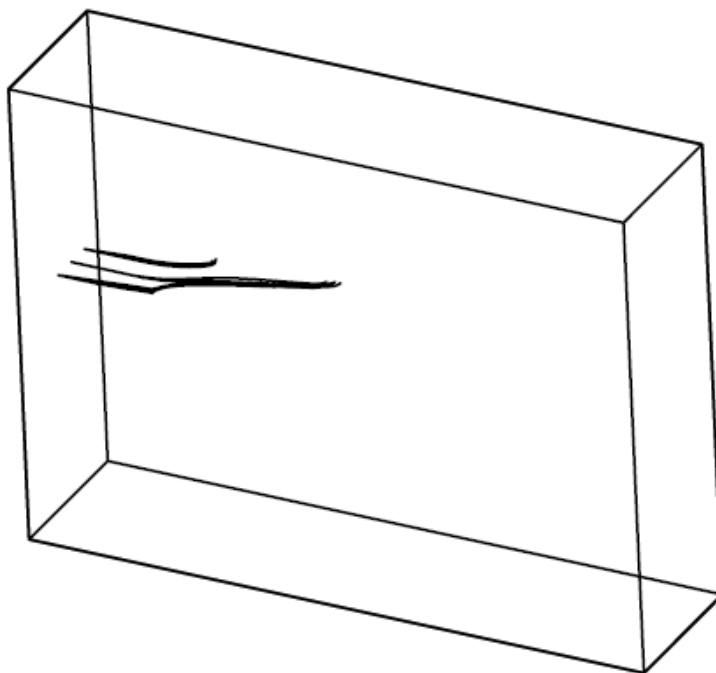
(c) $5\mu\text{m}$ (d) $10\mu\text{m}$

Figure 12. Trajectories of different sized particles in the ESP.

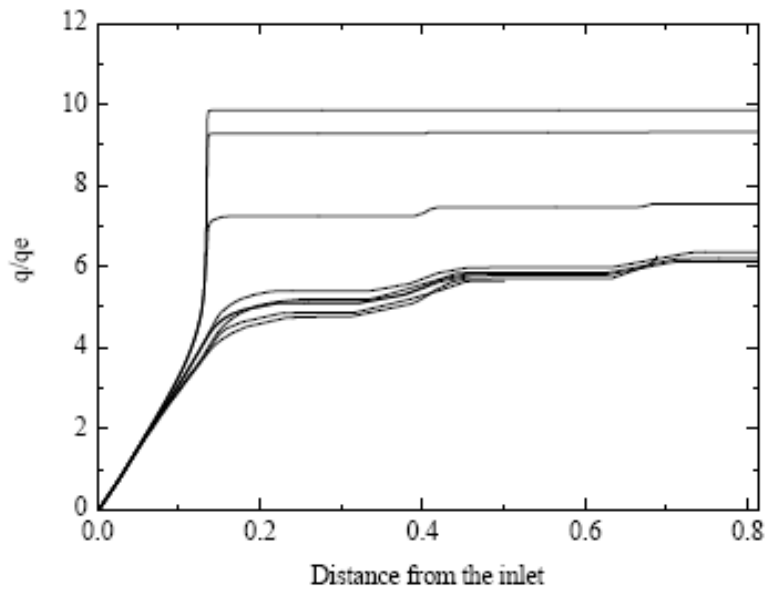
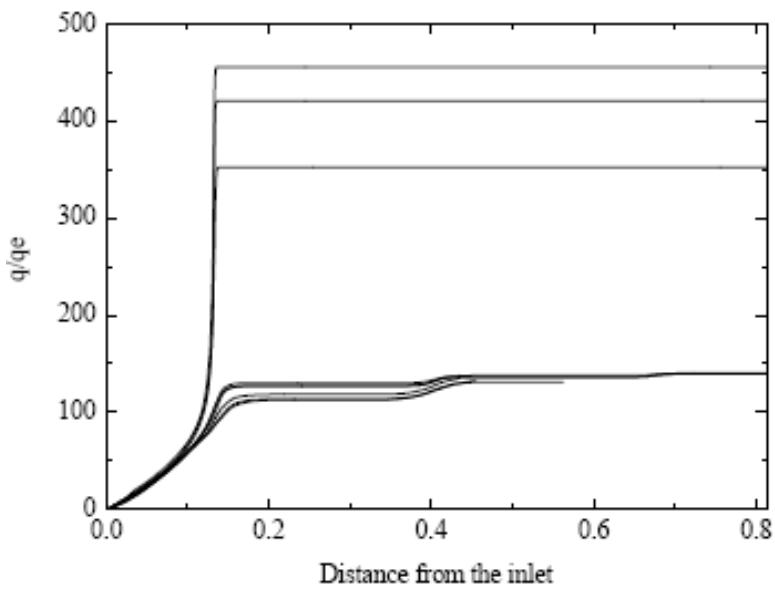
(a) $0.1\mu\text{m}$ (b) $1\mu\text{m}$

Figure 13. Continued on next page.

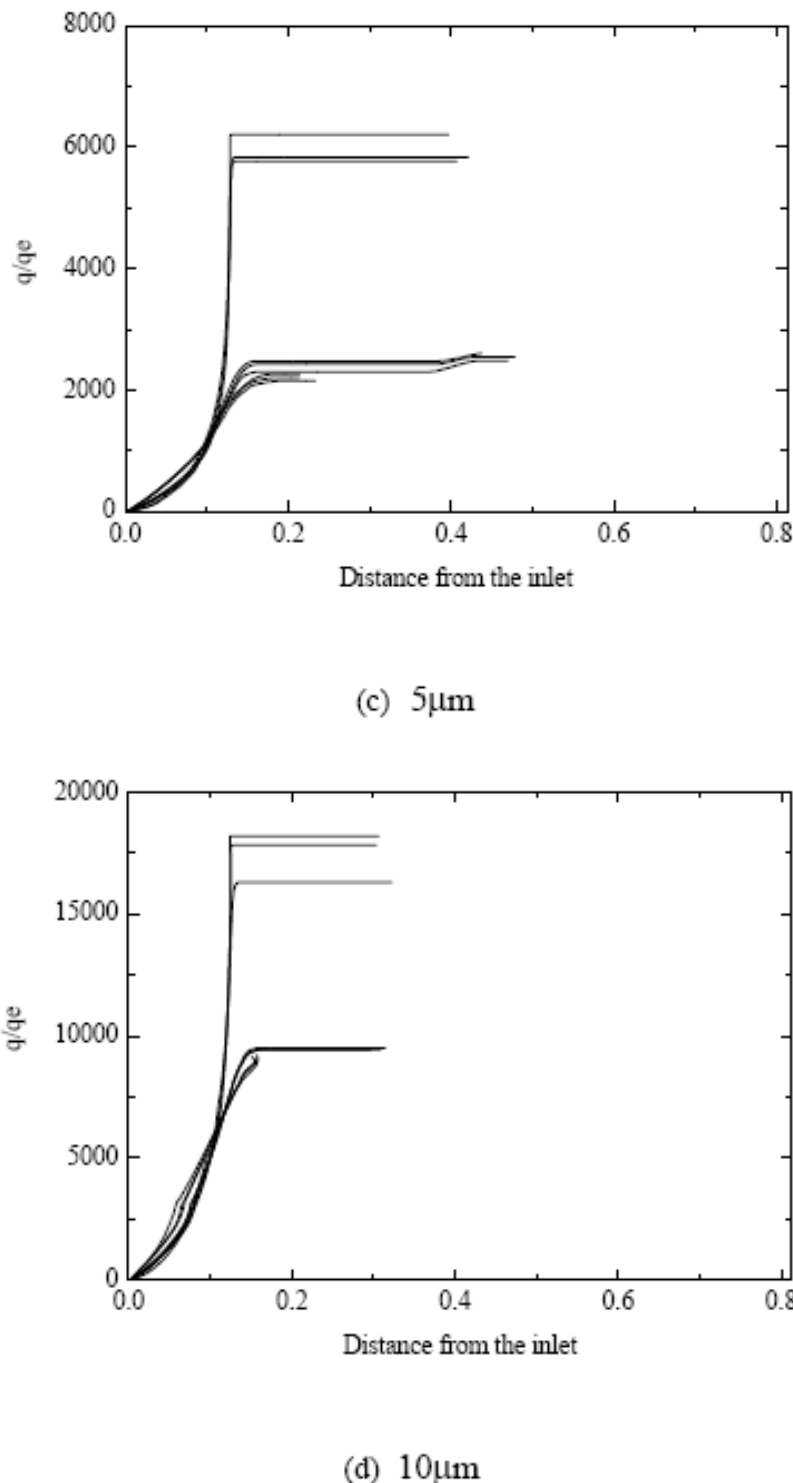


Figure 13. Particle charging history along with its trajectory.

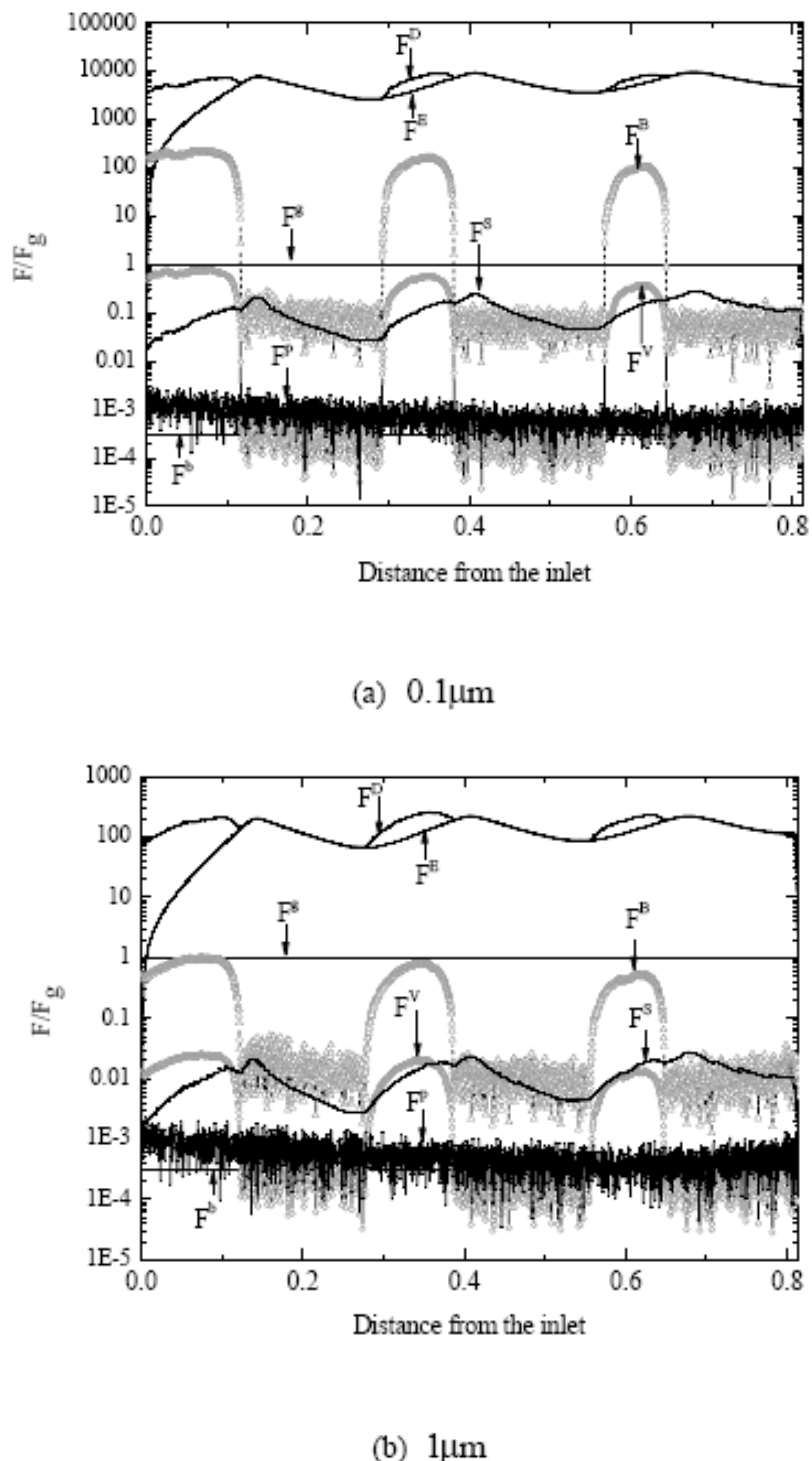


Figure 14. Continued on next page.

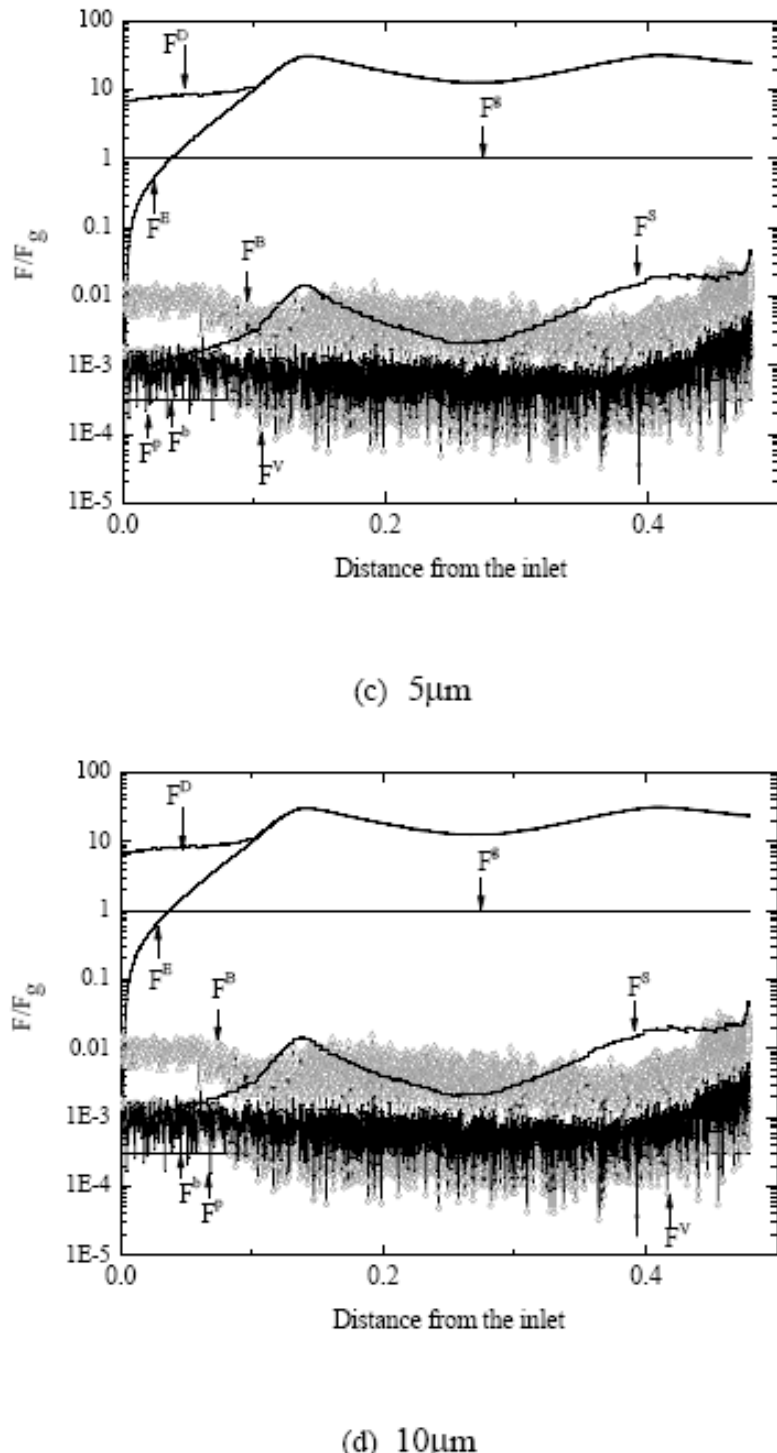


Figure 14. Forces acting on the particle along with its trajectory.

One group is the electric field force, the drag force and the Saffman lift forces. Among these forces, the electric field force depends on the distribution of electrostatic field and the

others are related to the relative velocity of the particle and the flow field. Another group is the Basset history force and the virtual mass forces, which are related to the relative acceleration of the particle and the flow field. (6) During the movement of the particle, the buoyancy force, the virtual mass force, the pressure gradient force and the Saffman lift force are always far less than the gravitational force. (7) Two kinds of forces are distinguished along with the particle trajectory. During the initial stage of particle's movement, the electric field force is the greatest in the absolute value variation. Another distinguished force is the Basset history force, whose order variation is up to four orders for the $0.1\mu\text{m}$ particle.

The electrostatic body force grows with particle diameter, so the larger particles are deflected towards the wall, and then push towards the wall stronger than the smaller particles. For example, the particles, whose size is greater than $5\mu\text{m}$, are trapped by the grounded plate before they pass the third corona wire. In other words, the bigger particle can not follow the flow field because it has greater inertia and more charges than the smaller one. And the particles' trajectories are shortened with the increase of particle diameter.

The effect of the turbulence on the particle tracing and charging depends on the particle diameter. For the particles smaller than $0.1\mu\text{m}$, their movements are sensitive to the turbulence because the smaller particle has less inertia. But the diffusion charging is the dominant mechanism, so their charging curves are smooth and the difference of the charge among them is not obvious. It should be noted that particle's charges at the terminal position are less than one elementary charge for the particles smaller than $0.01\mu\text{m}$. In other words, a portion of the small particles are not charged. If the particle's diameter is greater than $10\mu\text{m}$, the effect of turbulence on its movements is not obvious. And the field charging is the dominant mechanism, so their charges reach saturated state quickly after they pass the first corona wire. On this condition, the difference of the charge among them is also not obvious. For the particles around $1\mu\text{m}$, their movements are sensitive to the fluid turbulence, and diffusion charging and field charging are operating at the same time. Thus, their trajectories and charging histories are much more complicated. For the particles with the same size, they are released from the same starting point, but they have different trajectories and different charging rates, especially when they are in the vicinity of the corona wire because they get high charged by the strong electric field near the wires.

Conclusion

- (1) The control-volume method can be applied to solve three-dimensional unsymmetrical electrical condition in an electrostatic precipitator without knowing the electric-field direction a priori by using upwind (or downwind) scheme for the positive(or negative) corona. The present method complies with the physical facts that the positive charges move in the direction of electric-field strength and the negative charges move in the opposite direction of the electric-field strength.
- (2) The electric wind in a wire-plate ESP has arrays of large-scale, spanwise counter-rotating vertical structures, and each wire generates four equal circulatory cells. The cross-flow modifies the EHD flows in ESP. When N_{EHD} is from 7.3 to 116.0, only

one circulatory cell remains near every separation point. When N_{EHD} is below 1.8, the structure of EHD flow disappears.

- (3) For the particles smaller than $0.1\mu\text{m}$, their movements are sensitive to the fluid turbulence but the difference of the charge among the particles is not obvious. For the particles larger than $10\mu\text{m}$, their movements are not sensitive to the turbulence, and their charges reach saturated state quickly after they pass the first corona wire, so the precharge assumption can be applied only for the particles larger than $10\mu\text{m}$. For the particles between $0.1\mu\text{m}$ and $10\mu\text{m}$, their movements and charging history are much more complicated.
- (4) The gravitational force and the Basset history force play important roles for the motion of the particles less than $1\mu\text{m}$.
- (5) Two groups of forces follow the same variation rule along with the particle's trajectory. One group is the electric field force, the drag force and the Saffman lift force, another group is the Basset history force and the virtual mass force.
- (6) The variation frequencies of the Basset history force, the virtual mass force and the pressure gradient force are very high.

References

- [1] Leutert, G.; Bohlen, B. Der raumliche verlauf von elektrischer feldstarke und raumladdungsdichte im platten-elektrofilter, *Staub Reinhalt Luft*. 1972, 32(7): 297-301.
- [2] McDonald, J. R.; Smith, W. B.; Spencer III H. W.; Sparks L. E. A mathematical model for calculating electrical conditions in wire-duct electrostatic precipitation devices, *J. Appl. Phys.* 1977, 48(6): 2231-2243.
- [3] Lawless, P. A.; Sparks, L. E. A mathematical model for calculating effects of back corona in wire-duct electrostatic precipitators, *J. Appl. Phys.* 1980, 51(1): 242-256.
- [4] Kallio, G. A.; Stock, E. D. Computation of electrical conditions inside wire-duct electrostatic precipitators using a combined finite-element, finite-difference technique, *J Appl. Phys.* 1986, 59(6): 1799-1806.
- [5] Liang, W. J.; Lin, T. H. The characteristics of ionic wind and its effect on electrostatic precipitators, *Aerosol Sci. Technol.* 1994, 20(4): 330-344.
- [6] Lami, E.; Mattachini, F.; Sala, R.; Vigl, H. A mathematical model of electrostatic field in wires-plate electrostatic precipitators, *J. Electrostat.* 1997, 39(1): 1-21.
- [7] Yamamoto, T.; Velkoff, H. R. Electrohydrodynamics in an electrostatic precipitator. *J. Fluid Mech.*, 1981, 108, 1-18.
- [8] Lai, F. C.; Mckinney P. J.; Davidson J. H. Oscillatory electrohydrodynamic gas flows. *J. Fluid Eng.* 1995, 117(3): 491-497.
- [9] Goo, J. H.; Lee, J. W. Stochastic simulation of particle charging and collection characteristics for a wire-plate electrostatic precipitator of short length. *J. Aerosol Sci.* 1997, 28(5): 875-893.
- [10] Lu, C.; Huang, H. A sectional model to predict performance of a plate-wire electrostatic precipitator for collecting polydisperse particles. *J. Aerosol Sci.* 1998, 29(3): 295-308.

- [11] Park, S. J.; Kim, S. S. Electrohydrodynamic flow and particle transport mechanism in electrostatic precipitator with cavity walls. *Aerosol Sci. Technol.* 2000, 33(3): 205-221.
- [12] Soldati, A.; Banerjee, S. Turbulence modification by large-scale organized electrohydrodynamic flows. *Phys. Fluids*, 1998, 10(7): 1742-1756.
- [13] Soldati, A. On the Effects of electrohydrodynamic flows and turbulence on aerosol transport and collection in wire-plate electrostatic precipitators. *J. Aerosol Sci.* 2000, 31(3): 293-305.
- [14] Yoo, K. H.; Lee, J. S.; Oh, M. D. Charging and Collection of Submicron Particles in Two-Stage Parallel-Plate Electrostatic Precipitators. *Aerosol Sci. Technol.*, 1997, 27(3): 308-323.
- [15] Lei, H.; Wang, L. Z.; Wu, Z. N. Applications of upwind and downwind schemes for calculating electrical conditions in a wire-plate electrostatic precipitator. *J. Comput. Phys.* 2004, 193(2): 697-707.
- [16] Lei, H. Charge-current-conservation model for calculating electrical conditions in a wire-plate electrostatic precipitator. *IEEE Trans. Dielect. Elec. Insul.*, 2006, 13(4): 795-802.
- [17] Lei, H.; Xu, G. J.; He J. C. Magnetic field, flow field and inclusion collision growth in a continuous caster with EMBR. *Chem. Eng. Technol.* 2007, 30(12): 1650-1658.
- [18] Patankar S. V. *Numerical Heat Transfer and Fluid Flow*. Series in computational method in mechanics and thermal sciences, Hemisphere Pub. Co: Washington, 1980; pp 36-39.
- [19] Peek, F. W. *Dielectric phenomena in high-voltage engineering*, McGraw-Hill, New York, 1929; pp 48-84.
- [20] Kallio, G. A.; Stock, D. E. Interaction of electrostatic and fluid dynamic fields in wire-plate electrostatic precipitators. *J. Fluid Mech.* 1992, 240: 133-166.
- [21] Kallio, G. A.; Stock, D. E. Flow visualization inside a wire-plate electrostatic precipitator, *IEEE Trans. Indust. Appl.* 1990, 26(3): 503-514.
- [22] Penney G. W.; Matlick R. E. Potentials in D-C Corona Fields. *Trans. AIEE*. 1960, 79(5): 91-99.
- [23] Choi, B. S.; Fletcher C. A. J. Computation of particle transport in an electrostatic precipitator. *J. Electrostat.* 1997, 40and41: 413-418.
- [24] Gallimberti, I. Recent advancements in the physical modelling of electrostatic precipitators. *J. Electrostat.* 1998, 43(4): 219-247.
- [25] Talaie, M. R. Mathematical modeling of double-stage electrostatic precipitators based on a modified Eulerian approach. *Aerosol Sci. Technol.* 2001, 34(6): 512-519.
- [26] Schmid, H. J.; Vogel, L. On the modelling of the particle dynamics in electro-hydrodynamic flow-fields: I. Comparison of Eulerian and Lagrangian modelling approach. *Powder Technol.* 2003, 135and136: 118-135.
- [27] Schmid, H. J.; On the modelling of the particle dynamics in electro-hydrodynamic flow fields: II. Influences of inhomogeneities on electrostatic precipitation. *Powder Technol.* 2003, 135and136: 136-149.
- [28] Suh, Y. J.; Kim, S. S. Effect of obstructions on the particle collection efficiency in a two-stage electrostatic precipitator, *J. Aerosol Sci.* 1993, 27(1): 61-74.
- [29] Lei, H.; Wang L. Z.; Wu, Z. N. EHD turbulent flow and Monte-Carlo simulation for particle charging and tracing in a wire-plate electrostatic precipitator. *J. Electrostat.* 2008, 66(3-4): 130-141.

-
- [30] Zhang, X.; Wang, L.; Zhu, K. Particle tracking and particle-wall collision in a wire-plate electrostatic precipitator, *J. Electrostat.* 2005, 63(11): 1057-1071.
 - [31] Launder, B. E.; Spalding, D. B. Mathematical Models of Turbulence, Academic Press, London, 1972, pp. 967-982.
 - [32] Leonard, G. L.; Mitchner, M.; Self, S. A. An experimental study of the electrohydrodynamic flow in electrostatic precipitators, *J. Fluid Mech.* 1983, 127: 123-140.
 - [33] Hinds W.C. Aerosol Technology, John Wiley and Sons Inc. New York, 1999, pp. 49-50 and 323-327.
 - [34] Lawless, P. A. Particle charging bounds, symmetry relations, and an analytic charging rate model for the continuum regime, *J. Aerosol Sci.* 1996, 27(2): 191-215.
 - [35] Crowe, C.; Sommerfeld, M.; Tsuji Y. Multiphase flows with droplets and particles, CRC Press, Florida, 1997, pp. 95-96.
 - [36] Pope, S. B. Turbulent flows, Cambridge University Press, UK, 2000, pp.485-487.
 - [37] Lu, Q. Q.; Fontaine, J. R.; Aubertin, G. A lagrangian model for solid particles in turbulent flows, *Int. J. Multiphase Flow.* 1993, 19(2): 347-367.
 - [38] Lu, Q. Q.; Fontaine, J. R.; Aubertin, G. Particle motion in two-dimensional confined turbulent flows, *Aerosol Sci. Technol.* 1992, 17(3): 169-185.

Chapter 4

ESD PROTECTION DESIGNS WITH LOW-CAPACITANCE CONSIDERATION FOR RADIO-FREQUENCY INTEGRATED CIRCUITS

Ming-Dou Ker, Chun-Yu Lin and Yuan-Wen Hsiao

Nanoelectronics and Gigascale Systems Laboratory,
Institute of Electronics, National Chiao-Tung University, Taiwan

Abstract

Radio-frequency (RF) circuits have been widely designed and fabricated in CMOS processes due to the advantages of high integration and low cost for mass production. Electrostatic discharge (ESD), which has become one of the most important reliability issues in IC products, must be taken into consideration during the design phase of all ICs, including the RF front-end circuits. Without ESD protection circuits at all I/O pads, the RF performance of a wireless transceiver can be easily damaged by ESD stresses, because RF front-end circuits are always fabricated in advanced CMOS processes. Usually the I/O pads are connected to the gate terminal of MOS transistor or silicided drain/source terminal, which leads to a very low ESD robustness if no ESD protection design is applied to the I/O pad. Once the RF front-end circuit is damaged by ESD, it can not be recovered and the RF functionality is lost. Therefore, on-chip ESD protection circuits must be provided for all I/O pads in RF ICs.

1. Introduction

The typical on-chip double-diode ESD protection scheme is shown in Figure 1, which two ESD diodes at I/O pad are co-designed with the power-rail ESD clamp circuit to prevent internal circuits from ESD damage [1]-[5]. In Figure 1, a P+/N-well diode (D_P) and an N+/P-well diode or an N-well/P-substrate diode (D_N) are placed at input pad or output pad. When the D_P and D_N are under forward-biased condition, they can provide discharge paths from I/O pad to VDD and from VSS to I/O pad, respectively.

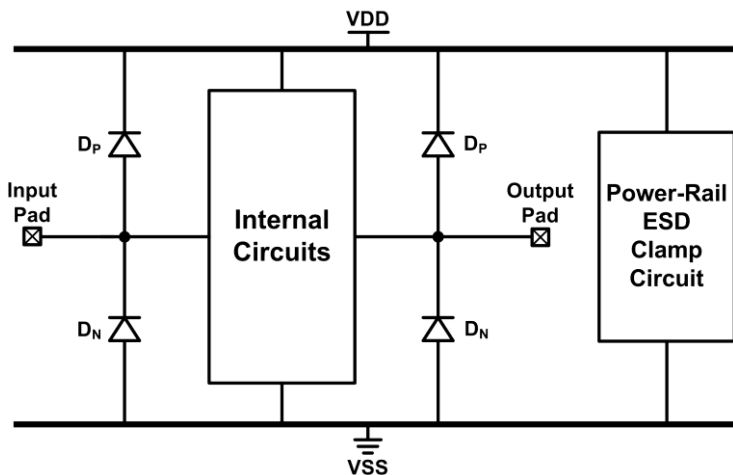


Figure 1. Typical double-diode ESD protection scheme.

Under positive-to-VDD mode (PD-mode) and negative-to-VSS mode (NS-mode) ESD stresses, ESD current is discharged through the forward-biased D_P and D_N , respectively. To avoid the ESD diodes from being operated under breakdown condition during positive-to-VSS mode (PS-mode) and negative-to-VDD mode (ND-mode) ESD stresses, which results in a substantially lower ESD robustness, the power-rail ESD clamp circuit is used between VDD and VSS to provide ESD current paths between the power rails [6], [7]. Thus, ESD current is discharged from the I/O pad through the forward-biased D_P to VDD, and discharged to the grounded VSS pin through the turn-on efficient power-rail ESD clamp circuit during PS-mode ESD stresses. Similarly, ESD current is discharged from the VDD pin through the turn-on efficient power-rail ESD clamp circuit and the forward-biased D_N to the I/O pad during ND-mode ESD stresses.

Although using power-rail ESD clamp circuit between VDD and VSS does not cause any effect on the internal circuits, applying ESD protection devices at the I/O pads inevitably introduce some negative impacts to circuit performance due to their parasitic effects. The main parasitic effect caused by ESD protection devices which deteriorates the RF performance is the parasitic capacitance [4], [8]. The negative impacts of ESD protection devices to RF circuit performance had been investigated, which had demonstrated that the RF performance such as power gain and noise figure are significantly degraded by the parasitic capacitance of ESD protection devices [9], [10]. A typical request on the maximum loading capacitance of ESD protection device for a 2-GHz RF input pin was specified as only ~200 fF, which includes the parasitic capacitances of bond pad and ESD protection device [4], [11]. The specification is even stricter for the RF circuits applied to higher frequency band. Thus, the parasitic capacitance of ESD protection device must be minimized in ESD protection design for RF applications.

2. Design Considerations for RF ESD Protections

ESD protection circuits cause RF performance degradation with several undesired effects, which are discussed in the following. Parasitic capacitance is one of the most

important design considerations for RF ICs. Conventional ESD protection devices with large dimensions have the parasitic capacitance which is too large to be tolerated for RF front-end circuits. As shown in Figure 2, the parasitic capacitance of ESD protection devices causes signal loss from the pad to ground. Moreover, the parasitic capacitance also changes the input matching condition. Consequently, the noise figure is deteriorated and the power gain is decreased.

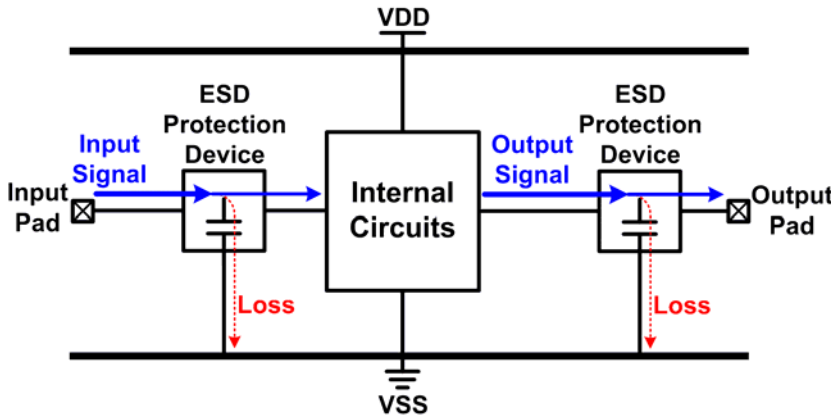


Figure 2. Signal loss at input and output pads of IC with ESD protection devices.

Noise factor is one of the most important merits for RF receivers. Since the RF receiver is a cascade of several stages, the overall noise factor of the RF receiver can be obtained in terms of the noise factor and power gain of each stage in the receiver. For example, if there are m stages cascaded in the RF receiver, the total noise factor of the RF receiver can be expressed as [12]

$$F_{total} = 1 + (F_1 - 1) + \frac{F_2 - 1}{G_{p1}} + \dots + \frac{F_m - 1}{G_{p1} \dots G_{p(m-1)}} \quad (1)$$

where F_i and G_{pi} are the noise factor and the power gain of the i -th stage, respectively. According to Eq. (1), the noise factor contributed by the first stage is the dominant factor to the total noise factor of the RF receiver (F_{total}). With the ESD protection circuit added at the input pad to protect the RF receiver IC against ESD damages, the ESD protection circuit becomes the first stage in the RF receiver IC, which is shown in Figure 3. For simplicity, only the first two stages, which are the ESD protection circuit and the low-noise amplifier (LNA), are taken into consideration, as shown in Figure 4. The overall noise factor (F_{LNA_ESD}) of the LNA with ESD protection circuit is

$$F_{LNA_ESD} = F_{ESD} + \frac{F_{LNA} - 1}{G} \quad (2)$$

where G is the power gain of the LNA, and F_{ESD} and F_{LNA} denote the noise factors of the ESD protection and LNA circuits, respectively. Thus, the noise factor of the ESD protection circuit

must be minimized, because it directly increases the total noise factor of the RF receiver and the increased noise factor can not be suppressed by the power gains of succeeding stages. Moreover, the signal loss due to the ESD protection circuit would also cause power gain degradation in RF circuits.

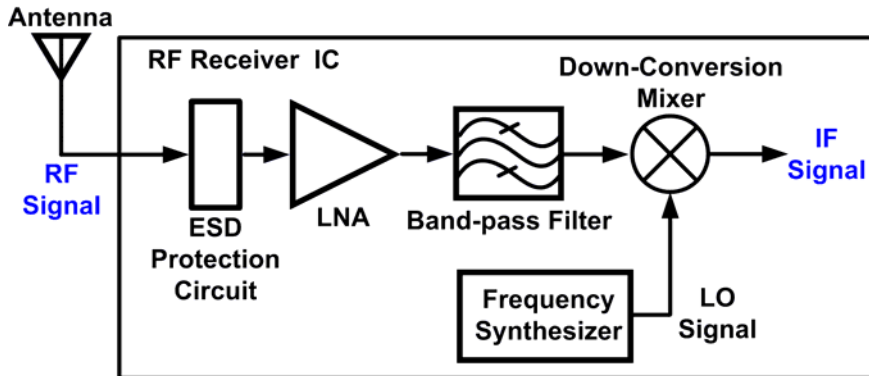


Figure 3. Block diagram of an ESD-protected RF receiver.

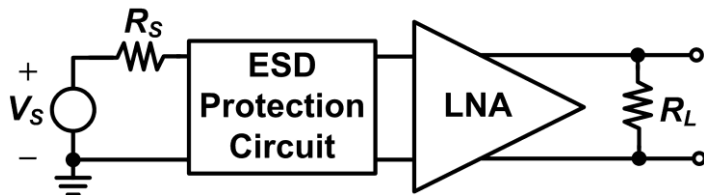


Figure 4. Block diagram of an LNA with ESD protection circuit. V_s , R_s , and R_L denote the source voltage, source resistance, and load resistance, respectively.

Another negative impact caused by the ESD protection circuit is the input impedance mismatching, which is particularly critical for narrow band RF circuits. With the ESD protection circuit added at the input node, the original input matching condition is changed by the parasitic capacitance from the ESD protection circuit. As a result, the center frequency of the narrow band RF circuit is shifted and the power gain is decreased due to impedance mismatching. The impedance mismatching due to ESD protection devices can be mitigated by co-designing the ESD protection circuit and the input matching network. With the co-design of ESD protection scheme and input matching network, the operating frequency can be tuned to the desired frequency. However, the noise figure is definitely increased after ESD protection circuit is added because more devices indicate more noise sources.

In addition to parasitic capacitance, the requirements of ESD protection device characteristics under ESD stresses introduce some design considerations. To provide effective ESD protection, the voltage across the ESD protection device during ESD stresses should be carefully designed. First, the trigger voltage and holding voltage of ESD protection device must be designed lower than the gate-oxide breakdown voltage of MOS transistors to prevent the internal circuits from damage before the ESD protection device is turned on during ESD stresses. Second, the trigger voltage and holding voltage of the ESD protection device must be higher than the power-supply voltage of the IC to prevent the ESD protection devices from

being mis-triggered under normal circuit operating conditions. Moreover, the turn-on resistance of ESD protection device should be minimized in order to reduce the joule heat generated in the ESD protection device and the voltage across the ESD protection device during ESD stresses. As CMOS process is continuously scaled down, the power-supply voltage is decreased and the gate oxide becomes thinner, which leads to reduced gate-oxide breakdown voltage of MOS transistor. Typically, the gate-oxide breakdown voltage is decreased to only ~5 V in a 65-nm CMOS process with gate-oxide thickness of ~15 Å. As a result, the ESD design window, defined as the difference between the gate-oxide breakdown voltage of the MOSFET and the power-supply voltage of the IC, becomes narrower in nanoscale CMOS technologies. Furthermore, ESD protection circuits need to be quickly turned on during ESD stresses in order to provide efficient discharge paths in time. In summary, ESD protection design becomes more challenging in nanoscale CMOS technologies.

To mitigate the performance degradation due to ESD protection devices, some design techniques had been used to reduce the parasitic capacitance from the ESD protection device. In this chapter, the RF ESD protection designs in CMOS processes are reviewed.

3. RF ESD Protection Designs by Layout Solutions

Layout solutions had been utilized to reduce the parasitic capacitance of ESD protection devices. By utilizing layout solutions, some silicon area might be shared to lower the total chip area. Furthermore, no process modification is needed and the ESD protection scheme does not need to be changed by using layout solutions.

3.1. Low-Capacitance Layout Structure for MOSFET

The layout structure for MOSFET with low parasitic capacitance had been proposed [13]. The layout top view is shown in Figure 5. The P-well region is defined between the two dotted rectangles in Figure 5. Figure 6 shows the cross-sectional view of the low-capacitance MOSFET.

The dotted line in Figure 6 denotes the depletion region edge of the PN-junction under the drain region. The P-well is designed not to lie below most of the drain area, which is connected to the I/O pad. Since the P-well does not exist under the N+ drain region of the NMOS transistor, the space charge region between the N+ drain diffusion and the P-substrate is larger than that of the N+/P-well junction. Thus, the parasitic capacitance is reduced by eliminating the P-well from existing under the drain region. During ESD stresses, the snapback breakdown occurs in the NMOS transistor, which turns on the parasitic NPN BJT in the NMOS transistor to sink ESD current. Because of the relatively low doping level in the PN-junction, the breakdown voltage of the drain-to-substrate junction is higher than that of the drain-to-well junction, resulting in degraded ESD robustness. Thus, a tradeoff exists between the parasitic capacitance and ESD robustness in this design.

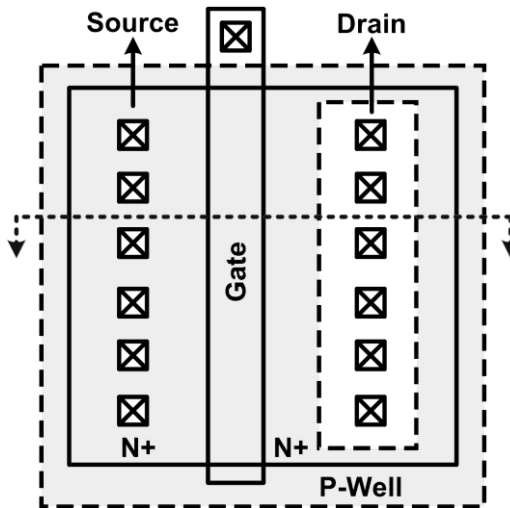


Figure 5. Layout top view of the low-capacitance NMOS transistor.

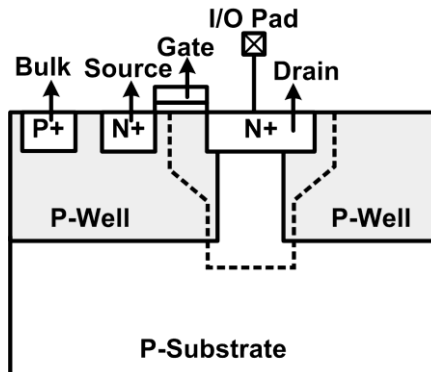


Figure 6. Cross-sectional view of the low-capacitance NMOS transistor.

3.2. Low-Capacitance Layout Structure for SCR

SCR had been demonstrated to be suitable for ESD protection for high-frequency applications, because it has both high ESD robustness and low parasitic capacitance under a small layout area [14], [15]. Layout structures which can reduce the parasitic capacitance of SCR had been investigated [16]-[18]. The layout top view and cross-sectional view of the low-capacitance SCR are shown in Figure 7. The SCR structure in Figure 7 is similar to that of the low-voltage triggering SCR (LVTSCR) [19], [20]. With a low trigger voltage, the LVTSCR can be quickly turned on to protect the internal circuits against ESD damage. During PS-mode ESD stresses, the snapback breakdown occurs in the embedded NMOS, which turns on the parasitic NPN BJTs Q_{2a} and Q_{2b} (formed by the N+ diffusion, P-well, and N+ diffusion) in the embedded NMOS. The current boosts the base voltage of Q_{2a} and Q_{2b} because of the voltage drop across the P-well resistance (R_{Well}).

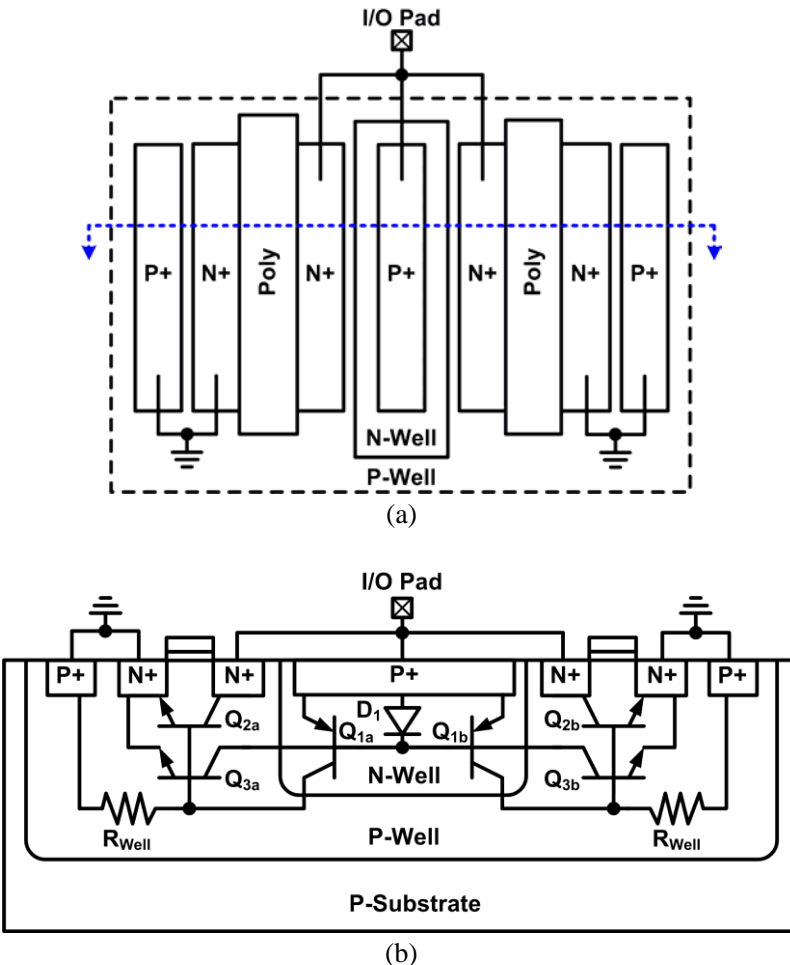


Figure 7. Low-capacitance SCR: (a) layout top view, and (b) cross-sectional view.

As the voltage across R_{Well} exceeds the cut-in voltage of the base-emitter junction diodes in the parasitic NPN BJTs Q_{3a} and Q_{3b} , which are formed by the N-well, P-well, and N+ diffusion, Q_{3a} and Q_{3b} are turned on. Consequently, two SCRs composed of Q_{1a} and Q_{3a} , and Q_{1b} and Q_{3b} are turned on to sink ESD current. With some area overhead, the ESD protection capability can be ideally doubled by splitting the current paths. The parasitic capacitance of the SCR primarily comes from the N-well/P-well junction and from the N+ diffusion (drain of the NMOS) to P-well junction. In order to reduce the parasitic capacitance, the shallow-trench isolation (STI) has been utilized in the modified design [21]. As shown in Figure 8, the inserted STI reduces the drain-to-well sidewall area and the N-well-to-P-well boundary area, which leads to reduced parasitic capacitance.

Another ESD protection design utilizing the parasitic SCR is shown in Figure 9 [22]. The cascoded NMOS transistors M_1 and M_2 are used for mixed-voltage I/O applications, which can receive $2 \times VDD$ input signal by using only $1 \times VDD$ devices without the gate-oxide reliability issue [23], [24]. The diode D_1 is used to provide ESD current path from the I/O pad to VDD. The cross-sectional view of this ESD protection design is shown in Figure 9(b), where the NMOS transistors M_1 and M_2 are realized with multi-finger structure. The P+

diffusion, N-well, and P-substrate form the vertical PNP BJT Q_1 , and the N-well, P-substrate, and N+ diffusion form the lateral NPN BJT Q_2 . In such a layout structure, the P+ diffusion, N-well, P-substrate, and N+ diffusion form the parasitic SCR to provide ESD current path from the I/O pad to VSS.

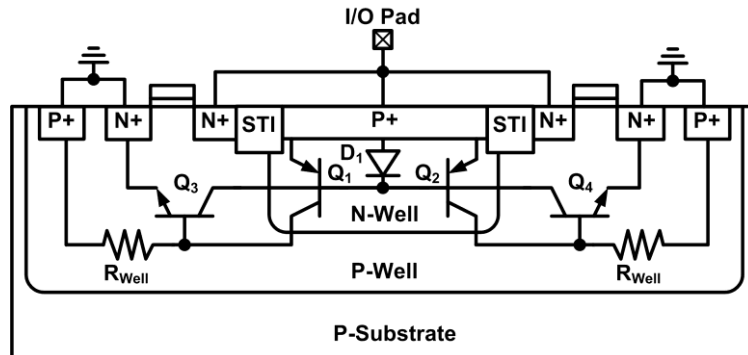


Figure 8. Cross-sectional view of the modified low-capacitance SCR with STI.

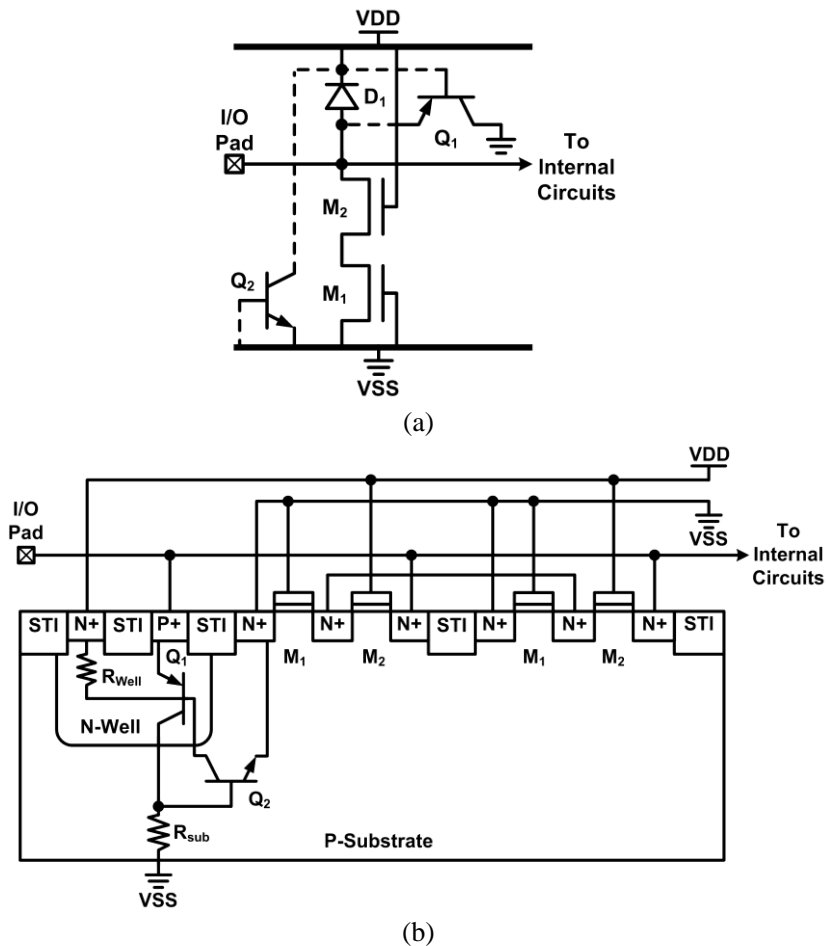


Figure 9. ESD protection design with a parasitic SCR: (a) circuit schematic, and (b) cross-sectional view.

Since the base terminal of Q_1 is biased to VDD, which is the highest potential in the IC, the reverse-biased base-emitter junction capacitance of Q_1 is reduced. Moreover, the emitter, base, and collector and base terminals of Q_2 are connected to the ac ground nodes VDD or VSS. Thus, the parasitic capacitance of Q_2 does not have any impact to the internal circuits.

3.3. Waffle Layout Structure

To save the silicon area and reduce the parasitic capacitance, the MOSFETs realized with the waffle structure had been studied [25], [26]. Similarly, the ESD protection devices had been realized with the waffle structure to optimize ESD robustness. The ESD protection device with the maximum ratio of perimeter to area is preferred, because it has the maximum ratio of ESD robustness to parasitic capacitance. The ESD protection diode realized with the waffle structure had been proposed [27]-[30]. To maximize the ratio of perimeter to area, small square diffusions are used. The layout top view and cross-sectional view of the P+/N-well waffle diode are shown in Figure 10. The arrows in Figure 10 show the ESD current paths. The P+ diffusion is implemented in the N-well region and surrounded by the N+ diffusion. Thus, ESD current can be discharged through four directions from the P+ diffusion. To scale the ESD protection capability, multiple P+ diffusions can be connected in parallel to form the waffle diode structure. Under the same ESD robustness, the waffle diode has the reduced parasitic capacitance than that of the traditional ESD diode.

Besides waffle diodes, SCR with waffle layout structure had been reported [31], [32]. The layout top view and cross-sectional view of the waffle SCR are shown in Figure 11. Compared with the waffle diode, the layout of waffle SCR is more complicated, especially the metal routing with multiple waffle SCRs in parallel. It had been verified that the waffle SCR can achieve smaller parasitic capacitance under the same ESD robustness.

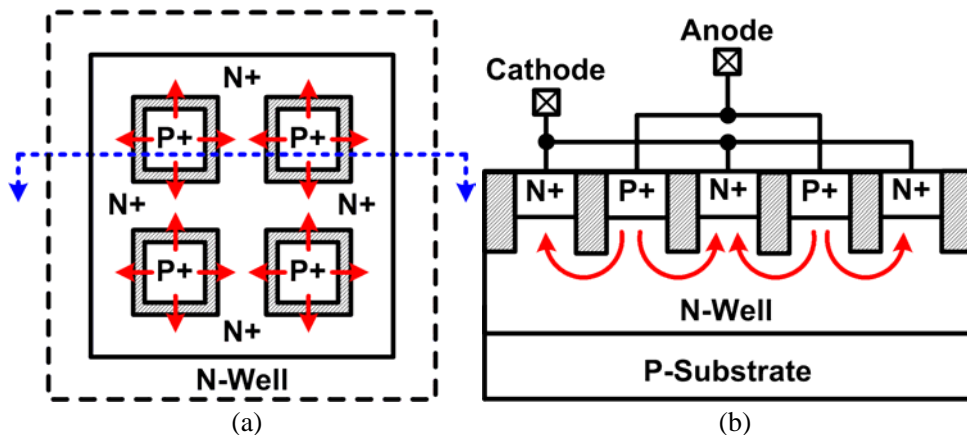


Figure 10. P+/N-well waffle diode: (a) layout top view, and (b) cross-sectional view.

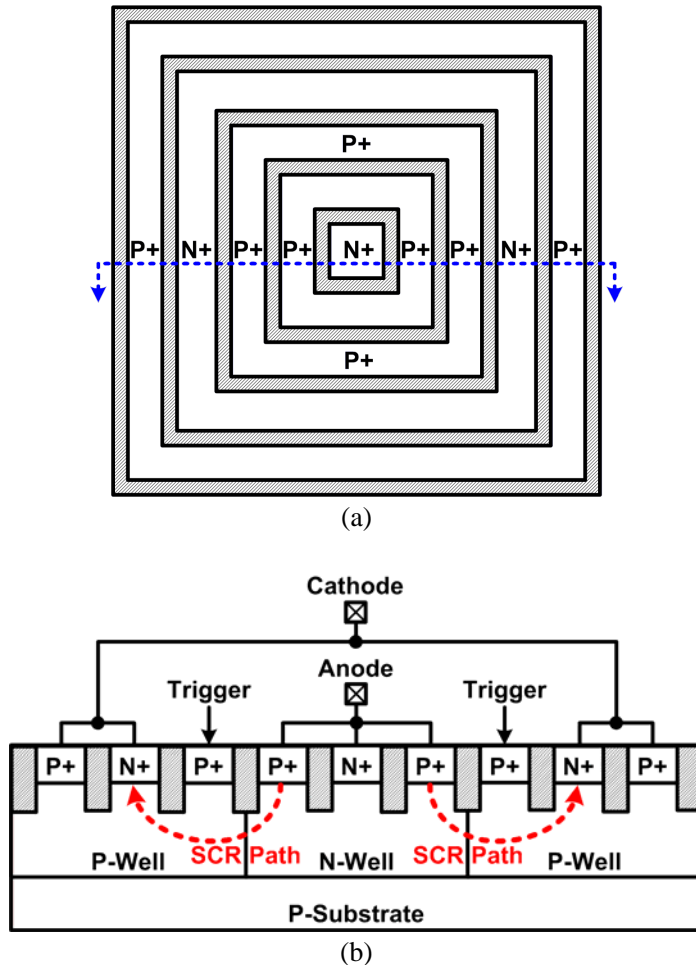


Figure 11. Waffle SCR: (a) layout top view, and (b) cross-sectional view.

3.4. ESD Protection Device Under I/O Pad

To reduce the chip area, ESD protection devices can be placed under the I/O pad, as shown in Figure 12 [33].

The contacts in Figure 12(a) connect the diffusion regions to the I/O pad. Figure 12(b) illustrates the schematic circuit diagram. The parasitic diodes D_1 and D_2 provide ESD current paths during PD- and NS-mode ESD stresses, respectively. During PS-mode ESD stresses, the BJT Q_3 is turned on when breakdown occurs in the reverse-biased base-collector junction. After Q_3 is turned on, the SCR formed by Q_3 and Q_4 is turned on to discharge ESD current. Similarly, the SCR composed of Q_1 and Q_2 is turned on during ND-mode ESD stresses to provide ESD protection. With the ESD protection circuit under the bond pad, the parasitic capacitances of the bond pad and ESD protection circuit are series connected from the I/O pad to substrate, resulting in reduced equivalent parasitic capacitance. Thus, the total parasitic capacitance of the I/O pad and ESD protection circuit is reduced, as compared with the ESD protection device placed beside the I/O pad.

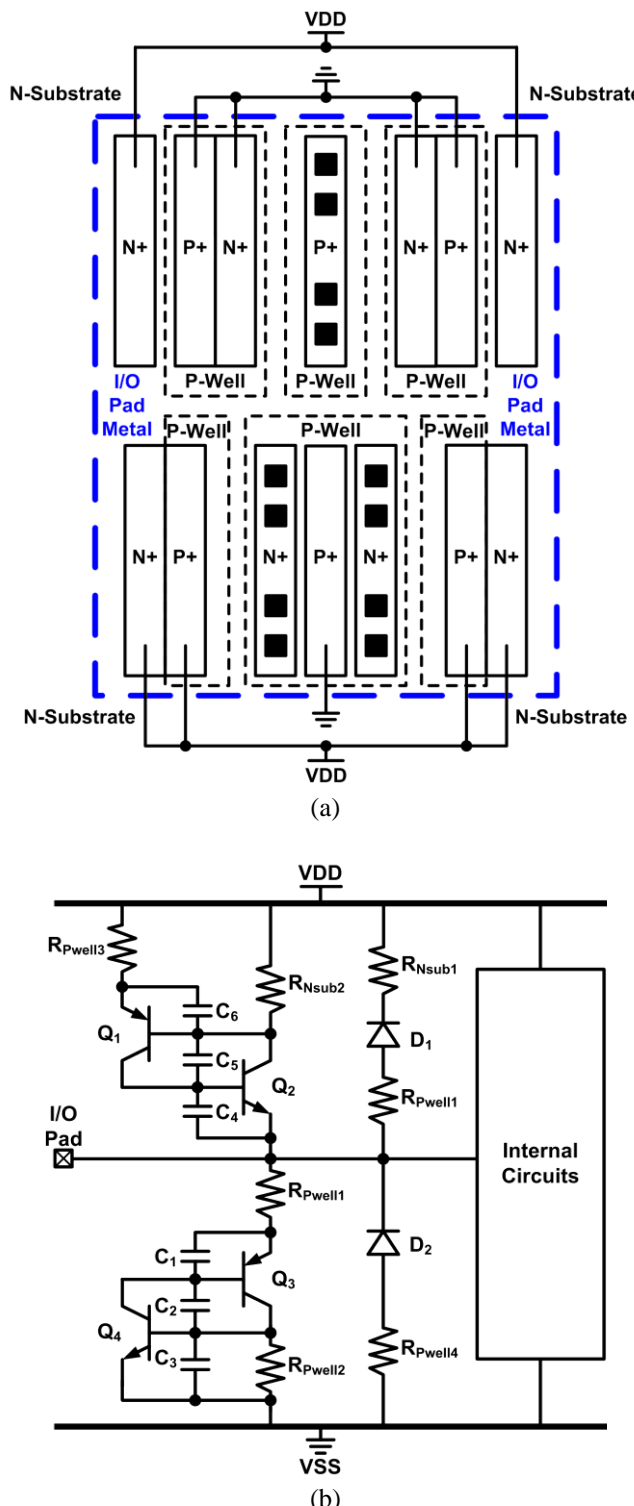


Figure 12. ESD protection device under the I/O pad: (a) layout top view, and (b) schematic circuit diagram.

Another ESD protection circuit under the bond pad had been proposed, with its layout top view shown in Figure 13(a) [34]. Figure 13(b) shows the schematic circuit diagram. The diode D_1 is formed by the P-well/N-well junction. The PNP BJT Q_1 is formed by the P+ diffusion, N-well and P-well, and the NPN BJT Q_2 is formed by the N-well, P-well, and N+ diffusion. Q_1 and Q_2 form an SCR from the I/O pad to VSS. During PS-mode ESD stresses, the junction breakdown occurs in D_1 , which turns on the SCR to discharge ESD current. The parasitic capacitance connected to the I/O pad is only the P+/N-well junction capacitance, which is the base-emitter junction capacitance of Q_1 . Moreover, the parasitic capacitance from the I/O pad to the grounded P-well region is reduced because the ESD protection circuit is placed under the bond pad.

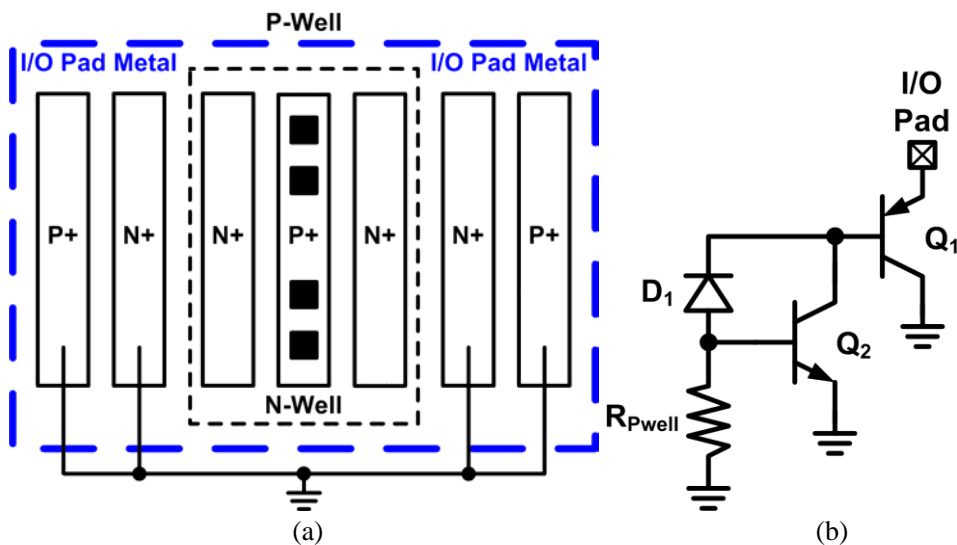


Figure 13. Another ESD protection device under the I/O pad: (a) layout top view, and (b) schematic circuit diagram.

4. RF ESD Protection Designs by Circuit Solutions

Besides layout solutions, circuit solutions had also been utilized to reduce the parasitic capacitance of ESD protection devices. The silicon area may be increased due to the additional components of extra circuit design. However, with the extra circuit design, the parasitic capacitance of the ESD protection device can be significantly reduced or even cancelled. Furthermore, no process modification is needed by using the circuit design techniques to reduce the parasitic capacitance.

4.1. Stacked ESD Protection Devices

Figure 1 has shown the conventional double-diode ESD protection design for RF frond-end circuits; however, it is only suitable for small ESD protection devices [35]. The device dimensions of ESD diodes should be decreased to reduce the parasitic capacitance at I/O pad,

and then the performance degradation caused by the parasitic capacitances from the ESD diodes could be reduced.

However, ESD robustness needs to be maintained, so the minimum device dimensions of ESD diodes can not be shrunk unlimitedly. In order to further reduce the parasitic capacitance from ESD diodes without sacrificing ESD robustness, the ESD diodes in stacked configuration had been proposed, as shown in Figure 14 [36], [37].

The overall equivalent parasitic capacitance will theoretically becomes C_{ESD}/n , where C_{ESD} is the parasitic capacitance of each ESD protection device and n ESD protection devices are stacked.

Thus, more stacked ESD devices lead to the more significant parasitic capacitance reduction. Besides reducing parasitic capacitance, using the stacked configuration can also reduce the leakage current of ESD diodes under normal circuit operating conditions. Although stacked ESD protection devices can reduce the parasitic capacitance and leakage current, this technique is adverse to ESD protection because the overall turn-on resistance and the voltage across the stacked ESD protection devices during ESD stresses were increased as well.

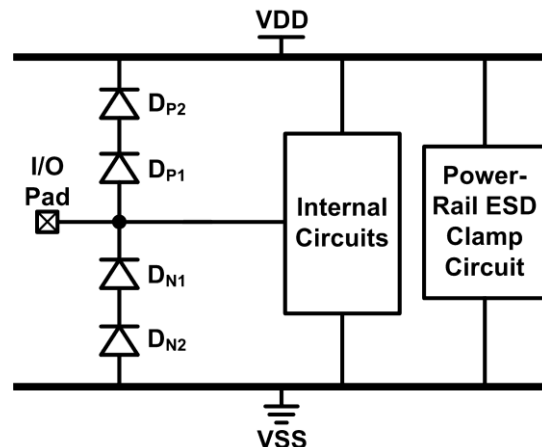


Figure 14. Stacked ESD protection devices to reduce the parasitic capacitance.

4.2. Parallel LC Resonator

This technique was also called the impedance cancellation, which was composed of a resonator with the parallel inductor and capacitor. In such a resonator, the resonant frequency (ω_o) is

$$\omega_o = \frac{1}{\sqrt{LC}} \quad (3)$$

where L and C denote inductance and capacitance, respectively. An ideal parallel LC resonator and the simulated S₂₁-parameters under different frequencies are shown in Figure 15.

The signal loss at the resonant frequency is ideally zero, which means that the equivalent capacitance at the resonant frequency is zero. Based on this concept, the ESD protection circuit with a parallel inductor had been proposed, as shown in Figure 16 [38]-[41]. Using the inductance of L_1 , it was designed to resonate with the parasitic capacitance of the ESD protection device at the operating frequency of the RF front-end circuit. With the parallel LC network resonating at the operating frequency, the shunt impedance of the resonator becomes very large, which can effectively suppress signal loss. Therefore, the ESD protection design using parallel LC resonator can mitigate the impacts on RF performances for circuits operating in a narrow frequency band.

Besides the bondwire inductor L_1 , the inductor can also be realized by the on-chip inductor [42]. Furthermore, the inductor can not only resonates with the parasitic capacitance of the ESD protection device but also serves as an ESD protection device by itself. In this configuration, the parallel LC resonator can be realized as shown in Figure 17 [43].

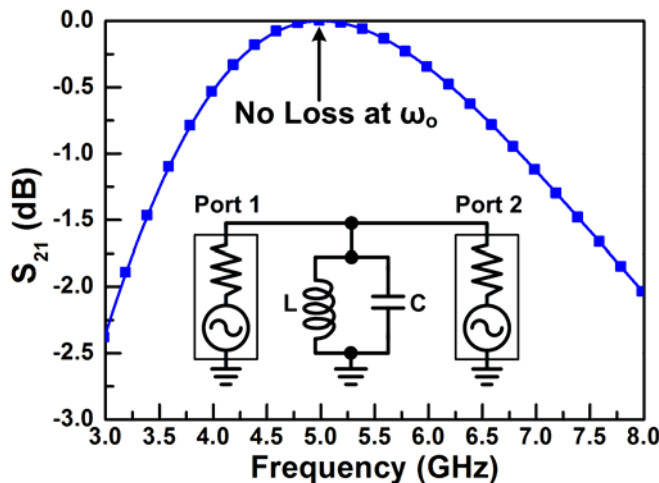


Figure 15. An ideal parallel LC resonator and its simulated S_{21} -parameters under different frequencies.

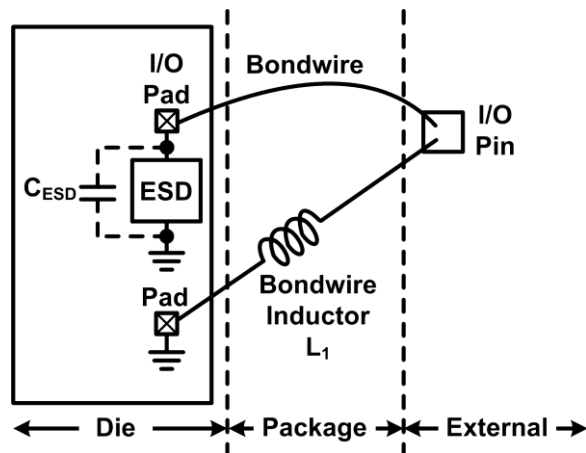


Figure 16. An example of ESD protection design with the parallel LC resonator.

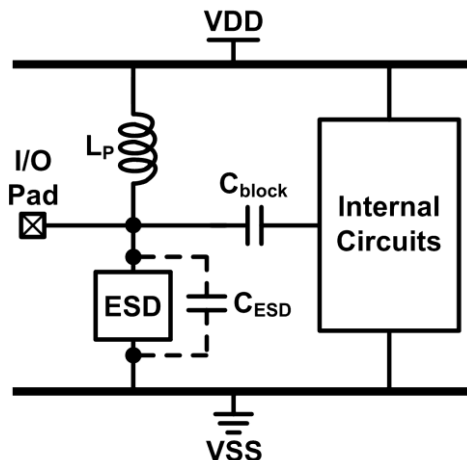


Figure 17. Another example of ESD protection design with the parallel LC resonator, where the inductor L_P provides ESD current path between VDD and the I/O pad.

Since VDD is an ac ground node, the inductor L_P is connected between the I/O pad and VDD with the ESD protection device between the I/O pad and VSS to form a parallel LC resonator. The inductor L_P also serves as an ESD protection device between I/O pad and VDD. The inductor and the parasitic capacitance of the ESD protection device are designed to resonate at the operating frequency of the RF front-end circuit to minimize performance degradation caused by the ESD protection device.

With an inductor directly connected between the I/O pad and VDD, the ESD protection device is reverse biased with the largest possible dc voltage under normal circuit operating conditions, which leads to the minimum the parasitic PN-junction capacitance in the ESD protection device.

The placement of the inductor and the ESD protection device can be interchanged to provide the same function. It should be noted that the dc biases in this configuration must be equal on both sides of the inductor. A dc blocking capacitor (C_{block}) is required to provide a separated dc bias for the internal circuits.

4.3. LC-Tank

LC-tank has been reported for the low-capacitance ESD protection design, which consists of an inductor, a capacitor, and an ESD diode [44]-[49]. As shown in Figure 18(a), a pair of the LC-tanks was placed at the I/O pad. One LC-tank consists of the inductor L_P and the capacitor C_1 , which is placed between the I/O pad and ESD diodes D_P . Another LC-tank consists of the inductor L_N and the capacitor C_2 , which is placed between the I/O pad and ESD diodes D_N . These ESD diodes D_P and D_N are used to block the steady leakage current path from VDD to VSS under normal circuit operating conditions. At the resonant frequency of the LC-tank, there is ideally infinite impedance from the signal path to the ESD diode. Consequently, the parasitic capacitances of the ESD protection devices are isolated, which can mitigate the parasitic effects from the ESD protection devices. In this configuration, the

metal width of the inductors should be wide enough to enhance the current handling capability under ESD stress conditions.

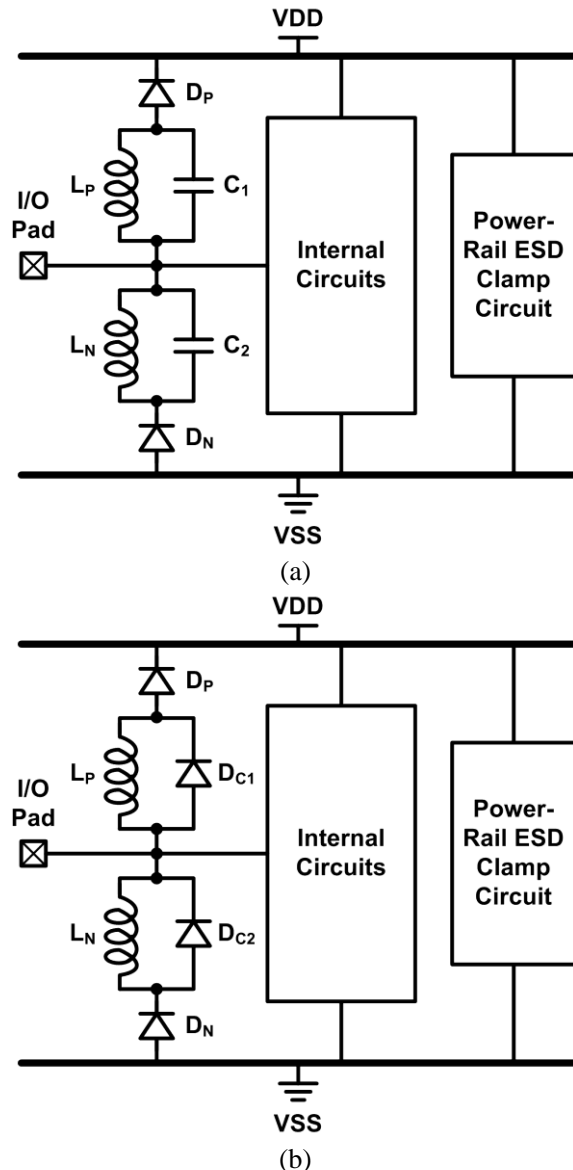


Figure 18. ESD protection design with a pair of LC-tanks, where the LC consists of (a) inductor and capacitor, and (b) inductor and diode.

Besides the above-mentioned LC-tank, the capacitors C_1 and C_2 can also be realized with the ESD protection devices. As shown in Figure 18(b), one LC-tank consists of the inductor L_P and the diode D_{C1} , which is placed between the I/O pad and ESD diodes D_P . The other LC-tank consists of the inductor L_N and the diode D_{C2} , which is placed between the I/O pad and ESD diodes D_N . With the additional ESD protection devices D_{C1} and D_{C2} , this configuration can more efficiently bypass the ESD current. So the ESD robustness can be improved.

To further reduce the parasitic capacitance from the ESD protection devices, the modified design with stacked LC-tanks had also been proposed, as shown in Figure 19 [45]-[48]. Two or more LC-tanks are stacked to provide better impedance isolation at resonant frequency, and the impacts of the ESD protection devices can be significantly reduced.

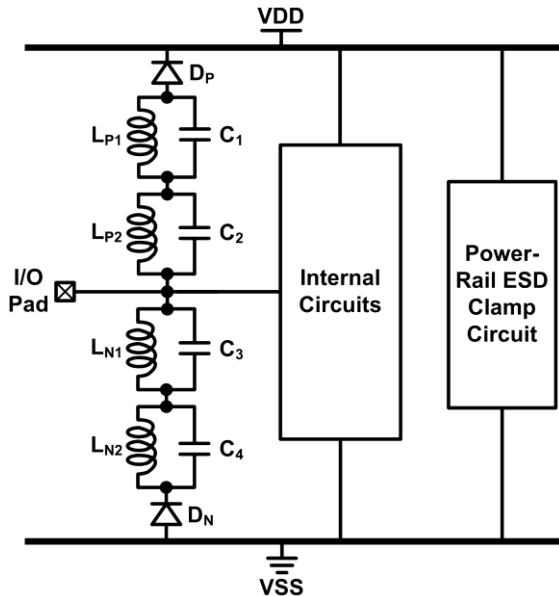


Figure 19. ESD protection design with stacked LC-tanks.

4.4. Series LC Resonator

The narrow band ESD protection design can be achieved by using the parallel LC resonator. For the wideband RF front-end circuits, the series LC resonator can be used for ESD protection. The simulated S_{21} -parameter of an ideal series LC resonator under different frequencies is shown in Figure 20.

With inductance L and capacitance C in the series LC resonator, the resonant frequency (ω_0) is identical to that shown in Eq. (3). There is a notch at the resonant frequency, where the signal loss is very large, and the signal will be totally lost. However, at frequencies above the resonant frequency, the magnitude of impedance increases, which means the signal loss becomes much smaller.

Thus, wideband ESD protection can be achieved by designing the application band of the series LC resonator to cover the frequency band of the RF signal. Figure 21 shows the ESD protection design utilizes the series LC resonator [38]-[41]. The inductance of L_1 and the parasitic capacitance of the ESD protection device (C_{ESD}) are designed to resonate. During ESD stresses, the ESD current can be discharged through the inductor L_1 and the ESD protection device.

Another example of ESD protection design utilizing the series LC resonator is shown in Figure 22 [50]-[52], where a pair of the series LC resonators was placed at the I/O pad. ESD

current paths from the I/O pad to both VDD and VSS are provided by the inductors and the ESD protection devices.

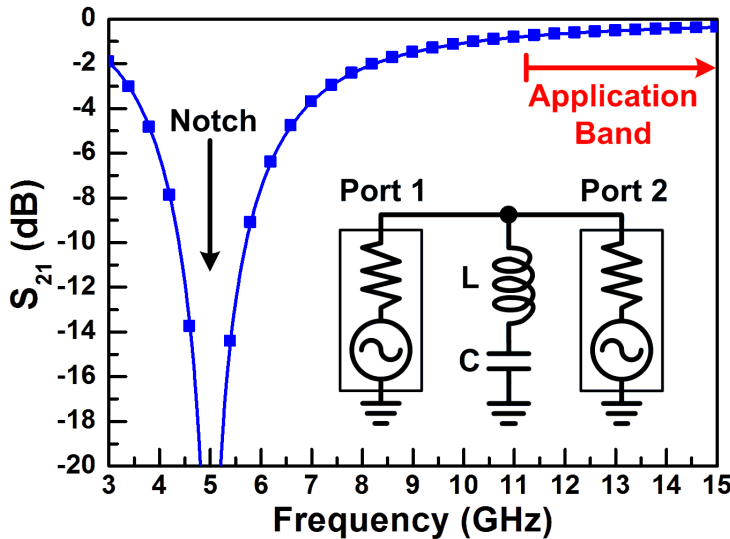


Figure 20. An ideal series LC resonator and its simulated S_{21} -parameters under different frequencies.

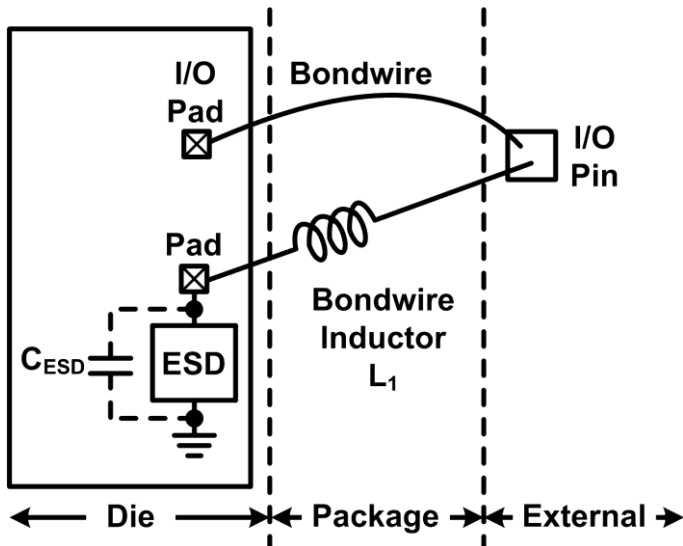


Figure 21. An example of ESD protection design with the series LC resonator.

To reduce the inductors used in the series LC resonators, a modified design used only one inductor is shown in Figure 23 [50]-[52]. One inductor is connected in series with two ESD protection devices connected to VDD and VSS.

Because the capacitance in the series LC resonator is the sum of the parasitic capacitances of two ESD protection devices, the inductance used in Figure 23 is smaller than that used in Figure 22 under the same resonant frequency. Consequently, total cost can be reduced in this modified design.

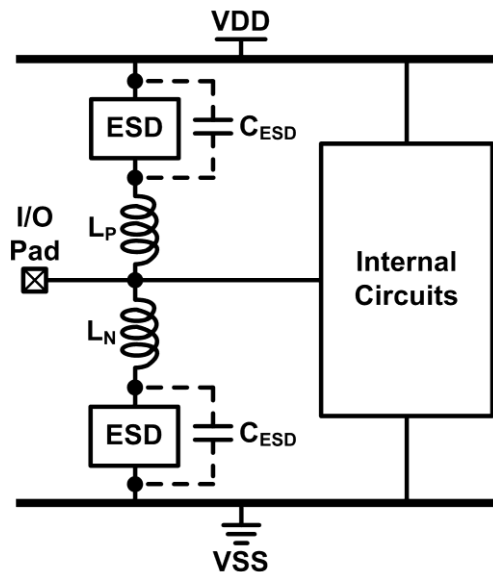


Figure 22. Another example of ESD protection design with the series LC resonator.

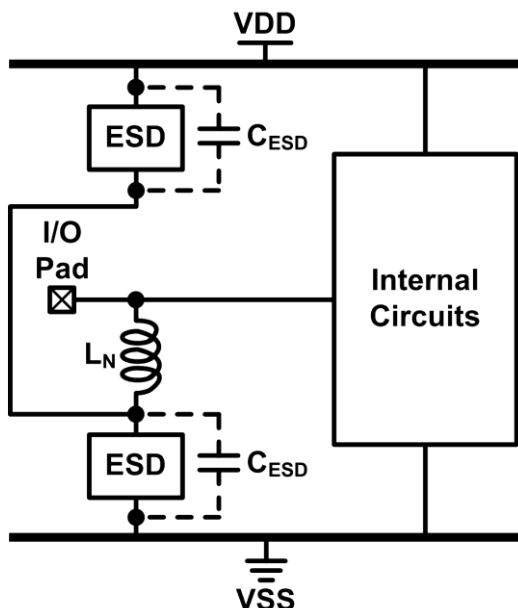


Figure 23. ESD protection design with modified series LC resonator, where only one inductor is connected in series with two ESD protection devices.

4.5. Impedance Matching

The size of ESD protection devices must be large enough to perform good ESD robustness. However, parasitic effects will increase with the large ESD protection devices. To solve this dilemma, ESD protection devices can be treated as a part of the impedance

matching network. By co-designing the ESD protection circuit and the impedance matching network, large ESD protection devices can be used to achieve high ESD robustness with their parasitic capacitance matched. The impedance matching technique of ESD protection device had been proposed. Figure 24 shows the ESD protection circuit with the impedance matching design [53], [54]. In this design, ESD current can be discharged from the I/O pad through the ESD protection devices to VDD and VSS. The combined impedance of the shunt and series impedance is designed to provide impedance matching at the I/O pad with ESD protection. The shunt and series impedance can be realized by various circuit components.

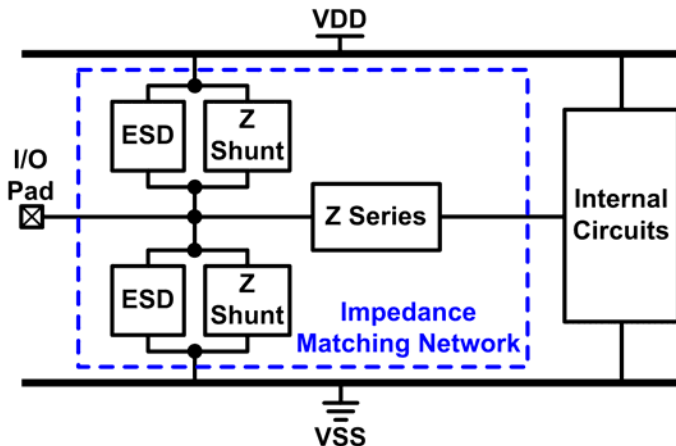


Figure 24. ESD protection design with impedance matching by using shunt and series components.

One example of ESD protection design with impedance matching technique is shown in Figure 25 [55], where uses inductance to match the parasitic capacitances of ESD protection devices. The ESD protection devices are placed next to the I/O pad, and provide ESD protection for the internal circuits. The transmission line (T-Line) connects to the external components. The inductive component L, which can be an inductor or a transmission line, is connected in series with the signal line, and matches the parasitic capacitances of the ESD protection devices, internal circuits, bond pad, and termination element (R_T). The small-signal equivalent circuit model of this matching network is shown in Figure 26, where the inductive component L separates two parasitic capacitances C_1 and C_2 . These C_1 and C_2 are

$$C_1 = C_{\text{int}} + C_{RT} \quad (4)$$

and

$$C_2 = C_{Pad} + C_{ESD} \quad (5)$$

where C_{int} , C_{RT} , C_{Pad} , and C_{ESD} denote the parasitic capacitance at the input node of the internal circuit, the parasitic capacitances of the termination element, bond pad, and ESD protection devices, respectively. The design goal is to neutralize the capacitance of C_1 and C_2 at the operating frequency by using the inductance of L. Therefore, the design target is

$$X_{C1} + X_{C2} + X_L = 0 \quad (6)$$

where X_{C1} , X_{C2} , and X_L are the reactance of C_1 , C_2 , and L , respectively. The overall impedance matching can be achieved as Eq. (6) holds.

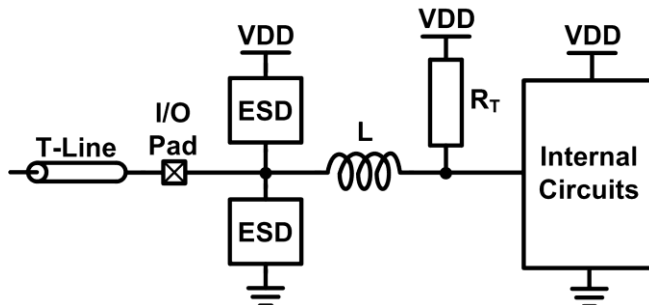


Figure 25. An example of ESD protection design with impedance matching.

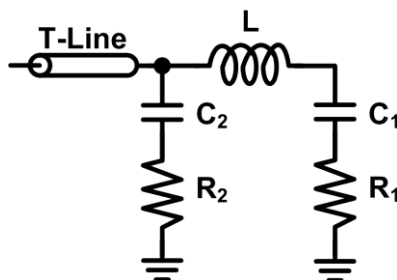


Figure 26. Equivalent small-signal model of the schematic shown in Figure 25.

4.6. Inductive ESD Protection

ESD protection design for RF circuits by using inductor as the ESD protection device has been reported [56], [57]. In Figure 27, the ESD protection inductor (L_{ESD}) is placed between the input pad and VSS. Inductors exhibits higher impedance at higher frequencies. Since the frequency component of ESD is much lower than that of the RF signal, the inductor can pass the ESD currents while block the RF signal.

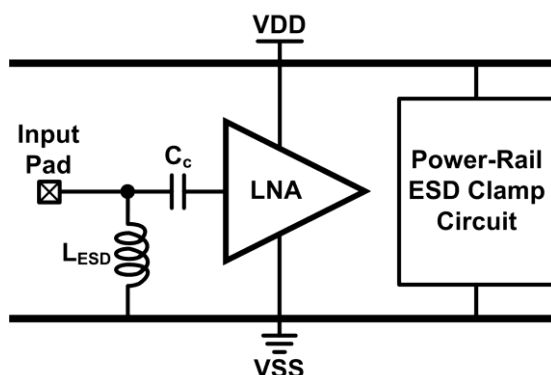


Figure 27. Inductive ESD protection design for an LNA.

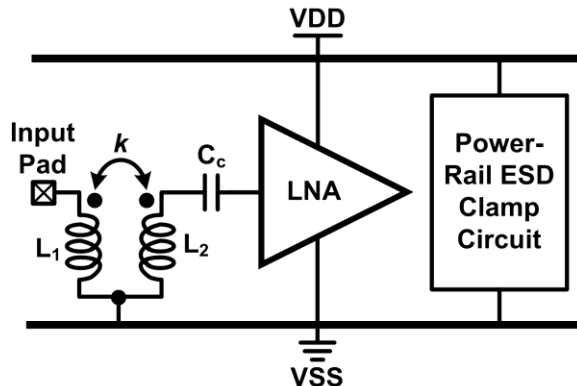


Figure 28. Inductive ESD protection design with transformer.

In the inductor-based ESD protection design, L_{ESD} was selected to resonate with the parasitic capacitances at the RF operating frequency. Therefore, the parasitic effects of the ESD protection inductor are compensated.

To efficiently sink the ESD current, the metal width of the ESD protection inductor should be wide enough to enhance the current handling capability and the parasitic series resistance. However, inductors realized very wide metal traces occupy large chip area. This is the main design concern in the inductor-based ESD protection. Besides, an ac coupling capacitor C_c is needed in this design to avoid the steady leakage current through the ESD protection inductor.

Another inductor-based ESD protection design is shown in Figure 28 [58], [59]. The ESD protection inductor can be merged with the gate inductor to save the chip area, since most of the LNAs need a gate inductor connected between the input pad and the gate terminal of the input MOS transistor. The ESD protection inductor is placed under the gate inductor to form a transformer. Consequently, the transformer-based ESD protection design provides not only the gate inductor in the impedance matching network, but also the ESD protection for the input pad.

4.7. T-Coil

The ESD protection design with T-coil for wideband applications had been reported [60]. As shown in Figure 29, this circuit can provide a purely resistive input impedance of R_T , under the proper impedance matching design. Once the following conditions hold, the input impedance Z_{in} remains resistive at all frequencies:

$$L_1 = L_2 = \frac{C_L R_T^2}{4} \left(1 + \frac{1}{4\zeta^2} \right) \quad (7)$$

$$C_B = \frac{C_L}{16\zeta^2} \quad (8)$$

and

$$k = \frac{4\zeta^2 - 1}{4\zeta^2 + 1} \quad (9)$$

where ζ is the damping factor of the network transfer function V_X/I_{in} . In the T-coil-based ESD protection design, C_L can be realized by the parasitic capacitance of ESD protection device. Therefore, large ESD protection device can be used without degrading the RF performances. The NMOS and PMOS transistors with gate-coupled technique is used in the first ESD protection design with T-coil. Recently, the silicon-controlled rectifier (SCR) has been used as the ESD protection device in the T-coil-based ESD protection design for a high-speed transmitter [61]. The return loss of the transmitter was improved with the T-coil to compensate the parasitic effects of the SCR.

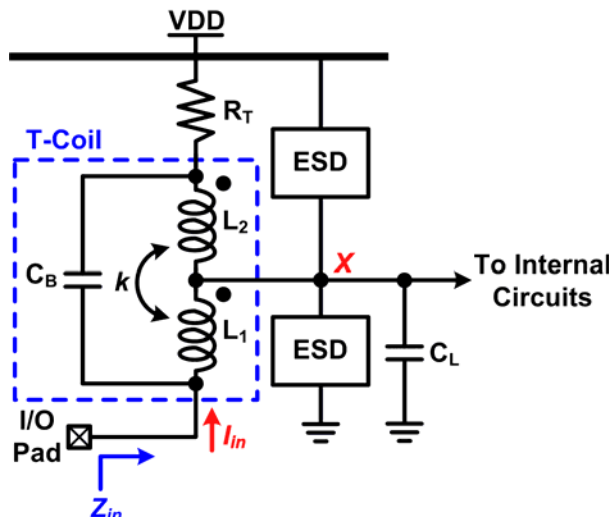


Figure 29. ESD protection design with T-coil.

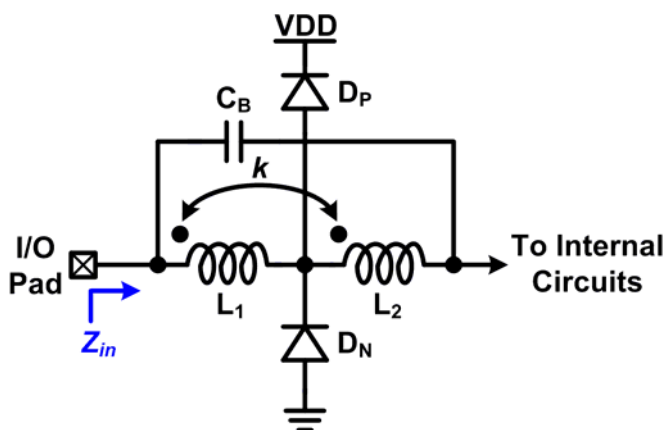


Figure 30. ESD protection with T-diode.

It has been reported that the transformer plus diode (T-diode) is used to protect the wideband LNA, as shown in Figure 30 [62]. This is another T-coil-based ESD protection design. In this design, the capacitor C_B in the T-diode was realized with the parasitic capacitance between the inductors L_1 and L_2 .

Since the T-coil and the T-diode can overcome the band-limiting problems in the narrow band ESD protection circuits, they are suitable for wideband RF front-end circuits. However, the design concern for the T-coil-based ESD protection was the inductor L_1 , which must be realized by wide metal trace and occupied large chip area.

4.8. Distributed ESD Protection

The distributed ESD protection scheme had been proposed to achieve wideband impedance matching with ESD protection devices [63]-[65]. The ESD protection devices are divided into several sections and are impedance matched by the transmission lines (T-lines) or inductors, as shown in Figure 31. With the ESD protection devices divided into small sections and matched by the transmission lines, such a distributed ESD protection scheme can achieve wideband impedance matching. The number of ESD protection devices can be varied to optimize the performance. The first reported distributed ESD protection scheme is the equal-size distributed ESD (ES-DES) protection scheme with ESD diodes, as shown in Figure 32.

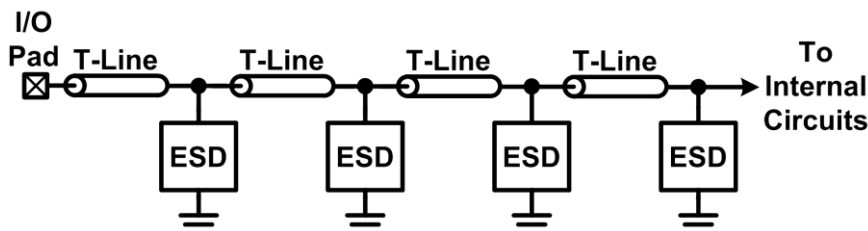


Figure 31. Distribute ESD protection scheme.

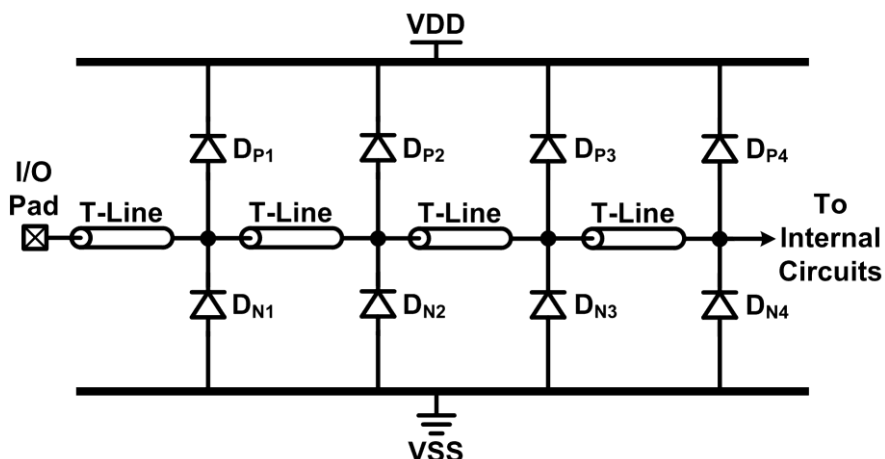


Figure 32. Distribute ESD protection scheme with equal-size ESD diodes.

In the ES-DESD protection scheme, the ESD protection diodes are equally divided into four sections. However, most of ESD current is expected to flow through the section which is closest to the I/O pad. To improve ESD robustness of distributed ESD protection scheme, the modified design of the decreasing-size distributed ESD (DS-DESD) protection scheme had been reported [66].

The DS-DESD protection scheme is shown in Figure 33, which allocates the ESD protection devices with decreasing sizes from the I/O pad to the internal circuit. With larger ESD protection devices close to the I/O pad, ESD robustness is improved. Because the first section of the ESD protection devices in the DS-DESD protection scheme is larger than that in the ES-DESD protection scheme, the DS-DESD protection scheme had been proven to have higher ESD robustness than that of the ES-DESD protection scheme under the same total parasitic capacitance of the ESD protection devices.

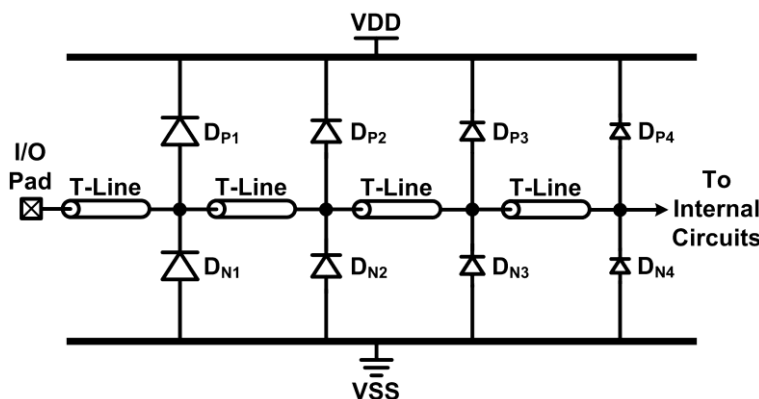


Figure 33. Distribute ESD protection scheme with decreasing-size ESD diodes.

Moreover, it had also been verified that good wideband impedance matching is still maintained in the DS-DESD protection scheme. However, in these ES-DESD and DS-DESD protection circuits, the de-embedding calculation must be executed to remove the parasitic effects of the I/O pads, and extract the intrinsic characteristics.

Considering the parasitic capacitance of I/O pad (C_{Pad}), the π -model ESD protection scheme was shown in Figure 34 [67]. The π -model ESD protection scheme consists of one set of ESD protection devices close to the I/O pad, the other set close to the internal circuits, and a transmission line matching these parasitic capacitances. The π -model ESD protection scheme can also be designed to achieve good wideband impedance matching with ESD protection devices.

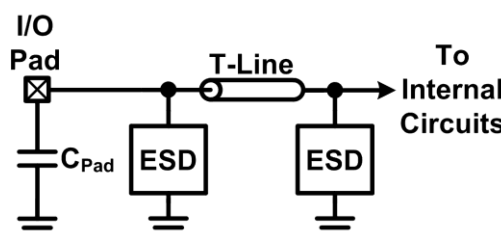


Figure 34. π -model ESD protection scheme.

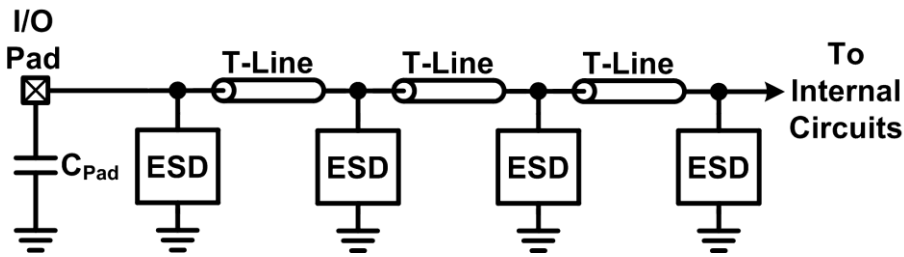


Figure 35. Distributed ESD protection scheme with the consideration for parasitic capacitance of I/O pad.

Another distributed ESD protection scheme with the consideration of the capacitive I/O pad is shown in Figure 35 [68]. The wideband impedance matching can be obtained by scaling these ESD protection devices and the transmission lines. Besides, this scheme can be suitable for wideband RF ESD protection with the large tolerance for the parasitic capacitance of I/O pad.

5. RF ESD Protection Designs by Process Solutions

The third approach to reduce the parasitic capacitance from the ESD protection device is to modify the fabrication process. Besides standard CMOS processes, ESD protection devices fabricated in some modified processes had been reported to reduce the parasitic capacitance. However, chip fabrication cost will be increased because of process modification.

5.1. Symmetrical SCR Structure

Figure 36(a) shows the cross-sectional view of a symmetrical SCR structure in the process with the N+ buried layer and P- layer [69].

With the high-concentration N+ buried layer, the clamping voltage of the SCR is reduced, which leads to more efficient ESD protection. Moreover, the deep-trench isolation separates the symmetrical SCR structure from the internal circuits, which is beneficial for latchup prevention. In the ESD protection device, the anode and cathode sides are junction-isolated, which reduces the parasitic capacitance. The overall reduction in parasitic capacitance is due to its smaller junction area and the series-connected parasitic capacitances of the two P-well/N+ buried layer junctions.

Figure 36(b) shows the schematic circuit diagram of this ESD protection device, in which the anode is connect to the I/O pad, and the cathode is connected to VSS. P-Well_1, N+ buried layer, P-Well_2, and N+ diffusion form the first SCR from anode to cathode. P-Well_2, N+ buried layer, P-Well_1, and N+ diffusion form the second SCR from cathode to anode. The N+ diffusion which is connected to anode, P-Well_1, and N+ buried layer form the NPN BJT Q₄. The N+ diffusion which is connected to cathode, P-well_2, and N+ buried layer form the NPN BJT Q₂. The N+ buried layer and N-well form the base of the BJT Q₁, and the P-Well_1 and P-Well_2 form the emitter and collector of the BJT Q₁, respectively. The first vertical BJT Q₅ is formed by the P- layer, N+ buried layer, and P-Well_1. The second vertical BJT Q₃ is formed by the P- layer, N+ buried layer, and P-Well_2. During PS-

mode ESD stresses, The avalanche breakdown occurs at the N+ buried layer/ P-Well_2 junction in Q₁, increasing current through Q₁. As current flows through the parasitic resistance in P-Well_2 (R_{Pwell_2}), the voltage across the base-emitter junction of Q2 increases. When the voltage across the base-emitter junction of Q₂ exceeds its cut-in voltage, Q₂ is turned on, and the SCR composed of Q₁ and Q₂ is turned on to sink ESD current. Similarly, the SCR composed of Q₁ and Q₄ is turned on to sink ESD current during NS-mode ESD stresses.

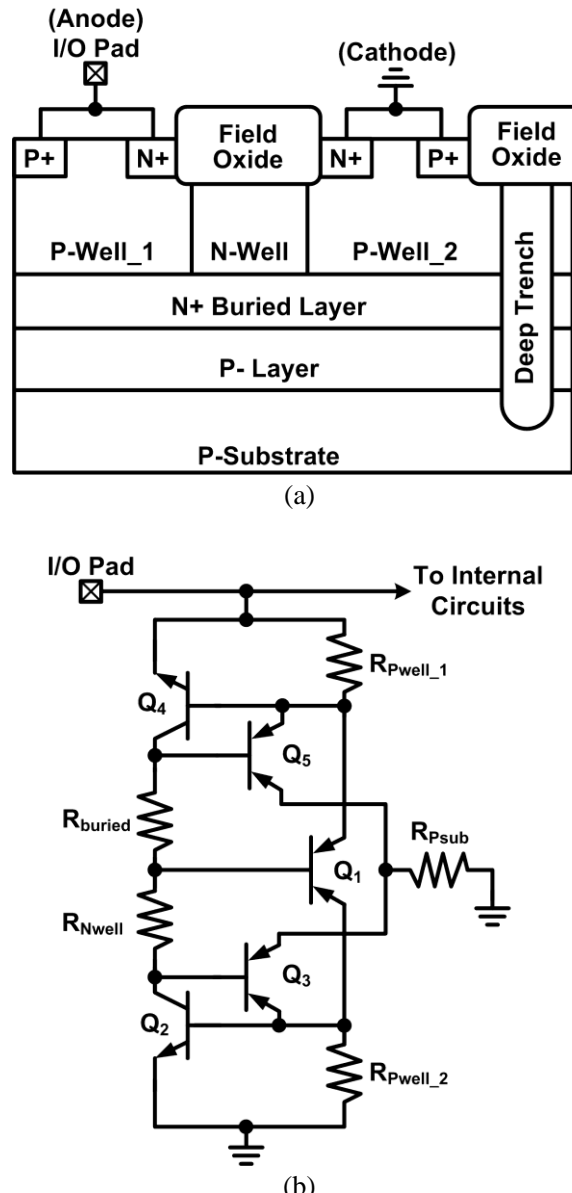


Figure 36. ESD protection device with symmetrical SCR: (a) cross-sectional view, and (b) schematic circuit diagram.

5.2. Low-Capacitance MOSFET

In section 3.1, it has been mentioned that the parasitic capacitance can be reduced by lowering the concentration of the PN-junction. The similar idea using an extra mask to lower the concentration at the drain-to-well junction had been proposed [70]. The cross-sectional view of the low-capacitance PMOS transistor is shown in Figure 37.

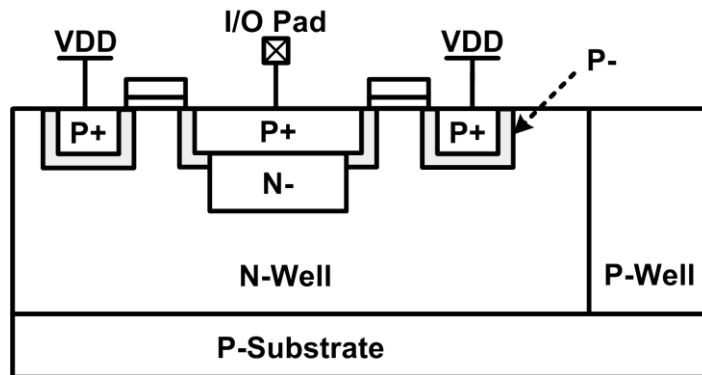


Figure 37. Cross-sectional view of the low-capacitance PMOS.

The drain and source regions are surrounded by the lightly-doped P-type (P-) regions. The N- region under the drain is counter-doped with P-type material to reduce the effective N-type concentration. Since the depletion region of the P+/N- junction is larger than that of the P+/N-well junction, the parasitic capacitance is reduced.

6. Discussion and Comparison

The comparison among various ESD protection designs for RF front-end circuits is summarized in Table 1. The evaluated parameters are explained as following.

- Design Complexity:
 - “Low”: The stand-alone ESD protection device is the ESD protection circuit without extra auxiliary component.
 - “Moderate”: The stand-alone ESD protection device is the ESD protection circuit without extra auxiliary component, but the layout of the ESD protection device needs careful consideration.
 - “High”: Besides the ESD protection device, extra auxiliary components are needed, and the auxiliary components should be carefully designed.
- Parasitic Capacitance:
 - “Small”: The parasitic capacitance of the ESD protection circuit at the I/O pad can be very small with proper design.
 - “Moderate”: The parasitic capacitance of the ESD protection circuit at the I/O pad is moderate for high-frequency applications.

- “Large”: The parasitic capacitance of the ESD protection circuit at the I/O pad is large for high-frequency applications.
- ESD Robustness:
 - “Poor”: ESD robustness of the ESD protection design is poor.
 - “Moderate”: ESD robustness of the ESD protection design is moderate.
 - “Good”: ESD robustness of the ESD protection design is good.
 - “Adjustable”: For some ESD protection designs by circuit solutions, ESD robustness can be adjusted by using different ESD protection devices and dimensions.
- Area Efficiency:
 - “Poor”: The area efficiency of the ESD protection design is poor.
 - “Moderate”: The area efficiency of the ESD protection design is moderate.
 - “Good”: The area efficiency of the ESD protection design is good.

According to Table 1, most of the reported ESD protection designs utilize circuit solutions to mitigate the impacts caused by the ESD protection circuit. By utilizing the circuit solutions, the ESD protection device can be realized with large device dimensions to achieve good ESD robustness, because the parasitic capacitance from the ESD protection device can be compensated or cancelled.

Table 1. Comparison Among the ESD Protection Designs for RF Circuits

ESD Protection Design		Design Complexity	Parasitic Capacitance	ESD Robustness	Area Efficiency
Layout Solutions	Low-C Layout Structure for MOSFET	Moderate	Large	Poor	Moderate
	Low-C Layout Structure for SCR	Moderate	Moderate	Good	Good
	Waffle Layout Structure	Moderate	Moderate	Moderate	Good
	ESD Protection Device Under I/O Pad	Moderate	Moderate	Moderate	Good
Circuit Solutions	Stacked ESD Protection Devices	Low	Moderate	Moderate	Good
	Parallel LC Resonator	High	Small	Adjustable	Poor
	LC-Tank	High	Small	Adjustable	Poor
	Series LC Resonator	High	Small	Adjustable	Poor
	Impedance Matching	High	Small	Adjustable	Poor
	Inductive ESD Protection	High	Small	Adjustable	Poor
	T-Coil	High	Small	Adjustable	Poor
	Distributed ESD Protection	High	Small	Adjustable	Poor
Process Solutions	Symmetrical SCR Structure	Low	Small	Good	Good
	Low-Capacitance MOSFET	Low	Moderate	Poor	Moderate

However, circuit solutions often need additional components. As a result, the chip area is substantially increased, which in turn increases the fabrication cost. Moreover, characteristics of the ESD protection device and the additional components need to be carefully investigated to minimize the undesired effects.

Summary

A comprehensive overview in the field of ESD protection design for RF circuits has been presented. To optimize both RF circuit performance and high enough ESD robustness simultaneously, the undesired parasitic effects from ESD protection devices must be minimized or cancelled. Furthermore, the ESD protection circuits and RF circuits should be co-designed to achieve both good circuit performance and high ESD robustness. As the operating frequencies of ICs are further increased, on-chip ESD protection design for RF applications will continuously be an important design task.

References

- [1] Y.-W. Hsiao and M.-D. Ker. (2009). A 5-GHz differential low-noise amplifier with high pin-to-pin ESD robustness in a 130-nm CMOS process. *IEEE Trans. Microw. Theory Tech.*, vol. 57 no. 5, pp. 1044-1053.
- [2] B. Huang, C. Wang, C. Chen, M. Lei, P. Huang, K. Lin, and H. Wang. (2009). Design and analysis for a 60-GHz low-noise amplifier with RF ESD protection. *IEEE Trans. Microw. Theory Tech.*, vol. 57 no. 2, pp. 298-305.
- [3] J. Borremans, S. Thijs, P. Wambacq, Y. Rolain, D. Linten, and M. Kuijk. (2009). A fully integrated 7.3 kV HBM ESD-protected transformer-based 4.5-6 GHz CMOS LNA. *IEEE J. Solid-State Circuits*, vol. 44 no. 2, pp. 344-353.
- [4] W. Soldner, M. Streibl, U. Hodel, M. Tiebout, H. Gossner, D. Schmitt-Landsiedel, J. Chun, C. Ito, and R. Dutton. (2007). RF ESD protection strategies: Codesign vs. low-C protection. *J. Microelectronics Reliability*, vol. 47 no. 7, pp. 1008-1015.
- [5] M.-D. Ker, Y.-W. Hsiao, and W.-L. Wu. (2006). ESD-protection design with extra low-leakage-current diode string for RF circuits in SiGe BiCMOS process. *IEEE Trans. Device and Materials Reliability*, vol. 6 no. 4, pp. 517-527.
- [6] M.-D. Ker. (1999). Whole-chip ESD protection design with efficient VDD-to-VSS ESD clamp circuits for submicron CMOS VLSI. *IEEE Trans. Electron Devices*, vol. 46 no. 1, pp. 173-183.
- [7] C.-T. Wang and M.-D. Ker. (2009). Design of power-rail ESD clamp circuit with ultra-low standby leakage current in nanoscale CMOS technology. *IEEE J. Solid-State Circuits*, vol. 44 no. 3, pp. 956-964.
- [8] A. Wang, H. Feng, R. Zhan, H. Xie, G. Chen, Q. Wu, X. Guan, Z. Wang, and C. Zhang. (2005). A review on RF ESD protection design. *IEEE Trans. Electron Devices*, vol. 52 no. 7, pp. 1304-1311.
- [9] M.-D. Ker and C.-M. Lee. (2003). Interference of ESD protection diodes on RF performance in giga-Hz RF circuits. *Proc. of IEEE Int. Symp. Circuits and Systems*, pp. 297-300.

- [10] K. Gong, H. Feng, R. Zhan, and A. Wang. (2002). A study of parasitic effects of ESD protection on RF ICs. *IEEE Trans. Microw. Theory Tech.*, vol. 50 no. 1, pp. 393-402.
- [11] C. Richier, P. Salome, G. Mabboux, I. Zaza, A. Juge, and P. Mortini. (2002). Investigation on different ESD protection strategies devoted to 3.3 V RF applications (2 GHz) in a 0.18 μ m CMOS process. *J. Electrostatics*, vol. 54 no. 1, pp. 55-71.
- [12] B. Razavi. *RF Microelectronics*. Englewood Cliffs, NJ: Prentice-Hall, 1998.
- [13] A. London. (2002). Low capacitance ESD structure having a source inside a well and the bottom portion of the drain inside a substrate. U.S. Patent 6,114,731.
- [14] M. Mergens, C. Russ, K. Verhaege, J. Armer, P. Jozwiak, R. Mohn, B. Keppens, and C. Trinh. (2005). Speed optimized diode-triggered SCR (DTSCR) for RF ESD protection of ultra-sensitive IC nodes in advanced technologies. *IEEE Trans. Device and Materials Reliability*, vol. 5 no. 3, pp. 235-249.
- [15] M.-D. Ker and K.-C. Hsu. (2005). Overview of on-chip electrostatic discharge protection design with SCR-based devices in CMOS integrated circuits. *IEEE Trans. Device and Materials Reliability*, vol. 5 no. 2, pp. 235-249.
- [16] J.-H. Lee, K.-R. Peng, and S.-C. Wong. (2002). Low capacitance ESD protection device. U.S. Patent 6,448,123.
- [17] J.-H. Lee, K.-R. Peng, and S.-C. Wong. (2003). Low capacitance ESD protection device. U.S. Patent 6,661,060.
- [18] J.-H. Lee, Y.-H. Wu, K.-R. Peng, R.-Y. Chang, T.-L. Yu, and T.-C. Ong. (2002). The embedded SCR NMOS and low capacitance ESD protection device for self-protection scheme and RF application. *Proc. of Custom Integrated Circuits Conf.*, pp. 93-96.
- [19] A. Chatterjee and T. Polgreen. (1991). A low-voltage triggering SCR for on-chip ESD protection at output and input pads. *IEEE Electron Device Lett.*, vol. 12 no. 1, pp. 21-22.
- [20] M.-D. Ker, C.-Y. Wu, and H.-H. Chang. (1996). Complementary-LVTSCR ESD protection circuit for submicron CMOS VLSI/ULSI. *IEEE Trans. Electron Devices*, vol. 43 no. 4, pp. 588-598.
- [21] K. Peng and J. Lee. (2003). Depletion mode SCR for low capacitance ESD input protection. U.S. Patent 6,610,262.
- [22] C. Salling and C. Duvvury. (2005). Efficient ESD protection with application for low capacitance I/O pads. U.S. Patent 6,858,902.
- [23] M.-D. Ker, S.-L. Chen, and C.-S. Tsai. (2005). Overview and design of mixed-voltage I/O buffers with low-voltage thin-oxide CMOS transistors. *IEEE Trans. Circuits and Systems I: Regular Papers*, vol. 53 no. 9, pp. 1934-1945.
- [24] D. Seo, H. Dabag, Y. Guo, M. Mishra, and G. McAllister. (2007). High-voltage-tolerant analog circuits design in deep-submicrometer CMOS technologies. *IEEE Trans. Circuits and Systems I: Regular Papers*, vol. 54 no. 10, pp. 2159-2166.
- [25] X. Zhang, S. Lam, P. Ko, and M. Chan. (2002). High-speed mixed signal and RF circuits design with compact waffle MOSFET. *Proc. of IEEE Hong Kong Electron Devices Meeting*, pp. 103-106.
- [26] L. Baker, R. Currence, S. Law, M. Le, C. Lee, S. Lin, and M. Teene. (1989). A "waffle" layout technique strengthens the ESD hardness of the NMOS output transistor. *Proc. of EOS/ESD Symp.*, pp. 175-181.
- [27] S. Dabral and K. Seshan. (2000). Diode and transistor design for high speed I/O. U.S. Patent 6,137,143.

- [28] S. Dabral and K. Seshan. (2006). Diode and transistor design for high speed I/O. U.S. Patent 7,012,304.
- [29] K. Bhatia and E. Rosenbaum. (2007). Layout guidelines for optimized ESD protection diodes. *Proc. of EOS/ESD Symp.*, pp. 19-27.
- [30] K. Bhatia, N. Jack, and E. Rosenbaum. (2009). Layout optimization of ESD protection diodes for high-frequency I/Os. *IEEE Trans. Device and Materials Reliability*, vol. 9 no. 3, pp. 465-475.
- [31] M.-D. Ker and C.-Y. Lin. (2008). Low-capacitance SCR with waffle layout structure for on-chip ESD protection in RF ICs. *IEEE Trans. Microw. Theory Tech.*, vol. 56 no. 5, pp. 1286-1294.
- [32] C.-Y. Lin, M.-D. Ker, and G.-X. Meng. (2008). Low-capacitance and fast turn-on SCR for RF ESD protection. *IEICE Trans. Electronics*, vol. E91-C no. 8, pp. 1321-1330.
- [33] C. Lee. (1998). ESD protection circuit located under protected bonding pad. U.S. Patent 5,838,043.
- [34] R. Yach. (2006). Low capacitance ESD-protection structure under a bond pad. U.S. Patent 7,002,218.
- [35] P. Leroux, M. Steyaert, V. Vassilev, and G. Groeseneken. (2002). A 1.3dB NF CMOS LNA for GPS with 3kV HBM ESD-protection. *Proc. of Eur. Solid-State Circuits Conf.*, pp. 335-338.
- [36] M.-D. Ker, T.-Y. Chen, and C.-Y. Chang. (2001). ESD protection design for CMOS RF integrated circuits. *Proc. of EOS/ESD Symp.*, pp. 346-354.
- [37] M.-D. Ker and C.-Y. Chang. (2002). ESD protection design for CMOS RF integrated circuits using polysilicon diodes. *J. Microelectronics Reliability*, vol. 42 no. 6, pp. 863-872.
- [38] X. Jin, L. Tse, K. Tsai, G. Chien, and S. Wei. (2005). Methods and apparatus for improving high frequency input/output performance. U.S. Patent 6,911,739.
- [39] X. Jin, L. Tse, K. Tsai, G. Chien, and S. Wei. (2005). Methods and apparatus for improving high frequency input/output performance. U.S. Patent 6,977,444.
- [40] X. Jin, L. Tse, K. Tsai, G. Chien, and S. Wei. (2006). Methods and apparatus for improving high frequency input/output performance. U.S. Patent 6,987,326.
- [41] X. Jin, L. Tse, K. Tsai, G. Chien, and S. Wei. (2006). Methods and apparatus for improving high frequency input/output performance. U.S. Patent 7,009,308.
- [42] S. Hyvonen, S. Joshi, and E. Rosenbaum. (2005). Comprehensive ESD protection for RF inputs. *J. Microelectronics Reliability*, vol. 45 no. 2, pp. 245-254.
- [43] S. Hyvonen and E. Rosenbaum. (2005). Diode-based tuned ESD protection for 5.25-GHz CMOS LNAs. *Proc. of EOS/ESD Symp.*, pp. 9-17.
- [44] T. Tsukada, Y. Hashimoto, K. Sakata, H. Okada, and K. Ishibashi. (2005). An on-chip active decoupling circuit to suppress crosstalk in deep-submicron CMOS mixed-signal SoCs. *IEEE J. Solid-State Circuits*, vol. 40 no. 1, pp. 67-79.
- [45] M.-D. Ker, C.-M. Lee, and W.-Y. Lo. (2005). Electrostatic discharge protection device for giga-Hz radio frequency integrated circuits with varactor-LC tanks. U.S. Patent 6,885,534.
- [46] M.-D. Ker, C.-M. Lee, and T.-Y. Chen. (2006). Electrostatic discharge protection designs with parallel LC tank for giga-Hz RF integrated circuits. U.S. Patent 7,009,826.
- [47] M.-D. Ker, C.-M. Lee, and T.-Y. Chen. (2006). ESD protection designs with parallel LC tank for giga-Hz RF integrated circuits. U.S. Patent 7,023,677.

- [48] M.-D. Ker, C.-M. Lee, and T.-Y. Chen. (2006). ESD protection designs with parallel LC tank for giga-Hz RF integrated circuits. U.S. Patent 7,023,678.
- [49] M.-D. Ker, C.-I. Chou, and C.-M. Lee. (2003). A novel LC-tank ESD protection design for giga-Hz RF circuits. *Proc. of IEEE Radio Freq. Integrated Circuit Symp.*, pp. 115-118.
- [50] C. Yue, S. Wong, D. Su, and W. McFarland. (2003). System for providing electrostatic discharge protection for high-speed integrated circuits. U.S. Patent 6,509,779.
- [51] C. Yue, S. Wong, D. Su, and W. McFarland. (2003). System for providing electrostatic discharge protection for high-speed integrated circuits. U.S. Patent 6,593,794.
- [52] C. Yue, S. Wong, D. Su, and W. McFarland. (2003). System for providing electrostatic discharge protection for high-speed integrated circuits. U.S. Patent 6,597,227.
- [53] J. Leete. (2004). Electrostatic protection circuit with impedance matching for radio frequency integrated circuits. U.S. Patent 6,771,475.
- [54] B.-S. Huang and M.-D. Ker. (2006). New matching methodology of low-noise amplifier with ESD protection. *Proc. of IEEE Int. Symp. Circuits and Systems*, pp. 4891-4894.
- [55] J. Zerbe, V. Stojanovic, M. Horowitz, and P. Chau. (2006). Input/output circuit with on-chip inductor to reduce parasitic capacitance. U.S. Patent 7,005,939.
- [56] D. Linten, S. Thijs, M. Natarajan, P. Wambacq, W. Jeamsaksiri, J. Ramos, A. Mercha, S. Jenei, S. Donnay, and S. Decoutere. (2005). A 5-GHz fully integrated ESD-protected low-noise amplifier in 90-nm RF CMOS. *IEEE J. Solid-State Circuits*, vol. 40 no. 7, pp. 1434-1442.
- [57] P. Leroux and M. Steyaert. (2004). A 5 GHz CMOS low-noise amplifier with inductive ESD protection exceeding 3 kV HBM. *Proc. of Eur. Solid-State Circuits Conf.*, pp. 295-298.
- [58] J. Borremans, S. Thijs, P. Wambacq, Y. Rolain, D. Linten, and M. Kuijk. (2009). A fully integrated 7.3 kV HBM ESD-protected transformer-based 4.5-6 GHz CMOS LNA. *IEEE J. Solid-State Circuits*, vol. 44 no. 2, pp. 344-353.
- [59] J. Borremans, S. Thijs, P. Wambacq, D. Linten, Y. Rolain, and M. Kuijk. (2007). A 5 kV HBM transformer-based ESD protected 5-6 GHz LNA. *Symp. VLSI Circuits Dig. Tech. Papers*, pp. 100-101.
- [60] S. Galal and B. Razavi. (2003). Broadband ESD protection circuits in CMOS technology. *IEEE J. Solid-State Circuits*, vol. 38 no. 12, pp. 2334-2340.
- [61] M. Kossel, C. Menolfi, J. Weiss, P. Buchmann, G. von Bueren, L. Rodoni, T. Morf, T. Toifl, and M. Schmatz. (2008). A T-coil-enhanced 8.5Gb/s high-swing source-series-terminated transmitter in 65nm bulk CMOS. *IEEE Int. Solid-State Circuits Conf. Dig. Tech. Papers*, pp. 110-111.
- [62] D. Linten, S. Thijs, J. Borremans, M. Dehan, D. Tremouilles, M. Scholz, M. Natarajan, P. Wambacq, and G. Groeseneken. (2007). T-diodes - a novel plug-and-play wideband RF circuit ESD protection methodology. *Proc. of EOS/ESD Symp.*, pp. 242-249.
- [63] B. Kleveland and T. Lee. (1999). Distributed ESD protection device for high speed integrated circuits. U.S. Patent 5,969,929.
- [64] B. Kleveland, T. Maloney, I. Morgan, L. Madden, T. Lee, and S. Wong. (2000). Distributed ESD protection for high-speed integrated circuits. *IEEE Electron Device Lett.*, vol. 21 no. 8, pp. 390-392.

- [65] C. Ito, K. Banerjee, and R. Dutton. (2002). Analysis and design of distributed ESD protection circuits for high-speed mixed-signal and RF ICs. *IEEE Trans. Electron Devices*, vol. 49 no. 8, pp. 1444-1454.
- [66] M.-D. Ker and B.-J. Kuo. (2005). Decreasing-size distributed ESD protection scheme for broadband RF circuits. *IEEE Trans. Microw. Theory Tech.*, vol. 53 no. 2, pp. 582-589.
- [67] M.-D. Ker, B.-J. Kuo, and Y.-W. Hsiao. (2006). Optimization of broadband RF performance and ESD robustness by π -model distributed ESD protection scheme. *J. Electrostatics*, vol. 64 no. 2, pp. 80-87.
- [68] M.-D. Ker and C.-M. Lee. (2006). ESD protection circuits with impedance matching for radio-frequency applications. U.S. Patent 2006/0256489 A1.
- [69] E. Stefanov and R. Escoffier. (2006). Symmetrical high frequency SCR structure. U.S. Patent 6,989,572.
- [70] J. McCollum and F. Dhaoui. (2006). Low-capacitance input/output and electrostatic discharge circuit for protecting an integrated circuit from electrostatic discharge. U.S. Patent 7,019,368.

Chapter 5

FOOD INDUSTRY ELECTROSTATIC POWDER COATING

Nutsuda Sumonsiri and Sheryl A. Barringer*

Department of Food Science and Technology,
The Ohio State University, Columbus, OH, USA

Abstract

Powder coating is an important process in the food industry, especially for snack foods. Powder coating creates variety in food, producing different flavors and appearance. Electrostatic coating has been adopted in order to provide better efficiency and lower the dust produced during coating. Electrostatic coating is usually done with a corona system to charge the powder. There are two systems used to coat the food: a tumble drum coating system and a conveyor belt coating system. The tumble drum coating system is used to coat all sides of the food product. The conveyor belt coating system only coats one side of the product but most consumers do not notice this. The efficiency of electrostatic coating is affected by characteristics of the powder, including particle size, density, resistivity, and flowability. Surface characteristics of the food to be coated are also important. These factors affect the transfer efficiency, adhesion, dust, evenness, and functionality of the powder on the targets. An understanding of these factors can be used to predict the coating performance in food production and help the processor choose the best system for coating food products.

1. Introduction

Electrostatic powder coating was introduced to the food industry from the painting industry in the 1960s (Bailey 1998). The main purposes of electrostatic coating are to produce evenly coated products, improve powder adhesion, minimize dust, minimize overuse and waste of expensive food powders. The coating on the food target is more even because charged powder particles repel one another to form a cloud which evenly disperses the coating across the surface (Biehl and Barringer 2003; Ricks and others 2002). According to Coulomb's law, the attraction force increases when the distance decreases. Therefore, the

* E-mail address: barringer.11@osu.edu, Tel. 614-688-3462, Fax. 614-292-0218

charge on the powders produces better adhesion between powders and the target surface (Hughes 1997). Dust creates worker health issues and an explosion risk. Electrostatic coating reduces dust and powder build up because charged powders seek out and land on the target surface, rather than remaining in the air and eventually settling on other surfaces. The reduction of dust and powder build up can shorten the cleaning process; as a result, it can reduce the operating costs.

Powder coating of food products is most often used in the snack food industry. Examples of powder coated foods include potato chips, cakes, donuts, shredded cheese, crackers, and pretzels. Powder coating is used to produce better taste and appearance, as well as to create more variety in foods to enhance consumer acceptability. Thus a sufficient amount of food powder or seasoning evenly dispersed on these foods is critical.

One of the advantages of electrostatic over nonelectrostatic coating is more even coating. Evenness of coating is used to indicate how well food powder is dispersed on the target, which affects the appearance of food and consumer acceptability (Hughes 1997). In a study of the uniformity of salt applied on crackers, the variation in salt content between crackers from nonelectrostatic coating was higher than the variation from electrostatic coating, which indicates that the electrostatic coating provides more even dispersion of salt on crackers because powder particles repel each other due to the negative charge given by the coater (Strietelmeier and Reynolds 1969). There are two coating systems that are usually used in snack food seasoning processes: a tumble drum coating system and a conveyor belt coating system (Hanify 2001). The tumble drum is a rotating stainless steel cylinder with internal baffles to flip the pieces, increasing the ability of the system to coat all sides of the target (Figure 1). The powder is charged and dispersed inside the drum by a gun, auger or vibratory feeder to create a spray or curtain of powder. The metal drum is grounded to attract the powder to the bed of food pieces tumbling underneath the powder dispenser.



Figure 1. A tumble drum coating system used in coating popcorn with salt.



Figure 2. Saltine crackers being coated in a conveyor belt coating system.

The other coating system is the conveyor belt coating system (Figure 2). The gun, waterfall or pneumatic sprayer is positioned over the conveyor belt. The belt is metal or made of conducting plastic to attract the charged powder. The belt system is designed to coat only one side of the target; however, the other sides of the product can be coated by using equipment to flip the target over. Frequently, though, the consumer doesn't notice that only one side is coated.

Most application methods use a charging gun or wire. The powder is blown from a reservoir to a feed pipe and through a powder dispenser with an electrode to create the electrostatic field, to coat the target (Bailey 1998). The electrostatic field can be created by a wire in the coating chamber or electrode at the end of a gun. While there is some use of tribocharging and induction charging in other industries, in the food industry almost all powder charging occurs by corona charging. Corona charging involves the ionization of the air, which carries the charge to the powder particles while passing through the exit region of the powder dispenser, because of the Coulombic force of the intense electric field between the corona gun and the target (Bailey 1998). During electrostatic coating, the air flow provides the aerodynamic force which combines with inertia and Coulombic forces to carry the charged powder particles from the coater to the target (Bailey 1998). These forces are greatly affected by the physical properties of the powders.

Under appropriate conditions, powder particles can not only cover the surface of the target but also coat down the sides of the target (Bailey 1998), which can lead to efficient side coating of powders on a thick target (Figure 3). This wrap around effect is possible because of particle inertial forces and space charge (Bailey 1998). In contrast, the Faraday Cage effect can decrease coating on a target with an uneven surface. Charged food powders do not deposit inside crevices on the target where there is a strong electrical field between the charging electrode and target, resulting in poor deposition and evenness on the surface (Figure 3), especially on targets with complicated geometry (Boncza-Tomaszewski and

Penczek 2002; Mayr and Barringer 2006). There is also a self-limiting phenomenon occurring during electrostatic coating in a corona system due to the back ionization effect. When the total charge in the powder layer exceeds the dielectric strength of the air, powder is blown off the target, producing an uneven layer of powder (Figure 3) (Horinka 1995).

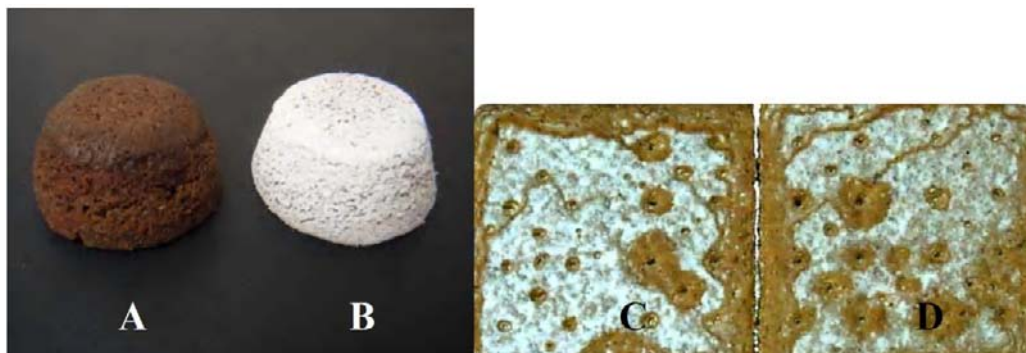


Figure 3. A: Wrap around effect on food targets. Chocolate fudge brownie without coating. B: Electrostatically coated brownie. C, D: Faraday cage and back ionization effects on electrostatically coated graham crackers.

The physical properties of the powders, including particle size, shape, charge, density, flow characteristics, and resistivity, affect the transfer efficiency, dust, adhesion, evenness and functionality of the electrostatically coated powder layer. These properties generally cannot be changed because the powder was chosen to deliver a certain sensory profile. Thus the design of the equipment must be altered to adapt to the powder used.

2. Effect of Powder Properties on Electrostatic Coating

2.1. Particle Size

Particle size plays an important role in electrostatic coating just as it does in nonelectrostatic coating. During nonelectrostatic coating, the transfer efficiency may increase or decrease with particle size, depending on whether gravity or aerodynamic forces dominate during coating (Figure 4). An example of a gravity system is in Figure 1, where powder falls out of a tube. Figure 2 is an aerodynamic system, where powder is blown onto the food. With addition of electrostatics, the transfer efficiency increases. With an aerodynamic system, the percent improvement with electrostatic coating increases as the particle size decreases from 330 to 5 μm using salt, corn starch, maltodextrin, cellulose powder, soy flour, cocoa (Ratanatriwong and Barringer 2007; Ricks and others 2002), sugar (Mayr and Barringer 2006), barbecue, salsa, salt and vinegar, and nacho cheese seasoning (Ratanatriwong and Barringer 2003). Smaller particles under the same charging conditions produce a higher charge to mass ratio than large particles, thus the electrostatic forces have more influence over smaller particles than larger particles. For small particles, electrostatic forces overcome the gravitational and aerodynamic forces so that the powder particles land on the targets rather than stay in the air as dust. When particles are large enough, gravitational forces

overcome electrostatic forces resulting in no or little difference in transfer efficiency between nonelectrostatic and electrostatic coating (Ricks and others 2002). With a gravity fed system, the electrostatic transfer efficiency increased as the particle size decreased from 145 to 13 μm using cornstarch, flour, maltodextrin, powdered sugar, salt, and cellulose. However, the percent improvement with electrostatic coating stayed constant at approximately 15% (Biehl and Barringer 2003).

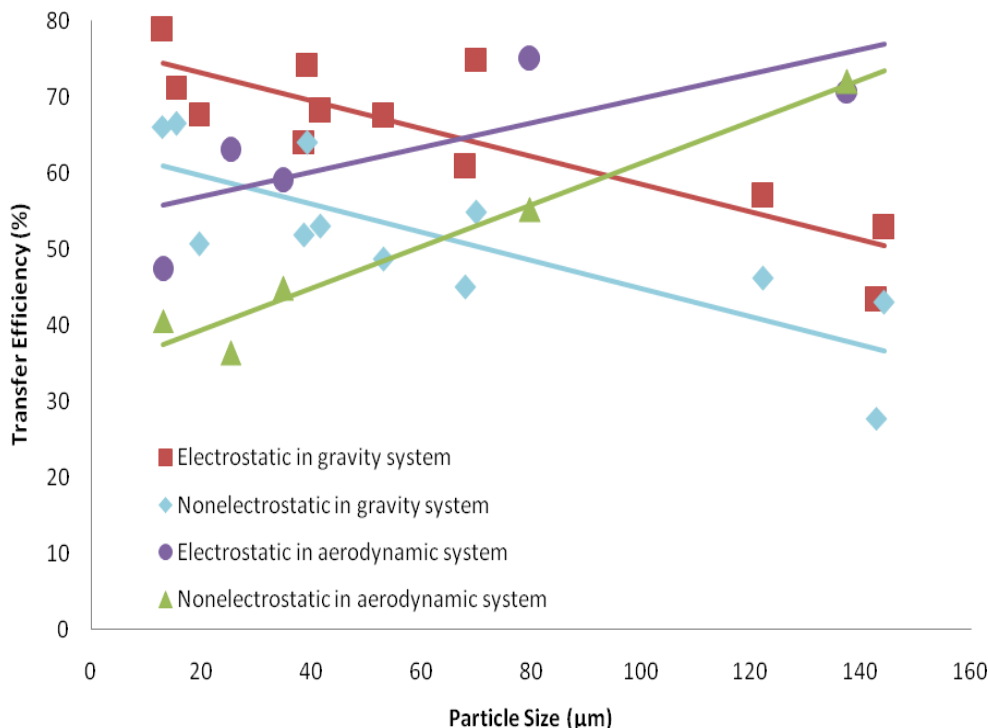


Figure 4. Effect of particle size on transfer efficiency in a gravity and aerodynamic coating system (data from Biehl and Barringer 2003; Mayr and Barringer 2006).

The improvement in adhesion with electrostatic coating is also particle size dependent. The adhesion of electrostatically coated sugar decreased as the particle size increased from 20 to 150 μm (Halim and Barringer 2007). Increasing the particle size greater than 200 μm produced no improvement of adhesion by electrostatics. Larger powders have a lower charge-to-mass ratio, and therefore lower attraction force between particles and the target surface. The adhesion of electrostatically coated salts on potato chips also significantly decreased when large particle sizes, 258 and 388 μm , were used (Buck and Barringer 2007).

Since electrostatic forces are strongest on small particles, electrostatics is very efficient at decreasing the dustiness of a process. Dust increases as particle size decreases. The use of electrostatic coating has been shown to create a significant dust reduction in most powders, such as corn flour, cellulose powder, salt, soy flour, corn starch, cocoa powder (Ricks and others 2002), sugar (Mayr and Barringer 2006), barbecue, sour cream, salt and vinegar, nacho cheese (Ratanatriwong and others 2003), and a variety of protein powders (Sumawi and Barringer 2005).

2.2. Powder Density

Power density can influence the performance of powder coating; however, it depends on the powders used and the coating system. Among food powders, salt is the most dense, at 2.29 g/cm^3 . Other food powders range from only 1.3 to 1.69 g/cm^3 . Frequently, density is found to have no significant effect on electrostatic coating, whether because of the small range of densities possible or because particle size and other factors are a larger effect (Biehl and Barringer 2004). In a computer simulation, electrostatic transfer efficiency increased when the particle density increased (Figure 5) (Yousuf and Barringer 2007).

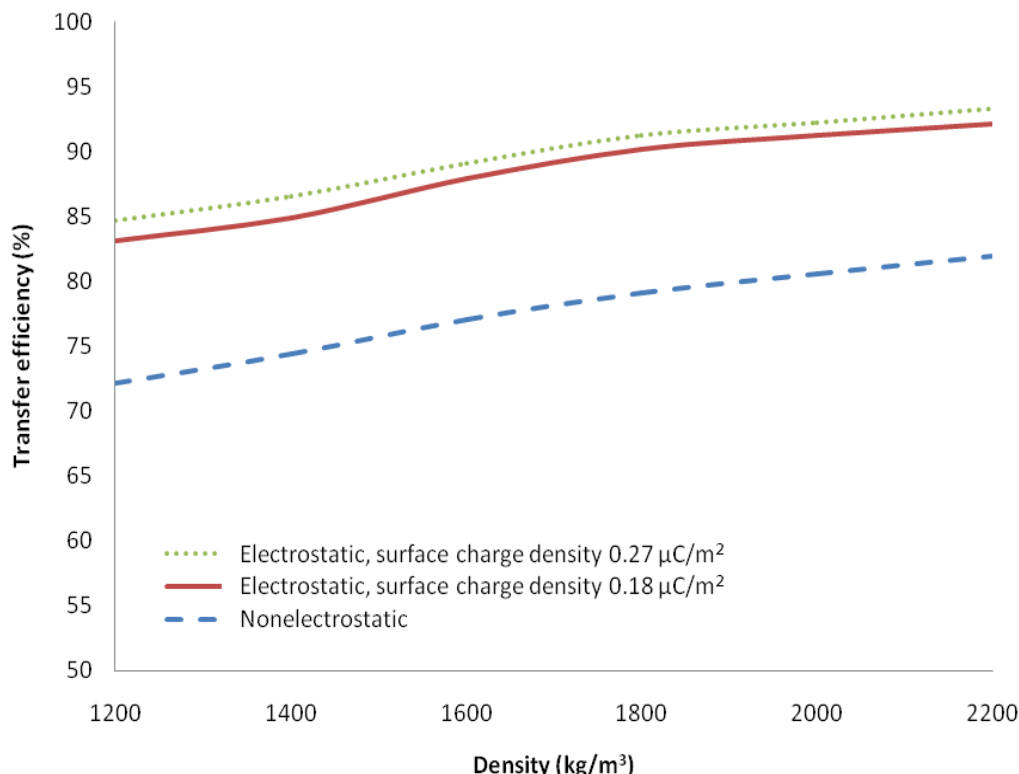


Figure 5. Effect of particle density on nonelectrostatic and electrostatic transfer efficiency in a computer simulation (data from Yousuf and Barringer 2007).

2.3. Powder Charge

The amount of charge on the powder affects particle velocity, transfer efficiency, coating thickness, and adhesion of electrostatic coating (Masui and Murata 1982). How well a powder charges is affected by the powder resistivity, and can be measured by the charge-to-mass ratio. There are three ranges of powder resistivity: greater than $10^{13} \Omega\text{m}$, between 10^{13} and $10^{10} \Omega\text{m}$, and below $10^{10} \Omega\text{m}$ (Bailey 1998). Powders with resistivity above $10^{13} \Omega\text{m}$ provide good adhesion since they are insulating and have a slow charge decay time (Bailey 1998). Cocoa powder is one of the few examples of a food powder that has resistivity in this range.

Powder particles with resistivity from 10^{13} to 10^{10} Ωm have a short charge decay time and poor adhesion (Bailey 1998). The performance of these powders is hard to predict because good adhesion might occur with these powders if other factors are in favor of adhesion. Most food powders have an intermediate resistivity. Powders with resistivity lower than 10^{10} Ωm are conductive so charge easily but lose their charge quickly on the target (Bailey 1998). Salts are the only food powders with resistivity below 10^{10} Ωm . During charging, the lower the resistivity, the more charge is deposited on the powder, and therefore a lower resistivity is desired. On the other hand, after the powders are charged, the higher the resistivity, the slower the charge decay rate and the better the adhesion force between particles and the target therefore a higher resistivity is desired (Hughes 1997). Unlike powders developed for photocopying, the resistivity of food powders cannot be changed during coating.

Resistivity is important in determining the adhesion of food powders. Powders with low resistivity, including salt and maltodextrin, did not produce a significant difference in adhesion between electrostatic and nonelectrostatic coating (Halim and Barringer 2007). However, most powders with resistivity between 10^{11} and 10^{13} Ωm produced a significant improvement in adhesion with electrostatic coating. Cocoa powder, with a resistivity of 10^{13} Ωm , showed the greatest increase in adhesion with electrostatic coating. Relative humidity also affects resistivity. As the relative humidity increases, the resistivity of cocoa powder decreases because of the water absorbing onto the surface (Halim and Barringer 2007). When the relative humidity increases and the resistivity of powders decreases, electrostatic adhesion is lower (Xu and Barringer 2008).

Charge-to-mass ratio is the most common method to indicate how efficiently the powders are charged during electrostatic coating (Hughes 1997). Charge-to-mass ratio increases as the particle size decreases. A higher charge-to-mass ratio produces a greater radial trajectory; therefore, powders with a larger charge-to-mass ratio can disperse more evenly and produce more uniform deposition (Ali and others 2000). Moreover, powders with large charge-to-mass ratio have better attraction to the target; thus, producing higher electrostatic transfer efficiency (Mazumder and others 1997). Many food powders, including powdered sugar, NaCl, cellulose powder, maltodextrin, whole wheat flour, and soy flour, show an increase in electrostatic transfer efficiency as the charge-to-mass ratio increases (Biehl and Barringer 2003). The charge-to-mass ratio needs to be at least 0.2 $\mu\text{C/g}$ to have good adhesion on the target (Singh 1978).

2.4. Flowability

Powder flowability also affects the performance of nonelectrostatic and electrostatic coating. There are numerous methods to measure flow characteristics of powders, including cohesion, flow index, angle of repose, and Hausner ratio. Cohesion represents the affinity of powder particles for each other and determinates how sticky the powders are (Rennie 1999). Cohesion is measured by using either the annular shear cell (Jenike 1964) or the unconfined yield test (Head 1982). A higher value of cohesion indicates that powders are stickier. The flow index is used to indicate how easily powder particles can flow. The angle of repose represents the angle which is formed at the highest peak of a pile of powder (Teunou and others 1999). The Hausner ratio is the ratio between the untapped and tapped bulk density of powder.

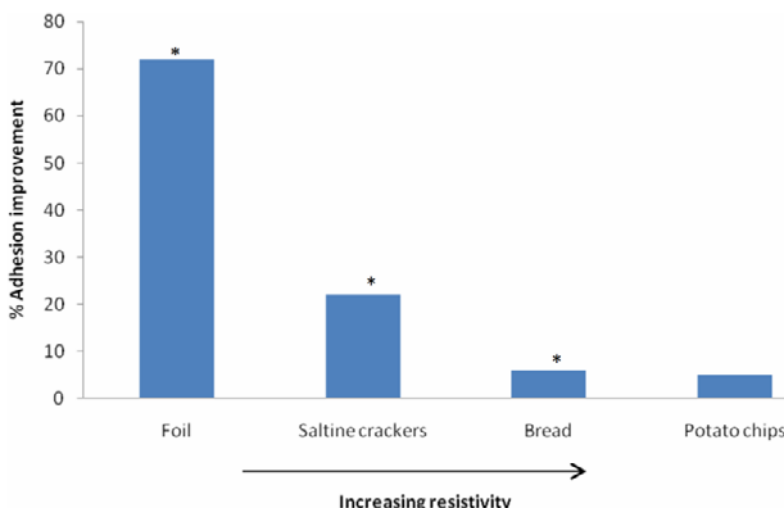
The flow properties of powders can be divided into three ranges: non-flowing, cohesive, and free-flowing. Non-flowing powders have a flow index less than 2, angle of repose greater than 50° and Hausner ratio more than 1.4 (de Jong and others 1999; Peleg 1977; Teunou and others 1999). Cohesive powders have a flow index between 2 and 4, angle of repose from 40° to 50°, and Hausner ratio between 1.25 and 1.4. Free-flowing powders have a flow index from 4 to 10, angle of repose less than 40°, and Hausner ratio from 1 to 1.25.

Flowability is an important factor to indicate the cohesiveness of powders and predict how efficiently and evenly powder particles deposit onto a target, which affects the transfer efficiency, adhesion, and dust reduction in coating (Biehl and Barringer 2003). During electrostatic coating, the transfer efficiency increases as powders become more free-flowing because they can be evenly dispersed across the target (Amefia and others 2006; Biehl and Barringer 2004; Ratanatriwong and Barringer 2007). However, since free-flowing powders also perform well in nonelectrostatic coating, the greatest improvement in electrostatic transfer efficiency occurs when the powders are cohesive (Ratanatriwong and others 2003; Ricks and others 2002). The charged particles repel each other, minimizing clumping, which results in the improvement in transfer efficiency. As expected, adhesion increased when the cohesiveness of powders increased (Sumawi and Barringer 2005). Flowability of powders also significantly affects the amount of dust. Free-flowing powders produce more dust than cohesive powders, but electrostatic coating produces a large reduction in dust for both free-flowing and cohesive powders.

3. Effect of Surface Characteristics of the Target on Electrostatic Coating

The characteristics of the target must be considered to achieve the best coating (Bailey 1998). The roughness of the target surface affects the adhesion forces between powders and target (Podczeck 1998). When the roughness of the target surface increases, the adhesion between powder particles and the target surface frequently decreases. This happens because there is less contact area, resulting in less van der Waals force between powders and target (Podczeck 1998).

The oil content on a potato chip's surface influences the adhesion created by electrostatics because a surface with high oil content has high capillary forces which overcome the electrostatic forces. Electrostatic coating on chips with a high surface oil content showed no improvement in adhesion over nonelectrostatic coating, while there was a significant improvement in adhesion when electrostatic coating was used on chips without free surface oil (Buck and Barringer 2007). However, oil also has high resistivity that can lead to charge building up on the surface of targets. This charge repels charged particles when they land on the target and lower the adhesion between particles and the target surface (Buck and Barringer 2007). Targets with lower resistivity provide better charge flow from the ground and better attraction between the powder and the target surface (Sims and others 2000). Most food targets have a resistivity in the range of 10^8 to 10^{10} Ωm . As food target resistivity increases, the percent electrostatic adhesion improvement increases (Figure 6).



* indicates significant improvement in adhesion (data from Halim and Barringer 2007).

Figure 6. Effect of target resistivity on percent electrostatic adhesion improvement with powdered sugar.

4. Evenness in Electrostatic Coating

Evenness of coating is important because it affects the appearance and functionality of the powder. In a study of coating evenness of various seasonings on potato chips and on banana chips, electrostatic coating produced a more even color on the surface at the same amount of seasoning (Figure 7) (Ratanatriwong and others 2003; 2009).

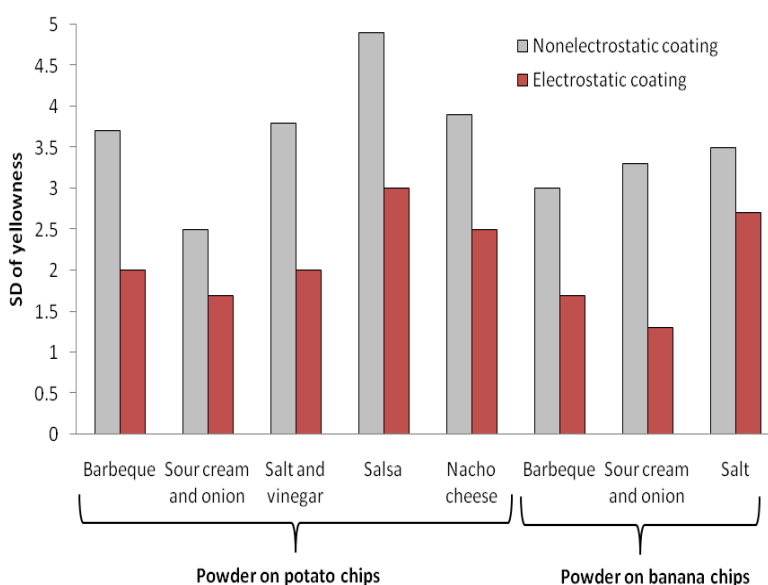


Figure 7. Standard deviation (SD) of yellowness of seasoned potato chips and banana chips. A higher SD indicates more uneven coating (data from Ratanatriwong and others 2003; 2009).

Consumers can see this difference, and significantly preferred electrostatically coated chips over nonelectrostatically coated ones. Meats electrostatically coated with the same amount of sodium erythorbate and/or glucono-delta-lactone were redder than nonelectrostatically coated meats (Barringer and others 2005). Electrostatic coating with glucose or smoke extract produced French fries with a more even color than nonelectrostatic coating (Amefia and others 2006). Electrostatic coating of cheese with a mold inhibitor produced a significantly longer shelf life than nonelectrostatic coating, for the same amount of inhibitor on the cheese (Amefia and others 2006). Similarly, electrostatic coating of meats with antimicrobial agents produced a significantly greater reduction in microbial counts than nonelectrostatic coating.

Conclusion

There are several factors that can influence the efficiency of electrostatic coating during food production, especially the characteristics of the powders used for coating. The greatest improvement with electrostatic coating occurs when using small and cohesive food powders with large charge-to-mass ratio. These parameters play significant roles in the performance of the coating and help the processor to design the optimum system to produce coated food products with the maximum transfer efficiency and minimum operating costs. Moreover, these factors can be used for the prediction of the coating performance of various food powders.

References

- Ali FS, Base TE, Inculet II. 2000. Mathematics modeling of powder paint particle trajectories in electrostatic painting. *IEEE T Ind. Appl.* **36**(4):992-997.
- Amefia AE, Abu-Ali JM, Barringer SA. 2006. Improved functionality of food additives with electrostatic coating. *Innov. Food Sci. Emerg. Technol.* **7**(3):176-181.
- Bailey AG. 1998. The science and technology of electrostatic powder spraying transport and coating. *J. Electrostat.* **45**(2):85-120.
- Barringer SA, Abu-Ali J, Chung H. 2005. Electrostatic powder coating of sodium erythorbate and GDL to improve color and decrease microbial counts on meats. *Innov. Food Sci. Emerg. Technol.* **6**(2):189-193.
- Biehl HL, Barringer SA. 2003. Physical properties important to electrostatic and nonelectrostatic powder transfer efficiency in a tumble drum. *J. Food Sci.* **68**(8):2512-2515.
- Biehl HL, Barringer SA. 2004. Comparison of the effect of powder properties on coating transfer efficiency and dustiness in two nonelectrostatic and electrostatic system. *Innov. Food Sci. Eng. Technol.* **5**(2):2512-2515.
- Boncza-Tomaszewski Z, Penczek P. 2002. Tribo charging powder coating. *Macromol. Symp.* **187**:417-425.
- Buck VE, Barringer SA. 2007. Factors dominating adhesion of NaCl onto potato chips. *J. Food Sci.* **72**(8):435-441.

- de Jong JAH, Hoffmann AC, Finkers HJ. 1999. Properly determine powder flowability to maximize plant output. *Chem Eng Prog* **95**(4):25-34.
- Halim F, Barringer SA. 2007. Electrostatic adhesion in food. *J. Electrostat* **65**(3):168-173.
- Hanify DE. 2001. Snack seasoning application. In: Lusas EW, Rooney LW, editors. *Snack Foods Processing*. Lanchester PA: Technomic Publishing Co. Inc. p 517-527.
- Head KH. 1982. Manual of soil laboratory testing vol.2. London: Pentech Press. p 581-585.
- Horinka PR. 1995. Powder particle size: its role in electrostatic coating. *Powder Coat* **4**:51-56.
- Hughes JF. 1997. Electrostatic particle charging: industrial and healthcare applications. Taunton, Somerset, England: Research Studies Press, Ltd. 170p.
- Jenike AW. 1964. Storage and flow of solids. Bulletin no. 123 of the Utah Engineering Experiment Station. Salt Lake City, UT: Univ of Utah. 198p.
- Masui N, Murata Y. 1986. Method for measuring the powder charge in the electrostatic powder-coating process. *Rev. Sci. Instrum* **53**(4):532-533.
- Mayr MB, Barringer SA. 2006. Corona compared with triboelectric charging for electrostatic powder coating. *J. Food Sci.* **71**(4):171-177.
- Mazumder MK, Wankum DL, Sims RA, Mountain JR, Chen H, Pettit, Chaser T. 1997. Influence of powder properties on the performance of electrostatic coating process. *J. Electrostat* **40-41**:369-374.
- Peleg M. 1977. Flowability of food powders and methods for its evaluation – a review. *J. Food Process Engl.* **1**(4):303-328.
- Podczeck F. 1998. Particle-particle adhesion in pharmaceutical powder handling. London: Imperial College Press. 243p.
- Ratanatriwong P, Barringer SA. 2007. Particle size, cohesiveness and charging effects on electrostatic and nonelectrostatic powder coating. *J. Electrostat*. **65**(10/11):704-708.
- Ratanatriwong P, Barringer SA, Delwiche J. 2003. Sensory preference, coating evenness, dustiness, and transfer efficiency of electrostatically coated potato chips. *J. Food Sci.* **68**(4):1542-1547.
- Ratanatriwong P, Suwansri S, Barringer SA, Tanasukarn P. 2009. Effect of electrostatic coating on consumer acceptance and process efficiency of seasoned coated snacks. *As J. Food Ag-Ind.* **2**(01):51-64.
- Rennie PR, Chen XD, Hargreaves C, Mackereth AR. 1999. A study of the cohesion of dairy powders. *J. Food Eng.* **39**(3):277-284.
- Ricks NP, Barringer SA, Fitzpatrick JJ. 2002. Food powder characteristics important to nonelectrostatic and electrostatic coating and dustiness. *J. Food Sci.* **67**(6):2256-2263.
- Sims RA, Mazumder MK, Biris AS, Sharma R, Kumar D. 2000. Effect of electric resistivity on the adhesion and thickness of electrostatically deposited powder layers. *IEEE Ind. Appl. Conf.* **2**:82-83.
- Singh S, O'Neil BC, Bright AW. 1978. A parametric study of electrostatic powder coating. *J. Electrostat* **4**(4):325-334.
- Strietelmeier DM, Reynolds JW. 1969. On electrostatic salting. *Snack Food*. **58**(9):46-48.
- Sumawi H, Barringer SA. 2005. Positive vs negative electrostatic coating using food powders. *J. Electrostat* **63**(6-10):815-821.
- Teunou E, Fitzpatrick JJ, Synnott EC. 1999. Characterization of food powder flowability. *J. Food Eng.* **39**(1):31-37.

- Xu Y, Barringer SA. 2008. Effect of relative humidity on coating efficiency in nonelectrostatic and electrostatic coating. *J. Food Sci.* **73**(6):297-303.
- Yousuf S, Barringer SA. 2007. Modeling nonelectrostatic and electrostatic powder coating. *J. Food Eng.* **83**(4):550-561.

Chapter 6

ELECTROSTATIC CAPACITANCE EXTRACTION OF ARBITRARY-SHAPED CONDUCTING BODIES USING METHOD OF MOMENTS WITH RECTANGULAR SUBDOMAIN MODELING

Saswati Ghosh*

Department of Electronics and Communication Engineering
Durgapur Institute of Advanced Technology and Management,
Durgapur-713212, West Bengal, India
Former Scientist, Kalpana Chawla Space Technology Cell,
Indian Institute of Technology, Kharagpur-721302, India

Abstract

This chapter presents the evaluation of capacitance of arbitrary-shaped conducting bodies using Method of Moments. The conducting surfaces are modeled by planar rectangular subdomains in which the charge density is assumed to be constant over each subsection. The exact formulation for the matrix element is evaluated for rectangular subsection. The capacitances of different conducting structures, e.g. square, circular, triangular, wedge-shaped plate and also multiconducting bodies e.g. transmission lines with square, circular cross section are evaluated here. In the next part of the chapter, work is extended for the evaluation of static charge distribution and capacitance of conducting bodies from the measured electric field components due the same. The computed results show good agreement with other available results in literature.

Introduction

The increased space development and production has led to significant interest in the evaluation of capacitance of arbitrary-shaped conducting bodies located in free space. The capacitance is used for the determination of spacecraft equivalent circuit model for the

* E mail address: saswatikgp@gmail.com

prediction of electrostatic discharge. Therefore, the improvement of accurate and efficient computational method to evaluate the capacitance of conducting bodies of different shapes becomes an important area of research in spacecraft technology. Considerable work was already performed on the evaluation of capacitance of conducting objects such as square plate, cylinder, circular disc etc. and also for three dimensional multiconductor systems and high voltage electrode configurations [1 – 9]. The conducting surfaces were modeled by square, triangular, cylindrical or rectangular subsections [5 – 9]. In the present chapter, the author has presented the numerical technique for the evaluation of capacitance of arbitrary – shaped e.g. square, triangular, circular, wedge-shaped conducting bodies and transmission lines of square and circular cross sections using Method of Moments. The conducting structures are modeled with a more generalized and simple elemental rectangular sub sectional shape. The exact formulation for the evaluation of the impedance matrix for rectangular subdomain is determined. The Method of Moments with Pulse basis function and Point Matching is used to evaluate the charge distribution and hence the capacitance of various conducting bodies. The capacitances of different conducting structures such as square plates, circular disc are compared with other available data in literature [5, 10] etc. Later the same method is extended for the capacitance evaluation of transmission lines with square and circular cross sections. In the next part of the chapter, the static charge distributions and capacitances of conducting bodies are evaluated from the electric field components due the same. To perform this method theoretically, the electric field at a measurement plane is evaluated due to the charge distribution on the conducting body. The same rectangular subsection modelling is used considering all of the charge being concentrated at the center of the subsection. Then the reverse procedure is applied to evaluate the charge distribution and hence the capacitance of the conducting body from the electric field data. Errors are intentionally incorporated in the electric field data to evaluate errors in the resultant capacitance value. This method may be useful for evaluating the capacitance from measured electrostatic field data.

Theory

Evaluation of Charge Distribution and Capacitance

The potential Φ at a point due to charge distribution $\sigma(r')$ on a conducting body is presented by the following equation [5]

$$\Phi = \iint_S \frac{\sigma(r')}{4\pi\epsilon|r - r'|} ds' \quad (1)$$

Here r and r' are the position vectors corresponding to observation and charge source points respectively, ds' is an element of surface S and ϵ is the permittivity of free space.

For a conducting body charged to a potential V , the potential on the conducting surface is written as follows

$$V = \iint_S \frac{\sigma(r')}{4\pi\epsilon|r - r'|} ds' \quad (2)$$

The unknown surface charge density distribution $\sigma(r')$ can be determined by solving equation (2).

The conducting bodies are approximated by planar rectangular subdomains (Figure 1). The Method of Moments with pulse basis function and point matching is then used to determine the approximate charge distribution [5]. The charge density $\sigma(r')$ is approximated as constant over each subsection and is represented in terms of a pulse expansion function $P_n(r)$ as follows

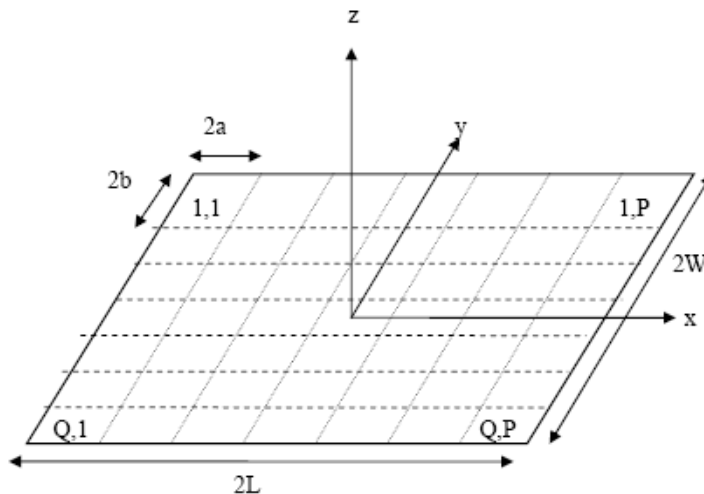


Figure 1. (a) Rectangular conducting plate divided into rectangular subsections.

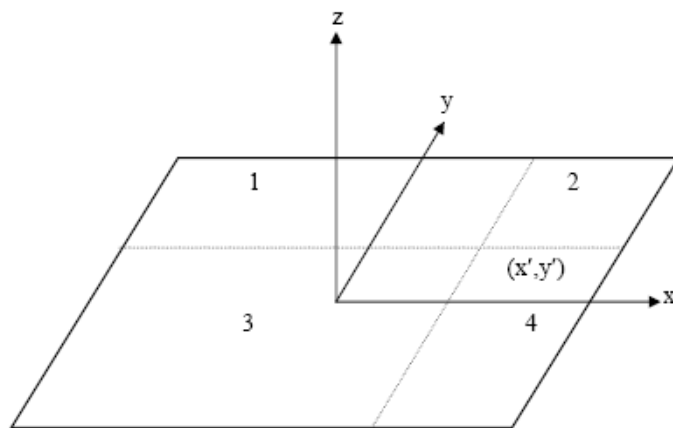


Figure 1. (b) Rectangular conducting plate divided into four distinct regions according to the position of (x_m, y_m) point : 1. $x_m > x'$; $y_m < y'$, 2. $x_m > x'$; $y_m > y'$, 3. $x_m < x'$; $y_m < y'$, 4. $x_m < x'$; $y_m > y'$.

$$\sigma(r') = \sum_{n=1}^N \sigma_n P_n(r') \quad \text{where} \quad P_n = \begin{cases} 1 & \text{for } n\text{-th subsection} \\ 0 & \text{elsewhere} \end{cases} \quad (3)$$

Here $N = PXQ$ is the number of rectangles modelling the surface and σ_n 's are the unknown weights (charge density).

Substituting the charge expansion (3) in (2) and point matching the resulting functional equation, an $N \times N$ system of linear equations is achieved in the following form

$$[V] = [K][Q] \quad (4)$$

Here $[K]$ is an $N \times N$ matrix and $[Q]$ and $[V]$ are column vectors of length N . The elements of $[K]$, $[Q]$ and $[V]$ are given as follows

$$K_{mn} = \iint_{\text{rectangle}} \frac{1}{4\pi\epsilon |r_m - r'|} dA' \quad (5)$$

$Q_n = \sigma_n$ = unknown charge density in subdomain n

$V_n = V$

r_m denotes the position vector of the center of the m th rectangle. A' is the area of the source rectangle.

$$|r_m - r'| = \sqrt{(x_m - x')^2 + (y_m - y')^2}$$

Here we have considered the conducting surface at $z=0$ plane.

The numerical formulation of (2) via the Method of Moments is available in other literature [5] and is avoided here. We consider only the evaluation of the element of the moment matrix as given by equation (5). Each element of the matrix corresponds to the potential at some point in space, $r = (x, y, z)$, due to a rectangular patch of surface charge of unit charge density. In general, the patch is arbitrarily positioned and oriented in space.

Performing tedious integration, the diagonal elements of the matrix is evaluated as follows [9]

$$K_{nn} = \frac{1}{\pi\epsilon} \left(a \ln \left(\frac{b}{a} + \sqrt{\frac{b^2}{a^2} + 1} \right) + b \ln \left(\frac{a}{b} + \sqrt{\frac{a^2}{b^2} + 1} \right) \right) \quad (6)$$

Here $2a$ and $2b$ are the sides of each rectangular subsection.

For the accurate evaluation of the elements of K_{nn} matrix, the plate is divided into four regions according to the location of the source and field points (Figure 1(b)). Using the standard integral formula the non-diagonal elements are evaluated as follows

$$K_{mn} = \frac{1}{4\pi\epsilon} \begin{cases} - \left[\frac{|x_m - x'| \ln \frac{(|y_m - y_n + b| + \sqrt{(x_m - x')^2 + (y_m - y_n + b)^2})}{(|y_m - y_n - b| + \sqrt{(x_m - x')^2 + (y_m - y_n - b)^2})}}{x_n - a} \right]^{x_n + a} \\ - \left[\frac{|y_m - y'| \ln \frac{(|x_m - x_n + a| + \sqrt{(y_m - y')^2 + (x_m - x_n + a)^2})}{(|x_m - x_n - a| + \sqrt{(y_m - y')^2 + (x_m - x_n - a)^2})}}{y_n - b} \right]^{y_n + b} \end{cases} \quad (7)$$

Here the source point is (x_n, y_n) and the field point is (x_m, y_m) . The x' and y' of equation (7) are replaced by their respective limits. Solution of the matrix equation (4) yields values for the surface charge density at the centres of the subdomains. The capacitance, C , of the conducting surface is obtained from the following equation

$$C = \frac{Q}{V} = \frac{1}{V} \sum_{n=1}^N \sigma_n A_n \quad (8)$$

Here N is the total number of rectangular subsections.

The same method for a single conductor is extended for evaluating the capacitance of multiconducting structures e.g. parallel plates and wedge-shaped plate (Figure 2 – 3). We consider two parallel rectangular conducting plates ($2L \times 2W$) each divided into equal number of subsections (Figure 2).

For multiconductors the matrix equation is modified as follows

$$[K_{mn}] [Q_n] = [V_n] \quad (9)$$

$$\text{Here } [K_{mn}] = \begin{bmatrix} [K_{mn}^{11}] & \dots & [K_{mn}^{1N}] \\ \dots & \dots & \dots \\ [K_{mn}^{N1}] & \dots & [K_{mn}^{NN}] \end{bmatrix}; [Q_n] = \begin{bmatrix} [Q_n^1] \\ \vdots \\ [Q_n^N] \end{bmatrix}; [V_n] = \begin{bmatrix} [V_n^1] \\ \vdots \\ [V_n^N] \end{bmatrix}$$

$$K_{mn} = \frac{1}{4\pi\epsilon} \int_{x_n-a}^{x_n+a} dx \int_{y_n-b}^{y_n+b} dy \quad (10)$$

Where

The diagonal sub matrices represent the effect of the plate itself and the non diagonal sub matrices represent the mutual interaction between the plates. The elements of the diagonal matrix remain same as the single element case.

For two plates, the elements of the non-diagonal matrix are evaluated as follows

$$\begin{aligned}
 K_{nn}^{12} &= K_{nn}^{21} \\
 &= \frac{I}{\pi \epsilon} \left(a \ln \frac{b + \sqrt{a^2 + b^2 + d^2}}{\sqrt{a^2 + d^2}} + b \ln \frac{a + \sqrt{a^2 + b^2 + d^2}}{\sqrt{b^2 + d^2}} \right) \\
 &\quad + \frac{2d}{\pi \epsilon} \left(\tan^{-1} \left(\frac{\sqrt{b^2 + d^2}}{d} \right) + b \left(\frac{1}{2} \tan^{-1} \frac{a}{\sqrt{b^2 + d^2}} \right) - \frac{1}{2} \tan^{-1} \frac{a}{d} \right)
 \end{aligned} \tag{11}$$

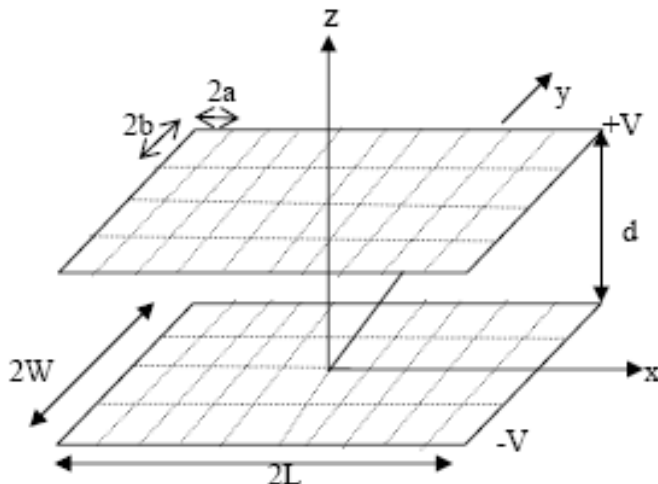


Figure 2. Parallel rectangular conducting plates divided into rectangular subsections.

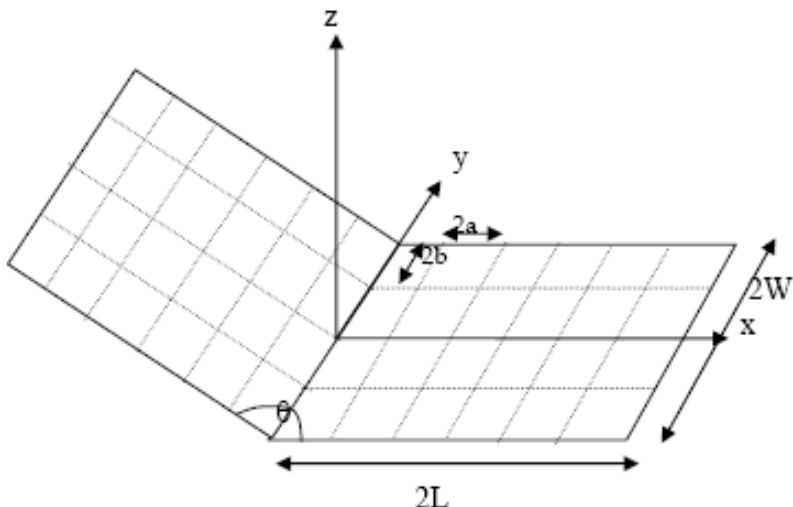


Figure 3. Inclined plate divided into rectangular subsections.

$$\begin{aligned}
K_{mn}^{12} &= K^2 I_{mn} \\
&= \frac{I}{4\pi\epsilon} \left[\begin{array}{l} |x_m - x_n + a| \ln \left(\frac{|y_m - y_n + b| + \sqrt{(x_m - x_n + a)^2 + (y_m - y_n + b)^2 + d^2}}{|y_m - y_n - b| + \sqrt{(x_m - x_n + a)^2 + (y_m - y_n - b)^2 + d^2}} \right) \\ - |x_m - x_n - a| \ln \left(\frac{|y_m - y_n + b| + \sqrt{(x_m - x_n - a)^2 + (y_m - y_n + b)^2 + d^2}}{|y_m - y_n - b| + \sqrt{(x_m - x_n - a)^2 + (y_m - y_n - b)^2 + d^2}} \right) \\ - |y_m - y_n + b| \ln \left(\frac{|x_m - x_n - a| + \sqrt{(x_m - x_n - a)^2 + (y_m - y_n + b)^2 + d^2}}{|x_m - x_n + a| + \sqrt{(x_m - x_n + a)^2 + (y_m - y_n + b)^2 + d^2}} \right) \\ + |y_m - y_n - b| \ln \left(\frac{|x_m - x_n + a| + \sqrt{(x_m - x_n + a)^2 + (y_m - y_n - b)^2 + d^2}}{|x_m - x_n - a| + \sqrt{(x_m - x_n - a)^2 + (y_m - y_n - b)^2 + d^2}} \right) \end{array} \right] \\
&\quad \left[\begin{array}{l} \tan^{-1} \left(\frac{\sqrt{(y_m - y_n + b)^2 + d^2} + |y_m - y_n + b|}{d} \tan \left(\frac{1}{2} \tan^{-1} \frac{|x_m - x_n + a|}{\sqrt{(y_m - y_n + b)^2 + d^2}} \right) \right) \\ - \tan^{-1} \left(\frac{\sqrt{(y_m - y_n - b)^2 + d^2} + |y_m - y_n - b|}{d} \tan \left(\frac{1}{2} \tan^{-1} \frac{|x_m - x_n + a|}{\sqrt{(y_m - y_n - b)^2 + d^2}} \right) \right) \\ - \tan^{-1} \left(\frac{\sqrt{(y_m - y_n + b)^2 + d^2} + |y_m - y_n + b|}{d} \tan \left(\frac{1}{2} \tan^{-1} \frac{|x_m - x_n - a|}{\sqrt{(y_m - y_n + b)^2 + d^2}} \right) \right) \\ + \tan^{-1} \left(\frac{\sqrt{(y_m - y_n - b)^2 + d^2} + |y_m - y_n - b|}{d} \tan \left(\frac{1}{2} \tan^{-1} \frac{|x_m - x_n - a|}{\sqrt{(y_m - y_n - b)^2 + d^2}} \right) \right) \end{array} \right] \quad (12)
\end{aligned}$$

For two inclined plates (Figure 3), the expression for the non diagonal element remains almost same as for parallel plates, the only difference is that the value of d does not remain constant – it varies with the positions of the subsections.

Evaluation of Charge Distribution from Electric Field Data

For the theory, we consider a perfectly conducting surface is charged to a potential V (Figure 4). The electric field at a point P due to the charged plate is evaluated using the following formula

$$E_p \vec{u}_p = \frac{Q_m}{4\pi\epsilon_0\epsilon_r} \cdot \frac{1}{r^2} \vec{u}_p \quad (13)$$

where

$$r^2 = \left\{ \left(x_p - x_m \right)^2 + \left(y_p - y_m \right)^2 + \left(z_p - z_m \right)^2 \right\}$$

Here Q_m is the total charge in m-th subsection of the plate with centre at (x_m, y_m, z_m)

and \vec{u}_p is the direction of \vec{E}_p which is along the outward radial from the charge Q_m . The components of \vec{E}_p along x, y and z coordinate axes can be achieved by multiplying \vec{E}_p with the direction cosines. The direction cosines are represented as follows

$$\cos \alpha = \frac{x_p - x_m}{r} \quad (14a)$$

$$\cos \beta = \frac{y_p - y_m}{r} \quad (14b)$$

$$\cos \gamma = \frac{z_p - z_m}{r} \quad (14c)$$

respectively.

The electric field components are presented in terms of the direction cosines as follows

$$\hat{E}_{xp} = E_p \cos \alpha \hat{u}_x \quad (15a)$$

$$\vec{E}_{yp} = E_p \cos \beta \vec{u}_y \quad (15b)$$

$$\vec{E}_{zp} = E_p \cos \gamma \vec{u}_z \quad (15c)$$

$$\vec{E}_{xp} = E_p \frac{\left(x_p - x_m \right)}{\sqrt{\left(x_p - x_m \right)^2 + \left(y_p - y_m \right)^2 + \left(z_p - z_m \right)^2}} \vec{u}_x \quad (16a)$$

$$\vec{E}_{yp} = E_p \frac{\left(y_p - y_m \right)}{\sqrt{\left(x_p - x_m \right)^2 + \left(y_p - y_m \right)^2 + \left(z_p - z_m \right)^2}} \vec{u}_y \quad (16b)$$

$$\vec{E}_{zp} = E_p \frac{\left(z_p - z_m \right) \vec{u}_z}{\sqrt{\left(x_p - x_m \right)^2 + \left(y_p - y_m \right)^2 + \left(z_p - z_m \right)^2}} \quad (16c)$$

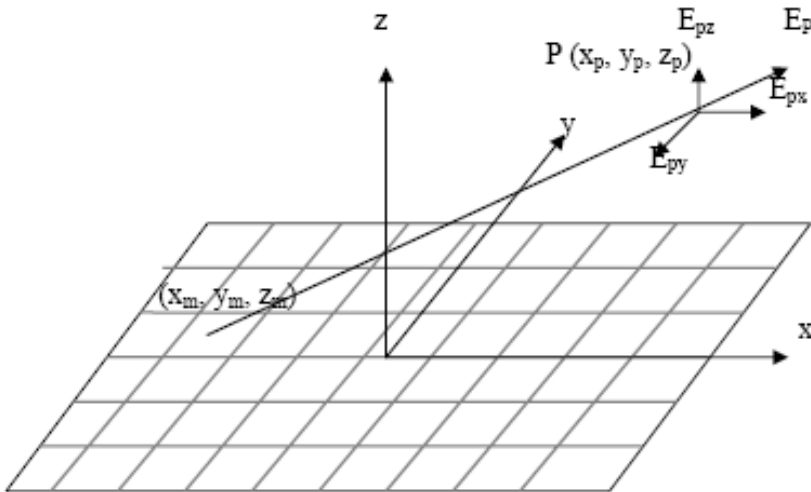


Figure 4. Electric field at a point P due to a rectangular conducting plate divided into rectangular subsection with excitation voltage = 1 V.

Any of the components may be along (-) ve direction of x, y or z but the resultant electric field \vec{E}_p must be always along the outward radial from the charge Q_m (in this case positive). Consequently the field components at a point due to the entire plate will be the sum of the contribution of the individual subsections of the conducting body. Equation (16) shows that the charge density on individual subsections on the conducting plate can be evaluated from the value of electric field at any point on a scan plane due to the charged conductor.

Combining equation (13 – 16), the electric field components at the point P are written as follows

$$\vec{E}_{xp} = \Delta s_m \alpha_m \cdot \frac{1}{4\pi\epsilon_0\epsilon_r} \cdot \frac{\left(x_p - x_m \right)}{\left\{ \left(x_p - x_m \right)^2 + \left(y_p - y_m \right)^2 + \left(z_p - z_m \right)^2 \right\}^{3/2}} \vec{u}_x = \alpha_m \cdot A_{pm} \vec{u}_x \quad (17a)$$

Here α_m is the charge density of that particular subsection, Δs_m is the area and A_m is a function of the co-ordinates of source point and field point.

$$A_{pm} = \Delta s_m \cdot \frac{1}{4\pi\epsilon_0\epsilon_r} \cdot \frac{\left(x_p - x_m \right)}{\left\{ \left(x_p - x_m \right)^2 + \left(y_p - y_m \right)^2 + \left(z_p - z_m \right)^2 \right\}^{3/2}} \quad (17b)$$

Similarly the other field components are written as follows

$$\vec{E}_{yp} = \alpha_m \cdot B_{pm} \vec{u}_y \quad (18a)$$

$$B_{pm} = \Delta s_m \cdot \frac{1}{4\pi\epsilon_0\epsilon_r} \cdot \frac{\left(y_p - y_m \right)}{\left\{ \left(x_p - x_m \right)^2 + \left(y_p - y_m \right)^2 + \left(z_p - z_m \right)^2 \right\}^{3/2}} \quad (18b)$$

$$\vec{E}_{zp} = \alpha_m \cdot C_{pm} \vec{u}_z \quad (19a)$$

$$C_{pm} = \Delta s_m \cdot \frac{1}{4\pi\epsilon_0\epsilon_r} \cdot \frac{\left(z_p - z_m \right)}{\left\{ \left(x_p - x_m \right)^2 + \left(y_p - y_m \right)^2 + \left(z_p - z_m \right)^2 \right\}^{3/2}} \quad (19b)$$

The electric field components at any particular point on the scan plane are the sum of the corresponding field components due to all charges concentrated at the centre of the grids. When both the conducting plate and the scanning plane (which is at a plane with nonzero z) are divided into equal number of subsections N ($N_s = N_f = N$), then the field equations are written as follows

$$\begin{aligned} E_{x1} &= A_{11}\alpha_1 + A_{12}\alpha_2 + A_{13}\alpha_3 + \dots + A_{1N}\alpha_N \\ E_{x2} &= A_{21}\alpha_1 + A_{22}\alpha_2 + A_{23}\alpha_3 + \dots + A_{2N}\alpha_N \\ &\vdots \\ E_{xN} &= A_{N1}\alpha_1 + A_{N2}\alpha_2 + A_{N3}\alpha_3 + \dots + A_{NN}\alpha_N \end{aligned} \quad (20)$$

The above equations are written in matrix form as follows

$$\begin{bmatrix} E_{x1} \\ \cdot \\ \cdot \\ \cdot \\ E_{xN} \end{bmatrix} = \begin{bmatrix} A_{11} & A_{12} & \dots & A_{1N} \\ \cdot & \cdot & & \cdot \\ \cdot & \cdot & \cdot & \cdot \\ \cdot & \cdot & \cdot & \cdot \\ A_{N1} & A_{N2} & \dots & A_{NN} \end{bmatrix} \begin{bmatrix} \alpha_1 \\ \alpha_2 \\ \cdot \\ \cdot \\ \alpha_N \end{bmatrix}$$

$$\begin{bmatrix} E_x \end{bmatrix} = [A] [\alpha] \quad (21)$$

Here $\begin{bmatrix} E_x \end{bmatrix}$ is a column matrix with N number of rows; $[A]$ is a $N \times N$ square matrix and $[\alpha]$ is a column matrix with N number of rows. Similarly we have

$$\begin{bmatrix} E_y \end{bmatrix} = [B] [\alpha] \quad (22)$$

$$\begin{bmatrix} E_z \end{bmatrix} = [C] [\alpha] \quad (23)$$

The charge distribution can be achieved from the above equations using simple matrix inversion formula as follows

$$[\alpha] = [A]^{-1} \begin{bmatrix} E_x \end{bmatrix} \quad (24)$$

$$[\alpha] = [B]^{-1} \begin{bmatrix} E_y \end{bmatrix} \quad (25)$$

$$[\alpha] = [C]^{-1} \begin{bmatrix} E_z \end{bmatrix} \quad (26)$$

It should be noted that the points on the scan plane where the electric fields are evaluated, should be suitably chosen so that the diagonal elements of the matrices $[A]$, $[B]$ and $[C]$ become non zero. For unequal number of source points and field points, the matrices $[A]$, $[B]$ and $[C]$ no longer become square matrices and hence equation (24 – 26) can not be used for this case. Equations (21 – 23) are reduced to a square system by premultiplying through the transpose matrices $[A]', [B]'$ and $[C]'$ respectively

$$[A]' [E_x] = [A]' [A][\alpha] \quad (27)$$

i.e.

$$[A]' [E_x] = [\mathbf{A}][\alpha] \quad (28)$$

Here $[A]' [A] = [\mathbf{A}]$ is a square matrix

Therefore

$$[\alpha] = [\mathbf{A}]^{-1} [A]' [E_x] \quad (29)$$

The equations for the other field components are achieved in a similar way.

Once the charge distribution matrix is evaluated, the capacitance is evaluated using the standard formulation (equation (8)).

Numerical Results and Discussions

The charge distribution and hence the capacitance of arbitrary shaped conducting bodies is evaluated using a computer program based on the preceding formulation. The capacitance of arbitrary shaped conducting bodies e.g. square, triangle, circular disc (Figure 5) are evaluated (Table 1 – 3).

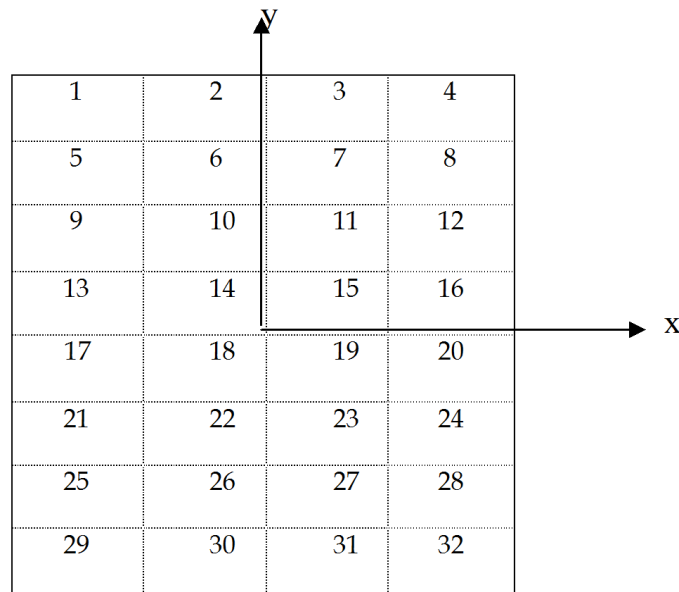


Figure 5. (a) Square conducting plate divided into rectangular subsections.

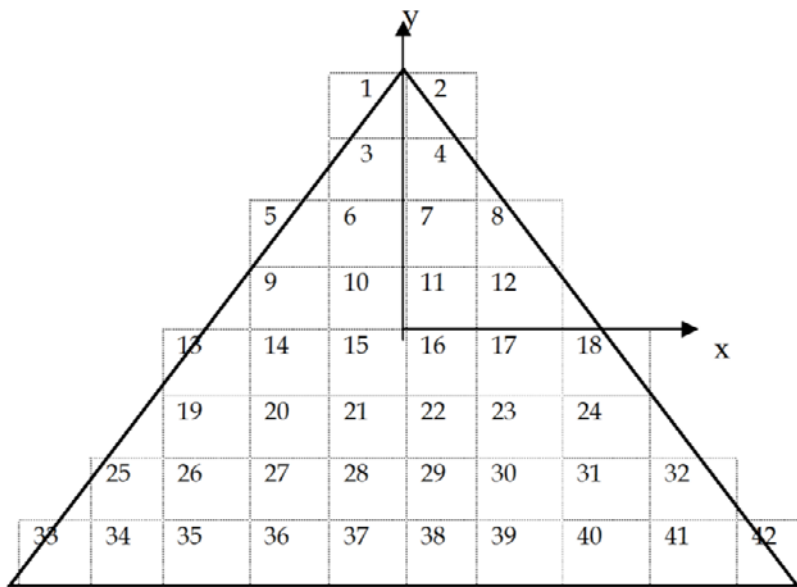


Figure 5. (b) Triangular conducting plate divided into rectangular subsections.

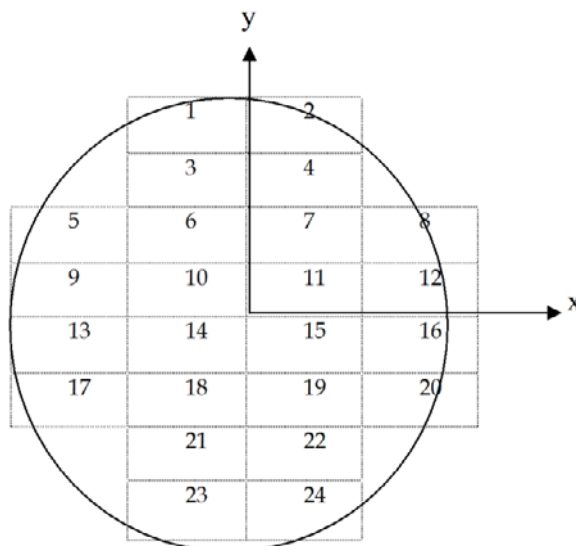


Figure 5. (c) Circular conducting plate divided into rectangular subsections.

The capacitance data for square and circular plate agree with the available data in literature [5, 8, 10]. Next the same method is extended for the evaluation of capacitance of wedge and also multiconducting bodies e.g. co-axial conductors with square and circular cross-section (Figure 6).

The results for capacitance is presented in Table 4 – 6. For co-axial conductors of finite length, there is appreciable fringing effect. The per unit length capacitance of the circular coaxial line is found by evaluating the capacitance of various lengths and then subtracting the contribution due to the fringing effect.

Table 1. Capacitance of square conducting plate with $2L=2W=1m$

No. of subsections	Capacitance in pF using rectangular subsection	Capacitance in pF using square subsection [5]
16	37.68	37.7
32	38.4	
36	38.8	38.7

Table 2. Capacitance of equilateral triangular conducting plate with sides= $1m$

No. of subsections	Capacitance in pF using rectangular subsection
8	22.7
15	23.2
42	27.1

Table 3. Capacitance of circular conducting disc with radius= $1m$

No. of subsections	Capacitance in pF using rectangular subsection	C/ ϵR
12	64.85	7.335
24	66.36	7.505
48	68.56	7.753

Table 4. Capacitance of two square ($1m \times 1m$) plates connected in the form of a wedge with angle of 90 degree

No. of subsections	Capacitance in pF using rectangular subsection	Capacitance in pF using approximate formula
8	51.65	48.58
16	52.33	49.14

Table 5. Capacitance of circular coaxial lines (radius= $1m$)

Ratio of outer to inner dimension	Capacitance / unit length in pF/meter	Analytical value $C=2\pi\epsilon/\ln(b/a)$ pF/meter
2.2	69.44	70.46
2.4	64.1	63.46
2.6	58.48	58.14
2.8	53.76	53.95
3.0	50.5	50.57
3.2	47.62	47.76
3.4	44.45	45.39
3.5	43.86	44.35

For circular coaxial conductor, each circular cylinder is replaced by a cylinder with octagonal structure of surface area equal to that of the circular cylinder. Each side of the octagonal cylinder is divided into rectangular subsections.

The results for the circular conductor are in well agreement with analytical values (Table 5).

The fringing field has appreciable contribution in the case of coaxial line of finite length. The per unit length capacitance for this type of coaxial lines are evaluated by subtracting the capacitance values of various lengths.

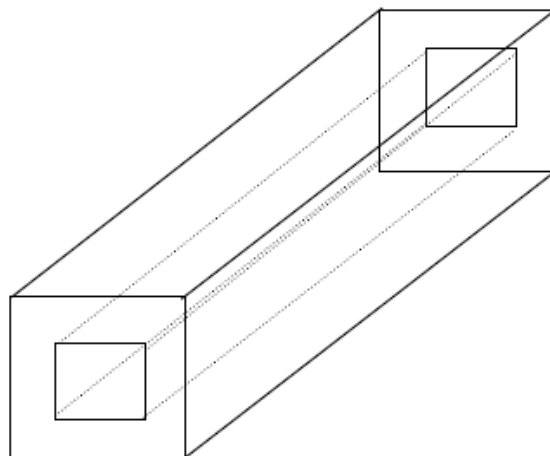


Figure 6. (a) Square coaxial line.

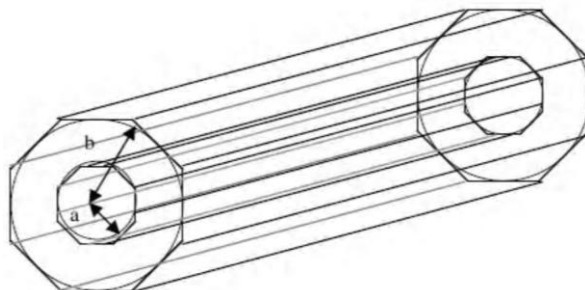


Figure 6. (b) Circular coaxial line approximated with octagonal cross-sectional coaxial structure.

Table 6. Capacitance of square coaxial lines (each sides=1m)

Ratio of outer to inner dimension	Capacitance / unit length in pF/meter
2.5	66.67
3.0	54.64
3.5	47.62

Capacitance from Electric Field Data

A computer program based on the preceding formulation is developed to determine the charge distribution and hence capacitance from the electric field data. The results are compared with other results available in literature. Table 7 shows the computational results achieved by dividing the conducting square plate ($1\text{m} \times 1\text{m}$) at $z = 0$ plane into sixteen equal subsections and also dividing the scanning plane of same size at $z = d = 1\text{m}$ into sixteen subsections. The results for capacitance obtained from x-component of electric field (E_x) data are in well agreement with the capacitance value achieved using exact formulation and also with the data given by Harrington [5]. Similar results are achieved for the capacitance evaluated from other field components.

Table 7. Capacitance of a unit square plate evaluated from electric field data

No. of subsections	Capacitance in pF	Capacitance in pF (from electric field data)
1	31.5	31.5
16	37.7	37.68

Conclusion

This chapter presents the evaluation of electrostatic capacitance of different planar and non planar conducting structures using Method of Moments with rectangular subsection modeling. The data for capacitance of different conducting structures agree well with their analytical value. To achieve better accuracy with lesser computing time, the conducting structures may be divided into larger rectangular subsections at the central part and smaller subsections at the edges.

Acknowledgment

The author would like to gratefully acknowledge the valuable comments of Prof. Ajay Chakrabarty, Professor, Department of Electronics and Electrical Communication Engineering, Indian Institute of Technology, Kharagpur, India on various technical aspects of this work.

References

- [1] J.C. Maxwell, A Treatise on Electricity and Magnetism, third ed., vol.1, Oxford University Press.
- [2] W.R. Smythe, Static and Dynamic Electricity, McGraw-Hill Book Co., 1968.
- [3] A.E. Ruehli, P.A. Brennan, Efficient capacitance calculations for three-dimensional multiconductor systems, *IEEE Trans. Microwave Theory Tech.* **21** (2) (1973) 76–82.

- [4] P.S. Maruvada, N. Hylte'n-Cavallius, Capacitance calculations for some basic high voltage electrode configurations, *IEEE Trans. Power Apparatus Syst. PAS-94* (5) (1975) 1708–1713.
- [5] R. F Harrington, Field Computation by Moment Method, Krieger Publishing Company, Florida, 1985.
- [6] S. M. Rao, Allen W. Glisson, D. R. Wilton, B. Vidula, “A Simple Numerical Solution Procedure for Static Problems involving arbitrary shaped surfaces”, *IEEE Transaction on Antennas and Propagation*, Vol.-AP-27, No. 5, pp. 604-608, September 1979.
- [7] Chaitali Chakrabarty, D. R. Poddar, A. Chakrabarty and B. N. Das, “Electrostatic Charge distribution and Capacitance of Isolated Cylinders and Truncated Cones in Free Space”, *IEEE Trans. on Electromagnetic Compatibility*, Volume 35, Issue 1, Feb. 1993 Page(s): 98 - 102.
- [8] V. K. Hariharan, S. V. K. Shastry, Ajay Chakrabarty and V. R. Katti, “Free Space Capacitance of Conducting Surfaces”, *Journal of Spacecraft Technology*, Vol. 8, No. 1, pp. 61-73, January 1998.
- [9] S. Ghosh, A. Chakrabarty, “Estimation of capacitance of different conducting bodies by the method of rectangular subareas”, *Journal of Electrostatics* **66** (2008) 142–146.
- [10] N. Nishiyama, M. Nakamura, Capacitance of disk capacitors by the boundary element method, in: Proceedings of the First European Conference on Numerical Methods in Engineering, 1992.

Chapter 7

ELECTROSTATICS OF PLANAR SYSTEM OF CONDUCTING STRIPS

Yuriy Tasinkevych

Polish Academy of Science, IPPT, Pawińskiego 5b,
Warsaw, 02-106 Poland

Abstract

The spatial distributions of electric field and charge are the most frequent subjects of classical electrostatic problems. Here, the spatial spectrum of the charge distribution on planar systems of strips is studied. Due to the charge singularities at the strip edges and strong dependence of the spectrum on the distribution details over the entire system, the direct application of the Fourier transformation to the charge spatial distribution yields results with unsatisfactory accuracy. Here a method of direct evaluation of the charge spatial spectrum is proposed and discussed; the spatial distribution is obtained from it by the inverse Fourier transformation for certain auxiliary purposes and final verification of numerical results. The solution is constructed as a linear combination of the template functions, evaluated in spectral domain, satisfying the electric boundary conditions on the strips, and having known spatial spectrum. The same functions are applied in the solution of the complementary problem of strips in external electric field. The flexibility of the method is illustrated in two examples. Namely, the quasi-periodic system of strips with periodicity broken by inclusion of one narrower strip is considered first. Also, the problem of acoustic beam forming analysis is treated by the presented method.

1. Introduction

Electrostatic analysis of planar systems of perfectly conducting strips may explain fundamental features of microwave [1] and micro-acoustic [2] devices. It also provides the approximated solution to diffraction problems in a long-wavelength limit [3]. In this case the induced electric charge distribution on strips varies according to the incident electric field. In classical electrostatics, the boundary value problem is formulated for electric field or its potential governed by the Laplace equation appended by the boundary conditions on the system of strips. The solution provides the electric field in the space around strips and the electric induction (the electric charge density) distribution on their surface [4]. Another

approach exploits the theory of complex functions [5]. Both these methods are not applicable for the diffraction problems mentioned above. Hence, yet another approach is necessary that is presented here—the spectral theory. Here we discuss in detail a different method for direct evaluation of the spatial spectrum of the charge distribution on planar system of strips; the spatial distribution is obtained from it by the inverse Fourier transformation. The former is often of great importance in applications (e.g., for modeling of the frequency response of SAW transducers, beam pattern of acoustic transducers, etc.). In the case of planar system of periodic strips having arbitrary potentials or charge distributions, the spectrum can be obtained using the so-called generalized BIS-expansion method [6], [7]. For finite system of strips of arbitrary width and spacing a set of the so-called spectral template functions, being independent solutions to the charge distributions on the plane of strips expressed in the spectral domain, is developed. The superposition of them is searched to satisfy the circuit equations: given potentials or charges [8]. The same template functions are used to find the solution of the complementary problem of strips in external electric field, assumed to be spatially variable (harmonic). This makes the problem analogous to the wave scattering one, and this justifies the application of wave-scattering terminology (“radiation conditions”, for instance) in the considered “electrostatic scattering” problem. In this case the strip total charge is evaluated as well as the Bloch harmonics of the “scattered” field in wide spectral domain. Also some aspects of the efficient numerical evaluation of the template functions for the case of finite system of strips of arbitrary width and spacing between them are given. Finally, some examples of application of the above methods are presented. First, a solution for planar system of strips originating from an infinite periodic system by inclusion of the narrower strip and spacing in the middle of the system is given. Such a system is called quasi-periodic. Also we present an example of application of the above spectral technique in the beam forming analysis of the acoustic transducers. Typical transducer array is an alternate set of acoustically different materials: piezoelectric, which responds to the incident waves by electric signal, and acoustically isolating material (like epoxy) between them [9, 10]. Piezoelectric materials are closer to hard, and epoxy is closer to soft acoustic materials. The idea of beam forming is simple: excite the wave-field by a system of point-like sources distributed on certain, usually flat surface with their strength chosen such that the wave radiated into the body evolves into the required wave beam-shape. In further approximation, the point-like sources are replaced by periodic vibrating strips of finite widths (a periodic baffle system). Such system was recently investigated in [11]. A similar system of periodic strips, or baffles, is considered here, and the interaction between them is accounted for in the full-wave analysis of the wave excitation by rigorous formulation of the corresponding boundary-value problem. The case of wave generation is considered in order to demonstrate the method flexibility. The scattering problem can be also addressed by this approach.

The chapter is organized as follows. The next section contains the preliminary matter introducing the spatial spectrum of the electric field on the plane of strips, and the planar harmonic Green's function that, establishing certain relation between the field components, replaces the Laplace equation in the considered boundary-value problem. In Sec. 3. the basic solution for a conducting half-plane is deduced and the concept of complex field function is introduced. In Sec. 4. a finite system of strips is considered. The template functions are developed and aspects of their efficient numerical evaluation are discussed briefly. Sec. 5.

deals with a periodic system of strips, and in Sec. 6. the problem of strips in external electric field is considered both for periodic (Sec. 6.1.) and finite (Sec. 6.2.) systems. Finally, in Sec. 7. the examples of the method application are demonstrated. Namely, Sec. 7.1. presents the solution to the problem of quasi-periodic system of strips and Sec. 7.2. illustrates the ability of the method to solve the problem of acoustic beam forming.

2. Basic Solutions for Planar Systems

Let a harmonic potential on the plane $y = 0$, assumed independent of z , be of the form $e^{-j k x}$, where k is an arbitrary spatial spectral variable. On the basis of the Laplace equation for the potential of electric field $\vec{E} = -\nabla \varphi$

$$\Delta \varphi = 0, \quad (1)$$

it is seen that the y -dependence of the solution for φ vanishing with growing distance from the plane $y = 0$ (in other words, satisfying the equivalent “radiation condition” for electromagnetic waves) is $e^{-|ky|}$. Assuming a vacuum space of dielectric constant ϵ_0 , the following equations for the field components, as a function of spectral variable, are obtained on the plane $y = 0+$ (just above the plane)

$$E_x(k) = jk\varphi(k), \quad E_y(k) = kS_k\varphi(k), \quad (2)$$

where $S_k = 1$ for $k \geq 0$ and -1 otherwise is adopted ($kS_k = |k|$; k is assumed to be real). Note that the surface charge on $y = 0$ plane is $2D_y$ because the induction at $y = -0$ is $-D_y$. It is convenient to introduce the planar harmonic Green’s function [7], [12]

$$G(k) = E(k)/D(k) = jS_k \quad (3)$$

defined for the field components on the plane $y = 0$: the tangential and normal field components $E = E_x$ and $D = E_y = D_y/\epsilon_0$ vanishing at $|y| \rightarrow \infty$ or, alternatively, satisfying the “radiation condition”. The other, complementary class of the field satisfying the opposite condition

$$E^I(k) = -G(k)D^I(k), \quad (4)$$

that is growing at infinity, will be considered later in the problem of strips embedded in external electric field (so-called “electrostatic scattering” problem; E^I , D^I denote the components of the external or “incident” field which source resides outside the planar structure, at infinity). The Green’s function $G(k)$ will replace the Laplace equation in all the analysis that follows for the fields on the plane $y = 0$.

3. Solution for a Half-Plane

The simplest surface structure we start our consideration with is a perfectly conducting half-plane occupying the domain e.g. $x < 0$. It is known [13] that the charged half-plane

$x < 0$ induces the following field on the plane $y = 0 +$:

$$\begin{aligned} E^{(0)}(x) &= \begin{cases} 1/\sqrt{x}, & x > 0 \\ 0, & x < 0 \end{cases}, & E^{(0)}(k) &= \frac{1}{2\sqrt{\pi|k|}} \begin{cases} e^{j\pi/4}, & k > 0 \\ e^{-j\pi/4}, & k < 0 \end{cases}, \\ D^{(0)}(x) &= \begin{cases} 0, & x > 0 \\ 1/\sqrt{-x}, & x < 0 \end{cases}, & D^{(0)}(k) &= \frac{1}{2\sqrt{\pi|k|}} \begin{cases} e^{-j\pi/4}, & k > 0 \\ e^{j\pi/4}, & k < 0 \end{cases} \end{aligned} \quad (5)$$

in the spatial, and spectral (at the right) representations. It is convenient to introduce the complex field defined by

$$\Phi = D - jE, \quad (6)$$

in both the spatial and spectral domains that yields for the half-plane

$$\Phi^{(0)}(x) = \frac{1}{\sqrt{-x}} = \begin{cases} -j/\sqrt{|x|}, & x > 0 \\ 1/\sqrt{|x|}, & x < 0 \end{cases}, \quad \Phi^{(0)}(k) = \begin{cases} e^{-j\pi/4}/\sqrt{\pi k}, & k > 0, \\ 0, & k < 0 \end{cases}. \quad (7)$$

The square-root value is chosen to be positive for $x \geq 0$, and $\sqrt{-1} = j$ otherwise. The above follows the well-known electrostatic theorem that real and imaginary parts of any harmonic function represent a solution of a certain electrostatic problem. The boundary conditions for the considered problem here are

$$E(x) = 0 \text{ on strips, } D(x) = 0 \text{ otherwise,} \quad (8)$$

appended by the condition that the field vanishes at $|y| \rightarrow \infty$ or the “radiation condition”.

This idea is exploited further below. Concerning the spectral representation, it is very important to note that it has a semi-finite support, the feature of great importance for further numerical analysis. Namely, it results from Eq.(3) that $\Phi(k) = D(k) - jE(k) = (1 + S_k)D(k)$ that is zero for $k < 0$, for fields vanishing at $|y| \rightarrow \infty$ (satisfying the “radiation condition”, Eq.(3)). The definition Eq.(6) has been chosen to obtain the convenient support $k \geq 0$. For given $\Phi(k)$, the representation of D and E in spectral domain can be inferred from the above results as

$$D(k) = \frac{1}{2} \begin{cases} \Phi(k), & k \geq 0 \\ \Phi^*(-k), & k < 0 \end{cases}, \quad E(k) = jS_k D(k) = \frac{j}{2} \begin{cases} \Phi(k), & k \geq 0 \\ -\Phi^*(-k), & k < 0 \end{cases}, \quad (9)$$

which can be easily checked by substitution to Eqs.(6) and (3). Moreover, functions $\{D(k-p), E(k-p)\}$ are constituents of another harmonic function $[D(x) - jE(x)]e^{-jpx}$ satisfying Eq.(1), but not necessarily Eq.(3) (this will be exploited later in Sec. 6.2.).

4. Finite System of Strips

First, we consider a strip of width $2a > 0$ on the plane $y = 0$ centered at $x = 0$. The spatial field distribution [13] is described by

$$\begin{aligned} \Phi^{(1)}(x; a) &= \Phi^{(0)}(x+a)\Phi^{(0)}(a-x) = \begin{cases} |a^2 - x^2|^{-1/2}, & |x| < a, \\ jS_x|a^2 - x^2|^{-1/2}, & |x| > a, \end{cases} \\ \Phi^{(1)}(k; a) &= [\Phi^{(0)}(k)e^{jka}] * [\Phi^{(0)}(k)e^{jka}]^* \end{aligned} \quad (10)$$

(the superscript * means the complex conjugation), respectively in the spatial and spectral domains, as resulting from the known convolution theorem for the Fourier transforms. Taking into account the semi-finite support of $\Phi(k)$, the convolution, Eq.(10), is explicitly (hint: change the variable into $y - k/2$)

$$\Phi^{(1)}(k; a) = \int_0^k \frac{e^{j(k-y)a} e^{-j\pi/4}}{\sqrt{\pi(k-y)}} \frac{e^{-jya}}{\sqrt{\pi y}} e^{j\pi/4} dy = J_0(ka), \quad (11)$$

where J_0 is the Bessel function. It immediately results from the above relation that higher harmonic components (over k) of the convolved functions do not contribute to the lower spectrum (at k and below) of the resulting function. This property is advantageous for the numerical analysis of Sec. 4.2., allowing one to truncate the convolved functions.

4.1. Template Functions

Now we attempt to develop the solution for a system of strips of arbitrary width and spacing between them. Following the same steps as above in the case of single strip, one easily obtains a similar expression for the system of two strips:

$$\Phi^{(2)}(k) = [\Phi^{(1)}(k; a_1)e^{jkb_1}] * [i\Phi^{(1)}(k; a_2)e^{jkb_2}], \quad (12)$$

where $a_{1,2}$ and $b_{1,2}$ are the corresponding widths and displacements of strips having the shifted spatial field representation, Eq.(10). The coefficient i is introduced in the second term to obtain $D(x) = \text{Re}\{\Phi(x)\}$ and $E(x) = \text{Im}\{\Phi(x)\}$, conveniently analogous to Eq.(7).

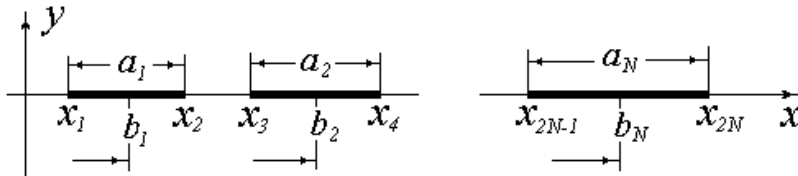


Figure 1. Finite system of strips.

For three or more strips ($N \geq 3$) (see Fig. 1), we have

$$\begin{aligned} \Phi^{(N)}(k) &= [\Phi^{(N-1)}(k)] * \left[j\Phi^{(1)}(k; a_N)e^{jkb_N} \right], \\ \Phi^{(N)}(x) &\sim [| (x - x_1)(x - x_2) \dots (x - x_{2N}) |]^{-1/2}, \end{aligned} \quad (13)$$

for spectral and spatial representations, respectively, where x_{2i-1}, x_{2i} are the i th strip's edges.

As it can be easily checked, the field discussed above vanishes fast with $|x| \rightarrow \infty$, indicating the multi-pole character of the charge distribution on the strips. Thus, it cannot form a basis of complete representation of the arbitrary field generated by the system of strips. The system can, for instance, possess a net charge different from zero, inducing the electric field vanishing at infinity like $1/x$. The harmonic function representing such cases and

exhibiting square-root singularity at the strip edges is the above derived function $\Phi(x)$ multiplied by a polynomial function of a degree not exceeding $N - 1$. Hence, N independent template solutions result, all satisfying the boundary and “radiation” conditions, Eq.(3),

$$\begin{aligned}\Phi^{(N,0)}(x) &= \Phi^{(N)}(x), \quad \Phi^{(N,1)}(x) = x\Phi^{(N)}(x), \dots, \\ \Phi^{(N,n)}(x) &= x^n\Phi^{(N)}(x), \dots,\end{aligned}\quad (14)$$

which yield the corresponding field components $E^{(n)}(x)$ and $D^{(n)}(x)$ on the plane $y = 0$. Applying the known Fourier transform theorem stating that multiplication by x in spatial domain corresponds to differentiation in spectral domain, one formally obtains the above functions in the spectral domain

$$\begin{aligned}\Phi^{(N,0)}(k) &= \Phi^{(N)}(k), \quad \Phi^{(N,1)}(k) = -j\frac{d}{dk}\Phi^{(N)}(k), \dots, \\ \Phi^{(N,n)}(k) &= (-j)^n\frac{d^n}{dk^n}\Phi^{(N)}(k), \quad n < N,\end{aligned}\quad (15)$$

yielding the spectral field representations $E^{(n)}(k)$ and $D^{(n)}(k)$, according to Eq.(9) (in Sec. 4.2., these functions will be redefined for numerical advantage). The superposition of these N independent functions suffices for representation of an arbitrary field that can be generated by the system of N strips subjected to N circuit constraints: given strip voltages or charges, or interconnections. A convenient method for evaluation of the above spectral template functions for practical use is presented in the Sec. 4.2.. Their spatial counterparts can be computed by means of FFT, if necessary.

In practical systems, both the source terminals are connected to other strips in the system, rendering the system electric neutrality (the currents flowing into and out of the system are in perfect balance as flowing through the same source). This means that the distant field excited by the charge distribution on strips behaves like the field generated by an electric dipole, at most, vanishing faster than $1/x$. Hence, the field spectral representation must vanish at $k = 0$. It is evident that the function $\Phi^{(N,N-1)}(x)$, having the Fourier transform $\Phi^{(N,N-1)}(k = 0) \neq 0$, must be excluded from the set of functions representing the charge distributions on strips because this and only this function represents a field vanishing like $1/x$ at infinity. The above is evident from Eq.(13):

$$\begin{aligned}D^{(N-1)}(k) &= \frac{1}{2} \begin{cases} \Phi^{(N,N-1)}(k), & k \geq 0, \\ \Phi^{(N,N-1)*}(-k), & k < 0, \end{cases} \\ D^{(N-1)}(x) &= \mathcal{F}^{-1}\{D^{(N-1)}(k)\} \sim 1/|x| \text{ at } |x| \rightarrow \infty\end{aligned}\quad (16)$$

(\mathcal{F}^{-1} means the inverse Fourier transform). The other functions represent field vanishing like x^{-k} , $k = 2, \dots, N$, and their spectral representations behave like k^n , $n = 1, \dots, N - 1$ at $k \rightarrow 0$, according to the limit theorem for the Fourier transforms.

The above shows that at our disposal is a set of $N - 1$ template functions the superposition of which, with certain coefficients, must satisfy the circuit equations. Let each strip be connected to either of the source terminals. It is clear that the conditions can be set only on the strip potential differences or voltages between strips, not on the potentials of strips itself. This shows that there are $N - 1$ circuit equations in this case, and we have a complete system of equations for evaluation of all superposition coefficients mentioned

earlier. To formulate the equations however, we need to evaluate voltages V_i and charges Q_i for fields represented by each template function. Details concerning the formulation and solution of the circuit equations are presented in Sec. 4.3.. It is worth to note here that in applications, we need to know the spatial spectrum of electric charge on strips in finite domain only $(0, k_u)$, where k_u , for example in the case of surface acoustic wave devices is $k_u = \omega_u/v_{SAW}$ and ω_u is the upper edge of the interesting frequency band of the considered surface acoustic wave transducer. The value of k_u however, must be considerably enlarged for the purpose of evaluation of the strips' charges and potentials by means of the inverse Fourier transformation (FFT). This evaluation provides a good verification tool of the entire result of quite extensive computations involved. But formally, evaluation of $\Phi(k)$ can be constrained to rather small domain $(0, k_u)$, provided that the strips' charges and potentials are evaluated by integration of the square-root singular spatial representations of surface electric fields, $D(x)$ and $E(x)$.

Below we consider the field components $D^{(0)}$ and $E^{(0)}$ evaluated from Eq.(9) using $\Phi^{(N,0)}$ in place of Φ : $D^{(0)}(k) = \Phi^{(N,0)}(k)/2, k \geq 0$ or $\Phi^{(N,0)*}(-k)/2, k < 0$, yielding results marked by the upper index (0); the analysis for the other functions, involving multiplication by x^n in Eq.(14) and indexed by (n), is similar. According to the definition of the electric potential $E = -d\varphi/dx$, the strip potentials can be obtained by integration of $E^{(0)}(x)$, what in spectral domain corresponds to the division by k of the $E^{(0)}(k)$ (with accuracy to an unimportant constant due to the potential difference being only involved in the circuit equations). As concerns the strip charge $Q^{(0)}(x)$ being the integral of $\Delta D_y = D_y(y+0) - D_y(y-0) = 2\epsilon_0 D^{(0)}$ (since $D_2(y-0) = -D_2(y+0) = -\epsilon_0 D$), using the Green's function (3), one obtains:

$$\begin{aligned}\varphi^{(0)}(x) &= \mathcal{F}^{-1}\{-jE(k)/k\} = \frac{1}{2\pi} \int_{-\infty}^{\infty} |k|^{-1} D^{(0)}(k) e^{-jkx} dk, \\ Q^{(0)}(x) &= \mathcal{F}^{-1}\{2j\epsilon_0 D(k)/k\} = \frac{j\epsilon_0}{\pi} \int_{-\infty}^{\infty} k^{-1} D^{(0)}(k) e^{-jkx} dk.\end{aligned}\quad (17)$$

Naturally, $\varphi(x)$ is constant on the strips because $E(x) = 0$ there, and $Q(x)$ is constant between the strips because $D(x) = 0$ there. Thus we apply for the voltage V_i between the i th and $(i+1)$ th strips and the charge Q_i of the i th strip

$$V_i^{(0)} = \varphi^{(0)}(\xi_{i+1}) - \varphi^{(0)}(\xi_i), \quad Q_i^{(0)} = [Q^{(0)}(\zeta_i) - Q^{(0)}(\zeta_{i-1})], \quad i = 1, \dots, N, \quad (18)$$

where ξ_m is a point within the m th strip domain (best - at its center), and ζ_m can be at the center of spacing between two neighboring strips, the $(m+1)$ th and m th; they can be easily evaluated from the strip edges x_m , except ζ_0 and ζ_N the value of which can be applied at certain distances in front of the first strip and after the last one; both values are equal because $Q^{(N)}(x \rightarrow \pm\infty)$ are equal. Note that all the above evaluations involve only the spectral representation of $D^{(0)}(k)$. The other advantage of this approach is that we may not bother with the square-root sign of Eq.(13) to evaluate the correct values of V_i, Q_i .

4.2. Numerical Evaluation of Template Functions

As seen from the above discussion, the template functions $\Phi^{(N,i)}(k)$, $i = 1\dots N-1$ are crucial for evaluation of the charge spatial spectrum $D(k)$, requiring numerical eval-

ation of $N - 1$ derivatives in Eq.(15). They can however, be redefined to avoid numerical differentiation [14]. The new definitions considered hereinafter are:

$$\begin{aligned}\Phi^{(N,0)}(x) &= j^{N-1} \prod_{i=1}^N \Phi^{(1)}(x - b_i, a_i) = \Phi^{(N)}(x) \\ \Phi^{(N,1)}(x) &= (x - b_1)\Phi^{(N)}(x) \\ \Phi^{(N,2)}(x) &= (x - b_1)(x - b_2)\Phi^{(N)}(x) \\ &\dots \\ \Phi^{(N,N-1)}(x) &= \Phi^{(N)}(x) \prod_{i=1}^{N-1} (x - b_i)\end{aligned}\quad (19)$$

where $b_i = (x_{2i} + x_{2i-1})/2$ is the i th strips center position and $a_i = (x_{2i} - x_{2i-1})/2$ is the i th strips half-width; x_{2i-1}, x_{2i} are the i th strip edges position (see Fig. 1). The new functions are apparently combinations of the old ones, Eq.(14). Here to form the function $\Phi^{(N,i)}(x)$ we multiply the basic template solution $\Phi^{(N)}(x)$ by the polynomial $\prod_{k=1}^i (x - b_k)$ instead of x^i as it was done earlier. The modified template functions take real values on the strips (representing the charge distribution there), and imaginary values between them (representing electric field there). They can be rewritten in the form of a product of similar terms

$$\Phi^{(N,i)}(x) = -j \prod_{m=1}^i \frac{j(x - b_m)}{\sqrt{a_m^2 - (x - b_m)^2}} \prod_{m=i+1}^N \frac{j}{\sqrt{a_m^2 - (x - b_m)^2}}, \quad i = 0, \dots, N-1, \quad (20)$$

The first product in Eq.(20) disappears for $i = 0$. The spectral representation of $\Phi^{(N,i)}$ is

$$\Phi^{(N,i)}(k) = \Phi'_1(k) * \dots * \Phi'_i(k) * \Phi_{i+1} * \dots * \Phi_N(k), \quad (21)$$

where (see Appendix A)

$$\begin{aligned}\Phi_m(k) &= \mathcal{F} \left\{ \frac{1}{\sqrt{a_m^2 - (x - b_m)^2}} \right\} = \begin{cases} J_0(ka_m) e^{jkb_m}, & k \geq 0, \\ 0, & k < 0, \end{cases} \\ \Phi'_m(k) &= \mathcal{F} \left\{ \frac{x - b_m}{\sqrt{a_m^2 - (x - b_m)^2}} \right\} = \begin{cases} -j[\delta(k) - a_m J_1(ka_m)] e^{jkb_m}, & k \geq 0, \\ 0, & k < 0. \end{cases}\end{aligned}\quad (22)$$

It is due to the Dirac δ -function in $\Phi'_m(k)$ that the evaluation order in Eq.(21) is important: the convolutions of functions $\Phi_m(k)$ should be evaluated first (counting from the right to the left) to obtain an integrable product of regular and δ functions. The algorithm would run as follows: $\Phi_{N-1} * \Phi_N \Rightarrow \Phi, \dots, \Phi_{i+1} * \Phi \Rightarrow \Phi, \Phi'_i * \Phi \Rightarrow \Phi, \dots, \Phi'_1 * \Phi \Rightarrow \Phi^{(N,i)}(k)$. In fact, the definition of $\Phi^{(N,i)}$ can be made in various ways, with a_m, b_m chosen in arbitrary order, not necessarily for subsequent strips. This is equivalent to choosing $\Phi'_m + c_m \Phi_m$ instead of Φ'_m in Eq.(21), with arbitrary c_m , resulting in arbitrary polynomials $P_n(x)$ of degree n in Eq.(19) defining $\Phi^{(N,n)}(x)$. This possibility will be exploited later in order to improve the numerical accuracy of the analysis. It is worth to note here that in the original definition, Eq.(14), $P_n = x^n$.

The modified template functions $\Phi^{(N,i)}(k)$, $i = 0, \dots, N - 1$ require only numerical evaluation of multiple convolutions. Nevertheless, it is still a rather difficult numerical task, especially for the case of large N . Here, the convolutions are evaluated using the convolution theorem:

$$\begin{aligned} \int_{-\infty}^{\infty} f_1(k - k') f_2(k') dk' &= \mathcal{F}\{f_1(x) f_2(x)\}, \quad f_i(x) = \mathcal{F}^{-1}\{f_i(k)\}, \\ f(x) &\approx \kappa \sum_{i=0}^{M-1} f_i e^{-jxk_i}, \quad \kappa = k_M/M, \quad k_i = i\kappa; \quad f_i = f(k_i), \quad i = 0, \dots, M-1, \end{aligned} \quad (23)$$

where the FFT algorithm is used for numerical Fourier transformations. Its input data is the set of samples of the transformed function evaluated at $k_i = i\kappa$, $i = 0 \dots M - 1$, where M is typically a power of 2. Thus, the function $f(k)$ is truncated at some $k_M = \kappa M$ (chosen large enough if we want to verify the analysis with the figures of the spatial field distributions like the ones presented later on). Neglecting this purpose, the function $f(k)$ could be truncated at lower k_u mentioned in Sec. 4.1..

The FFT algorithm is used mainly to take advantage of its speed, but due to the exploited trapezoidal rule of integration, the resulting accuracy of computations is not satisfactory for the case of larger number of strips, above 20 [15]. Better interpolation of the integrated function is necessary to overcome this difficulty. Typically, changing the integration rule would require integration section by section [14], but it is shown below that the FFT can still be applied, provided that its output data are appropriately modified. This subject is discussed below, after [16].

The transformed function can be approximated between its samples by means of higher order interpolation as follows

$$f(k) = \sum_{i=m}^{(M-1)-m} f_i \psi\left(\frac{k - k_i}{\kappa}\right) + \sum_{i=0}^m \left[f_i \bar{\psi}_i\left(\frac{k - k_i}{\kappa}\right) + f_{M-1-i} \bar{\psi}_{M-1-i}\left(\frac{k - k_i}{\kappa}\right) \right], \quad (24)$$

where $\psi(0) = 1$ and $\psi(m) = 0$, $m \pm 1, \pm 2, \dots$; since the interpolation must yield the value of the sampled function at k_i . The so-called kernel function ψ is assumed taking non-zero value only for k in domain between the first and the last samples used for its evaluation. For the case of cubic interpolation, $m = 3$, there are four samples f_i the kernel function ψ depends on. The explicit formula for ψ is presented in Appendix B after [16], which can be applied in the interior domains of k where $s \in (-2, 2)$.

A different, non-centered interpolation formula must be applied for intervals close to the integral limits, 0 and k_M , resulting in the kernel functions $\bar{\psi}_i(s)$, $\bar{\psi}_{M-1-i}(s)$, respectively (Appendix B). Finally, the approximation of the function $f(k)$, Eq.(24) is:

$$f(k) = \sum_{i=0}^{M-1} f_i \psi(s) + \sum_{i=0}^m \{f_i \bar{\psi}'_i(s) + f_{M-1-i} \bar{\psi}'_{M-1-i}(s)\}, \quad s = \frac{k - k_i}{\kappa}, \quad (25)$$

where the first sum includes only the kernel $\psi(s)$, and the last one depends on $\bar{\psi}'(s)$ being the difference between the boundary kernels $\bar{\psi}(s)$ and the interior kernel $\psi(s)$, presented again in the Appendix B. This is a formula analogous to Eq.(23) with the exception of the

kernel functions ψ and $\bar{\psi}'$ which are convolved with f_i (note that $s \sim k - k_i$). This allows one to write:

$$\begin{aligned} f(x) &\approx \kappa[W(\Theta) \sum_{i=0}^{M-1} f_i e^{-ji\Theta} + \sum_{i=0}^{M_1} \{f_i \alpha_i(\Theta) + f_{M-1-i} \alpha_{M-1-i}^*(\Theta)\}], \quad \Theta = x\kappa, \\ W(\Theta) &= \int_W e^{-js\Theta} \psi(s) ds, \quad \alpha_i(\Theta) = \int_{\bar{\psi}'_i} e^{-js\Theta} \bar{\psi}'_i(s-i) ds, \\ \text{and } \alpha_{M-1-i}(\Theta) &= e^{-j(M-1)\Theta} \alpha_i^*(\Theta) \text{ since } \bar{\psi}'_{M-1-i}(s) = \bar{\psi}'_i(-s), \end{aligned} \quad (26)$$

where the integration limits result directly from the support of the integrated functions presented in Appendix B. Applying the FFT algorithm to evaluate the first sum in Eq.(26) by analogy to Eq.(23), we finally obtain the algorithm of Fourier transform evaluation exploiting the cubic interpolation:

$$[f(x_n)] = \kappa\{W(\Theta)[FFT(f_0 \dots f_{M-1}, \underbrace{0, \dots, 0}_M)] + \sum_{i=0}^3 (\alpha_i(\Theta) f_i + \alpha_i^*(\Theta) f_{M-1-i})\} \quad (27)$$

(note the so-called zero-padding the data set with an M -long array of zeros to avoid the so-called circular convolution that may spoil the most important lower spectrum of f ; this doubles at least the FFT data set). Here $[f(x_n)]$ is the data vector of the sampled $f(x)$ at $x = n\pi/M$, $n = 0, \dots, 2M-1$. The independence of $W(\Theta)$ and $\alpha_i(\Theta)$ (presented explicitly in Appendix B) of the transformed functions (f_i) means that they can be evaluated only once. Examples of the template functions evaluated by means of the cubic interpolation method are shown in Fig. 2, and compared with the ones computed by standard FFT (dashed curve).

4.3. Spatial Spectrum of Complex Electric Field

The linear combination of template functions

$$\begin{aligned} \Phi(x) &= \sum_{j=0}^{N-2} \alpha_j \Phi^{(N,j)}(x), \quad D(x) = \sum_{j=0}^{N-2} \alpha_j \operatorname{Re}\{\Phi^{(N,j)}(x)\}, \\ E(x) &= - \sum_{j=0}^{N-2} \alpha_j \operatorname{Im}\{\Phi^{(N,j)}(x)\}, \end{aligned} \quad (28)$$

according to Eq.(6) represents the spatial field distribution. The unknown coefficients α_j are to be found from the equations resulting from the circuit theory. To formulate these equations, one needs to know the potential differences or voltages between the neighboring strips $V_i = \varphi_{i+1} - \varphi_i$, $i = 1, \dots, N-1$. Apparently, the coefficients can be determined from the known strip charges Q_i (see Eq.18). In the most frequent case of given voltages V_i the circuit theory yields the system of linear equations for unknown coefficients α_j which in matrix form can be written as follows 5circuit theory yields the matrix equation:

$$\begin{aligned} \mathbf{A}\boldsymbol{\alpha} &= \mathbf{V}, \quad \mathbf{V} = [V_i], \quad \mathbf{A} = [A_{ij}], \quad i, j = 1, \dots, N-1. \\ A_{ij} &= \int_{b_i+a_i}^{b_{i+1}-a_{i+1}} \operatorname{Im}\{\Phi^{(N,j-1)}(x)\} dx, \quad V_i = - \int_{b_i+a_i}^{b_{i+1}-a_{i+1}} E(x) dx. \end{aligned} \quad (29)$$

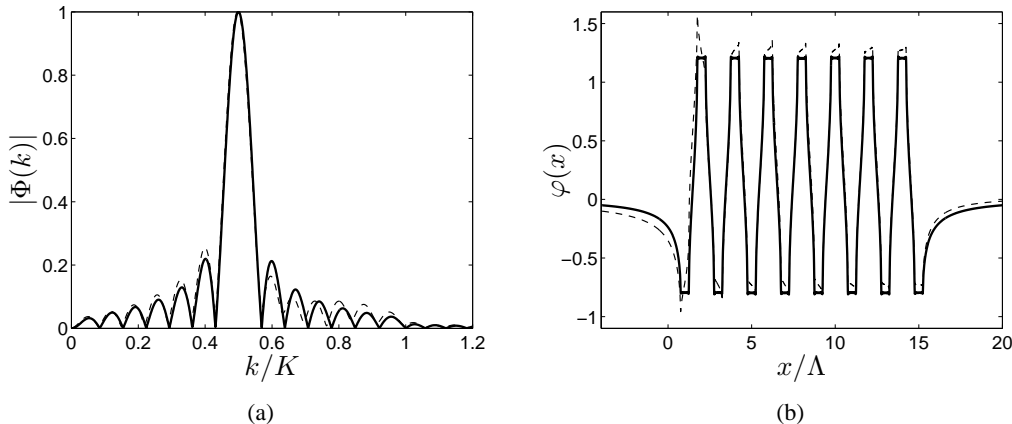


Figure 2. (a) Comparison of the results obtained with the template functions $\tilde{\Phi}^{(N,i)}(k)$ evaluated by means of the standard FFT (dash lines) and using cubic interpolation (solid line), for 15 equidistant strips of equal width and $M = 2^{14}$ samples in the domain $(0, 35K)$, $K = 2\pi/\Lambda$, Λ - strips pitch. (b) Their inverse Fourier transforms show the characteristic distortion of the potential distribution resulting from the inaccuracy of the standard FFT is removed when using the cubic interpolation.

The above integrands are square-root singular at both integration limits. This poses certain difficulty in evaluation of the matrix elements A_{ij} with sufficient accuracy in order to solve the system of equations. The difficulty can be overcome using the Gaussian quadrature formula [17] or other appropriate methods [2]; the iterative integration scheme based on the so-called extended midpoint rule has been found to be promising [15].

Another favorable method of evaluation of the integrals, Eq.(29), exploits the correspondence of integration in spatial domain, and division by spectral variable k in spectral domain. This applied to $E(k)$ and $D(k)$ yields the formula analogous to Eq.(17) for the corresponding functions $\varphi^{(N,j)}(x)$ and $Q^{(N,j)}(x)$ evaluated from $\Phi^{(N,j)}(k)$ according to Eq.(9). This yields the matrix components, explicitly:

$$A_{ij} = \varphi^{(N,j-1)}(b_{i+1}) - \varphi^{(N,j-1)}(b_i), \quad (30)$$

without an extra numerical integration in spatial domain, but taking advantage of an earlier effort of evaluation of the spatial spectrum with high accuracy, and subsequent application of the FFT in order to evaluate $\varphi^{(N,j)}(x)$ in discrete representation. The value of $\varphi^{(N,j)}(b_i)$ is taken from the corresponding nearest point of the FFT output series. After solving the system of equations, Eq.(29), the spatial spectrum $D(k)$ is evaluated from Eq.(9)

$$\Phi(k) = \sum_{j=0}^{N-2} \alpha_j \Phi^{(N,j)}(k). \quad (31)$$

It must be remarked here that the template functions, Eqs.(19)–(22), span large range of values for larger number of strips N . In the case of 30 equidistant strips of equal width, for example, the components in the sum in Eq.(31) differ by 12 orders of magnitude. Thus,

its numerical evaluation may become severely inaccurate even though the double precision arithmetic is used. The nature of this problem originates from the functional form of $\Phi^{(N,j)}(x)$, Eq.(19). To overcome this difficulty, we can take advantage of a certain degree of freedom, mentioned earlier, allowing us to choose arbitrary polynomials in numerators of these functions within the same order j . It is evident that polynomials having zeros distributed uniformly over the domain occupied by the strip system would temper the growth of $\Phi^{(N,j)}(x)$ over subsequent strips or spacing where φ and Q are evaluated, thus they would temper the values of the matrix coefficients A_{ij} . For example, roots can be placed on the selected strip centers [15]. The polynomials of higher template functions (larger index j) would have roots placed on almost all strips, whereas for lower j only on some of them chosen to obtain quasi-uniform root distribution. The order of magnitude of $\Phi^{(N,j)}(x)$ with larger j is however, generally lower and the roots distribution is less significant. The method is effective enough to reduce the above mentioned span of orders of magnitude from the value of 12 to lower and acceptable value of 7 (in the case of 30 equidistant strips of equal width). The corresponding examples are shown in Fig. 3.

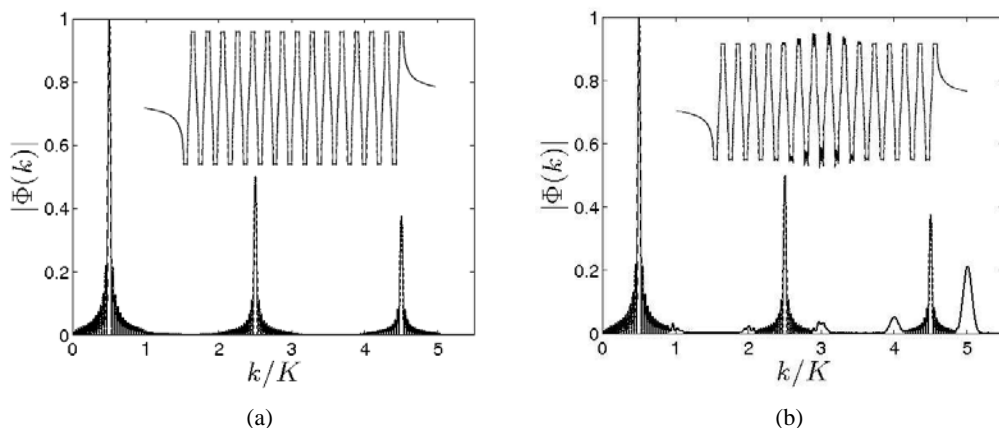


Figure 3. (a) The erroneous charge spectrum of 30 equidistant strips of equal width caused by loss of numerical precision in evaluation of the sum in Eq.(31) which components span several orders of magnitude. (b) The modification of the numerator polynomials corrects the problem. The insets represent the corresponding potential spatial distributions. This confirms the value of verification of numerical results by the inverse Fourier transformation of the evaluated spectrum, lacking one when the spatial distribution is computed first, and then transformed to obtain the spectrum (note that the problem with magnitude span concerns both methods because the evaluation of strip potentials is necessary in both). $K = 2\pi/\Lambda$, Λ - strips pitch.

5. Periodic System of Strips

Let us now consider the case of infinite Λ -periodic system of strips of width $2a$. The spatial complex field function $\Phi(x)$ results from the known identity [18]

$$\Gamma(1/2 - \mu) \sum_{n=0}^{\infty} P_n^{\mu}(\cos \theta) \cos(n + 1/2)v = \begin{cases} \frac{\sqrt{\pi/2} \sin^{\mu} \theta}{(\cos \theta - \cos v)^{\mu+1/2}}, & 0 \leq v < \theta, \\ 0, & \theta < v < \pi, \end{cases} \quad (32)$$

$0 < \theta < \pi$, $\operatorname{Re}\{\mu\} < 1/2$. The Legendre function $P_n^{\mu} = P_n$ for $\mu = 0$ has the properties (for v arbitrary real and n integer)

$$P_{-\nu-1} = P_{\nu}, \quad P_n(-x) = (-1)^n S_n P_n(x), \quad S_n = \begin{cases} 1, & n \geq 0, \\ -1, & n < 0, \end{cases} \quad (33)$$

which allow to transform the above identity into the following one [19]

$$\sum_{n=-\infty}^{\infty} P_n(\Delta) e^{-jnKx} = \begin{cases} \frac{\sqrt{2} e^{jKx/2}}{\sqrt{\cos Kx - \Delta}}, & |x| < a, \\ 0, & a < |x| < \Lambda/2. \end{cases} \quad (34)$$

Substituting $\Delta \rightarrow \Delta - \pi$ and $\theta \rightarrow \theta - \pi$ into Eq.(34) we readily obtain another equation

$$\sum_{n=-\infty}^{\infty} S_n P_n(\Delta) e^{-jnKx} = \begin{cases} 0, & |x| < a, \\ \frac{-j S_x \sqrt{2} e^{jKx/2}}{\sqrt{\Delta - \cos Kx}}, & a < |x| < \Lambda/2. \end{cases} \quad (35)$$

In Eqs.(34), (35) the variables Kx instead of θ and $\Delta = \cos Ka$ where introduced for consistency with our definition of the strips geometry. Here K is a spectral wavenumber of the periodic system, $K = 2\pi/\Lambda$. Multiplying the above equations by $e^{-jr x}$, $r \in (0, K)$ we obtain the spectral functions defined on the entire k -axis, $k = r + nK$, by

$$D(k) = P_{[k/K]}(\Delta), \quad E(k) = jS_k D(k), \text{ and } \Phi(k) = D(k) - jE(k) = 2P_{[k/K]}(\Delta) \quad (36)$$

(note, $S_n = S_{nK+r}$ for $r \in (0, K)$) $[k/K]$ is an integer floor of k/K . In Eq.(36) $\Phi(k)$ is the spectral representation of the complex field function for periodic system of strips satisfying the boundary conditions in corresponding domains of x . The corresponding spatial representations are as follows

$$\begin{aligned} D(x) &= \sum_{n=-\infty}^{\infty} P_n(\Delta) e^{-j(r+nK)x} = \frac{\sqrt{2} e^{-j(r-K/2)x}}{\sqrt{\cos Kx - \Delta}} \quad (\text{on strips}), \\ E(x) &= \sum_{n=-\infty}^{\infty} jS_n P_n(\Delta) e^{-j(r+nK)x} = S_x \frac{\sqrt{2} e^{-j(r-K/2)x}}{\sqrt{\Delta - \cos Kx}} \quad (\text{between strips}). \end{aligned} \quad (37)$$

Thus, the complex field function in the spatial domain is

$$\Phi(x) = 2 \sum_{n=0}^{\infty} P_n(\Delta) e^{-j(r+nK)x}. \quad (38)$$

Using the spatial representations of the electric field, Eq.(37), the strip charges and potentials can be easily evaluated. Let us consider a strip centered at the point $i\Lambda$. Integration of the first equation of Eq.(37) with respect to x over the interval $(i\Lambda - a, i\Lambda + a)$ yields

$$Q_i(r) = Q_r e^{-jri\Lambda}, \quad Q_r = 2\epsilon_0 \int_{-a}^a D(x) dx = 2\epsilon_0 \int_{-\Lambda/2}^{\Lambda/2} \sum_{n=-\infty}^{\infty} P_n(\Delta) e^{-j(r+nK)x} dx. \quad (39)$$

Changing the order of summation and integration an integrating term by term we obtain

$$Q_r = 4\epsilon_0 \sin(\pi r/K) \sum_{n=-\infty}^{\infty} \frac{(-1)^n P_n(\Delta)}{r + nK}. \quad (40)$$

Note, that integration in Eq.(39) has been performed over a period since $D(x) = 0$ outside the domain occupied by the strip. Similarly, the value of the integral in the second equation of Eq.(37) at the point $x = i\Lambda$ yields the potential of the strip:

$$\varphi_i(r) = \varphi_r e^{-jri\Lambda}, \quad \varphi_r = - \int E(x) dx|_{x=0} = -j \int \sum_{n=-\infty}^{\infty} S_n P_n(\Delta) e^{-j(r+nK)x} dx|_{x=0}. \quad (41)$$

Integration of Eq.(41) term by term yields

$$\varphi_r = \sum_{n=-\infty}^{\infty} \frac{S_n P_n(\Delta)}{r + nK}. \quad (42)$$

The sums in Eqs.(40), (42) can be performed analytically using Dougall identity (see Appendix B for details) which yields

$$Q_r(r) = -2\epsilon_0 \Lambda P_{-r/K}(\Delta), \quad \varphi_r(r) = -\frac{\pi}{K} \frac{P_{-r/K}(-\Delta)}{\sin(\pi r/K)}. \quad (43)$$

Note that both Q_r and φ_r are spectral functions of r . They in fact can be interpreted as the Fourier transforms of discrete functions Q_i and φ_i taking values at the strip centers $x = i\Lambda$. In real systems some of the strips may have given potentials while the rest of them are grounded (zero potential). The solution for arbitrary distribution of strip potentials along the system can still be obtained using the superposition principle over the domain of $r \in (0, K)$ with some weighting function $\alpha(r)$ defined for $r \in (0, K)$

$$\varphi_i = \frac{1}{K} \int_0^K \alpha(r) \varphi_r(r) e^{-jri\Lambda} dr = \varphi_l \delta_{li}, \quad (44)$$

where δ is the Kronecker delta, φ_l is the given potential of the strip centered at $x = l\Lambda$. Applying

$$\alpha(r) = \varphi_l \frac{e^{jrl\Lambda}}{\varphi_r(r)} \quad (45)$$

Eq.(44) can be satisfied, because the integral is zero for $i \neq l$, and it is φ_l for $i = l$. The function $\alpha(r)$ modifies the spectral representation of the electric charge

$$Q(r) = \alpha(r)Q_r \quad (46)$$

yielding the charge of the strip centered at $x = i\Lambda$ resulting from the given potential of the strip centered at $x = l\Lambda$

$$Q_i = \frac{1}{K} \int_0^K Q(r)dr = \frac{4\epsilon_0}{K} \varphi_l \int_0^K \frac{P_{-r/K}(\Delta)}{P_{-r/K}(-\Delta)} e^{-jr(i-l)\Lambda} \sin(\pi r/K) dr. \quad (47)$$

Another formulation of the electrostatic problem can be stated in terms of given charges Q_l and the resulting voltages between neighboring strips, $V_i = \varphi_{i+1} - \varphi_i$ as unknown quantities. The spectral representation of V_i is

$$V_r = \varphi_r e^{-jr\Lambda} - \varphi_r = j\Lambda P_{-r/K}(-\Delta) e^{-j\pi r/K}. \quad (48)$$

The weighting function $\alpha(r)$ can be deduced from the following condition, similar to Eq.(44). Namely, in terms of given charges Q_l

$$Q_i = \frac{1}{K} \int_0^K \alpha(r)Q_r(r)e^{-jr(i\Lambda)} = Q_l \delta_{il} \quad (49)$$

this yields

$$\alpha(r) = Q_l \frac{e^{jr(l\Lambda)}}{Q_r(r)}. \quad (50)$$

Taking into account that $V(r) = V_r(r)\alpha(r)$ and integrating from 0 to K in spectral domain we obtain the following expression for the voltage between neighboring strips V_i resulting from the given charge of the strip centered at $x = l\Lambda$

$$V_i = \frac{jQ_l}{2\epsilon_0 K} \int_0^K \frac{P_{-r/K}(-\Delta)}{P_{-r/K}(\Delta)} e^{-jr(i-l+1/2)\Lambda} dr. \quad (51)$$

The function $\alpha(r)$, depending on the strips excitation, modifies the spectral representation of the complex field function $\Phi(k)$ in the entire domain (see Eq.(36))

$$\begin{aligned} \Phi(k) &= 2\alpha(r)P_n(\Delta) & D(k) &= \alpha(r)P_n(\Delta), & E(k) &= \alpha(r)S_nP_n(\Delta), \\ k &= r + nK, & r &\in (0, K), & S_n &= S_k, \end{aligned} \quad (52)$$

defined in subsequent domains of width K . It is worth noting that in real systems of strips the total charge of all strips vanishes. Since the charge is defined as the integral of $D(x)$ with respect to x

$$Q(x) = 2\epsilon_0 \int_{-\infty}^x D(x)dx \quad (53)$$

its spectral representation is

$$Q(k) = 2j\epsilon_0 D(k)/k. \quad (54)$$

The total charge in the plane of strips is $Q(\infty)$, and if the limit exists in spectral domain

$$\lim_{k \rightarrow 0} D(k)/k = 0 \quad (55)$$

then the total charge of the system vanishes. Thus, for real systems $\alpha(0) = 0$, because $P_0(\Delta) = 1$.

6. Strips in External Electric Field

In this Section we use the concept of the template functions discussed earlier to approach the problem of strips embedded into external spatially variable (harmonic) field. This makes the problem analogous to the wave-scattering one. So, in what follows, the corresponding terminology (“radiation conditions”, “incident” or “scattered” field and so on) in the considered “electrostatic scattering” problem is adopted. The strip total charge is evaluated as well as the Bloch harmonics of the “scattered” field in wide spectral domain. We first consider the case of periodic system in Sec. 6.1. and in Sec. 6.2. a similar “electrostatic scattering” problem is solved for the case of finite system of strips.

6.1. Periodic System

Here we consider the planar periodic system of conducting strips in external harmonic electric field. It is convenient to consider the external field on the plane of strips as an incident wave field in the theory of electromagnetic wave scattering: $(D^I, E^I)e^{-jk^Ix}$, $k^I \neq 0$, where $k_I = r + IK$, $r \in (0; K)$, r is a reduced “wave number” from the first Brillouin zone and I is arbitrary integer. In contrast to the “scattered” field resulting from the induced strip charges and satisfying the “radiation condition”, that is vanishing at $|y| \rightarrow \infty$, the “incident” field grows there, being the function of type $e^{|k_I y|}$. The components of the “scattered” field (D^s, E^s) and “incident” field (D^I, E^I) on the plane of strips obey the conditions given by Eq.(3) and Eq.(4) respectively. In the “electrostatic scattering” problem considered here (D^I, E^I) are known and the total field is the sum of external and induced fields

$$(D, E) = (D^I, E^I) + (D^s, E^s). \quad (56)$$

Applying a harmonic expansion we obtain

$$\sum_n (D_n, E_n) e^{-j(r+nK)x} = \sum_n (D^I, E^I) \delta_{nI} e^{-j(r+nK)x} + \sum_n (D_n^s, E_n^s) e^{-j(r+nK)x} \quad (57)$$

The harmonic amplitudes of the total field satisfying the boundary conditions, Eq.(8), can be expanded into series (see Eq.(111), Appendix D) as follows:

$$D_n = \sum_m \alpha_m P_{n-m}(\Delta), \quad E_n = j \sum_m \alpha_m S_{n-m} P_{n-m}(\Delta). \quad (58)$$

Substitution of Eq.(58) into Eq.(57) yields for the n th harmonic field component

$$\begin{aligned} \sum_m \alpha_m P_{n-m} &= D^I \delta_{In} + D_n^s, \\ \sum_m \alpha_m S_{n-m} P_{n-m} &= D^I \delta_{In} + E_n^s, \end{aligned} \quad (59)$$

where $E_n^s = j S_n D_n^s$ (vanishing at infinity) and $E_n^I = -j S_n D_n^I$ (growing at infinity). Accounting for the above relations and combining both equations in Eq.(59) we obtain an infinite system of equations for unknown coefficients α_m

$$\sum_m \alpha_m (1 - S_n S_{n-m}) P_{n-m} = 2 D^I \delta_{nI}. \quad (60)$$

However, only the finite number of equations are nontrivial, for n in certain domain dependent on I [2]. Particularly, for large $|n| > \max\{|m|, I\}$, the equations are identically satisfied due to $1 - S_{n-m}S_n = 0$ and $\delta_{nI} = 0$. The detailed discussion can be found elsewhere [2, 19]. Here we only state the main results obtained in the cited works. Namely, if we apply the “incident” harmonics somewhere in the domain $I \in [N^-; N^+]$, it results that we must account for $m \in [N^-; N^+ + 1]$. Outside these limits the equations for α_m are satisfied directly, what can be checked by inspection (note, it must be $N > |I|$). Hence, Eq.(60) yields $2N + 1$ equations and $2(N + 1)$ unknowns α_m . The last equation can be obtained from the condition of the system electric neutrality (zero net charge). For this purpose it is convenient to exploit Eqs.(53), (55). Taking into account Eq.(57) we can write for the total charge of the considered system in external electric field

$$Q(x) = 2j\epsilon_0 \sum_n \frac{D_n e^{-j(r+nK)x}}{r + nK}; Q(k) = 2j\epsilon_0 D_{\lfloor k/K \rfloor}/k, \quad k = r + nK, \quad (61)$$

where $\lfloor k/K \rfloor$ is an integer floor of k/K as in Eq.(36). Substituting the expansion of harmonics D_n from Eq.(58), the spectral representation of charge distribution can be rewritten as follows

$$Q(k) = 2j\epsilon_0 \sum_m \alpha_m P_{\lfloor k/K \rfloor - m}(\Delta)/k. \quad (62)$$

Accounting for the above equation the condition of the system electric neutrality Eq.(55) yields

$$\sum_m \alpha_m P_{-m}(\Delta) = 0. \quad (63)$$

This is the last equation that must be appended to the system of equations for α_m , Eq.(60), in order to obtain equal number of equations and unknowns. Now, we can evaluate α_m dependent on given (D^I, E^I) , and finally, we can evaluate the wave-field at $y = 0$ and elsewhere in the media.

6.2. Finite System

In the previous Section we have considered the problem of periodic system of strips embedded into external electric field. This section strongly relies on the paper [2] presenting the “electrostatic scattering” problem for periodic system of groups of strips. with period $\Lambda = 2\pi/K$. The template functions defined in the cited work, due to the system periodicity, are actually the discrete spectral functions represented by the Fourier series F_n being the convolutions like these in Eqs.(10) and (21) but involving Legendre polynomials $P_n(\cdot)$ instead of Bessel function $J_0(ka)$ (for simple periodic system, considered in previous Section $F_n = P_n$). On the strength of the asymptotic expansion [18]

$$P_n(\cos \theta) = J_0([2n + 1] \sin[\theta/2]) + O(\sin^2[\theta/2]), \quad \theta \sim aK \rightarrow 0, \quad (64)$$

we infer that the difference between the functions obtained in both cases vanish if $k = nK, K \rightarrow 0$. We are going to exploit this approximation for K small but finite, in developing the solution of the “scattering” problem using the earlier evaluated function $D^{(N-1)}(k)$, Eq.(16), which will be denote as $\mathcal{D}(k)$ hereinafter. As presented in Sec. 4.2., this function

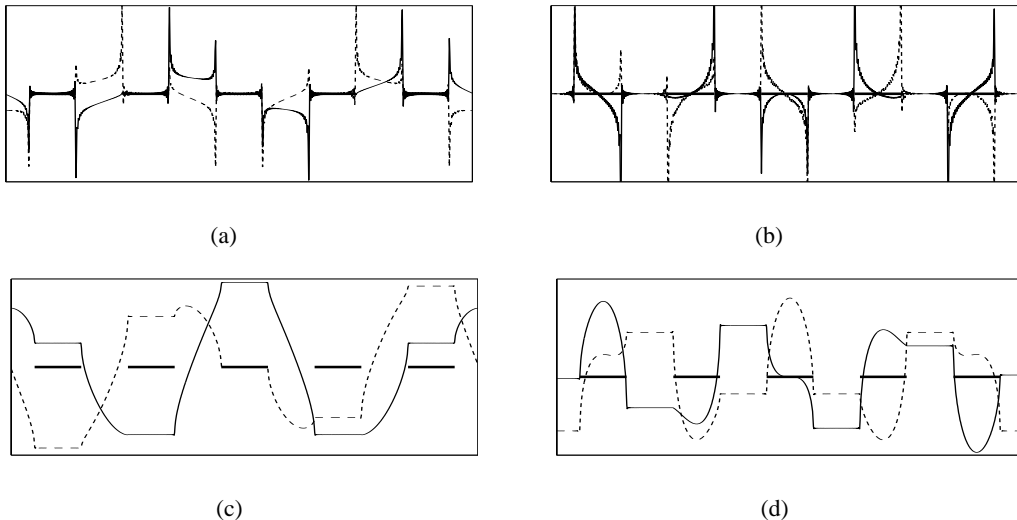


Figure 4. “Electrostatic scattering” by periodic system of strips of width $2a = \Lambda/2$: (a) the surface electric field $E_x(x)$, and (b) the normal induction $D_y(x)$. The surface spatial distributions of (c) the electric potential $\varphi(x)$ (note its constant values on strips) and (d) the charge $Q(x)$. Solid and dot lines represent real and imaginary values, respectively. Vertical scales are arbitrary; thick lines in lower figures represent the strips (at the zero level of the corresponding integrals).

is evaluated at discrete values of the spectral variable $k = i\kappa$. Thus, it is the discrete series in the numerical analysis and it actually represents, on the basis of the theory of FFT [16], the periodic function in spatial domain with a certain large period $2\pi/\kappa$. This enables us to introduce the notations

$$\mathcal{D}_i = \mathcal{D}(i\kappa), \quad \mathcal{E}_i = jS_i \mathcal{D}_i; \quad \mathcal{D}_{-i} = \mathcal{D}_i^*. \quad (65)$$

As it will be shown below, the series \mathcal{D}_i introduced in Eq.(65), with $\mathcal{D}_0 \neq 0$, will play an important role in the solution of the considered problem of strips in external electric field. Note that the pair of functions with shifted indices \mathcal{D}_{n-m} and \mathcal{E}_{n-m} places the values $\mathcal{D}_0, \mathcal{E}_0$ at the spectral line $k = m\kappa$, what corresponds to multiplication by e^{-jmKx} in the spatial domain. Naturally, such multiplied functions still satisfy the boundary conditions on the plane of strips, Eq.(8). This property will be exploited below with this important remark that D and E evaluated from Eq.(9) using the shifted \mathcal{D}_{i-m}

$$D_i = \mathcal{D}_{i-m} \text{ and } E_i = \mathcal{E}_{i-m} = jS_{i-m} \mathcal{D}_{i-m} \quad (66)$$

fail to satisfy Eq.(3) ($E_i \neq jS_i D_i$, this can be easily verified by inspection), and thus they fail to satisfy the “radiation condition” (the corresponding field does not vanish at $|y| \rightarrow \infty$). Note however that this failure takes place only due to the spectral lines $0 \leq i \leq m$; all other lines satisfy well Eq.(3).

To proceed further, the “incident” (external) harmonic field of wavenumber $k_I = IK$ and complex amplitudes D^I and E^I is introduced. This field does not vanish at infinity;

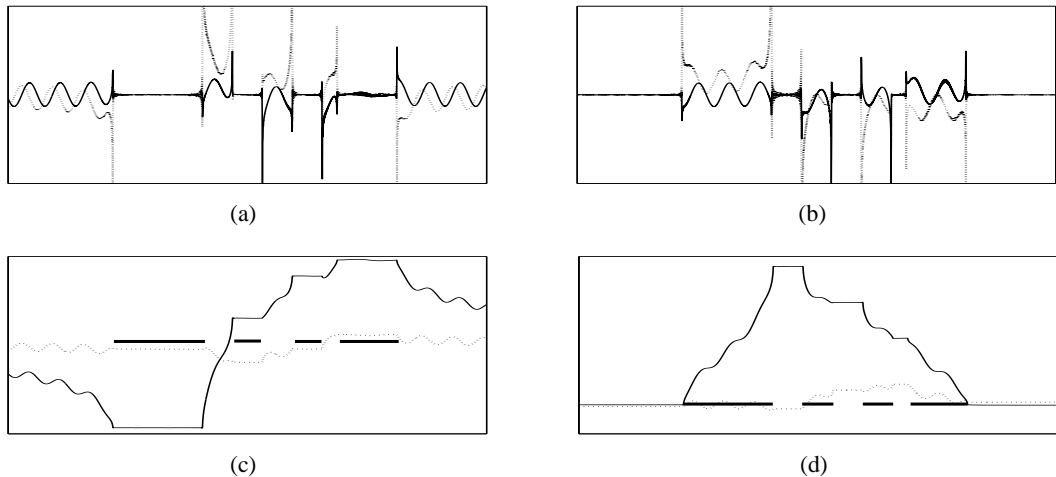


Figure 5. “Electrostatic scattering” by 4 strips: (a) the surface electric field $E_x(x)$, and (b) the normal induction $D_y(x)$. The surface spatial distributions of (c) the electric potential $\varphi(x)$ (note its constant values on strips) and (d) the charge $Q(x)$; equal values of $Q(x)$ on both sides of the structure indicates the structure electric neutrality. Solid and dot lines represent real and imaginary values, respectively. Vertical scales are arbitrary; thick lines in lower figures represent the strips (at the zero level of the corresponding integrals).

being the “incident” one, it rather grows with $|y| \rightarrow \infty$ and thus is a function of type $e^{|k_I y|}$. In contrast to the “scattered” field, the “incident” field obeys:

$$E^I = -G(IK)D = -jS_I D^I. \quad (67)$$

To simplify the analysis, $I > 0$ is applied in this chapter.

The field on the strip plane $y = 0$ is the sum of the “scattered” (marked below by the upper index s) and “incident” spatial waves; it must satisfy the boundary conditions on this plane. Noticing that the field $(\mathcal{D}_{i-m}, \mathcal{E}_{i-m})$ does it, we attempt to express the surface field by the combination (the summation convention applied over repeated indices)

$$\begin{aligned} E_i &= E_i^s + E^I \delta_{iI} = j\alpha_m S_{i-m} \mathcal{D}_{i-m}, \\ D_i &= D_i^s + D^I \delta_{iI} = \alpha_m \mathcal{D}_{i-m}, \end{aligned} \quad (68)$$

where δ is the Kronecker delta and α_m are unknown coefficients. One needs only to add the requirement that the “scattered” field obeys Eq.(3), that is $E_i^s = jS_i D_i^s$; explicitly

$$\alpha_m (1 - S_i S_{i-m}) \mathcal{D}_{i-m} = 2D^I \delta_{iI}. \quad (69)$$

It may be checked by inspection that the solution to this infinite system of equations (for i in infinite limits) can be solved with $\alpha_m, 1 \leq m \leq I + 1$, for the assumed $I > 0$. Indeed, for any $i > I$, the term in bracket turns to zero satisfying the homogeneous equation ($\delta_{I,i} \delta_{I,I} = 0$), and similarly for any $i \leq 0$, provided that m takes values in the above limits. For $i = I$ we have $\alpha_{I+1} = 1/\mathcal{D}_1^*$. Other α_m can be evaluated in recursive manner, starting with equation $i = I$ down to $i = 1$.

The resulting field distribution may include a net charge, $D_0 \neq 0$. To assure the system electric neutrality, one needs to add $\alpha_0 D_i$ to the evaluated D_i with coefficient α_0 chosen to obtain

$$D_0 + \alpha_0 D_0 = 0. \quad (70)$$

This completes the solution of the “scattering” problem; the resulting surface field in the spectral representation

$$D_i = \alpha_m D_{i-m}, E_i = j \alpha_m S_{i-m} D_{i-m}; 0 \leq m \leq I + 1, \quad (71)$$

satisfies the boundary conditions on the plane of strips. Moreover, the induced strip voltages and charges can be evaluated in the already presented manner, Eq.(17), in the corresponding discrete form ($k = i\kappa$). These should be treated like originating from the negative external voltage source. If, for example the i th strip is assumed to be grounded but gets certain potential due to the “incident” field, then a combination of template functions $\Phi^{(N,n)}$ must be added with proper coefficients evaluated in the Sec. 4.3..

7. Examples

In this Section we illustrate the presented method on two examples. First, we solve the electrostatic problem for the so-called quasi-periodic system of strips (Sec. 7.1.). And the second example concerns the application of the spectral approach to the beam forming analysis of the acoustic transducers (Sec. 7.2.).

7.1. Quasi-Periodic System of Strips

In this section we consider the periodic system with broken periodicity by inclusion of certain narrower strip and spacing in the middle of the system (Fig.6). Far from this inclusion, the system remains “periodic”, although the positions of strips and spacings at the left-hand side of the inclusion are interchanged with respect to the original periodic structure.

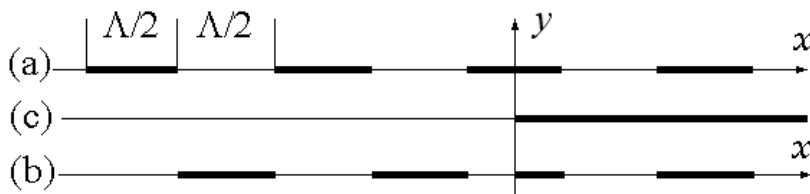


Figure 6. A periodic system of strips (a), and its quasi-periodic counterpart (b). E_y takes real values on strips (thick lines), and E_x is real in the other domains. The position of the conducting half-plane discussed in Sec. 3. is shown in (c).

The defective periodic structures are known in physics; they are used in the Fabry-Perot resonators of solid-state lasers, for instance. Two distributed reflectors (which are periodic structures) are placed there at certain distance (a cavity region), usually of $\Lambda/2 + n\Lambda$ length,

where Λ is the structural period of the reflectors. In the considered system of strips, this cavity region is $\Lambda/2$ wide where Λ is the strip period.

The basic solution for the field in periodic system of strips arranged on $y = 0$ plane was derived in Sec. 5., Eq.(37) and the corresponding complex field function is given by Eq.(38). The basic electrostatic solution for the half-plane $x > 0$, by analogy with Eq.(7), can be written in the following way

$$\Phi_h(x) = \frac{1}{\sqrt{x}}, \quad \Phi_h(k) = \frac{(1+j)}{\sqrt{2\pi k}}, \quad k > 0. \quad (72)$$

The product of two complex field functions, Eq.(37) and Eq.(72) is also a valid solution for certain electrostatic problem, like the product of two laterally shifted $\Phi_h(x)$ resulting in the solution for a strip (see Sec. 4.1., Eq.(10)). This is because the product of analytic functions is an analytic one, hence describing certain electrostatic field (this can be easily checked by inspection). Thus, multiplication of Eq.(37) and Eq.(72) yields a basic solution for the quasi-periodic system of strips, shown in Fig. 6(b)

$$\Phi(x) = \Phi_p(x)\Phi_h(x), \quad (73)$$

where Φ_p denotes the solutions for periodic system, Eq.(37). It results from Eq.(3) that $D(x)$ evaluated form the corresponding $\Phi(x)$ in Eq.(73) using Eq.(9) remains real-valued in the same domains of $x > 0$ as it was presented in previous sections because of the real-valued $1/\sqrt{x}$. For $x < 0$ however, the value of $1/\sqrt{x}$ is imaginary causing that the domains of real and imaginary values of the field resulting from $\Phi(x)$ are interchanged with respect to the earlier discussed fields for periodic system. Concluding, the field components correspond to the system of strips looking like the one presented in Fig. 6(b). Note that the original strip placed at $x = 0$ is divided: its part placed at $x > 0$ remains the strip where $E(x) = 0$ and $D(x) \neq 0$, and the other part placed at $x < 0$ becomes the spacing, where $E(x) \neq 0$ and $D(x) = 0$. The system is no longer periodic and is called quasi-periodic because outside this perturbation at $x \approx 0$ the remaining strips are “periodic”. The spectral representation of $\Phi(x)$ is a convolution of two spectral functions that corresponds to multiplication in spatial domain:

$$\Phi(k) = \Phi_p(k) * \Phi_h(k). \quad (74)$$

Due to half-infinite support of both spectral functions and simple form of $\Phi_p(k)$, Eq.(38) and $\Phi_h(k)$, Eq.(72), the convolution can be easily evaluated [19], as presented below schematically:

$$\begin{aligned} \int_0^p \frac{P_{[\xi]}}{\sqrt{p-\xi}} d\xi &= \sum_{n=0}^{|p|-1} 2P_n \left(-\sqrt{p-n-\xi} \right)_0^1 + \int_{|p|}^p \frac{P_{[p]}}{\sqrt{p-\xi}} d\xi, \\ \Phi(k) &= \frac{4(1+j)}{\sqrt{\Lambda}} \left(\sum_{n=0}^{|p|-1} \frac{P_n}{\sqrt{p-n+\sqrt{p-n-1}}} + P_{[p]} \sqrt{p-|p|} \right), \quad p = \frac{k}{K}, \end{aligned} \quad (75)$$

from which the spectral representations of the field components are evaluated using Eq.(9). The integration of the field in spatial domain corresponds to division by k in spectral domain. The solution for arbitrary distribution of strip potentials along the system can be

obtained using the same technique as in Sec. 5., Eq.(44). For this purpose, we multiply the complex field $\Phi(x)$ in Eq.(73) by arbitrary real-valued function $\alpha(x)$ having its spectral representation closed within domain $k \in (0, K)$

$$\Phi(x) = \alpha(x)\Phi_p(x)\Phi_h(x), \quad \Phi(k) = \alpha(x) * \Phi_p(k) * \Phi_h(k). \quad (76)$$

Particularly, for $\alpha(k) = 1, k \in (0, K)$, the function $\Phi(x)$ has its spectrum distributed over the entire positive semi-axis $k > 0$ (Fig.7).

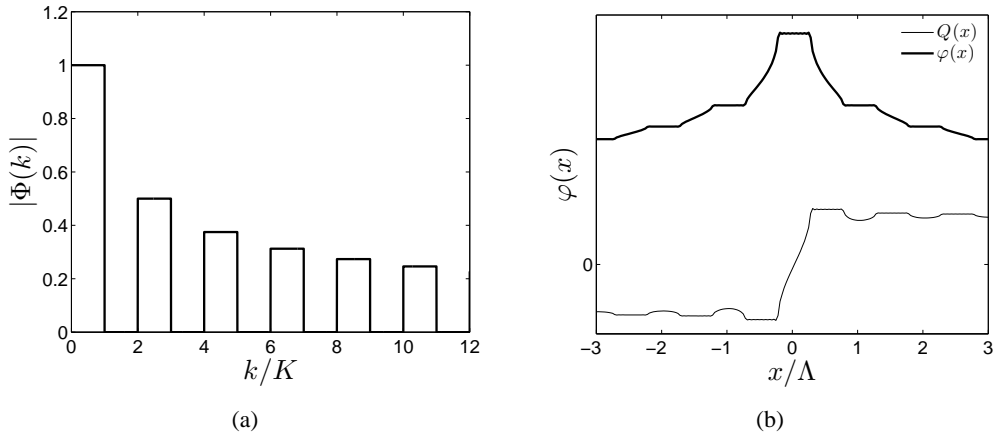


Figure 7. (a) The applied spectral function $|\Phi_r(k)|$ for periodic system of planar strips. (b) The spatial distribution of electric potential $\varphi(x)$ (thick line); thin line presents the spatial charge distribution $Q(x)$.

In general case arbitrary function $\alpha(k)$ can be conveniently approximated by a step function taking constant values in subsequent sub-domains. This will enable us to evaluate the convolution integrals like in Eq.(75), which corresponds to the function $\alpha(k)$ taking unitary value in one domain. Such the function can be conveniently represented by the series of Walsh functions, for instance, taking constant values α_i on the subintervals $((i-1)\kappa < k \leq i\kappa)$ of the interval $(0; K)$, where $\kappa = K/M$ and M is the number of such subintervals. By analogy to Eq.(75) (which corresponds to the case $M = 1$), each component of $\alpha(k)$ contributes to the convolution integral by:

$$\int_{i/M}^{(i+1)/M} \frac{\alpha_i P_{[\xi]}}{\sqrt{p-\xi}} d\xi = 2\alpha_i \sum_{n=0}^{|p|-1} P_n \left(-\sqrt{p-n-\xi} \right)_{i/M}^{(i+1)/M} + \int_{[p]+i/M}^b \frac{\alpha_i P_{[p]}}{\sqrt{p-\xi}} d\xi, \quad p = \frac{k}{K}, \quad (77)$$

where the second integral appears in the equation only if $k > |p| + i/M$, in which case $b = \min(k, |p| + (i+1)/M)$. Also note that the first component (the sum) disappears if $|p| = 0$. The above discussion presents how to obtain $\Phi^{(i)}(k)$ for each α_i and for any value of $k = k_n = n\kappa, n = 0, 1, 2, \dots, N$ used in computations, with adequate small κ and sufficiently large N required by the numerical FFT algorithm. The final $\Phi(k)$ is the series

$$\Phi(k) = \sum_{i=0}^{M-1} \alpha_i \Phi^{(i)}(k), \quad k = n\kappa, \quad \Phi_n^{(i)} = \Phi^{(i)}(k_n),$$

truncated here to finite M . The truncated function is represented by its values at discrete points $k_n = n\kappa$ (typically, $N = 2^{N'}$), yielding a numerical vector of data Φ_n :

$$\Phi_n = \sum_{i=0}^{M-1} \alpha_i \Phi_n^{(i)}. \quad (78)$$

It results from Eq.(77) that $\Phi^{(i)}(0) = 0$ hence $\Phi_0 = 0$.

Applying Eq.(9), one easily obtains the analogous vector data of length $2N$ for electric field $E(k_n)$, $k_n = n\kappa$, $n = -N + 1, \dots, 0, \dots, N$, and similarly for $D(k_n)$. Taking into account that

$$E(x) = -\partial\varphi/\partial x, \quad E(k) = jk\varphi(k), \quad (79)$$

in spatial and spectral domains, respectively, where φ is the electric potential distribution in the plane of strips $y = 0$, the strip potentials can be evaluated with the help of FFT algorithm in a similar manner as discussed in Sec. 4.3.

$$[\varphi_n] = \alpha_i \text{FFT}\{[-jE(k_n)/k_n]\}, \quad \Phi_0/k_0 \rightarrow 0, \quad (80)$$

where the numerical data vectors are denoted by $[.]$. The evaluated φ_n are the potentials at discrete spatial points $x \sim n(N\kappa)^{-1}$ in the plane of strips; let m denote these values of n corresponding to the points nearest to the centers of strips. The immediate verification of the computation accuracy, depending on both κ and N , is whether $\varphi_n = \text{const}$ on strips (certain violation of this condition cannot be avoided at the strip edges even for the smallest κ and largest N possible due to the known Gibbs phenomenon). The values of α_i is obtained by solving the above equation from the condition that φ_m takes given values.

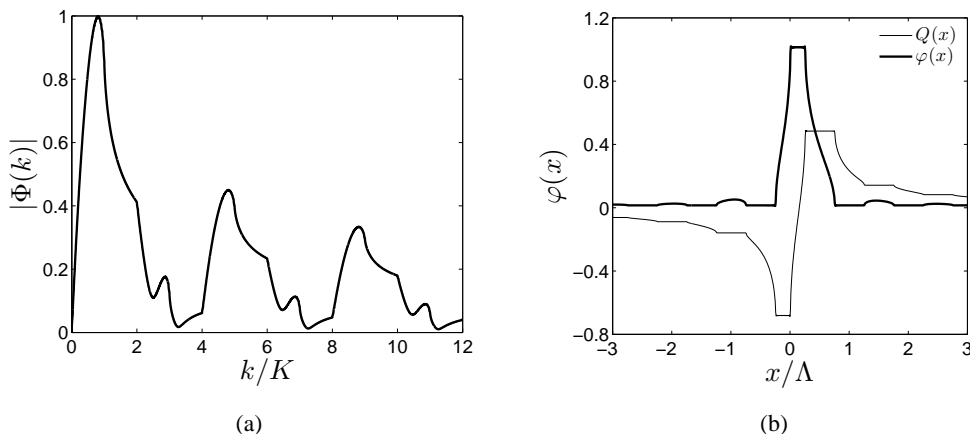


Figure 8. (a) The evaluated spectrum $|\Phi(k)|$, and (b) the spatial distribution of electric potential $\varphi(x)$ (solid line); thin line presents the spatial charge distribution $Q(x)$.

In Fig. 8 the numerical example is shown for the case when the unity potential is given only to the narrow strip at $x \in (0, \Lambda/4)$; the other strips are assumed grounded. The results shown in Fig. 8 present both $\Phi(k)$ and $\varphi(x)$. The constant values of the potential on strips (thick line) can be easily noticed, as well as good accuracy concerning the strip voltages. In

the presented examples we applied $M = 2^5$ and $\kappa = 2\pi/32$, $N = 2^{16}$. Computations show that the evaluated strip potentials vanishes fast for farther strips from the system center. This justifies the above mentioned truncation of the vector of unknowns α_i . The thin line presents the spatial charge distribution being the integral of $2\epsilon_0 D(x)$.

7.2. Acoustic Beam Forming

In this section we give an example of application of the method presented above to the case of acoustic transducers beam forming analysis. The idea of beam forming is based on excitation of the wave-field by a system of point-like sources distributed on certain surface. Their strength and phase is chosen such that the wave radiated into the body evolves into the required wave beam-shape. In further approximation, the point-like sources are replaced by periodic vibrating strips of finite widths (a periodic baffle system).

A similar system is considered here, and the interaction between strips (baffles) is accounted for in the full-wave analysis of the wave excitation problem by rigorous formulation of the corresponding boundary-value problem. The considered system consists of periodic acoustically hard strips (baffles) where the normal acoustic vibration vanish [20], and between them are acoustically soft domains where the acoustic pressure is given constant or vanishes in the scattering problem. This is a mixed (Dirichlet-Neuman) boundary-value problem that we deal with here: the given pressure between baffles models the wave-beam generation, and the pressure exerted on the acoustically hard baffles by the incident and scattered waves, in the case of scattering problem, models the response signal from the piezoelectric transducer element. To demonstrate the flexibility of the presented method we consider the problem of wave generation by the system of baffles. The scattering problem can also be addressed by this approach.

7.2.1. Surface Harmonic Impedance of an Acoustic Half-Space

Two-dimensional harmonic wave-field $e^{j\omega t} e^{-j\xi x - j\eta y}$ is considered independent of z in the acoustic media governed by equations for acoustic potential φ , pressure p and particle velocity \vec{v}

$$\begin{aligned}\nabla^2 \varphi + k^2 \varphi &= 0, \\ \vec{v} &= -\nabla \varphi, \quad p = j\omega \rho_a \varphi,\end{aligned}\tag{81}$$

where $k = \omega/c$ is the acoustic wave number. Standard notations are applied: c is the sound velocity in the media, ρ_a - its mass density.

Assuming known $p \exp(-j\xi x)$ at the plane $y = 0$, the resulting y -component of the particle velocity $v = v_y$ in the upper half-space of acoustic media can be easily evaluated:

$$\begin{aligned}v &= v_y = Gp, \quad G(\xi) = \eta/(\omega \rho_a), \\ \eta &= \sqrt{k^2 - \xi^2} = -j\sqrt{\xi^2 - k^2}\end{aligned}\tag{82}$$

neglecting the exponential term $\exp(j\omega t - j\xi x)$. In the above equations η is chosen in order to satisfy the “radiation condition” of the acoustic field at $y \rightarrow \infty$. Inside the media, the acoustic potential generated by p at $y = 0$ is

$$\varphi(x, y) = -j \frac{p}{\omega \rho_a} e^{-j\xi x - j\eta y}.\tag{83}$$

To apply the presented method of analysis, we will need the x -derivative of pressure $p(x)$ at $y = 0$, which is in somewhat symbolic notation $q = p_{,x} = -j\xi p$, thus in spectral domain:

$$v = (jG/\xi)p_{,x} = g(\xi)q; \quad g(\xi \rightarrow \pm\infty) = g_\infty S_\xi, \quad (84)$$

where $g_\infty = 1/(\omega\rho_a)$ is the acoustic admittance, and $S_\nu = 1$ for $\nu \geq 0$ and -1 otherwise.

7.2.2. Boundary Conditions at the Baffle Plane

In the presented formulation, the periodic system of the acoustically hard baffles (y -component of the particle velocity on baffles vanishes), are placed on the surface of acoustic medium $y > 0$. In the slot between baffles, a harmonic pressure of constant amplitude p_l excite the wave-field in the medium, where l determine the position of the slot along x -axis: $l\Lambda$ is the slot center.

For $\Lambda - w$ wide baffles centered at $= l\Lambda + \Lambda/2$, l - any integer number, the boundary conditions at $y = 0$ are:

$$\begin{aligned} q &= 0, \quad x \in (-w/2, w/2) + l\Lambda \text{ between strips}, \\ v &= 0, \quad x \notin (-w/2, w/2) + l\Lambda \text{ on strips}, \\ p(l\Lambda) &= p_l, \quad \text{in the middle between strips}, \end{aligned} \quad (85)$$

which p_l are given values. They are constant in given slots between baffles due to the condition $q = 0$ there. The solutions to the boundary-value problem of interest are functions $p(x)$ and $v(x)$ at $y = 0$ plane, which will be searched in the form of Bloch series, natural for the considered periodic system. The field inside the medium, $y > 0$, is evaluated applying Eq.(83) (in spectral representation).

7.2.3. Application of Electrostatic Method

In periodic systems with period $\Lambda = 2\pi/K$, the wave-field is represented by the Bloch series like

$$p(x) = \sum_{n=-\infty}^{\infty} p_n e^{-j(r+nK)x}, \quad r \in (0, K) \quad (86)$$

(for example of acoustic pressure p) where r is an arbitrary wave-number constrained to one Brillouin zone for the sake of uniqueness of the representation. The Bloch components p_n are expanded again in the finite series of Legendre polynomials (see Sec. 5. and Appendix D, Eq.(111))

$$\begin{aligned} \sum_{n=-\infty}^{\infty} S_n P_n(-\cos \Delta) e^{-jnKx} &= 0 \text{ for } |x| < w/2, \text{ and} \\ \sum_{n=-\infty}^{\infty} P_n(-\cos \Delta) e^{-jnKx} &= 0 \text{ for } |x| > w/2, \end{aligned} \quad (87)$$

where $\Delta = \pi w/\Lambda$. For $(\Lambda - w)$ -wide strips centered at $x = l\Lambda + \Lambda/2$, the corresponding field expansion at $y = 0$ applied in the solution to the boundary-value problem formulated

above, Eq.(85), is

$$\begin{aligned} q &= \sum_{n=-\infty}^{\infty} q_n e^{-j(r+nK)x}, \quad q_n = \sum_m \alpha_m S_{n-m} P_{n-m}(-\cos \Delta), \\ v &= \sum_{n=-\infty}^{\infty} v_n e^{-j(r+nK)x}, \quad v_n = \sum_m \beta_m P_{n-m}(-\cos \Delta). \end{aligned} \quad (88)$$

The boundary conditions, Eq.(85), are fulfilled on the strength of Eq.(87). Now, we need only to check if the applied wave-field solution satisfies the wave equation inside the media, which equation is represented at the plane $y = 0$ by the harmonic admittance $G(r + nK)$ or more convenient, by its version g , Eq.(84). Only this part of the wave-field (q, v) which satisfies the radiation condition at $y \rightarrow \infty$ is involved in Eq.(84). This yields the relation for the n th Bloch component having wave-number $r + nK$ (δ_{ij} is the Kronecker delta)

$$v_n = g(r + nK)q_n, \quad r \in (0, K), \quad (89)$$

which must be satisfied for all n , particularly for large $|n| \gg |I|$ where

$$g(r \pm NK) = \pm g_{\infty} \quad (90)$$

(formally, $N = \infty$, but in the applied approximation, N is assumed large but finite - this is the only approximation applied in the method). This is only possible if [6]:

$$\beta_m = g_{\infty} \alpha_m \quad (91)$$

which substituted into the earlier equation yields:

$$\sum_m \alpha_m [g(r + nK)S_{n-m} - g_{\infty}] P_{n-m}(-\cos \Delta) = 0. \quad (92)$$

Accounting for Eq.(90), the equations for α_m outside the limits $n \in [-N, N]$ and $m \in [-N, N+1]$ (moreover it must be $N > |I|$) are satisfied automatically, what can be checked by inspection [6]. Hence, Eq.(92) yields the system of $2N + 1$ equations for $2(N + 1)$ unknowns. It can be now explained what is the source of advantage of the presented method over other methods applied for similar problems. The boundary conditions are satisfied exactly by the proposed solution, Eq.(88), but certain departure is made concerning the equation of motion which is represented here by the harmonic admittance G or g , Eqs.(82)–(84). This departure relies on the approximation that $g(r + nK) \equiv g_{\infty}$ for $r + nK$ greater than certain large but finite value (far above the domain of existence of propagating modes in the media). In fact, $g(x) \rightarrow g_{\infty}$ like $1/x^2$ and indeed this approximation can be applied in general. In the consequence of it, the wave-field on the baffle plane is represented by the finite Fourier series and the larger the number of terms involved, that is the larger the applied N is, the better approximation is achieved. Usually, for $K \approx k$, N can be chosen quite small. The resulting system of equations Eq.(92) appended by the one resulting from the last boundary conditions in Eq.(85), can be easily solved. This last equation can be evaluated by integration of $q = p_{,x}$, Eq.(88), using the Dougall identity, Eq.(105) of Appendix C

$$p_r(l\Lambda) = \sum_n j \frac{q_n e^{-jrl\Lambda}}{r + nK} = \sum_m j \frac{\pi (-1)^m \alpha_m e^{-jrl\Lambda}}{K \sin \pi r / K} P_{-r/K-m}(\cos \Delta), \quad (93)$$

which, being constant between neighboring baffles, is evaluated at $x = l\Lambda$; note the dependence on r indicating its spectral-domain origin. The solution we seek, must satisfy the condition that the pressure at the different slot between baffles take different (given) values p_l , dependent on l . This requires integration of the above equation over $r \in (0, K)$, which is the inverse Fourier transform of discrete function $p_l = p(l\Lambda)$ defined by (note that the harmonic term $\exp(-jrl\Lambda)$ is already included in the p_r evaluated above):

$$\frac{1}{K} \int_0^K p_r(l\Lambda) dr = p_l. \quad (94)$$

This finally yields the last condition for α_m dependent on r (p_l are given):

$$\sum_m (-1)^m \alpha_m P_{-r/K-m}(\cos \Delta) = -j \frac{K}{\pi} p_l e^{jrl\Lambda} \sin \pi r / K; \quad (95)$$

simple substitution into Eq.(93) verifies that Eq.(94) is satisfied. This is the last equation that must be appended to the system, Eq.(92), in order to obtain equal number of equations and unknowns. Now, we can evaluate α_m dependent on given p_l , and finally, we can evaluate the wave-field at $y = 0$ and everywhere in the media $y > 0$ using Eq.(88) and Eq.(83).

7.2.4. Beam Forming by Chosen Pressure between Baffles

In contrast to the earlier cited papers [21, 22, 23], the applied method of analysis yields spatial spectrum of the acoustic pressure at the baffle plane. Taking advantage of this, the far-field radiation pattern of $p(\xi)$ dependent on the wave number $\xi = r + nK$, Eq.(81), can be simply evaluated from the inverse Fourier transform (as already defined in Eq.(94) on the baffle plane). At the level y above the baffle plane $y = 0$, the acoustic pressure behaves according to Eq.(83), thus introducing spatial angular variables: $x = R \sin \theta$, $y = R \cos \theta$, and η given in Eq.(82), the pressure in angular coordinates is:

$$p_R(\theta) = \int_{-\infty}^{\infty} p(\xi) e^{-jR\xi \sin \theta} e^{-jR\eta \cos \theta} d\xi / K. \quad (96)$$

At large distance $R \rightarrow \infty$, we may drop this part of the integral which depends on imaginary valued η (representing the localized field at the baffle plane). This is made by constraining θ to the domain $(-\pi/2, \pi/2)$ in the transformed integration where $\xi = k \sin \vartheta$, $\eta = k \cos \vartheta$:

$$p_R(\theta) = \int_{-\pi/2}^{\pi/2} (k/K) p(k \sin \vartheta) \cos \vartheta e^{-jkR \cos(\vartheta-\theta)} d\vartheta, \quad (97)$$

which integral can be easily evaluated by the stationary phase method [24, 25] (the stationary point of interest here is $\theta = \vartheta$):

$$p_R(\theta) = p(k \sin \theta) \cos \theta \frac{k}{K} \sqrt{\frac{j2\pi}{kR}} e^{-jkR}. \quad (98)$$

This is an alternate method of evaluation of angular radiation characteristics to the one presented in [21, 22, 23]. It can be however evaluated more efficiently as explained below.

Solving Eqs.(89)–(95), we obtain n th Bloch order of the acoustic pressure, $p_n = jq_n/(r + nK)$ for given r , Eq.(88). This is the wave pressure radiated into the half-space $y > 0$ at the direction described by the corresponding wave numbers ($\xi_n = r + nK, \eta_n = \sqrt{k^2 - (r + nK)^2}$) provided that η_n is real. Hence, only limited values of n contribute to the angular radiation pattern at $\theta = \text{atan}((r + nK)/\eta_n)$ (there are multiple directions for small K). Repeating this for all allowed $r \in (0, K)$ in Eq.(86) (followed by evaluation of α_m from Eqs.(85)–(95) and q_n from Eq.(88) in the manner presented above), the angular radiation pattern can be fully reconstructed.

In the numerical examples presented in Fig. 9 both the pressure on the baffle plane $p(x)$ and the radiation pattern $|p(\theta)|$ are presented computed for several values of slot width w and for the baffle period $\Lambda = 0.5\lambda$. In the above examples we applied given pressure in one

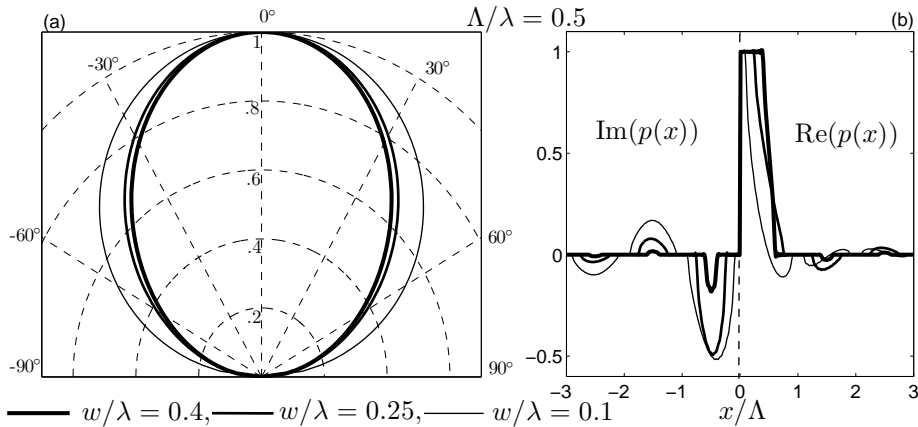


Figure 9. Radiation pattern (a) $|p(\theta)|$ and pressure distribution (b) on the baffle plane $p(x)$ for $\Lambda/\lambda = 0.5$, and different slot width w .

slot only: $p_l = \delta_{l0}$.

In Fig. 10 the radiation pattern is computed for the case of 5 active slots excited with the chosen phase shift $p_l = \exp(jk\Lambda \sin \theta)$, for $l = -2, \dots, 2$ and $p_l = 0$ otherwise. The deflection angle is chosen $\theta = 30^\circ$ and 0° for comparison. The deflection angle differs slightly from the applied value $\theta = 30^\circ$. This difference can be diminished by taking more active slots. At the same time the width of the main lobe gets smaller and the side lobe level remains unchanged. In Fig. 10(b) the corresponding distribution of the pressure field on the baffle plane is presented.

8. Conclusion

The electrostatic problem is solved by a novel method exploiting the special template functions constructed in spectral domain and satisfying the electric boundary conditions on the strips. The cases of periodic and finite systems are considered. In both cases the template functions are the partial solution of corresponding electrostatic problems. For a finite system they are in the form of multiple convolutions of Bessel functions of the first kind whereas for a periodic system the template functions are expressed via properly chosen Legendre polynomials. The method is applied to solve the problem of strips in external

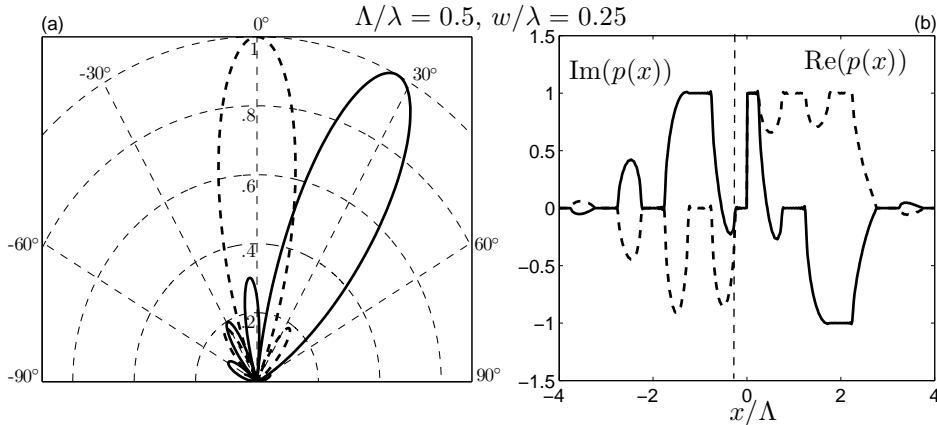


Figure 10. Radiation pattern $|p(\theta)|$ (a) and pressure distribution (b) for $\Lambda/\lambda = 0.5$, $w/\lambda = 0.25$ and 5 active slots excited with linear phase shift and deflection angle $\theta = 30^\circ$ (solid line) and 0° (dashed line).

electric field. It can be successfully used for evaluation of the field on the plane of strips embedded in any spatial-variable external field represented by a series of spatial harmonics.

In contrast to standard electrostatics, here we construct solutions in the spectral domain. Note that the field spatial distribution is often the least important in applications: measured are either the mutual strip capacitances depending on the total strip charges (the integrals of the charge distribution), or the spatial spectrum (in the scattering cases, like the Bragg scattering by strips or frequency characteristics of surface wave transducers). The solution constructed in spectral domain with satisfactory accuracy is advantageous as compared with the standard evaluation of spatial charge distribution at least in the latter case, because of high sensitivity of the charge spectrum on the charge distribution details over the entire system. Having the spatial spectrum, one can easily evaluate the spatial distribution and its integral (in order to evaluate the measured total charges of strips) with similar high accuracy, what is not true in the reverse way. Moreover, the inverse Fourier transformation yields the tool for verification of the spectral results, lacking in the standard analysis [26, 27, 28].

The presented examples confirm that the applied method is worth considering not only for pure electrostatic problems but for numerical experiments concerning the beam forming systems as well. It is very efficient numerically, yielding all interesting characteristics of the system within the same simple analysis, and yields results satisfying the energy conservation law, the valuable feature allowing one to check the computed results easily.

Appendix A

It is known that [18]

$$\mathcal{F} \left\{ \frac{1}{\sqrt{a_m^2 - (x - b_m)^2}} \right\} = \int_{-\infty}^{\infty} \frac{e^{j k x} dx}{\sqrt{a_m^2 - (x - b_m)^2}} = J_0(ka_m)e^{jkb_m}, \quad k \geq 0, \quad (99)$$

and 0 for $k < 0$ (note the exponential term resulting from the displacement b_m). The generalized transform of the function $(x - b_m)/\sqrt{a_m^2 - (x - b_m)^2}$ can be found using the

rule $\mathcal{F}\{xf(x)\} = -jd F(k)/dk$, yielding

$$\mathcal{F}\{x/\sqrt{a_m^2 - x^2}\} = -j \frac{d}{dk} J_0(ka_m) = -j[\delta(k) - a_m J_1(ka_m)]. \quad (100)$$

Finally, for the shifted function:

$$\mathcal{F}\{(x - b_m)/\sqrt{a_m^2 - (x - b_m)^2}\} = -j[\delta(k) - a_m J_1(ka_m)]e^{jk b_m}. \quad (101)$$

Appendix B

The cubic interpolation functions are, after [16]:

$$\psi(s) = \begin{cases} (s+3)(s+2)(s+1)/6, & s \in (-2, -1), \\ -(s+2)(s+1)(s-1)/2, & s \in (-1, 0), \\ (s+1)(s-1)(s-2)/2, & s \in (0, 1), \\ -(s-1)(s-2)(s-3)/6, & s \in (1, 2), \end{cases} \quad (102)$$

$$\begin{aligned} \bar{\psi}_0(s) &= \begin{cases} -(s-1)(s-2)(s-3)/6, & s \in (0, 1), \\ \psi(s), & s \in (1, 2), \end{cases} \\ \bar{\psi}_1(s) &= \begin{cases} (s+1)(s-1)(s-2)/2, & s \in (-1, 0), \\ \psi(s), & s \in (0, 2), \end{cases} \\ \bar{\psi}_2(s) &= \begin{cases} -(s+2)(s+1)(s-1)/2, & s \in (-2, -1), \\ \psi(s), & s \in (-1, 2), \end{cases} \\ \bar{\psi}_3(s) &= \begin{cases} (s+3)(s+2)(s+1)/6, & s \in (-3, -2), \\ \psi(s), & s \in (-2, 2), \end{cases} \\ \bar{\psi}_{M-1-i}(s) &= \bar{\psi}_i(-s), \quad i = 1, \dots, m = 3, \\ \bar{\psi}'_0(s) &= \begin{cases} -\psi(s), & s \in (-2, 0), \\ -2s(s-1)(s-2)/3, & s \in (0, 1), \end{cases} \\ \bar{\psi}'_1(s) &= \begin{cases} -\psi(s), & s \in (-2, -1), \\ s(s+1)(s-1), & s \in (-1, 0), \end{cases} \\ \bar{\psi}'_2(s) &= -2s(s+2)(s+1)/3, \quad s \in (-2, -1), \\ \bar{\psi}'_3(s) &= (s+3)(s+2)(s+1)/6, \quad s \in (-3, -2), \\ \bar{\psi}'_{M-1-i}(s) &= \bar{\psi}'_i(-s), \quad i = 1, \dots, m = 3. \end{aligned} \quad (103)$$

The functions $W(\Theta)$ and α_m are:

$$\begin{aligned} W(\Theta) &= \frac{6 + \Theta^2}{3\Theta^4}(3 - 4 \cos \Theta + \cos 2\Theta); \\ \alpha_0 &= \frac{(-42 + 5\Theta^2) + (6 + \Theta^2)(8 \cos \Theta - \cos 2\Theta)}{6\Theta^4} + \\ &\quad + j \frac{(-12\Theta + 6\Theta^3) + (6 + \Theta^2) \sin 2\Theta}{6\Theta^4}, \\ \alpha_1 &= \frac{14(3 - \Theta^2) - 7(6 + \Theta^2) \cos \Theta}{6\Theta^4} + j \frac{30\Theta - 5(6 + \Theta^2) \sin \Theta}{6\Theta^4}, \\ \alpha_2 &= \frac{-4(3 - \Theta^2) + 2(6 + \Theta^2) \cos \Theta}{3\Theta^4} + j \frac{-12\Theta + 2(6 + \Theta^2) \sin \Theta}{3\Theta^4}, \\ \alpha_3 &= \frac{2(3 - \Theta^2) - (6 + \Theta^2) \cos \Theta}{6\Theta^4} + j \frac{6\Theta - (6 + \Theta^2) \sin \Theta}{6\Theta^4}; \end{aligned} \quad (104)$$

the functions α_i can also be easily expanded in the convenient power series.

Appendix C

To obtain Eq.(43) we used the Dougall identity [18]

$$P_{\nu}^{-\mu}(\cos \theta) = \frac{\sin \nu \pi}{\pi} \sum_{n=0}^{\infty} (-1)^n \left(\frac{1}{\nu - n} - \frac{1}{\nu + n + 1} \right) P_n^{-\mu}(\cos \theta), \quad (105)$$

$-\pi < \theta < \pi$, $\mu \geq 0$, that can be rewritten as follows

$$P_{-\nu}(\cos \theta) = -\frac{\sin \nu \pi}{\pi} \sum_{n=-\infty}^{\infty} \frac{(-1)^n P_n(\cos \theta)}{\nu + n} \quad (106)$$

using the first identity from Eq.(33). Substitution of Eq.(106) into Eq.(40) (with $\cos \theta = \Delta$) yields the first equation in Eq.(43). Eq.(106) can be further transformed using the second identity from Eq.(33)

$$P_{-\nu}(-\cos \theta) = -\frac{\sin \nu \pi}{\pi} \sum_{n=-\infty}^{\infty} \frac{S_n P_n(\cos \theta)}{\nu + n}. \quad (107)$$

Substitution of Eq.(107) into Eq.(42) yields the second equation in Eq.(43).

Appendix D

The functions $D(x)$ and $E(x)$ introduced in Sec. 5., Eq.(37) satisfy the boundary conditions, Eq.(8), and in spectral domain (compare with Eq.(3))

$$E = j S_k D, S_k = k / \sqrt{k^2} \quad (108)$$

representing the field vanishing at infinity. Multiplying $D(x)$ and $E(x)$ by e^{-jmKx} we obtain the new functions $D'(x)$ and $E'(x)$

$$D'(x) = \sum_n P_n e^{-j(r+(n+m)K)x}, E'(x) = j \sum_n S_n P_n e^{-j(r+(n+m)K)x}. \quad (109)$$

which, after introduction of a new summation variable $n \Rightarrow n + m$ and straightforward rearrangement of sums can be rewritten as follows

$$D'(x) = \sum_n P_{n-m} e^{-j(r+nK)x}, E'(x) = j \sum_n S_{n-m} P_{n-m} e^{-j(r+nK)x}. \quad (110)$$

Taking a linear combination of terms like in Eq.(110) yields an arbitrary electric field components $D(x), E(x)$

$$D(x) = \sum_m \alpha_m \sum_n P_{n-m} e^{-j(r+nK)x}, E(x) = \sum_m \alpha_m \sum_n S_{n-m} P_{n-m} e^{-j(r+nK)x} \quad (111)$$

being the constituents of certain harmonic function $\Phi(x) = D(x) - jE(x)$, satisfying the boundary conditions, Eq.(8), but not necessarily Eq.(108). This property is exploited in Sec. 6.1. to represent the total field being the sum of the induced (“scattered” field) vanishing at infinity and external field (“incident” field) growing there.

References

- [1] Collin, R. E. *Field theory of guided waves*; McGraw-Hill: New York, NY, 1960.
- [2] Danicki, E.J. *IEEE Trans.* 2004, UFFC-51, 444–452.
- [3] Jones, D. S. *The Theory of Electromagnetism*; Pergamon Press: Oxford-London-New York-Paris, 1964.
- [4] Green, N. G.; Ramos, A.; Morgan, H. , *J. Electrostatics* 2002, 56, 235–254.
- [5] Mushelishvili, N. I. *Singular integral equations*; Nauka: Moscow, 1946.
- [6] Bløtekjær, K.; Ingebrigtsen, K. A.; Skeie, H. *IEEE Trans.* 1973, ED-20, 1133–1138.
- [7] Danicki, E.; Tasinkevych, Y. *J. Electrostatics* 2006, 64, 386—391.
- [8] Danicki, E. J.; Tasinkevych, Y. *J. Tech. Phys.* 2005, 46, 175-193.
- [9] Yen, J. T.; Steinberg, J. P.; Smith, W. *IEEE Trans.* 2000, UFFC-47, 93–110.
- [10] Seo, C. H.; Yen, J. T. *IEEE Ultrason. Symp. Proc.* 2007, 2381–2384.
- [11] Kühnicke, E. *Wave Motion* 2007, 44, 248–261.
- [12] Morgan, D. P. *Surface acoustic wave devices*; Elsevier Science Publishers B. V.: Amsterdam, 1991.
- [13] Moon, P.; Spencer, D. E. *Field theory for engineers*; D. Van Nostrand Company Inc.:Princeton, 1961.
- [14] Danicki, E. *IEEE Ultras. Symp. Proc.* 1996, 193–196.
- [15] Tasinkevych, Y. *Numerical efficiency of interdigital transducers charge spatial spectrum evaluation methods*; PhD thesis; IPPT PAN: Warsaw, 2004.
- [16] Press, W. H.; Teukolsky, S. A.; Vetterling, W. T.; Flannery, B. P. *Numerical Recipes in C. The art of scientific computing*; second ed.; Cambridge University Press, 1992.
- [17] Bausk, E.; Kolosovsky, E.; Kozlov, A.; Solie, L. *IEEE Trans.* 2002, UFFC-49, 1–10.
- [18] Erdélyi, A.; Magnus, W.; Oberhettinger, F.; Tricomi, F. G. *Higher Transcendental Functions*; McGraw Hill: New York: NY, 1953, Vol. 1.
- [19] Danicki, E. J. (2006). *Spectral theory of interdigital transducers of surface acoustic waves*. <http://www.ippt.gov.pl/~edanicki/danickibook.pdf>, Chapt. 3.
- [20] Erbas. B. *Wave Motion* 2007, 44, 282–303.
- [21] Crombie, P.; Bascom, P. A.; Cobbold, J. R. *IEEE Trans.* 1997, UFFC-44, 997–1009.
- [22] Arendt, J.; Svendsen, N. B. *IEEE Trans.* 1992, UFFC-39, 262–267.

- [23] Selfridge, A. R.; Kino, G. S.; Khuri-Yakub, B. T. *Appl. Phys. Lett.* 1980, 37, 35–36.
- [24] Fedoryuk, M. W. *The Steepest Descent Method*; Nauka: Moscow, 1977, Chapt. 3.
- [25] Felsen, L. B.; Marcuvitz, N. *Radiation and Scattering of Waves*; Prentice Hall: Englewood Cliffs, 1973, Vol. 1, Chapt. 4.
- [26] Abbott, B. P.; Hartmann, C. S. *IEEE Ultras. Symp. Proc.* 1993, 157–160.
- [27] Biryukov, S. V.; Polevoi, V. G. *IEEE Ultras. Symp. Proc.* 1997, 225–228.
- [28] Peach, R. C. *IEEE Trans.* 1981, SU-28, 96–105.

Chapter 8

REVIEW OF ELECTROPORATION

Sadhana Talele

The University of Waikato, New Zealand

Abstract

Electroporation also called *Electropermeabilization*, is the use of high magnitude electric field pulses to alter the permeability of a cell membrane. This change in permeability is achieved by using an electric field pulse to induce nanoscopic ‘pores’ in the cell membrane. These pores are commonly called ‘electropores,’ which is why the process is commonly referred to as *electroporation*.

Many biotechnological applications and research require transport of macromolecules such as genes, antibodies, and chemical drugs, into a host cell. For any particular application, choosing a given transfer process is based on its efficacy, ease of use and side effects. A characteristic shared by most of the chemical and biological techniques is that they are usually cell-type dependent and have relatively poor efficiencies. Therefore, methods which are both versatile and efficient are being searched for and investigated. Electroporation, first reported in 1982 (Neumann *et al.*, 1982), is one of the methods reported to be effective for such delivery. Since its inception, this method has been a valuable tool for *in vitro* delivery of small and large molecules into a large variety of cells. During this time, electroporation has been performed on living plants, animals, and humans (*in vivo* electroporation), with an increasing focus on therapeutic uses (Dev *et al.*, 2000; Smith and Nordstrom, 2000; Muramatsu *et al.*, 1998).

This chapter covers important aspects of electroporation including induced transmembrane potential, formation of pores, relation between pore radii and pore energy, pore density and current through electropores. This knowledge is useful for simulating electroporation results which can be helpful for making informed decisions about electroporation system parameters.

1. Introduction

1.1. The Cell Membrane

Biological membranes are the most common cellular structures in animals and plants. Characteristics of these membranes can be summarised (Israelachvili, 1992; Cotterill, 2002; Curtis and Barnes, 1983; Russell *et al.*, 2008; Grimnes and Martinsen, 2000) as follows

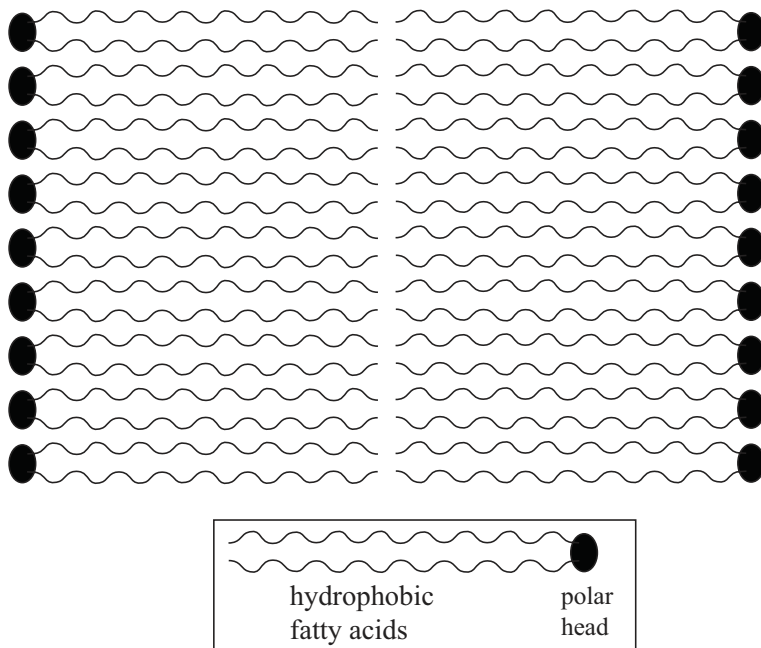


Figure 1. Bilayer lipid membrane (Adapted from (Grimnes and Martinsen, 2000)).

in the rest of the subsection. Membranes are involved in a number of cellular functions, and are complex and varied. A membrane is made mostly from a double layer of lipids (hydrophobic fatty acid chain molecules) and hydrophilic phosphorus molecules. Hence, the membrane is called a phospholipid bilayer. Lipids are water soluble, oily (greasy) organic substances, and are the most important storage forms of chemical energy in the body. A major component of the cell membrane are polar lipids. The cell membrane also is the basis for the capacitive nature of cells and tissues.

As seen in Figure 1, the phospho-heads cover the two surfaces of the bilayer and the fatty acid tails constitute the interior of the bilayer (Israelachvili, 1992; Grimnes and Martinsen, 2000). In Figure 2 the membrane embedded proteins, and sodium ionic channels are shown. The proteins are mostly involved with selective molecule transport across the membrane. Sodium ionic channels are involved in the electrogenic pump action explained below. Membranes commonly contain a number of proteins, a number of phospholipids and glycolipids with various headgroups, number of chains and chain lengths. In spite of the various complexities, membranes can be generalized to have the significant property that they exist as thin bilayer membranes. As the biological lipids tend to self-assemble, these structures are not fixed and are part of a very dynamic system.

A bilayer lipid membrane (BLM) has a very low electric conductivity and is thus closed for ion transport. The membrane thickness is about 5 nm, thus the membrane capacitance is very high, and the breakdown potential is low (Grimnes and Martinsen, 2000).

Membranes change their lipid composition in response to external stimuli. Under stress, a membrane may form a pore or a non-bilayer structure. More information on the membrane can be found in the book on intermolecular and surface forces by Israelachvili (1992); Grimnes and Martinsen (2000).

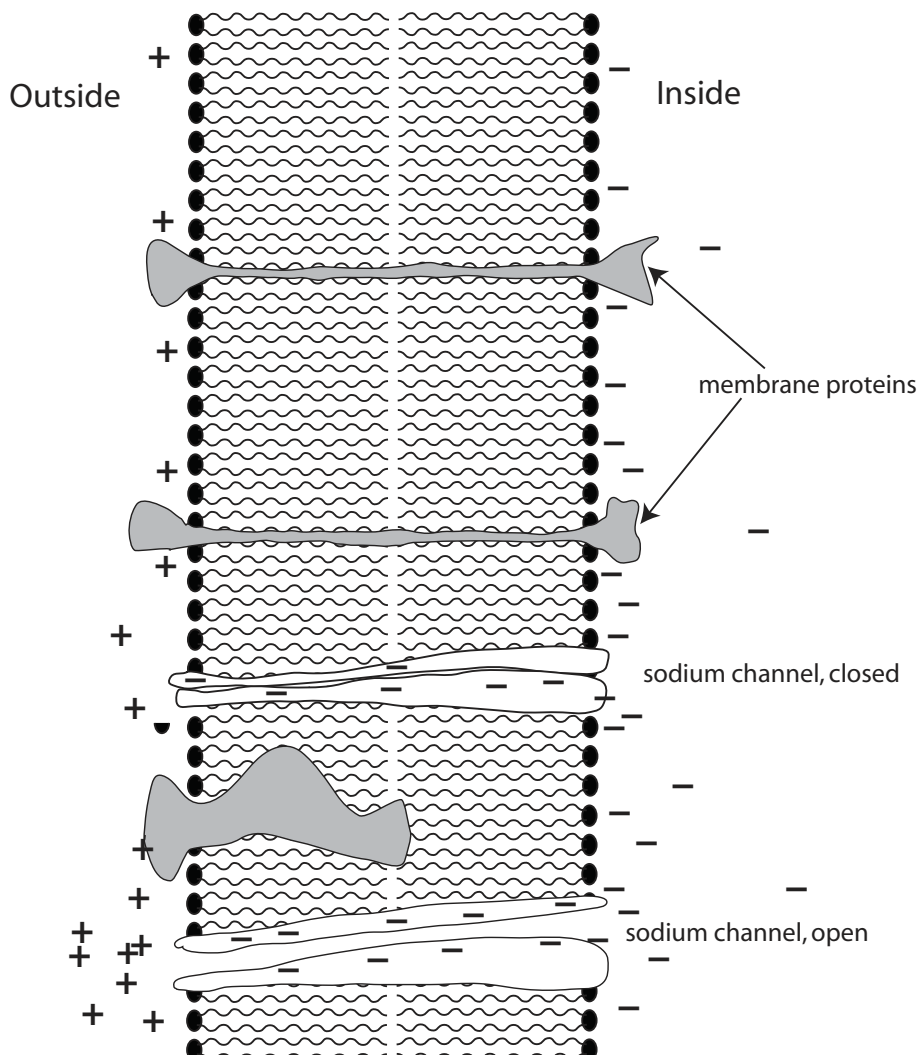


Figure 2. Bilayer lipid membrane with embedded proteins and sodium channels (Adapted from (Grimnes and Martinsen, 2000)).

1.2. Ion Pumps

Ion pumps consist mainly of sodium or potassium pumps that are embedded in the cell membrane (Grimnes and Martinsen, 2000; Israelachvili, 1992). Each pump translocates a greater electric charge (three Na^+ ions per cycle) in one direction than in the other (two K^+ ions per cycle)(Grimnes and Martinsen, 2000). Many such pumps operate in parallel in the cell membrane, thus together they are capable of generating an electrical potential difference of up to -90 to -40 mV across the membrane, the interior being at negative potential with respect to the extracellular liquid. As shown in Figure 3, for excitable cells (muscle and nerve cell) this potential is about -70 mV, for non-excitable cells only -10 to -20 mV (Grimnes and Martinsen, 2000).

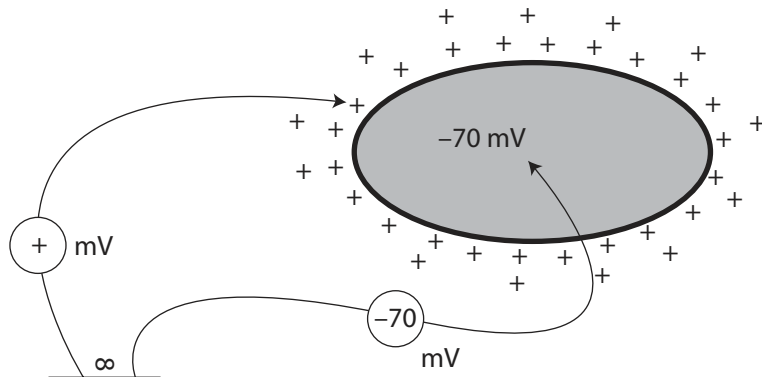


Figure 3. Rest potential: Intra and extra cellular potential of a cell under normal conditions.

2. Electroporation

It is possible to induce the formation of hole in a cell membrane by applying a sufficiently strong electric field pulse. This is known as electroporation. The effect is reversible when the cell membrane is temporarily permeated. Irreversible electroporation occurs when the cell membrane poration is of such a nature as to induce cell death. Section 3. discusses electroporation in more detail. Polarization is one of the basic mechanisms of interactions of membranes with electric fields, leading to electroporation and related phenomena of dielectrophoresis (Pohl, 1978; Neumann *et al.*, 1989) and electrofusion (Zimmermann, 1982; Neumann *et al.*, 1989; Zimmermann and Neil, 1996).

2.1. Polarization of Membranes

Polarization of membranes underlies their destabilization. Polarization is due to restricted motion of charges: electric fields exert forces on charges. These charges can either move if they are free (material is conductive) or accumulate if they are limited in their movement. This charge redistribution in a particular limited space leads to polarization. Figure 4 shows polarization of a single cell due to restriction by the cell membrane to the motion of ions.

2.2. Electric Field Interaction with Polarized Membranes

The interaction of external electric field with the polarized membranes results in forces which can induce motions inside particles. This motion can result in structural rearrangement or fracture in the material. This can subsequently lead to electroporation and related phenomenon in case of cell membranes (Pohl, 1978; Dimitrov, 1995). Membranes have low polarizability (relative dielectric constant about 5) and low conductivity (3×10^{-7} S/m) (Kotnik *et al.*, 1998). The cell membrane is generally bounded (externally and internally) by a medium of high dielectric constant (about 80) and a high conductivity (about 1.2 S/m). Application of external fields leads to accumulation of charge at the membrane surfaces; this creates an electric field inside the membrane that is much stronger than the surrounding

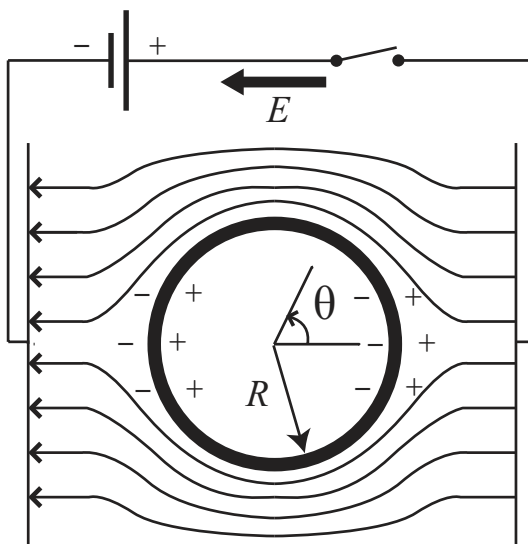


Figure 4. Spherical particle in electric field, E is the electric field (Adapted from (Dimitrov, 1995; Kinoshita *et al.*, 1992)).

field. The polarized membrane interacts with this field, resulting in structural rearrangements which can cause membrane poration.

2.3. Applications of Electroporation

There are many applications of electroporation/electropermeabilization (EP) in biotechnology, biochemistry, molecular biology, medicine and other biological research. Some of the applications are as follows:

1. Electrochemotherapy (ECT): In cancer chemotherapy, some drugs do not exhibit anti-tumour effects because of insufficient transport through the cell membrane (Miklavčič and Kotnik, 2004). A combined use of chemotherapeutic drugs and application of electric pulses is known as electrochemotherapy and is useful for local tumour control. Especially, bleomycin has been reported to have shown a 700-fold increased cytotoxicity when used in ECT (Cemazar *et al.*, 1998; Serša, 2000). This helps to achieve a substantial anti-tumour effect with a small amount of drug, that limits its side effects (Serša *et al.*, 1993). Bleomycin and cisplatin have proven to be much more effective in electrochemotherapy than in standard chemotherapy when applied to tumour cell lines *in vitro*, as well as *in vivo* on tumours in mice (Mir *et al.*, 1991, 1995; Serša *et al.*, 1995). Clinical trials have been carried out with encouraging results (Glass *et al.*, 1996; Serša *et al.*, 2000; Gothelf *et al.*, 2003; Kranjc *et al.*, 2005; Tozon *et al.*, 2005; Snoj *et al.*, 2005).
2. Electrogenetransfection (EGT): Application of electroporation for transfer of DNA into cells to effect some form of gene therapy, often referred to as electrogenetransfection, is currently being applied in some pre-clinical trials (Mir, 2000). It is presently considered to have large potential as a non-viral method to deliver genetic material

- into cells, the process aimed at correcting genetic diseases (Budak-Alpdogan *et al.*, 2005; Bertino, 2008).
3. Electrofusion (EF): Under appropriate physical conditions, delivery of electric pulses can lead to membrane fusion in close-contact adjacent cells. EF results in the encapsulation of both original cells' intracellular material within a single enclosed membrane and can be used to produce genetic hybrids or hybridomas (Zimmermann, 1982). Hybridomas are hybrid cells produced by the fusion of an antibody secreting stimulated B-lymphocytes, with a tumour cell that grows well in culture. The hybridoma is then able to continue to grow in culture, and a large amount of specific desired antibodies can be recovered after processing. Electrofusion has proved to be a successful approach in the production of vaccines (Scott-Taylor *et al.*, 2000; Orentas *et al.*, 2001), antibodies (Schmidt *et al.*, 2001), and reconstructed embryos in mammalian cloning (Gaynor *et al.*, 2005).
 4. Transdermal drug delivery (TDD): Application of high-voltage pulses to the skin allows a large increase in induced ionic and molecular transport across the skin barrier (Prausnitz *et al.*, 1993). This has been applied for transdermal delivery of drugs, such as metoprolol (Vanbever *et al.*, 1994), and also works for larger molecules, for example, DNA oligonucleotides (Vanbever *et al.*, 1994).
 5. Electroinsertion (EI): Another application of electroporation is insertion of molecules into the cell membrane. As the electric field induced membrane pores reseal, they entrap some of the transported molecules. Experiments on electroinsertion suggest the possibility of using the process to study certain physiological properties of these cells and understanding aspects of the lipid-protein interactions of the cell plasma membrane (Mouneimne *et al.*, 1992).

3. Overview of Electroporation

The phenomenon of the electric modification of cell membrane conductivity has been known since the 1940s (Cole, 1972). Sale and Hamilton (1967, 1968) observed that treatment of cells with intense electric field pulses led to cell lysis, and suggested that the cell membranes were damaged by the transmembrane potential induced by the applied electric field.

The transmembrane potential V_m was estimated from the equation, often referred to as the (steady-state) Schwan's equation (Schwan, 1957),

$$V_m = \frac{3}{2} E a \cos \theta, \quad (1)$$

where E is the applied external electric field, a is the radius of the cell, and θ is the angle between the direction of the field and the normal to the cell surface. The critical transmembrane potential built up for electroporation to occur was found to be about ± 1 V. The phenomenon was called 'electric breakdown' by Sale and Hamilton (1968).

It soon became apparent that a field-induced permeability increase is transient in nature although long-lived compared with the field duration. The term 'electropermeabilization' was used to explain the occurrence of permeability changes introduced by electrical

impulses in vesicular membranes (Neumann and Rosenheck, 1972). It was later shown by Rosenheck *et al.* (1975) that the electric field induced change was transient. The resistance changes in the membrane were attributed to dielectric breakdown (Zimmermann *et al.*, 1973).

Subsequent studies showed that the cell membranes of pulse treated cells were permeable to molecules of a size smaller than a certain limit, suggesting the creation of a porous membrane structure (Neumann and Rosenheck, 1972; Zimmermann *et al.*, 1973; Kinoshita and Tsong, 1977b). It was also found that under appropriate conditions, the cells could recover, which implied that these electropores were resealable and could be induced without permanent damage to the cell (Zimmermann *et al.*, 1980), and the cytoplasmic macromolecular contents could be retained (Kinoshita and Tsong, 1977a,b). Since then, a number of research groups have studied mechanisms of pore formation and detailed characteristics of the cell membranes modified by electric fields (Abidor *et al.*, 1979; Chernomordik *et al.*, 1983; Glaser *et al.*, 1988; Schwister and Deuticke, 1985).

However, the pores themselves were not observed until the invention of rapid freezing electron microscopy in the 1990s. Chang and Reese (1990) were the first to observe them. Other aspects of electroporation, for example, visualization of transmembrane potential and its evolution in space and time, resealing of pores and asymmetry in permeability of porated cells (sea urchin egg and liposomes) with the help of an optical microscope, were also reported (Kinoshita *et al.*, 1992; Hibino *et al.*, 1993). These microscopes have a time resolution of sub-microseconds suitable for studying electroporation.

3.1. Important Aspects of Electroporation

During the formative years of modern micro- and molecular biology, chemical and biological techniques were developed to transfer selected material through cellular membranes (Ausubel *et al.*, 1990). The ability to perform transmembrane transport of material is critical to many areas of research. Much of this research requires transport of macromolecules such as DNA, RNA, antibodies, chemical drugs, metabolites, molecular probes and various vesicles.

Research that is closely associated with electroporation, and has attracted more study among cell biologists and biophysicists, is that high voltage electric pulses can induce fusion of cells. The viable giant cells were first obtained by Neumann *et al.* (1980) by simple electro-pulsing of a suspension of cells. Later, it was suggested to make use of the phenomenon of dielectrophoresis (Pohl, 1978), to acquire close contact between cells (Scheurich and Zimmermann, 1981). Dielectrophoresis is the movement of relatively non-conducting or charged particles (cells) in a non-uniform AC electric field (Pohl, 1978). If a number of particles are present, appropriate particle size, density of particles, electric field magnitude and frequency can induce cells to aggregate in long chains (pearl chain) in an alternating electric field (Zimmermann, 1982).

In 1982, transfection of a foreign gene into eukaryotic cells by the electroporation method was reported (Neumann *et al.*, 1982). Transfection involves opening transient pores in the cell plasma membrane, to allow the uptake of genetic material. It was also reported that the transfected gene was expressed in the host cells (Neumann *et al.*, 1982). Since then, electroporation has become accepted as an effective technique for introduction of for-

eign DNA into cells of any origin (Potter, 1988; Neumann *et al.*, 1989). The ease of the electroporation technique and its applicability to a variety of cells has led to investigations of DNA electrotransfer into various tissues. The utility of *in vivo* electroporation for entry of molecules has been demonstrated through an increasing number of new applications that have been developed each year (Jaroszeski *et al.*, 2000; Saulis and Šatkauskas, 2004b; Talele and Gaynor, 2008).

Experiments in 1989 on frog skin showed that electroporation could be made to occur repeatedly in a tissue without evident damage (Powell *et al.*, 1989). Further research has shown that the electroporation of the skin could be used to enhance transdermal drug delivery (Prausnitz *et al.*, 1993, 1994).

In 1989 it was reported that upon application of electric fields pulses on a suspension of cells in the presence of a selected membrane protein, implantation of the protein in the cell's plasma membrane was possible (Mouneimne *et al.*, 1989). This phenomenon is called electroinsertion. Later, electroporation of excitable membranes was observed (O'Neil and Tung, 1991). Electrically induced membrane breakdown of isolated cardiac cells was reported. Chen and Lee (1994) reported the asymmetrical electroporabilization of frog skeletal muscle fibres with respect to the stimulation pulse polarity.

A method of electroporation has been applied *in vivo* to introduce anticancer drugs to tumorous tissue in order to obtain therapeutic effects (Mir *et al.*, 1991). The main factors that play a crucial role in obtaining high responses of the treatment are the drug used in the treatment and the appropriate electric pulses delivered to the tumour. This phenomenon is called electrochemotherapy.

Electroporation has been investigated and refined to an extent that, for most applications, it is simpler and more efficient than rival chemical and biological processes (Chang *et al.*, 1992; Neumann *et al.*, 1989). However, the mechanisms of electroporation are still not fully understood and there are aspects of the process which are, as yet, suboptimal in their possible performance. Optimization of the parameters of electric pulses for any specific application is still needed (Jaroszeski *et al.*, 2000; Saulis and Šatkauskas, 2004b)

4. Response of Cell to Electrical Field

From an electrical point of view, the cell can be described as an electrolyte (the cytoplasm) surrounded by an electrically insulating cover (the cell membrane). Under physiological conditions, extracellular space is also an electrolyte. As a simple approximation, one may treat the membrane as non-conducting (purely dielectric), and the intracellular and the extracellular space as purely conductive (having insignificant dielectric permittivity).

4.1. Membrane Rest Potential

Under physiological conditions, a potential in the range of -90 mV up to -40 mV (most commonly -70 mV) is always present on the cell membrane (Cole, 1972). This potential is caused by a tiny deficit of positive ions in the cytoplasm leading to a charge imbalance that is a consequence of the transport of specific ions (Na^+ and K^+) across the membrane. This transport is driven towards the electrical and ion concentration equilibrium. Once this equilibrium is reached, the electrical slope across the membrane determines the

resting transmembrane potential. This is the normal physiological condition of any healthy cell. The unbalanced ions responsible for the membrane rest potential represent a very small fraction of all the ions in the cytoplasm, so that the osmotic pressure difference (hydrostatic pressure produced by a difference in concentration between solutions on the two sides of a semipermeable membrane) generated by this imbalance is negligible (Kotnik, 2003). The membrane also acts as a charged capacitor, with the unbalanced ions accumulating close to its surface, so that the cytoplasm can in general be viewed as electrically neutral.

4.2. Induced Transmembrane Potential

When a biological cell is exposed to an electric field, a local distortion of the field in the cell and its vicinity takes place. Due to the low membrane conductivity, the field is concentrated in the cell membrane, where it is several orders of magnitude larger than in the cytoplasm and the extracellular region. This results in an induced transmembrane potential V_m , this transmembrane potential superimposes to the membrane rest potential (Kotnik, 2003). When an isolated spherical cell is exposed to a DC homogeneous electric field, the voltage induced on the cell membrane is determined by solving Laplace's equation. For the first approximation, the cell membrane can also be treated as initially nonconductive. Under these assumptions, the transmembrane potential is given by Schwan's Equation, see Equation 1 (Schwan, 1957). Schwan's equation implies that the transmembrane potential varies proportionally to the cosine of the angle and the maximum potential is induced at the points where the electric field is perpendicular to the membrane, namely at $\theta = 0^\circ$ and $\theta = 180^\circ$, the points referred to as the 'poles' of the cell. The formula describes the static situation, and can safely be applied to yield the steady-state value of the induced transmembrane potential.

4.3. Effect of Membrane Rest Potential on Induced Transmembrane Potential

Recall that the transmembrane potential superimposes to the membrane rest potential. If an applied electric field produces a transmembrane potential of the same orientation of the inherent rest potential, then they add. Conversely, if the applied electric field produces a transmembrane potential in the opposite orientation of the inherent rest potential, then they subtract. Thus one pole is likely to experience a transmembrane potential about 140 mV (assuming a rest potential of -70 mV) lower than the other pole, and can result in asymmetry in permeability around the cell.

5. Formation of Pores

Equation 1 for the transmembrane potential is valid only until pores are formed. Once enough pores are formed, the membrane conductivity changes and Schwan's equation is no longer valid. This phenomenon of electroporation has often been referred to as 'electrical breakdown' or electropermeabilization.

A few well observed and documented characteristics of the cell membrane electroporation can be summarised as follows:

1. The transmembrane potential must exceed a certain threshold value $V_{m(cr)}$ for electroporation to occur (Hibino *et al.*, 1991; Kinoshita *et al.*, 1992).
2. It is thought, most probably, that it is the lipid part of the biological membrane which is transiently permeabilized by an electroporation pulse (Chernomordik *et al.*, 1987; Chang and Reese, 1990).
3. Electropore formation can be asymmetrical: pore populations in two hemispheres may differ in the size and (or) number of pores (Kinoshita *et al.*, 1992).
4. The change of the membrane permeability caused by the pore formation can be fully reversed. When the pulse parameters, number of pulses and the medium properties are properly chosen, electropores have a finite lifetime (Swezey and Epel, 1989; Kinoshita and Tsong, 1977a,b; Saulis and Šatkauskas, 1977; Saulis *et al.*, 1991).
5. The increased permeability can be sufficient enough to allow ions and small molecules as well as macromolecules to enter or leave the cell (Kinoshita and Tsong, 1977b; Liang *et al.*, 1988; Graziadei *et al.*, 1991; Sheng *et al.*, 1995; Swezey and Epel, 1989; Yumura *et al.*, 1995).
6. The uptake through pores is greater in a solution of low ionic strength (Kinoshita and Tsong, 1977a; Rols and Teissié, 1989; Teissié and Tsong, 1981).
7. Permeability is bidirectional, that is, intracellular compounds (e.g., ions, glycine, ATP, proteins) can leak from electroporated cells (Moser *et al.*, 1995; Neumann and Rosenheck, 1972; Schwister and Deuticke, 1985), while foreign substances can enter the cell (Kinoshita and Tsong, 1977a,b; Swezey and Epel, 1989; Zimmermann *et al.*, 1980).
8. Phospholipids in the membrane exhibit major structural changes under electroporation conditions (Neumann *et al.*, 1992). There appears to be a rapid transition (within 1 μ s) from hydrophobic to hydrophilic pores (see section 5.1.).

This dependence of pore number, size, and evolution characteristics are researched theoretically with results reported in detail in the research articles Talele and Gaynor (2007); Krassowska and Filev (2007); Smith *et al.* (2004). In early years a basic concept of the transient aqueous pore hypothesis was that they are membrane ‘defects’ or ‘membrane perforations’ (Neumann, 1989), that are created with rapidly increasing rate as transmembrane potential V_m is increased. If the magnitude of V_m increases from zero due to the applied external electric field, then the additional membrane energy associated with V_m leads to increased pore creation probability. The rate of pore creation increases nonlinearly with larger V_m . A pore population described by a pore density function quickly increases with respect to increasing V_m , and gives the cell membrane rapidly changing electrical conductance thus reducing the rate at which pores can be created.

5.1. Types of Pores and Their Characteristics

Based on the observation by Chang and Reese (1990) where a rapid freezing electron microscopy was used to show volcano-shaped pores in erythrocyte membranes exposed to

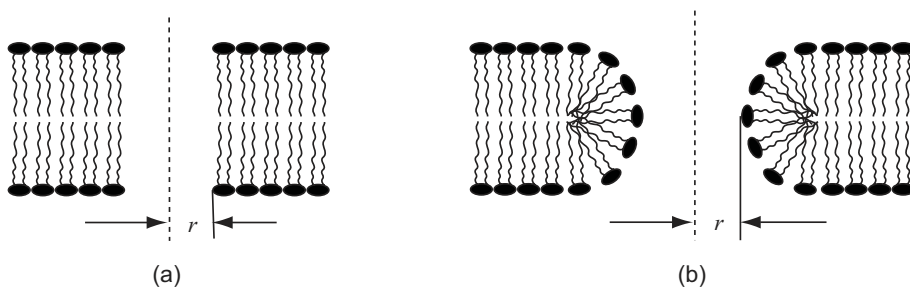


Figure 5. Types of electropores: (a) Hydrophobic (nonconducting pore), (b) Hydrophilic pore (conducting pore).

an intense electric pulse (Weaver and Barnett., 1992; Kakorin *et al.*, 1996), it is currently thought that initial electroporation involves the rearrangement of clusters of lipids' pore structures (Tekle *et al.*, 2001; Saulis and Šatkauškas, 2004a) with minimum pore size in the order of a few nanometres. This is in agreement with the results obtained from other pore models. These pore models take into consideration energy changes in the bilayer membrane due to pore formation.

The pores are assumed to be hydrophobic or hydrophilic. The hydrophobic pores, as shown in Figure 5a (Abidor *et al.*, 1979; Neu and Krassowska, 1999; Glaser *et al.*, 1988), are simply gaps in the lipid bilayer of the membrane, formed as a result of thermal fluctuations. The primary pores that participate in electrical behaviour and molecular transport are thought to be hydrophilic pores, with a minimum radius of about 1 nm, and a reasonable probability of various pore sizes much larger (Weaver, 1993). The 'hydrophilic' or 'inverted pores,' as shown in Figure 5b, have their walls lined with the water-attracting heads of lipid molecules. Hence, the hydrophilic pores allow the passage of water-soluble substances, such as ions, while the hydrophobic pores do not. In the remainder of this chapter, the hydrophilic pores will be referred to as conducting, and the hydrophobic pores, as nonconducting. Similar notation is used in the literature (Abidor *et al.*, 1979; Neu and Krassowska, 1999; Glaser *et al.*, 1988; Weaver and Chizmadzhev, 1996).

5.2. Relation between Pore Radius and Pore Energy

Research has established that pore radius and pore energy are related (Abidor *et al.*, 1979; Glaser *et al.*, 1988; Weaver and Chizmadzhev, 1996; Neu and Krassowska, 1999) as shown in Figure 6.

5.2.1. Energy of a Pore

The energy function consists of two parts, $u(r)$ for the energy of non-conducting pores and $w_c(r)$ the energy of conducting pores as shown in Figure 6a. The energy $w(r)$ of a pore of radius r is the lesser of $u(r)$ and $w_c(r)$ (see Figure 6b) (Neu and Krassowska, 1999). This is the pore energy in absence of an applied external V_m . The pore energy $w(r)$ has two maxima, at r_* and r_d , and a local minimum at r_m . The pore energies at r_* , r_m , and r_d are denoted by $w_* = w(r_*)$, $w_m = w(r_m)$, and $w_d = w(r_d)$. This plot in Figure 6 is

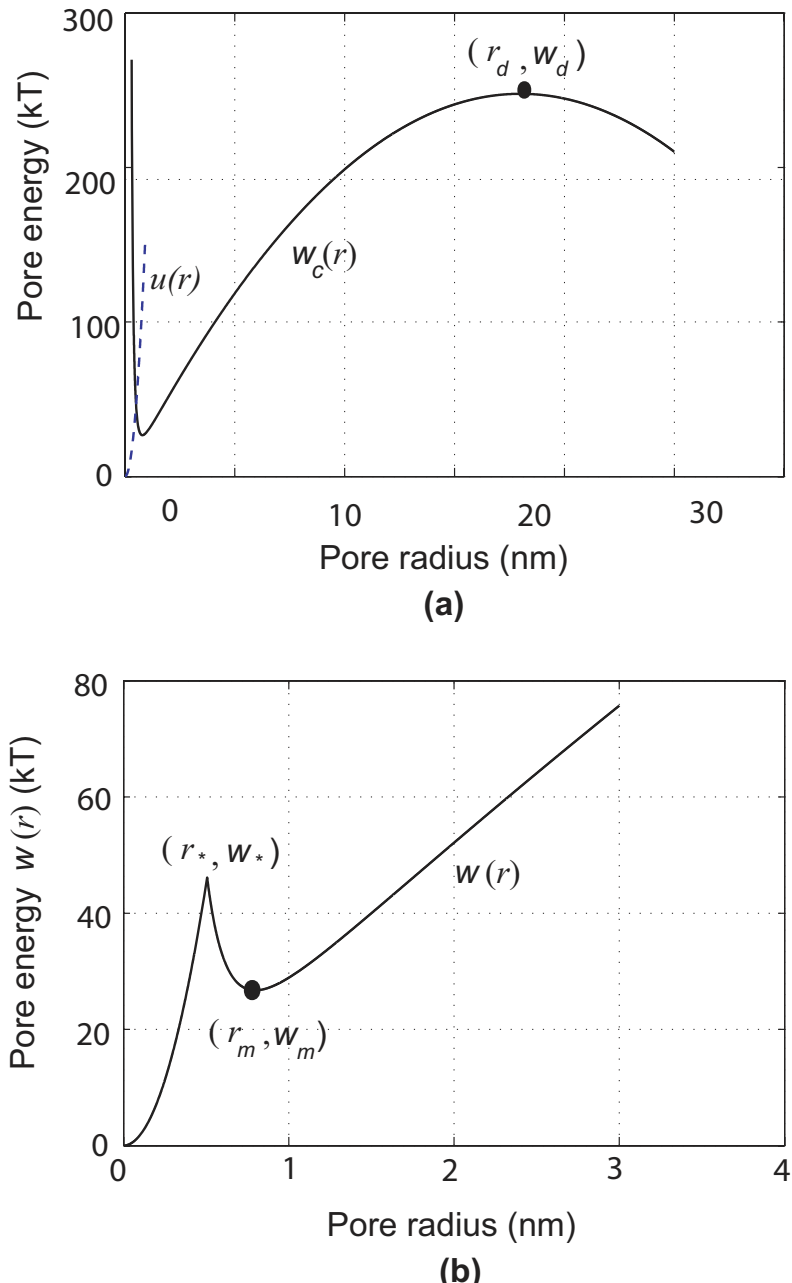


Figure 6. Pore-energy function at zero transmembrane potential: (a) The pore-energy function of a non-conducting (dotted line) and conducting (solid line) pore. Adapted from (Abidor *et al.*, 1979; Glaser *et al.*, 1988; Weaver and Chizmadzhev, 1996; Neu and Krasowska, 1999). (b) Lesser energy of the conducting and non-conducting pore. Pore-energy function is enlarged for a shorter range of radius.

calculated using the values of parameters in Table 1 and the form of $w(r)$ given by Neu and Krassowska (1999).

5.2.2. Energy of the Nonconducting Pores

The energy $u(r)$ of the nonconducting pores is given in the literature in terms of Bessel functions, and is well approximated by the quadratic function (Neu and Krassowska, 1999),

$$u(r) = w_* \left(\frac{r}{r_*} \right)^2. \quad (2)$$

5.2.3. Energy of the Conducting Pores

The energy $w_c(r)$ of conducting pores is given by (Neu and Krassowska, 1999)

$$w_c(r) = 2\pi w_{ed}r - \pi\xi_0 r^2 + \left(\frac{w_{stc}}{r} \right)^4. \quad (3)$$

The theory of electroporation of the cell membrane is similar to the theory of soap film rupture. If one imagines a membrane with surface tension ξ_0 and then cuts a hole of radius r , the energy change in the system due to the hole is given by the first two terms in Equation 3. The lipid head groups are assumed to line the pore interior, thus the pores are conducting. The appearance of a circular pore in a membrane with surface tension ξ_0 is balanced by the presence of two competing energy terms: increase in energy barrier by a linear edge component proportional to pore edge of length $2\pi r$ (Weaver and Powell, 1989; Glaser *et al.*, 1988; Abidor *et al.*, 1979) (first term Equation 3) and reduction in energy barrier proportional to removal of pore area πr^2 (second term in Equation 3). Here w_{ed} is the energy per unit length of the pore perimeter (pore edge energy) and ξ_0 is the tension of a membrane without pores.

The lipid head groups which line the pore interior, tend to repel each other due to steric and/or electrostatic interactions (Weaver and Chizmadzhev, 1996; Israelachvili, 1992) and are taken into account by adding the third term (Neu and Krassowska, 1999) of Equation 3. This steric repulsion is responsible for the increase in pore energy with shrinking radius (Weaver and Chizmadzhev, 1996; Neu and Krassowska, 1999), since it gives a local minimum of w at non-zero radius. Here w_{stc} is the steric repulsion energy constant. In absence of the steric repulsion term the pores would shrink to zero radius, whereas in reality their radii are about 0.76 nm, which corresponds to the local energy minimum (DeBruin and Krassowska, 1999; Neu and Krassowska, 2003; Krassowska and Filev, 2007).

5.2.4. Energy of a Pore in the Presence of Non-zero Transmembrane Potential

The existence of transmembrane potential diminishes the energy barrier to pore formation and thus the energy of a pore is modified in the presence of V_m as given by (Abidor *et al.*, 1979; Neu and Krassowska, 1999; Weaver and Mintzer, 1981)

$$w(r, t) = w(r) - \pi a_p V_m^2(t) r^2, \quad (4)$$

where the second term represents an energy drop across the capacitive membrane (Abidor *et al.*, 1979). The coefficient a_p is a property of the membrane and its aqueous environment.

Table 1. Values of parameters used to plot Figure 6

Symbol	Value	Description
r_*	0.51×10^{-9} (m)	minimum radius of hydrophilic pores ^a
r_m	0.76×10^{-9} (m)	minimum energy radius at $V_m=0$ ^a
r_d	18 (nm)	radius at global maximum ^a
w_*	45 (kT)	energy at local maximum ^a
w_m	25.6 (kT)	energy at local maximum ^a
w_d	238 (kT)	energy at global maximum ^a
a_p	6.9×10^{-2} (Fm $^{-2}$)	constant to calculate energy drop across membrane ^b
w_{stc}	9.67×10^{-15} (J $^{1/4}m$)	steric repulsion energy constant ^b
w_{ed}	1.8×10^{-11} (Jm $^{-1}$)	edge energy ^b
ξ_0	1×10^{-3} (Jm $^{-2}$)	tension of the bilayer without pores ^b

^aValues taken from Glaser *et al.* (1988).

^bValues taken from Neu and Krassowska (1999).

Here, the time dependence of the energy is due to the temporal variation of V_m . Also, as seen in Figure 7, the radius corresponding to the local energy minimum increases for higher transmembrane potential. All pores are initially created hydrophobic at a rate determined by their energy as shown in Figure 6 (Smith *et al.*, 2004). Most of them are quickly destroyed by lipid fluctuations. But if hydrophobic pores of radius $r > r_*$ are created, they spontaneously convert to long lived hydrophilic pores. The hydrophilic pores are created within a small range of radii just above r_* and immediately move (expand) toward minimum energy status of radius r_m (Glaser *et al.*, 1988; Neu and Krassowska, 1999, 2003; Smith *et al.*, 2004; Krassowska and Filev, 2007). This is the scenario considered in the model discussed by Talele and Gaynor (2007).

5.2.5. Bilayer Membrane Energy

The most important entity that affects the pore formation, growth and decay is the pore energy, $w(r)$ at any given time. This energy is a function of pore radius which is a function of space and time. Formation of pores cause dynamic changes in transmembrane potential V_m , that must be included. The pores also affect surface tension which also must be included. Theoretical accuracy of prediction of pores can be only as accurate as the correctness of pore energy, $w(r)$. This theory of the energy function $w(r)$ is applicable only to a single pore, as it does not account of any interactions between the pores. As the radius of any pore of the cell increases, it relaxes the tension of the other pores, decreasing the effective tension experienced by each pore. It follows that pore formation will lead to variations in the tension. This is in agreement with Benachir and Lafleur (1996), whose experimental results suggested that the membrane surface tension must be variable. This tension coupling can be taken into account in terms of the total area A_p occupied by all the pores at any given time. Thus Equation 3 is suitably modified and reported by Smith *et al.*

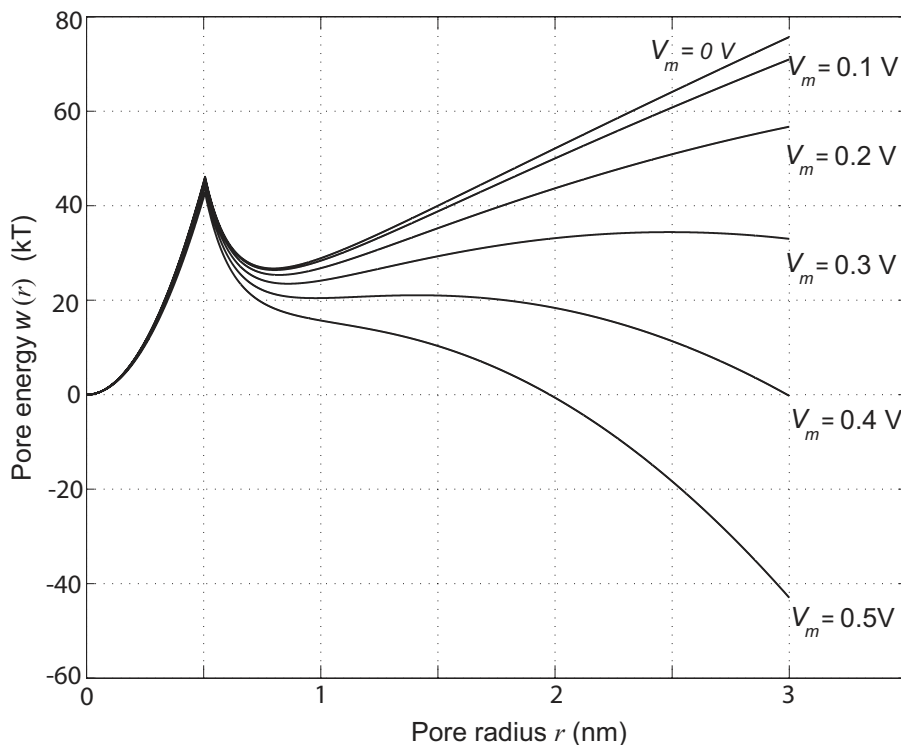


Figure 7. The pore-energy function of a pore at transmembrane potential $V_m = 0, 0.1, 0.2, 0.3, 0.4$, and 0.5 V based on references (Abidor *et al.*, 1979; Glaser *et al.*, 1988; Weaver and Chizmadzhev, 1996; Smith *et al.*, 2004). This plot uses the values of parameters in Table 1 as per literature (Neu and Krassowska, 1999)

(2004), to accommodate pores of various sizes. The bilayer energy is then given by,

$$w_m = \sum_{q=1}^Q \left[w_{st} \left(\frac{r_*}{r_q} \right)^4 + 2\pi w_{ed} r_q - \pi \xi_{eff}(A_p) r_q^2 + \int_0^{r_q} F_p(r_q, V_m) dr \right], \quad (5)$$

where summation is over the Q pores in the bilayer membrane. The terms in this equation are explained in the following paragraphs.

The lipid head groups which line the pore interior, tend to repel each other due to steric and/or electrostatic interactions (Weaver and Chizmadzhev, 1996; Israelachvili, 1992; Neu and Krassowska, 1999) and are taken into account by the first term in Equation 5, where w_{st} is the steric repulsion energy (Neu and Krassowska, 2003).

The appearance of a circular pore in a membrane is balanced by the presence of two competing energy terms: reduction in energy barrier proportional to removal of pore area πr_q^2 (third term in Equation 5) and increase in energy barrier by a linear edge component proportional to pore edge of length $2\pi r_q$ (Weaver and Powell, 1989; Glaser *et al.*, 1988; Abidor *et al.*, 1979) (second term in Equation 5). Here, w_{ed} is the pore edge energy, and ξ_{eff}

is the effective tension of the membrane given by

$$\xi_{\text{eff}}(A_p) = 2\xi' - \frac{2\xi' - \xi_0}{\left(1 - \frac{A_p}{A}\right)^2} \quad (6)$$

where ξ' is the energy per area of the hydrocarbon-water interface (Israelachvili, 1992; Neu and Krassowska, 2003), ξ_0 is the tension of a membrane without pores and A is the total area of the lipid bilayer. A varying value of the total area A_p occupied by the pores at any given time is given by

$$A_p = \sum_{q=1}^Q \pi r_q^2 \quad (7)$$

and contributes to a dynamic effect of pore formation both temporally and spatially.

The last term in Equation 5 is the contribution of the membrane potential to the bilayer energy (Neu and Krassowska, 2003). Assuming the inner surface of a pore as toroidal (Kandušer *et al.*, 2003; Neu and Krassowska, 2003), the electric force F_p acting on the pore is given by

$$F_p(r, V_m) = \frac{F_{\max}}{\left(1 + \frac{r_h}{r+r_t}\right)} V_m^2. \quad (8)$$

This equation is a heuristic approximation (Neu and Krassowska, 2003) of the numerical solution which the authors have computed for the electrical force acting on a pore derived from first principles; r_h and r_t are constants taken from Neu and Krassowska (2003). This equation is thought to be appropriate for larger pores as it predicts that F_p approaches a constant value F_{\max} as the pore radius increases, rather than increase linearly (Abidor *et al.*, 1979), or decrease to zero (Barnett and Weaver, 1991; Joshi *et al.*, 2002; Pastushenko and Chizmadzhev, 1982) as radius increases. The Equation 5 is useful for modelling electroporation.

6. Calculation of Pore Density

The theoretical understanding of the electroporation process is based on the partial differential equation (PDE) known as the Smoluchowski equation (SE), (Freeman *et al.*, 1994; Barnett and Weaver, 1991; Pastushenko *et al.*, 1979; Weaver and Mintzer, 1981). The SE describes the evolution of membrane pore population density in terms of the number and size of the pores. Solution of this PDE requires several constants whose values can neither be measured directly nor are known accurately (Barnett and Weaver, 1991), thus the SE is useful in giving only a qualitative picture of electroporation, for a spatially clamped uniformly polarised membrane area (Neu and Krassowska, 1999).

As seen in Figure 6 and 7, the radius at the minimum pore energy r_m only weakly depends on the transmembrane potential V_m , hence can be considered to be independent of V_m . For the purpose of the mathematical modelling electroporation, initially pores are assumed to be formed with the minimum-energy radius $r_m = 0.76$ nm (as measured from the graph in Figure 6b), at the rate given by DeBruin and Krassowska (1999); Smith *et al.*

(2004); Krassowska and Filev (2007),

$$\frac{dN}{dt} = \psi e^{(V_m/V_{ep})^2} \left(1 - \frac{N}{N_{eq}(V_m)} \right), \quad (9)$$

where N is the pore density of the initial small pores formed, ψ is the creation rate coefficient and N_{eq} is the equilibrium pore density for a potential V_m given by

$$N_{eq}(V_m) = N_0 e^{b(V_m/V_{ep})^2}. \quad (10)$$

Here, N_0 is the initial pore density with no applied electric field, V_{ep} is the characteristic voltage of electroporation and

$$b = (r_m/r_*)^2 \quad (11)$$

is the pore creation constant where r_* is the minimum radius of hydrophilic pores and r_m the minimum-energy radius (Neu and Krassowska, 2003). The value of constant V_{ep} is given by DeBruin and Krassowska (1999), who had chosen it to fit experimental data. Further details of this equation are given by Neu and Krassowska (1999), who take the pore density equation to be a result of the asymptotic model that is an approximation to the Smoluchowski Equation (SE)-based models. The asymptotic ordinary differential equation (ODE) described here is easier to solve, requires constants which can be easily related to experimental measurements, and has been shown to be valid even if the applied electric field has frequency in the megahertz range (Neu and Krassowska, 1999).

6.1. Current through a Single Pore

In order to model the response of a single cell to an applied electric field, it is important to be able to find the value of electric current i_{sml} , that flows through each pore of the cell membrane. As mentioned above, the cell membrane is embedded in an electrolytic solution. Figure 8 shows a cross section of the membrane through the centre of a pore. As mentioned by Barnett and Weaver (1991) and Glaser *et al.* (1988), the mathematical formulation of this three dimensional problem consists of a set of coupled differential equations that cannot be solved analytically. However, if the potential across the membrane can be found, then the Nernst-Planck equation of the corresponding one dimensional problem can be reduced and further used to solve the three dimensional case. The following discussion in this section draws heavily upon Barnett and Weaver (1991), Glaser *et al.* (1988) and DeBruin and Krassowska (1999). The Nernst-Planck equation for the current density in the pore is

$$j_x = -z_x F D_f \left(\nabla \kappa_x + \frac{z_x F \kappa_x}{RT} \nabla \Phi \right) \quad (12)$$

for an ion species x with valence z_x where D_f is the diffusion constant, F is Faraday's constant, R is the universal gas constant, T is the absolute temperature, $\kappa_x(x, y, z)$ is the concentration of the ion species and $\Phi(x, y, z)$ is the electric potential. In order to model the interior of a pore in a cell membrane, we take the z-axis perpendicular to the membrane and assume cylindrical symmetry around the z-axis. Thus $\kappa = \kappa(z)$ and $\Phi = \Phi(z)$. Now

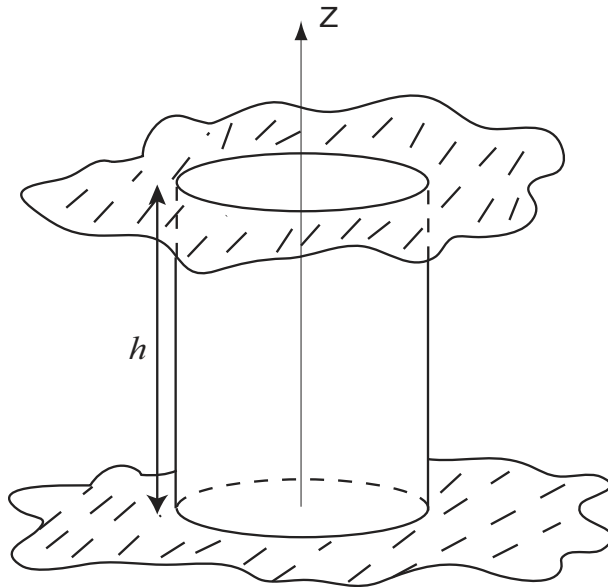


Figure 8. Cross section of a pore in the membrane.

the z -component of Equation 12 is,

$$\begin{aligned} j_x &= M \left(\frac{d\kappa}{dz} + \varrho\kappa \frac{d\Phi}{dz} \right) \\ &= M \exp[-\varrho\Phi] \frac{d}{dz} (\kappa \exp[\varrho\Phi]) \end{aligned} \quad (13)$$

where $M = -z_x F D_f$ and $\varrho = z_x F / RT$. Hence

$$\begin{aligned} \frac{j_x}{M} \int_0^h \exp[\varrho\Phi] dz &= \int_0^h \frac{d}{dz} (\kappa \exp[\varrho\Phi]) dz \\ &= \kappa(h) \exp[\varrho\Phi(h)] - \kappa(0) \exp[\varrho\Phi(0)] \end{aligned} \quad (14)$$

where h is the thickness of the cell membrane, $z = 0$ is taken to be the inner surface of the membrane and $z = h$ the outer surface. Thus

$$\begin{aligned} j_x &= M \frac{\kappa(h) \exp[\varrho\Phi(h)] - \kappa(0) \exp[\varrho\Phi(0)]}{\int_0^h \exp[\varrho\Phi(z)] dz} \\ &= M \frac{\kappa(h) - \kappa(0) \exp[\varrho\Phi(0) - \varrho\Phi(h)]}{\int_0^h \exp[\varrho\Phi(z) - \varrho\Phi(h)] dz} \\ &= z_x D_f F \frac{[x]_{\text{in}} \exp\left(\frac{z_x F}{RT} [\Phi(0) - \Phi(h)]\right) - [x]_{\text{ex}}}{\int_0^h \exp\left(\frac{z_x F}{RT} [\Phi(z) - \Phi(h)]\right)} dz \end{aligned} \quad (15)$$

where $\kappa(0) \equiv [x]_{\text{in}}$ is the internal concentration of ion x and $\kappa(h) \equiv [x]_{\text{ex}}$ is the external concentration. To evaluate the integral in the denominator one must know the form $\Phi(z)$

takes. Let us assume $\Phi(z) = \Phi_{\text{ext}}(z) + \Phi_B(z)$, namely the sum of the potential due to the applied electric field and the Born energy caused by the interactions of the ions with the pore walls. Φ_{ext} can be taken to be varying linearly across the membrane, with $\Phi_{\text{ext}}(0) = \Phi_{\text{in}}$ and $\Phi_{\text{ext}}(h) = \Phi_{\text{ex}}$. Thus

$$\Phi_{\text{ext}}(z) = \Phi_{\text{in}} - [\Phi_{\text{in}} - \Phi_{\text{ex}}] \frac{z}{h}. \quad (16)$$

So

$$\begin{aligned} \frac{z_x F}{RT} [\Phi_{\text{ext}}(z) - \Phi_{\text{ext}}(h)] &= \frac{z_x F}{RT} [\Phi_{\text{in}} - \Phi_{\text{ex}}] \left(1 - \frac{z}{h}\right) \\ &= z_x v_m \left(1 - \frac{z}{h}\right) \end{aligned} \quad (17)$$

As for the Born energy, we follow Glaser *et al.* (1988), and assume $\Phi_B(z) = z_x t_B(z)$, where $t_B(z)$ is a trapezoidal function. This is based on the assumption that the interactions of the ion type x with the walls of the pore are described by an energy barrier given by,

$$w(z) = \frac{F}{RT} [t_B(z) - t_B(h)] = \begin{cases} w_0 \frac{z}{d} & 0 \leq z < d \\ w_0 & d \leq z < h-d \\ w_0 \frac{h-z}{d} & h-d \leq z \leq h, \end{cases} \quad (18)$$

where w_0 is the energy barrier within the pore. The Born energy function is shown in Figure 9. Thus

$$\frac{z_x F}{RT} [\Phi_B(z) - \Phi_B(h)] = z_x^2 w(z). \quad (19)$$

Now, using these assumptions in Equations 16 to 19, the integral in the denominator of Equation 15 can be evaluated as follows.

$$\begin{aligned} I &= \int_0^h \exp \left(\frac{z_x F}{RT} [\Phi(z) - \Phi(h)] \right) dz \\ &= \int_0^d \exp \left(z_x v_m - z_x \left[\frac{v_m}{h} - \frac{z_x w_0}{d} \right] z \right) dz \\ &\quad + \int_d^{h-d} \exp \left(z_x v_m + z_x^2 w_0 - \frac{z_x v_m}{h} z \right) dz \\ &\quad + \int_{h-d}^h \exp \left(z_x v_m + \frac{z_x^2 w_0 h}{d} - z_x \left[\frac{v_m}{h} + \frac{z_x w_0}{d} \right] z \right) dz \\ &= \frac{hn}{z_x^2 w_0 - z_x v_m n} (\exp[z_x v_m + z_x^2 w_0 - nz_x v_m] - \exp[z_x v_m]) \\ &\quad - \frac{hn}{z_x v_m n} (\exp[z_x^2 w_0 + nz_x v_m] - \exp[z_x v_m + z_x^2 w_0 - nz_x v_m]) \\ &\quad - \frac{hn}{z_x^2 w_0 + z_x v_m n} (1 - \exp[z_x^2 w_0 + nz_x v_m]), \end{aligned} \quad (21)$$

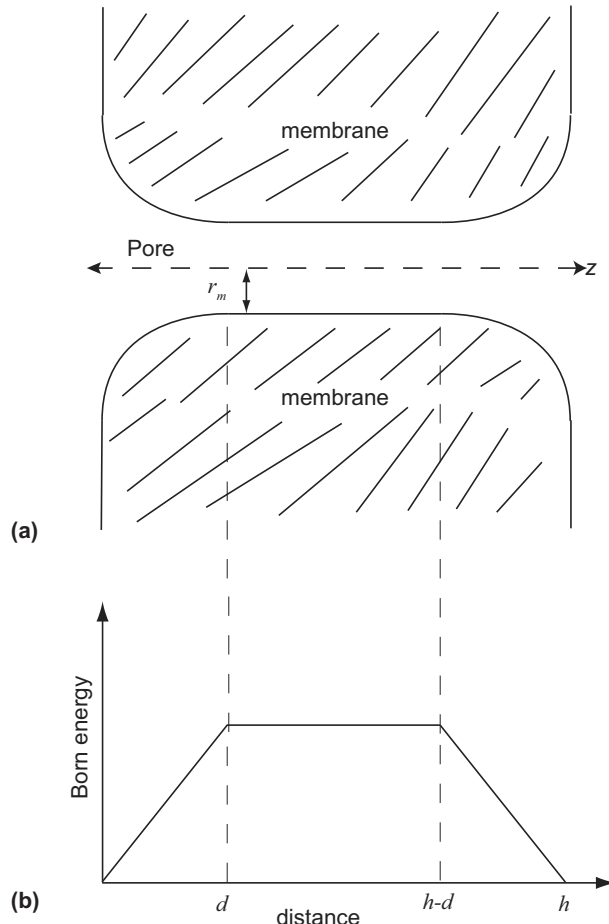


Figure 9. Born energy of a pore: (a) Cross section of a pore (b) Energy profile of a hydrophilic pore as a function of its position along the axis of the pore.

where $n = d/h$, is the relative entrance length of the pore as shown in Figure 9. This expression simplifies to

$$I = \frac{h}{z_x v_m} \left(\frac{w_0 z_x \exp[z_x(w_0 z_x - n v_m)] - n v_m}{w_0 z_x - n v_m} \right) \exp(z_x v_m) - \frac{h}{z_x v_m} \left(\frac{w_0 z_x \exp[z_x(w_0 z_x + n v_m)] + n v_m}{w_0 z_x + n v_m} \right). \quad (22)$$

The total current i_{sml} through the pore is the current density in the pore multiplied by the cross sectional area of the pore. Further simplification using the Nernst-Einstein equation gives

$$i_{\text{sml}} = \frac{\pi r_m^2 \sigma_{ps} v_m R T}{F h} \frac{(e^{v_m} - 1)}{\left(\frac{w_0 e^{w_0 - n v_m} - n v_m}{w_0 - n v_m} e^{v_m} - \frac{w_0 e^{w_0 + n v_m} + n v_m}{w_0 + n v_m} \right)}, \quad (23)$$

where r_m is the radius of the pore at its narrowest part, σ_{ps} is the conductivity of the aqueous solution that fills the pore, $v_m = z_x V_m / RT$, and $V_m = \Phi_{in} - \Phi_{ex}$ is the transmembrane potential. Thus the formula for pore current is valid only for small pores up to 1 nm radius, and accounts only for the diffusion current due to interaction of ions with the pore walls. Current through larger pores has to be modelled differently. The above derivation for pore current is based upon those of Barnett and Weaver (1991), Glaser *et al.* (1988) and DeBruin and Krassowska (1999). Equation 23 for current through small pores is useful for modelling electroporation. A model based on the assumption of all created pores being small in radius, is useful for comparing onset of pore density depending on various independent parameters like cell radius, peak electric field, extracellular and intracellular fluid conductivity.

7. Calculation of Transmembrane Potential

Small spherical particles in the size range 1 μm –1000 μm are very important in today's world. They are used in manufacturing operations like powder coating, and powder injection molding. A number of raw materials used in the agricultural, food, mining, and metallurgical industries are received in particulate form, and are to be processed further. Particles of biological origin, such as cells and DNA are of common interest, for further use in biomedical applications. This section introduces the reader to some of the mathematical formulae related to the effect of the electric field on biological cells. These formulae are useful to build and extend models of electroporation of a single spherical cell.

7.1. Electric Field Interaction with a Cell as a Particle

Further discussion in this section is heavily based on the text by Jones (1995). Imagine a spherical particle of radius R , suspended in a dielectric fluid and subject to a uniform electric field E_0 orientated in the z -direction as illustrated in Figure 10. The dielectric permittivity inside and outside the cell is ε_{in} and ε_{ex} , respectively. The field polarizes the particle, inducing a moment in it. The effective dipole moment P_{eff} , is defined as the moment of an equivalent, point dipole that, when immersed in the same dielectric medium and positioned at the centre of the original particle, produces the same electrostatic potential. The electrostatic potential Φ due to a point dipole of moment P_{eff} in a dielectric medium of permittivity ε_{ex} is

$$\Phi(r, \theta) = \frac{P_{eff} \cos \theta}{4\pi \varepsilon_{ex} r^2}, \quad (24)$$

where θ is the polar angle measured from the positive pointing pole of the dipole and r is the distance from the origin. This is the standard solution of Laplace's equation in the far-field of a dipole source. This approximation may have to be modified if the potential at the centre of the cell is to be calculated. However, modelling electroporation requires the potential, just inside and outside the cell membrane, thus the approximation is valid.

7.2. Effective Dipole Moment of a Dielectric Sphere in a Dielectric Medium

This electric potential due to the effective dipole moment can be determined by solving the boundary value problem as follows. The following assumptions are made: that there is

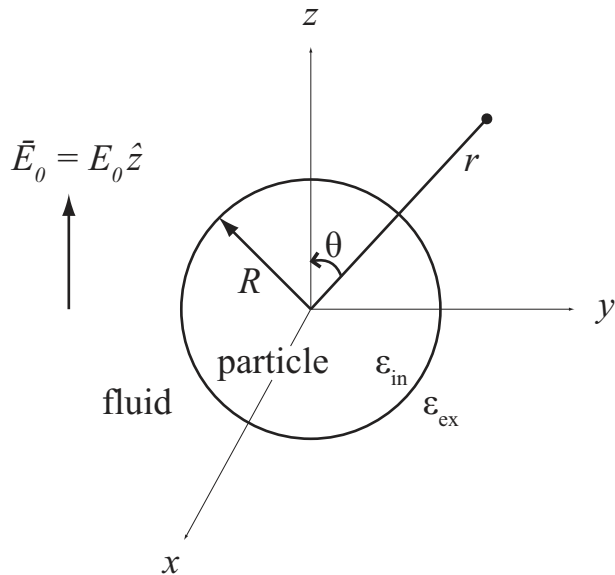


Figure 10. Spherical particle in electric field.

an applied external uniform electric field E_0 ; that there is no free charge anywhere in the sphere or dielectric liquid; and that the presence of the particle does not disturb the system of source charges that create E_0 . With these assumptions the electrostatic potential satisfies Laplace's equation everywhere. The solutions for the potential outside Φ_{ex} , and inside Φ_{in} the sphere, of radius a take the form:

$$\Phi_{\text{ex}}(r, \theta) = -E_0 r \cos \theta + \frac{A \cos \theta}{r^2}, \quad r > a \quad (25)$$

$$\Phi_{\text{in}}(r, \theta) = -Br \cos \theta, \quad r < a \quad (26)$$

where A and B are coefficients, that can be determined using the boundary conditions. The first term in Equation 25 is the imposed uniform electrostatic field, and the second term is the induced dipole of the particle. Comparing Equation 24 with this second term links the coefficient A and the effective dipole moment, by the equation,

$$P_{\text{eff}} = 4\pi\epsilon_{\text{ex}} A. \quad (27)$$

The boundary conditions are applied at the surface of the particle. The first condition is that the potential must be continuous across the surface of the cell, namely

$$\Phi_{\text{ex}}(a, \theta) = \Phi_{\text{in}}(a, \theta). \quad (28)$$

The second condition is that, the normal component of the displacement flux must be continuous across the boundary, hence

$$\epsilon_{\text{ex}} \frac{\partial \Phi_{\text{ex}}}{\partial r} = \epsilon_{\text{in}} \frac{\partial \Phi_{\text{in}}}{\partial r}, \quad (29)$$

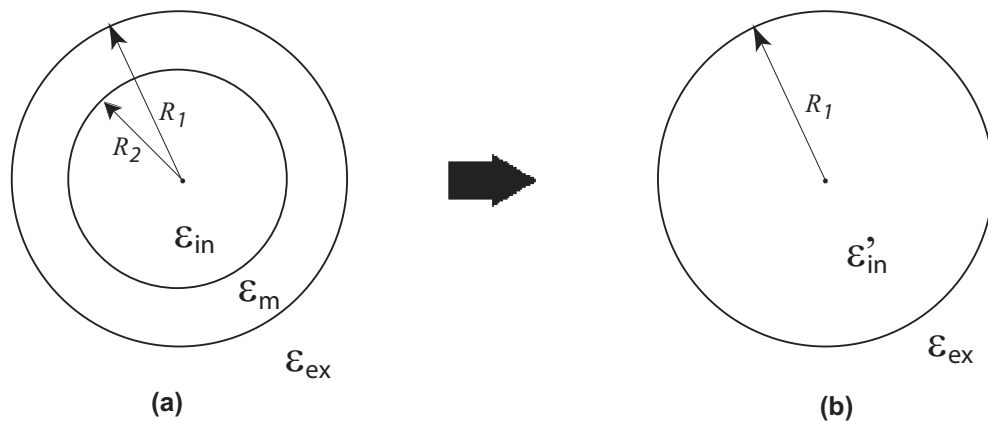


Figure 11. Spherically concentric dielectric shell and its homogeneous equivalent (a) cell with membrane (b) equivalent cell.

where ε_1 is the extracellular permittivity, and ε_2 is the intracellular permittivity. Equations 25, 26, 28 and 29 are solved by Jones (1995) to obtain

$$A = \frac{(\varepsilon_{\text{in}} - \varepsilon_{\text{ex}})}{(\varepsilon_{\text{in}} + 2\varepsilon_{\text{ex}})} a^3 E_0 \quad \text{and} \quad B = \frac{3\varepsilon_{\text{ex}}}{(\varepsilon_{\text{in}} + 2\varepsilon_{\text{ex}})} E_0. \quad (30)$$

Thus the effective dipole moment can be written as

$$P_{\text{eff}} = 4\pi\varepsilon_{\text{ex}} \frac{(\varepsilon_{\text{in}} - \varepsilon_{\text{ex}})}{(\varepsilon_{\text{in}} + 2\varepsilon_{\text{ex}})} a^3 E_0. \quad (31)$$

In general form, for a homogeneous dielectric sphere the expression for the effective dipole moment is

$$P_{\text{eff}} = 4\pi\varepsilon_{\text{ex}} K a^3 E_0. \quad (32)$$

where K , known as the Clausius-Mossotti function, provides a measure of the strength of the effective polarization of a spherical particle. As seen, K is a function of the permittivities of the sphere and the fluid in which the sphere is immersed, viz

$$K(\varepsilon_{\text{in}}, \varepsilon_{\text{ex}}) = \frac{\varepsilon_{\text{in}} - \varepsilon_{\text{ex}}}{\varepsilon_{\text{in}} + 2\varepsilon_{\text{ex}}}. \quad (33)$$

7.3. Multilayered Particles

The above model of the cell is over simplified—in reality the biological cell has at least an outer cell wall, known as the membrane. The membrane should be modelled as an extra layer. To calculate the effective dipole moment of a layered particle, we assume that the particle is spherically symmetrical as shown in Figure 11. Here, ε_{ex} is the extracellular permittivity, ε_m is the membrane permittivity and ε_{in} is the intracellular permittivity. R_1 and R_2 are the outer and inner radii respectively, of the particle. We can approximate the three layer model ($\varepsilon_{\text{ex}}, \varepsilon_m, \varepsilon_{\text{in}}$) with a two layer model ($\varepsilon_{\text{ex}}, \varepsilon'_{\text{in}}$) where ε'_{in} is a revised ε_{in} from this simplification. We only need the potential Φ at the membrane boundary, as the

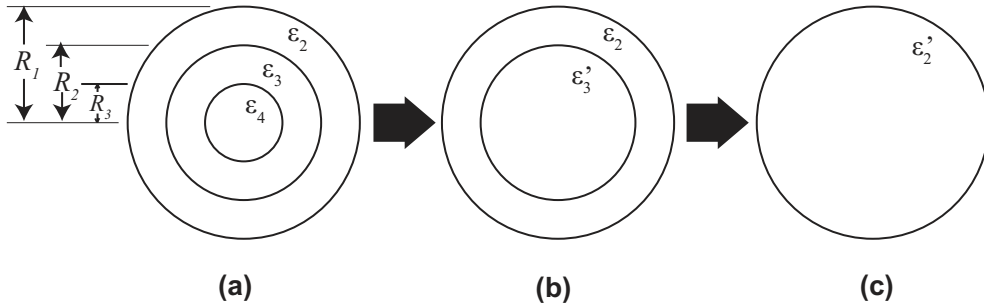


Figure 12. Multilayered spherical concentric dielectric shell and its homogeneous equivalent (a) Multilayered shell (b) Intermediate equivalent particle (c) Equivalent particle.

membrane is very thin compared with the cell radius, thus this approximation is suitable. The effective permittivity of the equivalent particle as given by Jones (1995) is

$$\varepsilon_{in}' = \varepsilon_m \left\{ \frac{a_r^3 + 2 \left(\frac{\varepsilon_{in} - \varepsilon_m}{\varepsilon_{in} + 2\varepsilon_m} \right)}{a_r^3 - \left(\frac{\varepsilon_{in} - \varepsilon_m}{\varepsilon_{in} + 2\varepsilon_m} \right)} \right\}, \quad (34)$$

where

$$a_r = \frac{R_1}{R_2}.$$

This method can be easily applied to multilayered shells using the approach illustrated in Figure 12. One starts at the innermost layer and by repeatedly applying Equation 34, eventually arrives at the expression for the permittivity of the equivalent homogeneous sphere.

7.4. Lossless Spherical Shell in a Uniform Field, Calculation of Potentials

Consider a layered spherical particle as in Figure 11, subjected to an applied uniform electric field E_0 , oriented in the z-direction. Assume that there is no free electric charge anywhere. To solve this boundary value problem, we solve Laplace's equation for the electrostatic potential in the three regions. Then Φ_{ex} the extracellular potential, Φ_m the potential in the membrane, and Φ_{in} the intracellular potential are given by,

$$\Phi_{ex}(r, \theta) = \left(-E_0 r + \frac{A}{r^2} \right) \cos \theta, \quad r > R_1 \quad (35)$$

$$\Phi_m(r, \theta) = \left(-Br + \frac{C}{r^2} \right) \cos \theta, \quad R_1 > r > R_2 \quad (36)$$

$$\Phi_{in}(r, \theta) = -Dr \cos \theta, \quad r < R_2. \quad (37)$$

where A , B , C and D are unknown coefficients to be determined using the boundary conditions. The boundary conditions at the two dielectric surfaces are

$$\Phi_{\text{ex}} = \Phi_{\text{in}} \quad \text{and} \quad \varepsilon_{\text{ex}} \frac{\partial \Phi_{\text{ex}}}{\partial r} = \varepsilon_m \frac{\partial \Phi_m}{\partial r} \quad \text{at} \quad r = R_1 \quad (38)$$

$$\Phi_m = \Phi_{\text{in}} \quad \text{and} \quad \varepsilon_m \frac{\partial \Phi_m}{\partial r} = \varepsilon_{\text{in}} \frac{\partial \Phi_{\text{in}}}{\partial r} \quad \text{at} \quad r = R_2. \quad (39)$$

The above solutions and the boundary conditions can be solved to give,

$$A = \frac{\varepsilon'_{\text{in}} - \varepsilon_{\text{ex}}}{\varepsilon'_{\text{in}} + 2\varepsilon_{\text{ex}}} R_1^3 E_0, \quad (40)$$

$$B = \frac{-3\varepsilon_{\text{ex}} a_r^3}{(\varepsilon'_{\text{in}} + 2\varepsilon_{\text{ex}})(a_r^3 - K)} E_0, \quad (41)$$

$$C = \frac{-3\varepsilon_{\text{ex}} K a_r^3}{(\varepsilon'_{\text{in}} + 2\varepsilon_{\text{ex}})(a_r^3 - K)} E_0, \quad (42)$$

$$D = \frac{-3\varepsilon_{\text{ex}}(1 - K) a_r^3}{(\varepsilon'_{\text{in}} + 2\varepsilon_{\text{ex}})(a_r^3 - K)} E_0, \quad (43)$$

where

$$a_r = \frac{R_1}{R_2} \quad \text{and} \quad K = \frac{\varepsilon'_{\text{in}} - \varepsilon_{\text{ex}}}{\varepsilon'_{\text{in}} + 2\varepsilon_{\text{ex}}}. \quad (44)$$

7.5. Spherical Shell with Ohmic Loss in Uniform Field

Typically cells are multilayered and have finite conductivities. In such cases, an effective complex permittivity may be substituted for any layered sphere. In the preceding sections, the spherical particle and the medium have been assumed to be perfectly dielectric (zero conductivity). In fact, biological cells and the medium have finite conductivities (σ_{in} and σ_{ex}) in addition to their dielectric permittivities. This contributes to losses in the system and influences the cell behaviour in an electric field. When loss is present, the dipole moment of a particle in a field exhibits either a time delay when the electric field is suddenly applied or a phase lag when the electric field is a continuous time varying cyclic signal. Imagine the layered dielectric sphere in Figure 11 with permittivities ε_{in} , ε_m and ε_{ex} and conductivities σ_{in} , σ_m and σ_{ex} . Then, as shown in Figure 13, in each of the n separate dielectric layers, where ε is the dielectric permittivity, σ is the dielectric conductivity and $i = \sqrt{-1}$, the complex permittivity can be used as

$$\bar{\varepsilon}_n = \varepsilon_n + \frac{\sigma_n}{i\omega} \quad n \in \{\text{in}, \text{m}, \text{ex}\}. \quad (45)$$

The boundary conditions in Equations 28 and 29 are modified by replacing the permittivities with their complex equivalents. Solving Laplace's equation for the three region problem with complex permittivities, results in new coefficients, \bar{A} , \bar{B} , \bar{C} , and \bar{D} to be used in the

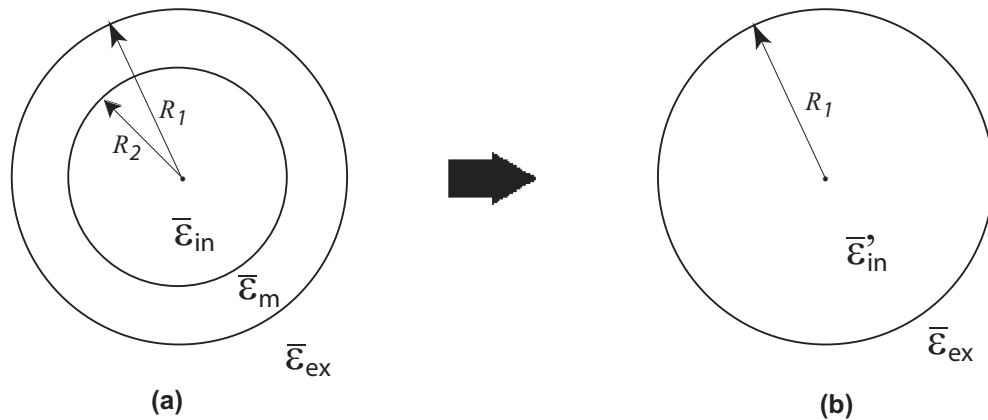


Figure 13. Multilayered spherical concentric lossy shell and its homogeneous equivalent
(a) Multilayered shell (b) Equivalent particle.

solutions for Φ_{in} , Φ_m and Φ_{ex} . They are:

$$\bar{A} = \frac{\bar{\varepsilon}_{\text{in}} - \bar{\varepsilon}_{\text{ex}}}{\bar{\varepsilon}_{\text{in}} + 2\bar{\varepsilon}_{\text{ex}}} R_1^3 E_0 \quad (46)$$

$$\bar{B} = \frac{-3\bar{\varepsilon}_{\text{ex}} a_r^3}{(\bar{\varepsilon}_{\text{in}} + 2\bar{\varepsilon}_{\text{ex}})(a_r^3 - K)} E_0 \quad (47)$$

$$\bar{C} = \frac{-3\bar{\varepsilon}_{\text{ex}} K a_r^3}{(\bar{\varepsilon}_{\text{in}} + 2\bar{\varepsilon}_{\text{ex}})(a_r^3 - K)} E_0 \quad (48)$$

$$\bar{D} = \frac{-3\bar{\varepsilon}_{\text{ex}}(1-K) a_r^3}{(\bar{\varepsilon}_{\text{in}} + 2\bar{\varepsilon}_{\text{ex}})(a_r^3 - K)} E_0 \quad (49)$$

where

$$a_r = \frac{R_1}{R_2} \quad \text{and} \quad K = \frac{\bar{\varepsilon}_{\text{in}} - \bar{\varepsilon}_{\text{ex}}}{\bar{\varepsilon}_{\text{in}} + 2\bar{\varepsilon}_{\text{ex}}}. \quad (50)$$

The effective homogeneous dielectric permittivity is replaced by its complex equivalent as follows:

$$\bar{\varepsilon}_{\text{in}} = \bar{\varepsilon}_m \left\{ \frac{a_r^3 + 2 \left(\frac{\bar{\varepsilon}_{\text{in}} - \bar{\varepsilon}_m}{\bar{\varepsilon}_{\text{in}} + 2\bar{\varepsilon}_m} \right)}{a_r^3 - \left(\frac{\bar{\varepsilon}_{\text{in}} - \bar{\varepsilon}_m}{\bar{\varepsilon}_{\text{in}} + 2\bar{\varepsilon}_m} \right)} \right\} = \varepsilon_{\text{in}} + \frac{\sigma_{\text{in}}}{i\omega} \quad (51)$$

7.6. Transient Response of Lossy Dielectric Sphere to a Suddenly Applied Electric Field

Imagine an ohmic sphere exposed to an electric field that is suddenly turned on, namely, $E(t) = E_0 u(t)$, where $u(t)$ is the unit step function. It turns out that the potentials inside

and outside are unchanged in their form; the coefficients just become functions of time, namely A is replaced by $A(t)$ and B replaced by $B(t)$.

The boundary conditions are as usual (and true for all time)

$$\Phi_{\text{ex}}(a, \theta) = \Phi_{\text{in}}(a, \theta). \quad (52)$$

Now Equation 29 must be replaced by a charge continuity condition because finite conductivity allows accumulation of free electrical charge on a surface. The instantaneous charge conservation condition is

$$\sigma_{\text{ex}} \left(-\frac{\partial \Phi_{\text{ex}}}{\partial r} \right) - \sigma_{\text{in}} \left(-\frac{\partial \Phi_{\text{in}}}{\partial r} \right) + \frac{\partial \sigma_f}{\partial t} = 0 \quad \text{at } r = a, \quad (53)$$

where σ_f is the free electric surface charge as defined by

$$\sigma_f = \varepsilon_{\text{ex}} \frac{\partial \Phi_{\text{ex}}}{\partial r} - \varepsilon_{\text{in}} \frac{\partial \Phi_{\text{in}}}{\partial r} \quad \text{at } r = a. \quad (54)$$

Here, $\frac{\partial \Phi_{\text{ex}}}{\partial r}$ and $\frac{\partial \Phi_{\text{in}}}{\partial r}$ are the normal components of the ohmic current outside and inside of the sphere respectively. Combining these equations give a set of differential equations that can be solved for the time dependent coefficient $A(t)$ to give

$$A(t) = \frac{\sigma'_{\text{in}} - \sigma_{\text{ex}}}{\sigma'_{\text{in}} + 2\sigma_{\text{ex}}} R_1^3 E_0 \left(1 - \exp \left(\frac{-t}{\tau_{mw}} \right) \right) + \frac{\varepsilon'_{\text{in}} - \varepsilon_{\text{ex}}}{\varepsilon'_{\text{in}} + 2\varepsilon_{\text{ex}}} R_1^3 E_0 \exp \left(\frac{-t}{\tau_{mw}} \right) \quad (55)$$

where

$$\tau_{mw} = \frac{\varepsilon'_{\text{in}} + \varepsilon_{\text{ex}}}{\sigma'_{\text{in}} + 2\sigma_{\text{ex}}} \quad (56)$$

is the membrane relaxation time constant.

By careful observation of Equations 40 and 55, by analogy the time dependent coefficient $D(t)$ is

$$D(t) = -\frac{3\sigma_{\text{ex}}(1 - K_I)}{(\sigma'_{\text{in}} + 2\sigma_{\text{ex}})(a_r^3 - K_I)} a_r^3 E_0 \left(1 - \exp \left(\frac{-t}{\tau_{mw}} \right) \right) - \frac{3\varepsilon_{\text{ex}}(1 - K_R)}{(\varepsilon'_{\text{in}} + 2\varepsilon_{\text{ex}})(a_r^3 - K_R)} a_r^3 E_0 \exp \left(\frac{-t}{\tau_{mw}} \right), \quad (57)$$

where K_I and K_R are the imaginary and real component of K respectively. These equations for $A(t)$ and $D(t)$ can be used to model transmembrane potential defined as the potential across the membrane, given by

$$V_m = \Phi_{\text{in}} - \Phi_{\text{ex}}. \quad (58)$$

As seen from Equations 35 and 37, to calculate Φ_{in} and Φ_{ex} we only need the constants $A(t)$ and $D(t)$, thus the other two constants $B(t)$ and $C(t)$ are not relevant.

7.7. Analytical Solutions for Transmembrane Potential

Assuming the cell dielectric properties are known, here I detail the analytical solutions for the potentials inside and outside a spherical cell as available in literature (Schwan, 1989). These are useful for validating numerical modelling results. Once again, consider a spherical cell with external radius R_1 and internal radius R_2 as in the previous section. The cell membrane thickness is then $h = R_1 - R_2$. Assume E_0 is the external applied electric field. Imagine the cell with permittivities (ϵ_{in} , ϵ_m , ϵ_{ex}) and conductivities (σ_{in} , σ_m , σ_{ex}). Then in each of the separate dielectric regions, the specific admittance is given by

$$\varpi = \sigma - i\omega\epsilon \quad (59)$$

to give the specific admittivities ϖ_{in} , ϖ_m and ϖ_{ex} . Potentials just inside and outside the cell membrane are given by

$$\Phi_{in} = \vartheta R_2, \quad (60)$$

$$\Phi_{ex} = E_0(R_1 - \nu/(R_1)^2). \quad (61)$$

The constants ϑ and ν are calculated as,

$$\vartheta = 9\varpi_{ex}\varpi_m E_0/\varsigma, \quad (62)$$

where

$$\begin{aligned} \varsigma = & ((\varpi_m + 2\varpi_{ex})(2\varpi_m + \varpi_{in}) \\ & + 2(R_2/R_1)^3(\varpi_m - \varpi_{ex})(\varpi_{in} - \varpi_m)), \end{aligned} \quad (63)$$

and

$$\begin{aligned} \nu = & ((R_1)^3(2\varpi_m + \varpi_{in})(\varpi_{ex} - \varpi_m) \\ & + R_2^3(2\varpi_m + \varpi_{ex})(\varpi_m - \varpi_{in}))/\varsigma. \end{aligned} \quad (64)$$

Equations 59 to 64 can be used to calculate transmembrane potential as a passive response to an applied sinusoidal electric field.

If the cell membrane parameter is specified as specific membrane capacitance C_m and only the intracellular and extracellular conductivities for a cell of radius a are known, then the following Equation 65 by Holzapfel *et al.* (1982) can be used to calculate analytical solution for the induced transmembrane potential as a passive response to an applied sinusoidal electric field.

$$V_m(t) = \frac{1.5Ea}{1 + (\omega\tau_r)^2}(\cos\omega t + \omega\tau_r \sin\omega t) \quad (65)$$

where the membrane relaxation time constant is

$$\tau_r = aC_m \left(\frac{1}{\sigma_{in}} + \frac{1}{2\sigma_{ex}} \right). \quad (66)$$

8. Conclusion

In this chapter the reader is introduced to a number of important aspects of and the various mathematical relations within the various terms during the phenomenon of electroporation. This information is important for mathematical modelling of the electroporation which may help predict results of electroporation based processes so as to optimize experimental parameters.

References

- Abidor, I. G., V. B. Arakelyan, L. V. Chernomordik, Y. A. Chizmadzhev, V. F. Pastushenko, and M. R. Tarasevich. Electric breakdown of bilayer membranes: I. The main experimental facts and their qualitative discussion. *Bioelectrochemistry and Bioenergetics*, **6**, pp. 37–52 (1979).
- Ausubel, F. M., R. Brent, R. E. Kingston, D. D. Moore, J. Seidman, J. A. Smith, and K. Struhl. *Current Protocols in Molecular Biology*. Wiley, New York (1990).
- Barnett, A. and J. C. Weaver. Electroporation: A unified, quantitative theory of reversible electrical breakdown and mechanical rupture in artificial planar bilayer membranes. *Bioelectrochemistry and Bioenergetics*, **25**, pp. 163–182 (1991).
- Benachir, T. and M. Lafleur. Osmotic and pH transmembrane gradients control the lytic power of melittin. *Biophysical Journal*, **70**, pp. 831–840 (1996).
- Bertino, J. R. Transfer of drug resistance genes into hematopoietic stem cells for marrow protection. *The Oncologist*, **13**, pp. 1036–1042 (2008).
- Budak-Alpdogan, T., D. Banerjee, and J. R. Bertino. Hematopoietic stem cell gene therapy with drug resistance genes: An update. *Cancer Gene Therapy*, **12**, pp. 849–863 (2005).
- Cemažar, M., D. Miklavčič, and G. Serša. Intrinsic sensitivity of tumor cells to bleomycin as an indicator of tumor response to electrochemotherapy. *Japanese Journal of Cancer Research*, **89**, pp. 328–333 (1998).
- Chang, D. C., B. M. Chassy, J. A. Saunders, and A. E. Sowers, editors. *Guide to Electroporation and Electrofusion*. Academic Press, San Diego, CA (1992).
- Chang, D. C. and T. S. Reese. Changes in membrane structure induced by electroporation as revealed by rapid-freezing electron microscopy. *Biophysical Journal*, **58**, pp. 1–12 (1990).
- Chen, W. and R. C. Lee. Electromediated permeabilization of frog skeletal muscle cell membrane: Effect of voltage-gated ion channels. *Bioelectrochemistry and Bioenergetics*, **34**, pp. 157–167 (1994).
- Chernomordik, L. V., S. I. Sukharev, I. G. Abidor, and Y. A. Chizmadzhev. Breakdown of lipid bilayer membranes in an electric field. *Biochim Biophys Acta*, **736**, pp. 203–213 (1983).

- Chernomordik, L. V., S. I. Sukharev, S. V. Popov, V. F. Pastushenko, A. V. Sokirko, I. G. Abidor, and Y. A. Chizmadzhev. The electrical breakdown of cell and lipid membranes: The similarity of phenomenologies. *Biochim Biophys Acta*, **902**, pp. 360–373 (1987).
- Cole, K. S. *Membranes ions and impulses*. University of California Press, Berkeley, CA (1972).
- Cotterill, R. *Biophysics An Introduction*. John Wiley and Sons Ltd, West Sussex, England (2002).
- Curtis, H. and N. S. Barnes. *Biology, fourth edition*. Worth Publishing, New York (1983).
- DeBruin, K. A. and W. Krassowska. Modeling electroporation in a single cell. I. Effects of field strength and rest potential. *Biophysical Journal*, **77**, pp. 1213–1224 (1999).
- Dev, S. B., D. P. Widera, and G. A. Hofmann. Medical applications of electroporation. *IEEE Transactions on Plasma Science*, **28**, pp. 206–223 (2000).
- Dimitrov, D. S. Electroporation and electrofusion of membranes. In: *Handbook of Physics of Biological Systems*, edited by R. Lipowsky and E. Sackmann, volume 1, pp. 854–895. Elsevier (1995).
- Freeman, S. A., M. A. Wang, and J. C. Weaver. Theory of electroporation of planar bilayer membranes: Predictions of the aqueous area, change in capacitance, and pore-pore separation. *Biophysical Journal*, **67**, pp. 42–56 (1994).
- Gaynor, P., D. N. Wells, and B. Oback. Couplet alignment and improved electrofusion by dielectrophoresis for a zona-free high-throughput cloned embryo production system. *Medical and Biological Engineering and Computing*, **43**, pp. 150–154 (2005).
- Glaser, R. W., S. L. Leikin, L. V. Chernomordik, V. F. Pastushenko, , and A. I. Sokirko. Reversible electrical breakdown of lipid bilayers: Formation and evolution of pores. *Biochim Biophys Acta*, **940**, p. 275287 (1988).
- Glass, L. F., N. A. Fenske, M. Jaroszeski, R. Perrott, D. T. Harvey, D. S. Reintgen, and R. Heller. Bleomycin-mediated electrochemotherapy of basal cell carcinoma. *Journal of the American Academy of Dermatology*, **34**, pp. 82–86 (1996).
- Gotheff, A., L. M. Mir, and J. Gehl. Electrochemotherapy: Results of cancer treatment using enhanced delivery of bleomycin by electroporation. *Cancer Treatment Reviews*, pp. 1–17 (2003).
- Graziadei, L., P. Burfeind, and D. Bar-Sagi. Introduction of unlabeled proteins into living cells by electroporation and isolation of viable protein-loaded cells using dextran-fluorescein isothiocyanate as a marker for protein uptake. *Analytical Biochemistry*, **194**, pp. 198–203 (1991).
- Grimnes, S. and O. G. Martinsen. *Bioimpedance and Bioelectricity basics*. Academic Press, San Diego, NY (2000).

- Hibino, M., H. Itoh, and K. J. Kinosita. Time courses of cell electroporation as revealed by submicrosecond imaging of transmembrane potential. *Biophysical Journal*, **64**, pp. 1789–1800 (1993).
- Hibino, M., M. Shigemori, H. Itoh, K. Nagayama, and K. Kinosita, Jr. Membrane conductance of an electroporated cell analyzed by submicrosecond imaging of transmembrane potential. *Biophysical Journal*, **59**, pp. 209–220 (1991).
- Holzapfel, C., J. Vienken, and U. Zimmermann. Rotation of cells in an electric field. *Journal of Membrane Biology*, **67**, pp. 13–26 (1982).
- Israelachvili, J. *Intermolecular and Surface Forces*. Academic Press, London, UK (1992).
- Jaroszeski, M. J., R. Gilbert, and R. Heller. *Methods in Molecular Medicine: Electrochemotherapy, Electrogenetherapy, and Transdermal Drug Delivery Electrically Mediated Delivery of Molecules to Cells*. Humana Press, Totowa, New Jersey (2000).
- Jones, T. B. *Electromechanics of particles*. Cambridge University Press, New York (1995).
- Joshi, R. P., Q. Hu, K. H. Schoenbach, and H. P. Hjalmarson. Improved energy model for membrane electroporation in biological cells subjected to electrical pulses. *Physical Review E*, **65(4)**, pp. 041920–041928 (2002).
- Kakorin, S., S. P. Stoylov, and E. Neumann. Electro-optics of membrane electroporation in diphenylhexatriene-doped lipid bilayer vesicles. *Biophysical Chemistry*, **58**, pp. 109–116 (1996).
- Kandušer, M., M. Fošnaria, M. Šentjurc, V. Kralj-Iglič, H. Hägerstrand, A. Iglič, and D. Miklavčič. Effect of surfactant polyoxyethylene glycol C₁₂E₈ on electroporation of cell line DC3F. *Colloids and Surfaces A*, **214**, pp. 205–217 (2003).
- Kinosita, K. and T. Y. Tsong. Voltage-induced pore formation and hemolysis of human erythrocytes. *Biochim Biophys Acta*, **471**, pp. 227–242 (1977a).
- Kinosita, K. and T. Y. Tsong. Formation and resealing of pores of controlled sizes in human erythrocyte membrane. *Nature*, **268**, pp. 438–441 (1977b).
- Kinosita, K., Jr., M. Hibino, H. Itoh, M. Shigemori, K. Hirano, Y. Kirinoand, and T. Hayakawa. Events of membrane electroporation visualized on a time scale from microsecond to seconds. In: *Guide to Electroporation and Electrofusion*, edited by D. C. Chang, B. M. Chassy, J. A. . Saunders, and A. E. Sowers, chapter 3, pp. 29–46. Academic Press, San Diego, CA (1992).
- Kotnik, T. Biological cells in electric fields. In: *Proceedings of the Electroporation based Technologies and Treatments*, edited by P. Kramar and D. Miklavčič, pp. 7–12. Bioelectrochemical society IGEA, Ljubljana, Slovenia (2003).
- Kotnik, T., D. Miklavčič, and T. Slivnik. Time course of transmembrane voltage induced by time-varying electric fields: a method for theoretical analysis and its application. *Bioelectrochemistry and Bioenergetics*, **45**, pp. 3–16 (1998).

- Kranjc, S., M. Cemažar, A. Grosel, M. Sentjurc, and G. Serša. Radiosensitising effect of electrochemotherapy with bleomycin in LPB sarcoma cells and tumors in mice. *BMC Cancer* (2005).
- Krassowska, W. and P. D. Filev. Modeling electroporation in a single cell. *Biophysical Journal*, **92**, pp. 404–417 (2007).
- Liang, H., W. J. Purucker, D. A. Stenger, R. T. Kubiniec, and S. W. Hui. Uptake of fluorescense-labeled dextrans by 10T 1/2 fibroblasts following permeation by rectangular and exponential-decay electric field pulses. *Biotechniques*, **6**, pp. 550–558 (1988).
- Miklavčič, D. and T. Kotnik. Electroporation for electrochemotherapy and gene therapy. In: *Bioelectromagnetic Medicine*, edited by M. S. Markov, chapter 40, pp. 637–656. Marcel Dekker, New York (2004).
- Mir, L. M. Therapeutic perspectives of *in vivo* cell electroporabilization. *Bioelectrochemistry*, **53**, pp. 1–10 (2000).
- Mir, L. M., S. Orlowski, J. Belehradek, and C. Paoletti. Electrochemotherapy potentiation of antitumour effect of bleomycin by local electric pulses. *European Journal of cancer*, **27**, pp. 68–72 (1991).
- Mir, L. M., S. Orlowski, J. J. Belehradek, J. Teissié, M. Rols, G. Serša, D. Miklavčič, R. Gilbert, and R. Heller. Biomedical applications of electric pulses with special emphasis on antitumor electrochemotherapy. *Bioelectrochemistry and Bioenergetics*, **38**, pp. 203–207 (1995).
- Moser, D., D. Zarka, C. Hedman, and T. Kallar. Plasmid and chromosomal dna recovery by electroextraction of cyanobacteria. *FEMS Microbiology Letters*, **128**, pp. 307–313 (1995).
- Mouneimne, Y., P. F. Tosi, R. Barhoumi, and C. Nicolau. Electroinsertion: An electrical method for protein implantation into cell membranes. In: *Guide to Electroporation and Electrofusion*, edited by D. C. Chang, B. M. Chassy, J. A. Saunders, and A. E. Sowers, chapter 20, pp. 327–346. Academic Press, San Diego, CA (1992).
- Mouneimne, Y., P. F. Tosi, Y. Gazitt, and C. Nicolau. Electro-insertion of xeno-glycophorin into the red blood cell membrane. *Biochemical and Biophysical Research Communications*, **159**, pp. 34–40 (1989).
- Muramatsu, T., A. Nakamura, and H. M. Park. *in vivo* electroporation: A powerful and convinient means of non viral gene transfer to tissues of living animals (Review). *International Journal of Molecular Medicine*, **1**, pp. 55–62 (1998).
- Neu, J. C. and W. Krassowska. Asymptotic model of electroporation. *Physical Review E*, **59**, pp. 3471–3482 (1999).
- Neu, J. C. and W. Krassowska. Modeling postshock evolution of large electropores. *Physical Review E*, **67**, pp. 1–12 (2003).

- Neumann, E. The relaxation hysteresis of membrane electroporation. In: *Electroporation and Electrofusion in Cell Biology*, edited by E. Neumann, A. E. Sowers, and C. A. Jordan, chapter 4, pp. 61–82. Plenum Press, New York (1989).
- Neumann, E., G. Gerisch, and K. Opatz. Cell fusion induced by high electric impulses applied to dictyostelium. *Naturwissenschaften*, **67**, pp. 414–415 (1980).
- Neumann, E. and K. Rosenheck. Permeability changes induced by electric impulses in vesicular membranes. *Journal of Membrane Biology*, **10**, pp. 279–290 (1972).
- Neumann, E., M. Schaefer-Ridder, Y. Wang, and P. H. Hofschneider. Gene transfer into mouse lymphoma cells by electroporation in high electric fields. *European Molecular Biology Organization Journal*, **1**, pp. 841–845 (1982).
- Neumann, E., A. E. Sowers, , and C. A. Jordan, editors. *Electroporation and Electrofusion in Cell Biology*. Plenum Press, New York (1989).
- O’Neil, R. J. and L. Tung. Cell-attached patch clamp study of the electropermeabilization of amphibian cardiac cells. *Biophysical Journal*, **59**, pp. 1028–1039 (1991).
- Orentas, R., D. Schauer, Q. Bin, and B. D. Johnson. Electrofusion of a weakly immunogenic neuroblastoma with dendritic cells produces a tumor vaccine. *Cellular Immunology*, **213**, pp. 4–13 (2001).
- Pastushenko, V. F. and Y. A. Chizmadzhev. Stabilization of conducting pores in BLM by electric current. *General Physiology and Biophysics*, **1**, pp. 43–52 (1982).
- Pastushenko, V. F., Y. A. Chizmadzhev, and V. B. Arakelyan. Electric breakdown of bilayer lipid membranes.II. Calculation of the membrane lifetime in the steady-state diffusion approximations. *Bioelectrochemistry and Bioenergetics*, **6**, pp. 53–62 (1979).
- Pohl, H. A. *Dielectrophoresis, the Behavior of Matter in Non-uniform Electric Fields*. Cambridge University Press, Cambridge (1978).
- Potter, H. Electroporation in biology: Methods, applications and instrumentation. *Analytical Biochemistry*, **174**, pp. 361–373 (1988).
- Powell, K. T., A. W. Morgenthaler, and J. C. Weaver. Tissue electroporation: Observation of reversible electrical breakdown in viable frog skin. *Biophysical Journal*, **56**, pp. 1163–1171 (1989).
- Prausnitz, M. R., V. G. Bose, R. Langer, and J. C. Weaver. Electroporation of mammalian skin: A mechanism to enhance transdermal drug delivery. *Proceedings of the National Academy of Sciences*, **90**, pp. 10504–10508 (1993).
- Prausnitz, M. R., U. Pliquett, R. Langer, and J. C. Weaver. Rapid temporal control of transdermal drug delivery by electroporation. *Pharmacological Research*, **11**, pp. 1834–1837 (1994).

- Rols, M. P. and J. Teissié. Ionic-strength modulation of electrically induced permeabilization and associated fusion of mammalian cells. *European Journal of Biochemistry*, **179**, pp. 109–115 (1989).
- Rosenheck, K., P. Lindner, and I. Pecht. Effect of electric fields on light-scattering and fluorescence of chromaffin granules. *Journal of Membrane Biology*, **20**, pp. 1–12 (1975).
- Russell, P. J., S. L. Wolfe, P. E. hertz, C. Starr, and B. McMillan. *Biology, the dynamic science*. Thomson Publishing, USA (2008).
- Sale, A. J. H. and W. A. Hamilton. Effects of high electric fields on microorganisms: I. Killing of bacteria and yeasts. *Biochim Biophys Acta*, **148**, pp. 781–788 (1967).
- Sale, A. J. H. and W. A. Hamilton. Effects of high electric fields on microorganisms:III. Lysis of erythricuytes and protoplasts. *Biochim Biophys Acta*, **163**, pp. 37–43 (1968).
- Saulis, G., J. Naktinis, and M. Venslauskas. Kinetics of pore resealing in cell membranes after elrc troporation. *Bioelectrochemistry and Bioenergetics*, **26**, pp. 1–13 (1991).
- Saulis, G. and S. Šatkauskas. Pore disappearance in a cell after electroporation: Theoretical simulation and comparison with experiments. *Biophysical Journal*, **73**, pp. 1299–1309 (1977).
- Saulis, G. and S. Šatkauskas. Electroporation of biological membranes. *Veterinarija ir Zootechnika*, **26**, pp. 82–88 (2004a).
- Saulis, S. and G. Šatkauskas. Electroporation as a tool for biotechnology and medicine with specific emphasize on its application for drug and gene delivery: Review. *Veterinarija ir Zootechnika*, **26**, pp. 74–81 (2004b).
- Scheurich, P. and U. Zimmermann. Electrically stimulated fusion of different plant cell protoplasts. *Plant Physiology*, **67**, pp. 849–853 (1981).
- Schmidt, E., U. Leinfelder, P. Gessner, D. Zillikens, E. B. Brocker, and U. Zimmermann. CD19+ B lymphocytes are the major source of human antibody-secreting hybridomas generated by electrofusion. *Journal of Immunological Methods*, **255**, pp. 93–102 (2001).
- Schwan, H. P. Electrical properties of tissue and cell suspensions. *Advances in Biological and Medical Physics*, **5**, pp. 147–209 (1957).
- Schwan, H. P. Dielectrophoresis and rotation of cells. In: *Electroporation and Electrofusion in Cell Biology*, edited by E. Neumann, A. E. Sowers, , and C. A. Jordan, chapter 1, pp. 3–22. Plenum Press, New York (1989).
- Schwister, K. and B. Deuticke. Formation and properties of aqueous leaks induced in human erythrocytes by electrical breakdown. *Biochim Biophys Acta*, **816**, pp. 332–348 (1985).
- Scott-Taylor, T. H., R. Pettengell, I. Clarke, G. Stuhler, M. C. L. Barthe, P. Walden, and A. G. Dalgleish. Human tumour and dendritic cell hybrids generated by electrofusion: Potential for cancer vaccines. *Biochim Biophys Acta*, **1500**, pp. 265–267 (2000).

- Serša, G. Electrochemotherapy. In: *Electrochemotherapy, Electrogenetherapy, and Transdermal Drug Delivery : Electrically Mediated Delivery of Molecules to Cells (Methods in Molecular medicine)*, edited by M. J. Jaroszeski, R. Heller, and R. Gilbert, chapter 6, pp. 119–133. Humana Press, Totowa, New Jersey (2000).
- Serša, G., M. Cemažar, and D. Miklavčič. Antitumor effectiveness of electrochemotherapy with cisdiamminedichloroplatinum(II) in mice. *Cancer Research*, **55**, pp. 3450–3455 (1995).
- Serša, G., S. Novaković, and D. Miklavčič. Potentiation of bleomycin antitumor effectiveness by electrotherapy. *Cancer Letters*, **69**, pp. 81–84 (1993).
- Serša, G., B. Stabuč, M. Cemažar, D. Miklavčič, and Z. Rudolf. Electrochemotherapy with cisplatin: the systemic antitumour effectiveness of cisplatin can be potentiated locally by the application of electric pulses in the treatment of malignant melanoma skin metastases. *Melanoma Research*, **10**, pp. 381–385 (2000).
- Sheng, Y., V. Mancino, and B. Birren. Transformation of escherichia coli with large DNA molecules by electroporation. *Nucleic Acids Research*, **23**, pp. 1990–1996 (1995).
- Smith, K. C., J. C. Neu, and W. Krassowska. Model of creation and evolution of stable electropores for DNA delivery. *Biophysical Journal*, **86**, pp. 2813–2826 (2004).
- Smith, L. and J. Nordstrom. Advances in plasmid gene delivery and expression in skeletal muscle. *Current Opinion in Molecular Therapeutics*, **2**, pp. 150–154 (2000).
- Snoj, M., Z. Rudolf, M. Cemažar, B. Jancar, and G. Serša. Successful sphincter-saving treatment of anorectal malignant melanoma with electrochemotherapy, local excision and adjuvant brachytherapy. *Anti-Cancer Drugs*, **16**, pp. 345–348 (2005).
- Swezey, R. and D. Epel. Stable, resealable pores formed in sea urchin eggs by electric discharge (electroporation) permit substrate loading for assay of enzymes *in vivo*. *Cell Regulation*, **1**, pp. 65–74 (1989).
- Talele, S. and P. Gaynor. Nonlinear time domain model of electropermeabilization: Response of a single cell to an arbitrary applied electric field. *Journal of Electrostatics*, **65**, pp. 775–784 (2007).
- Talele, S. and P. Gaynor. Non-linear time domain model of electropermeabilization: Effect of extracellular conductivity and applied electric field parameters. *Journal of Electrostatics*, **66**, pp. 328–334 (2008).
- Teissié, J. and T. Y. Tsong. Electric field induced transient pores in phospholipid bilayer vesicles. *Biochemistry*, **20**, pp. 1548–1554 (1981).
- Tekle, E., R. D. Astumian, W. A. Friauf, and P. B. Chock. Asymmetric pore distribution and loss of membrane lipid in electroporated DOPC vesicles. *Biophysical Journal*, **81**, pp. 960–968 (2001).

- Tozon, N., V. Kodre, G. Ser  a, and M. Cema  ar. Effective treatment of perianal tumors in dogs with electrochemotherapy. *Anticancer Research*, **25**, pp. 839–946 (2005).
- Vanbever, R., N. Lecouturier, and V. Preat. Transdermal delivery of metoprolol by electroporation. *Pharmacological Research*, **11**, pp. 1657–1662 (1994).
- Weaver, J. C. Electroporation: a general phenomenon for manipulating cells and tissues. *Journal of Cellular Biochemistry*, **51**, pp. 426–435 (1993).
- Weaver, J. C. and A. Barnett. Progress towards a theoretical model for electroporation: Membrane electrical behavior and molecular transport. In: *Guide to Electroporation and Electrofusion*, edited by D. C. Chang, B. M. Chassy, J. A. Saunders, and A. E. Sowers, chapter 7, pp. 91–118. Academic Press, San Diego, CA (1992).
- Weaver, J. C. and Y. Chizmadzhev. Theory of electroporation: a review. *Bioelectrochemistry and Bioenergetics*, **41**, pp. 135–160 (1996).
- Weaver, J. C. and R. A. Mintzer. Decreased bilayer stability due to transmembrane potentials. *Physics Letters A*, **86A**, pp. 57–59 (1981).
- Weaver, J. C. and K. T. Powell. Theory of electroporation. In: *Electroporation and Electrofusion in Cell Biology*, edited by E. Neumann, A. E. Sowers, and C. A. Jordan, chapter 7, pp. 111–126. Plenum Press, New York (1989).
- Yumura, S., R. Matsuzaki, and T. Kitanishi-Yumura. Introduction of macromolecules into living dictyostelium cells by electroporation. *Cell Structure and Function*, **20**, pp. 185–190 (1995).
- Zimmermann, U. Electric field-mediated fusion and related electrical phenomena. *Biochim Biophys Acta*, **694**, pp. 227–277 (1982).
- Zimmermann, U. and G. A. Neil. *Electromanipulation of Cells*. CRC Press, Boca Raton, Florida (1996).
- Zimmermann, U., J. Schulz, and G. Pilwat. Transcellular Ion Flow in Escherichia coli B and Electrical Sizing of Bacterias. *Biophysical Journal*, **13(10)**, pp. 1005–1013 (1973).
- Zimmermann, U., J. Vienken, and G. Pilwat. Development of drug carrier systems: electric field induced effects in cell membranes. *Journal of Electroanalytical Chemistry*, pp. 553–574 (1980).

Chapter 9

MEASUREMENTS ON THE PRINCIPAL ELECTRIC PARAMETERS OF THE ATMOSPHERE

Florian Mandija

Department of Physics, Faculty of Natural Sciences,
University of Shkodra "Luigj Gurakuqi", Shkodër, Albania

Abstract

In the latest research developments, a great interest in the scientific community is dedicated also on study of the atmospheric state in the lower part of the troposphere. This part of the atmosphere is our living environment, and so it is the source of our breathing air. The atmospheric studies are a multidisciplinary science. It concerns on the measurement of both, the physical and chemical atmospheric parameters. In my research activity I'm concentrated on the continuous monitoring of the physical atmospheric parameters, especially electrical parameters of lower part of the troposphere. The principal electrical parameters of the atmosphere are atmospheric ion concentration, density current, atmospheric electric fields, aerosol concentration, etc.

Atmospheric ion and aerosol concentration are the principal electrical parameters monitored in my measurement campaigns. Atmospheric ions belong on the small air ion group. In the case of aerosol monitoring, there are done two types of measurements; aerosol number concentration, for the aerosol particles in the size interval (0.3-100 μm), and aerosol mass concentration, for three aerosol groups PM1, PM2.5 and PM10.

The electrical state of the atmosphere is strongly connected with the area category. So, all the monitoring process is carried out in four main areas; urban, rural, seashore and mountain.

Based on the measurement results, I've studied the daily and annual variation of the atmospheric ion and aerosol particle concentration.

During the measurements are recorded also the principal meteorological parameters. These parameters are air temperature, atmospheric pressure, relative humidity and wind speed. There are carried out the correlations among atmospheric and aerosol concentration and the above mentioned meteorological parameters.

Analyzing the variation of the concentrations, I've determinate the recombination and the attachment coefficients, so giving a clear picture of the electrostatic interaction among atmospheric ions and aerosol particles in certain areas.

The concentrations of both atmospheric ions and aerosol particles are also altitude dependent, in the exponentially decay form. The measurements on the different altitudes enable to determine the scale height of their concentrations and the analytical functions.

It is important to mention that my research activities on the atmospheric electricity are developed mainly in the fair weather conditions of the atmosphere.

Introduction

Atmospheric electricity is a very interesting branch of electrostatic physics. It deals with a gaseous dielectric, like atmospheric air [1-3]. Atmospheric electricity by itself is composed by several components, where most important are; atmospheric electric charge like atmospheric ions and aerosol particles, atmospheric current and atmospheric electric field in fair-weather and thunderstorm meteorological conditions, atmospheric discharges like lightning, and many other atmospheric effects related with the atmospheric electricity [3-5].

First of all we have to understand the concept of global electric circuit. It can be simplified on a giant capacitor composed by two spherical “electrodes”, one on the Earth surface and another on the Ionosphere in the altitude about 60km [6-8]. The simplified scheme of this circuit is given by the figure 1.

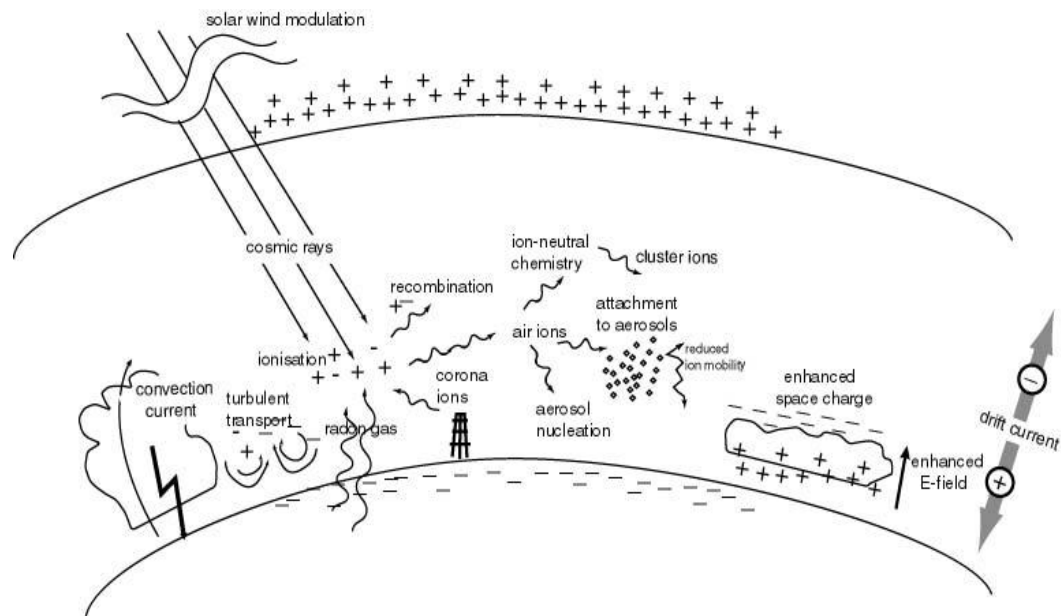


Figure 1. The global electric circuit.

The Earth surface is negatively charged, as the Ionosphere is positively charged [8-10]. Based on its electrical structure, in this part of Atmosphere exists an electric field:

$$\vec{E} = -\overrightarrow{\text{grad}}\varphi \quad (1)$$

where φ is electrostatic potential.

Electrical carriers in this medium (gaseous dielectric) are atmospheric ions and small aerosol particles [11-12]. The sizes of small air ions are in the nanometric interval, as the aerosol sizes are in the nanometric, submicron and micron interval. Immediately in second

fractions after the ionization of the air molecules, the bare ions collect nearly 10-12 water molecules [13-15]. These structures are called group-ions, and these are the real atmospheric ions [16-19]. Meanwhile maximum aerosol size can be as far as $100\mu\text{m}$.

One of the most principal parameters of electrical carriers is their electrical mobility:

$$B = \frac{\vec{V}}{\vec{E}} \quad (2)$$

Due to their greater electrical motilities μ ($\text{cm}^2\text{V}^{-1}\text{s}^{-1}$), because of their smaller size, atmospheric ions give the major contribution on the atmospheric current [20-23]. Positive ions have smaller electrical mobility, but due to their greater concentration, the contribution of two polarities on the atmospheric current is almost equal [24-27].

The electrical current in the atmosphere is given by the equation:

$$J_C = V \cdot \sigma \quad (3)$$

where V is the difference of electric potentials between Earth surface and Ionosphere, and σ is the electrical conductivity of air:

$$\sigma = \mu_i n_i e + \sum_a \mu_a N_a Q_a = \sigma_o + \sigma_a \quad (4)$$

where the first term gives the small air ion contribution on the conductivity of the atmosphere, and the second term gives the aerosol contribution [28-31].

The contribution of the small air ions can be expressed separating two polarities of the ions:

$$\sigma = \sigma_+ + \sigma_- = e(\mu_+ n_+ + \mu_- n_-) \quad (5)$$

Electrical resistance of the atmosphere is determined based on the classic Ohm law:

$$R_C = \frac{V}{J_C} \quad (6)$$

Table 1. The electric parameters of the global circuit

Electric parameter	Symbol	Value
Potential gradient	E	120 V/m
Vertical current density	J_z	3 pA/m ²
Air electric conductivity	σ	20 fS/m
Ionosphere potential	V_I	250 kV
Atmospheric resistance	R_T	230 Ω
Earth-Air current	I	1800 A
Air column resistance	R_C	120 p Ω /m ²
Time constant	RC	10 min
Earth electric charge	Q	$0.5 \cdot 10^6$ C

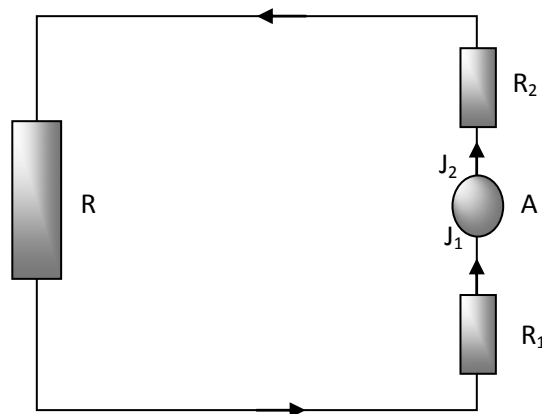


Figure 2. Electric scheme of the global circuit

In the table 1 are given the details of the electrical global circuit.

Where; R is electric resistance in fair-weather meteorological conditions, R_1 is electric resistance between clouds and Earth surface in disturb conditions, R_2 is electric resistance between clouds and Ionosphere in disturb conditions, J_1 and J_2 are respective electric currents, and A is “electric generator” [32-37].

The electrical scheme of global electric circuit is presented by the figure 2.

The concentration of all electric carriers in the atmosphere is determined by the balance equation, which in its simplest form is given by the equation (7):

$$\frac{dn(t)}{dt} = q(t) - \alpha(t)n^2(t) - \beta(t)n(t)N(t) \quad (7)$$

where $q(t)$ is the ion production ($\text{cm}^{-3}\text{s}^{-1}$), $\alpha(t)$ is the recombination coefficient (cm^3s^{-1}), $\beta(t)$ is the attachment coefficient (cm^3s^{-1}), $n(t)$ is the concentration of atmospheric ions (cm^{-3}), and $N(t)$ is the concentration of aerosol particles (cm^{-3}).

In stationary cases, $\frac{dn(t)}{dt} = 0$ the balance equation becomes:

$$q - \alpha n^2 - \beta n N = 0 \quad (8)$$

and solving this equation we can find the concentration of the atmospheric ions in stationary conditions:

$$n = \frac{1}{2\alpha} \left[-\beta N + \sqrt{(\beta N)^2 + 4\alpha q} \right] \quad (9)$$

There are two limit cases of the balance equation;
recombination limit:

$$\alpha n^2 \gg n\beta Z \quad (10)$$

And attachment limit:

$$\alpha n^2 \ll n\beta Z \quad (11)$$

All the above mentioned situations correspond on the fair-weather conditions.

In the cases of intense thunderstorms, the electric field rises more intense and they may alter their horizontal orientation [38-41].

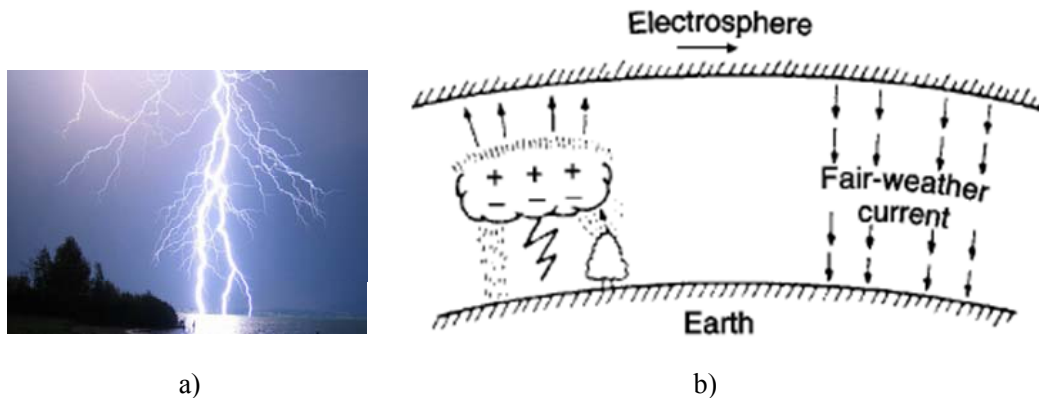


Figure 3. a) A spectacular view of lightning b) Lightning effects on the global electric circuit.

Lightning are a very usual phenomenon in these cases (fig.3.a). Are these atmospheric discharges that play the role of the batteries in the electric global circuit, because they compensate the lost of the electric charge during the fair weather (fig.3.b).

It is important to say that atmospheric ions contribute not only on the atmospheric current, but also in the new particle formation, due to ion induced nucleation mechanism [60-66]. But the aerosol particles due to the attachment processes, contributes in the reduction of the ion concentration. The major sources of the atmospheric ions are; cosmic rays (40%), radon in the air (40%) and the external radiation (40%) from the radioactive elements in the ground. All these sources are dependent on the local conditions. The sources of the aerosol particles are volcanic explosions, desert dust storms, marine salt, and human made activities. The concentration of atmospheric ions and aerosol particles decreases with the height, in the lower part of the Troposphere. The concentration of both atmospheric ions and aerosol particles are strongly correlated with the meteorological parameters [42-46].

Atmospheric ions are categorized in several groups according their sizes.

In the table 2 are listed the size categories of atmospheric ions.

Table 2. Atmospheric ion classification

	Category	Electric mobility ($\text{cm}^2\text{V}^{-1}\text{s}^{-1}$)	Size (nm)
1.	Small group-ions	>1	<1.32
2.	Small intermediate group-ions	0.01-1	1.32-15.6
3.	Large intermediate group-ions	0.001-0.1	15.6-50
4.	Large group-ions	0.00025-0.001	50-114
5.	Ultra large group-ions	<0.00025	114 - 200

The statistical size distribution of atmospheric ions is given in figure 4.

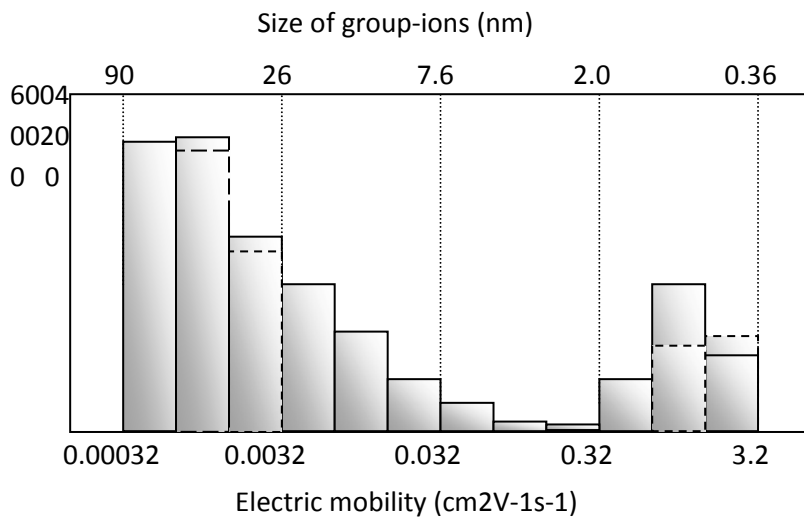


Figure 4. Size distribution of the atmospheric ions.

As atmospheric ions have their own size distribution, also the aerosol particles have several size distributions [47-51]. Some of them are log-normal size distribution,

$$\text{power law size distribution } n_N^o(\log D_p) = \frac{C}{D^\alpha}$$

$$\text{gamma size distribution } \frac{dN(r)}{dr} = \frac{N_o}{\Gamma(\alpha+1)\beta^{\alpha+1}} r^\alpha \exp\left(-\frac{r}{\beta}\right), \text{ etc.}$$

The most important among them is log-normal size distribution. Its analytical form is given by the equation:

$$df = \frac{1}{\sqrt{2\pi}\ln\sigma_g} \exp\left(-\frac{(\ln d_p - \ln \bar{d})^2}{2(\ln\sigma_g)^2}\right) d(\ln d_p) \quad (12)$$

where $\bar{d} = \exp\left(\frac{\sum n_p \ln d_p}{N}\right)$ is the mean diameter, $\sigma_g = \exp\left(\sqrt{\frac{\sum n_p (\ln d_p - \ln \bar{d})^2}{N-1}}\right)$ is the standard deviation of the size distribution, d_p is the size of the aerosol, and N is the number of modes.

There exist several modes in the size distributions of the aerosol particles [51-55]. These modes depend on the meteorological factors and the regions where the distribution measurements are carried out. But four of them are more important (fig.5);

Nucleation mode	$d < 0.01 \mu\text{m}$
Aitken mode	$0.01 \mu\text{m} < d < 0.1 \mu\text{m}$
Accumulation mode	$0.1 \mu\text{m} < d < 1 \mu\text{m}$
Coarse mode	$d > 1 \mu\text{m}$

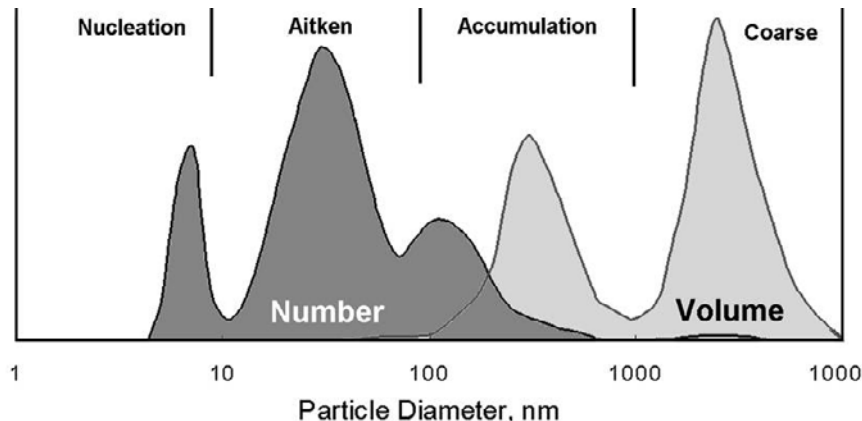


Figure 5. Four more important modes in aerosol size distribution.

The more evident modes, especially in the mass distribution are:

Fine mode	$d < 2.5 \mu\text{m}$
Coarse mode	$2.5 \mu\text{m} < d$

This is the case of the binomial aerosol distribution (fig.6).

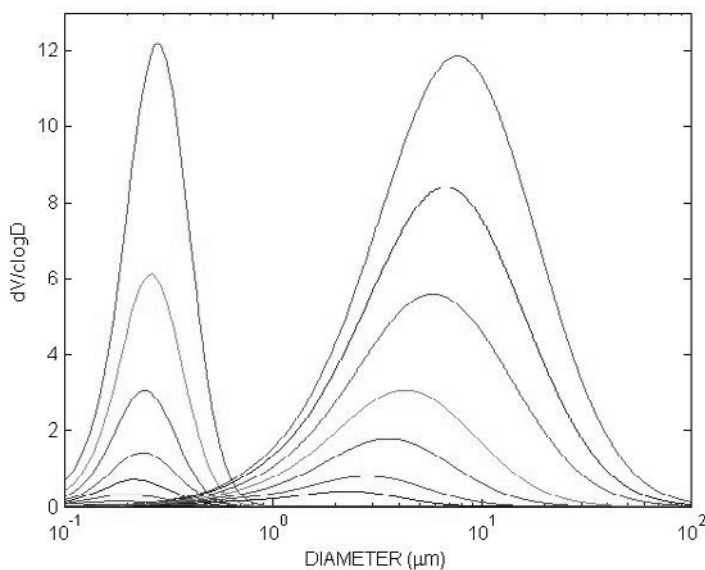


Figure 6. Binomial aerosol distribution.

In the same manner we can justify the distributions for the aerosol surface and aerosol volume [56-59]:

$$n_s^e(d_p) = \frac{\pi d_p^2 N}{\sqrt{2\pi} d_p \ln \sigma_g} \exp \left[-\frac{(ln d_p - ln \bar{d}_{pg})^2}{2 \ln^2 \sigma_g} \right] \quad (13)$$

$$n_v^e(d_p) = \frac{\pi d_p^3 N}{6\sqrt{2\pi} d_p \ln \sigma_g} \exp \left[-\frac{(ln d_p - ln \bar{d}_{pg})^2}{2 \ln^2 \sigma_g} \right] \quad (14)$$

Some aerosol particles sizes are listed in the table 3.

Table 3. Some aerosol particles

No.	Particles	Sizee (μm)
1	Viruse	0.001-0.07
2	Atiken particles	0.001-0.2
3	Combustion gases	0.001-0.3
4	Fog	0.001-1
5	Smoke	0.001-1
6	Sea salt	0.03-0.4
7	Bactere	0.07-30
8	Ash	1-100
9	Spore	10-100
10	Water droplet	10-100

The main sources of the atmospheric aerosols are reported in the table 4.

Both atmospheric ions and aerosol particles can penetrate deep into our respiratory system [60-63]. The amount of the air ions (especially for the negative polarity) in an ambient is an important indicator for quality of air, and this is the reason that atmospheric ions are called vitamins of the air. They have a direct impact on serotonin, a neuro-hormone that controls the physiological state of the humans [64-67]. From the other side, the amounts of the aerosol particles in the air aggravate the quality of air, because they can worse the respiratory system. Internationally are ruled many environmental limits on the mass concentration of aerosol particles, as are PM2.5 and PM10 [68-73].

Aerosols influence on the radiative balance in direct and indirect mechanisms [74-76]. The direct mechanism is based on the fact that aerosols reflect sunlight back into space (especially sulphates), and reduce the amount of solar radiation that reaches the surface cause the Earth's surface temperature to cool down [77-80]. In the indirect mechanism aerosols contribute to cloud formation. These mechanisms are presented in the figure 7.

Table 4. Principal aerosol sources

Source	Flux Tg/yr	Cathegory
Natural		
Primary		
Soil dust	1500	Mostly coarse
Sea salt	1300	Coarse
Biological fractions	50	Coarse
Volcanic ash	30	Coarse
Secondary		
Sulphates	210	Fine
Organic materials	200	Fine
Nitrates from	50	Fine and coarse
Total Natural	3100	
Source	Flux Tg/yr	Cathegory
Antropogenic		
Primary		
Industrial dust	100	Fine and coarse
Smoke and soot	10	Mostly fine
Secondary		
Sulphates	190	Fine
Combustions of biomasses	90	Fine
Nitrates	50	Mostly Coarse
Total Antropogenic	450	
TOTAL	36000	

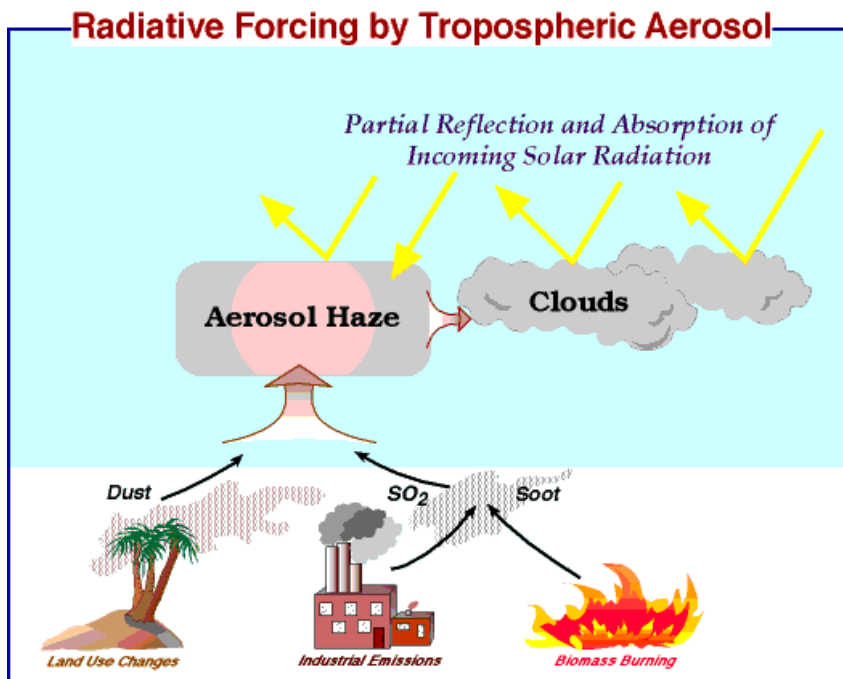


Figure 7. The scheme of radiative forcing by aerosols.

But aerosols can influence also in warming our eco-system. Carbonic aerosols let solar radiation to enter in atmosphere, but don't allow Earth radiation to escape.

In the brief we can say that the electrical condition of the atmosphere plays an important role on the behavior of its physical parameters, determining the ecology and the quality of our living environment.

Method and Instruments

Method

There are realized several measurement campaigns during the period February 2006–November 2009. Principal factors monitored in these campaigns are atmospheric ions and aerosol particles.

The measurements include:

1. Ion and aerosol concentrations in indoor ambient.
 - Living room
 - Bar
 - School
 - Hospital
 - Factory
2. Ion and aerosol concentrations in outdoor ambient.
 - Urban centre
 - Suburban zone
 - Rural area
 - Mountain
 - Seashore
3. Daily variation of the ion and aerosol concentration.
4. Analyses of dust mass concentration.
5. Determination of the interaction intensity among atmospheric ions and aerosol particles.
6. Determination of the dependence of atmospheric ion concentration from the altitude.
7. Radon concentration monitoring
8. Meteorological parameters continuous monitoring.

Meteorological parameters during the measurements are selected far-weather.

So during the measurements, the stationary condition was fulfilled.

But, for further analyses we have selected also disturb meteorological conditions.

Instruments

Principal instruments used in measurements campaigns are:

- Air Ion Counter (model Digital Air Ion Counter ITC-201A)



Figure 8. Air Ion Counter ITC-201A.

Specifications

Measures positive ions and negative ions Light weight and compact design (approx. 400g) Displays date, time, temperature and humidity Data storage Rechargeable Lithium-ion battery Automatic range selection Made in Japan

Dimensions: W80xH180xD35 (mm) Internal power supply: Rechargeable Li-ion battery External power supply: AC adaptor 100-240VAC (50/60Hz) input, 6VDC output Battery Life: 2 hours continuously when fully charged and no back light use Consumption power: Less than 2.1W Detectable ion: Positive/Negative air ions Size of Ion: Small ion (Nano size) Measurement method: Ion mobility conversion method Mobility: 0.6 (cm^2/Vs) Measurement range: 10 to 1,236,000 (pcs/cc) Measurement tolerance: approx. +/-13% (Estimated value with electrical/mechanical factors considered) Minimum detectable density: 10 (pcs/cc) Data collection interval: approx. 0.25 sec Warming up time: approx. 30 sec (when turned on or the Start/Stop button is pushed) Data memory capacity: Max.27,000 records (ion count, temperature, humidity, time, date) Display: Semi transmissive TN LCD with back light Air flow rate: 500 (cc/sec) Operating temperature range: 5-35C (41-95F) Operating humidity range: 85% R.H. or below (no condensation)

- Air ion Counter (model IC-1000)

Ion counts are digitally displayed on the LCD. The 3 measurement ranges provide accurate measurement. Up to 2,000,000 (pcs/cc) ions can be measured. Product name: Air Ion Counter IC-1000 Detectable ion: Positive/Negative small air ions Air flow rate: 400 (cm^3/sec) Efficiency of ion collections: 65% Input resistance: 1010 Ohms. Battery: One 9V alkaline. Current drain is about 5mA on STANDBY, and 40mA on Measurement range: 10 - 1,999,000 (pcs/cc). Measurement method: Parallel flat plates method Mobility: 0.8 (cm^2/VS) Noise level: (2 second-weighting) approximately 10 ions/ cm^3 Accuracy: +/-25% for fast ions (mobility greater than 0.8 (cm^2/VS)) - these are the most numerous ions. This ion counter is less sensitive to "slow" ions such as charged pieces of dust). Minimum detectable density: 10 (pcs/cc) Setting time: approx. 2 seconds (response time), and 10 sec (after switchover between "+" and "-") Ion Selectivity (crosstalk): 1:5000.



Figure 9. Air ion Counter IC-1000.

Specifications

Operating temperature range: 0-50C (14-122F) Operating humidity range: 90% R.H. or below (no condensation) Weight: approx. 460g Dimensions: W90xH160xD58 (mm)

- Particle Counter (model Handilaz mini 301)



Figure 10. HandiLaz mini301.

ISO14644" certification of cleanrooms
Detecting local particle sources
Dust monitoring
Portable particle counting
Filter testing and leak detection
Low-cost alternative for spot monitoring
Versatile and useful for many applications
Low cost of ownership
Batteries allow continuous use with no downtime
Diode laser eliminates need for frequent cleaning
Particle measurements made in seconds
Intuitive, easy-to-learn user interface
Interfaces directly by cable to optional printer or PC
Easy data transfer to Excel
Quick and easy leak detection
Compact and Portable
Weighs only 1.5 lb. (0.68 kg)
Uses standard AA batteries to provide easy mobility, extend testing periods, reduce costs, and simplify repurchasing

- Environmental Dust Monitor (model 107)

Measures instantly PM1, PM2.5, PM10
Fully Automatic
Portable



Figure 11. EDM 107

31 channels
Air temperature sensor
Relative humidity sensor
Air pressure sensor
Data logger card
RS-232
Battery operated

- Multifunction Environmental Meter (model 4-DLAF8000b)



Figure 12. Environmental meter.

Measures meteorological parameters:

Handheld

air temperature

relative humidity

wind speed.

- Atmospheric pressure is measured with Pressure Meter Testo 511.



Figure 13. Pressure meter.

Measures the atmospheric pressure.

Handheld

Perform pressurization risk assessments for combustion air zones as well as room-to-room pressurization tests without running a reference hose.

Pressure Range: 8.86 to 35.44 in Hg

Units: hPa, mbar, Pa, mmH₂O,

mmHg in H₂O, in Hg, PSI

- Radon Monitor (Model RadStar 300)



Figure 14. Radon Monitor RadStar 300.

Internal memory

Portable

Software for download data

AC power operation

Sensitivity 0.2cpm/Pci/L

Ionization chamber detector

Measurement Results

Let us present in a concise way the measurement results taken in the all measurement campaigns.

1. Ion and aerosol concentrations (average values) in indoor environments are presented the table 5.

Table 5. Average values of the ion and aerosol concentrations in several indoor environments

	Dwellings	Schools	Hospitals	Bars	Factories
PM 0.3 (10^6 m^{-3})	5.46	5.55	5.77	5.82	7.32
PM 0.5 (10^6 m^{-3})	4.87	4.46	3.72	5.18	5.64
PM 5.0 (10^4 m^{-3})	9.90	65.9	53.66	30.71	1081.39
Positive ions (cm^{-3})	844.8	719.6	380.0	157.9	26715.6
Negative ions (cm^{-3})	775.4	632.8	303.3	137.9	22518.8
Total ions (cm^{-3})	1620.2	1352.4	683.3	295.7	49234.4

For the sixth column of the table 5, there are chooses wood, paper, marble, and cement factories.

2. Ion and aerosol concentrations (average values) in outdoor environments are presented the table 6.

Table 6. Average values of the ion and aerosol concentrations in several outdoor environments

	Urban	Suburban	Seashore	Rural	Mountain
PM 0.3 (10^6 m^{-3})	5.09	4.79	5.07	5.01	4.89
PM 0.5 (10^6 m^{-3})	1.96	1.47	1.60	1.15	0.86
PM 5.0 (10^4 m^{-3})	40.11	9.57	10.24	1.55	1.84
Positive ions (cm^{-3})	462.9	743.8	623.9	1272.5	877.8
Negative ions (cm^{-3})	328.5	664.9	347.1	666.6	1404.4
Total ions (cm^{-3})	791.3	1408.8	951.0	1952.2	2282.2

Urban measurements are done mainly in the cities of Albania with populations around 100,000-800,000; meanwhile in the seashore the measurements are concentrated in the Albanian Adriatic seashore. Rural and especially mountain regions are characterized by scarce population. The maximum altitude of the mountain measurement locations are around 1000m. In the seashore the measurements are realized mainly during the summer season, which is the most populated season. The urban centers can not be considered as industrial centers, because of their low industrial activities carried out in these areas.

3. Daily variations of the air ion concentration of both polarities (seashore measurements) are given in figure 15-18.

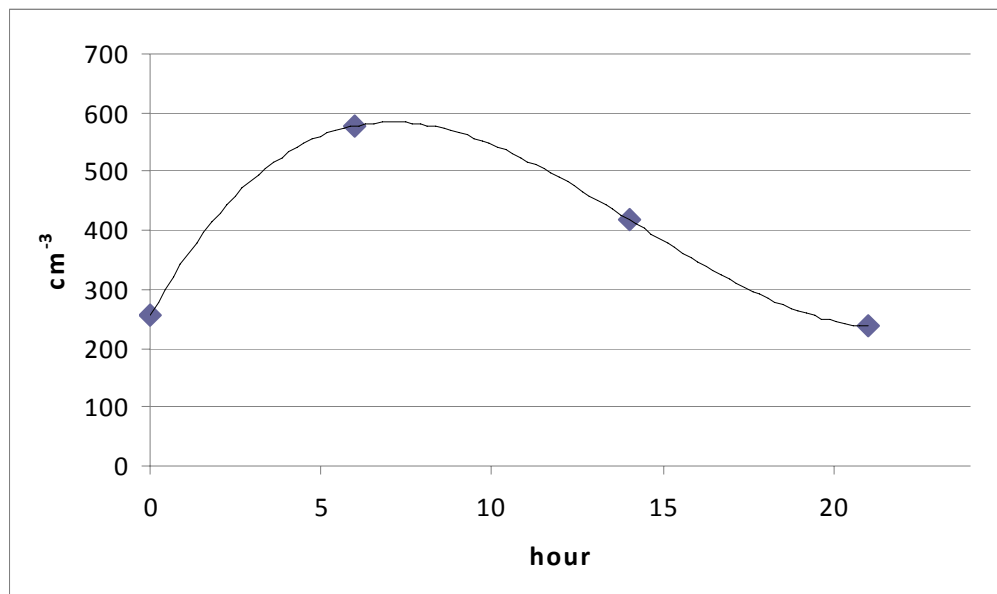


Figure 15. Daily variation of negative ion concentration.

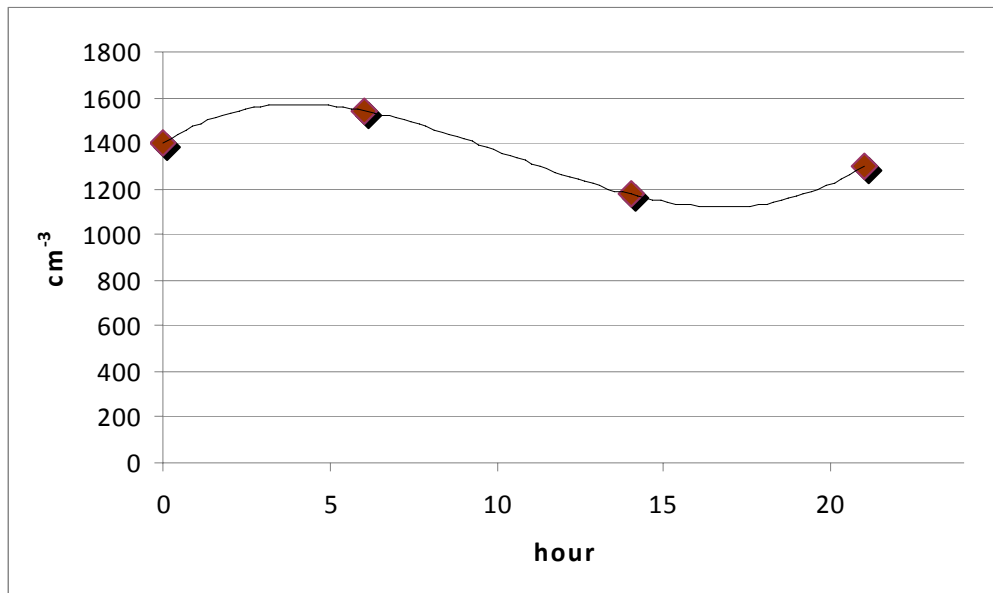


Figure 16. Daily variation of positive ion concentration

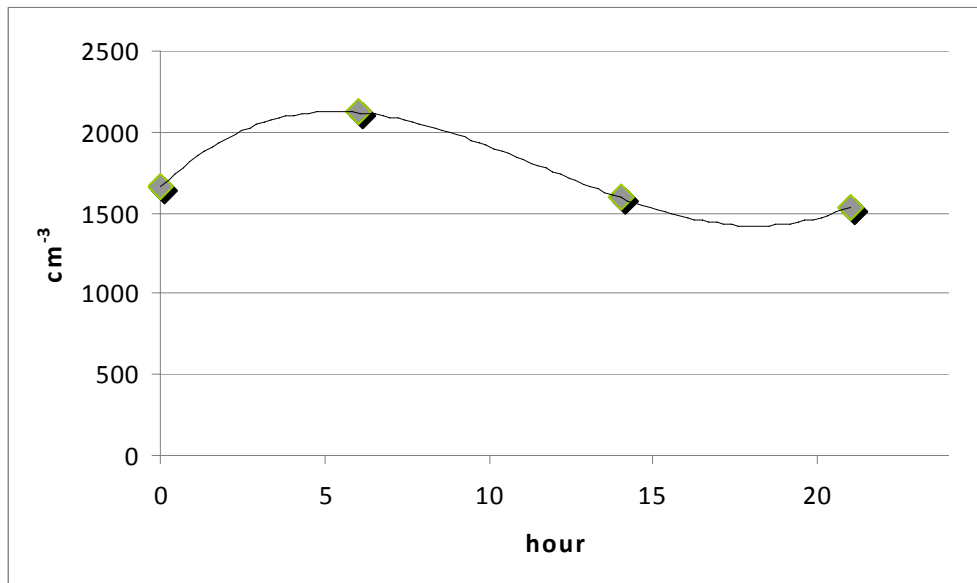


Figure 17. Daily variation of atmospheric ion concentration

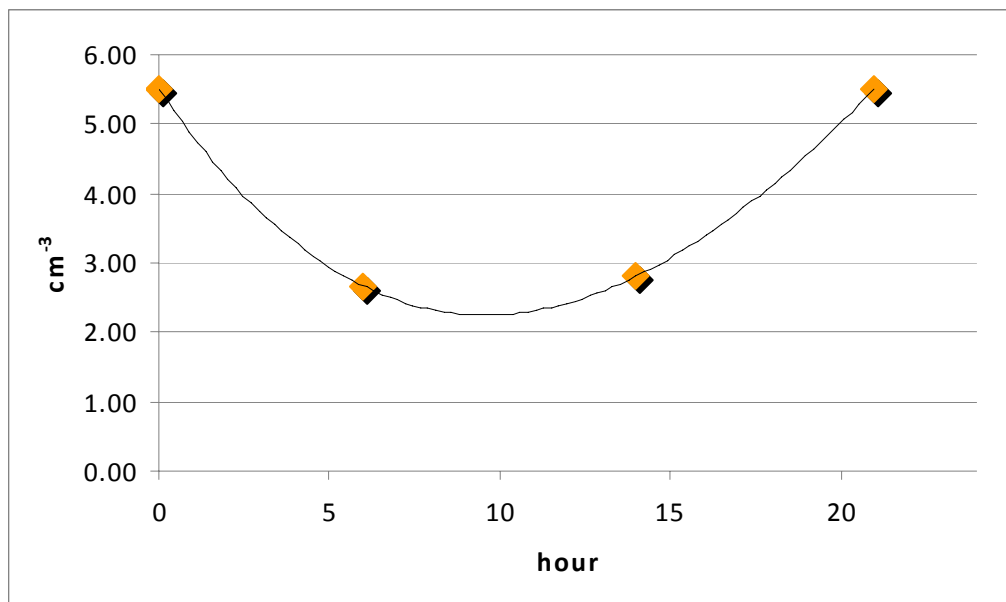


Figure 18. Daily variation of unipolarity factor

Numerical aerosol concentrations (seashore measurements) for three particle sizes are presented in figure 19.

The measurements to determine the daily variation of the ion and aerosol concentration are realized in four hours of the day, characterizing morning, noon, evening and night hours. In the above graphics are presented the average values of these concentrations in the above mentioned hours. In order to obtain more precise results it must be chooses more measurement hours, especially during the afternoon hours, time which many human activities take place. Meanwhile the late evening and early morning hours are characterized by a very minor human activity, and so they have very little variations in the ion and aerosol concentration. Even more the only variation in the ion and aerosol concentrations is the continuously and uniformly decrease.

The ion and aerosol measurements have been done instantly during these measurement hours. This fact let us to have a more accurate determination of the correlation between their concentrations.

In the figure 19, PM0.3, PM0.5 and PM5.0 indicate the concentrations of the aerosols with diameters (sizes) respectively form $0.3\mu\text{m}$, $0.5\mu\text{m}$ and $5.0\mu\text{m}$, up to the maximum measured diameter $100\mu\text{m}$.

The trend lines connecting the result points are the approximation lines in the form of polynomial of order 3.

4. Analyses of dust mass concentration

The daily variations of the aerosol mass concentration (PM1, PM2.5 and PM10) are given by the figure 20-23. It must be noted that because of the urban measurements of this variation, it takes into account also the traffic effects and other human made particulate sources.

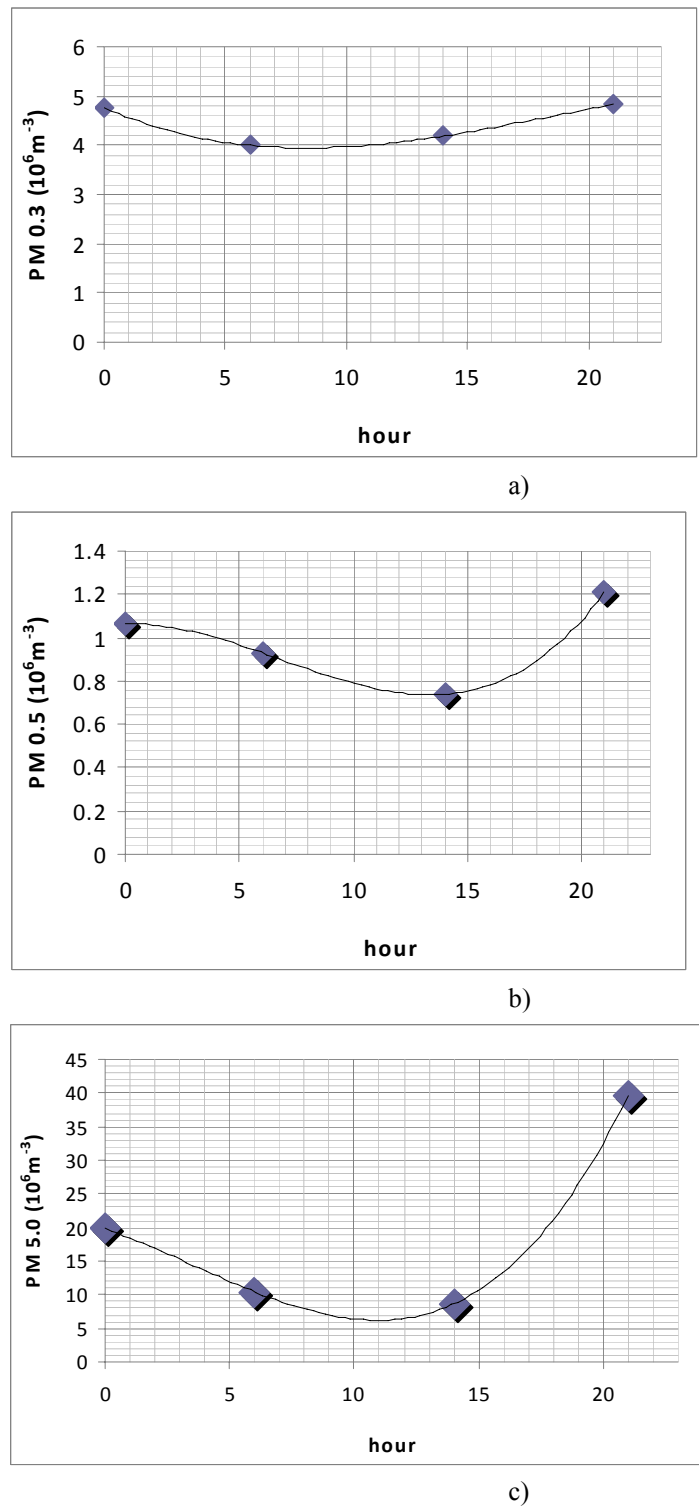


Figure 19. a) Daily variation of PM 0.3 (particles greater than $0.3\mu\text{m}$). b) Daily variation of PM 0.5 (particles greater than $0.5\mu\text{m}$), c) Daily variation of PM 5.0 (particles greater than $5.0\mu\text{m}$).

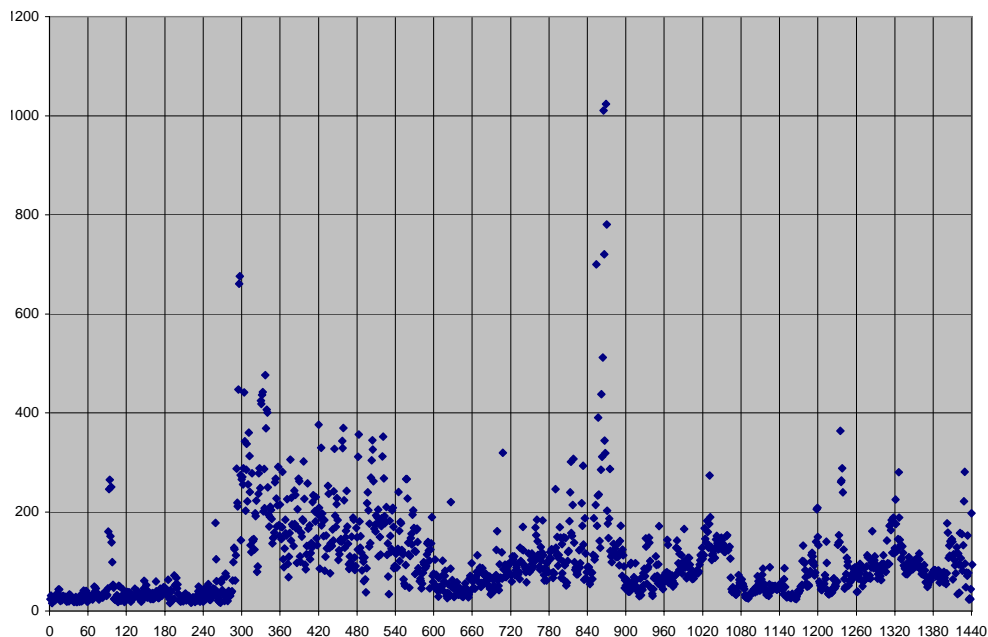


Figure 20. Daily variation of the PM1.

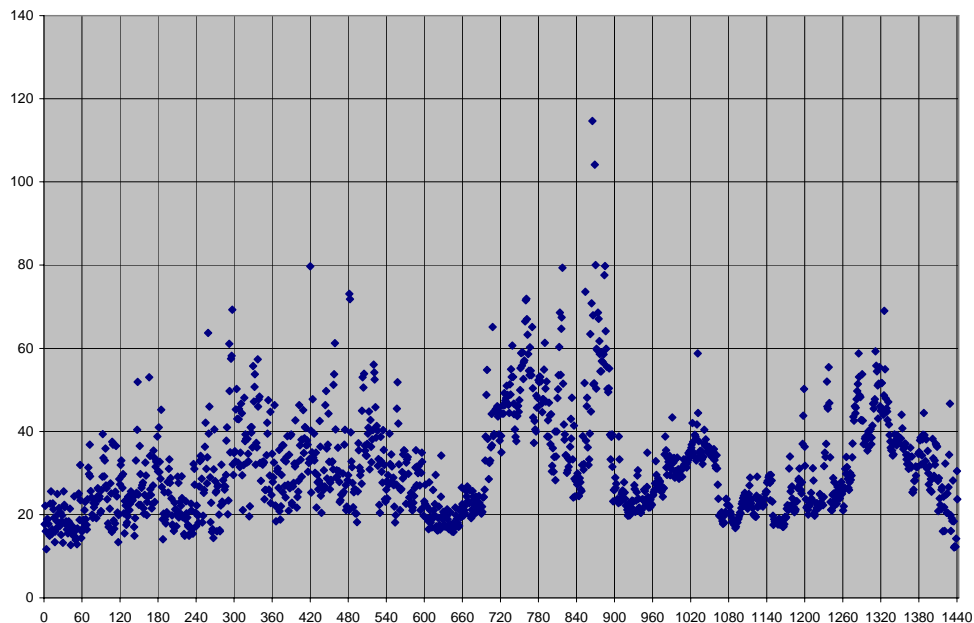


Figure 21. Daily variation of the PM2.5.

In the graphics (fig.20-23), the mass concentrations are expressed in $\mu\text{g}/\text{m}^3$, and the time in minutes. Measurements are realized in the urban areas, in the kerbsides. PM1, PM2.5 and PM 10 indicate the concentrations of the aerosols respectively within in the size intervals ($0.25\mu\text{m} - 1\mu\text{m}$), ($0.25\mu\text{m} - 2.5\mu\text{m}$) and ($0.25\mu\text{m} - 10\mu\text{m}$). Time 0, in the PM graphics, corresponds to the time of measurement beginning (09^{th} local time). The time interval is

1min, and during the all daily cycle we have 1440 measurement values. For more ease visualization, it can be averaged during one hour, and so can be presented only 24 measurement values in one day cycle. To eliminate the random fluctuations, which don't carry a net physical interpretation (like an accidental strong wind or when someone approaches to the measurement instrument), we can cancel the extreme (maximum) values of the PM concentrations.

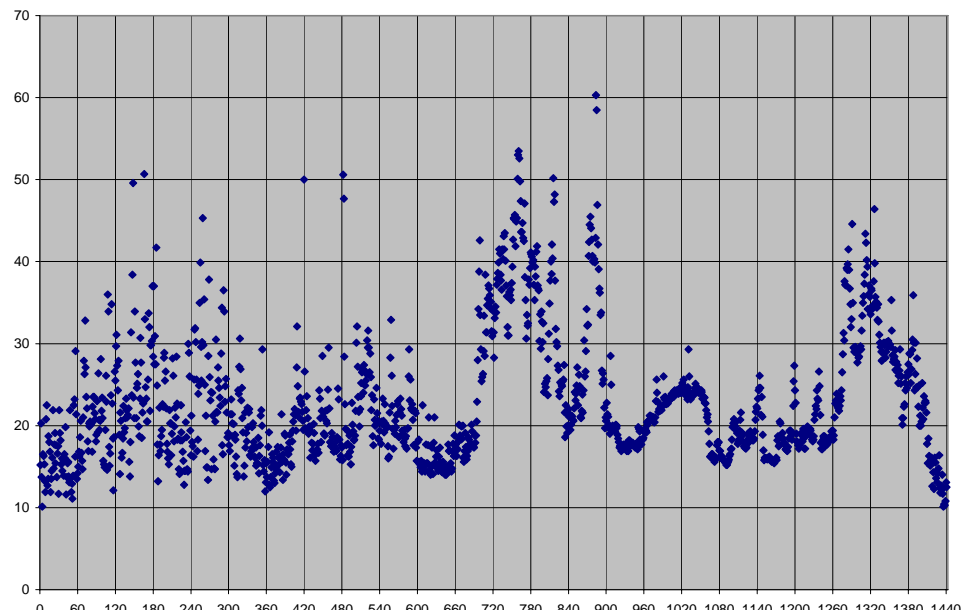


Figure 22. Daily variation of the PM10.

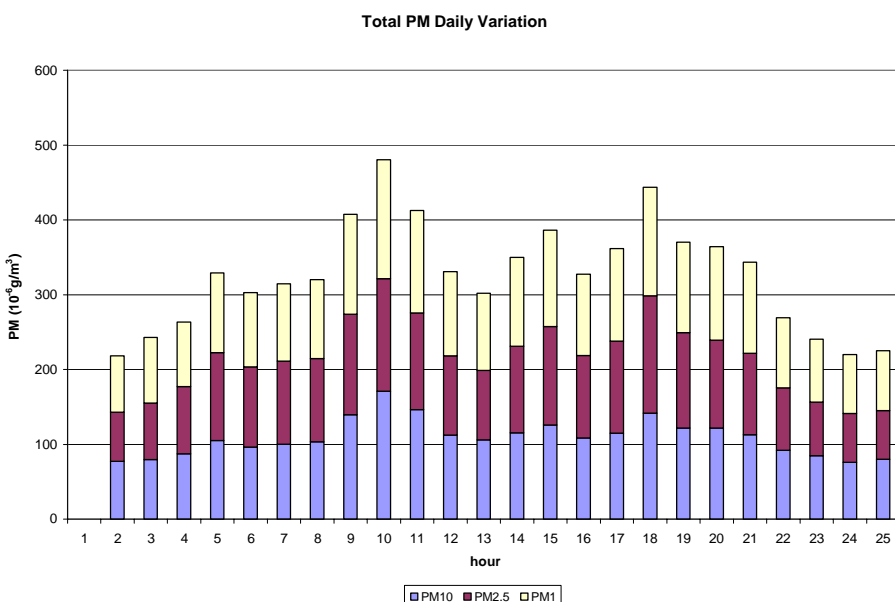


Figure 23. The averaged daily variation of PM1, PM2.5 and PM10.

The averaged over all time measurement values of the daily variation of PM1, PM2.5 and PM10 mass concentrations are presented by the figure 23.

5. The determination of the interactions intensity among atmospheric ions and aerosol particles

In order to make good predictions about the intensity of interactions among atmospheric ions and aerosol particles, one must determine the attachment coefficients β . Having this in mind it is formed a system of four equations and four variables; α , β , β_+ , and β_- .

$$\begin{aligned} \alpha n_+ n_- + \beta n N &= q \\ \alpha n_+ n_- + \beta_+ n_+ \frac{N}{2} &= \frac{q}{2} \\ \alpha n_+ n_- + \beta_- n_- \frac{N}{2} &= \frac{q}{2} \\ n_+ \beta_+ + n_- \beta_- &= n \beta \end{aligned} \quad (15)$$

where α is the ion-ion recombination coefficient, β is the ion-aerosol attachment coefficient, β_+ is the attachment coefficient for the positive polarity, and β_- is the attachment coefficient for the negative polarity.

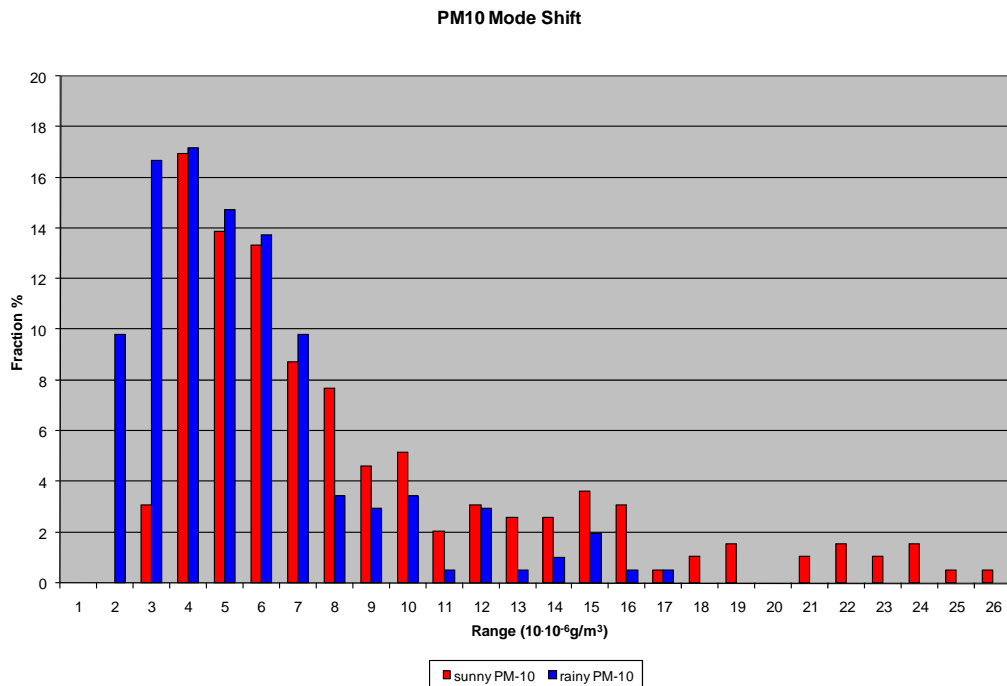


Figure 24. Mode shift during rainy days.

This system is constructed assuming that half of particles interact with positive ions and another half with negative ions, so the positive and the negative ions interact with the same number of aerosols. The solution of the system (15) gives the values of the attachment β and recombination α coefficients:

$$\alpha = \frac{q}{3n_- n_+} \quad (16)$$

$$\beta = \frac{2q}{3nN} \quad (17)$$

$$\beta_+ = \frac{q}{3n_+ N} \quad (18)$$

$$\beta_- = \frac{q}{3n_- N} \quad (19)$$

Obtaining these values of the attachment coefficients, we can “measure” the intensity of interaction among atmospheric ions and aerosol particles. This is a theoretical interpretation of the interaction and it must be compared with measurement data to evaluate its accuracy.

It can be seen that the ion-ion recombination coefficient is related with the ion production rate q (the intensity of the radiation sources) and the total ion concentration ($n = n_+ + n_-$). The ion-aerosol attachment coefficient is related with the ion production rate q and total ion concentration too, but also with the aerosol concentration. If we find large values in the ion and aerosol concentrations in the constant ion production rate, the coefficients of their attachment processes have to be very low, and vice versa.

This is a statistical interpretation (based on the measurement data) of the recombination and attachment coefficients. Their magnitudes depend not only on their concentrations (n and N) but also on their physical and chemical properties, like size, shape, electric charge, chemical composition, etc.

6. Determination of the dependence of atmospheric ion concentration from the altitude.

Altitude dependencies of the atmospheric air ions, in the lower part of the Troposphere are generally expressed in the exponential decay form.

$$C(z) = C_o e^{-\frac{z}{H}} \quad (20)$$

where C_o is the concentration in quote zero, and H is the scale height for ions and aerosols.

These altitude dependencies are determined based on the seashore and suburbs measurements carried out in the summer season. The altitude dependencies of atmospheric ions are presented by the graphics and respective analytical functions:

Graphically the dependencies for the seashore measurements are presented by the figures 25-27.

The blue lines represent measurement values, as the red ones the theoretical values.

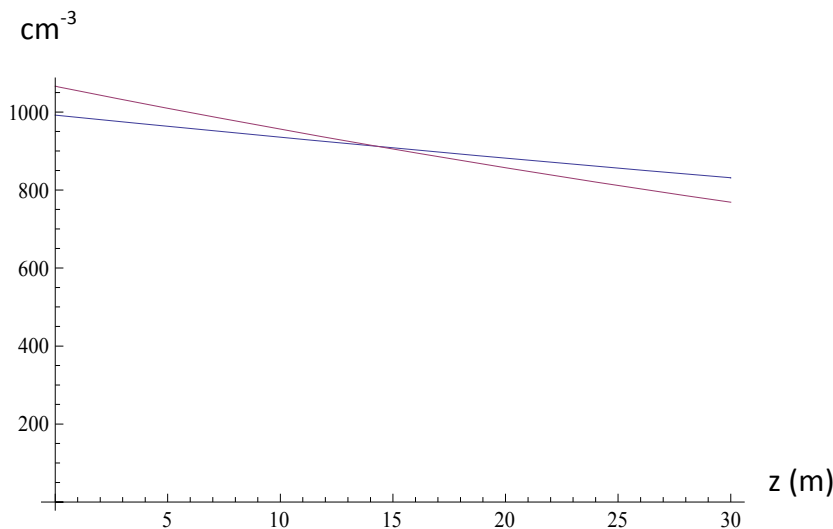


Figure 25. Altitude dependence of the concentration of positive atmospheric ions.

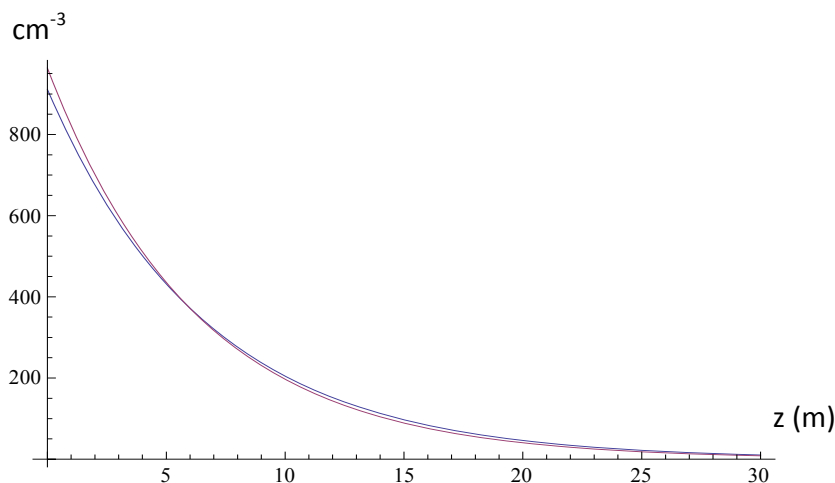


Figure 26. Altitude dependence of the concentration of negative atmospheric ions.

The analytical functions of the altitude dependencies for atmospheric ion, in the seashore measurement campaign, are given by the equations 21-23.

$$n^+(z) = 992.15 \cdot e^{-\frac{z}{169.5}} \quad (21)$$

$$n^-(z) = 911 \cdot e^{-\frac{z}{6.7}} \quad (22)$$

$$n(z) = 1847.7 \cdot e^{-\frac{z}{23.9}} \quad (23)$$

The scale height for the atmospheric ions near the ground in this case is:

$$H_+ = 169.5 \text{ m}, H_- = 6.7 \text{ m} \text{ and } H = 23.9 \text{ m}.$$

In the equations 21-23 there are approximated the experimental results with the final exponential decay form.

The measurement location is characterized by a relatively high population concentration. This is because the measurements in the seashore are carried out in the summer season in the Adriatic seashore. This fact indicates the high concentrations of the aerosols composed by the marine sea salt and the anthropogenic sources like traffic effects, etc.

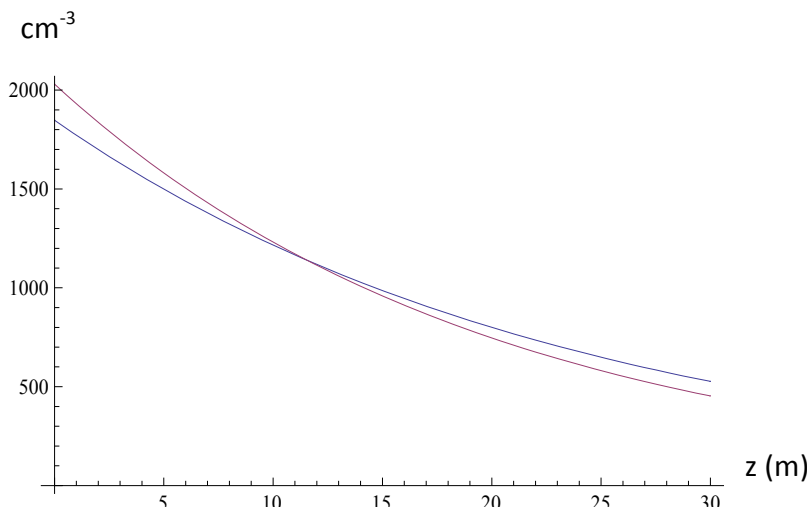


Figure 27. Altitude dependence of the concentration of atmospheric ions.

The dependencies for the suburbs measurements are presented by the figures 28-30.

The analytical functions of the altitude dependencies for atmospheric ion, in the suburbs measurement campaign, are given by the equations 24-26.

$$n^+(z) = 101.1 \cdot e^{-\frac{z}{14.1}} \quad (24)$$

$$n^-(z) = 64.6 \cdot e^{-\frac{z}{23.4}} \quad (25)$$

$$n(z) = 174.4 \cdot e^{-\frac{z}{16.6}} \quad (26)$$

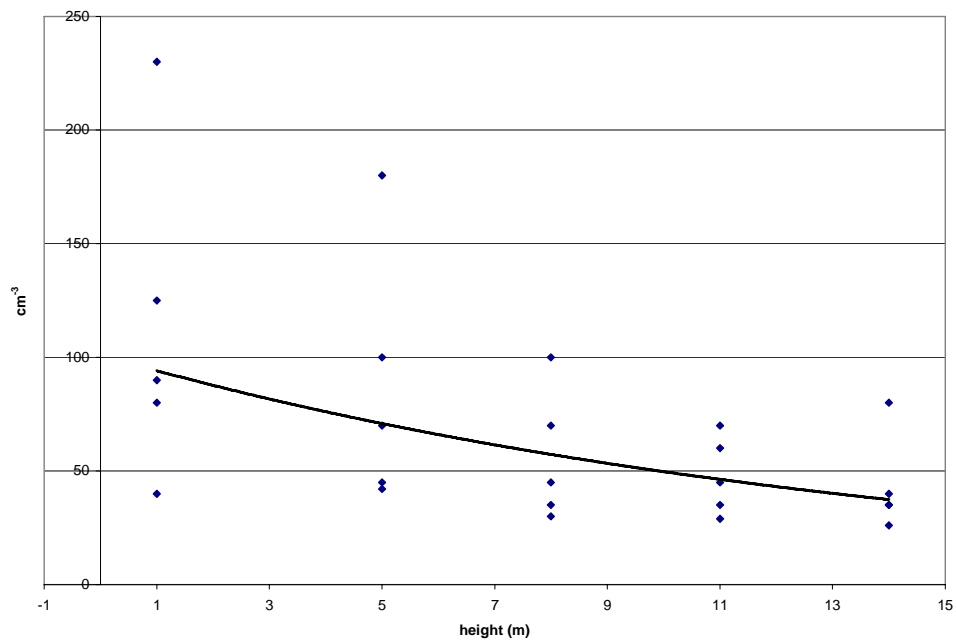


Figure 28. Altitude dependence of the concentration of positive atmospheric ions.

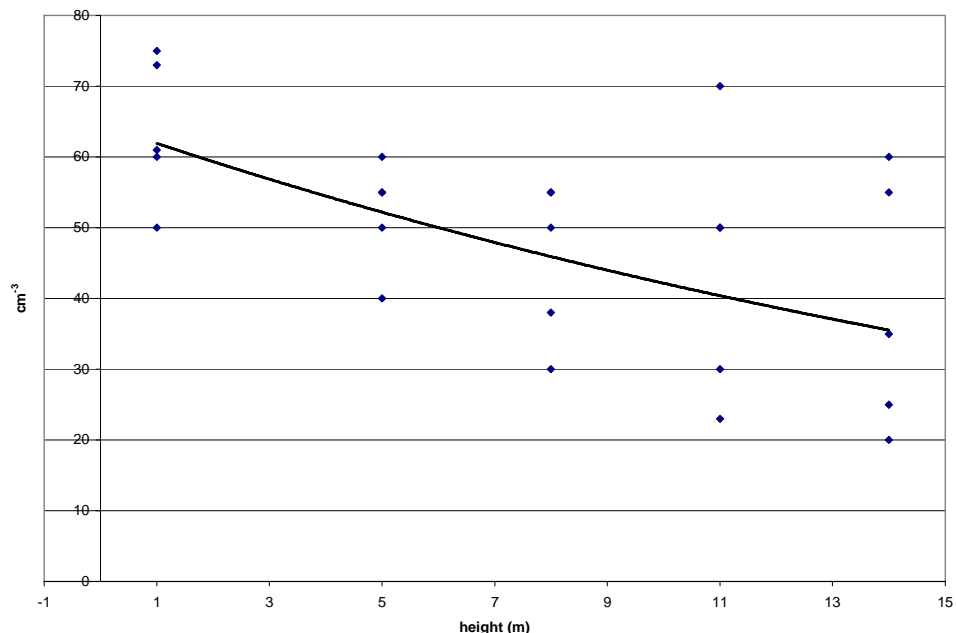


Figure 29. Altitude dependence of the concentration of negative atmospheric ions.

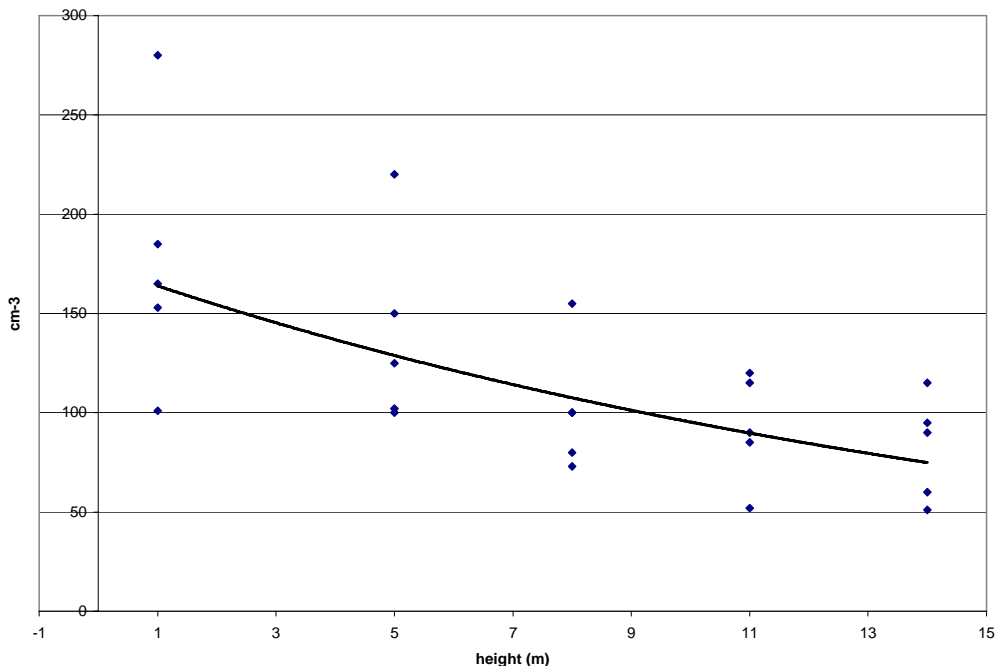


Figure 30. Altitude dependence of the concentration of atmospheric ions.

The scale height for the atmospheric ions near the ground in this case is:

$$H_+ = 14.1 \text{ m} \text{ and } H_+ = 23.4 \text{ m} \text{ mo. } H_+ = 16.6 \text{ m} .$$

The measurements are carried out in the suburbs of a relatively small city. This city has around 100,000 habitants, and so the human contribution on the aerosol concentration increase is somewhat low. Another characteristic of the measurement zone is the vicinity of the lake. It influences mostly in reduction of the aerosol concentration and in the ion production also.

It can be inferred that the most important variable parameter in the seashore and suburbs (include also the presence of lake) areas seems to be the different aerosol concentration in these areas.

7. Radon concentration monitoring

Radon Rn-222 is a radioactive noble gas, invisible, colorless and odorless. It has a half-life of 3.823 days and decomposes by alpha particle emission into Po-218. Its concentration is 150 atoms in every ml air, or 6×10^{-20} radon atoms for every air molecules. Radon is derived from the radium decay which itself is derived form the decay of uranium found in the soil. Uranium concentration in the soil varies 0.5-5.0ppm, depending on the soil properties. Some types of rocks have higher than average uranium contents [81-83]. These include light-colored volcanic rocks, granites, dark shale, sedimentary rocks that contain phosphate, and metamorphic rocks derived from these rocks. These rocks and their soil may contain as much

as 100 ppm uranium. Radon is responsible for about 55% of natural background radioactivity, contributing by 10 mSv/yr. Because of its mass density is approximately eight times greater than mean air density, radon is accumulated mostly in the lowest part of the troposphere. Because of this spatial distribution and the fact that this gas is an indicator of the air quality, the monitoring of the radon concentration becomes of great importance. Rn-222 contributes also on 40% of the atmospheric ion production, determining so on the electrical conductivity of the atmosphere [83-85]. The radioactivity levels in the outdoor ambient are less than indoor ambient, with respective values 10 and 40 Bq/m³ [85-87].

Radon influences indirectly on the human health. Its decay products polonium-218 and polonium-214, are attached on the aerosol particles are inhaled on the respiratory system. Inside the respiratory organs the radon decay products emits alpha particles which destroy the DNA and consequently causes cancer. According to the EPA, radon is the second most important factor, after smoking, causing cancer. Lung cancer is much higher when radon exposure is combined with smoking. EPA establishes the alarm level of the radon concentration is 4pCi/L. In the European Union the alarm level is 400Bq/m³.

The alarm limits of the radon in the water are respectively, 300 pCi/L and 1000 Bq/l ($1\text{pCi/L} = 37 \text{ Bq/m}^3$). The radon concentrations in the underground water are many times greater than the radon concentrations in the surface water. So the monitoring of the radon concentration can be a key indicator on the study of the underground water. In order to evaluate the presence of radon in the outdoor environments, it has been monitored the region of Shkodra Lake (near the city of Shkodra) in the period January-April 2009.



Figure 31. The satellite photograph of Shkodra Lake (Google Earth).

There are selected several locations around the waterside, both in Albanian and Montenegro part of the lake. The principal meteorological parameters during the measurement campaign are presented in the table 7.

Table 7. The meteorological parameters during the measurement campaign

	Minimal	Maximal	Mean
Air temperature (°C)	5.2	24	14.8
Relative humidity (%)	27.1	68	43.5
Atmospheric pressure (hPa)	1010.8	1015.3	1011.5
Wind speed (km/h)	0.0	9.3	2.07

The fundamental parameters indicating the radon presence in the air are its concentration and the alpha particle emission. These two radiation parameters are measured around the perimeter of the Shkodra Lake.

The values of radon concentration, alpha particles detection and the respective meteorological parameters are presented in the table 8.

Table 8. Values of the measurement campaign

Location	Radon (Bq/m³)	Alpha particles/hour	Weather condition	Temperature (°C)	Relative humidity (%)	Wind speed (km/h)
Zogaj	22	14	Cloudy	11.3	66.1	1.40
Zogaj	18	12	Sunny	6.5	43.4	3.52
Shiroke	25	16	Rain	10.3	78.9	1.22
Shiroke	22	14	Sunny	10.0	36.4	4.20
Shkoder	18	12	Sunny	22.0	30.3	1.20
Demiraj	33	19	Sunny	21.0	41.7	1.00
Koplik	14	10	Sunny	22.7	28.8	0.7
Shegan	25	15	Cloudy	12.7	45.3	3.53
Bozhaj	62	35	Sunny	17.3	30.0	2.00
Bozhaj	7	6	Cloudy	16.8	29.4	0.70
Vranje	29	17	Cloudy	19.5	33.3	1.90
Shkoder	16.5	11.2	Sunny	19	70	0.5
Shkoder	15.5	10.9	Sunny	23	60	0.3
Velipoje	11	8	Sunny	22	65	7
Razem	14	10	Sunny	22	52	4

In the last two rows of the table 8 are presented the radon values respectively in the seashore and mountain campaigns.

In order to compare the mean values obtained on the measurements near the Shkodra Lake, we have make measurements in the city of Shkodra and in the remote areas like mountains and seashores.

The mean value of the radon concentration around the Shkodra Lake, in the city of Shkodra, and in the remote areas (mountain and seashore) is given in table 9.

Table 9. Mean values of the radon and alpha particles in the Shkodra Lake and city of Shkodra

	Radon (Bq/m³)	Alpha particles
Shkodra Lake	25.0	15.45
City of Shkodra	9.25	7.96
Remote areas	12.5	9.00

From the above values (table 9), it's clearly seen that the values obtained near the Shkodra Lake are greater than the values in the center of city of Shkodra, indicating different geological structures of the alluviums in these zones. These values are also greater than the remote areas values, despite the minor differences with these zones.

But all the above values lay in the relatively narrow interval, even the measurement values of the remote areas.

The importance of these radon measurements are not only on the environmental concern (because the Shkodra Lake is the greatest lake in the Balkan Peninsula), but also in the determination of the radiation budget near the ground in suchlike regions. This radiation budget lets us to determine indirectly the ion production rate, which constitutes the principal factor on the electricity of the lower part of the Troposphere.

It must be mentioned that the altitude of the measurements are only some cm above the ground surface. This is done to determine also the cracks on the rocks, which gives a very high radon concentration from the profoundness of the ground. In these locations are frequently found underground water sources, where the water bubbles and releases radon in the air. It is this fact that we have found greater radon concentration in these locations.

8. Meteorological parameters continuous monitoring.

During the air ion measurements are recorded also the meteorological parameters, as air temperature, relative humidity and atmospheric pressure. Because of large interval of measurements, almost during all the annual variations, there are taken extremely values of the meteorological parameters. The variations of the air ions of both polarities with the meteorological parameters are presented by the figures 32-34.

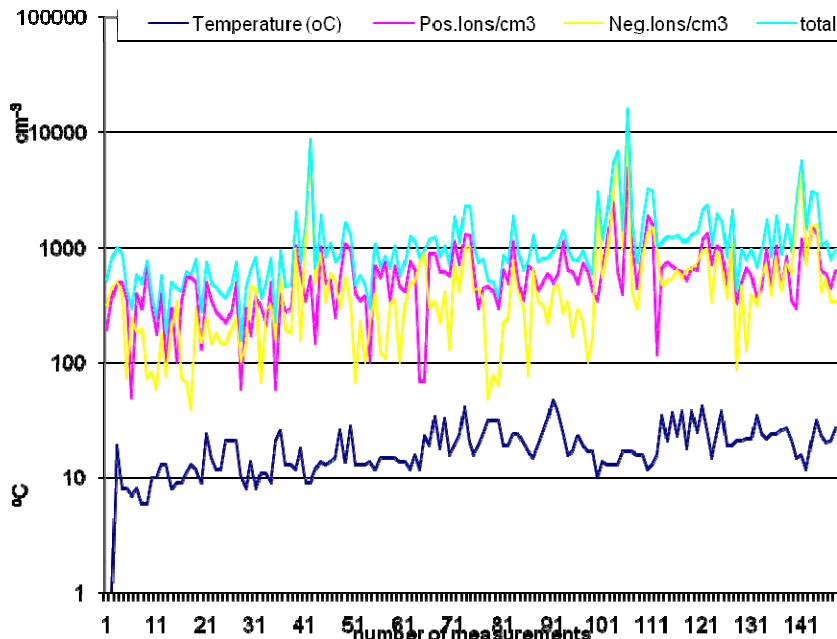


Figure 32. Variation of atmospheric ion concentration with air temperature.

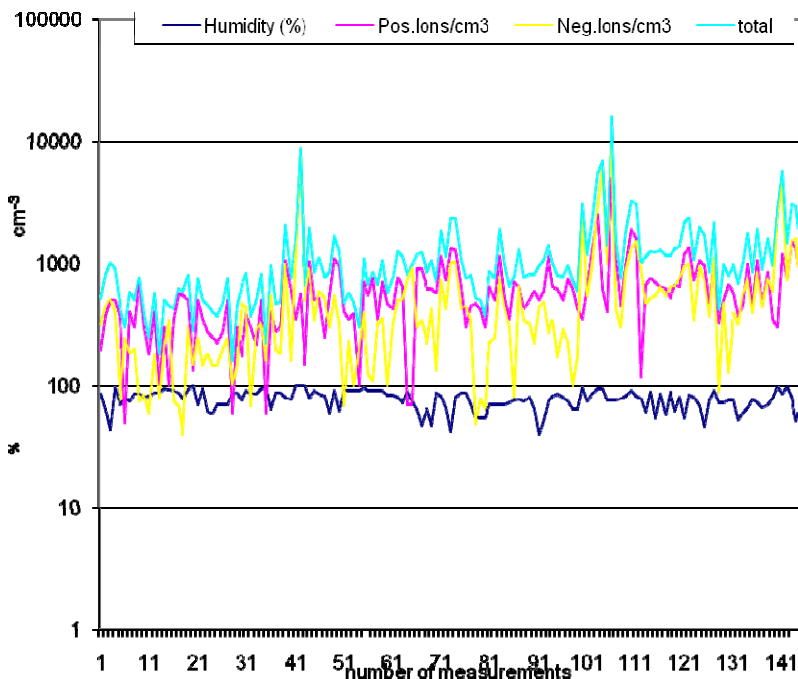


Figure 33. Variation of atmospheric ion concentration with relative humidity.

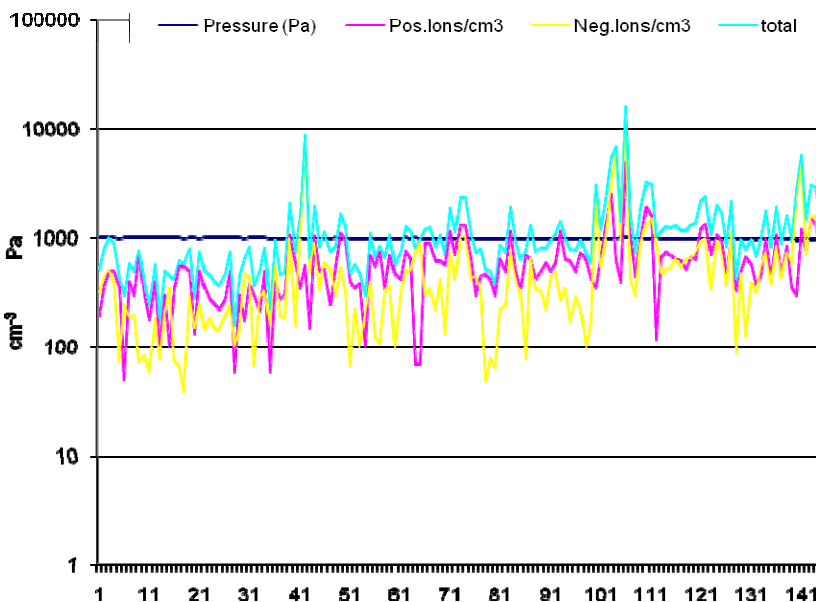


Figure 34. Variation of atmospheric ion concentration with atmospheric pressure.

The lines in the figures 32-34, indicating the relationship between the atmospheric ions and the principal meteorological parameters, are approximation lines which connect the measurement points. In order that the presentation of the graphics is clear, are used the logarithmic scale. In the y-axis are presented both the atmospheric ion concentration and the

values of the air temperature, relative humidity and the atmospheric pressure. In the x-axis are listed the number of the measurements.

In the figure 34, due to the relative low variability of the atmospheric pressure, its variation line is almost a horizontal line (around the value 1000 Pa).

Discussion

From values of the tables 5-6 can be easily verified that aerosol concentration in bars and notably in factories is much more greater than in other indoor ambients. Measurements in several types of factories signify the fact that the aerosol concentrations depend mainly on the sources of the particles. In the case of factories the primary particle sources are machinery engines that depend on the type of the factory. In the case of bars the smoke constitutes the major part of the aerosol. Because their relative tightly places, another aerosol source in the bars is also the respiratory exhaust and inhalation. Theoretically the concentrations of the air ions and aerosol particles must be inversely proportional, but when one measures the charge space, especially in the indoor ambient, it can be found that this quantity is proportional with the concentrations of the aerosol particles. In heavy pollution indoor ambient a large amount of space charge is not in the form of air ions but in the form of charges aerosol particles. That is why in heavy pollution ambient (mostly in the indoor ambient) can be measured high "ion" concentrations. The large amount of air ions and the deficiency in aerosols is a good indicator of air quality, notably in outdoor ambient. Based on the results of tables 4-5, it can be clearly seen that the dwellings, hospitals and schools have relatively cleaner air than bars and particularly factories.

Such a high aerosol concentrations are rarely found in outdoor ambient, even in highly polluted industrial centers, and in these cases the space electric charge is mostly in the form of air/atmospheric ions. So the situation in these environments is in a good accordance with the theoretical predictions, in which ion and aerosol concentrations are inverse proportional related (this is due to the attachment processes of atmospheric ions on aerosol particles). The measurement results show that in the urban centers can be found the higher aerosol concentrations, and so these areas are called heavy polluted areas. The mountains due to their lowest aerosol concentration are the cleanest areas. Rural and seashore have both relatively high atmospheric ion concentrations, but in the second case the aerosol concentration is higher mostly due to the sea salt contribution, and this factor cannot be considered as a pollution factor. Meanwhile in the suburban areas the primarily pollution factors are the influence of the near urban centre, and the roads connecting these areas with urban centers. A minor factor in the suburban areas comes from the human activities carried out in these areas. Both these two areas, seashore and rural, are considered relatively with clean air compared with urban centers.

Daily variations of the atmospheric ions show maximums for both positive and negative polarities in the early morning hours. This is due to the presence of high radon concentrations and low aerosol concentrations in these hours. During the night hours there is an accumulation process of the radon, and the human activities, which elevate the aerosol concentration, are in their lower phase. The minimums are achieved in the afternoon for the positive polarity and some hours later for the negative polarity. Since the unipolarity factor is greater than unity, the total atmospheric ion concentration experiences its minimum on the

afternoon hours, approximately at the same time when the minimum for the positive polarity occurs. The unipolarity factor takes minimum values in the time interval morning-noon. This is thanks to a large presence of negative ions respect to the positive polarity. But the unipolarity even these hours doesn't take values less than unity, showing the predominance of the positive polarity of atmospheric ions during all the measuring time. The lower values of the unipolarity factor can be found in the disturbed meteorological conditions, or when we make measurements on other locations, like mountains, etc. The maximum values of the unipolarity factor are achieved on the afternoon and evening hours.

For all the particle number concentrations (PM0.3, PM0.5 and PM5.0) the maximum occurs on the evening hours. The particulate sources are activated mostly in the daytime hours. But if we take into account the fact that measurements are performed in the seashore, and the distances among measurement points and particulate sources (mostly traffic roads) are relatively long, it lets to conclude that the maximum concentrations may be postponed by some hours. Probably in these hours occurs the steady state between the particle formation and particle precipitation/deposition. For the same reason the minimum of aerosol concentration comes in the interval from morning hours till the noon. The minimum in the PM0.3 concentration comes some hours earlier than the maximum of the PM5.0, because the smaller particles the greater are their effectiveness in diffusion and transportation. It is important to emphasize that PM0.3 and PM0.5 particles lays in accumulation and coarse modes, meanwhile PM5.0 particles lay only in the coarse mode. Observing the daily variations of the ion and particle number concentrations may be concluded with a certain approximation, that two concentrations have inverse proportional relationship. The correlation coefficients between aerosol concentrations PM0.3, PM0.5, PM5.0, and air ion concentrations are given in table 10.

Table 10. The correlation coefficients between concentration of aerosol particles and atmospheric ions

	Positive Ions	Negative Ions
PM 0.3	-0.213	-0.973
PM 0.5	0.284	-0.654
PM 5.0	-0.117	-0.755

The reason of these three threshold channels ($0.3\mu\text{m}$, $0.5\mu\text{m}$ and $5.0\mu\text{m}$) are the cleanroom classifications. Cleanrooms are classified according to the number and size of particles permitted per volume of air. Large numbers like "class 100" or "class 1000" refer to FED-STD-209E, and denote the number of particles of size $0.5\mu\text{m}$ or larger permitted per cubic foot of air. The standard also allows interpolation, so it is possible to describe e.g. "class 2000". Small numbers refer to ISO 14644-1 standards, which specify the decimal logarithm of the number of particles $0.1\mu\text{m}$ or larger permitted per cubic meter of air. Both FS 209E and ISO 14644-1 assume log-log relationships between particle size and particle concentration. For that reason, there is no such thing as a "zero" particle concentration. The locations (table 11-12) without entries are N/A ("not applicable") combinations of particle sizes and cleanliness classes, and should not be read as zero. Because 1 m^3 is approximately 35 ft^3 , the two standards are mostly equivalent when measuring $0.5\mu\text{m}$ particles, although the testing standards differ. It must be mentioned that ordinary room air is approximately class 1,000,000 or ISO 9.

Table 11. US federal cleanrooms standards

Class	maximum particles/ft ³					ISO equivalent
	≥0.1 μm	≥0.2 μm	≥0.3 μm	≥0.5 μm	≥5 μm	
1	35	7	3	1		ISO 3
10	350	75	30	10		ISO 4
100		750	300	100		ISO 5
1,000				1,000	7	ISO 6
10,000				10,000	70	ISO 7
100,000				100,000	700	ISO 8

US FED STD 209E was officially cancelled by the General Services Administration of the US Department of Commerce November 29, 2001, but is still widely used.

Comparing the results of the tables 1-2, and referential values of the tables 11-12, it can be deduced that air conditions in all indoor environments are outside the ISO standards. Meanwhile in outdoor environments, urban, suburban and seashore are classified as Class 9 and rural and mountains are classified as Class 8.

Table 12. ISO 14644-1 cleanroom standards

Class	maximum particles/m ³						FED STD 209E equivalent
	≥0.1 μm	≥0.2 μm	≥0.3 μm	≥0.5 μm	≥1 μm	≥5 μm	
ISO 1	10	2					
ISO 2	100	24	10	4			
ISO 3	1,000	237	102	35	8		Class 1
ISO 4	10,000	2,370	1,020	352	83		Class 10
ISO 5	100,000	23,700	10,200	3,520	832	29	Class 100
ISO 6	1,000,000	237,000	102,000	35,200	8,320	293	Class 1000
ISO 7				352,000	83,200	2,930	Class 10,000
ISO 8				3,520,000	832,000	29,300	Class 100,000
ISO 9				35,200,000	8,320,000	293,000	Room air

The daily variation of the aerosol mass concentrations (dust components PM1, PM2.5 and PM10) are well correlated with the presence of particulate sources. In outdoor ambient these sources may be traffic contributions, as machines exhaust or re-suspended dust, and non traffic contributions like wind dust, etc. In the dust monitoring are selected fair weather days (low wind days), and so the last contribution may be neglected. The first two traffic effects enter in action at simultaneity. Having a look to the graphics of the figures 20-22, can be seen that the highest aerosol mass concentrations occurs in the morning hours (07⁰⁰-09⁰⁰), around the noon (12⁰⁰-14⁰⁰), and in the evening hours (19⁰⁰-20⁰⁰). These are local hours that people usually use respectively to go in work, to return from work, and to take outgoing. The graphic

in figure 24 presents the frequency distribution of the different aerosol mass concentrations, in the size interval $20\mu\text{m}$ in sunny and rainy days. From that graphics can be noted that the concentrations in both meteorological conditions are log-normally distributed.

The distribution parameters are given in the tables 14-15 (PM units, $\mu\text{g}/\text{m}^3$).

- Sunny days

Table 14. Distribution parameters in sunny days

	Mean	Minimal	Maximal	Median	Mode	St. Deviation
PM 10	114.67	2.7	6500	88.1	91.8	129.96
PM 2.5	38.74	2.2	1678.6	32.7	20.7	28.22
PM 1	28.80	1.9	393.4	22.9	15.4	19.88

- Rainy days

Table 15. Distribution parameters in rainy days

	Mean	Minimal	Maximal	Median	Mode	St. Deviation
PM 10	82.55	1.5	4052.6	56.15	15.70	103.59
PM 2.5	29.75	1.2	683.2	23.4	9.0	24.51
PM 1	22.15	0.8	203.4	16.6	5.7	18.46

From the graphic 24 and tables 14–15 it can be seen that the mean, median, mode, standard deviations, and minimal and maximal values are reduced in the rainy days respect to the sunny days. The mode in the rainy days moves toward the lower values (to the left of the graphic in the figure 24).

There are determined also the scale height for PM1, PM2.5 and PM10 aerosol mass concentrations in the urban areas. The final calculations of the measurement results in different altitudes (in the range 1-14m) give the exponential decay form of their altitude profile:

$$\text{PM} = \text{PM}(0) \cdot e^{-\frac{z}{H}} \quad (27)$$

where $\text{PM}(0)$ is the PM concentration near the ground (quote zero) and H is scale height of the PM altitude profile. Scale height of their altitude profiles are given in the table 16.

Table 16. PM-s scale heights

	PM 10	PM 2.5	PM 1
Scale height (m)	40.02	132.83	285.53

Values of the table 16 height indicate that smaller particles have greater scale height, a result which is in a good accordance with the gravitational Boltzman distribution of the aerosol particles.

The figure 24 shows the statistical distribution of mass concentration in different meteorological conditions; fair weather and during precipitations. Both distributions are of

log-normal type, where in the rainy days the mode of distribution is reduced compared with the mode in sunny days. Maximum reductions are obtained for PM10 distributions. This is thanks to the greater effectiveness of interaction between larger particles and water droplets, because their greater cross sections. During precipitations the larger and smaller limits of the distribution are also reduced. This happens because large concentrations are rarely found in these meteorological conditions, and small concentrations happen more frequently. The average value of the distributions is also reduced in rainy days.

During foggy days the distribution of aerosol mass concentration is somewhat not regular. There are found much greater concentrations of all PM-s.

In the table 17-18 are listed principal values of the distributions in sunny and foggy days.

- Sunny days

Table 17. Distribution parameters in sunny days

	Mean	Minimal	Maximal	Median	Mode	St. Deviation
PM 10	128.0	63.4	315.9	116.4	85.1	47.32
PM 2.5	60.9	35.6	136.4	62.1	42.3	13.91
PM 1	53.2	31.1	130.0	52.1	40.1	13.26

- Foggy days

Table 18. Distribution parameters in foggy days

	Mean	Minimal	Maximal	Median	Mode	St. Deviation
PM 10	1941	110.2	6500	1620	110.2	1563
PM 2.5	123.5	72.9	231.3	118.1	72.9	38.8
PM 1	78.7	65.5	96.8	79.1	65.5	8.20

Mean values of PM concentrations in urban, rural areas and international limits are presented in the table 19.

- Sunny days

Table 19. Aerosol mass concentrations in sunny days

	Urban	Rural	WHO	EPA
PM 10	114.67	47.6	20	50
PM 2.5	38.74	29.3	10	15

The annual mean aerosol concentrations in urban centre of Shkodra, Albania are well outside the recommendations of both WHO and EPA. In rural areas around, 7km from city of Shkodra, concentration values are also somewhat outside above mentioned recommendations.

The balance equation connect ion production rate by all sources and factors which reduce ion concentration. The principal sources of ion production in the lower part of the Troposphere are radon, cosmic rays and radioactive material on the Earth surface. Radon concentration has an exponential decay altitude profile thanks to its specific mass greater than air in normal conditions. Cosmic rays contribute almost uniformly in this part of Atmosphere

(their variation in the ion production contribution begins in the higher part of the atmosphere). The radiation from the radioactive material on the Earth surface contributes in the ion production only in relatively very lower altitudes (inverse square law). Reduction factors are the processes of the recombination among ions with opposite polarity and attachment among ions and aerosols. In the limit cases; in clean environments the recombination process becomes dominant, but in heavy polluted environments the attachment process is dominant. In both cases aerosol altitude profile is exponential decay. The natural aerosol particles may be charged (positive or negative) or uncharged (electrically neutral). In the theoretically model it is assumed that atmospheric ions of either polarity n_{\pm} interacts with half number of aerosols $N/2$. This situation emerges when air ions interacts only with aerosols (charged particles) with opposite polarity and the number of positive charged aerosols to be equal with the number of negative charged aerosols $N_{\pm} = \frac{N}{2}$ (N_c is the number of charged aerosols).

Another possibility to occur this situation is that air ions interact with uncharged aerosol particles, but their interaction doesn't depend on their polarity. So the balance equation can be written for total ion concentration and for the concentration of both polarities. In this stage there are three equations with four variables; α , β , β_+ , and β_- :

$$\begin{aligned}\alpha n_+ n_- + \beta n N &= q \\ \alpha n_+ n_- + \beta_+ n_+ \frac{N}{2} &= \frac{q}{2} \\ \alpha n_+ n_- + \beta_- n_- \frac{N}{2} &= \frac{q}{2}\end{aligned}\tag{28}$$

In order to have a valid solution (the determination of the required coefficients) in the system (28) it must be added another equation. The fourth equation comes from the condition that the interaction of atmospheric ions with aerosol particles is composed by the two components, one for the positive polarity and another for the negative polarity.

$$n_+ \beta_+ + n_- \beta_- = n \beta\tag{29}$$

Having now for equations with four variables, we can find the solutions for the required coefficients. All these coefficients depends to the ion production rate q , ion concentrations n , n_+ , n_- , and aerosol number concentration N . To have more accurate solutions it must separate aerosol particles based on their charge and size distributions. Also it must be known the atmospheric ion size distribution. This is because the interaction among atmospheric ions and aerosol particles depends on their electric charge and on their size distributions.

One of the most important topics in this study is the altitude profile of the atmospheric ions. It depends on several factors, such as the altitude profiles of the ion sources and altitude profiles of reductions mechanisms. The altitude diapason of in the measurements is 1-15m in suburbs and seashore. We have to make some assumptions about the dependence in this altitude range of the above mentioned factors. Above the height 1m the contribution on the

ion production of the radioactive materials in the Earth surface can be neglected. This is because of the inverse square law of the radioactivity intensity $I = \frac{A}{d^2}$, where A is a constant and d is the distance from the radioactivity source.

Cosmic ray exerts a constant effect on the ion production in all this range of altitudes (table 20).

Table 20. Altitude Dependence of Cosmic Ray Dose (dose equivalent; does not include the neutron component)

Altitude, m (ft)	Dose Rate, mrem/y
Sea level	31
1,525 (5,000)	55
3,050 (10,000)	137
9,140 (30,000)	1900
15,240 (50,000)	8750
24,340 (80,000)	12,200

Radon concentration has a exponentially decay altitude profile (Boltzman altitude distribution). So these three principal contributors on the ion production are expressed by a sum of a constant term (cosmic ray contribution) and a exponentially decay term (radon contribution):

$$\text{ion production}(z) = a + b \cdot e^{-\frac{z}{c}} \quad (30)$$

The principal factors on the ion reduction are their aerosol attachment and the precipitation/deposition. The attachment process is related with the aerosol concentration, which has an exponentially decay altitude profile. Precipitation of the atmospheric ions on the Earth surface depends on the air parameters, meteorological conditions, atmospheric electric field, etc. Meteorological conditions are selected fair-weather, and so the atmospheric electric field, wind speed and air parameters are in a stationary state. In order to evaluate the precipitation factor, we must give the table of the forces acting on the air ion. The principal forces are electric force, drag force and gravitational force:

$$\vec{F} = \vec{F}_e + \vec{F}_d + \vec{F}_g \quad (31)$$

where:

$\vec{F}_e = q\vec{E}$ is the electric force, q is ion electric charge, $\vec{F}_d = -6\pi\eta r_s$ is the drag force, η is air dynamic viscosity ($\eta = 1.846 \cdot 10^{-5}$ kg/ms in $t = 23^\circ\text{C}$), $r_s = \frac{kT}{6\pi\eta D}$ is Stokes radius, $D = \frac{kT}{q}\mu$ is diffusion coefficient, $\mu = \frac{\vec{v}}{\vec{E}}$ is electric mobility, \vec{v} is ion relative ion

radius, $D = \frac{kT}{q}\mu$ is diffusion coefficient, $\mu = \frac{\vec{v}}{\vec{E}}$ is electric mobility, \vec{v} is ion relative ion

velocity to the air, and \vec{E} is atmospheric electric field. Substituting all the parameters of small atmospheric ions, we obtain the condition $\vec{F}_g \ll \vec{F}_e$. So the dry precipitation factor can be neglected from our calculations. Finally, the reducing factors have only the exponentially decay term. Combining production and reduction factors, the air ion concentration may be expressed by sum of a constant term (cosmic ray contribution), and two exponentially decay terms (radon and aerosol contributions). To simplify the situation, there are treated only limit cases. The treatment of the limit cases is done using the balance equation:

$$\alpha n^2 + \beta N n = q \quad (32)$$

Recombination limit (clean areas):

$$\alpha n^2 = q \quad (33)$$

$$n = \sqrt{\frac{q}{\alpha}} = \sqrt{\frac{1}{\alpha}} \sqrt{q_o + q_1 e^{-\frac{z}{h_r}}} = \sqrt{\frac{q_o}{\alpha}} \sqrt{1 + \frac{q_1}{q_o} e^{-\frac{z}{h_r}}} \quad (34)$$

where h_r is the scale height of the radon concentration.

Because the term $\frac{q_1}{q_o} e^{-\frac{z}{h_q}}$ is much smaller than 1, we can make approximations:

$$n \approx \sqrt{\frac{q_o}{\alpha}} \left(1 + \frac{q_1}{2q_o} e^{-\frac{z}{h_q}} \right) = \sqrt{\frac{q_o}{\alpha}} + \frac{q_1}{2\sqrt{\alpha q_o}} e^{-\frac{z}{h_r}} \quad (35)$$

or

$$n(z) = n_o + n_1 e^{-\frac{z}{h}} \quad (36)$$

where the ion and radon scale height are equal.

In this case the altitude profile of atmospheric is composed by a constant term and an exponential term.

- Attachment limit (polluted areas)

$$\beta N n = q \quad (37)$$

$$n = \frac{q}{\beta N} = \frac{q_o + q_1 e^{-\frac{z}{h_r}}}{\beta N_o e^{-\frac{z}{h_a}}} \quad (38)$$

Where h_a is the aerosol scale height, and $h_a \approx h_r$. Having this fact in mind we can obtain this final result for the ion concentration for in the attachment limit:

$$n = \left(\frac{q_o}{\beta N_o} \right) e^{\frac{z}{h_a}} + \left(\frac{q_1}{\beta N_o} \right) e^{-\left(\frac{z}{h_r} - \frac{z}{h_a} \right)} \quad (39)$$

In this case the altitude profile of atmospheric ions is composed by the sum of two exponential terms.

The radioactive materials in the ground are a fundamental ion production source. Each time an atom of the radioactive minerals in the ground decays near the air, it produces 50,000 - 500,000 air ion pairs [77]. But we are dealing with another important factor; radon. The evaluation of the radon presence in the outdoor ambient is a crucial point in the study of the electric properties of the air. Airborne radioactive materials such are radon, thoron, etc. are determinant factors on the generation of the space charge. Another problem concerning the presence of radon is environmental, because of its very dangerous impact on the human health, especially on the smokers [78]. Let us concentrate on the first problem, the electrostatic problem. Radon in the air produces about 250,000 ion pairs for each decays of radon atom, and the number of ions is directly proportional to radon concentration and the average ion lifetime [79]. The regions monitored for the presence of radon are predominantly rural, but also suburbs, urban seashore and mountain are monitored. The measurement results show that the radon concentrations in these regions are generally within allowed intervals.

The mean radon concentration in these regions is:

$$C = 25.03 \text{ Bq/m}^3 \quad (40)$$

and the standard deviation of these measurement values is:

$$\sigma = 14.18 \text{ Bq/m}^3 \quad (41)$$

The standard deviation has low value, indicating the fact that radon concentration values are included in narrow intervals. Since radon concentration depends on the soil properties, the low value of the standard deviation is due also the relatively small measurement area (around 1000 km²). This fact, and the well known fact of uniform ion production of cosmic rays (in the lower part of Troposphere); signify with a certain approximation the relatively uniform distribution of ion production sources in the measurement region. The ion production from the cosmic rays can be approximated with the Chapman function:

$$Ch(x, \chi) = \sqrt{\frac{\pi x}{2} \sin \chi} \exp\left(\frac{\cos^2 \chi}{2}\right) \left(1 \pm \operatorname{erf} \sqrt{\frac{1}{2} x \cos^2 \chi}\right) \quad (42)$$

where $x = \frac{R + h}{H}$, R is the Earth radius, H is height scale, h is the altitude, χ is the zenith angle (angle with the vertical) and erf is the error function.

Comparing these measurement results on the radon concentration with the precaution values in different countries, given in table 21, it can be easily seen that the radon concentration in the measurement regions is within the allowed values.

Table 21. Domestic radon concentrations and Action Levels in different countries

Country	Action Level (Bq/m^3)	Country	Action Level (Bq/m^3)
Czech Republic	200	Norway	200
Finland	400	Poland	400
Germany	250	Sweden Switzerland	400
Ireland	200	United Kingdom	400
Israel	200	European Community	200
Lithuania	100	USA	400
Luxembourg	250	Canada	150

Theoretically it is known the relationship of radon presence and the meteorological parameters. Experimentally there are derived the correlation coefficients of the radon concentration and the air temperature, relative humidity and the atmospheric pressure (table 22).

Table 22. Correlation coefficients of radon concentration with some meteorological parameters.

	Air temperature ($^{\circ}\text{C}$)	Relative humidity (%)	Wind speed (km/h)
Radon (Bq/m^3)	0.09	-0.04	0.11

The very low values of correlation coefficients are due to relatively low number of measurements of radon concentration in this region and don't indicate the low influence of the meteorological parameters on the radon concentration over the ground. Based on these values, it may not be concluded that the radon concentration doesn't depend very much on the meteorological parameters, or the dependence is very weak. This inference is based also on the well known fact that radon concentration and the atmospheric pressure have an inverse proportional relationship.

$$C(Rn) = \sqrt{a + b \cdot p} \quad (43)$$

Where p is the atmospheric pressure, and a and b are constants.

It is important to emphasize that the measurements of radon concentration are realized in different meteorological conditions; sunny, cloudy, windy and rainy days.

The correlations between meteorological parameters (air temperature, relative humidity and atmospheric pressure) and atmospheric ion concentrations (negative, positive and total) are presented by the table 23.

Table 23. Correlation coefficients of atmospheric concentrations with some meteorological parameters.

	Air temperature (°C)	Relative humidity (%)	Atmospheric pressure (Pa)
Negative ion (cm ⁻³)	-0.05	0.14	-0.15
Positive ion (cm ⁻³)	0.17	-0.10	-0.19
Total ion (cm ⁻³)	0.01	0.08	-0.17
Unipolarity factor	-0.04	-0.08	-0.08

The low value of the correlation coefficients doesn't point out the invariance of these magnitudes, but because the natural meteorological air temperatures, relative humidity and atmospheric pressure vary in relatively narrow intervals, and so the correlation coefficients will have so low values. It is seen from the table 20 that air temperature and relative humidity doesn't affect so much the ion concentrations of both polarities. But the atmospheric pressure is in inverse proportionality with ion concentrations of two polarities and the total concentration. This is in a good accordance with the theoretical evaluations, because the greater values of the atmospheric pressure, the lower are the values of the radon concentration, and so the lower will be also the values of the ion concentration [80]. Theoretically the relative humidity reduces the ion concentration. This fact is evidenced only for the positive polarity by the table 20. The experimental facts for the negative polarity are related with the meteorological conditions, especially in the high and very high relative humidity values. In these conditions the measurements are realized mostly in rainy days. So the reducing effect of high relative humidity is counterbalanced by the fact that the rain process is an intensive ion production (especially for negative polarity) source. The intervals of the air temperature are relatively narrow, and it doesn't let make a good decisions about these correlations. It is seen from the table 24 the air temperature positive correlation with positive ions and negative correlation with negative ion concentrations. This fact is related with the proportionality of the aerosol concentration with air temperature, and the fact that a great part of the space electric charge is in the form of attached on the aerosol particles. Taking into account the fact that aerosols are mostly positive charged, we can argue the correlation coefficients of the air temperature with ion concentrations.

Conclusion

In this chapter there are presented several elaborated data from the many measurement campaigns on the atmospheric electricity parameters. These data are part of a full database on air ion concentration, aerosol concentration and related factors research in the lower part of the Troposphere. The aerosol number and mass concentrations are measured in the 0.25 µm - 100 µm size interval, which covers a part of the accumulation mode and whole coarse mode. This chapter is divided in eight general topics; Ion and aerosol concentrations in the indoor and outdoor ambient, daily variations of the ion and aerosol concentration, analyses of dust mass concentration, determination of the interaction intensity among atmospheric ions and aerosol particles, determination of the atmospheric ion concentration altitude profile, radon concentration monitoring and meteorological parameters continuous monitoring.

In the indoor monitoring, the highest aerosol concentrations are found in the heavy polluted ambient like factories, but also in the bars and other high densely ambients. The space charge in these ambient is mainly in the form of charged aerosols. The minimal aerosol concentrations are found in the cleanest ambient, like hospitals, dwellings or schools, and the space charge in these ambient exist mostly in the form of air ions.

Outdoor aerosol concentrations show the lower differences. In urban or industrial centers are found the maximum aerosol concentrations whereas the minimum concentrations are found mostly in the mountain and remote areas. The atmospheric ion concentration shows an inverse distribution; maximums are found in the mountain and remote areas and minimum concentrations are found in the much polluted areas like urban and industrial centers. The space charges almost in all outdoor ambient is in the atmospheric ions, but also in the charged aerosol form.

The daily variations of atmospheric ions and aerosol particle concentrations (in outdoor ambient) are inverse proportionally with each other. In early morning hours, due to the high radon accumulation, can be evidenced the maximum atmospheric ion concentration. The minimum of the atmospheric ion concentration is achieved on afternoon, when aerosol particles have their daily maximum concentration. Daily variation of the two atmospheric ion polarities has a small difference, only by some hours. The aerosol particle acquires their minimum concentration on the late night or early in the morning, the hours, when the traffic effect is in its minimum.

The interaction between atmospheric ions and aerosol particles determines their concentration, especially the ion concentrations. Due the attachment processes, aerosols reduce the concentration of air ions. But the presence of air ions influence on the new particle formation (ion mediated nucleation), and so increase the aerosol concentration too.

Altitude profile of aerosol concentration is exponentially decayed. Radon has also an exponentially decay altitude profile. Cosmic rays influence uniformly on the ion production. So taking into account all these reduction and production factors, it can be derived a quite complex altitude profile of atmospheric ions. But the situations relatively facilitated when are treated the limit cases; the recombination and the attachment limits.

The radon presence around the monitoring regions is within the normal values. Also the alpha particle concentrations in these regions don't exhibit any abrupt changes, except on any rills.

During the monitoring of the meteorological parameters, are obtained negative correlations between air ions and atmospheric pressure. But the correlations between ion concentrations, air temperature and relative humidity are very weak and also indicate several irregularities. This is mostly due the low interval values of the above mentioned meteorological parameters.

As conclusion it must be mentioned that there are monitored continuously the concentrations of both atmospheric ions and aerosol particles in different locations, different meteorological conditions, monitored their daily variations, determined their altitude profiles, and determined the correlations among atmospheric ion and aerosol concentrations, and the principal meteorological parameters.

Analyzes of all these measurement results and their theoretical interpretations, gives the opportunity to have a clear table of air particle properties (charged and uncharged) and their distributions, so evaluating in an accurate way the electrical properties of the lower part of the Atmosphere.

References

- [1] L. Wahlin, *Atmospheric Electrostatics*, Colutron Research Corporation, Boulder, Colorado, USA, Wiley and Sons, 1989.
- [2] S. V. Anisimov and E. M. Dmitriev, *Aero electrical altitude profile in limit of regular convection*, GEMM Laboratory, Geophysical Observatory, Shmidt Inst. of Earth Physics, RAS Borok, Yaroslavl, Russia, 1997.
- [3] F.Vila & F.Mandija, *Effects of Atmospheric Electricity*, Conference on Natural Sciences and Didactics, pp 23, Shkodër, Albania, 2004.
- [4] R. G. Harrison, Electrical properties of surface atmospheric air at Eskdalemuir, 1909–1911, *Atmospheric Research* **84** (2007) 182–188.
- [5] F.Mandija & F.Vila, *Studies about atmospheric electricity*, American Institute of Physics, AIP Conference Proceedings, Volume 899, pp.755.Melville, New York, USA, 2007.
- [6] J. Chalmers, *Atmospheric Electricity*, Pergamon Press, London, 1957.
- [7] G. Deshpande, A. K. Kamra, The atmospheric electric conductivity and aerosol measurements during fog over the Indian Ocean, *Atmospheric Research* **70** (2004) 77–87.
- [8] R. G. Harrison, Long-range correlations in measurements of the global atmospheric electric circuit, *Journal of Atmospheric and Solar-Terrestrial Physics* **66** (2004) 1127–1133.
- [9] S. Israelsson, H. Tammet, Variation of fair weather atmospheric electricity at Marsta Observatory, Sweden, 1993–1998, *Journal of Atmospheric and Solar-Terrestrial Physics* **63** (2001) 1693–1703.
- [10] B. A. Tinsley, On the variability of the stratospheric column resistance in the global electric circuit, *Atmospheric Research* **76** (2005) 78–94.
- [11] M.J. Rycroft, S. Israelsson, C. Price, The global atmospheric electric circuit, solar activity and climate change, *Journal of Atmospheric and Solar-Terrestrial Physics* **62** (2000) 1563–1576.
- [12] D. Siinigh, V. Gopalakrishnan, R.P. Singh, A.K. Kamra, Sh. Singh, V. Pant, R. Singh, A.K. Singh, The atmospheric global electric circuit: An overview, *Atmospheric Research* **84** (2007) 91–110.
- [13] T. Hussein, M. Dal Maso, T. Petäjä, I. K. Koponen, P. Paatero, P. P. Aalto, K. Hämeri, M. Kulmala, Evaluation of an automatic algorithm for fitting the particle number size distributions, *BOREAL ENVIRONMENT RESEARCH* **10**: 337–355, 2005.
- [14] U. Horrak, P. P. Aalto, J. Salm, J. M. Makela, L. Laakso, M. Kulmala, Characterization of air ions in boreal forest air during BIOFOR III campaign, *Atmos. Chem. Phys. Discuss.*, 5, 2749–2790, 2005.
- [15] E.R. Jayaratne, F.O. J-Fatokun, L. Morawska, Air ion concentrations under overhead high-voltage transmission lines, *Atmospheric Environment* **42** (2008) 1846–1856.
- [16] Hirsikko, T. Yli-Juuti, T. Nieminen, T. Vartianinen, L.Laakso, T. Hussein, M. Kulmala, Indoor and outdoor air ions and aerosol particles in the urban atmosphere of Helsinki; characteristics, sources and formation, *Boreal Environment Research*, **12**: 295–310, 2007.
- [17] P. Tiitta, P. Miettinen, P. Vaattovaara, A. Laaksonen, J. Joutsenaari, A. Hirsikko, P. Aalto, M. Kulmala, Road-side measurements of aerosol and ion number size

- distributions: a comparison with remote site measurements, *Boreal Environment Research*, **12**: 311–321, 2007.
- [18] D. L. Henshaw, Does our electricity distribution system pose a serious risk to public health? *Medical Hypotheses* (2002) 59(1), 39–51.
 - [19] Y. I. Stozhkov, V. I. Ermakov, and V. S. Makhmutov, *Cosmic rays and atmospheric processes*, Proceedings of ICRC 2001: 4157 c Copernicus Gesellschaft, 2001.
 - [20] I.G. Usoskina, O.G. Gladyshevab, G.A. Kovaltsov, Cosmic ray-induced ionization in the atmosphere: spatial and temporal changes, *Journal of Atmospheric and Solar-Terrestrial Physics* **66** (2004) 1791–1796.
 - [21] N. Jonassen, "Neutralization of Static Charges by Air Ions: Part 1, Theory" in Mr. Static, *Compliance Engineering* **19**, no. 4 (2002): 28–31.
 - [22] *Sick Building Syndrome: causes, effects and control* - Chapter 3 © 1990 London Hazards Centre, Interchange Studios, Hampstead Town Hall Centre, 213 Haverstock Hill, London NW3 4QP, UK
 - [23] H. Svensmark, J. O. P. Pedersen, N. D. Marsh, Experimental evidence for the role of ions in particle nucleation under atmospheric conditions, *Proc. R. Soc. A* (2007) 463, 385–396.
 - [24] Petrignani, *Dissociative Recombination of Atmospheric Ions*, PhD Thesis, Amsterdam, Nederland, 2005.
 - [25] U. Horrak, *Air ion mobility spectra at a rural area*, PhD Thesis, University of Tartu, Estonia, 2001.
 - [26] R. G. Harrison, K. L. Aplin, Water vapor changes and atmospheric cluster ions, *Atmospheric Research* **85** (2007) 199–208.
 - [27] F. Yu, Nucleation rate of particles in the lower atmosphere: Estimated time needed to reach pseudo-steady state and sensitivity to H_2SO_4 gas concentration, *Geophysical Research Letters*, Vol.30, No. 10, 1526, doi:10.1029/2003GL017084, 2003.
 - [28] K. Y. Konradiev, *Atmospheric aerosol properties, formation, processes and impacts*, Springer, Chichester, UK, 2006.
 - [29] T. Hayasaka, K. Aoki, A. Shimizu, N. Sugimoto, I. Matsui, Sh. Satake, Y. Muraji, *Vertical distribution and optical properties of the aerosol observed over Japan spring*, 2005.
 - [30] M. Dal Maso, M. Kulmala, K. E. J. Lehtinen, J. M. Maakelaa, P. Aalto, C. D.O'Dowd, Condensation and coagulation sinks and formation of nucleation mode particles in coastal and boreal forest boundary layers, *Journal of Geophysical Research*, pp 1–7, 2001.
 - [31] O. Preining, The science of ultrafine aerosols, *Pure & Appl. Chem*, Vol. 64, No.11, pp.1679–1684, 1992.
 - [32] Luts, J. Salm, *Air ions and Electrical Aerosol Analysis*, University of Tratu, Estonia, 1992.
 - [33] R. B. Husar, *The Emergence of the Bimodal Distribution Concept*, Second Symposium on the History of Aerosol Science, Portland, OR, October, 2001.
 - [34] Virtanen, T. Ronkko, J. Kannisto, J. Ristimaki, J. M. Makela, J. Keskinen, T. Pakkanen, R. Hillamo, L. Pirjola and K. Hameri, Winter and summer time size distributions and densities of traffic-related aerosol particles at a busy highway in Helsinki, *Atmos. Chem. Phys.*, **6**, 2411–2421, 2006.

- [35] F.Mandija, The correlation between air ion concentration and altitude in suburbs areas, *Journal of Physics Students*, Vol 2, No 3 (2008).
- [36] L. Laakso, T. Petaja, K. E. J. Lehtinen, M. Kulmala, J. Paatero, U. Horrak, H. Tammet, and J. Joutsensaari, Ion production rate in a boreal forest based on ion, particle and radiation measurements, *Atmos. Chem. Phys. Discuss.*, **4**, 3947–3973, 2004.
- [37] H. Tammet, U. Horrak, L. Laakso, and M. Kulmala, Factors of air ion balance in a coniferous forest according to measurements in Hyvitala, Finland, *Atmos. Chem. Phys. Discuss.*, **6**, 3135–3174, 2006.
- [38] M. B. Enghoff and H. Svensmark, The role of atmospheric ions in aerosol nucleation , A review, *Atmos. Chem. Phys. Discuss.*, **8**, 7477–7508, 2008.
- [39] M. G. Talavera, B. Quintana, E. G. Diez, F. Fernandez, Studies on radioactivity in aerosols as a function of meteorological variables in Salamanca (Spain), *Atmospheric Environment* **35** (2001) 221}229, 2000.
- [40] K. Zhang, S. Anthony, S. Wexler, Y. Zhu, C. William, W. Hinds, C. Sioutas, Evolution of particle number distribution near roadways. Part II: the ‘Road-to-Ambient’ process, *Atmospheric Environment* **38** (2004) 6655–6665.
- [41] F.Yu, *Atmospheric Sciences Research Center*, State University of New York, Albany, New York, 2001.
- [42] W. Hinds, *Aerosol Technology, Properties, behavior and measurement of airborne particles*, Second Edition, John Wiley & Sons, USA, 1998.
- [43] R.J. Wilding, R.G. Harrison, Aerosol modulation of small ion growth in coastal air, *Atmospheric Environment* **39** (2005) 5876–5883.
- [44] M. Alfarra, *Insights Into Atmospheric Organic Aerosols Using An Aerosol Mass Spectrometer*, PhD Thesis, University of Manchester Institute of Science and Technology, UK, 2004.
- [45] M. Dal Maso, *Analisis of Atmospheric Particle Formation, Report Series in Aerosol Science*, No.85, Division of Atmospheric Sciences, Department of Physical Sciences, Faculty of Science , University of Helsinki, Finland, 2006.
- [46] J. Seinfeld & S. Pandis, *Atmospheric Chemistry and Physics, From air pollution to Climate change, Second Edition*, Wiley & Sons, USA, 2006.
- [47] R. G. Harrison , K. L. Aplin, Atmospheric condensation nuclei formation and high-energy radiation, *Journal of Atmospheric and Solar-Terrestrial Physics* **63** (2001) 1811–1819.
- [48] F.Mandija & F.Vila, Studies about atmospheric electricity, the dependence between air ionisation level and altitude in different locations, *Proceedings of the 13th International Conference on Atmospheric Electricity*, pp 150-153, ICAE, Beijing, China, 2007.
- [49] M. Kulmala, K. E. J. Lehtinen, L. Laakso, G. Mordas, K. Hämeri, On the existence of neutral atmospheric clusters, *Boreal Environment Research* **10**: 79–87, 2005.
- [50] C. Andronache, Diffusion and electric charge contributions to below-cloud wet removal of atmospheric ultra-fine aerosol particles, *Aerosol Science* **35** (2004) 1467–1482.
- [51] S. N. Tripathi, R. G. Harrison, Enhancement of contact nucleation by scavenging of charged aerosol particles, *Atmospheric Research* **62** (2002) 57–70.
- [52] D. Hillel, *Environmental Soil Physics*, Academic Press, San Diego, CA, USA, 1998.
- [53] F.Vila & F.Mandija, The altitude profile of atmospheric ion concentration, and the determination of the recombination and attachment coefficients in the suburbs areas, *Journal of Electrostatics*, Vol.67, Issues 2+3, p.492-495, 2009.

- [54] H. Gadhavi, *Experimental investigation of aerosol properties and modeling of its impact on radiation budget*, Physical Research Laboratory Ahmedabad 380 009 India, 2005.
- [55] M. Jones, R. M. Harrison, Interpretation of particulate elemental and organic carbon concentrations at rural, urban and kerbside sites, *Atmospheric Environment* **39** (2005) 7114–7126.
- [56] R. J. Wilding, A. Ellis, R. G. Harrison, *Ionisation as a precursor to aerosol formation*, Department of Meteorology, The University of Reading, UK.
- [57] L. Laakso, J. M. Makela, L. Pirjola, and M. Kulmala, Model studies on ion-induced nucleation in the atmosphere, *Journal of Geophysical Research*, Vol.107, No. d20, 4427, doi:10.1029/2002JD002140, 2002.
- [58] R. G. Harrison, *Ionisers and electrical aerosol removal*, Proc. Xth Ann. Conf., The Aerosol Society, Swansea, April 1996, pp38-43.
- [59] T. Maryama, T. Katayama, Transfer of small negative atmospheric ions, *Journal of Applied Physics*, Vol.94, No. 11, 2003.
- [60] J. H. Park, *Multiple Scattering Measurements using multi-static lidar*, PhD Thesis, The Pennsylvania State University, 2008.
- [61] O. Otsuki, G. Dodbiba, T. Fujita, Effect of particle size distribution on formation of linear configuration of dielectric fine particles under the electric field, *Journal of Physics: Conference Series* **147** (2009) 012003 doi:10.1088/1742-6596/147/1/012003.
- [62] G. Biskos, *Calibration – Modification of the Fast Mobility Spectrometer*, PhD thesis, University of Cambridge, UK, 2001.
- [63] L. Laasko, *Kinetics and Dynamics of Atmospheric Ions, Clusters and Aerosols*, Report Series, No.70, (2004).
- [64] K. L. Aplin, *Instrumentation for atmospheric measurements*, PhD Thesis, University of Reading, Department of Meteorology, UK, 2000.
- [65] T. Hussein, A. Karppinen, J. Kukkonen, J. Harkonen, P. P. Aalto, K. Hameri, V. M. Kerminen, M. Kulmala, Meteorological dependence of size-fractionated number concentrations of urban aerosol particles, *Atmospheric Environment* **40** (2006) 1427–1440.
- [66] H. Tammet, *Size and mobility of nanometer particles, clusters and ions*, Department of Environmental Physics, Tartu University, 18 Ülikooli Str., Tartu EE 2400 Estonia, 1993.
- [67] B. Lie-Svendsen, T. A. Blix, U. P. Hoppel, E. V. Thrane, *Direct modeling the small-scale plasma response to the presence of heavy aerosol particles*, doi: 10.1016/SO273-1177(03)00.
- [68] R. M. Harrison, J. Stedman, D. Derwent, New Directions: Why are PM10 concentrations in Europe not falling? *Atmospheric Environment* **42** (2008) 603–606.
- [69] P. Monkkonen, *Observations of urban aerosols in India*, Report Series, No.72, Division of Atmospheric Sciences, Department of Physical Sciences, Faculty of Science , University of Helsinki, Finland (2005).
- [70] J. M. Makela, I. K. Koponen, P. Aalto, M. Kulmala, One-year data of submicron size modes of tropospheric background aerosol in southern Finland, *J. Aerosol Sci.* Vol. 31, No. 5, pp. 595-611, 2000.
- [71] P. J.T. Verheijen, *Statistical Distributions in Particle Technology*, Department of Chemical Engineering, Technical University Delft, Netherlands, 2001.

- [72] Kousa, *PM2.5 and NO₂ exposure assessment of urban population in the Helsinki metropolitan area and other European urban areas*, Report Series in Aerosol Science, No.57, Division of Atmospheric Sciences, Department of Physical Sciences, Faculty of Science , University of Helsinki, Finland, 2002.
- [73] T. Schneider, K. A. Jensen, P. A. Clausen, A. Afshari, L. Gunnarsen, P. Wahlin, M. Glasius, F. Palmgren, O. J. Nielsen, C. L. Fogh, Prediction of indoor concentration of 0.5–4 mm particles of outdoor origin in an uninhabited apartment, *Atmospheric Environment* **38** (2004) 6349–6359.
- [74] F.Mandija, Sh.Ahmetaga, F.Vila, *Atmospheric monitoring on the Adriatic seashore*, Book of Abstracts of the 7th General Conference of the Balkan Physical Union, Alexandropoulos, Greece, 2009.
- [75] R. G. Harrison, *Aerosol charging and radioactivity*, PhD Thesis, Air Pollution Group, Department of Mechanical Engineering, Imperial College of Science, Technology and Medicine, University of London, UK, 1997.
- [76] X. Querol, A. Alastuey, C.R. Ruiz, B. Artinano, H.C. Hansson, R.M. Harrison, E. Buringh, H.M. Brink, M. Lutz, P. Bruckmann, P. Straehl, J. Schneider, Speciation and origin of PM10 and PM2.5 in selected European cities, *Atmospheric Environment* **38** (2004) 6547–6555.
- [77] K. E J. Lehtinen, H. Korhonen, M. Dal Maso, M. Kulmala, On the concept of sink diameter, *Boreal Environonment Research*, 6, 405-411, 2003.
- [78] J. N. Smith, R. L. Mauldin III, F. L. Eisele, Growth rates of freshly nucleated atmospheric particles in Atlanta, *Journal of Geophysical Research*, Vol.110, d22S05, doi:10.1029/2005JD005935, 2005.
- [79] M. Jones, R. M. Harrison, The effects of meteorological factors on atmospheric bio-aerosol concentrations- a review, *Science of the Total Environment* **326** (2004) 151–180.
- [80] P. A. Jacques, C. S. Kim, Measurement of total lung deposition of inhaled ultrafine particles in healthy men and women, *Inhalation Toxicology*, **12**:715±731, 2000.
- [81] R. G. Harrison, Urban smoke concentrations at Kew, London, 1898–2004, *Atmospheric Environment* **40** (2006) 3327–3332.
- [82] T. Ahonen, P. Aalto, O. Rannik, M. Kulmala, E. D. Nilsson, S. Palmroth, H. Ylitalo, P. Hari, Variations and vertical profiles of trace gas and aerosol concentrations and CO₂ exhange in eastern Lapland, *Atmospheric Environment* Vol. 31, No. 20, pp. 3351-3362, 1997.
- [83] J. Planini, V. Radoli, D. Culo, *Searching for an earthquake precursor: Temporal variations of radon in soil and water*, *Fizika B*, **2**, 25-82Zagreb, 2000.
- [84] Iannucci, *Investigation of low energy cosmic rays with NINA missions at low Earth orbit*, Universita degli Studi di Roma "Tor Vergata", Facolta di Scienze Matematiche, Fisiche, Naturali, 2002.
- [85] V. M. Sorokin, A. K. Yaschenko, M. Hayakawa, A perturbation of DC electric field caused by light ion adhesion to aerosols during the growth in seismic-related atmospheric radioactivity, *Nat. Hazards Earth Syst. Sci.*, **7**, 155–163, 2007.
- [86] F. Mandija, D. Ulqini, Sh. Ahmetaga, F. Vila, *A rough estimation of the radon concentration in the air in the region of Shkodra Lake*, Proceedings of the International Conference on Lakes and Nutrient Loads, Pogradec, Albania, 2009.

- [87] M. Kulmala, I. Riipinen, M. Sipilä, H. E. Manninen, T. Petäjä, H. Junninen, M. Dal Maso, G. Mordas, A. Mirme, M. Vana, A. Hirsikko, L. Laakso, R. M. Harrison, I. Hanson, C. Leung,, K. E. J. Lehtinen, V.-M. Kerminen, Toward *Direct Measurement of Atmospheric Nucleation*, *Science Express*, 2007.

Chapter 10

A ROUTE TO MOLECULAR ELECTROSTATICS THROUGH ATOMIC CHARGES GENERATED BY MEANS OF FAST AND ROBUST EMPIRICAL SCHEMES

***Dmitry A. Shulga,* Alexandr A. Oliferenko, Sergey A. Pisarev,
Vladimir A. Palyulin and Nikolay S. Zefirov***

Institute of Physiologically Active Compounds
Russian Academy of Sciences, Chernogolovka, Russia
Department of Chemistry
M.V. Lomonosov Moscow State University, Russia

Abstract

Two general approaches to derivation of empirical schemes for partial atomic charge calculation in diverse organic molecules have been presented. Both are fast, simple and scalable and guarantee dependence of charges on chemical environment and obey topological symmetry constraints. Parameters of the two schemes have been fitted to reproduce 6-31G(d) molecular electrostatic potential simultaneously around a set of diverse organic structures. Therefore the charges obtained are directly applicable to molecular modeling based on classical force fields such as AMBER, CHARMM, MMFF94, GROMOS, etc. as well as scoring functions.

Keywords: Molecular dynamics, Empirical schemes, Partial atomic charge, Molecular electrostatic potential, Force fields.

1. Introduction

Partial atomic charges have long been used to describe electrostatic interactions as a major non-bonding energy contribution in many molecular modeling applications ranging from qualitative host-guest electrostatic complementarity comparison, to QSAR/QSPR

*E-mail address: shulga@qsar.chem.msu.ru

studies, to quantitative protein-ligand interaction modeling by means of Molecular Dynamics or Monte Carlo approaches based on molecular mechanics force fields, to combined Quantum/Molecular mechanics studies (QM/MM). Due to lack of strict definition of atomic charges in terms of Quantum Mechanics a great number of schemes for charge calculation have come into being. However, among the others, atomic charges that best reproduce *ab initio* electrostatic potential around a molecule of interest (molecular electrostatic potential, MEP) by means of classical point charge Coulomb term are most soundly defined theoretically and appeared to have been the most fruitful in obtaining accurate results of applied modelling [1–3]. In particular, electrostatic potential derived (ESP-derived) charges, fitted to reproduce RHF/6-31G(d) electrostatic potential on a grid of points in space around molecules, have been used to obtain parameters of the classical (non-polarizable) molecular mechanics force fields such as AMBER [4, 5], MMFF94 [6, 7], CHARMM [8, 9], GROMOS [10, 11]. The combination of level of theory and basis set results in 10-15% overpolarization in organic species, which effectively mimics polarization caused by their immersion into water media. Approximately the same amount of overpolarization has been incorporated into the widespread used water models (TIP3P, TIP4P, TIP5P, SPC). Thus a consistent implicit description of polarization is introduced into molecular modeling based on classical force fields.

However, ESP-derived charges (MK-ESP [12, 13], CHELP, CHELPG and partially RESP [14, 15]) have well known deficiencies. First, a need for resource consuming Quantum Chemical calculations may become a bottleneck in applications requiring high throughput. Second, charges on "buried" centers are ill-conditioned by least squares equations during the fit, which usually lead to unreasonably high in magnitude and non-transferable values of charges, hampering their use. Third, ESP-derived charges are not topologically symmetric, i.e. chemically equivalent atoms do not have the same values. The latter may lead to qualitatively incorrect results of modeling where extensive sampling of conformational space is assumed. The RESP scheme applies topological symmetry as constraints during the fit procedure in expense of requiring expert user intervention.

On the other hand, existing empirical charge schemes, often based on Electronegativity Equalization (EE) principle, either do not produce topologically symmetric charges or fail to reproduce (in original parameterization) the RHF/6-31G(d) MEP with reasonable accuracy. As an additional demand caused by recent development of multiscale approaches, an empirical charge scheme should be simple, fast and scalable, which would admit creating models with desired ratio of accuracy to resources spent.

In what follows we outline two approaches to construction of topologically symmetric empirical charge schemes. The first is based on complete electronegativity equalization with topologically symmetric energy function (TSEF). The second - on a new dynamic electronegativity relaxation (DENR) principle. Then the results on their parameters optimization to reproduce RHF/6-31G(d) MEP on a set of structures are presented, and compared to those based on the charge schemes known from the literature.

2. Theory

2.1. Common Consideration

Following the conceptual density functional theory (DFT) [16, 17], it is assumed the existence of relationship (1) between the energy of a molecular system and its charge density, approximated in the simplest way by a set of partial atomic charges, \mathbf{q} . The charges are constrained (2) to give total molecular charge, Q_{tot} , zero for neutral species:

$$E_{mol} = E_{mol}(\mathbf{q}) \quad (1)$$

$$\mathbf{1}^T \mathbf{q} = Q_{tot} \quad (2)$$

It is natural to find atomic charges as those minimizing (1) under the constraint (2). Employing Lagrange multiplier technique one gets simultaneous Equations (3), which can be solved for \mathbf{q} and λ :

$$\begin{cases} \frac{\partial E_{mol}(\mathbf{q})}{\partial q_i} + \lambda = 0, & i = 1 \dots N_{at} \\ \sum_j^{N_{at}} q_j = Q_{tot} \end{cases} \quad (3)$$

where N_{at} is the number of atoms in a molecules, q_i is the charge on atom i , λ is the Lagrange multiplier related to molecular electronegativity in DFT [16, 17].

The presented formalism lays the grounds [18, 19] for empirical charge schemes based on *complete EE principle*, major differences being in representation of energy function (1). Note, that effective atomic electronegativity (EN) is given [20] by

$$\chi_i^{eff}(\mathbf{q}) = \frac{\partial E_{mol}(\mathbf{q})}{\partial q_i}. \quad (4)$$

If $E_{mol}(\mathbf{q})$ is approximated with quadratic function (5), system (3) becomes a system of linear simultaneous equations with a square matrix, which is solved readily to get a single solution corresponding to the global minimum of (5)

$$E_{mol}(\mathbf{q}) = E_0 + \chi_0^T \mathbf{q} + \frac{1}{2} \mathbf{q}^T H \mathbf{q} \quad (5)$$

where χ_0 is the vector of atomic electronegativities χ_i^0 , and H is the positive definite hardness kernel matrix.

Most widespread implementations of the charge schemes based on the EE principle, despite being extremely fast compared to techniques relying on QC calculations, possess known deficiencies. First, charges on atoms are either independent of chemical environment (for diagonal H) or may incorrectly reflect the effect [7], otherwise. Off-diagonal elements of H depend on interatomic separations [21] and thus require knowledge of molecular geometry. However, in e.g. virtual screening and QSAR studies generation of reasonable molecular geometries may prove both cumbersome and ambiguous. Moreover the charges obtained are not topologically symmetric as corresponding to a certain conformer. Therefore methods that do not require geometry would have certain benefits. Second, the

charge transfer between distant atoms is exaggerated [7,22]. Third, the charges of empirical schemes poorly reproduce MEP and hence are not directly applicable to general use with the force fields [7].

Below the two novel approaches to constructing empirical charge schemes with desired properties are proposed: (a) use of complete EE with topologically symmetric energy function (TSEF), and (b) dynamical EN relaxation (DENR). Their parameters were then subjected to optimization to reduce error in simultaneous MEP reproduction on a set of 196 and then validated on a set of 30 diverse organic structures. Both schemes give topologically symmetric charges and do not require knowledge of molecular geometry. The topological symmetry means that equivalent in a chemical structure (weighed graph) vertices receive equal charge values. This is important so that e.g. equivalent rotational conformers to have the same energy within the force field treatment.

2.2. Complete Electronegativity Equalization with Topologically Symmetric Energy Function (TSEF)

The main idea of the approach is to construct energy function that would by definition reflect topological symmetry. Then application of complete EE framework would automatically produce topologically symmetric charges. At the same time the charges have to be dependent of its near chemical environment. Consider an approximation of energy function (6) as a particular form of (5)

$$E_{mol}(\mathbf{q}) = \sum_i^{N_{at}} \left(\chi_i^0 q_i + \frac{1}{2} \eta_i^0 q_i^2 + \frac{1}{2} \sum_{j \neq i}^{N_{at}} \phi_{ij} q_i q_j \right) \quad (6)$$

where χ_i^0 and η_i^0 are the EN and hardness of atom i ; ϕ_{ij} is the interaction parameter between q_i and q_j charges, here $H_{ii} = \eta_i^0$, and $H_{ij} = H_{ji} = \phi_{ij}$.

The first two terms in parentheses of (6) describe attraction of charge to given atom i , whereas the last one is responsible for intercharge interaction. In fact ϕ_{ij} is the parameter of electrostatic interaction and therefore should behave as $1/R_{ij}$ at long separations between i and j . Note that on omitting the last term and applying complete EE procedure one gets values of charges that do not depend on chemical environment: all atoms of the same sort (type) share the same value of charge. Straightforward use of $1/R_{ij}$ has also proven problematic. First, a reasonable geometric structure is needed (might require its generation). Second, off-diagonal elements of the hardness kernel matrix, H , may become too large in presence of short interatom distances, resulting in ill-conditioned charge values due to breaking of diagonal dominance (and positive definiteness) of the matrix. Third, the charges obtained do not reflect topological symmetry as they are based on a set of R_{ij} distances pertinent to a certain conformer.

Here we propose an approach to overcome several difficulties by expressing intercharge interaction parameter ϕ_{ij} entirely in terms of molecular graph topology (i.e. topology of chemical bonds). To that end ϕ_{ij} is related to Minial Distance Path (MDP) defined as a minimum number of bonds separating the two atoms i and j . For simplicity a linear dependence of mean interatomic distance in organic molecules on the corresponding MDP

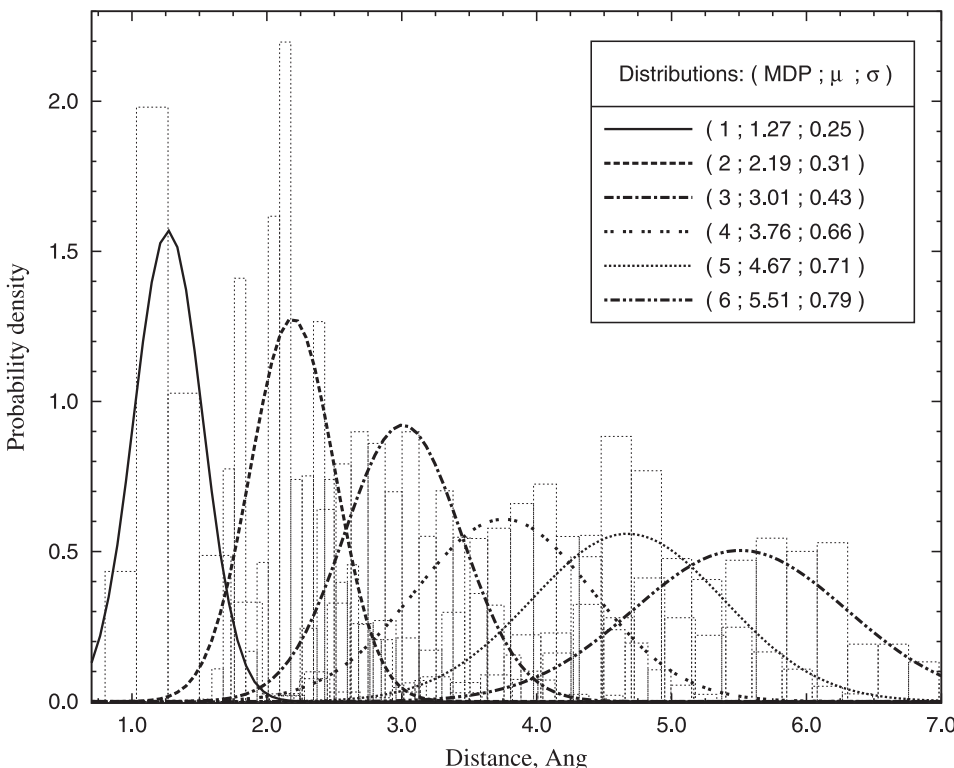


Figure 1. Distributions of interatomic distances for MDP=1, 2, 3, 4, 5 and 6.

values was sought. For that reason the interatomic distances in the set of 226 diverse RHF/6-31G(d) optimized organic structures were checked and collected for all pairs of 1, 2, 3, 4, 5 and 6 bond separated atoms, giving rise to distributions of distance values for six different MDP values.

The distributions were approximated with Gaussians whose mean values gave excellent correlation to the corresponding MDP values (7):

$$\begin{aligned}\mu(MDP) &= 0.84 \cdot MDP + 0.46 \\ R^2 &= 0.9993, s = 0.04,\end{aligned}\tag{7}$$

which can be used to obtain an approximation for ϕ_{ij} in a rather general form

$$\phi_{ij} = \alpha \cdot K(MDP_{ij}) \frac{1}{0.84 \cdot MDP_{ij} + 0.46},\tag{8}$$

where MDP_{ij} is the minimal distance path (in bonds) between atoms i and j ; $K(MDP_{ij})$ is the set (for $MDP_{ij} = 1, 2, 3, 4, 5$ and 6) of factors for softening pure Coulombic potential at short separations (set to unity to recover pure $1/R$ behavior); α is the units conversion factor to make agreement between the first two and the last term of (6), i.e. χ_i^0 and η_h^0 .

Substitution of (8) into (6) results in an expression of energy function, which is completely topologically symmetric, thus giving topologically symmetric charges upon application of the complete EE formalism (3). Besides, the charges thus obtained depend on

chemical environment and account to some extent (in a mean way) mutual polarization of charges in a molecule.

The linear system is solved numerically. Initial values for atomic EN and hardness (corresponding to energy in eV) were taken from Goddard [23]. Therefore α is 14.4 [eV· Å]. The set of softening factors $K(1 \dots 6) = [0.652; 0.903; 0.967; 0.990; 1.000; 1.000]$ was obtained by relating Slater's integral [23] to $1/R$ at distances corresponding to the Gaussian means.

2.3. Dynamic Electronegativity Relaxation (DENR)

The second approach is based effectively on *incomplete EN equalization* that is aimed at diminishing differences of effective EN values for directly connected (neighboring) atoms via redistributing charges along the network of chemical bonds. The resulting charge distribution thus properly reflects molecular topology and its dependence of each atom's chemical environment.

The simplest yet very practical implementation of the idea is the bond charge increment/correction (BCI/BCC) schemes such as e.g. MMFF94 [6] and AM1-BCC [24]. A more elaborated approach of the sort is Gasteiger's iterative partial equalization of orbital electronegativity (PEOE) [25], in which complete equalization is prevented by successively increasing attenuation of charge transfer between atoms. Even though Gasteiger charges have proven to well correlate to chemical properties associated with charge distribution, the physical meaning of the dumping factor used is less theoretically justified. The novel EN relaxation approach to generate atomic charges, based on a simplified solution of the Laplace equation with Dirichlet boundary conditions was described [19] and compared to complete EN equalization.

Here we propose a dynamical relaxation approach admitting further development and modification which has much in common with the above mentioned ones and is based on the following assumptions. Initial charge distribution \mathbf{q}_0 , satisfying constraint (2) and possessing symmetry that is no less than provided by molecular topology, is redistributed along chemical bonds to lower $E_{mol}(\mathbf{q})$. The total charge, Q_{tot} , is conserved with the local charge conservation Equations (9), where the last equality means that the charge transfer is allowed only between immediately bonded atoms

$$\frac{dq_i}{dt} = \sum_j^{N_{at}} \Delta q_{ij} \cong \sum_{j \in \{i,j\}}^{\text{bonds of } i} \Delta q_{ij}, \quad (9)$$

where $\frac{dq_i}{dt}$ is the change of charge q_i on atom i during the evolution in effective time t ; Δq_{ij} is the elementary charge transfer from atom j to atom i ; we demand also detailed balance $\Delta q_{ij} = -\Delta q_{ji}$.

Assuming that Δq_{ij} is proportional to the slope of lowering of the energy function in direction of the charge transfer, one gets [26] a system of Ordinary Differential Equations (10), which can be more conveniently expressed in a matrix form (11):

$$\frac{dq_i}{dt} = -c \cdot \sum_{j \in \{i,j\}}^{\text{bonds}} \left(\frac{\partial E_{mol}(\mathbf{q})}{\partial q_i} - \frac{\partial E_{mol}(\mathbf{q})}{\partial q_j} \right) = -c \cdot \sum_{j \in \{i,j\}}^{\text{bonds}} \left(\chi_i^{\text{eff}}(\mathbf{q}) - \chi_j^{\text{eff}}(\mathbf{q}) \right) \quad (10)$$

$$\frac{d\mathbf{q}}{dt} = -c \cdot L\chi^{eff}(\mathbf{q}) \quad (11)$$

where $L = D - A$ is the symmetric Laplace matrix, well known from the literature [27]; D is the diagonal matrix of vertex orders; A is the adjacency matrix of a molecular graph; c is the positive constant; $\chi^{eff}(\mathbf{q})$ is the vector of atomic effective EN's.

Laplace matrix has well known properties and spectrum [27], which facilitates investigation of the system (11). The eigenvalues are non-negative, with the first - in ascending order - always equal to zero, $0 \equiv \lambda_1 \leq \lambda_2 \leq \dots \leq \lambda_{N_{at}}$. The first eigenvalue is comprised of equal values, $\mathbf{V}_1 = v \cdot \{1, 1, \dots, 1\}^T$. In the other eigenvectors inhomogeneity of components related to the adjacent vertices grows as the corresponding eigenvalue increases.

A stationary solution of (11) is obtained when all time derivatives vanish, which is equivalent to eigenproblem with zero eigenvalue

$$L\chi_{st} = 0 \cdot \chi_{st}, \quad (12)$$

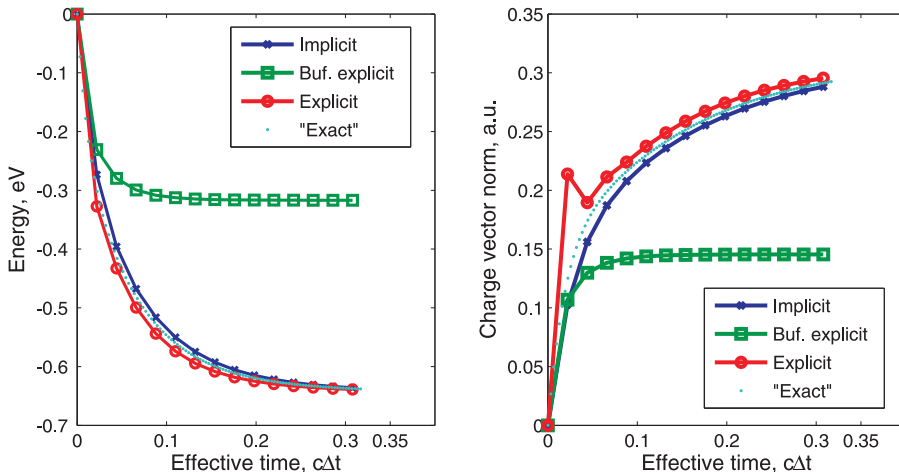
where χ_{st} is the vector of stationary effective atomic EN's.

Such a solution always exists since the Laplace matrix of a molecular graph always has zero eigenvalue with equal components eigenvector \mathbf{V}_1 defined up to a normalizing constant. Thus in the stationary solution all effective EN's must be equal to each other, hence it assumes *complete EN equalization*. The stationary solution, $\chi_{st}(\mathbf{q}_{st})$, is Lyapunov stable if \mathbf{q}_{st} corresponds to a local minimum of energy function and has at least one divergent exponent in case of a saddle point.

Analytical non-stationary solution to (11) was obtained [26] for a simplified energy function (6) assuming $\eta_i \cong 1, \phi_{ij} = 0$ as a decomposition in term of Laplace matrix eigenvectors. Its investigation enabled to make a series of important observations. First, contributions of all eigenvectors decay exponentially with effective time with exponents proportional to the corresponding eigenvalues. Second, in the limit of $t \rightarrow \infty$ only the stationary solution is obtained, whereas during the process the contributions from the components related to significant differences of effective EN values on adjacent vertices (atoms) decay faster than the other contributions. Case studies carried out with several chemical structures and appropriate EN values have revealed additional peculiarities. First, the most significant energy drop occurs on early stages of system evolution effectively at finite times, at which effective atomic EN's still differ significantly (approaching the same value in the limit). Second, topological symmetry of a solution is preserved during the evolution but is lost in the limit.

Summarizing the above observations and noting a very coarse nature of energy function used (making search for its exact minimum senseless) one arrives at the *principle of dynamic EN relaxation*: to obtain topologically symmetric and environment dependent charges it is reasonable to relax the system according to (11) until the most energetically unfavorable components decrease. Pragmatically, relaxation can be stopped when the drop in energy becomes comparable to errors due to inaccuracy of energy function approximation.

For applied charge calculation with arbitrary energy function it is proposed [26] to relax a system by means of finite difference integration of (11). Although a wealth of schemes for finite difference integration exists, approximate nature of relaxation and intention to use charge calculation schemes in high throughput molecular modeling suggest that the most



overall parsimonious to resources scheme would be more beneficial. For that reason the simplest energy function (13) [a form of (6) with $\phi_{ij} = 0$] was proposed and the two simplest schemes of ODE integration are considered: explicit (16) and implicit (17) Euler ones, which differ in from which time step k the charges $\mathbf{q}^{(k)}$ are used in the right hand part of (15):

$$E_{mol}(\mathbf{q}) = \sum_i^{N_{at}} \left(\chi_i^0 q_i + \frac{1}{2} \eta_i^0 q_i^2 \right) \quad (13)$$

$$\chi^{eff}(\mathbf{q}) = \chi_0 + \eta_0 \mathbf{q} \quad (14)$$

$$\mathbf{q}^{(n+1)} - \mathbf{q}^{(n)} = -c\Delta t \cdot \left(L\chi_0 + L\eta_0 \mathbf{q}^{(k)} \right) \quad (15)$$

$$\mathbf{q}^{(n+1)} = (I - c\Delta t \cdot B_0) \cdot \mathbf{q}^{(n)} - c\Delta t \cdot \mathbf{a}_0 \quad (16)$$

$$\mathbf{q}^{(n+1)} = (I + c\Delta t \cdot B_0)^{-1} \cdot \left(\mathbf{q}^{(n)} - c\Delta t \cdot \mathbf{a}_0 \right) \quad (17)$$

where $B_0 = L\eta_0$ and $\mathbf{a}_0 = L\chi_0$.

Though implicit scheme (17) requires more calculations since it involves one matrix inversion in case of (13) and solving a set of nonlinear equations at each iteration for an arbitrary energy function, it permits taking larger time steps Δt without significant loss of stability and accuracy. The latter is especially important for stiff systems [28]. For molecular graph based Laplace matrix, L , stiffness is determined by the ratio of the largest to smallest (nonzero) eigenvalues of L , which grows with increasing length of acyclic parts of a molecular graph. Use of small time steps results in unnecessarily detailed dynamics in view of a crude nature of (13). On the other hand, at larger time steps the explicit scheme loses stability whereas the implicit one does not.

To exemplify the above consider acetamide CH_3CONH_2 molecule, for which atomic EN and hardness values taken from [23] are (in eV) $\chi_{\text{C}}^0 = 5.343$; $\chi_{\text{N}}^0 = 6.899$; $\chi_{\text{O}}^0 = 8.741$; $\chi_{\text{H}}^0 = 4.528$; $\eta_{\text{C}}^0 = 10.126$; $\eta_{\text{N}}^0 = 11.760$; $\eta_{\text{O}}^0 = 13.364$; $\eta_{\text{H}}^0 = 13.890$. For the studied system the stiffness ($\lambda_{N_{at}}/\lambda_2$) is $\simeq 22.4$, which well exceeds unity, meaning the system is rather hard. Fig. 2 shows numerical results for effective time step, $c\Delta t$, equal 0.022

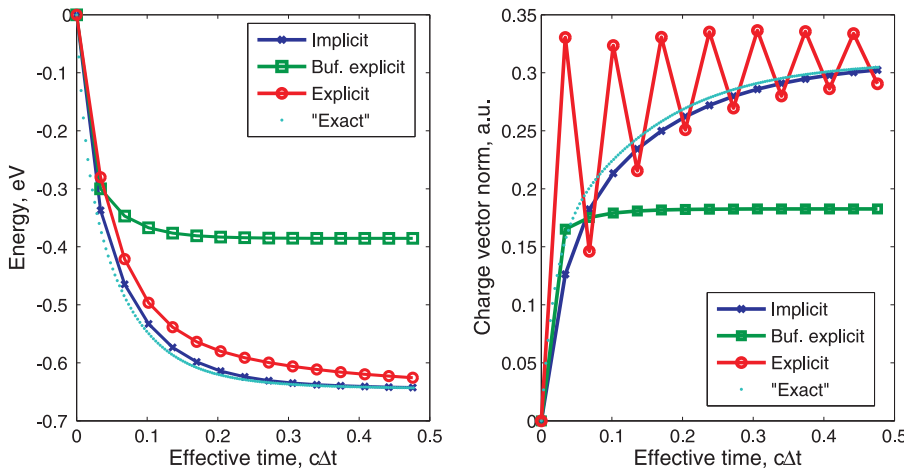


Figure 2. Different stability of integration schemes: the explicit and implicit Euler ones, the buffered explicit againts the "exact" solution (smaller time step).

and $0.034 [(\text{a.u.})^2/\text{eV}]$ in panels (a) and (b), respectively. Zero atomic charges were taken as initial values. At smaller time step both explicit and implicit schemes give comparable results. For the explicit scheme (red) the norm of vector of atomic charges exhibits a surge, which is recovered by the second iteration. At larger time step however the picture is different. The implicit scheme (blue) retains its stability while only marginally loosing in accuracy compared to the "exact" solution. On the contrary, the explicit scheme, still showing acceptable accuracy, loses its stability, which is manifested by huge oscillations in charge vector norm still converging to the "exact" solution in the limit for that time step. Even insignificant further increase of time step leads first to diverging oscillations and then to the catastrophic loss of accuracy (energy tends to infinity). Clearly, that for the puposes of dynamic EN relaxation only unconditionally stable finite difference methods are suitable due to the general stiffness of the arising systems. Thus the implicit Euler scheme has been chosen for further implementation in the DENR charge scheme.

The details of the implemented DENR scheme are as follows. Initial values for atomic EN and hardness were also taken from [23]. After a series of preliminary experiments, the effective time step, $c\Delta t$, was taken to be $0.05 [(\text{a.u.})^2/\text{eV}]$, and the number of iterations to carry out was set to two ($n = 2$).

Interestingly, but it can be shown that by admitting several insignificant simplifications, Gasteiger's charge scheme [25] equations can be recast in a form of buffered (dumped) explicit Euler scheme in conjunction with quadratic energy function:

$$\mathbf{q}^{(n+1)} = (I - c\Delta t \cdot \alpha^n \cdot B_0) \cdot \mathbf{q}^{(n)} - c\Delta t \cdot \alpha^n \cdot \mathbf{a}_0, \quad (18)$$

where α is the dumping factor, set to 0.5 in the original paper.

The form (18) suggests three major simplifications. First, $c\Delta t$ parameter is the same for all bonds, whereas in [25] it is associated with the EN value of the atomic positive ions and may differ for different bonds, although the maximum difference being of factor 2. Second, quadratic energy function is implied (linear effective EN), whereas in [25] cubic

energy function is implied by use of quadratic expansion of the effective EN's. On the other hand, actual values of coefficients at third powers of charge in the energy function implied by [25] are an order of magnitude smaller than at the first and second ones, thus justifying our assumption. Third, we used effective atomic EN and hardness values instead of orbital ones in the PEOE scheme [25].

Finite difference solution by means of the buffered explicit scheme (18) with the same initial conditions are also depicted in Fig. 2 in green. Successive dumping the charge transfer results in preventing the system from reaching the global minimum of the energy function related to the complete EN equalization solution. At the same time the solution becomes stable. Thus it can be inferred why Gasteiger had to resort to initially non-obvious dumping. First, it is used to obtain topologically symmetric and environment dependent charges, that cannot be obtained otherwise within complete EN equalization and the use of the energy function implied by the original equations. Second, it is used to ensure numerical stability to calculate charges on molecules of arbitrary length. Third, the dumping makes the charge transfer more local for ordinary organic molecules, which is what chemical knowledge suggests in consistently relating chemical and physical properties of arbitrary size molecules to certain groups of atoms.

3. Method

To validate and further study the two charge schemes TSEF and DENR both have been implemented and their parameters subjected to optimization aimed at reducing error in *ab initio* MEP reproduction simultaneously on the set of diverse organic structures. To that end the initial set of 226 structures was split into training set of 196 and test set of 30 structures, respectively. Each structure has been geometry optimized at RHF/6-31G(d) level, with PC GAMESS [29], followed by MEP calculation with the optimal wave function on a grid of Connolly surfaces as implemented in PC GAMESS (PTSEL=CONNOLLY) with radii multiple to 1.4, 1.6, 1.8, 2.0, 2.2 values of van der Waals radii for the corresponding elements and point surface density of 4 points per Å². Three objective functions have been used throughout the study: (a) the χ²-like (19), (b) the standard deviation like one (20), and (c) the absolute mean error (21)

$$F(\chi_0, \eta_0) = \sum_i^{N_{str}} \sum_j^{N_{grid,i}} \left(V_{ij}^{\text{qc}} - \sum_l^{N_{at,i}} \frac{q_{il}^{\text{calc}}}{r_{jl}} \right)^2 \quad (19)$$

$$q_{il}^{\text{calc}} = q_{il}^{\text{calc}}(\chi_0, \eta_0)$$

$$D_V = \left[\frac{1}{N_{str}} \sum_i^{N_{str}} D_i^2 \right]^{1/2} \quad (20)$$

$$D_i = \left[\frac{1}{N_{grid,i}} \sum_j^{N_{grid,i}} \left(V_{ij}^{\text{qc}} - \sum_l^{N_{at,i}} \frac{q_{il}^{\text{calc}}}{r_{jl}} \right)^2 \right]^{1/2}$$

$$ADV = \frac{1}{N_{str}} \sum_i^{N_{str}} \left(\frac{1}{N_{grid,i}} \sum_i^{N_{grid,i}} \left| V_{ij}^{\text{qc}} - \sum_l^{N_{at,i}} \frac{q_{il}^{\text{calc}}}{r_{jl}} \right| \right) \quad (21)$$

where N_{str} is the number of structures in the set; $N_{grid,i}$ is the number of grid points, at which the MEP is evaluated, defined for structure i ; V_{ij}^{qc} is the Quantum Chemical MEP evaluated at grid point j of structure i ; $N_{at,i}$ is the number of atoms in the structure i ; r_{jl} is the distance between the atom l and the grid point j ; q_{il}^{calc} is the charge on atom l in the structure i ; χ_0 and η_0 are the vectors EN and hardness values defined for the atom types used; D_i is the root-mean-square deviation of MEP description for structure i ; D_V and ADV are the root-mean-square and absolute mean deviation of MEP reproduction for a whole set.

The Simplex Annealing algorithm [28], which combines stochastic Simulated Annealing [30] and deterministic Simplex Method [31], was used to minimize the objective functions. This method both does not require any derivatives calculation and is suitable for global optimization.

Due to significant mutual dependence of parameters and quite different influence of the parameters pertinent to different atomic types the objective functions have very different curvatures (confirmed by numerical second derivative matrix investigation) with respect to change of parameter vector. Moreover, there exist collective modes, along which the objective functions change only negligibly. The latter complicates significantly the optimization process and results in non uniqueness of the parameters obtained.

To partially overcome the complication the parsimonious use of atomic types has been adhered. Initially, a broad set of atomic types has been defined on "element"/"valent state" basis. On the early stages of optimization all types pertinent to one element have been grouped to share the same parameters values. Split of groups was carried out only if it caused significant lowering of the objective function. Splitting was repeated several times to bring finer and well defined subgroups.

The overall optimization scheme was as follows. First, initial parameters of atomic EN and hardness were taken from Goddard's scheme [23]. Second, objective function (19) admitting faster calculations was optimized and parameters splitted after careful analysis of the results. This stage repeated several times. Third, objective function (21) was optimized starting with the parameters obtained at the previous step. Both (21) and (20) were used to assess the quality reached in MEP reproduction. Least squares estimator (19) is known to be biased toward outliers thus distorting the picture. Therefore absolute mean error estimator (21), which is known to give robust estimations, has been used after preliminary (and faster) optimization with (19). To estimate transferability of the finally obtained parameters they were utilized without any modification to evaluate (21) and (20) with the charges calculated for the test set structures. An overfitted model is undesirable, since it would have significantly better performance on the training rather than the test set, overall undermining its value in predictions.

4. Results and Discussion

To place results in a proper context the same calculations have been performed with the charges due to five different charge schemes taken for reference: MK-ESP [12, 13], RESP [14, 15], AM1-BCC [24], MMFF94 [6, 7], and Mulliken PA. Table 1 and Table 2 show the results obtained with the charge schemes studied for the training and test sets, respectively. Results obtained with both optimized (opt.) and initial (init.) values of EN and hardness parameters are presented for the currently proposed TSEF and DENR charges schemes. Distributions of actual D_i values among the both sets were approximated with Gaussians, whose mean and standard deviation values (μ and σ) are also presented in the Tables. Fig. 3 depicting the Gaussians for the test set of structures helps visually compare performance of different charge schemes in the MEP reproduction.

Table 1. Residual errors in the QC MEP reproduction [kJ/mol] on the training set of 196 structures, calculated with different point charges.

Charge scheme	AD_V	D_V	D_i , min ^a	D_i , max	μ^b	σ
MK-ESP	3.65	5.88	1.26	12.50	5.33	2.50
RESP	4.11	6.40	1.34	12.95	5.86	2.58
AM1-BCC	7.60	10.92	3.38	36.96	10.01	4.37
MMFF94 ^c	9.45	13.02	3.55	36.18	12.14	4.72
Mulliken PA	13.97	19.51	1.84	42.06	17.77	8.08
DENR(opt.)	7.81	10.95	1.57	30.94	10.21	3.97
TSEF(opt.)	9.35	13.17	2.47	33.56	12.14	5.14
DENR(init.)	21.73	29.78	3.79	58.69	27.37	11.75
TSEF(init.)	25.85	35.44	3.49	90.59	31.65	15.99

- ^a D_i , min and D_i , max are the minimum and maximum values of D_i on the structure set.
- ^b μ and σ are the parameters of Gaussians approximating distribution of D_i on the structure set.
- ^cSeven boron containing structures were excluded since the parameters are lacking.

Analysis of the Tables 1 and 2 and Fig. 3 suggests the following important observations. First, even charge schemes based on direct fit of charges to QC MEP for each structure separately (such as MK-ESP and RESP) produce rather substantial errors, which evidently set the lower limits achievable via approximation of the MEP with the point charge potential. Second, application of topological constraints on charge values in the least squares procedure of RESP method results in only negligible deterioration of the overall potential reproduction compared to results due to unconstrained MK-ESP fit charges. Third, Mulliken population analysis charges generally give the error three times as much as the direct fit methods give, despite the use of the same optimal wave function. Fourth, the empirical bond charge increment based schemes (AM1-BCC and MMFF94) produce errors twice as much as the direct fit ones, AM1-BCC performing noticeably better. Fifth, the proposed empirical charge schemes (TSEF and DENR), after their parameters had been optimized,

Table 2. Residual errors in the QC MEP reproduction [kJ/mol] on the test set of 30 structures, calculated with different point charges.

Charge scheme	AD_V	D_V	D_i, min	D_i, max	μ	σ
MK-ESP	3.65	5.88	1.26	12.50	5.33	2.50
RESP	4.11	6.40	1.34	12.95	5.86	2.58
AM1-BCC	7.60	10.92	3.38	36.96	10.01	4.37
MMFF94	9.45	13.02	3.55	36.18	12.14	4.72
Mulliken PA	13.97	19.51	1.84	42.06	17.77	8.08
DENR(opt.)	7.81	10.95	1.57	30.94	10.21	3.97
TSEF(opt.)	9.35	13.17	2.47	33.56	12.14	5.14
DENR(init.)	21.73	29.78	3.79	58.69	27.37	11.75
TSEF(init.)	25.85	35.44	3.49	90.59	31.65	15.99

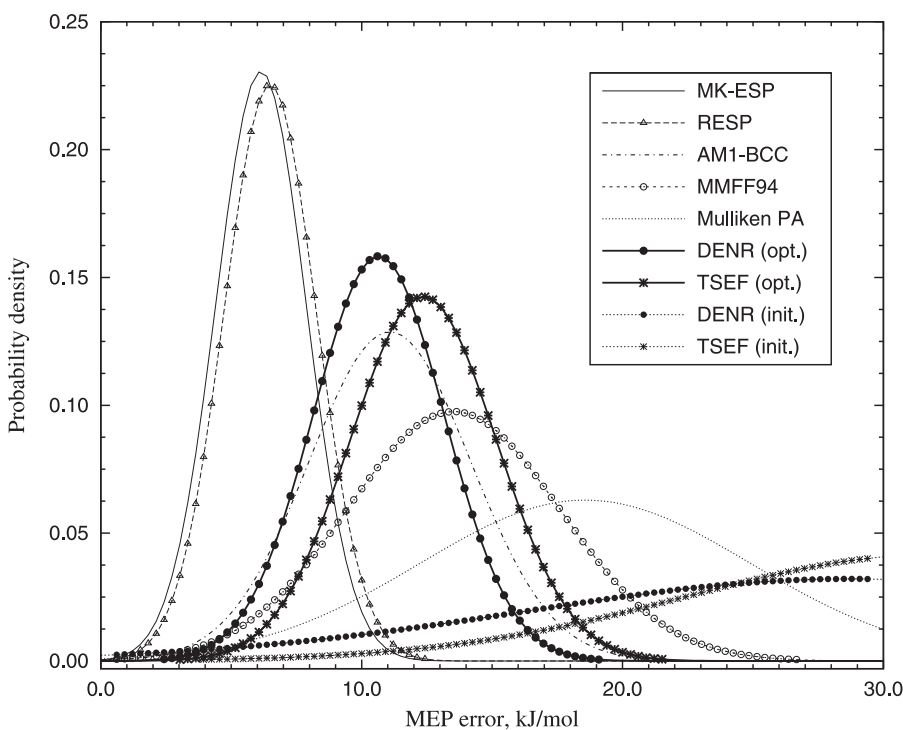


Figure 3. Gaussian approximations of D_i distributions on the test set calculated with charges of different schemes.

perform comparably to the BCI schemes (AM1-BCC, MMFF94), the DENR scheme being comparable to much more computation demanding AM1-BCC scheme, which requires providing a geometry to conduct its semi empirical optimization by means of AM1 to get initial charge values (subsequently corrected by the BCI's). Note, that AM1-BCC charges are not topologically symmetric. Sixth, characteristic features of the MEP reproduction er-

rors by DENR and TSEF did not change in going from the training to test sets indicating that the robust and transferable parameters of atomic EN and hardness had been obtained for both models.

It should be noted that the proposed charge schemes due to clarity of the assumptions are extensible and scalable (admitting theoretical and numerical complexity level tuning) and not requiring 3D structure geometry. The number of required empirical parameters (EN and hardness) scales as N versus N^2 for the BCI based schemes. The most tedious stage in both TSEF and DENR schemes is matrix inversion, which is very fast (split second) for small and medium size molecules. Application to large systems (e.g. proteins, polysaccharides) may require changing direct matrix inversion algorithms adopted for this study in favor of iterative ones, which should in full take advantage of sparse, diagonal predominant nature of the matrices emerged.

5. Conclusions

The two novel approaches to constructing fast empirical charge schemes based on Dynamic Electronegativity Relaxation (DENR) and complete EN equalization with Topologically Symmetric Energy Function (TSEF) have been presented. Both possess qualities required for successful application in molecular modeling: (1) they are fast, simple and scalable, (2) the charges produced depend on chemical environment and (3) are topologically symmetric, (4) no molecular geometry is required on input, (5) the parameters (EN and hardness) can be optimized to reduce a simultaneous error in the MEP reproduction on a set of structures and subsequently used on arbitrary structures comprised of atomic types, for which the optimal parameters had been obtained. We believe that dynamic EN relaxation as a special case of incomplete EN equalization provides a sound and promising framework for describing molecular charge distribution suitable for fast and robust estimation of molecular electrostatics.

Acknowledgements

The authors are thankful to Bezrukov D.S. for helpful discussions on the manuscript and Russian Foundation for Basic Research for partial financial support.

References

- [1] A.D. Mackerell, *Journal of Computational Chemistry*, **24** (2004), 1584.
- [2] P. Politzer, J.S. Murray, *Theoretical Chemistry Accounts: Theory, Computation, and Modeling*, **108** (2002), 134.
- [3] B. Hernandes, F. Luque, M. Orozco, *Journal of Computer-Aided Molecular Design*, **14** (2000), 329.
- [4] J.W. Ponder, D. Case, *Advances in Protein Chemistry*, **66** (2003), 27.

- [5] J. Wang, R.M. Wolf, J.W. Caldwell, P.A. Kollman, D.A. Case, *Journal of Computational Chemistry*, **25** (2004), 1157.
- [6] T.A. Halgren, *Journal of Computational Chemistry*, **20** (1999), 730.
- [7] T.A. Halgren, *Journal of Computational Chemistry*, **17** (1996), 520.
- [8] A.D. MacKerell, D. Bashford, A. Bellott, R.L. Dunbrack, J.D. Evanseck, M.J. Field, S. Fischer, J. Gao, H. Guo, S. Ha, et al., *The Journal of Physical Chemistry B*, **102** (1998), 3586.
- [9] A.D. MacKerell, N. Banavali, N. Foloppe, *Biopolymers*, **56** (2000), 257.
- [10] L.D. Schuler, X. Daura, W.F. van Gunsteren, *Journal of Computational Chemistry*, **22** (2001), 1205.
- [11] O. Chris, A. Villa, A.E. Mark, W.F. van Gunsteren, *Journal of Computational Chemistry*, **25** (2004), 1656.
- [12] C.U. Singh, P.A. Kollman, *Journal of Computational Chemistry*, **5** (1984), 129.
- [13] B.H. Besler, K.M. Merz, P.A. Kollman, *Journal of Computational Chemistry*, **11** (1990), 431.
- [14] C.I. Bayly, P. Cieplak, W.D. Cornell, P.A. Kollman, *Journal of Physical Chemistry*, **97** (1993), 10269.
- [15] W.D. Cornell, P. Cieplak, C.I. Bayly, P.A. Kollmann, *Journal of the American Chemical Society*, **115** (1993), 9620.
- [16] W. Kohn, A.D. Becke, R.G. Parr, *The Journal of Physical Chemistry*, **100** (1996), 12974.
- [17] P. Geerlings, F. DeProft, W. Langenaeker, *Chemical Reviews*, **103** (2003), 1793.
- [18] J. Morales, T.J. Martinez, *The Journal of Physical Chemistry A*, **105** (2001), 2842.
- [19] A.A. Oliferenko, S.A. Pisarev, V.A. Palyulin, N.S. Zefirov, *Advances in Quantum Chemistry*, **51** (2006), 139.
- [20] F. DeProft, W. Langenaeker, P. Geerlings, *Journal of Molecular Structure: THEOCHEM*, **339** (1995), 45.
- [21] W.J. Mortier, S.K. Ghosh, S. Shankar, *Journal of the American Chemical Society*, **108** (1986), 4315.
- [22] G.L. Warren, J.E. Davis, S. Patel, *The Journal of Chemical Physics*, **128** (2008), 144110.
- [23] A.K. Rappe, W.A. Goddard, *The Journal of Physical Chemistry*, **95** (1991), 3358.

-
- [24] A. Jakalian, D.B. Jack, C.I. Bayly, *Journal of Computational Chemistry*, **23** (2002), 1623.
 - [25] J. Gasteiger, M. Marsili, *Tetrahedron*, **36** (1980), 3219.
 - [26] D.A. Shulga, A.A. Oliferenko, S.A. Pisarev, V.A. Palyulin, N.S.Zefirov, *SAR and QSAR in Environmental Research*, **19** (2008), 153.
 - [27] R. Merris, *Linear Algebra and its Applications*, **278** (1998), 221.
 - [28] W.H. Press, B.P. Flannery, S.A. Teukolsky, W.T. Vetterling, *Numerical Recipes in C: The Art of Scientific Computing*, Cambridge University Press, (1992), 2nd edition.
 - [29] A. Granovsky, *PC GAMESS version 7.0*, (2006),
<http://classic.chem.msu.su/gran/gamess/index.html>.
 - [30] S. Kirkpatrick, C.D. Gelatt, M.P. Vecchi, *Science*, **220** (1983), 671.
 - [31] J.A. Nelder, R. Mead, *The Computer Journal*, **7** (1965), 308.

INDEX

A

accelerator, 14, 15, 40
acid, 68, 224
activation energy, 69
adhesion, x, 54, 55, 56, 159, 160, 162, 163, 164, 165, 166, 167, 168, 169, 306
adhesion force, 165, 166
adhesion properties, 56
adhesive properties, 69
adsorption, 59, 72, 73, 78
aerosols, 266, 267, 268, 276, 278, 281, 283, 290, 295, 300, 301, 303, 304, 305, 306
ageing, 64, 78
air quality, 286, 290
Albania, 259, 274, 294, 302, 306
alcohol, 54, 59, 61, 62, 64
algorithm, 94, 96, 102, 196, 197, 198, 210, 211, 302, 319
amphibia, 255
amplitude, 62, 213
antibody, 228
anticancer drug, 230
antitumor, 254, 257
applied research, 54, 78
arithmetic, 200
ash, 267
assessment, 306
assumptions, 61, 231, 241, 243, 244, 295, 314, 322
asymmetry, 229, 231
atmospheric pressure, xi, 55, 65, 67, 259, 272, 288, 289, 290, 299, 300, 301
atoms, 58, 285, 310, 311, 312, 313, 314, 315, 318, 319
ATP, 232
attachment, xi, 259, 262, 263, 280, 281, 290, 295, 296, 298, 301, 304

B

background, 286, 305
bacteria, 256
basal cell carcinoma, 252

batteries, 263, 271
beams, 64, 69, 74, 75, 78
behavior, ix, 66, 83, 84, 95, 99, 105, 258, 268, 304
Beijing, 304
biochemistry, 227
biological processes, 230
biomedical applications, 243
biotechnology, 227, 256
blood, 254
Boltzmann distribution, 106
bonding, 69, 104, 156
bonds, 62, 312, 313, 314, 317
boreal forest, 302, 303, 304
boundary value problem, 189, 243, 246
bounds, 123
brachytherapy, 257
breakdown, 65, 68, 126, 128, 129, 130, 134, 136, 151, 224, 228, 229, 230, 231, 251, 255
broadband, 158
Bulgaria, 53, 80

C

campaigns, xi, 259, 268, 273, 287, 300
Canada, 299
cancer, 227, 252, 254, 256, 286
capillary, 166
carbon, 305
carrier, 19, 30, 31, 32, 33, 34, 35, 36, 37, 38, 39, 40, 41, 42, 43, 44, 45, 258
cast, 91
casting, 74
cell, ix, x, 11, 16, 19, 26, 33, 42, 46, 47, 83, 105, 121, 165, 223, 224, 225, 226, 227, 228, 229, 230, 231, 232, 235, 236, 239, 240, 243, 244, 245, 246, 247, 250, 251, 252, 253, 254, 256, 257, 258
cell death, 226
cell line, 227, 253
cell membranes, 226, 229, 254, 256, 258
cell surface, 228
cellulose, 162, 163, 165
certification, 271
chain molecules, 224

- channels, 224, 225, 271, 291
 charge density, x, 33, 39, 46, 48, 56, 69, 88, 94, 95,
 97, 171, 173, 174, 175, 179, 311
 cheese, 160, 162, 163, 168
 chemical bonds, 312, 314
 chemical properties, 56, 281, 314
 chemical structures, 74
 chemotherapy, 227
 China, 83, 304
 clarity, 46, 322
 classes, 291
 classification, 263
 clean air, 290
 cleaning, 160, 271
 climate change, 302
 cloning, 228
 closure, 100
 clusters, 233, 304, 305
 CO₂, viii, 32, 54, 69, 70, 71, 72, 73, 78, 306
 coagulation, 106, 303
 cocoa, 162, 163, 165
 cohesion, 165, 169
 cohesiveness, 166, 169
 collisions, 106
 column vectors, 174
 combustion, 272
 community, xi, 259
 compensation, 55, 56
 complementarity, 309
 complexity, 322
 components, viii, x, 95, 102, 112, 136, 144, 152, 154,
 171, 172, 178, 179, 180, 182, 186, 190, 191, 193,
 194, 195, 199, 200, 204, 209, 213, 219, 249, 260,
 292, 295, 315
 composition, 56, 74, 224, 281
 compounds, 232
 computation, 110, 211, 321
 computational fluid dynamics, 84
 computer technology, 99
 computing, 186
 concentrates, 50
 concentration, xi, 50, 51, 84, 99, 105, 106, 107, 152,
 230, 231, 239, 240, 259, 261, 262, 263, 266, 268,
 274, 275, 276, 281, 282, 283, 284, 285, 286, 287,
 288, 289, 290, 291, 293, 294, 295, 296, 297, 298,
 299, 300, 301, 303, 304, 306
 conception, 40, 41
 concrete, viii, 2, 30, 34, 36, 39, 45
 condensation, 269, 270, 304
 conductance, 232, 253
 conductivity, 226, 228, 231, 243, 247, 249, 257, 261
 conductor, viii, viii, 1, 2, 3, 4, 5, 6, 7, 8, 9, 10, 11, 12,
 14, 15, 16, 18, 19, 22, 25, 26, 27, 29, 30, 33, 45,
 46, 48, 49, 50, 51, 52, 175, 179, 185
 conductors, viii, 1, 9, 10, 14, 26, 27, 28, 29, 45, 183
 confidence, 66, 67, 68, 72
 confidence interval, 67, 68, 72
 configuration, viii, 53, 64, 86, 137, 138, 139, 140,
 305
 conflict, 89
 conjugation, 193
 consensus, 28
 conservation, 91, 92, 99, 217, 249, 314
 construction, 310
 consumers, ix, 159
 consumption, 73
 continuity, 86, 87, 91, 92, 99, 100, 110, 249
 contradiction, 61
 control, 59, 84, 90, 227, 251, 255, 303
 convergence, vii, ix, 1, 7, 83, 89, 96, 102, 112
 convergence criteria, 96, 102, 112
 conversion, 46, 269, 313
 copper, 11, 34, 37, 70
 corn, 162, 163
 corona discharge, viii, 36, 39, 53, 55, 56, 57, 58, 59,
 60, 63, 64, 65, 70, 72, 74, 75, 77, 95
 correlation, 58, 110, 111, 276, 291, 299, 300, 304,
 313
 correlation coefficient, 291, 299, 300
 correlation function, 110, 111
 correlations, xi, 99, 259, 299, 300, 301, 302
 corrosion, 54
 cosmic rays, 263, 294, 298, 306
 costs, 160, 168, 271
 coupling, 74, 84, 99, 146, 236
 CPU, 85
 critical value, 60
 crystalline, 54
 culture, 228
 cytoplasm, 230, 231
 cytotoxicity, 227
 Czech Republic, 299

D

- damping, 147
 data set, 198
 data transfer, 271
 database, 300
 decay, viii, xi, 53, 54, 58, 64, 65, 66, 67, 68, 69, 78,
 164, 165, 236, 259, 281, 283, 285, 286, 293, 294,
 295, 296, 297, 301, 315
 decisions, xi, 223, 300
 decomposition, 315
 decoupling, 156
 defects, 62, 232
 deficiency, 84, 290
 deficit, 230
 definition, 192, 195, 196, 201, 310, 312
 deformation, 64, 78
 degradation, 126, 128, 129, 137, 139
 delivery, x, 223, 228, 230, 252, 256, 257, 258
 dendritic cell, 255, 256
 density, ix, xi, 39, 54, 85, 86, 87, 88, 89, 90, 91, 92,
 93, 94, 95, 96, 97, 98, 100, 102, 105, 108, 159,
 162, 164, 165, 189, 212, 223, 229, 232, 239, 242,
 243, 259, 261, 269, 286, 311, 318

- density functional theory, 311
 dependent variable, 90
 deposition, 58, 161, 165, 291, 296, 306
 derivatives, 196, 315, 319
 desorption, 58, 59, 65, 67, 72, 73, 78, 80
 detection, 271, 287
 deviation, 167, 319
 DFT, 311
 dielectric constant, 106, 191, 226
 dielectric permittivity, 230, 247, 248
 dielectric strength, 162
 differential equations, 85, 90, 102, 105, 239, 249
 differentiation, 194, 196
 diffraction, viii, 53, 54, 59, 60, 73, 74, 77, 78, 189, 190
 diffusion, 67, 90, 91, 92, 100, 106, 110, 120, 129, 130, 131, 132, 133, 134, 136, 150, 239, 243, 255, 291, 296
 diffusion region, 134
 diffusivity, 105
 diodes, 125, 126, 131, 133, 134, 136, 137, 139, 140, 148, 149, 154, 156
 discharges, 260, 263
 discretization, 91, 94
 discs, 35, 36, 38, 39
 dispersion, 160
 displacement, 217, 244
 distilled water, 54, 58
 distribution, x, 17, 18, 28, 29, 30, 55, 59, 61, 62, 63, 64, 68, 69, 78, 84, 86, 87, 96, 97, 102, 109, 111, 119, 171, 172, 173, 181, 182, 186, 187, 189, 190, 192, 193, 194, 196, 198, 199, 200, 202, 205, 208, 209, 210, 211, 212, 216, 217, 257, 264, 265, 286, 293, 294, 295, 296, 298, 301, 303, 304, 305, 314, 320
 division, 195, 199, 209
 DNA, 227, 228, 229, 230, 243, 257, 286
 dogs, 258
 dominance, 312
 doping, 129
 drawing, 38, 42, 46
 drug delivery, 228, 255
 drug resistance, 251
 drug use, 230
 drugs, x, 223, 227, 228, 229
 dumping, 314, 317, 318
 duration, 228
 dust storms, 263
 dynamic viscosity, 100, 296
- E**
- earth, viii, 2
 ecology, 268
 electric charge, vii, viii, 53, 54, 61, 73, 77, 84, 189, 195, 203, 225, 246, 260, 261, 263, 281, 290, 295, 296, 300, 304
 electric conductivity, 224, 261, 302
- electric current, 239, 255, 262
 electrical breakdown, 251, 252, 255, 256
 electrical conductivity, 261, 286
 electrical properties, 301
 electricity, viii, xi, 1, 260, 288, 300, 302, 303, 304
 electrodes, 3, 6, 10, 11, 12, 14, 15, 21, 22, 26, 32, 33, 34, 35, 36, 38, 40, 46, 55, 84, 86, 260
 electrolyte, 230
 electromagnetic, 191, 204
 electromagnetic waves, 191
 electron, 33, 229, 232, 251
 electron microscopy, 229, 251
 electrons, 29, 31, 84
 electroporation, x, xi, 223, 226, 227, 228, 229, 230, 231, 232, 233, 235, 238, 239, 243, 251, 252, 253, 254, 255, 256, 257, 258
 embryo, 252
 emission, 285, 287
 encapsulation, 228
 energy, viii, xi, 2, 31, 32, 34, 38, 39, 45, 53, 54, 69, 70, 71, 72, 73, 78, 100, 101, 102, 107, 111, 112, 217, 223, 224, 232, 233, 234, 235, 236, 237, 238, 241, 242, 253, 304, 306, 309, 310, 311, 312, 313, 314, 315, 316, 317, 318
 England, 169, 252
 environment, 235, 309, 311, 312, 314, 315, 318, 322
 enzymes, 257
 EPA, 286, 294
 equality, 314
 equilibrium, 106, 230, 239
 erythrocyte membranes, 232
 erythrocytes, 253, 256
 Estonia, 303, 305
 etching, 34, 36, 37, 39
 ethanol, 62
 ethylene, 54
 eukaryotic cell, 229
 Europe, 305
 European Community, 299
 European Union, 286
 evening, 276, 291, 292
 evolution, 229, 232, 238, 252, 254, 257, 314, 315
 excision, 257
 excitation, 56, 179, 190, 203, 212
 exposure, viii, 54, 73, 74, 75, 76, 77, 286, 306

F

- fabrication, 69, 150, 154
 failure, 206
 fatty acids, 224
 FFT, 194, 195, 197, 198, 199, 206, 210, 211
 fibroblasts, 254
 film thickness, 59
 films, viii, 53, 54, 56, 58, 59, 60, 61, 62, 65, 66, 67, 68, 69, 70, 72, 73, 74, 77, 78
 financial support, 322
 Finland, 299, 304, 305, 306

flexibility, x, 189, 190, 212
 floating, 12, 25, 46
 flour, 162, 163, 165
 flow field, 85, 86, 91, 95, 99, 103, 104, 105, 106, 109, 110, 120, 122
 fluctuations, 233, 236, 279
 fluid, ix, 83, 84, 90, 91, 99, 100, 101, 103, 104, 107, 108, 109, 110, 111, 112, 120, 121, 122, 243, 244, 245
 fluorescence, 256
 foils, 37
 food, vii, ix, x, 159, 160, 161, 162, 164, 165, 166, 168, 169, 243
 food additives, 168
 food industry, ix, 159, 160, 161
 food production, x, 168
 food products, x, 159, 160
 freedom, 200
 freezing, 36, 229, 232
 frequency distribution, 293
 friction, 39
 fusion, 228, 229, 255, 256, 258

G

gases, 266
 gene, 227, 229, 251, 254, 256, 257
 gene therapy, 227, 251, 254
 gene transfer, 254
 generation, 101, 190, 212, 298, 311, 312
 genes, x, 223, 251
 genetic disease, 228
 Germany, 299
 glucose, 168
 glycine, 232
 glycol, 253
 government, 84
 GPS, 156
 granules, 256
 graph, 26, 238, 312, 315, 316
 gratings, 73, 74, 75
 gravitational force, ix, 83, 108, 113, 120, 121, 162, 296
 gravity, 13, 17, 25, 100, 162, 163
 Greece, 306
 grids, 180
 grounding, 34
 groups, xi, 56, 57, 58, 60, 61, 62, 65, 66, 68, 72, 73, 75, 113, 121, 205, 229, 235, 237, 259, 263, 318, 319
 growth, 122, 200, 236, 304, 306
 guidelines, 156

H

hardness, 155, 311, 312, 314, 316, 317, 318, 319, 320, 322

health, 84, 160, 286, 298, 303
 heat, 129
 heating, 64, 78
 height, xi, 12, 16, 25, 33, 42, 259, 263, 281, 283, 284, 285, 293, 295, 297, 298, 299
 hematopoietic stem cells, 251
 Hong Kong, 155
 hospitals, 290, 301
 host, x, 223, 229
 human activity, 276
 humidity, viii, xi, 53, 55, 64, 165, 170, 259, 269, 270, 271, 272, 287, 288, 289, 290, 299, 300, 301
 hybrid, 228
 hybrid cell, 228
 hybridoma, 228
 hypothesis, 2, 6, 7, 15, 232
 hysteresis, 255

I

ideal, 3, 35, 137, 138, 141, 142
 identity, 201, 202, 214, 219
 image, vii, 1, 2, 15, 16, 17, 18, 37
 immersion, 310
 implementation, 111, 311, 314, 317
 in vitro, x, 223, 227
 in vivo, x, 223, 227, 230, 254, 257
 incidence, 59, 62
 inclusion, x, 122, 189, 190, 208
 independence, 198
 India, 171, 186, 305
 indication, 64
 indices, 206, 207
 induction, 19, 22, 29, 32, 33, 34, 36, 39, 161, 189, 191, 206, 207
 inductor, 137, 138, 139, 140, 141, 142, 143, 144, 145, 146, 148, 157
 industry, vii, 159
 inertia, 105, 120, 161
 infinite, 32, 139, 190, 201, 204, 207
 inhibitor, 168
 insertion, 228
 instruments, 268
 integrated circuits, 155, 156, 157
 integration, ix, 109, 125, 174, 195, 197, 198, 199, 202, 209, 214, 215, 315, 316, 317
 interaction, xi, 69, 72, 78, 99, 175, 190, 212, 226, 243, 259, 268, 281, 294, 295, 300, 301, 310, 312
 interactions, ix, 72, 83, 85, 103, 226, 228, 235, 236, 237, 241, 280, 309
 interface, 60, 92, 93, 95, 238, 271
 interference, 36, 59, 73
 interval, xi, 4, 8, 17, 18, 29, 34, 48, 110, 202, 210, 259, 260, 269, 278, 288, 291, 293, 300, 301
 intervention, 310
 inversion, 181, 316, 322
 ion channels, 251
 ion transport, 224

ionization, 95, 161, 162, 261, 303
ions, xi, 31, 36, 58, 64, 65, 72, 84, 85, 86, 96, 99, 106, 225, 226, 230, 231, 232, 233, 241, 243, 252, 259, 260, 261, 262, 263, 264, 266, 268, 269, 273, 274, 280, 281, 282, 283, 284, 285, 288, 289, 290, 291, 295, 296, 297, 298, 300, 301, 302, 303, 304, 305, 317
Ireland, 299
irradiation, viii, 53, 62, 64, 70, 71, 72, 73, 78
isolation, 131, 141, 150, 252
Israel, 299
iteration, 96, 113, 316, 317

J

Japan, 1, 52, 269, 303
Jordan, 255, 256, 258

K

K^+ , 96, 225, 230
kinetics, 73, 84

L

laminar, 84
land, 160, 162, 166
laser radiation, 69, 70, 71, 72, 78
lasers, viii, 54, 59, 70, 73, 78, 208
laws, 99
leakage, 137, 139, 146, 154
Leaks, 256
Least squares, 319
liberation, 68
lifetime, 32, 69, 232, 255, 298
line, 3, 12, 31, 36, 37, 38, 41, 46, 50, 56, 129, 144, 149, 183, 185, 199, 206, 210, 211, 212, 217, 234, 235, 237, 290
links, 244
lipids, 224, 233
liposomes, 229
Lithuania, 299
living environment, xi, 259, 268
lymphocytes, 256
lysis, 228

M

machinery, 290
macromolecules, x, 223, 229, 232, 258
magnetic effect, 86
magnetic field, 100
malignant melanoma, 257
manufacturing, vii, 30, 36, 39, 243
marrow, 251

mathematics, 80
matrix, x, 96, 102, 171, 172, 174, 175, 181, 182, 198, 199, 200, 311, 312, 314, 315, 316, 319, 322

Maxwell equations, 86
measurement, xi, 59, 70, 172, 259, 268, 269, 273, 274, 276, 278, 279, 280, 281, 282, 283, 285, 286, 287, 288, 289, 290, 291, 293, 298, 299, 300, 301, 304

measures, 290
media, viii, 54, 64, 73, 74, 77, 205, 212, 214, 215, 310

median, 104, 293

membrane permeability, 232

membranes, 223, 224, 226, 228, 229, 230, 251, 252, 255, 256

memory, 269, 273

memory capacity, 269

men, 306

metabolites, 229

mice, 227, 254, 257

micrometer, 74

microscope, 229

microscopy, 232

microstructures, 69

migration, 64, 86

mining, 243

Ministry of Education, 83

missions, 306

MMA, 74

mobility, 86, 96, 261, 263, 264, 269, 271, 296, 303, 305

model, ix, 83, 84, 85, 99, 100, 106, 109, 110, 111, 121, 122, 123, 144, 145, 171, 236, 239, 243, 245, 249, 253, 254, 257, 258, 268, 269, 270, 271, 295, 319

modeling, 84, 87, 122, 168, 186, 190, 305, 309, 310, 315, 322

models, 65, 99, 212, 233, 239, 243, 310, 322

modules, 85

moisture, 39

mold, 168

molecular biology, 227, 229

molecules, x, 84, 99, 106, 223, 224, 228, 229, 230, 232, 233, 257, 261, 285, 309, 310, 312, 318, 322

momentum, 84, 99, 100, 105, 107

Montenegro, 286

Moon, 220

morphology, 68

motion, ix, 83, 85, 86, 90, 92, 99, 100, 105, 106, 109, 112, 113, 121, 123, 214, 226

mountains, 287, 290, 291, 292

movement, ix, 83, 107, 113, 120, 226, 229

multiplication, 194, 195, 206, 209

multiplier, 311

N

NaCl, 165, 168

nanometer, 305
 nerve, 225
 Netherlands, 305
 network, 128, 138, 144, 146, 147, 314
 neuroblastoma, 255
 New Zealand, 223
 nitrogen, 56
 nodes, 95, 101, 102, 133, 155
 noise, 74, 126, 127, 128
 Norway, 299
 nucleation, 263, 301, 303, 304, 305
 nuclei, 304
 numerical analysis, 192, 193, 206

O

observations, 315, 320
 oil, 166
 one dimension, 88, 239
 optical properties, 59, 303
 optimization, 156, 310, 312, 318, 319, 321
 optoelectronics, 54, 55
 orbit, 306
 order, ix, 4, 58, 59, 61, 62, 64, 67, 75, 77, 78, 84, 86, 90, 95, 96, 103, 113, 120, 129, 131, 137, 159, 190, 196, 197, 199, 200, 202, 205, 212, 215, 216, 217, 230, 233, 239, 276, 280, 286, 287, 289, 295, 296, 315, 318
 orientation, 231, 263
 osmotic pressure, 231
 outliers, 319
 ownership, 271
 oxidation, 39
 oxygen, viii, 53, 58, 59, 62, 72, 73, 78

P

PAN, 220
 parameter, 67, 75, 103, 250, 261, 285, 312, 317, 319
 parameters, xi, 56, 59, 67, 152, 168, 223, 230, 232, 235, 236, 237, 243, 251, 257, 259, 261, 263, 268, 272, 286, 287, 288, 289, 293, 294, 296, 297, 299, 300, 301, 310, 312, 318, 319, 320, 322
 partial differential equations, 87, 91
 particle nucleation, 303
 particles, viii, ix, xi, 53, 59, 64, 72, 73, 83, 84, 85, 105, 106, 107, 112, 113, 115, 120, 121, 123, 159, 160, 161, 162, 163, 165, 166, 226, 229, 243, 253, 259, 260, 262, 263, 264, 266, 268, 277, 280, 281, 286, 287, 290, 291, 292, 293, 294, 295, 300, 301, 302, 303, 304, 305, 306
 passive, 250
 periodicity, x, 189, 205, 208
 permeability, x, 223, 228, 229, 231, 232
 permeation, 254
 permittivity, 2, 15, 48, 49, 56, 86, 172, 243, 245, 246, 247
 PET, 54, 58, 65, 66, 67, 68, 69
 phenol, 74
 phospholipids, 224
 phosphorus, 224
 photographs, 22
 photons, 70, 71
 physical properties, 161, 162, 318
 physics, 52, 208, 260
 pitch, 38, 199, 200
 plants, x, 84, 223
 plasma, 56, 228, 229, 230, 305
 plasma membrane, 229, 230
 plasmid, 257
 Poisson equation, 87, 91
 Poland, 189, 299
 polarity, 55, 57, 58, 60, 61, 62, 64, 66, 67, 70, 72, 84, 90, 230, 266, 280, 290, 291, 295, 300
 polarizability, viii, 54, 61, 73, 74, 77, 78, 226
 polarization, 62, 226, 245, 310, 314
 pollutants, 84
 pollution, 84, 290, 304
 polycarbonate, 11, 36, 37
 polymer, viii, 52, 53, 54, 55, 56, 58, 59, 64, 69, 74, 77, 78, 79
 polymer films, viii, 53, 54, 55, 59, 64, 69, 78
 polymer structure, 74
 polymerization, 74
 polymers, viii, 53, 54, 55, 58, 69, 74, 75, 78, 79
 polypropylene, viii, 53, 54, 56, 59, 60, 62, 69, 70
 poor, x, 153, 161, 165, 223
 population, 232, 238, 274, 283, 320
 population density, 238
 positive correlation, 300
 potassium, 225
 potato, 160, 163, 166, 167, 168, 169
 power, 11, 12, 14, 31, 38, 39, 40, 52, 70, 73, 76, 126, 127, 128, 197, 219, 251, 264, 269, 273
 precipitation, 121, 122, 291, 296, 297
 prediction, 30, 168, 172, 236
 preference, 169
 pressure, viii, ix, 53, 56, 58, 64, 65, 66, 67, 68, 69, 78, 83, 86, 90, 94, 100, 102, 108, 109, 113, 120, 121, 212, 213, 215, 216, 217, 231, 271, 272, 287, 300
 prevention, 150
 probability, 109, 112, 232, 233
 probability distribution, 112
 probe, 96
 production, viii, ix, 45, 53, 54, 68, 74, 125, 159, 171, 228, 252, 262, 281, 285, 286, 288, 294, 295, 296, 297, 298, 300, 301, 304
 production technology, 74
 program, 3, 6, 11, 182, 186
 proportionality, 300
 proteins, 224, 225, 232, 252, 322
 PTFE, 54, 56, 58, 65, 66, 67, 68
 pulse, x, 173, 223, 226, 229, 230, 232, 233
 pumps, 225
 PVP, 91

R

radiation, 69, 70, 72, 190, 191, 192, 194, 204, 206, 212, 214, 215, 216, 217, 221, 263, 266, 268, 281, 287, 288, 295, 304, 305
radical polymerization, 74
radio, 156, 157
radium, 285
radius, 6, 16, 19, 36, 48, 49, 50, 51, 94, 95, 96, 184, 228, 233, 234, 235, 236, 237, 238, 239, 243, 244, 246, 250, 296, 299
radon, 263, 285, 286, 287, 288, 290, 294, 296, 297, 298, 299, 300, 301, 306
range, 54, 55, 67, 74, 96, 164, 166, 199, 230, 234, 236, 239, 243, 269, 270, 293, 295, 296
raw materials, 243
reality, 41, 235, 245
reason, ix, 44, 59, 64, 77, 83, 266, 291, 313, 316
recombination, xi, 259, 262, 280, 281, 295, 301, 304
recovery, 31, 32, 33, 34, 36, 38, 254
redistribution, 226
reflection, 60
refractive index, 59, 60, 61, 62, 63, 64, 75, 77
region, 29, 66, 67, 87, 95, 99, 105, 129, 133, 136, 152, 161, 208, 209, 231, 247, 286, 298, 299, 306
relationship, 289, 291, 299, 311
relaxation, 58, 249, 250, 255, 310, 312, 314, 315, 317, 322
reliability, ix, 125, 131
relief, 68, 73, 74, 77
reproduction, 312, 318, 319, 320, 321, 322
residual error, 102
resistance, 39, 54, 128, 129, 130, 137, 146, 151, 229, 261, 262, 269, 302
resolution, 56, 60, 74, 229
resonator, 137, 138, 139, 141, 142, 143
resources, 105, 310, 316
respiratory, 84, 266, 286, 290
response time, 269
risk, 160, 272, 303
risk assessment, 272
RNA, 229
robustness, ix, 125, 126, 129, 130, 133, 137, 140, 143, 144, 149, 153, 154, 158
room temperature, viii, 53
root-mean-square, 319
roughness, 94, 166
routing, 133
rural areas, 294
Russia, 302, 309

S

salt, 160, 162, 163, 164, 165, 263, 266, 267, 283, 290
satellite, 286
saturation, 106
scaling, 150
scattering, 190, 191, 204, 205, 206, 207, 208, 212, 217
scientific computing, 220
semiconductor, 73
semiconductor lasers, 73
semiconductors, 73
sensitivity, viii, 54, 74, 77, 78, 217, 251, 303
separation, 104, 105, 121, 252
serotonin, 266
shape, vii, viii, 1, 2, 6, 7, 9, 10, 15, 19, 31, 40, 45, 46, 50, 70, 97, 105, 113, 162, 172, 190, 281
shear, 165
side effects, x, 223, 227
signs, 68
silicon, 129, 133, 136
silk, 11
simulation, vii, ix, 1, 3, 5, 6, 7, 9, 10, 11, 12, 14, 15, 16, 17, 18, 19, 24, 25, 26, 27, 28, 29, 30, 33, 34, 36, 39, 40, 42, 45, 46, 47, 48, 50, 52, 83, 84, 110, 121, 122, 164, 256
skeletal muscle, 230, 251
skin, 228, 230, 255, 257
smoke, 168, 290, 306
smokers, 298
smoking, 286
sodium, 168, 224, 225
soil, 169, 285, 298, 306
space, 35, 46, 47, 88, 94, 95, 97, 99, 129, 161, 171, 172, 174, 189, 191, 226, 229, 230, 236, 266, 290, 298, 300, 301, 310
Spain, 304
spatial frequency, 75, 77
species, 84, 239, 310, 311
specific gravity, 14
specific surface, 8, 62
spectrum, x, 57, 189, 190, 193, 195, 198, 199, 200, 210, 211, 215, 217, 220, 315
speed, xi, 36, 38, 39, 85, 155, 156, 157, 197, 259, 272, 287, 296, 299
stability, viii, 53, 54, 68, 258, 316, 317, 318
stabilization, 56
standard deviation, 66, 110, 264, 293, 298, 318, 320
standards, 80, 291, 292
starch, 162, 163
steel, 160
storage, viii, 54, 65, 68, 69, 73, 78, 224, 269
strategies, 154, 155
strength, 86, 89, 90, 92, 120, 190, 205, 212, 214, 232, 245, 252
stress, 140, 224
structural changes, 62, 64, 74, 232
subdomains, x, 171, 173, 175
subgroups, 319
substitution, 192, 215
substrates, 69, 74
sugar, 162, 163, 165, 167
summer, 274, 281, 283, 303
supply, 11, 12, 31, 39, 55, 62, 269
suppression, 105

surface area, 7, 9, 10, 47, 185
 surface layer, 68
 surface modification, viii, 53, 64, 78
 surface properties, 56
 surface structure, 191
 surface tension, 235, 236
 surfactant, 253
 suspensions, 256
 Sweden, 299, 302
 Switzerland, 299
 symmetry, ix, 83, 87, 101, 123, 239, 309, 310, 312, 314, 315
 synthesis, 74

T

Taiwan, 125
 tanks, 156
 targets, x, 159, 161, 162, 166
 temperature, xi, 54, 55, 56, 58, 68, 70, 72, 73, 75, 94, 239, 259, 266, 269, 270, 271, 272, 287, 288, 290, 299, 300, 301
 temperature dependence, 58
 tensile strength, 13
 tension, 235, 236, 238
 terminals, 133, 194
 thermal stability, 54
 threshold, 232, 291
 TIR, 60
 tissue, 230, 256
 topology, 312, 314
 total internal reflection, 60, 62
 tracking, 105, 107, 123
 traffic, 276, 283, 291, 292, 301
 training, 318, 319, 320, 322
 trajectory, 84, 109, 110, 113, 117, 119, 120, 121, 165
 transducer, 190, 195, 212
 transfection, 229
 transformation, x, 189, 190, 195, 200, 217
 transformations, 197
 transistor, ix, 125, 129, 130, 146, 152, 155, 156
 transition, 232
 transmission, x, 144, 148, 149, 150, 171, 172, 302
 transport, x, 84, 100, 105, 122, 168, 223, 224, 227, 228, 229, 230, 233, 258
 transportation, 14, 291
 tumor, 251, 255
 tumor cells, 251
 tumors, 227, 254, 258
 turbulence, ix, 83, 84, 85, 99, 100, 101, 105, 107, 111, 112, 120, 121, 122
 turbulent flows, 123

U

United Kingdom, 123, 299, 253, 303, 304, 305, 306
 universal gas constant, 239
 uranium, 285, 286
 urban areas, 278, 293, 306
 urban centers, 274, 290
 urban population, 306
 US Department of Commerce, 292

V

vaccine, 255
 vacuum, 39, 48, 49, 65, 68, 191
 valence, 239
 vapor, 70, 303
 variability, 290, 302
 variables, 6, 99, 111, 112, 201, 215, 280, 295, 304
 variance, 111
 vector, 87, 174, 198, 211, 212, 311, 315, 317, 319
 velocity, ix, 38, 39, 64, 83, 84, 86, 90, 99, 100, 101, 102, 103, 105, 106, 107, 108, 109, 110, 111, 112, 120, 164, 212, 213, 297
 vibration, 212
 viscosity, 90, 100
 visualization, 105, 122, 279
 vitamins, 266

W

wave number, 204, 212, 215, 216
 wavelengths, 59, 70
 wealth, 315
 wheat, 165
 wind, viii, ix, xi, 2, 40, 64, 83, 84, 85, 99, 103, 104, 120, 121, 259, 272, 279, 292, 296
 wires, 84, 94, 97, 99, 102, 104, 113, 120
 women, 306
 wood, 273

X

XPS, viii, 53, 56, 57, 58, 73